

Dissertation
submitted to the
Combined Faculties of the Natural Sciences and Mathematics
of the Ruperto-Carola-University of Heidelberg. Germany
for the degree of
Doctor of Natural Sciences

Put forward by
GUSTAVO ENRIQUE MEDINA TOLEDO
born in Santiago, Chile

Oral examination: November 3rd, 2022

UNVEILING THE MILKY WAY'S HISTORY USING
YOUNG & OLD POPULATION VARIABLE STARS

REFEREES: PROF. DR. EVA K. GREBEL

PRIV.-DOZ. DR. SABINE REFFERT

Abstract

This dissertation focuses on classical Cepheids and RR Lyrae stars as tracers of the recent star formation and the early assembly of the Milky Way, respectively.

I use data from the *Gaia* spacecraft to search for classical Cepheids in Galactic open clusters. I confirm (reject) several Cepheid-cluster associations considered in previous studies as bona-fide and identify new potential cluster Cepheid candidates. I also study the feasibility of using young cluster ages as tests of the Cepheid period-age relation, and conclude that their usage still faces difficulties due to their sparsely populated red giant branches, their stochastically sampled main-sequence turn-offs, and their quick dissolution.

I combine publicly available and proprietary data to study outer halo RR Lyrae stars, in the context of the Halo Outskirts with Variable Stars (HOWVAST) survey. Using Dark Energy Camera data, I search for distant halo RR Lyrae stars and detect ~ 500 candidates, $\sim 25\%$ of which are not reported in the literature, and 11 of which are new discoveries beyond 100 kpc. I use their pulsation properties and radial distribution to investigate the role that the accretion of satellites play in the formation and shape of the halo. Finally, I derive atmospheric parameters, chemical abundances, and kinematics for a sample of distant halo RR Lyrae stars using Magellan Inamori Kyocera Echelle spectra. I speculate about their origin, looking for hints of their association with satellites and stellar streams, and conclude that the accretion of sub-haloes contributes significantly to building up the outer halo.

The results of this thesis confirm the pivotal role of variable stars as tools to unveil the Milky Way's evolution.

Zusammenfassung

Diese Dissertation konzentriert sich auf klassische Cepheiden und RR-Lyrae-Sterne als Indikatoren für kürzliche Sternentstehung respektive den frühen Aufbau der Milchstraße.

Ich benutze Daten des *Gaia* Satelliten, um nach klassischen Cepheiden in Galaktischen offenen Sternhaufen zu suchen. Ich bestätige (und verwerfe) mehrere Cepheiden-Haufen-Assoziationen, die in früheren Studien als echt angesehen wurden, und identifiziere neue potenzielle Cepheiden-Haufen-Kandidaten. Ich untersuche auch die Möglichkeit, das Alter junger Sternhaufen als Test für die Beziehung zwischen Periode und Alter der Cepheiden zu verwenden, und komme zu dem Schluss, dass ihre Verwendung aufgrund ihrer dünn besiedelten Roten-Riesen-Äste, der stochastischen besiedelten Hauptreihen-Abzweigungen und ihrer schnellen Auflösung immer noch mit Schwierigkeiten verbunden ist.

Ich kombiniere öffentlich verfügbare und proprietäre Daten, um äußere Halo-RR-Lyrae-Sterne im Rahmen des Halo Outskirts with Variable Stars (HOWVAST) surveys zu untersuchen. Mit den Daten der Dark Energy Camera suche ich nach entfernten Halo-RR-Lyrae-Sternen und identifiziere ~ 500 Kandidaten, $\sim 25\%$ davon sind in der Literatur nicht beschrieben, und 11 davon sind Neuentdeckungen jenseits von 100 kpc. Ich verwende ihre Pulsationseigenschaften und radiale Verteilung, um die Rolle zu untersuchen, die die Akkretion von Satelliten bei der Bildung und Form des Halos spielt. Schließlich leite ich atmosphärische Parameter, chemische Zusammensetzungen und Kinematik für eine Stichprobe von entfernten Halo-RR-Lyrae-Sternen anhand von Magellan-Inamori-Kyocera-Echelle-Spektren ab. Ich spekuliere über ihren Ursprung, suche nach Hinweisen auf ihre Verbindung mit Satelliten und stellaren Strömen und komme zu dem Schluss, dass die Akkretion von Subhalos wesentlich zum Aufbau des äußeren Halos beiträgt.

Die Ergebnisse dieser Arbeit bestätigen die zentrale Rolle variabler Sterne als Werkzeuge zur Entschlüsselung der Entwicklung der Milchstraße.

Contents

LIST OF FIGURES	v
LIST OF TABLES	ix
1 Introduction	1
1.1 The Milky Way Galaxy	1
1.1.1 The Galaxy in a nutshell	2
1.2 Galactic archaeology: Stars as fossils of the Milky Way history	4
1.2.1 Chemodynamical tagging	5
Photometry	5
Spectroscopy	6
Astrometry	7
1.3 Cosmic nucleosynthesis	8
1.3.1 The first stars	10
1.3.2 Chemical enrichment via stellar evolution	10
1.3.3 The production of heavy elements	13
1.4 The disc and the halo of the Milky Way	14
1.4.1 The Galactic disc	14
1.4.2 The Galactic halo	16
1.5 Star clusters, dwarf galaxies, and streams as probes of stellar and Galactic evolution	19
1.5.1 Open clusters	21
1.5.2 Globular clusters	26
1.5.3 Dwarf galaxies	27
1.5.4 Streams	28
1.6 Variable stars	30
1.6.1 Classical Cepheids	35
Evolution	36
Classical Cepheids as standard candles	37
The period-age relation	40
On the importance of classical Cepheids for Galactic studies	41
1.6.2 RR Lyrae stars	42
Evolution	45
The Blazhko effect	45
RR Lyrae stars as standard candles	45
The Oosterhoff dichotomy	46

	On the importance of RR Lyrae stars for Galactic studies	48
1.7	This thesis	49
2	A study of Cepheids in open clusters and the Cepheid period-age relation in the <i>Gaia</i> era	53
2.1	Motivation	53
2.2	Cepheids and open clusters samples	55
2.2.1	Open clusters	55
2.2.2	Cepheids sample	57
2.3	Membership determination	57
2.3.1	On-sky selection and prior $P(A)$	58
2.3.2	The likelihood $P(B A)$	61
2.3.3	Differences with A13	62
2.4	The data	65
2.4.1	Parallaxes	65
2.4.2	Proper motions	65
2.4.3	Radial velocities	66
2.5	Membership determination: the outcome	67
2.5.1	A few bona fide combos from the literature	67
	The Cepheids around NGC 7790	67
	The Cepheids in NGC 6067	69
	GQ Vul and FSR 0158	69
2.5.2	Missed combos from the literature	70
2.5.3	Combos with high likelihood but low prior	72
2.5.4	Some combos of interest	72
	Clusters potentially hosting several Cepheids	72
	Gaia 5 and V0423 CMa	74
	Kronberger 84 and ASASSN-V J213533.70+533049.3	75
	UBC 130 and SV Vul	75
	UBC 229 and V0335 Pup	76
	LP 1937 and DF Cas	76
	UBC 106 and CM Sct	77
	UBC 290 and X Cru	77
2.6	Age determination of open clusters	77
2.6.1	Methodology	77
2.6.2	Results and comparison with previous studies	80
2.6.3	A critical view on cluster Cepheids to test period-age relations	82
2.6.4	Alternative methods for cluster age determination	87
2.6.5	The Cepheid period-age relation	88
2.7	Discussion and concluding remarks	89
3	RR Lyrae stars in the Halo Outskirts With Variable STars survey (HOWVAST)	93
3.1	Motivation	93
3.2	The data	96
3.2.1	Observations	96

3.2.2	Data processing	98
	Pre-processing	98
	Photometric calibration	98
3.3	Search and characterization of RR Lyrae stars	99
3.3.1	Selection of the RR Lyrae candidates	99
3.3.2	Distance determination	101
3.3.3	Classification and Bailey diagram	103
3.3.4	Comparison with previous surveys	105
3.4	RR Lyrae stars beyond 100 kpc	108
3.4.1	Main properties of the sample	108
3.4.2	Potential associations of distant RR Lyrae stars	110
3.5	Space density distribution	112
3.5.1	Radial density model	112
3.5.2	Number density profiles	113
3.6	Discussion and summary	117
4	Probing the Galactic outer halo using chemodynamics of RR Lyrae stars	121
4.1	Motivation	121
4.2	Sample selection and observations	123
4.2.1	Sample selection	123
4.2.2	Observation and data reduction	126
4.3	Spectral analysis	129
4.3.1	Radial velocities	129
4.3.2	Atmospheric parameters	130
Metallicities	131	
Effective temperatures	136	
Surface gravity - $\log g$	137	
Microturbulence - V_t	138	
4.3.3	Spectroscopic stellar parameters	138
4.3.4	Stellar parameters and uncertainties	140
4.3.5	Chemical abundances	144
4.3.6	Orbital analysis	145
4.4	Results	151
4.4.1	Chemical comparison	151
4.4.2	Kinematics	155
4.5	Discussion	156
4.5.1	J051424 and the LMC	157
4.5.2	J023001, Whiting 1, and Sagittarius	157
4.5.3	Association with known substructures	158
4.5.4	Streams and other associations	159
4.6	Summary and conclusions	165
5	Conclusions and future work	169
5.1	Summary and outlook	169
5.2	Future research directions	171
5.2.1	Cepheids and open clusters in the Milky Way and beyond	171

Contents

5.2.2	The Galactic outskirts: Pushing the boundaries with RR Lyrae stars	173
	A further exploration of the distant halo	173
	The hunt for ultra-faint dwarf galaxies and streams	175
5.3	Concluding remarks	176
Appendix A		178
A1	Complementary tables and figures	179
Appendix B		190
B1	Complementary material	191
Appendix C		206
C1	Additional spectral regions and line list	207
C2	Stellar parameters and chemodynamics of a subsample of our targets	212
	HD 76483	212
	J034239	212
	J023001	214
	HV205840	215
	J054653	216
Frequently used acronyms		218
List of publications		222
Bibliography		225
Acknowledgements		260

List of Figures

1.1	The Milky Way and its constituents	3
1.2	The story of our Universe in brief	9
1.3	Abundance of α -elements as a function of metallicity for disc stars	12
1.4	Velocity distribution of stars in the disc and the halo	15
1.5	Radial density of RR Lyrae in the halo from the DES	17
1.6	Relative fractions of structures in the halo	19
1.7	Absolute magnitude, physical size, and heliocentric distance comparison of resolved stellar systems	20
1.8	Open cluster disruption models as a function of time and star formation efficiency	22
1.9	Energy, angular momentum, and spatial distribution of stellar streams and globular clusters	29
1.10	Schematic of the Hertzsprung-Russel diagram and the instability strip	31
1.11	Example of a phased light curve from the OGLE survey	33
1.12	Comparison of different period detection methods for ab-type RR Lyrae stars	34
1.13	Post-main-sequence evolutionary tracks of intermediate mass stars	36
1.14	Period-luminosity relation of classical Cepheids and RR Lyrae stars in the MW	38
1.15	Theoretical period-age relation of Cepheids	41
1.16	Examples of RR Lyrae star light curves	43
1.17	Bailey diagram of RR Lyrae stars from the PS-1 survey	44
1.18	The Oosterhoff dichotomy	47
2.1	Spatial distribution of Cepheids and open clusters	56
2.2	Correlation of open cluster apparent radii r_1 and r_2	59
2.3	Comparison of proper motions, parallaxes, and radial velocities of cluster-Cepheid pairs with A13	63
2.4	<i>Gaia</i> -based astrometry and colour-magnitude diagrams for the combo Kronberger 84-ASASSN J213533.7	74
2.5	Same as Figure 2.4 but for the combo UBC 130-SV Vul	75
2.6	Same as Figure 2.4 but for the combo UBC 229-V0335 Pup	76
2.7	Colour-magnitude diagram of the cluster Ruprecht 100	80
2.8	Colour-magnitude diagrams of Collinder 394 and NGC 6067	81
2.9	Comparison between the $\log(t)$ from this work and previous studies, and residual dispersion in logarithmic scale	84

List of Figures

2.10	Colour-magnitude diagrams for a simulated cluster	86
2.11	The Cepheid period-age relation	89
3.1	Spatial distribution of the HiTS and the HOWVAST surveys	95
3.2	Significance test and periodogram of a source that passed the selection filters	100
3.3	Histogram of the mean magnitudes of the RRLs detected in this work	102
3.4	Spatial distribution of the RRL candidates detected in this work, colour-coded by their heliocentric distance	103
3.5	Bailey diagram of our full RRL sample	104
3.6	Folded light curves of our sample of RRLs with beyond 100 kpc	109
3.7	Binned RRL number density profiles of the individual regions studied in this work	113
3.8	Same as Figure 3.7 but the entire region studied in this work	114
3.9	Comparison between our best-fitting radial density profile parameters and those from other RRLs studies in the literature	116
4.1	Folded light curves of the RRLs used in our spectroscopic study	125
4.2	Signal-to-noise ratio of our target stars as a function of heliocentric distance, colour-coded by their phase of observation	126
4.3	Spectral region surrounding the H_α line for the stars observed during our second campaign	127
4.4	Spectral regions surrounding the Ca K, H_ϵ , and H_α lines for our radial velocity standard stars	128
4.5	Systemic velocity determination of one of our stars, based on Balmer and metallic lines	130
4.6	Iron abundance estimations from the ΔS method and different combinations of lines, for two stars in our sample	133
4.7	Empirical iron abundance estimations for the stars observed in our second observing campaign	134
4.8	Fourier decomposition of the light curves of two stars in our sample	135
4.9	Empirical effective temperature estimations for the stars observed in our sec- ond observing campaign	137
4.10	H_α and H_γ profiles of an RRL from our primary sample	139
4.11	Stellar parameters and uncertainties of the subsample of our program stars with higher resolution	141
4.12	Ba absorption line at 4554.03 Å for two of the program RRLs	144
4.13	Orbits of our RR Lyrae stars integrated for 3 Gyr forward and backward	147
4.14	Relative LTE abundance of α -elements as a function of iron abundance for our target stars	152
4.15	Same as Figure 4.14, but showing the abundance ratios of individual elements as a function of iron abundance	153
4.16	Abundance ratios of the n-capture process elements Sr and Ba of our stars	154
4.17	Total velocity as a function of Galactocentric distance and Toomre diagram for the stars in our sample and halo stars from APOGEE	156
4.18	Energy versus vertical angular momentum for the stars in our sample assuming a isolated and a perturbed potential	159

4.19	Positions and velocities of our sample in Galactic Cartesian coordinates . . .	160
4.20	Eccentricity of the integrated orbits of our RRLs as a function of their pericentric and apocentric distances	161
4.21	Footprint of 33 of the stream tracks in <i>galstreams</i> (Mateu, 2022) discussed in Section 4.5.4, in equatorial coordinates	162
4.22	Same as Figure 4.21, but with the stars and streams represented in Galactic coordinates	163
A1	<i>Gaia</i> -based astrometry and colour-magnitude diagrams for two of the combos described in Section 2.5.4	187
A2	Colour-magnitude diagrams of the clusters studied in Section 2.6	188
B1	Corner plot of the posterior probability distributions and MCMC chains for the radial density profile of our entire sample	192
B2	Same as Figure B1, but for HOWVAST 2017	193
B3	Same as Figure B1, but for HOWVAST 2018	194
B4	Spatial distribution of RRL candidates detected in the HOWVAST 2017 fields and the surveys used for completeness comparisons	195
B5	Same as Figure B4 but for the HOWVAST 2018A fields	196
B6	Same as Figure B4 but for the HOWVAST 2018B fields	197
C1	Spectral regions surrounding the Balmer lines for RRLs studied in this work	208
C2	Spectral regions containing metallic lines for RRLs studied in this work . . .	209
C3	Relative abundances and modeled orbits of the star J034239	213
C4	Same as Figure C3, but for the star J023001	214
C5	Same as Figure C3, but for the star HV205840	215
C6	Modeled orbits for the star J054653	216

List of Tables

2.1	Cluster-Cepheid pairs with membership probabilities $P(A B) > 0.10$	68
2.2	Age estimations for a reliable subsample of clusters	83
3.1	Equatorial coordinates of the DECam fields observed by HOWVAST in 2017 and 2018	97
3.2	Total number and recovered RRLs from previous surveys as a function of heliocentric distance	106
3.3	Main properties of the RRL candidates detected beyond 100 kpc	111
3.4	Simple and broken-power-law parameters from the sampled posterior probability distributions described in Section 3.5	115
4.1	Main properties of the RR Lyrae stars observed in our spectroscopic program	124
4.2	Radial velocity measurements for our targets	131
4.3	Atmospheric parameters determined for the RR Lyrae stars with higher S/N in our sample	142
4.4	Chemical abundance ratios for seven RR Lyrae stars in our sample	146
4.5	Orbital parameters of the stars in our sample, integrated for 3 Gyr using GALPY's <i>MWPotential2014</i>	149
4.6	Orbital parameters of the stars in our sample, integrated for 3 Gyr using the perturbed potential	150
4.7	Information of the stellar streams considered in Section 4.5.4	164
A1	Prior, likelihood and membership probability for literature combos	180
A2	Cluster-Cepheid pairs with membership probabilities $P(A B)$ between 0.01 and 0.10	181
A3	Same as Table A2 for combos with low priors $P(A)$, but high likelihood	183
B1	Main properties of the entire sample of RRLs detected in this work	198
C1	Line list of the elements detected for our RR Lyrae stars	210

Para B.I.M.T.

1

Introduction

The information presented in this chapter is extracted from the books [Carroll & Ostlie \(2007\)](#), [Sparke & Gallagher \(2007\)](#), and [Catelan & Smith \(2015\)](#), from the review papers [Bland-Hawthorn & Gerhard \(2016\)](#), [Frebel \(2018\)](#), [Simon \(2019\)](#), and [Cowan et al. \(2021\)](#), and from the works cited within each section.

Here, I introduce the reader to the state-of-the-art of the fields of Galactic archaeology and variable stars, which constitute the foundations of this dissertation. I start this chapter by putting our Galaxy into a broader cosmological context (Section 1.1), and highlighting the importance of the study of stellar populations and their origin as tools to disentangle the history of the Galaxy as a whole (Section 1.2). In the subsequent section (Section 1.3), a summary of the formation of chemical elements over the cosmic history is set out, as this represents an indispensable basis for the remainder of the present work. Next, I use the information provided in the previous sections to describe individually the Milky Way components relevant to this thesis (Section 1.4). Section 1.5 deals with the theoretical and observational framework required to understand stellar systems as donors of specific populations to the different constituents of our Galaxy, all in the context of gravitational interactions. Because this dissertation focuses on variable stars, I use Section 1.6 to describe the role that these stars play on the study of the Milky Way. Finally, in Section 1.7, I provide an outline of the studies presented in this thesis, and summarize the motivations and goals of each chapter.

1.1 The Milky Way Galaxy

The alluring nature of the night sky has captivated humanity for thousands of years, and understanding the phenomena responsible for its spectacular appearance has always been a topic of interest to place our existence into perspective with respect to the vast Universe. The discovery that our Galaxy¹, the Milky Way (MW), is one of many others in the Universe (e.g., [Hubble, 1926](#))² opened a field of study that became a cornerstone of contemporary astrophysics. Since then, astronomers have striven to decipher the puzzles concerning the formation of the galactic and stellar structures that we observe today. In order to unveil the

¹By convention, the word “galaxy” is written capitalised to refer to the Milky Way, and lower cased when referring to external galaxies.

²Before that, the term “nebulae” was used to make allusion of objects with a blurry appearance, including gas clouds, star clusters, planetary nebulae, and galaxies.

cosmic origins, investigating the Universe on small and large scales is essential to provide different perspectives on the principles that govern the Universe as a whole. This thesis is encapsulated in the framework of near-field cosmology (Bland-Hawthorn & Peebles, 2006), which focuses on the detailed study of the MW, its components, and its neighboring galaxies to better understand the conditions in which galaxies formed throughout the history of the Universe.

In the currently favoured cosmological paradigm, the Λ cold dark matter (Λ -CDM) model, galaxies are assembled hierarchically through the accretion of smaller structures (e.g., Searle & Zinn, 1978; White & Frenk, 1991; Kauffmann, White, & Guiderdoni, 1993; Cole et al., 1994; Bullock & Johnston, 2005; Fattahi et al., 2020). Indeed, when we scan the celestial sphere, we capture moments which appear frozen at a human timescale as snapshots of the cosmic history, and Galactic cannibalism appears wherever we look. By combining observations and models, we can predict the future of our Galaxy, but these tools can also be used to reconstruct its past. In this framework, the MW and similar galaxies (MW-like) have likely undergone violent mergers in their early history as part of their hierarchical formation (see e.g. Press & Schechter, 1974; Blumenthal et al., 1984; Bullock & Johnston, 2005; Montalbán et al., 2021; Malhan et al., 2022). Evidence of such interactions is imprinted in the stars that these galaxies contain. Moreover, stars formed under different conditions within the MW (e.g., in stellar systems) evolve dynamically and suffer from similar gravitational effects as accreted galaxies throughout their turbulent lifetimes. Thus, disentangling the formation and evolution of the Galaxy as a whole requires a detailed description of the distribution, dynamics, chemistry, and ages of the stars that inhabit its constituents. That is what motivates this dissertation.

1.1.1 The Galaxy in a nutshell

Together with the Andromeda (also known as M31; Messier, 1781) and Triangulum galaxies, the MW is one of the three largest members of the Local Group, a loosely bound group of > 100 galaxies (mostly of them satellite galaxies) distributed over $\sim 2 \times 10^6$ pc³. The MW is a typical barred spiral galaxy with a total mass of $\sim 10^{12}$ solar masses (M_{\odot})⁴ and an intricate structure. Our Solar system is located at roughly 8.27 kpc from the centre of the MW (Gravity Collaboration et al., 2021), orbiting the MW periodically over a hundred million years (with a velocity of ~ 220 km s⁻¹; Bovy et al. 2012) in the inner rim of the Orion Arm (Alves et al., 2020). The major constituents of our Galaxy and their main properties are illustrated in Figure 1.1.

The central region of the MW is known as the bulge: an elongated spheroid of stars that show cylindrical rotation and orbit the Galactic centre with a mean rotational velocity of ~ 100 km s⁻¹ (out to 2 kpc from the centre; see Bland-Hawthorn & Gerhard 2016 and references therein). The bulge is known for its high density of stars, and for containing a nuclear star cluster (Becklin & Neugebauer, 1968) that hosts a supermassive black hole (Sagittarius A*; Balick & Brown, 1974; EHT Collaboration et al., 2022). In spite of it containing significant amounts of dust (Baade, 1946), its presence is clear to the naked eye

³A parsec, pc, is defined as approximately 3.26 times the distance that the light covers in one year (a light-year), or 3.09×10^{16} m.

⁴One solar mass corresponds to approximately 1.99×10^{30} kg.

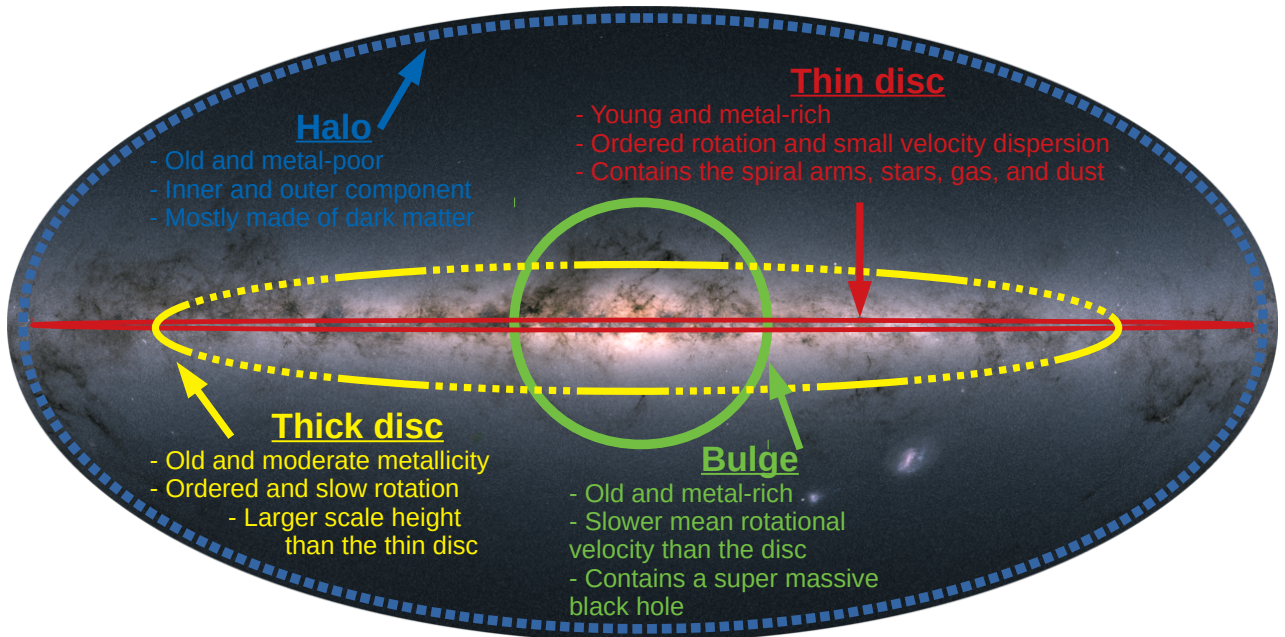


Figure 1.1: Map of our Galaxy depicting its main components (the bulge, the thin and thick discs, and the halo). A brief summary of their properties, as described in Sections 1.1.1 and 1.4, is also provided. The regions covered by each component do not represent accurate representations of their shapes and are only displayed for illustrative purposes. *Background Image Credit: Gaia Data Processing and Analysis Consortium (DPAC); A. Moitinho / A. F. Silva / M. Barros / C. Barata, University of Lisbon, Portugal; H. Saviotto, Fork Research, Portugal.*

from the southern hemisphere. The bulge of our Galaxy is made up predominantly by old stars with a broad range of metallicities⁵, with iron-to-hydrogen abundance ratios ($[\text{Fe}/\text{H}]$, as defined in Section 1.3) ranging between -3.0 and 1 dex (see e.g. Ness & Freeman, 2016). The majority of its stars, however, display $[\text{Fe}/\text{H}]$ between -1.5 and 0.5 dex (e.g., Zoccali et al., 2008). Nowadays, consistent evidence from the HI and CO gas distribution (Binney et al., 1991; Fux, 1999), the near-infrared light distribution (Blitz & Spergel, 1991; Weiland et al., 1994; Binney, Gerhard, & Spergel, 1997), and the spatial distribution of stars (McWilliam & Zoccali, 2010; Nataf et al., 2010) indicate that the MW’s bulge consists of a bar (Shen et al., 2010; Robin et al., 2012) and it is structured in an X-like boxy/peanut shape (Robin et al., 2012; Portail et al., 2017), which is a distinctive feature of pseudo-bulges among spiral galaxies (e.g., Barbuy, Chiappini, & Gerhard, 2018; Gargiulo et al., 2019; Yu et al., 2022).

A disc composed of star, gas, and dust encircles the bulge, and is characterized by its flat-rotating structure of ~ 30 kpc length across. The disc can be dissected into two components: a thin and a thick disc (Gilmore & Reid, 1983). The former is considered to be the main star factory of the MW, as it is home to the spiral arms and the big bright star forming clouds responsible for most of the active star formation that takes place in the Galaxy. The thin disc is composed of young and metal-rich stellar populations. Enclosing the thin disc, there

⁵In astronomical jargon, metals are all elements heavier than hydrogen and helium.

is a thick disc that extends a few 100 pc above and below its more slender counterpart. The thick disc is mainly made of stars (not gas) that orbit the main body of the Galaxy following more inclined trajectories than the thin disc's, and tend to have fewer heavy elements (which suggests an earlier formation; see Section 1.3). Both the bulge and the disc are surrounded by the halo, which has a spheroid-like shape and is much larger than the disc. The halo is sprinkled with stars and pristine satellites (globular clusters and dwarf galaxies), but it is mainly composed of dark matter, which comprises ~ 80 per cent of the MW mass. Because this dissertation focuses on disc and halo stars, a more detailed description of these components is provided in Section 1.4.

From our current understanding, galaxies in general are constituted by a combination of stellar populations (i.e., they are considered composite populations), which are ensembles of stars with common properties (e.g., ages, chemical abundances, kinematics, distances, and origins). These properties allow these stars to be used as probes of the conditions in which they were formed. Two types of stellar populations are commonly recognized within our Galaxy (Oort, 1926), based on the categories defined by Baade (1944). The so-called Population I stars are found predominantly in the spiral arms, usually rotating around the Galactic centre on regular and ordered elliptical orbits. These stars are known for being young and rich in metals. Our Sun is an example of a Population I star. Population II stars, on the other hand, are old and metal-deficient stars ubiquitous in globular clusters and the halo, and typically describe eccentric and more chaotic orbits around the MW. For this work I have chosen Population I and II stars to explore different regions of the MW, as a means to investigate its recent star formation history (Chapter 2) and its early assembly (Chapters 3 and 4).

1.2 Galactic archaeology: Stars as fossils of the Milky Way history

The MW is one of the most valuable laboratories that we have access to for studying galaxy formation, given its well-resolved constituents on which investigations can be carried out in great detail (Bland-Hawthorn & Gerhard, 2016). It might be argued that, living well within our Galaxy gives us a limited perspective of its structure, as compared with our complete view of nearby and distant galaxies. However, being embedded within the Galactic disc allows us to measure high precision stellar properties (e.g., the kinematics of stars; Johnston, Spergel, & Haydn, 2002; Bovy, Erkal, & Sanders, 2017; Bonaca et al., 2019), especially in the Solar neighborhood, while keeping a privileged view of the other Galactic components (e.g., the halo) and nearby galaxies⁶. With this information, it becomes feasible for us to employ both stars and galaxies as stringent tests of more general galaxy formation models (e.g., Guedes et al., 2011; Grand et al., 2017; Buck et al., 2021; Conroy et al., 2022).

Galactic archaeology uses present-day stellar populations as relics to reveal the history of the MW through their properties (chemical abundances, kinematics, and ages; see e.g. Freeman & Bland-Hawthorn, 2002; Matteucci, 2012; Belokurov, 2013; Lagarde et al., 2019; Hawkins et al., 2020). Piecing together the evidence provided by these stellar fossils can be,

⁶A big disadvantage, nevertheless, is that the far side of the Galactic disc and the bulge's very centre remain vastly unexplored due to the high stellar density and interstellar extinction toward those regions.

however, an arduous labour, as the information required to reconstruct the Galactic evolution is in some cases meticulously buried, for example, due to mixture of stars in the position and velocity space across the MW disc and halo. Thus, it becomes necessary to inspect the properties of stars from perspectives that allow the maximum amount of information to be extracted from the available resources.

1.2.1 Chemodynamical tagging

Tagging groups of stars according to their chemical compositions and motions through space allows astronomers to trace back their individual and collective histories, and in particular to investigate the presence of substructures in the Galaxy (see e.g. [Massari, Koppelman, & Helmi, 2019](#); [Koppelman et al., 2019](#)). This is notably useful to investigate stars that formed together but dispersed due to internal and external interactions, alongside with the processes responsible for their dissolution. Chemical tagging, akin DNA-tagging in biological life, uses information encoded in stars (in this case, element abundance patterns in their atmospheres) under the assumption that stars that are born together are chemically homogeneous ([Freeman & Bland-Hawthorn, 2002](#)). Weak chemical tagging suggests that it is possible to identify the Galactic component in which a star was born given their chemical patterns (e.g., [Mitschang et al., 2014](#); [Hawkins et al., 2015](#); [Garcia-Dias et al., 2019](#)), whereas strong chemical tagging propose that it is even possible to determine the exact conditions of the molecular clouds stars come from (e.g., [Freeman & Bland-Hawthorn, 2002](#); [Price-Jones et al., 2020](#); [Hogg et al., 2016](#); [Gudin et al., 2021](#); [Nelson et al., 2021](#)). Likewise, kinematical information (i.e., the velocities and orbits of stars) allows us to backtrack their motions to determine where stars come from based on their dynamics. Thus, combining both of these approaches, in what is now called chemodynamical tagging, pushes Galactic archaeology to its fullest potential by providing stringent constraints on the birth location of stars in the Galaxy, and subsequently on the MW formation.

In order to chemodynamically characterize stars for their use as Galactic tracers, a wealth of information is required. To address this necessity, intrinsically different but complementary observational techniques have been developed allowing astronomers to get insights on the physical properties of stars that, otherwise, would not be accessible. These techniques can be broadly branched into three categories: photometry, spectroscopy, and astrometry⁷.

Photometry

Photometry is the astronomical technique that quantifies the intensity of light emitted by a source as photons collected over time. Currently, at optical wavelengths this is achieved by using charge-coupled devices (CCDs) that are sensitive over specific wavelength ranges. The light captured in these passbands (*filters*) is then standardized as unitless quantities, or magnitudes (apparent or absolute), which can then be used to define colour indices as the difference in magnitude between two passbands. Because astronomical filters are optimized over limited wavelength ranges, magnitudes in different bands (and colours) are sensitive to different fundamental stellar parameters (e.g., luminosities, effective temperatures, and

⁷A branch that encapsulates the quantities measured by these techniques is time-domain astronomy, which quantifies how astronomical sources change in brightness over time (e.g., [Tyson, 2019](#)).

1 Introduction

chemical abundances) and other physical effects relevant to the study of stars (e.g., interstellar extinction). Photometry is the main technique used to describe the observable luminosity changes in variable stars, which are the object of study of this thesis and are described in detail in Section 1.6.

In the past few decades, numerous large-scale and dedicated surveys have been developed to map the optical/near infrared sky, motivated by a variety of science cases, usually systematically scanning it with deep, wide, and/or fast cadence observations. Examples of such surveys are the Sloan Digital Sky Survey (SDSS; [York et al., 2000](#)), the Two Micron All-Sky Survey (2MASS; [Skrutskie et al., 2006](#)), the Catalina Real-Time Transient Survey (CRTS; [Drake et al., 2009](#)), the Panoramic Survey Telescope And Rapid Response System (Pan-STARRS-1) imaging survey (PS-1; [Kaiser et al., 2002](#)), the Vista Variables in the Vía Láctea Survey (VVV; [Minniti et al., 2010](#)), the Dark Energy Survey (DES; [The Dark Energy Survey Collaboration, 2005](#)), the Optical Gravitational Lensing Experiment (OGLE; [Udalski, Szymański, & Szymański, 2015](#)), the Transiting Exoplanet Survey Satellite (TESS; [Ricker et al., 2015](#)), and the Zwicky Transient Facility (ZTF; [Bellm et al., 2019](#)). Surveys like the aforementioned have permitted the detection and classification of a plethora of point-like/extended sources of a diverse nature such as variable stars, exoplanets⁸, active galactic nuclei (AGNs), asteroids, and supernovae, allowing for the characterization of the physical processes responsible for their light emissions and changes, and setting the foundations for the continuous development of new instruments and telescopes (to be discussed in Chapter 5).

Spectroscopy

Spectroscopy is the field that studies the electromagnetic radiation emitted by a source as a function of wavelength. This dependence can be investigated by generating spectra from the dispersion of light of different wavelengths into different directions, or by analysing the wavelength distribution of such dispersion. Stars radiate their light across the spectrum in a continuum, which is then absorbed by chemical elements in the gas or dust on its path to the observer (e.g., when it crosses their atmospheres), producing dark regions (absorption features) at specific wavelengths over the spectrum. Radiation is also emitted (or re-emitted, after being absorbed) at specific wavelengths corresponding to the transition of electrons from a high energy state to a lower energy state. This information, encoded in a stellar spectrum, cannot be inferred by the naked eye, and can reveal an astonishing amount of details about the physical properties of stars. Fundamental stellar parameters, such as effective temperatures, surface gravities, and chemical abundances, can be determined, for example, by comparing the observed spectra with model atmospheres or by recognizing patterns in their shapes (e.g., [Gray & Johanson, 1991](#); [Hansen et al., 2012](#); [Snedden et al., 2012](#); [Blanco-Cuaresma et al., 2014a](#); [Hanke et al., 2018](#); [Guiglian et al., 2020](#)). By analysing the precise wavelength at which absorption and emission lines are detected, and contrasting them with their known wavelengths at rest (from laboratories on Earth), the systemic (line-of-sight) velocity of the emitting source can be determined via Doppler shift. Moreover, the width of these lines can be used to infer the internal velocity dispersion of the source.

⁸The presence of extrasolar planets can be inferred from the miniscule periodic dimming of the light received from their host star.

Designing spectroscopic campaigns (either large spectroscopic surveys or dedicated small programs) is not a simple task, as several trade-off decisions are required to balance the capabilities of the instruments/telescopes used to gather the data (as nicely illustrated in Figure I.1 from Hanke 2020), that is, to optimize their surveying strategies. These aspects include the spectral resolving power R (the spectrograph’s ability to distinguish features in the spectrum), the wavelength coverage, the survey depth, and the total number of stars observed, and define the suitability of the data obtained for specific science cases. For example, the most precise methods for abundance analysis require high-resolution spectra, and the choice of a wavelength range largely defines the set of lines that needs to be observed. Among the most important large spectroscopic surveys carried out in the last 20 years are the Radial Velocity Experiment (RAVE; Steinmetz et al., 2006), the Large Sky Area Multi-Object Fibre Spectroscopic Telescope (LAMOST) spectroscopic survey (Luo et al., 2015), the *Gaia*-ESO spectroscopic survey (GES; Gilmore et al., 2012), the Galactic Archaeology with HERMES (GALAH) survey (De Silva et al., 2015), and the Apache Point Observatory Galactic Evolution Experiment (APOGEE; Majewski et al., 2017)⁹. Upcoming spectroscopic surveys aiming at extending and complementing the aforementioned will be described in Chapter 5.

Astrometry

Astrometry is the branch of astronomy that concerns the precise tracking of the positions and movements (from the measurement of positions over time) of stellar objects. The position of a star on the celestial sphere can be defined in different coordinate systems. For example, the equatorial system represents the position of a celestial object in spherical coordinates (right ascension and declination) using the Earth as the centre of the sphere and the celestial equator as a fundamental plane, whereas the Galactic coordinate system (Galactic latitude and longitude) sets the Sun as the centre of the sphere and the Galactic plane as the fundamental plane. Measuring precise positions allows for the determination of the stellar parallax, which is the apparent shift of the position of an object, as seen from the Earth, against the cosmic background (from which its distance can be estimated, by geometrical triangulation) over a period of ~ 6 months¹⁰. The proper motion of an object is defined, on the other hand, as the change on its position as seen from the centre of mass of the Solar System. It is then natural to realize that both of these quantities depend on the distance of the source, and in general they become increasingly harder to measure with increasing distance (the apparent change in position becomes miniscule).

The field of astrometry took a significant leap with the launch of the High Precision Parallax Collecting Satellite (HIPPARCOS) mission from the European Space Agency (ESA; ESA, 1997), which was able to measure the positions for over 10^5 stars with an unprecedented level of detail. About two decades later, HIPPARCOS’ successor, the *Gaia* satellite (Gaia Collaboration et al., 2016), further revolutionized the field by delivering a full astrometric characterization (with five parameters, namely equatorial coordinates, parallaxes, and proper motions) and photometry (in *Gaia*’s passbands: G , BP , and RP) for over one billion stars

⁹RAVE and LAMOST are examples of low-resolution surveys, whereas *Gaia*-ESO, GALAH, and APOGEE are considered medium to high resolution.

¹⁰This change is caused by perspective, from the motion of the Earth around the Sun.

(Lindegren et al., 2018) through its second data release (DR2; Gaia Collaboration et al., 2018). This number was enlarged to ~ 1.5 billion stars with the so-called early third data release (eDR3; Gaia Collaboration et al., 2020), which also included an increased level of precision in their astrometric solutions. More recently, the third data release (DR3; Gaia Collaboration et al., 2022) pushed the boundaries even further by providing radial velocities for over 33 million objects, mean spectra for about a million sources (Katz et al., 2022), and the analysis of variability for ~ 10 million variable sources (Eyer et al., 2022), including hundreds of thousands of sources characterized by Specific Object Studies (e.g., Ripepi et al., 2022b; Clementini et al., 2022).

1.3 Cosmic nucleosynthesis

Throughout the ~ 13 Gyr of our Universe’s history, its chemical composition, as measured by the abundance of chemical elements, has not remained the same. Concrete evidence of the chemical evolution of the Universe can be observed in our everyday life. After the Big Bang, a primordial nucleosynthesis resulted in a Universe consisting predominantly of hydrogen and helium (~ 76 and 24 per cent, respectively), with trace amounts of deuterium, tritium, helium-3 and lithium. However, the elements that we observe today, including those that constitute the base of the organic chemistry and life as we know it (e.g., hydrogen, carbon, nitrogen, oxygen, and phosphorus), and the heavier chemical species that make technological development possible (e.g., aluminium, silicon, iron, copper, and zinc) clearly differ from our Universe’s primordial chemical composition. The atmosphere of our Sun, which formed 4.6 Gyr ago (Bouvier & Wadhwa, 2010), also shows a composition that is different to that of the Universe right after the Big Bang. Asplund et al. (2009), for example, used a time-dependent three-dimensional (3D) hydrodynamical model to find the solar mass fraction of hydrogen, helium, and other elements to be 73.8, 24.9, and 1.3 per cent, respectively. All of the aforementioned elements were formed in a variety of astrophysical sites (e.g., nucleosynthesis as a result of stellar evolution and neutron star mergers; Bethe, 1939; von Weizsäcker, 1951; Burbidge et al., 1957). This occurred over the course of a continuous cosmic enrichment which produced chemical species with increasing atomic numbers Z ¹¹, and constitute one of the cornerstones supporting the Big Bang theory and the Λ -CDM model (see e.g. Cyburt, 2004; Hinshaw et al., 2013; Fields et al., 2020). Thus, imprints of the formation and evolution of our Universe, and of our Galaxy in particular, can be deduced from elemental abundances observed in present-day stellar populations. A schematic of the cosmological history of the Universe is provided in Figure 1.2 as a reference for the content of this section.

Metallicity is a key concept to understand the chemical evolution of the Universe. Various notations exist to refer to the metal content of stars. One such representation utilizes the symbols X , Y , and Z as the mass fractions of hydrogen, helium, and metals in a star, respectively (with respect to the total amount of baryonic matter), so that $X + Y + Z = 1$. The chemical abundance ratio of specific elements is commonly calculated using the logarithm of the ratio of such elements compared to that of the Sun. For example, the ratio

¹¹The atomic number of an element represents the charge number of its nucleus, or the number of protons present in ordinary nuclei of that species.

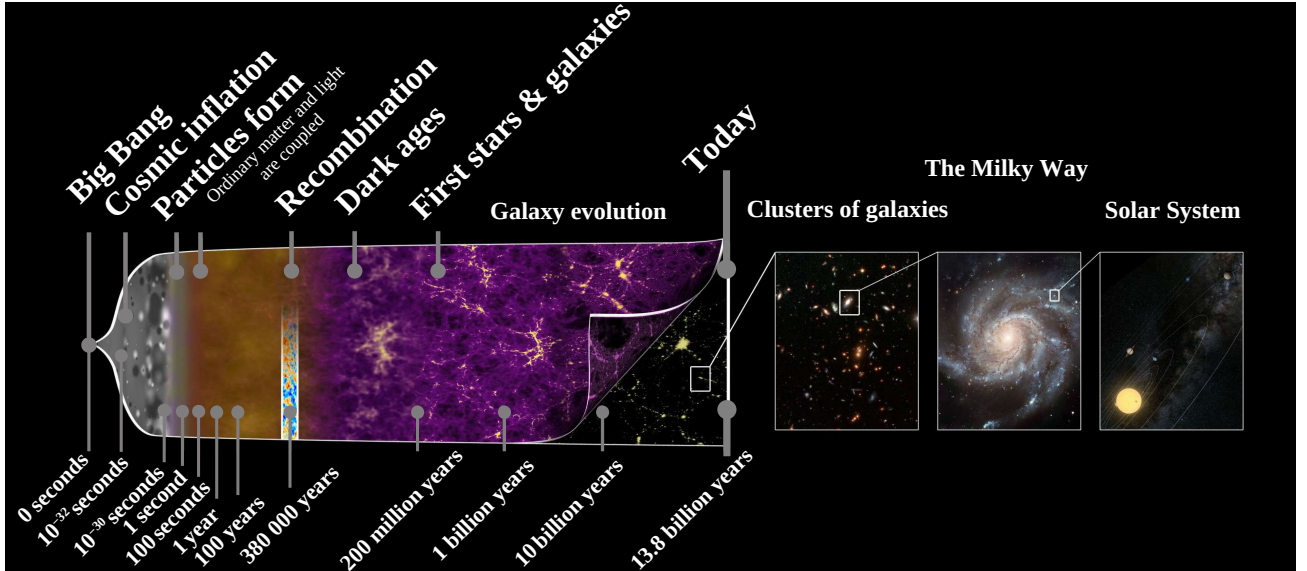


Figure 1.2: Summary of the history of our Universe starting from the Big Bang. This illustration highlights the main events that occurred in this period of time (as mentioned in Section 1.3), including the early expansion of the Universe, the moments in which primordial nucleosynthesis took place, the time when the CMB was emitted, and the times of the formation of galaxies and different generations of stars. *Image credit:* Figure adapted from [The Story of Our Universe](#): NASA/ESA/C. Carreau.

of Fe with respect to H for a given star is described by

$$[\text{Fe}/\text{H}] = \log\left(\frac{N_{\text{Fe}}}{N_{\text{H}}}\right)_{\text{star}} - \log\left(\frac{N_{\text{Fe}}}{N_{\text{H}}}\right)_{\text{Sun}}, \quad (1.1)$$

where the first and second terms denote the ratio of elemental abundances in the star and in the Sun (respectively), and N_{Fe} and N_{H} represent the corresponding number of atoms of iron and hydrogen per unit volume. Thus, a star with $[\text{Fe}/\text{H}] = 0$ dex (0^{th} decimal exponent) is said to be of solar metallicity, whereas $[\text{Fe}/\text{H}] = 1$ and -2 indicate that the given star possesses 10 times more and 100 times less (1 per cent) iron than the Sun, respectively. This also implies that $[\text{Fe}/\text{H}] = \log(Z/Z_{\odot})$. It is worth mentioning that it has become customary to use the fraction $[\text{Fe}/\text{H}]$ to refer to the overall metallicity of a star, $[\text{M}/\text{H}]$. This notation is extended to elements other than Fe and H (e.g., $[\text{Mg}/\text{Fe}]$ denotes the abundance ratio of magnesium with respect to iron).

It is now accepted that the amount of metals in a star depends on its formation time and birthplace, and that the overall metallicity of the Universe increases with time (e.g., [Frebel, 2018](#)). In our current cosmological paradigm, the first elements were synthesized from the condensation of plasma that cooled after the initial expansion of the Universe. About one second after the Big Bang, the neutron-to-proton ratio dropped to 1:6 as a consequence of a decrease in temperature (to $< 10^{10}$ K). This halted the transformation of protons into neutrons through weak interactions (see e.g. [Boesgaard & Steigman, 1985](#); [Bertulani, Fuqua, & Hussein, 2013](#)). Three minutes later, the temperatures decreased even further allowing neutrons and protons to combine, forming deuterium and helium. Elements with mass

numbers A ¹² heavier than eight could not form at this stage, because of the high binding energy of helium and the unstable nature of the elements with A between five and eight.

1.3.1 The first stars

After $\sim 380,000$ yr, the expansion and cooling of the Universe provided the conditions required for neutral hydrogen to form, allowing thermal radiation to decouple from ordinary matter. This was the moment when the radiation now observed as the cosmic microwave background (CMB) was emitted (Penzias & Wilson, 1965; Planck Collaboration et al., 2020). A few 100 Myr later, regions dominated by dark matter grew from small anisotropies to filamentary structures and overdensities in which H and He underwent gravitational collapse, forming the first stars. This first generation of stars are also known as Population III stars, and are composed of the primordial chemical elements in the Universe. Therefore, they are thought to be extremely metal-poor. Due to the dearth of metals, dust, and molecules like CO to act as coolant for the gravitational collapse within the primordial gas, cloud fragmentation did not take place and the formation of very massive stars (of masses $\sim 10^2$ - $10^3 M_{\odot}$) with high rotational velocities and short lifetimes (3-5 Myr; Siess, Livio, & Lattanzio, 2002; Umeda & Nomoto, 2003) was favoured instead (e.g., Jeans, 1902; Bromm & Larson, 2004). Recent simulations have shown, however, that accretion disc fragmentation around massive Population III protostars could also form stars at much lower masses ($< 1 M_{\odot}$; see e.g. Hartwig et al., 2015; Wollenberg et al., 2020), which could have survived until the present day (e.g., Schlaufman, Thompson, & Casey, 2018; Chandra & Schlaufman, 2021). Population III stars have not been observed yet, and they are considered one of the holy grails of modern astronomy, as they are the precursors of Population II and Population I stars (Baade, 1944) and therefore would provide direct evidence of the physical and chemical conditions in the early stage of the Universe’s evolution.

1.3.2 Chemical enrichment via stellar evolution

Stars are able to maintain their hydrostatic equilibrium by counteracting their gravitational collapse through the thermal pressure caused by exothermic nuclear fusion occurring in their stellar cores¹³ (Atkinson, 1931; Bethe, 1939; Gamow, 1939). During the lifetime of a star, continuous processes “burn” the existing chemical elements in its core and in shells surrounding it, forming new elements in the process, and expelling them to the interstellar medium (ISM) at the end of their lives. The ultimate fate of stars depends on stellar mass, and their evolution can be terminated by their collapse directly into a black hole due to endothermic photodesintegration (for masses $> 250 M_{\odot}$), as pair-instability supernovae explosions (130 - $250 M_{\odot}$), and as core-collapse supernovae (8 - $130 M_{\odot}$). After these stars finish their evolution, the next generations form from an ISM enriched with α -elements¹⁴, iron-peak

¹²The mass number A of an element corresponds to the sum of neutrons and protons that its nucleus contain.

¹³Notable deviations from these equilibrium states are those observed in pulsating variable stars, as better described in Section 1.6.

¹⁴ α -elements are stable elements that are synthesized by fusions with He nuclei (e.g., C, O, Ne, Mg, Si, Ca, and Ti).

elements (e.g., V, Cr, Mn, Fe, Co, and Ni), and heavier elements. The newly formed stars have masses typically ranging between 0.08 and $150 M_{\odot}$ ¹⁵, and follow a stochastic number distribution known as Initial Mass Function (IMF). In general, these number distributions decline with mass (most stars are low-mass, and massive stars are rare), and are well represented by a broken-power-law or a lognormal function at small masses and a steep power-law at high masses (see e.g. [Salpeter, 1955](#); [Kroupa, Aarseth, & Hurley, 2001](#); [Chabrier, 2003](#); [Banerjee & Kroupa, 2012](#)). These types of distributions imply that most of the mass of a given stellar population will be defined by its low-mass stars, whereas most of its light will be emitted by a few high-mass stars.

From the moment a star is born, its evolutionary path is defined by its mass, helium fraction, metallicity, elemental abundances, among other effects (e.g., rotation and binarity). Stars spend most of their lifetimes in hydrostatic equilibrium, burning H into He in their cores, on the so-called main sequence (MS). This sequence is observed as a nearly diagonal distribution of stars across the Hertzsprung-Russel (HR) diagram ([Hertzsprung, 1911](#); [Russel, 1914](#))¹⁶. The main reaction producing a star’s energy via fusion in MS stars is contingent upon its mass. In stars with masses $< 1.3 M_{\odot}$, the main channel of energy production is the proton-proton (p - p) chain. In this chain reaction, groups of four protons interact to form He nuclei through three possible chain of reactions branches (e.g., [Adelberger et al., 2011](#); [Wiescher, Käppeler, & Langanke, 2012](#)). More massive (i.e. hotter) stars, on the other hand, use C, N, and O as catalysts for reactions that require higher temperatures ($> 1.7 \times 10^7$ K) to produce most of their energy and to synthesize He from H, through the Carbon-Nitrogen-Oxygen (CNO) cycle. Although the latter dominates in the higher-mass regime, Population III stars could not undergo the CNO cycle due to the lack of heavy elements to originate this series of reactions.

Stars on the MS will continue burning H into He in their cores until their nuclear fuel is exhausted. The end of this process occurs within a Hubble time (~ 13.8 Gyr) for stars with masses $> 0.8 M_{\odot}$, and is the moment when the star evolves off the MS. At this stage, the star’s contracting core is composed of He and is surrounded by an H-burning shell, which expands and cools the star’s photosphere while maintaining a constant luminosity. This is observed as a horizontal movement of the star through the HR diagram to become a red giant. When the temperature at the stellar core reaches $\sim 10^8$ K, He burning ignites and the star contracts. For stars with masses similar to our Sun’s, the He fusion is triggered in a degenerate gas in which the increase of temperature does not lead to an increase of pressure, and the energy produced by nuclear reactions further increase the temperature, in a thermonuclear runaway that only ceases when the degeneracy is lifted (the so-called helium flash). The quiescent He burning phase is characterized by a clustering of red giants whose shape most notably depends on the star’s metallicity and mass (and is seen as a horizontal branch for low-mass stars). For more massive stars (stars with masses $> 2 M_{\odot}$ with non-degenerate cores), this transition involves a decrease in radius and a hotter surface, seen as a blue-wards evolution in the HR diagram. In this phase, the star converts He into C through the triple- α process, and also forms O from He and C. At the end of the He burning stage,

¹⁵These numbers represent the limits at which stars can maintain their hydrostatic equilibrium. Stars that do not reach the conditions to trigger nuclear fusion are called brown dwarfs.

¹⁶The HR diagram shows the dependence of the luminosity of stars in a given stellar population (or alternatively, their absolute magnitudes) on their spectral classifications, effective temperatures or colours.

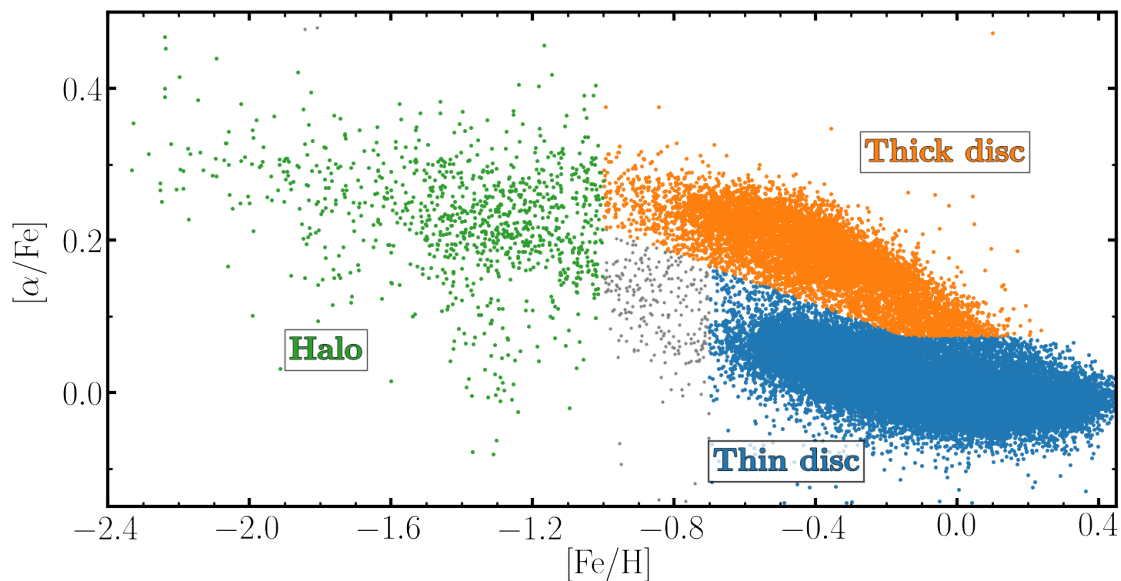


Figure 1.3: Chemical abundance ratios of MW stars from SDSS-IV/APOGEE DR16 (Ahumada et al., 2020) depicted in the $[\alpha/\text{Fe}]$ - $[\text{Fe}/\text{H}]$ space. Stars from the disc and the halo are separated by combining and adapting the selection criteria defined by Navarro et al. (2011) and Anguiano et al. (2020), which are based on the stars’ metallicities. From these cuts, stars lying in the region between the disc and halo distributions (plotted as grey dots) are considered tidal debris, following the definition of Navarro et al. (2011). This plot shows a clearly visible bi-modal distribution among the disc stars, which is used to dissect the disc into two components: one α -enhanced and the other α -depleted (thick and thin disc, respectively). A turn-over (or knee) in the overall distribution of α -element abundances is also visible, representing the transition between the two nucleosynthesis sites described in Section 1.3.2.

the star leaves an inert CO core with a He-burning shell. At this point, stars less massive than $8 M_{\odot}$ shed their outer layers, forming a planetary nebula that leaves behind the CO core as a white dwarf. If the initial mass of the star is between 8 and $10 M_{\odot}$, the higher temperatures will be enough to fuse C, which might result in an oxygen-neon-magnesium white dwarf (Werner & Drake, 2005).

After core He fusion, stars more massive than $8\text{-}10 M_{\odot}$ undergo a continuous and rapid set of core and shell burning stages involving heavier elements (e.g., Ne and O), which produces an onion-like structure in the stellar interior. These processes continue until the chain of reactions reaches the iron-peak (at $Z \sim 26$), where the nuclei are most strongly bound. This represents the point at which the star begins to fuse its core material into iron-peak elements via endothermic reactions. The star then ceases to be stable against its own gravity, and initiates a free-fall contraction that concludes with an explosion leaving a neutron star or a black hole as a remnant, depending on the initial stellar mass. This explosion (a Type II or core-collapse supernovae) occurs $10^6\text{-}10^7$ yr after the progenitors’ formation, and ejects material that enriches the ISM. This material is a key factor of the cycle responsible for the chemical enrichment of the Universe (in particular for elements with $14 \leq Z \leq 30$; e.g., Nomoto et al. 2006), becoming the supply for the formation of the following generations of stars.

An additional formation site for iron-peak elements involves thermonuclear Type Ia supernovae (SNe Ia; [Hoyle, 1960](#); [Soker, 2019](#); [Kobayashi, Leung, & Nomoto, 2020](#)), which are thought to occur predominantly in binary systems containing intermediate-mass stars that have become white dwarfs and exceed the Chandrasekhar mass ($\sim 1.38 M_{\odot}$), that is, the maximum stellar mass that degenerate electron pressure can support ([Chandrasekhar, 1931](#)). Given that the SN Ia are the aftermath of the entire evolution of intermediate-mass stars (long timescales) and core-collapse supernovae only require a few Myr to reach their final stage (short timescales), there is a time delay between both enrichment processes that characterizes chemically evolving systems. This delay is usually visible in the α -metallicity diagram (also referred as Tinsley-Wallerstein diagram; [Wallerstein, 1962](#); [Tinsley, 1979](#)), which depicts the average of the α elements over the iron abundance of stars as a function of their $[\text{Fe}/\text{H}]$. In this type of diagram, which is commonly used for the study of galaxies with sufficiently long star formation histories (including the MW), a “knee” separates two regimes: stars with high $[\alpha/\text{Fe}]$ and low $[\text{Fe}/\text{H}]$, and stars with decreasing $[\alpha/\text{Fe}]$ and increasing $[\text{Fe}/\text{H}]$ (e.g., [Koch et al., 2008](#); [Nissen & Schuster, 2010](#); [Mikolaitis et al., 2014](#); [Di Matteo et al., 2019](#); [Escala et al., 2020](#)). In these plots, the location of the turn-over in α -element abundances represents the transition between the two nucleosynthesis sites aforementioned. Stars with $[\text{Fe}/\text{H}]$ below that of the knee have been enriched by Type II SNe and have low iron-abundances (and high $[\alpha/\text{Fe}]$), whereas those with $[\text{Fe}/\text{H}]$ higher than that of the knee are formed after the time at which SNe Ia started contributing iron-peak elements to the ISM. The position of this point in the α -metallicity diagram roughly scales with galaxy mass (e.g., [Tolstoy, Hill, & Tosi, 2009](#)), since the more massive a system is, the higher the star-formation rate can be and therefore, the more Fe (and α -elements) can be produced before the SNe Ia begin to decrease the $[\alpha/\text{Fe}]$ ratio. This implies that, at a constant metallicity, low α -abundances trace star formation events that occurred in a low-mass system. The delay time is thought to be ~ 1 Gyr, and these diagrams have been widely used to disentangle the different components of the Galaxy, with a halo being predominantly metal-poor and α -rich, and a disc composed of metal-rich and α -poor populations (e.g., [Nissen & Schuster, 2010](#); [Adibekyan et al., 2013](#); [Hawkins et al., 2015](#); [Hayden et al., 2015](#); [Bland-Hawthorn & Gerhard, 2016](#); [Haywood et al., 2018](#); [Fernández-Alvar et al., 2019](#); [Hawkins, 2022](#)). An example of an α -metallicity diagram that could be used to dissect the components of the MW is provided in [Figure 1.3](#). The α -metallicity diagram has also been useful to explore, for instance, the assembly of the old, metal-rich MW halo, as the accretion of massive dwarf galaxies for which the $[\alpha/\text{Fe}]$ turn-over takes place at higher metallicities (see e.g. [de Boer et al., 2014](#); [Hawkins et al., 2022](#)).

1.3.3 The production of heavy elements

The majority of the elements heavier than the Fe peak group is not produced from the nucleosynthesis sites described above, but are the result of neutron capture processes taking place during the final stages of the evolution of stars ([Burbidge et al., 1957](#); [Cameron, 1957](#)). These are the so-called slow and rapid neutron capture processes (s - and r -process, respectively), which are separated based on their different capture rates with respect to the timescale of β -decay, and can explain the production of different sets of elements (see e.g. [Hansen, 2022](#); [Psaltis et al., 2022](#)). The s -process, for example, can explain the formation of

elements such as La, Ba, and Y, up to $Z \sim 83$ (bismuth), whereas the r -process is responsible for the production of elements heavier than Bi (e.g., Eu, Th, and U; Burbidge et al., 1957; Sneden, Cowan, & Gallino, 2008) and can also form lighter elements (e.g., Sr, Ag, and Eu; Arlandini et al., 1999). The former takes place in the low-mass asymptotic giant branch (AGB), and during the core He-burning and C-burning phases in massive stars (Gallino et al., 1998; Käppeler et al., 2011; Karakas & Lattanzio, 2014; Trippella et al., 2016; Vescovi & Reifarth, 2021), when the density of neutrons is of the order of $\sim 10^{10} \text{ cm}^{-3}$. The r -process, on the other hand, occurs on neutron capture timescales much shorter than that of β -decay, and therefore requires neutron densities of the order of $\sim 10^{20} \text{ cm}^{-3}$. Possible formation sites that could provide such high neutron-rich environments include magneto-hydrodynamic supernova explosions (MHD SN; Cameron, 2003; Cowan et al., 2021), neutron star mergers (Lattimer & Schramm, 1974; Chornock et al., 2017; Drout et al., 2017; Watson et al., 2019), and neutrino-driven winds in core-collapse SNe (Arcones, Janka, & Scheck, 2007; Wanajo, 2013; Guillaumon & Goldman, 2020). Unraveling the nature of the poorly constrained r -process remains one of the most addressed challenges in the study of stellar nucleosynthesis, and is presently an active topic of research (e.g., Hansen et al., 2012; Hansen, Montes, & Arcones, 2014; Sakari et al., 2018a,b; Ezzeddine et al., 2020; Gudin et al., 2021; Hirai et al., 2022). A comprehensive description of stellar evolution and cosmic nucleosynthesis, however, escapes the scope of this thesis, and I refer the reader to the vast literature available and to recent reviews (e.g., Frebel, 2018; Cowan et al., 2021).

1.4 The disc and the halo of the Milky Way

1.4.1 The Galactic disc

The Galactic disc is the flat and rotationally-supported structure that contains the majority of the gas, dust, and stars in the Galaxy, including our Sun (located slightly above the Galactic plane; Jurić et al., 2008). It has been known since the early 1980s that the disc harbors multiple populations which cannot be described by a single density profile (Gilmore & Reid, 1983). In fact, the existence of a thin and a thick disc has been confirmed by a plethora of studies using the chemical, kinematical, spatial, and age distribution of stars (Chiba & Beers, 2000; Nissen & Schuster, 2010; Bovy et al., 2012; Haywood et al., 2013; Conroy et al., 2022). This is visible, for example, in the distinct velocity distributions of thin and thick disc stars is shown in Figure 1.4. It is now known that the thin and thick discs are characterized by different scale heights, that is, the height above or below the plane at which the stellar density has dropped to $1/e$ (the scale height increases with age overall; e.g., Chen et al., 2001). For the former, the scale height is of the order of 300-400 pc (Bland-Hawthorn & Gerhard, 2016), whereas for the latter it is about twice as large (depending on the position in the Galaxy; Carroll & Ostlie, 2007). In terms of ages, stars in the thick disc tend to be older (on average) and with a smaller dispersion in ages than those in the thin disc (e.g., Haywood et al., 2013), which is a site of gas, dust, and active star formation (e.g., in stellar associations and open clusters; see Section 1.5.1). In terms of kinematics, thin disc stars are on average kinematically colder, and display an ordered rotation with a small velocity dispersion (the velocity dispersion of disc stars increases with age; Casagrande et al., 2011). Thick disc stars, on the other hand, are kinematically hotter but still with ordered

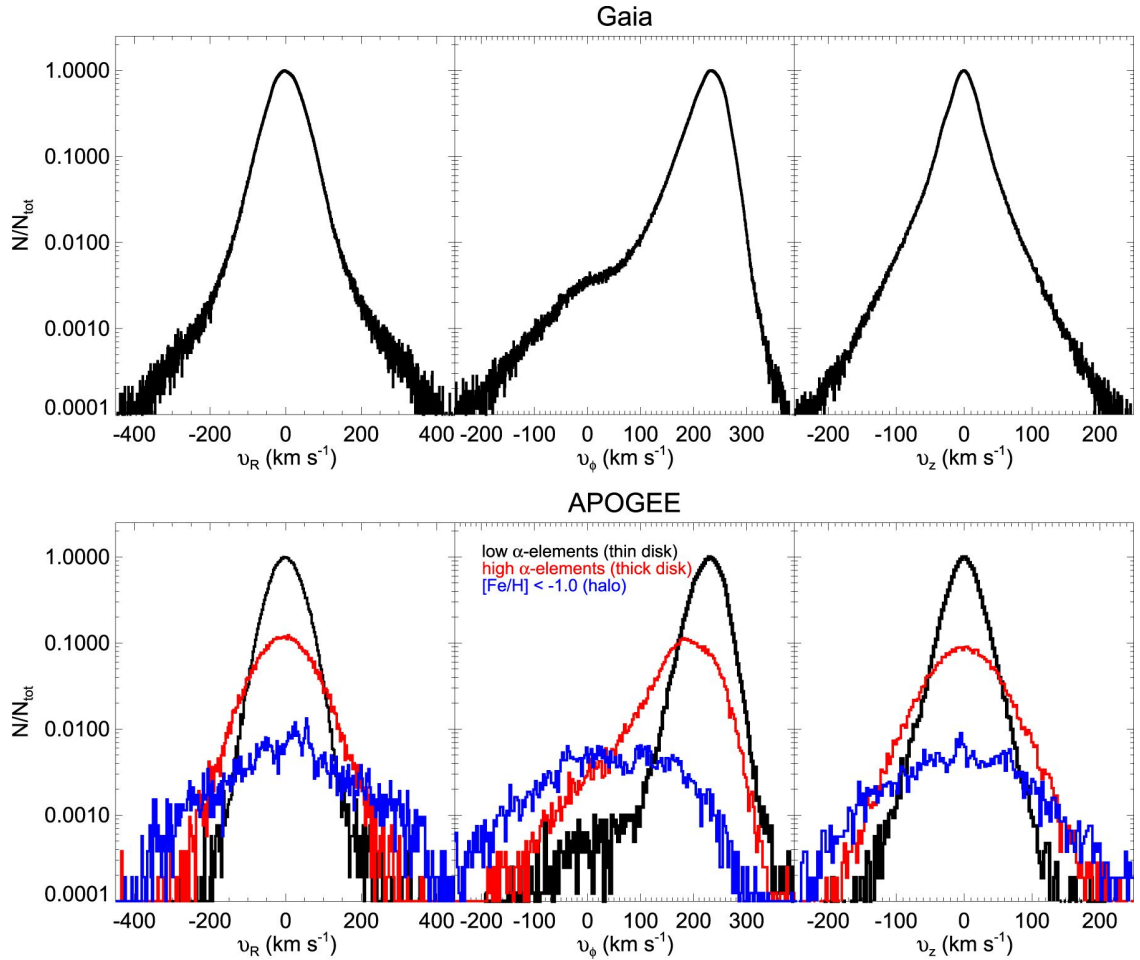


Figure 1.4: Relative distribution functions obtained for individual velocity components (in the cylindrical Galactic system) of thin disc, thick disc, and halo stars as defined by [Anguiano et al. \(2020\)](#). In these plots, v_R , v_ϕ , and v_z represent the radial, azimuthal, and vertical component of the velocities, respectively. The velocities shown in the *upper* panels are based on *Gaia* data, whereas those in the *lower* panels are taken from the APOGEE survey. For the distributions in the bottom panels, stars are assigned to the halo or to the thin/thick disc using their chemistry as a means to avoid cross-contamination between different Galactic components (similar to Figure 1.3). *Image credit:* Figure 2 in [Anguiano et al. \(2020\)](#). Reproduced by permission of the authors and the American Astronomical Society (AAS) journal.

rotation (Sparke & Gallagher, 2007). Regarding their chemical abundances, stars in the thin disc have decreasing $[\text{Fe}/\text{H}]$ with increasing Galactocentric distance (e.g., Friel et al., 1995; Lemasle et al., 2008; Hayden et al., 2015), have on average $[\text{Fe}/\text{H}]$ close to solar, and are depleted in α -elements (with $[\alpha/\text{Fe}]$ between 0 and 0.1; see e.g. Haywood 2008). The thick disc is on the other hand richer in $[\alpha/\text{Fe}]$ (between 0.15 and 0.30) with lower metallicities as compared with thin disc stars (Bensby, Feltzing, & Lundström, 2003; Hayden et al., 2015; Bland-Hawthorn et al., 2019). Additionally, a correlation exists between the metallicity and age for disc stars (decreasing metallicity with increasing age; Haywood et al., 2013). Such correlation is tighter and steeper for stars in the thick disc.

To explain the origin of the two disc populations, and their differences in kinematics, chemistry, and scale height in particular, several formation scenarios have been proposed. One hypothesis combines radial mixing (and/or a decline in the vertical dispersion of the gas with time) with a smooth evolution of the Galaxy (e.g., in terms of star formation rate) to explain the chemical dichotomy of the disc (Loebman et al., 2011; Sharma, Hayden, & Bland-Hawthorn, 2021). Other proposed explanations include the two-infall model, which invokes two phases of accretion separated in time by a pause in star formation episodes (Chiappini, Matteucci, & Gratton, 1997; Spitoni et al., 2019), and the idea that the majority of the thick disc was formed from the accretion of satellite galaxies (Abadi et al., 2003a,b). An additional scenario uses a violent merger event to explain this dichotomy (Villalobos & Helmi, 2008; Buck, 2020; Agertz et al., 2021). Such an event would be responsible for the kinematic heating of an already formed high- α disc, concurrently delivering gas to fuel the formation of low- α thin disc stars (e.g., Conroy et al., 2022). The discovery of evidence for events like these in recent years (e.g. the so-called Gaia-Sausage-Enceladus merger; Helmi et al., 2018; Belokurov et al., 2018b; Myeong et al., 2018) has permitted a general consensus on the origin of the thick disk of our MW.

1.4.2 The Galactic halo

The largest constituent of the MW, the nearly spherical Galactic halo, encompasses both the MW bulge and the disc, and is comprised of two main components: the stellar halo and the dark matter halo (Helmi, 2008). Even though it contains only ~ 1 per cent of the total stellar mass of the MW ($\leq 10^9 M_{\odot}$; see e.g. Deason, Belokurov, & Sanders 2019; Mackereth & Bovy 2020), the stellar halo is perhaps the component that contains the most useful information regarding its assembly history, as it is made up of the most metal-poor ($-5 < [\text{Fe}/\text{H}] < -1$; e.g., Frebel & Norris 2015) and the oldest stars in the Galaxy (Helmi, 2008; Youakim et al., 2020). Kinematically, these stars orbit the MW in highly eccentric orbits with a velocity distribution that is clearly distinct from those of the disc (Reddy, Lambert, & Allende Prieto, 2006; Lane, Bovy, & Mackereth, 2022), as depicted in Figure 1.4. Given that these stars retain the chemical and kinematic conditions of the environment in which they were born, they are fossils that provide us with a unique picture of the early stages of the MW evolution and the properties of the first stars in the Universe (see e.g. Freeman & Bland-Hawthorn, 2002; Frebel & Norris, 2015). Additionally, in the Λ cold dark matter cosmological framework stellar haloes are predicted to harbor the accreted debris of smaller systems with a wide range of masses (e.g., globular clusters and dwarf galaxies; Ibata, Gilmore, & Irwin, 1994; Belokurov et al., 2006; Jordi & Grebel, 2010; Malhan, Ibata, & Martin, 2018; Borsato,

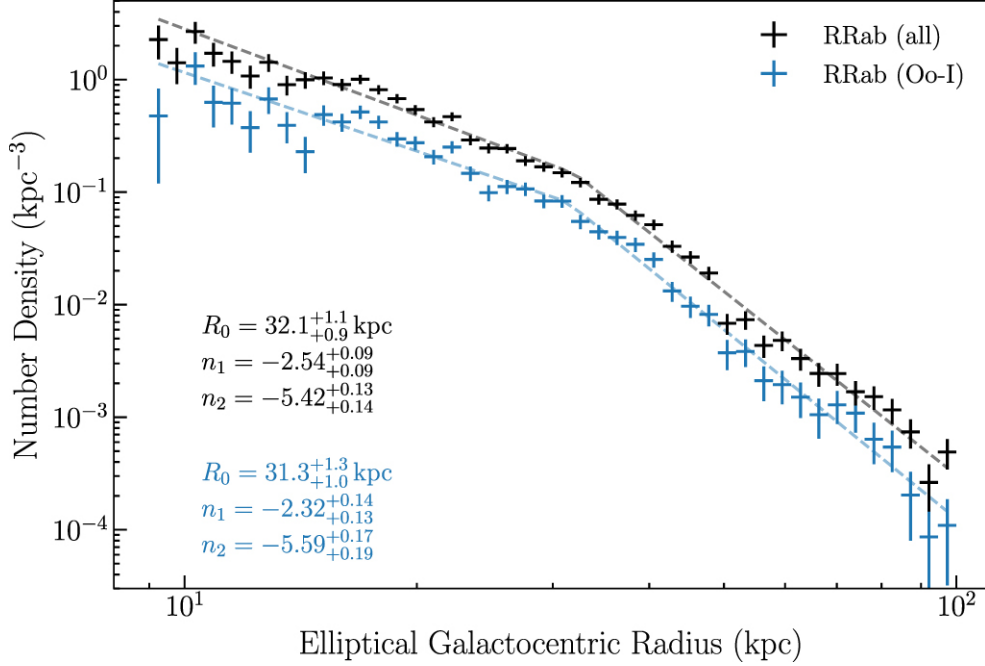


Figure 1.5: Number density of RRab from the DES as a function of Galactocentric radius (out to 100 kpc), for an elliptical model with flattening parameter $q = 0.7$. The figure displays two datasets based on RRLs: one in blue representing shorter period RRLs, and one in black not restricted by periods. The data is modeled with broken-power-laws. The resulting models find a break in the radial profile that separate the power-laws into an inner and outer component of slopes n_1 and n_2 , respectively. The break is detected at $R_0 \sim 30$ kpc from the Galactic centre in the region of the sky surveyed by the DES. *Image credit:* Figure 12 in [Stringer et al. \(2021\)](#). Reproduced by permission of the authors and the American Astronomical Society (AAS) journal.

[Martell, & Simpson, 2020](#)). Thus, studying the halo is essential to obtain a complete census of the accretion events that formed our the MW.

In our Galaxy, the halo is separated into an inner and an outer component (e.g., [Bovy et al., 2012](#)) at ~ 20 kpc from the Galactic centre (see e.g. [Watkins et al., 2009](#); [Sesar et al., 2011](#); [Xue et al., 2015](#); [Medina et al., 2018](#); [Stringer et al., 2021](#)). This kind of separation appears to be a common feature among other galaxies, too (e.g., [Koch et al., 2008](#); [Pillepich et al., 2014](#)). The inner component is thought to be comprised of a mixture of accreted stars and stars formed in-situ ([Nissen & Schuster, 2010, 2011](#); [Nissen et al., 2014](#); [Hawkins et al., 2014](#); [Helmi et al., 2019](#); [Belokurov et al., 2019](#)), is geometrically flattened (with an oblateness parameter $q = c/a = 0.65$, where a and c are the axes in the disk plane and along the vertical direction, respectively; [Bland-Hawthorn & Gerhard 2016](#)) and more metal-rich (with $[\text{Fe}/\text{H}] \sim -1.6$; [Beers et al. 2012](#)), In contrast, the outer component is thought to have originated mostly from accretion events ([Belokurov et al., 2006](#); [Carollo et al., 2010](#); [Beers, 2010](#); [Schönrich, Asplund, & Casagrande, 2011](#); [Naidu et al., 2020](#)), and is characterized by a more spherical density distribution with $q \sim 0.8$ and $[\text{Fe}/\text{H}] < -2$ dex ([Carollo et al., 2010, 2012](#); [Beers et al., 2012](#); [Bland-Hawthorn & Gerhard, 2016](#)). In terms of kinematics, the rotation velocity of halo stars decreases with height above and below the Galactic plane ([Chiba & Beers, 2000](#); [Deason et al., 2012](#)), with the inner halo having on average no rotation

1 Introduction

and the outer halo having a net retrograde rotation (e.g., [Ivezić, Beers, & Jurić, 2012](#)).

Measuring the shape of the Galactic radial density profile (i.e., the number of stars per unit volume) provides useful insights to reconstruct the accretion history of the outer halo (e.g., [Bullock & Johnston, 2005](#); [Cooper et al., 2013](#)), as it is sensitive to properties such as its formation time, the amount of stellar mass accreted, and how long ago the last mergers took place ([Pillepich et al., 2014](#)). An example of a halo radial density profile (from [Stringer et al. 2021](#), with data from the DES) measured with RR Lyrae stars is provided in [Figure 1.5](#). The slope of the density profile of outer halo stars, in particular, has been shown to be a parameter of cosmological significance, closely related to the halo accretion history of MW-like galaxies ([Jurić et al., 2008](#); [Pillepich et al., 2014](#); [Slater et al., 2016](#)), given that they are not expected to have formed at remote distances (e.g., [Naidu et al., 2020](#)). Furthermore, the presence of large-scale overdensities in the halo is thought to be a product of the collective response of the MW (“wakes”) to the infall of massive satellites (e.g., [Belokurov et al., 2019](#)). [Conroy et al. \(2021\)](#), for instance, predicted that the dynamical effect of the LMC should be visible as overdensities in all distant halo populations that probe the smooth halo (neglecting structures from unrelaxed debris). In fact, the degree of radial anisotropy is expected to increase with the distance from the centre of the host halo, and to reach a plateau beyond a specific radius ([Pandey, 2022](#)). Thus, studying the halo (an-)isotropies, and the morphology and strength of these wakes through the spatial distribution of distant stars helps to characterize the gravitational interactions that formed the halo (e.g., to help unveil the orbits of the infalling satellites) and the dynamical equilibrium of the halo (e.g., [Conroy et al., 2021](#)), and could also be used to constrain the nature of dark matter and gravity (see e.g. [Han et al., 2022b](#)).

The stellar halo notably contains valuable probes of the MW’s history and is thought to be comprised mainly of accreted substructures (e.g., [Rodriguez-Gomez et al., 2016](#); [Malhan, Ibata, & Martin, 2018](#); [Naidu et al., 2020](#)), making it a natural laboratory to study the evolution of the Galaxy as a whole. The expected relative contribution from individual accretion events to the formation of the halo is depicted in [Figure 1.6](#). In this context, it is important to consider that stars belonging to the same structure retain similar integrals of motion (e.g., energy, actions, and angular momenta) even if they are scattered across the sky, and tend to share similar chemical abundance patterns (e.g., [Venn et al., 2004](#); [Lee et al., 2015](#); [Naidu et al., 2020](#)). Thus, in order to reconstruct the assembly history of our Galaxy, it has become customary to study the observed six-dimensional phase-space (positions and velocities) of present-day stellar populations and overdensities as signatures of tidal stripping (e.g., [Li et al., 2021](#); [Cook et al., 2022](#)). This is particularly useful in the halo populations, given the relatively long dynamical time-scales resulting from partial phase mixing in this region. Dynamical information of halo stars can be used to look for groups of stars with similar properties, to study their connection with known or previously undiscovered structures, and even to determine the parent populations of single stars. In addition, halo stars contain evidence of the chemical composition of the environment in which old stars were formed, hence they are excellent tracers of the early chemical evolution of the Galaxy. In this thesis, I dedicate two chapters to the study of the halo using old variable stars ([Chapters 3 and 4](#)).

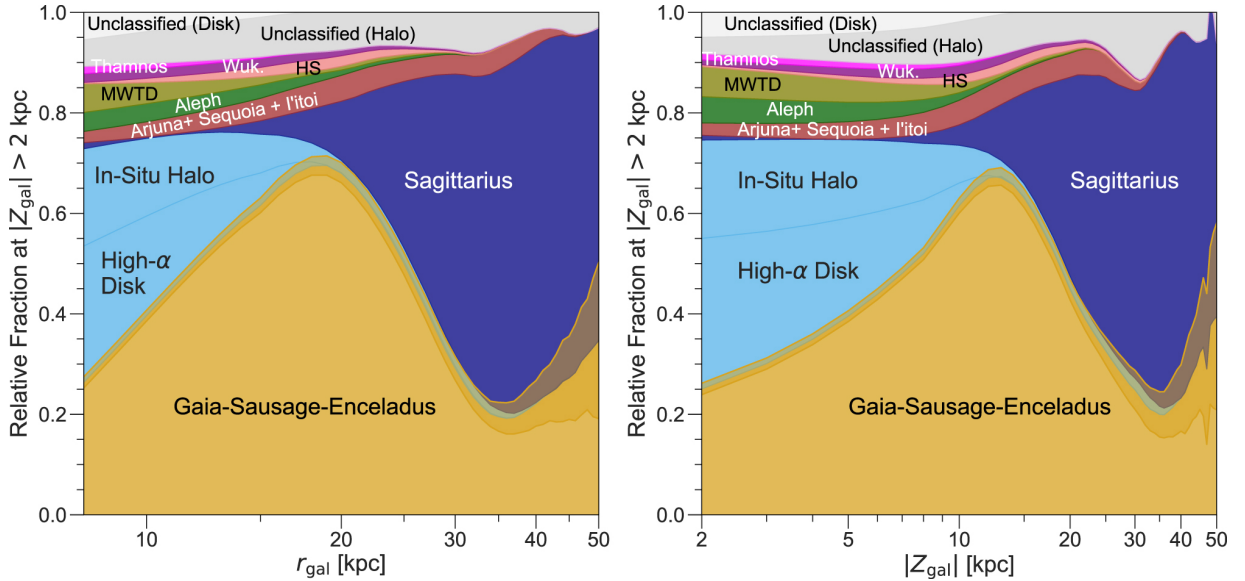


Figure 1.6: Relative fraction of stars belonging to MW structures (stars with similar energies, angular momenta, and actions) as a function of the distance from the Galactic centre (r_{gal} , *left*) and the plane ($|Z_{\text{gal}}|$, *right*), out to 50 kpc. The expected contribution from each structure is colour-coded. This plot shows that the majority of the stars in the inner halo are formed in-situ or are associated either with the high- α -disc or with the Gaia-Sausage-Enceladus merger event, whereas more distant stars are predominantly related to the Sagittarius dSph and its stream. *Image credit:* Figure 19 in [Naidu et al. \(2020\)](#). Reproduced by permission of the authors and the American Astronomical Society (AAS) journal.

1.5 Star clusters, dwarf galaxies, and streams as probes of stellar and Galactic evolution

Our Galaxy contains and is surrounded by a large number of smaller systems which constitute the basis of its baryonic stellar content, and serve as donors of stellar populations in a variety of evolutionary states (e.g., [Searle & Zinn, 1978](#); [White & Rees, 1978](#); [Côté, Marzke, & West, 1998](#); [Bullock & Johnston, 2005](#); [Oser et al., 2010](#)). The interactions between the MW and these smaller systems is predominantly ruled by gravity, which is the most important force in astrophysical systems at different scales (e.g., for star clusters, galaxies, and clusters of galaxies). But numerous and notable differences exist between these systems, as seen in their stellar, gas, and dark matter content, their formation, and their dynamical and chemical evolution. [Figure 1.8](#) shows their differences in terms of their absolute brightnesses, physical sizes, and distances from the Sun. Another significant difference comes from their dynamics, as two-body interactions of stars are important in driving the dynamical evolution of star clusters (hence they are considered “collisional”), whereas in galaxies, stars are typically more separated (and interact less often, as collisionless systems), mainly moving collectively in the gravitational field.

Star clusters are considered ideal laboratories for stellar dynamics and evolution, characterized by containing stars with similar properties (e.g., metallicities and ages) and for lacking dark matter. Two main types of star clusters are found in the Universe: open clus-

1 Introduction

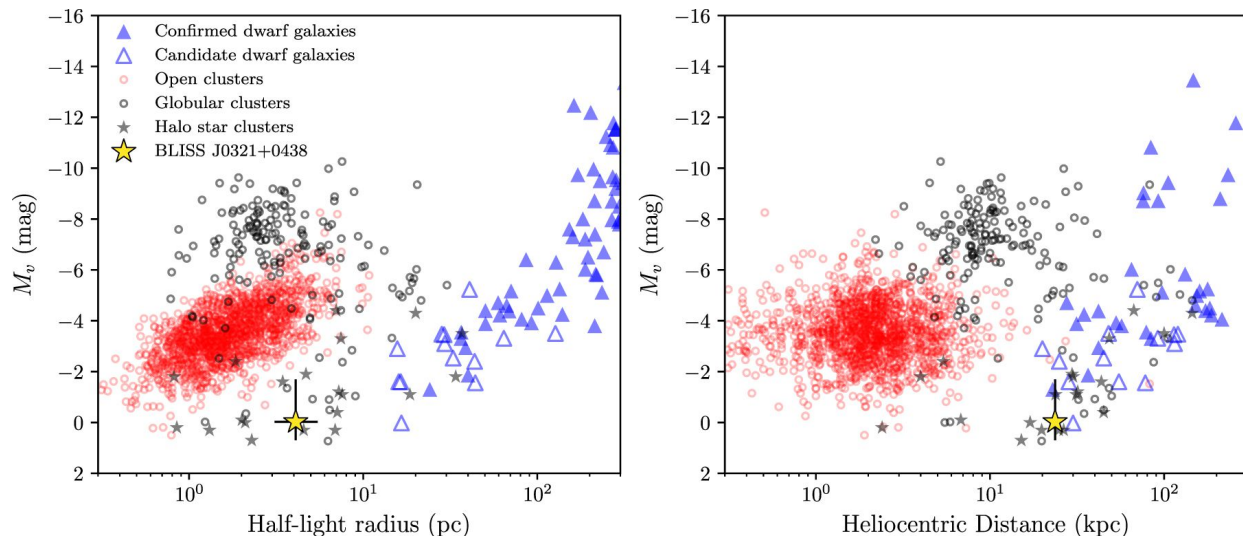


Figure 1.7: Absolute magnitude M_V as a function of physical size (*left* panel) and heliocentric distance (*right* panel) for resolved stellar systems in and around the MW. In these panels, globular and open clusters of the MW are shown as black and red circles, whereas recently discovered halo clusters are represented with black stars. Local Group dwarf galaxies are depicted as blue triangles (filled for confirmed dwarfs, and open for candidates without firm classifications). The yellow star indicates the position of the recently discovered faint halo cluster BLISS J0321+0438 (BLISS 1). The catalogues used in these plots are those compiled by [Mau et al. \(2019\)](#). The differences between open clusters, globular clusters, and dwarf galaxies based on the depicted parameters are mostly clear except for faint, extended, and distant stellar systems where the limit between globular clusters and dwarf galaxies blurs. *Image credit:* Figure 2 from [Mau et al. \(2019\)](#). Reproduced by permission of the authors and the American Astronomical Society (AAS) journal.

ters are groups of stars that are loosely bound, while globular clusters are more massive and tightly bound groups of older stars that are spherically distributed ([Fall & Zhang, 2001](#); [Baumgardt, 2001](#)). Other types of star clusters include nuclear star clusters, which are the densest known clusters in the Universe located near the center of mass of most spiral galaxies ([Böker, 2010](#)), believed to have formed by gravitational interactions near the galactic centre or by merging of other types of star clusters ([Capuzzo-Dolcetta, 1993](#); [Madigan et al., 2014](#)). Because the stellar densities and masses of star clusters can be significantly different, the dynamical effects that rule their evolution can also differ. For open and globular clusters, for instance, tidal shocks¹⁷ and dynamical relaxation¹⁸ are the most relevant effects to consider (with timescales between of $\sim 10^8$ - 10^9 yr and $\sim 10^8$ - 10^{10} yr, respectively). For nuclear clusters, dynamical friction¹⁹ is the most important effect owing to their higher densities (with timescales $\sim 10^7$ yr). The characteristic dynamical timescales of these systems, combined with their masses and densities, imply that open clusters are quickly dissolved and mixed

¹⁷Tidal shocks are gravitational perturbations occurring when a cluster interacts with objects with a large mass (e.g., interstellar clouds, or passages through the Galactic plane).

¹⁸The relaxation time is defined as the time required for the stars in a system to lose all memory of their initial orbits, due to equipartition of energy.

¹⁹Dynamical friction occurs when the gravitational force in high-density stellar systems slows down the orbital motion of stars.

with field stars, whereas globular clusters display a variety of dynamical evolution states. However, all these systems are affected by tidal interactions with their environment (e.g., their host galaxy), in one way or another.

Dwarf galaxies are systems that typically host from a few thousand to a few billion stars and orbit large galaxies (which can contain hundreds of billions of stars), such as the MW and Andromeda. Their formation is commonly associated with the effects of gravitational forces in the early Universe. Notable examples of dwarf galaxies are the Small and Large Magellanic Clouds (SMC and LMC, respectively), both of which can be observed by the naked-eye in the Southern hemisphere and have been referenced for more than one millennium. Regarding the distinctions between star clusters and dwarf galaxies, several criteria have been defined based on their differences in sizes, luminosities, and masses (van den Bergh, 2008; Da Costa, 2003). The boundaries between dwarf galaxies and globular clusters, based on their absolute V -band magnitudes and their physical radii, were clear and accepted until a flood of dwarf galaxies with exceedingly low luminosities and mass-to-light ratios began to be discovered (Willman et al., 2005a,b; Torrealba et al., 2019). These faint and diffuse galaxies are described later in this section. In terms of their content, the kinematics of stars (and gas) in dwarf galaxies reveals that they tend to be completely dominated by their dark matter haloes (unlike star clusters), when adopting a Newtonian dynamics framework (e.g., Battaglia & Nipoti, 2022). But if there is one aspect that dwarf galaxies and star clusters have in common, it is that they both interact gravitationally with their host galaxy, which results in tidal features hidden by phase-space mixing that arise from their partial/total disruption.

Understanding how the interactions between clusters, dwarf galaxies, and the MW took place (when, where, and under which conditions) is one of the main goals of Galactic archaeology. In the rest of this section, I describe the main properties of clusters and dwarf galaxies, and the stellar streams that result from their tidal dissolution. Specifically, I focus on their contributions to our current understanding of the evolution of stellar populations and the MW, and the open problems associated to their use in Galactic archaeology.

1.5.1 Open clusters

Open clusters are groupings composed of up to a few thousand gravitationally bound stars formed from the collapse of giant molecular clouds, more or less at the same time and under similar physical conditions (i.e., they are simple stellar populations). Open clusters are systems typically younger than 1 Gyr (van den Bergh, 1957; Oort, Kerr, & Westerhout, 1958; Lamers et al., 2005; Anders et al., 2021) found in star forming regions of spiral and irregular galaxies, and are characterized by their low-masses ($\sim 10^2$ - $10^3 M_\odot$; e.g., Parmentier & Baumgardt, 2012) and overall low-densities ($\sim 10 M_\odot \text{pc}^{-3}$; Seleznev 2016). Numerous studies have indicated that embedded clusters account for a significant fraction of all star formation taking place in the Galaxy (Lada, Lombardi, & Alves, 2010) and in other galaxies (De Grijs, 2010; Larsen, 2010).

Because these clusters are groups of stars (initially) chemically homogeneous, and because they cover a wide range of ages and chemical compositions²⁰, open clusters are excellent laboratories for the study of stellar populations, especially in the MW where their stars can be resolved. In fact, the study of open clusters has become a backbone of research in

²⁰Within a given galaxy, however, most clusters have roughly the same metallicity.

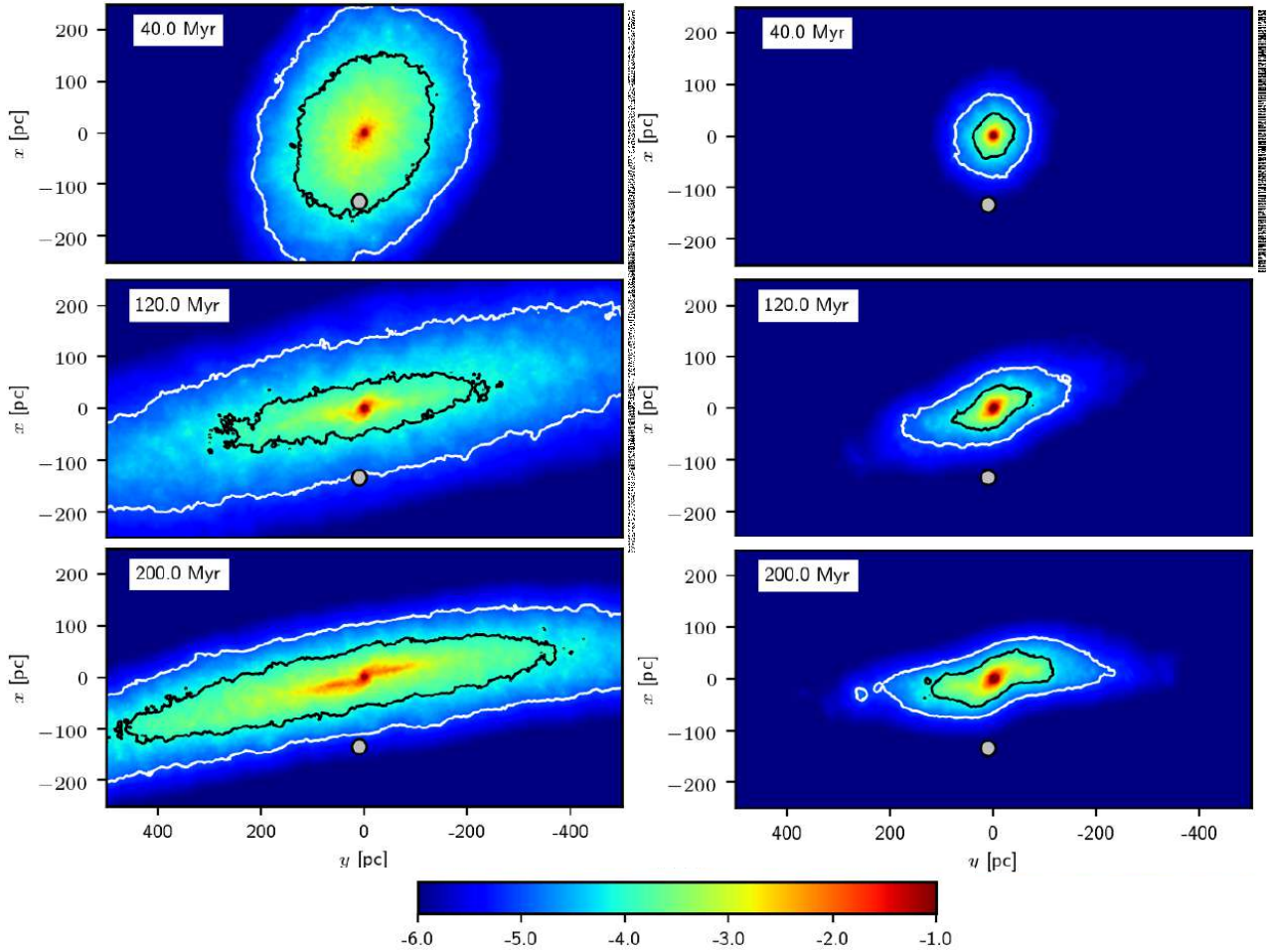


Figure 1.8: Evolution over time of the star number density in Cartesian coordinates (in the $z = 0$ plane) for a model open cluster of mass $1,400 M_{\odot}$, initial half light radius of 0.2 pc , and low star formation efficiency (33 per cent). The y coordinate is as defined positive in the direction of the Galactic rotation, and the x coordinate is negative towards the Galactic centre. The Sun’s position is marked by a large grey circle. The number density over the z plane is colour-coded in logarithmic scale (pc^{-3}). The model shown in the *left* panels is computed adopting a rapid gas expulsion, where the gas expulsion timescale τ_M is much shorter than the half-mass crossing time t_h (defined as cluster’s half-light radius over its velocity dispersion), and the *right* panels represent a cluster where gas expulsion occurs adiabatically (where $\tau_M \gg t_h$). These plots show that open clusters undergoing gas expulsion and tidal dissolution can become extended structures and lose a significant fraction of their initial stellar mass in timescales $< 120 \text{ Myr}$ (even when their initial masses are relatively high). Clusters of lower masses are expected to tidally disrupt more rapidly than those used for these simulations (under similar conditions), as shown by [Shukirgaliyev et al. \(2018\)](#). *Image credit:* Adapted from Figures 1 and 3 from [Dinnbier & Kroupa \(2020\)](#). Reproduced by permission of the authors and the Astronomy & Astrophysics (A&A) journal.

modern astrophysics with impact in numerous open issues, such as the details of the star formation process (Prisinzano et al., 2022), the assembly and evolution of the Galactic disc and other galaxies (e.g., Janes & Adler, 1982; Friel et al., 1995; Jacobson et al., 2016; Recio-Blanco et al., 2022), the kinematics of young stellar systems (e.g., Jeffries et al., 2014; Wright et al., 2019), stellar nucleosynthesis (Viscasillas Vázquez et al., 2022), and stellar evolution (Lagarde et al., 2017). In the last decade, the development of a large number of spectroscopic surveys allowed for the determination of chemical abundances, radial velocities, and other fundamental properties of stars in open clusters. The list of these surveys include, but is not limited to, the SDSS (Abdurro’uf et al., 2022), the GALAH survey (Buder et al., 2021), and the GES survey (Randich et al., 2022).

Clusters can be used to investigate the physics of transport processes occurring in stellar interiors (e.g., Magrini et al., 2021), including the impacts of rotational mixing on the chemical profile of stars (Palacios et al., 2003; Charbonnel & Lagarde, 2010; Bastian et al., 2018; Lagarde et al., 2019). In particular, they can be used to constrain the physics and efficiency of hydrodynamical transport processes of angular momentum (e.g., from photometric surveys focusing on young stars; Gallet & Bouvier, 2015; Amard et al., 2019) and chemical species in stellar interiors (e.g., the helium-to-metal enrichment ratio and lithium depletion; Cummings et al., 2017; Jeffries et al., 2017; Charbonnel et al., 2020; Tognelli et al., 2020). Also, a lithium dip has been observed in all open clusters older than ~ 200 Myr (e.g., Balachandran, 1995; Anthony-Twarog et al., 2009), which can be partially explained by a strong magnetic braking and rotation-induced mixing (e.g., Pasquini et al., 2004; Smiljanic et al., 2009) and internal gravity waves (Talon & Charbonnel, 2003). Furthermore, clusters have been used to study the effects of star spots and magnetic fields on the radius and age determination of pre-main-sequence stars (Franciosini et al., 2022), and as benchmarks to calibrate the relations between stellar mass, [C/N] ratio, age, and iron abundance for stars in different evolutionary states (Lagarde et al., 2017; Casali et al., 2019; Spoo et al., 2022). Even the properties of stellar interiors can be investigated through the study of stellar pulsation modes, through asteroseismology (Mosser et al., 2014; Vrad, Mosser, & Samadi, 2016; Gehan et al., 2018). For instance, Bossini et al. (2017) used asteroseismic observations of open clusters to probe various core-mixing scenarios of red-clump stars.

Several authors have combined precise astrometry with ground-based radial velocities, to study the kinematics of open clusters (e.g., Jeffries et al., 2014; Soubiran et al., 2018; Wright et al., 2019; Carrera et al., 2022). Da Rio et al. (2017), for instance, studied complex kinematic structures (subclusters) within young clusters, and Tarricq et al. (2021) investigated the orbital parameters, 3D kinematics, and age dependence of over 1,000 open clusters. Furthermore, by combining astrometric and kinematic information, the spiral arms of the MW can be traced using open clusters (Dias & Lépine, 2005), especially given that their mean parameters (e.g., position, kinematics, ages, and line-of-sight extinctions) are better determined than for single field stars. Becker & Fenkart (1970), for instance, used samples of clusters to trace the path of the MW spiral arms, and van den Bergh (1958) used clusters to study the evolution of the disc’s scale height. In the same vein, but more recently, Castro-Ginard et al. (2021) analysed open clusters and found evidence disfavoured classic density waves as the main drivers of the disc’s spiral structure, and implied that its nature is transient, which has also been suggested by other works using different tracers (e.g., classical Cepheids and molecular gas; Minniti et al., 2021; Colombo et al., 2022).

1 Introduction

Most stars are thought to be born in young embedded clusters that evolve dynamically over time (e.g., Lada & Lada, 2003; Porras et al., 2003; Megeath et al., 2016), and current models predict that these evolutions involve, among other effects, mass loss (Hénon, 1961) and expansion (Baumgardt, Hut, & Heggie, 2002; Gieles et al., 2010; Dinnbier & Kroupa, 2020). After star formation within its originally dense birth environment, a cluster relaxes and mass segregates (e.g., Spitzer, 1969; McMillan, Vesperini, & Portegies Zwart, 2007; Spera, Mapelli, & Jeffries, 2016), ejects stars as a result of close stellar interactions (e.g., Aarseth, 1971; Tanikawa et al., 2012; Oh, Kroupa, & Pflamm-Altenburg, 2015), and evaporates stars due to weak encounters between stars (Küpper et al., 2010). In addition, clusters lose stars by the depletion of the gas that was not consumed for the process of star formation (e.g., Lada, Margulis, & Dearborn, 1984; Baumgardt & Kroupa, 2007), which causes a sudden change of the gravitational potential of the cluster and a subsequent expansion (Goodwin, 1997; Kroupa, Aarseth, & Hurley, 2001), and by the gravitational interaction with the host galaxy (Baumgardt & Makino, 2003; Sollima, 2020). Moreover, galactic tidal forces shape the evaporated stars into tidal tails following the orbit of the cluster, and forming tidal tails that can be used to probe the gravitational potential of the host galaxy. The effects of gas expulsion and tidal dissolution for a relatively massive model open cluster are illustrated in Figure 1.8. These effects are expected to be even more prominent for clusters less massive than $< 1,000 M_{\odot}$ (Shukirgaliyev et al., 2018). In recent years, many of these extended features have been discovered, taking advantage of the exquisite astrometry of *Gaia* (see e.g. Röser & Schilbach, 2019; Yeh et al., 2019; Gao, 2020; Nikiforova et al., 2020; Sharma et al., 2020; Bhattacharya et al., 2021). The reconstruction of the kinematics and orbits of open clusters can also be used to shed light on the internal processes of heating (Gustafsson et al., 2016; Quillen et al., 2018), radial migration (Minchev, Chiappini, & Martig, 2016; Anders et al., 2017), the chemodynamical evolution of the disc, and to provide evidence for recent merger events and past accretions from outside the MW (Law & Majewski, 2010; Cantat-Gaudin et al., 2016). It is worth noting that the embedded-cluster phase lasts < 5 Myr and it is expected that the vast majority of embedded clusters formed in molecular clouds will dissolve within 10 Myr of their birth (Lada, Lombardi, & Alves, 2010), but in general terms, the timescales of cluster dissolution largely depend on their masses and orbits within the Galaxy.

Traditionally, stellar clusters are discovered as stellar overdensities (e.g., Messier, 1781). With the advent of the first *Gaia* data releases, the study of open clusters started a renaissance and the census of clusters in the MW has continuously been updated since, both in terms of new clusters discovered and of the rejection of cluster candidates in historical catalogues (e.g., Dias et al., 2002; Kharchenko et al., 2013). These studies, taking advantage of the precision and homogeneity of *Gaia*'s astrometry, have been possible through the development of machine-learning methods that systematically detect clusters in blind searches as overdensities in phase-space (e.g., Michalik et al., 2015; Cantat-Gaudin et al., 2018a, 2019; Castro-Ginard et al., 2019, 2020; Sim et al., 2019; Ferreira et al., 2020; Hunt & Reffert, 2021; Castro-Ginard et al., 2022). They have demonstrated that the detection of open clusters strongly rely on the assumptions made for the methods used, and that the census of MW clusters is still likely incomplete, especially at the faint end where remnants of disrupted clusters, and small and sparse objects can escape detection (Bica & Bonatto, 2011). This produces biases that prevent the detection of low-mass clusters, which are faint and do not

contain a large number of stars (e.g., [Moraux, 2016](#)). Moreover, these searches can result in false positives due to chance positional alignments and/or coincidental proper motions and parallaxes ([Carraro, Subramaniam, & Janes, 2006](#); [Carraro et al., 2017](#)).

One of the advantages of using open clusters to trace the structure of the MW is that, as simple stellar populations, their main properties (age, distance, extinction, and abundance of metals) can be derived from photometry in a relatively simple (albeit model dependent) manner (e.g., [Trumpler, 1930](#); [Janes & Adler, 1982](#); [Moitinho, 2010](#); [Buckner & Froebrich, 2014](#); [Cantat-Gaudin et al., 2018b, 2020](#)). In order to characterize open clusters from photometry, the most commonly used method relies on the comparison of the stars belonging to the clusters and stellar evolution models (main-sequence fitting; see e.g. [Chaboyer et al., 1996](#); [Grebel & Chu, 2000](#); [von Hippel et al., 2006](#); [Yen et al., 2018](#)). For this comparison, theoretical models representing stars of the same age and metallicity covering a wide range of masses (isochrones) are used. This is the point where the determination of the cluster parameters relies on the model, as the isochrone shapes and the computed evolutionary tracks (time evolution of a star with a given mass) depend on the input physics of the model (e.g., rotation, convective core overshooting, binary fractions, the photometric system, among others). Examples of stellar evolution models used for this purpose are the PAdova and TRieste Stellar Evolution Code (PARSEC; [Bressan et al., 2012](#)) and the Modules for Experiments in Stellar Astrophysics (MESA) Isochrones and Stellar Tracks (MIST; [Paxton et al., 2011, 2013](#); [Dotter, 2016](#); [Choi et al., 2016](#)).

Properly identifying cluster members by separating them from field (foreground or background) stars is key in reliably determining the properties of clusters, as their distribution in the colour-magnitude diagram is sensitive to various physical parameters. For instance, the presence of stars near the cluster’s main-sequence turn-off, and in the lower main sequence is important for obtaining the cluster’s age through isochrone fitting, and the width of the main sequence provides useful insights into the binary fraction assumed for the models and the interstellar reddening. Thus, missing stars in the census of cluster members, or considering field stars as part of a cluster (contamination) can directly affect the assessment of the cluster properties, especially for dissolving clusters, for clusters in crowded regions of the disc or in regions with high interstellar extinction. Identifying cluster members usually takes into account the position and proper motion of stars, together with their brightness and colours (e.g., [Malo et al., 2013](#); [Sarro et al., 2014](#); [Stott, 2018](#); [Seleznev, 2016](#)). This makes traditional methods that use maximum likelihood and Bayesian inference to determine cluster membership probabilities (e.g., [Sanders, 1971](#); [Stott, 2018](#)) work best for nearby clusters and brighter stars ([Krone-Martins & Moitinho, 2014](#); [Schmeja, 2011](#)). Machine-learning-based methods have also been used to compute updated membership lists ([Cantat-Gaudin et al., 2020](#); [Jaehnig, Bird, & Holley-Bockelmann, 2021](#)), and to characterize their astrophysical properties (e.g., [Bossini et al., 2019](#); [Dias et al., 2021](#)). Obtaining reliable member lists of open clusters is nowadays an active area of research that escapes the scope of this thesis. However, I dedicate a chapter (Chapter 2) to investigate the effects of the limitations on the age determination of young open clusters (specially younger than 150 Myr), and how this impacts empirical tests of the Cepheid period-age relation in the *Gaia* era.

1.5.2 Globular clusters

Globular clusters are spherical groups of $\sim 10^4$ - 10^6 tightly bound stars found in all types of galaxies, and in the MW they are found predominantly in the halo and the bulge. These systems are typically larger and more massive than open clusters (with radii from ~ 10 to 100 pc, and masses from 10^4 to $10^7 M_\odot$), and are characterized by being long-lived (> 10 Gyr), and metal-poor objects²¹ with high stellar densities ($\geq 10^3 M_\odot \text{pc}^{-3}$) that can survive tidal encounters and internal kinematics for over a Hubble time (Sparke & Gallagher, 2007). The traditional concept of globular clusters considered them alike with open clusters in terms of being comprised of simple stellar populations. This view, however, has been challenged since evidence of multiple stellar populations is continuously found in massive clusters, from significant light element abundance spreads that are not expected as a result of stellar evolutionary processes (e.g., in He, C, N, O, and Na), and from anticorrelations in chemical elements (e.g., C-N and Na-O; Charbonnel & Chantereau, 2016; Bastian & Lardo, 2018; Gratton et al., 2019; Milone & Marino, 2022).

A large number of globular clusters have been detected both in the MW and in external galaxies, which, together with their status as fossils of galactic evolution, make them key witnesses of accretion events contributing their stars onto the MW (e.g., Minniti et al., 2021). The current census of Galactic globular clusters, in particular, contains ~ 160 clusters²², and new entries are added to this catalogue from time to time (e.g., Koch, Kunder, & Wojno, 2017; Barbá et al., 2019; Mau et al., 2019). An example of the properties of a newly discovered cluster is provided in Figure 1.8. Up to this day, no consensus has been reached on the absolute number of clusters belonging to the Galaxy, owing to inherent complications of identifying clusters members in regions with significant extinction (e.g., towards the disc and bulge), and the challenges of recognizing cluster colour-magnitude diagrams in crowded (due to the contamination of field stars; Gran et al., 2022) and very distant regions (e.g., in the outermost Galaxy; Webb & Carlberg, 2021). Together with the detection of these systems, the structural parameters, ages, masses, positions, and kinematics of globular clusters can be determined from homogeneous datasets and dedicated studies, complementing our current understanding of these systems and their role in our Galaxy's assembly (e.g., Webbink, 1985; Harris et al., 1997; Recio-Blanco et al., 2005; Kharchenko et al., 2013; Baumgardt & Vasiliev, 2021; Vasiliev & Baumgardt, 2021). Their contribution to the hierarchical formation of the MW has been explored in numerical simulations (Kruijssen et al., 2019; Carlberg, 2020), which suggest that most of the stellar content of proto-globular clusters is in fact lost in the inner Galaxy (Baumgardt et al., 2019). Evidence of these contributions has been found in the Galactic disc, bulge, and halo, and is the product of the interaction of globular clusters with the strong gravitational potential of the MW that tear them apart as stellar tails and streams (Ibata et al., 2018; Hanke et al., 2020b; Price-Jones et al., 2020; Horta et al., 2021; Kisku et al., 2021; Martin et al., 2022a). Moreover, tightly-clumped groups of globular clusters in the action-energy space can be used to detect merger events, as was recently done for the Pontus structure, which is suggested to have originated from the accretion of a

²¹Exceptional cases of globular clusters with (super-)solar metallicities, masses $< 10^3 M_\odot$ or ages < 5 Gyr exist (Schweizer & Seitzer, 1998; Dinescu, Girard, & van Altena, 1999; Carraro, Subramaniam, & Janes, 2006; Forbes & Bridges, 2010).

²²A larger number of clusters, with significantly lower $[\text{Fe}/\text{H}]$ than observed today, is thought have existed in the past (e.g., Martin et al., 2022a).

satellite galaxy (Malhan et al., 2022).

1.5.3 Dwarf galaxies

Dwarf galaxies are the most abundant type of galaxies in the Universe. In the hierarchical structure formation scheme, these galaxies are considered the building blocks of massive galaxies (Bullock & Johnston, 2005), and the dwarfs surviving the gravitational pull of their more massive counterparts (and their remnants) are considered fossils of the formation and evolution of galaxies. Although a clear criterion to distinguish dwarf galaxies from “giant” galaxies has not been defined (e.g., in terms of luminosities or masses), a common choice to draw the line is to consider galaxies with absolute visual magnitudes M_V fainter than -18 dwarf galaxies (as adopted by Grebel, Gallagher, & Harbeck 2003 and McConnachie 2012). The Local Group hosts over 100 dwarf and satellite galaxies within a few Mpc, which are classified as dwarf irregular (dIrr), dwarf elliptical (dE), and dwarf spheroidal (dSph) galaxies²³ and, in spite of being the overwhelming majority of nearby galaxies, contain < 5 per cent of its total mass. Irregular dwarf galaxies are gas-rich systems dominated by star-forming HII regions and are typically found in low-density environments (e.g., the outer regions of galaxy clusters and in the field; Grebel, 2001a). Galaxies classified as dEs have spherical or elliptical shapes, are gas-deficient with long-lasting star formation, and are preferentially detected in high-density regions (e.g., around the Andromeda galaxy; Grebel, 2001a; Bidaran et al., 2020). Lastly, dSphs are gas-deficient and low-surface brightness galaxies (typically with half-light radii > 100 times larger than those of globular clusters of similar luminosity) with no ongoing star formation. In terms of numbers, dSph are the most numerous among the Local Group galaxies (> 83 dSph). These dwarfs, which can also contain globular clusters themselves, tend to be strongly dominated by dark matter, and manifest short- or long-lasting star formation episodes at early times, with large abundance spreads albeit low metallicities. (Grebel, 2001b). Around the MW alone, ~ 60 dwarf galaxies have been detected (McConnachie, 2012; McConnachie & Venn, 2020), most of which were discovered in the last two decades with the advent of large-scale and photometric surveys with unprecedented depth (e.g., the SDSS and the DES; Willman et al., 2005a,b; Zucker et al., 2006; Belokurov et al., 2009, 2010; Bechtol et al., 2015; Koposov et al., 2015; Torrealba et al., 2016; Luque et al., 2016; Mau et al., 2020). These satellites are classified as dIrrs and dSphs, have distances between 8 and 420 kpc (Martin et al., 2004; Irwin et al., 2007), and sizes that range from a few 10 pc to over 3 kpc (Muñoz et al., 2018; Torrealba et al., 2019).

The smallest and oldest dwarf galaxies are the so-called ultra-faint dwarf galaxies (UFDs), which are among the first galaxies formed (Frebel et al., 2010; Simon, 2019). These dwarf galaxies are the least luminous and most dark-matter-dominated objects in the Universe (thus, they have relatively large mass-to-light ratios; e.g., McConnachie, 2012; Drlica-Wagner et al., 2019), which makes them pristine laboratories for the study of dark matter (e.g., Albert et al., 2017), metal-poor stars (stars in low-mass galaxies are more metal-poor than those in higher-mass galaxies, in general; Kirby et al., 2013), and the initial conditions of the Universe. Moreover, owing to their low star formation efficiency and quenching from reionization, UFDs provide clean signatures of the formation sites of the r -process. For instance, UFDs that

²³Dwarf galaxies can also be classified as early- and late-type, based on properties such as their gas content and their star formation activity.

contain r -process enhanced stars (such as Reticulum II, Tucana III, and Grus II) can be used as evidence of r -process enrichment by neutron star mergers (Roederer et al., 2016; Hansen et al., 2020).

Since the MW is the best studied galaxy in the Universe (Bland-Hawthorn & Gerhard, 2016), it has become customary to compare its properties, in particular its dwarf galaxy population, to the results of cosmological simulations (e.g., Engler et al., 2021). This has led to one of the most serious challenges that CDM cosmologies face at small scales: an apparent lack of observed satellites at both ends of the mass spectrum, despite the large number of nearby satellites recently discovered in the MW and Andromeda (see e.g. Torrealba et al., 2019; Chandra et al., 2022). These challenges are known as the missing satellites problem and the too big to fail discrepancy. The former arises from the mismatch (of \sim two orders of magnitude) between the number of dark matter haloes predicted and the number of luminous satellite galaxies observed at the low-mass end of the satellite distributions (e.g., Moore et al., 1999; Simon & Geha, 2007). Possible solutions to this disagreement include the presence of dark matter haloes lacking baryons around massive galaxies, the existence of undetected baryonic structures (containing dark matter), and taking physical processes that remove the baryons required for star formation (e.g., reionization, photo-evaporation, and stellar feedback) into account in the simulations (e.g., Sawala et al., 2016). The too big to fail problem, on the other hand, stands at the high-mass end of the distribution of satellites (e.g., Boylan-Kolchin, Bullock, & Kaplinghat, 2011, 2012; Garrison-Kimmel et al., 2014; Bullock & Boylan-Kolchin, 2017), where more massive sub-haloes and with higher central densities are predicted, but not observed. A possible solution for this puzzle is to consider baryonic effects (such as stellar feedback) that can redistribute matter leading to shallower and cored dark matter distributions, also reducing the mass of each sub-halo (Tomozeiu, Mayer, & Quinn, 2016; Ostriker et al., 2019). In any case, increasing the number of known MW satellites and characterizing them remains one of the key tools to fully uncover the role of the physical processes that rule galaxy formation as we know it.

1.5.4 Streams

Stellar streams are long lived coherent structures that represent those rare circumstances where ensembles of stars directly trace out orbits in a galactic potential, and can be used to support the in-situ/ex-situ origin of stars in our Galaxy (e.g., Newberg & Carlin, 2016). As already mentioned, streams of stars are the outcome of the gravitational disruption of smaller systems with a variety of physical properties and from different galactic environments, and thus, serve as powerful probes of galaxy formation processes supporting the standard Λ -CDM cosmological model (Peebles, 1965; Blumenthal et al., 1984; Springel et al., 2008). In the MW, these streams originate from the accretion of systems with a varied range of masses, ranging from dwarf galaxies as massive as the Sagittarius dSph (Ibata, Gilmore, & Irwin, 1994; Belokurov et al., 2006; Vivas & Zinn, 2006), the Gaia-Sausage-Enceladus (Helmi et al., 2018; Belokurov et al., 2018b) or the Sequoia galaxies (Myeong et al., 2019), to star clusters that concluded their dissolution or are undergoing tidal disruption (Grillmair, 2006; Jordi & Grebel, 2010; Borsato, Martell, & Simpson, 2020; Shipp et al., 2020; Martin et al., 2022a). An example of the study of globular clusters as potential progenitors of a set of stellar streams is illustrated in Figure 1.9, based on the work of Bonaca et al. (2021). The

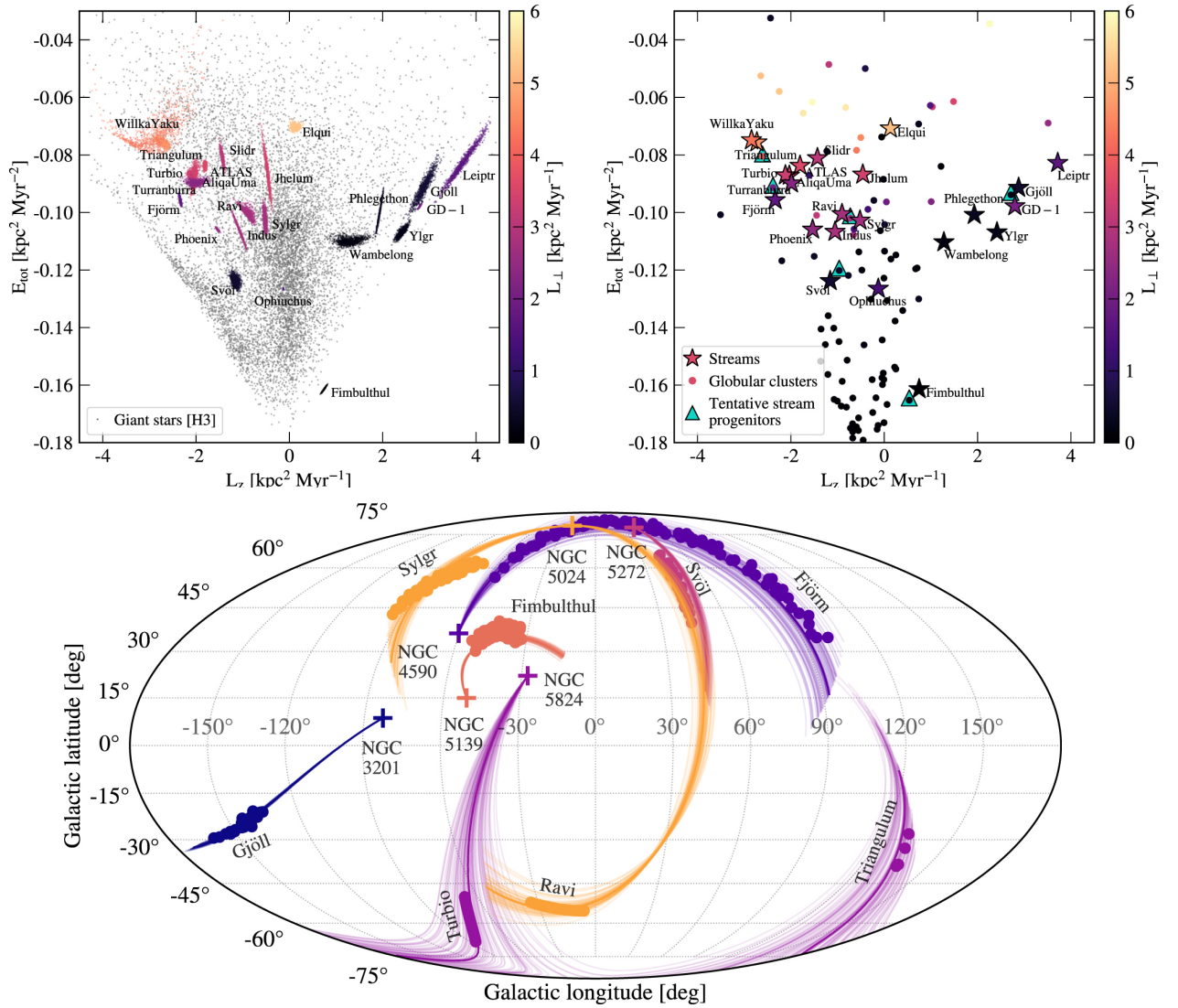


Figure 1.9: *Top left panel:* Orbital energy E_{tot} and vertical angular momentum L_z distribution for the sample of stellar streams studied by Bonaca et al. (2021), colour-coded by the average orthogonal component of the angular momentum. Stars from the field are shown as black dots. *Top right panel:* Median E_{tot} and L_z of the same stellar streams compared to those of globular clusters (black circles). *Bottom panel:* Sky positions (in Galactic coordinates) of streams (circles) and globular clusters (crosses). The coloured lines represent the orbits derived for the clusters. These plots are used to conjecture the plausible progenitors of the observed streams based on the coherence of their persistent features in energy, angular momentum, and spatial distribution with those of the clusters. *Image credit:* Figures 1 (top panels) and 4 (bottom panel) from Bonaca et al. (2021). Reproduced by permission of the authors and the American Astronomical Society (AAS) journal.

figure shows that the coherence in the energy, angular momentum, and spatial distribution of the stream members can be compared with those of globular clusters to assess their origins.

Throughout the last few decades, solid observational evidence has been found confirming the pivotal role of stellar streams to uncover the history and nature of the MW and its neighborhood. First, streams are (currently) detected and characterized from the complement of precise astrometric surveys (e.g., *Gaia*), deep photometric surveys, and spectroscopic surveys providing radial velocities and chemical abundances (Ibata et al., 2018; Shipp et al., 2018; Li et al., 2019, 2021; Ji et al., 2021; Mateu, 2022; Yang et al., 2022). The live view of the hierarchical formation that streams provide can be used for diverse science cases. Malhan, Valluri, & Freese (2021), for instance, used stellar streams from disrupting globular clusters to probe the nature of dark matter, as the morphological and dynamical properties of these streams are sensitive to the central dark matter density profile and the mass of the parent satellite. Other authors have used these persistent features as probes of dark matter sub-haloes (e.g., Ibata et al., 2002; Yoon, Johnston, & Hogg, 2011; Carlberg, 2012; Johnston & Carlberg, 2016; Bovy, Erkal, & Sanders, 2017; Erkal, Koposov, & Belokurov, 2017), or in a different vein, to test alternative theories of gravity (e.g., Kesden & Kamionkowski, 2006; Thomas et al., 2017). Stellar streams have also been used for other purposes, such as measuring the rotation of the MW bar (Hattori, Erkal, & Sanders, 2016; Pearson, Price-Whelan, & Johnston, 2017), shedding light onto the total matter surface density profile in our Galaxy (Erkal & Belokurov, 2015; Widmark et al., 2020), measuring the three-dimensional velocity of our sun (Malhan, Ibata, & Martin, 2020), detecting MW mergers (Bonaca et al., 2021; Malhan et al., 2022), understanding structure formation in the very early Universe (Martin et al., 2022a), identifying and characterizing wide binaries (Peñarrubia, 2021), and examining the too big to fail discrepancy (Shipp, 2022).

Identifying and describing stars in streams can be a challenging task (e.g., Brauer et al., 2022), especially at large distances (> 20 kpc). This is mostly due to the scarcity of tracers at large distances and the large uncertainties in the distance determinations for stars in regions where *Gaia* parallaxes (and proper motions) decrease their precision (in addition to other related instrumental limitations). Chemodynamically characterizing outer halo stars and assessing their cosmic origin from potential associations with clusters, dwarf galaxies, and streams, is one of the main goals of present-day Galactic archaeology studies, and is part of the motivation of this thesis.

1.6 Variable stars

Variable stars are objects whose observed brightness change significantly over time. In astronomy, many different types of stellar (and non-stellar) variability phenomena have been detected and studied throughout the years; from AGNs to pulsating variable stars, and from asteroids to eclipsing binaries and planetary transits. The variability classes (*intrinsic* or *extrinsic*) are defined based on the root that causes the variability, that is, if a star owes its variability to processes inherent to the star (intrinsic variables) or to phenomena external to it (extrinsic variables). Variable stars can be further classified as periodic, semi-regular, or irregular variables, according to the repeatability with which these changes occur.

Pulsating variable stars periodically expand and contract their surface layers, changing their sizes, effective temperatures, and spectral properties in the process. Thus, these stars

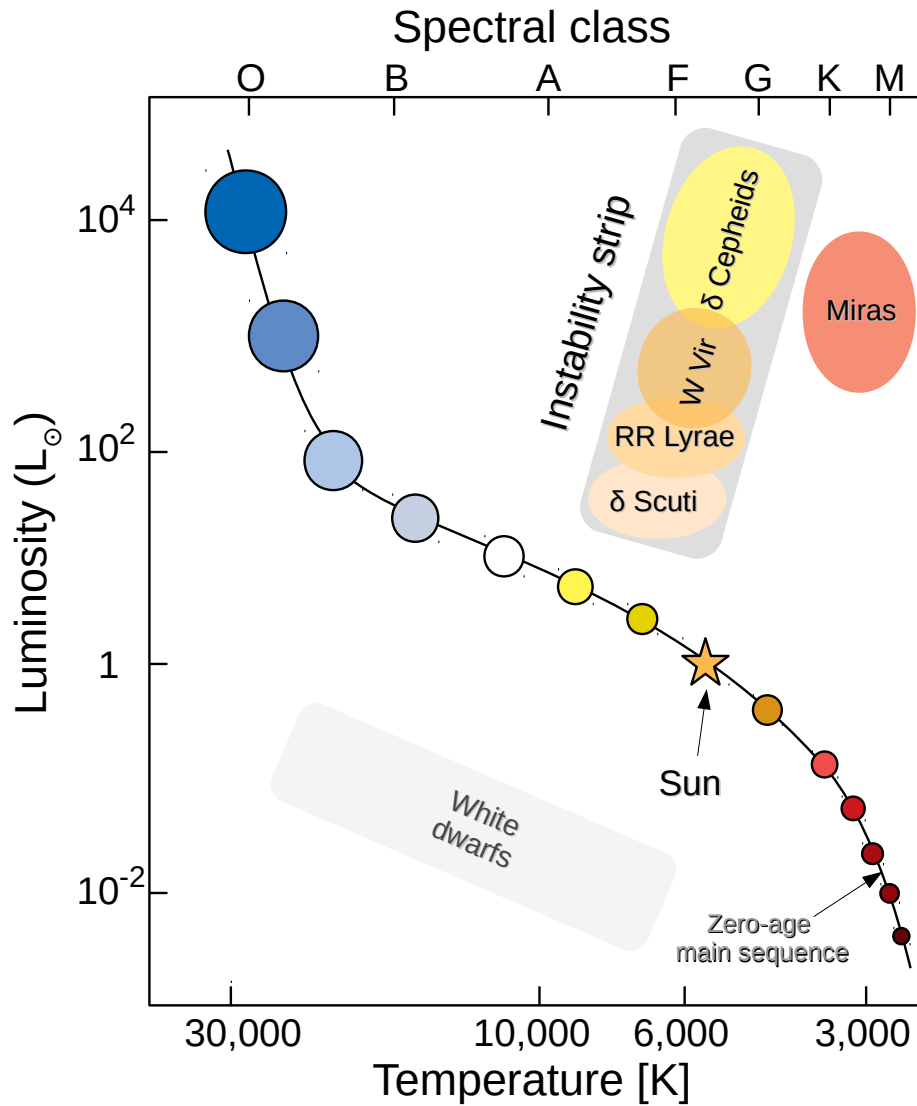


Figure 1.10: Schematic illustration of the position of the IS over the zero-age main sequence in the HR diagram. The figure depicts the approximate location of δ Cepheids and RRLs within the IS (among other types of variable stars), as well as other stellar objects such as the Sun (at $L = 1 L_{\odot}$ and $T \sim 5,700$ K), Miras, and white dwarfs. The star sizes displayed are not to scale, and the colours are only used for illustrative purposes.

1 Introduction

are classified as intrinsic variables. Stellar pulsations are present throughout the HR diagram, and therefore, numerous subdivisions belong the class of pulsating variable stars. For instance, they can be divided into radial and non-radial pulsators. Other criteria to classify these stars include their masses, their evolutionary status, and the excitation mechanism that drives their pulsations. Of particular importance is the instability strip (IS) above the MS, a region in the HR diagram in which pulsating variable stars with a wide range of masses lie (e.g., RR Lyrae stars, W Virginis stars, classical Cepheids, and RV Tauri stars). A schematic representation of the location of the IS in the HR diagram and the stars that it contains is depicted in Figure 1.10. In this thesis, I will focus on two of the most commonly used types of variable stars, both of which are classified as radially pulsating variable stars: classical Cepheids, and RR Lyrae stars.

For most stars, considering energy generation only (ϵ mechanism) is not sufficient to excite pulsations, hence one must consider energy transfer as the main mechanism responsible for stellar pulsations. In order for pulsations to be triggered, some layers of the star must gain energy during compression, and then release said energy during expansion. These layers are typically associated with H and He partial ionization zones. During the compression of a star, the rise in temperature causes the opacity of the normal layers of a star to decrease. This is implied by the following equation:

$$\kappa_{\text{R}} \propto \rho^n T^{-s}, \quad (1.2)$$

where κ_{R} is the Rossland mean opacity, ρ is the star's density, T is its temperature, and n and s are coefficients that determine the degree of opacity (where $n \sim 1$ and $s \sim 7/2$ for free-free absorptions in a non-degenerate, fully ionized gas). However, this behaviour is not valid throughout the star, as it features a few bumps in opacity at different layers (specially where $T \sim 20,000$ and $40,000$ K). In these regions, the trend is for the opacity to increase with increasing temperature ($s < 0$), which is caused by the ionization of H and the partial ionization of He. This increase in the opacity is known as the κ mechanism (Cox & Whitney, 1958; Baker & Kippenhahn, 1962; Zhevakin, 1963), and the increased ability of these layers to gain heat during compression is called the γ mechanism (Cox et al., 1966). The increase in opacity prevents the radiation flow from escaping, increasing the radiation pressure and subsequently leading to a “lift” of these layers. The expansion of the star then produces a decrease in opacity and a release of the damped radiation. As a consequence, the star contracts by gravity, triggering a new cycle of the pulsation. These mechanisms (sometimes referred as the *heat mechanisms* of a star) operate together and suffice to explain the excitation of pulsation instabilities of classical variable stars falling in the IS. An exhaustive description of the physics of stellar pulsation theory is beyond the scope of this thesis, and I refer the reader to the work by Catelan & Smith (2015) and the references therein for more information.

The term *light curve* is often used to characterize the brightness fluctuation of variable sources. A light curve represents the change in apparent magnitude as a function of time. If the variable object changes its brightness with a known period P , the phase of an observation can be computed from

$$\phi = \frac{t - T_0}{P} - \left[\frac{t - T_0}{P} \right], \quad (1.3)$$

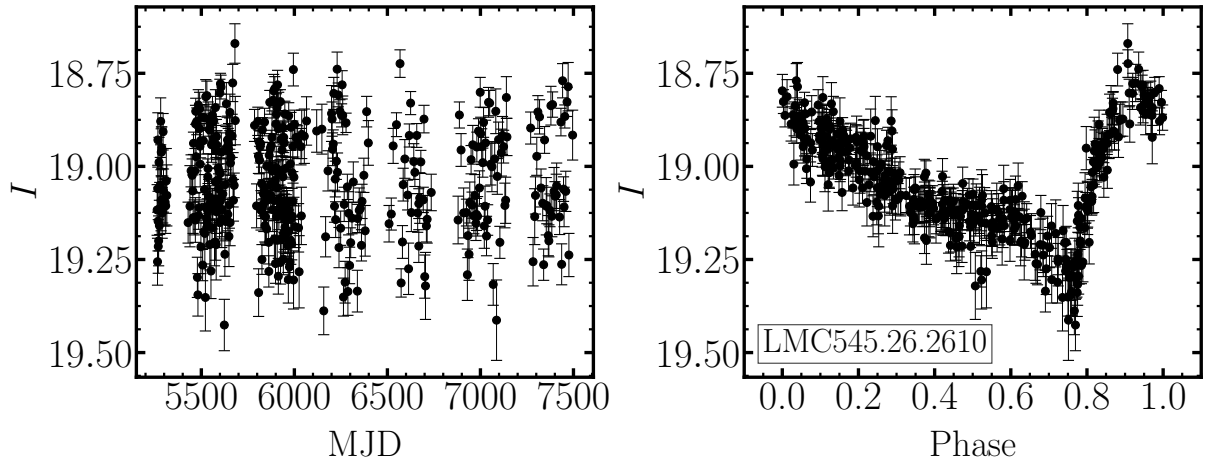


Figure 1.11: The light curve of the RR Lyrae star LMC545.26.2610, based on observations from the OGLE survey (Soszyński et al., 2016). In the *left* panel, the magnitude of this RR Lyrae star in the I -band is plotted vs. the Modified Julian Date (MJD) of the observations. In the *right* panel, the light curve of LMC545.26.2610 is shown phased with a period of 0.59839 d.

where ϕ is the phase, t is the time of a given observation, and T_0 is an adopted reference time (often chosen as the time of maximum light; Hoffmeister & Kholopov, 1985). The second term in this equation represents the integer part of the first term. Thus, from this definition, the phase is defined as the portion of $(t - T_0)/P$ after the decimal point, and a phased light curve shows the change in brightness of a source during a single cycle by assigning a ϕ value from 0 to 1 to each observation. This also means that, if a variable object varies with a period P of one day, a phase of 0.5 will represent its brightness 12 hr after the adopted start of its cycle ($P/2$). Figure 1.11 shows the light curve in the I -band of an RRL from the LMC (LMC545.26.2610), as an example of the phasing of a light curve.

One of the most important steps in the analysis of photometric or spectroscopic observational data of variable sources is the determination of their period (or multiple periods). Given that the data is commonly affected by various effects (and by different degrees), characterizing the time series that generate a light curve is a challenging task. For instance, the data are often irregularly sampled and have data gaps of different lengths, due to observation constraints. Not only that, but the available number of data points varies from study to study, and determines the precision with which the light curve variations are described (in particular for period determinations; e.g., Huijse et al., 2018). Furthermore, light curves are affected by correlated noise due to observations taken under different conditions (e.g., atmospheric conditions, changing air-mass, and other systematics; Pont, Zucker, & Queloz, 2006). In addition, the data are affected by several other noise sources, from background and photon noise to heteroscedastic errors (i.e., data that can be modeled with variance that changes between samples; Akritas, 1997).

Due to the irregular sampling of the data, conventional techniques (such as the Fast Fourier Transform, or FFT) cannot be directly applied in astronomical light curves for period determination. A variety of period determination methods have been developed to tackle this

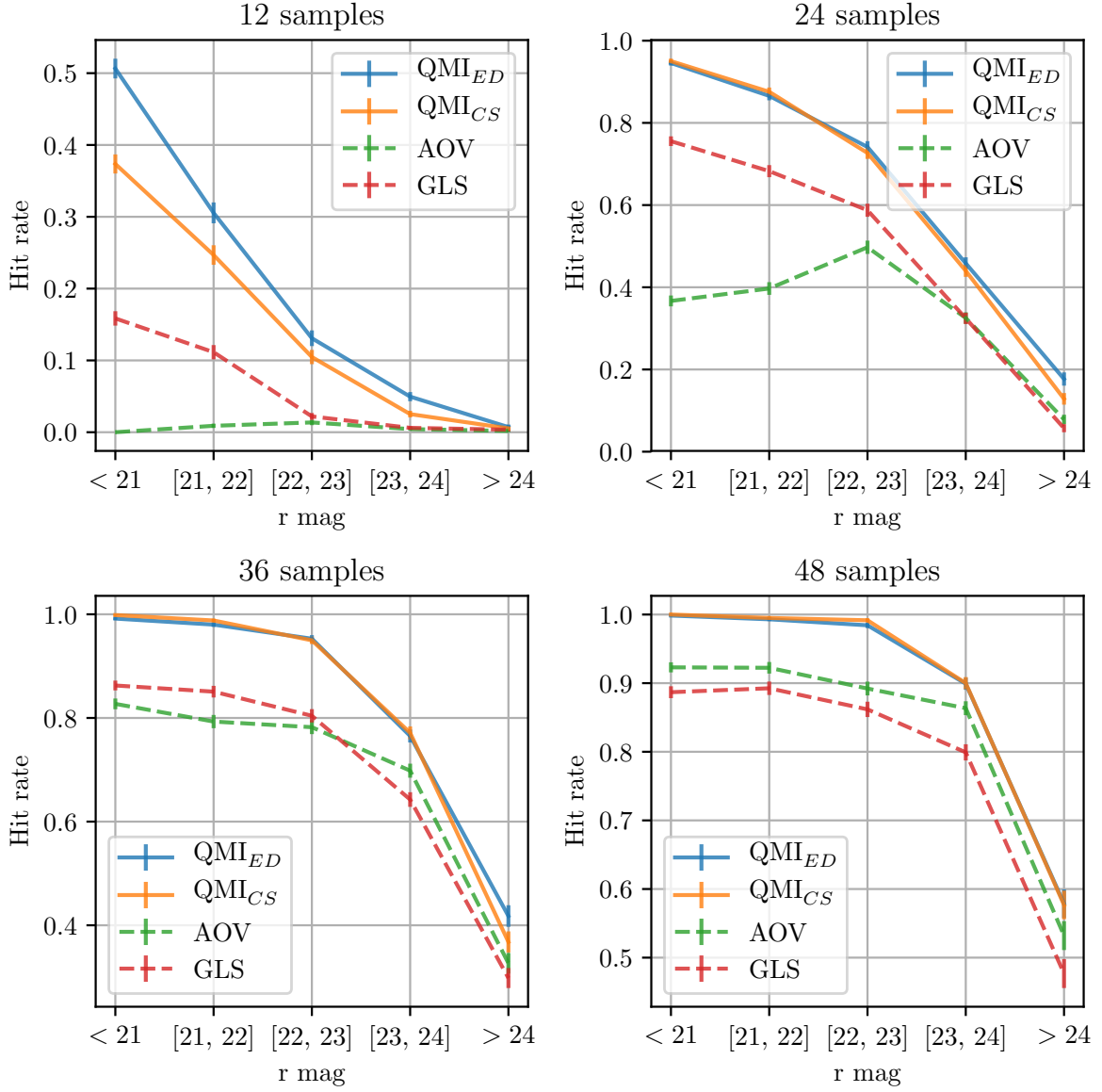


Figure 1.12: Ability to recover the true period of RRLs (hit rate) as a function of their mean r -band magnitude, for different period detection methods. The four panels represent the hit rate for ab-type RRLs with light curves containing 12, 24, 36, and 48 data points. These plots show that the Quadratic Mutual Information method (based on the Euclidean distance, ED, and the Cauchy-Schwarz divergence, CS) outperforms traditional period detection methods (the AoV and the GLS) regardless of the number of available observations. *Image credit:* Figure 7 from [Huijse et al. \(2018\)](#). Reproduced by permission of the authors and the American Astronomical Society (AAS) journal.

problem, and have been specifically employed on astronomical data (Graham et al., 2013a). Most of these techniques rely on selecting the period of the source from a *periodogram*, i.e., a diagram that depicts the goodness-of-fit of a period in contrast to other the trial values. Among the so-called parametric methods, the most widely used is the Lomb-Scargle (LS) periodogram (Scargle, 1982), which is equivalent to fitting sinusoidal models to the light curves and has been generalized to take into account more complex models (e.g., Truncated Fourier series; Palmer, 2009) and heteroscedastic errors (generalized LS, or GLS; Zechmeister & Kürster, 2009). These generalizations make the method less susceptible to effects associated to the sampling of the time series, such as aliasing (which occurs when the observations are coupled with the period nature of the source). Additional methods that fall into this category are based on Fourier fitting and Fourier-likelihood periodograms (e.g., Kovács & Kupi, 2007; Murakami et al., 2022) and the use of autoregressive moving averages (Kelly et al., 2014). Examples of non-parametric methods are the Phase Dispersion Minimization (Stellingwerf, 1978), the Analysis of Variance periodogram (AoV; Schwarzenberg-Czerny, 1996), and the Minimum String Length technique (Clarke, 2002), which do not rely on sinusoidal functions to model the data, but instead optimize a metric on the phase diagram of the light curves. Other non-parametric methods rely on information theory criteria. Zucker (2016), for instance, developed a statistical criterion based on the the cumulative distribution of the folded light curve, which outperforms the LS in sparsely sampled light curves. Other examples of these techniques are the Conditional Entropy periodogram (CE; Graham et al., 2013b), the Correntropy Kernelized periodogram (Huijse et al., 2012; Protopapas et al., 2015), and the Quadratic Mutual Information criterion (QMI; Huijse et al., 2018). The latter focuses on maximizing an indicator called the Cauchy-Schwarz QMI (e.g., Principe, 2010) between the phases and the magnitudes of a light curve to estimate the period, and has shown to outperform the generalizations of the LS and AoV periodograms when applied to simulated RR Lyrae stars and Cepheids multiband data. This is shown in Figure 1.12. The better performance in recovering the true period of the sources (hit rate) is significant for light curves that are composed of fewer than 30 observations, and is particularly relevant for the work presented in Chapter 3.

1.6.1 Classical Cepheids

Among the most studied types of variable stars are classical Cepheids, also known as δ Cepheids or type I Cepheids. These stars are luminous population I variables that lie in the IS, typically pulsating in the fundamental mode or in the first overtone, and with spectral types ranging from F-type (for the faintest Cepheids, with $M_V \sim -2$) to G or K type for the brightest Cepheids ($M_V \sim -6$; see e.g. Turner, 1996; Catelan & Smith, 2015). Classical Cepheids are stars more massive than the Sun that evolved from MS stars falling into the category of intermediate-mass stars, with masses between 2 and $20 M_\odot$. This range is often more restricted to $4\text{--}9 M_\odot$ for Cepheids in the MW. Overall, these stars are metal-rich and have (metal) abundances close to Solar (Lemasle et al., 2013) in our Galaxy, meanwhile in systems where the young stellar population is more metal deficient than in the solar neighborhood (e.g., in the Magellanic Clouds), classical Cepheids are more metal-poor.

The pulsation of classical Cepheids is driven by the κ and γ mechanisms. Thus, the region of the Cepheids where helium transitions from being singly to doubly ionized plays a crucial

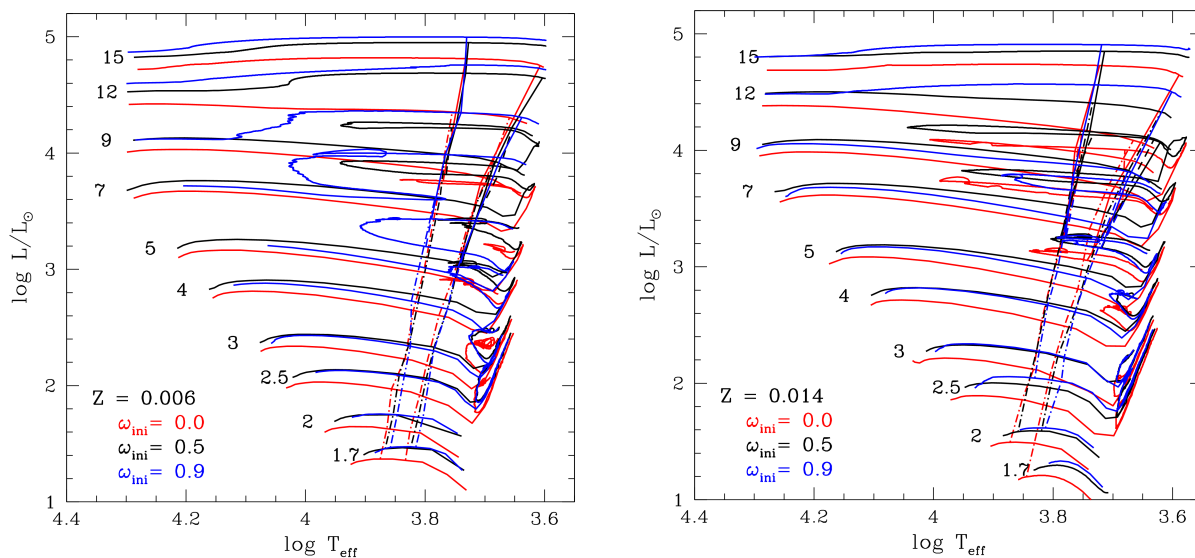


Figure 1.13: Theoretical evolutionary tracks (solid lines) and IS boundaries (dashed lines) from the models used by [Anderson et al. \(2016\)](#). These models are computed for stars with masses between 1.7 and $15 M_{\odot}$, for a system with different initial rotation rates (ω_{ini} , known alternatively as Ω_{ini}), and with initial Z of 0.006 and 0.014 (*left* and *right*, respectively). The initial rotation rate ω_{ini} is defined as $\omega_{\text{ZAMS}}/\omega_{\text{crit}}$, where ω_{ZAMS} is the surface angular velocity in the zero-age main sequence (ZAMS) and ω_{crit} (or Ω_{crit}) is the critical angular velocity (see e.g. [Georgy, Meynet, & Maeder, 2011](#)). Thus, solid lines $\omega_{\text{ini}} = 0$ represent models without rotation, and $\omega_{\text{ini}} = 0.5$ and 0.9 represent models with an initial rotation of 50 and 90 per cent of the critical rate. This figure shows that the expected number of IS crossings (including blue loops) depends on the initial mass, metallicity, and rotation rate of stars. *Image credit:* Figure 1 from [Anderson et al. \(2016\)](#). Reproduced by permission of the authors and the *Astronomy & Astrophysics (A&A)* journal.

role in the pulsation of the star. The pulsation periods of most δ Cepheids are often in the range 1-100 d, although longer and shorter periods have also been observed (e.g., [Ulaczyk et al., 2013](#)).

Evolution

The lifetimes of δ Cepheids are short. The ages of these relatively young stars range between $\sim 10^7$ yr (10 Myr) for the brightest and most massive Cepheids, to a few 10^8 yr (100 Myr) for the least massive ones. Thus, classical Cepheids are commonly found in systems and regions that have undergone recent star formation episodes (e.g., the MW disc and nearby galaxies that contain young stars, such as the Magellanic Clouds).

Mass is the property that defines the evolution of stars on and after the MS. Stars with masses in the range 2-20 M_{\odot} can cross the IS many times during their post-MS evolution, as shown in [Figure 1.13](#). After core hydrogen exhaustion, the progenitors of classical Cepheids evolve off the MS to the red giant branch (RGB). This constitutes their *first crossing* through the instability strip, from the blue (hotter) to the red (cooler) side of the HR diagram.

Owing to its largely dynamical nature, the overall contraction phase that intermediate-mass stars undergo immediately after the end of the MS (before the first crossing) takes place remarkably fast. For this reason, prominent gaps are found at the upper main sequence in photometric studies of open clusters, near the so-called *turn-off point* (e.g., [Eggen & Sandage, 1964](#); [Racine, 1971](#); [Sandquist, 2004](#)). As the inert core of a Cepheid progenitor progressively contracts, the hydrogen burning layer heats up and becomes thinner and, at the same time, the outer layers of the star expand. This shell-narrowing phase, involving a change of the position of the star in the HR diagram toward the RGB locus, occurs quickly. This phase lasts of order 2×10^6 yr ([Catelan & Smith, 2015](#)) for a star of mass $5 M_{\odot}$, which is less than 3 per cent of the total MS lifetime of the star. Thus, the first IS crossing occurs at a comparatively high evolutionary speed. This explains the dearth of stars between the MS turn-off and the RGB in the CMD of open clusters, and is the reason why relatively few classical Cepheids are expected to be observed at this stage in their evolution. This feature is known as the “Hertzsprung gap” ([Hoyle, 1960](#)).

After the initialization of helium burning in the core, intermediate-mass stars experience internal changes that carry them from the red giant region to the blue in the HR diagram, and back to the cooler regions after reaching the hottest points of these blueward excursions. As a consequence, prominent *blue loops* characterize the He burning phase in intermediate-mass stars. The blue loops involve repeatedly crossing the instability strip until the end of helium burning in their cores. These crossings normally occur at least a second and third time (*second* and *third crossing*), which once again gives rise to classical Cepheids. For instance, the theoretical evolutionary path of a $5 M_{\odot}$ star that becomes a classical Cepheid crosses the IS on its way to the RGB region (first crossing), during the blue ward loop as it fuses helium in its core (second crossing), and back to the red toward the AGB (third crossing). The luminosity of the blue loops is higher for higher mass stars (e.g., [Caputo et al., 2005](#); [Anderson et al., 2016](#)). Other details, such as the bluest point reached in these loops and the relative duration of these tracks depend mainly on the mass of the star, its chemical composition, and the physics adopted in the evolutionary model (e.g., [Bertelli, Bressan, & Chiosi, 1985](#); [Bono, Castellani, & Marconi, 2000](#); [Bertelli et al., 2009](#); [Halabi, El Eid, & Champagne, 2012](#)). In [Figure 1.13](#), the dependence of the IS crossings and the presence of blue loops on stellar mass, rotation, and metallicity is clearly visible.

Classical Cepheids as standard candles

Distance is undoubtedly one of the most important parameters in astronomy, as we rely on distance determinations of stars and stellar systems to reconstruct the shape and dimension of the Galaxy, as well as larger structures in the Universe. Distance is simultaneously, however, one of the most difficult parameters to measure. Nearly all measurements of astronomical distances rely directly or indirectly on the principle of triangulation²⁴. To estimate the distance to stars in our Galaxy, for instance, a purely geometrical method is the most commonly used: the stellar parallax (see [Section 1.2](#)). This technique is based on the change in the apparent position of a star as the earth moves from one side of its orbit to the other

²⁴As a side note, distance tracers can be separated into primary distance indicators, which provide a direct distance measurement (e.g., radar echo, main-sequence fitting, variable stars), and secondary distance indicators, which rely on the former to calibrate their distance determination methods (e.g., the Tully-Fisher relation, SNe, and the so-called fundamental-plane method).

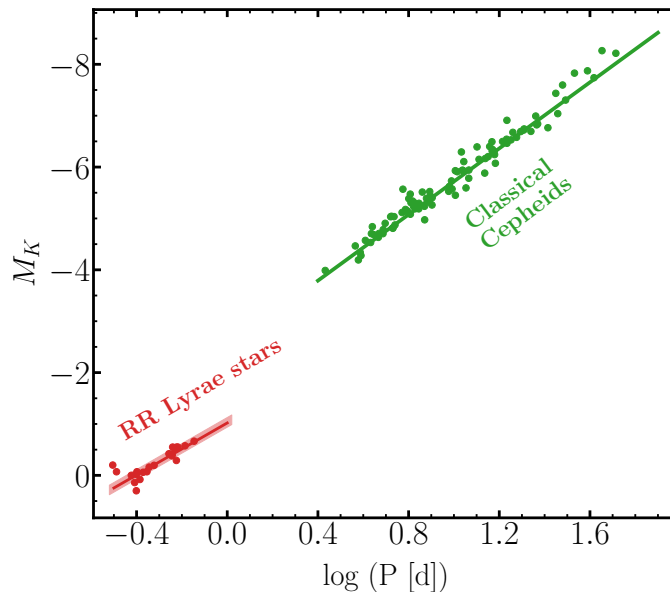


Figure 1.14: K -band PL relations of RRLs and classical Cepheids in the MW, based on the calibrations of [Muraveva et al. \(2015\)](#) and [Breuval et al. \(2021\)](#), respectively. A subsample of the stars used to derive the PL relations is also shown. The shaded area in the RRL relation depicts its shape when adopting $[\text{Fe}/\text{H}] = -2.5$ and 0.17 dex (the metallicity range explored by [Muraveva et al. 2015](#)), and shows that the dependence on metallicity is relatively small.

(forming a triangle of base 2 Astronomical Units). However, the stellar parallax can only be applied for relatively nearby objects with great precision, and the vast majority of all known stars are too distant for their parallaxes to be measured.

A wide variety of other methods have been developed to overcome the challenge of estimating distances to astronomical objects (see [De Grijs, 2011](#), for an exhaustive description). Some of these methods also rely on geometry as a means to derive distances (similar to the method of parallaxes). For instance, the distance to eclipsing binary systems can be obtained by comparing their angular diameters and their linear sizes, computed from their photometric and radial velocity curves, and from surface brightness-colour relations (e.g., [Lacy, 1977](#); [Guinan et al., 1998](#); [Fitzpatrick et al., 2003](#)). Other methods rely on knowing fundamental properties of the sources to determine their intrinsic brightness, with which distances can be determined from the inverse-square law of light. These sources are categorized as standard candles, a group that encompasses both Cepheids and RR Lyrae stars.

In general, the luminosity L of a star can be computed if its radius R and its effective temperature (i.e., the temperature of a black body with the same amount of radiation) T_{eff} are known, from the equation

$$L = 4\pi R^2 \sigma T_{\text{eff}}^4, \quad (1.4)$$

where σ is the Stefan–Boltzmann constant²⁵. This is also known as the Stefan–Boltzmann law ([Stefan, 1879](#); [Boltzmann, 1884](#)). Moreover, for pulsating variable stars (and for Cepheids in particular), because the macroscopic movement of their material is responsible for the

²⁵ $\sigma = 5.6704 \times 10^{-8} \text{ W m}^{-2} \text{ K}^{-4}$.

pulsations, combining fundamental equations (e.g., the propagation of sound waves in the stellar interior and the virial theorem) allows one to derive a relation between their period and the mean (mass) density $\langle \rho \rangle$:

$$P \sqrt{\langle \rho \rangle} = \sqrt{\frac{3\pi}{2\Gamma_1 G}}. \quad (1.5)$$

This is known as Ritter’s relation (Ritter, 1879). In this equation, P is the period, G is the gravitational constant²⁶, and Γ_1 is the first adiabatic component, which is defined as $\Gamma_1 \equiv (\delta \ln P / \delta \ln \rho)$ in adiabatic conditions (i.e., $dQ/dt = 0$, where Q is the rate of heat input/loss). The right side of Equation 1.5 is also known as the pulsation constant (Q). A detailed derivation of this equation is provided by Catelan & Smith (2015). By combining Equations 1.4 and 1.5 with the definition of mass density ($\langle \rho \rangle = M/V$, where M and V are the mass and volume of the star) and bolometric magnitude M_{bol} ($M_{\text{bol}} = -5 \log(R) - 10 \log(T_{\text{eff}}) + K$, where K is a constant), and adopting sensible assumptions for simplicity (e.g., correlations between M and M_{bol} , and mass-luminosity relations), one obtains:

$$M_{\text{bol}} = \alpha \log(P) + \beta \log(T_{\text{eff}}) + \gamma, \quad (1.6)$$

where α , β , and γ are constants. This equation constitutes the foundation of the period-luminosity (PL) relation of Cepheids and its dependence on the Cepheids’ colour, as the effective temperature term can be expressed using mean dereddened colour indices. It is worth noting that the colour term β is usually small given the relatively similar color of Cepheids due to the narrow width of the instability strip. Additionally, these relations imply that Cepheids with longer periods are intrinsically brighter and have higher masses, and subsequently shorter lives. Therefore, it is more likely to observe short period Cepheids rather than long period ones, which can in turn limit the calibration of the PL relation at larger distances. The overall shape of the PL relation of Cepheids and RR Lyrae stars is shown in Figure 1.14.

Because extinction from interstellar dust can significantly dim the brightness of Cepheids (specially near the Galactic bulge) and by different amounts (differential reddening), PL relations are often employed using reddening-free Wesenheit indices (e.g., Madore, 1982; Ngeow, 2012; Carini et al., 2017), in what is called period-Wesenheit (PW) relations (e.g., Ripepi et al., 2019, 2022).

Decades of work have striven to convincingly establish the (in-)sensitivity of the PL and PW relations to metallicity, determining theoretical and empirical period-luminosity-metallicity (PLZ) and period-Wesenheit-metallicity (PWZ) relations for Cepheids (e.g., Caputo et al., 2000; Fiorentino et al., 2002; Marconi, Musella, & Fiorentino, 2005; Sandage & Tammann, 2006; Bono et al., 2010; Freedman & Madore, 2011; Bono et al., 2016; Riess et al., 2016). Overall, the metallicity is expected to affect the slope and intercept of the PL and PW relations, especially in the optical. At the same time, the metallicity dependence of the PW relations is predicted to be weak when combining different bands, particularly in the near-infrared (see e.g. Fiorentino et al., 2007; Groenewegen, 2008, 2013; Fiorentino, Musella, & Marconi, 2013; Ngeow, 2012; Di Criscienzo et al., 2013; Gieren et al., 2018). Only recently, the advent of recent large and homogeneous datasets providing exquisite astrometric

²⁶ $G = 6.674 \times 10^{-11} \text{ m}^3 \text{ kg}^{-1} \text{ s}^{-2}$.

1 Introduction

precision (e.g., *Gaia*, further described in Section 1.2) has permitted precise estimations of such dependence (e.g., Breuval et al., 2021; Breuval, Riess, & Kervella, 2022; Riepi et al., 2022).

Finally, the distance in parsecs of a Cepheid from the sun, or heliocentric distance d (or d_{H}), can be determined once its apparent magnitude m (corrected by extinction) and its absolute magnitude M (from Equation 1.6) are known, by following

$$\begin{aligned}\mu &= m - M = 5 \log(d) - 5 \\ d &= 10^{(m-M+5)/5},\end{aligned}\tag{1.7}$$

where μ is the distance modulus of the star.

The period-age relation

Given that Cepheids follow a PL relation, it is also expected that they obey period-age (PA), period-age-colour (PAC), and period-age-metallicity relations, which has served to supplement their use as tracers of young stellar populations. This results from taking into account the correlation between period and luminosity, the stellar ages predicted by evolutionary models (mass-age relation), and the mass-luminosity relation (see e.g. Kippenhahn & Smith, 1969; Meyer-Hofmeister, 1969; Bono, Castellani, & Marconi, 2000). The exact shape of these relations, depicted in Figure 1.15 as a function of metallicity and initial rotation rate, depends on the Cepheid pulsation mode, and are (broadly speaking) of the form:

$$\log(t) = a + b \log(P).\tag{1.8}$$

Indeed, from a theoretical perspective, a longer pulsation period implies a higher luminosity and stellar mass, and thus, a younger age for the Cepheid. An empirical PA relation was derived by Tammann (1970) based on Galactic Cepheids and clusters, and later on by Efremov (1978) using MW, M31, and LMC clusters. Later, Magnier et al. (1997b) obtained a new semi-empirical relation using Cepheids in the M31 star-forming region NGC 206. Other authors have used larger samples of Cepheids and followed similar approaches to derive PA relations (see, e.g., Grebel & Brandner, 1998; Efremov, 2003; Senchyna et al., 2015; Inno et al., 2015). These studies, in addition to recent theoretical approaches (Bono et al., 2005; Anderson et al., 2016; De Somma et al., 2020b), support the use of PA and PA-colour relations to supply accurate age estimates based only on a few observables.

The existence of the PA relations makes Cepheids flexible tools for tracing star formation events (in the Galaxy and beyond) and the structure of the MW (e.g., Feast et al., 2014; Dékány et al., 2015; Senchyna et al., 2015), especially given their marginal dependence on reddening, distance, and photometric calibrations for age-dating (unlike, e.g., cluster isochrone fitting), and that they can be applied to individual objects. However, strong evidence of the consistency of PA relations derived directly from stellar evolution models (considering their underlying assumptions, e.g., the width of the IS and the initial stellar rotation rate) and those from empirical methods is still missing. In recent years, the advent of surveys providing rich and homogeneous datasets (such as those described in Section 1.2)

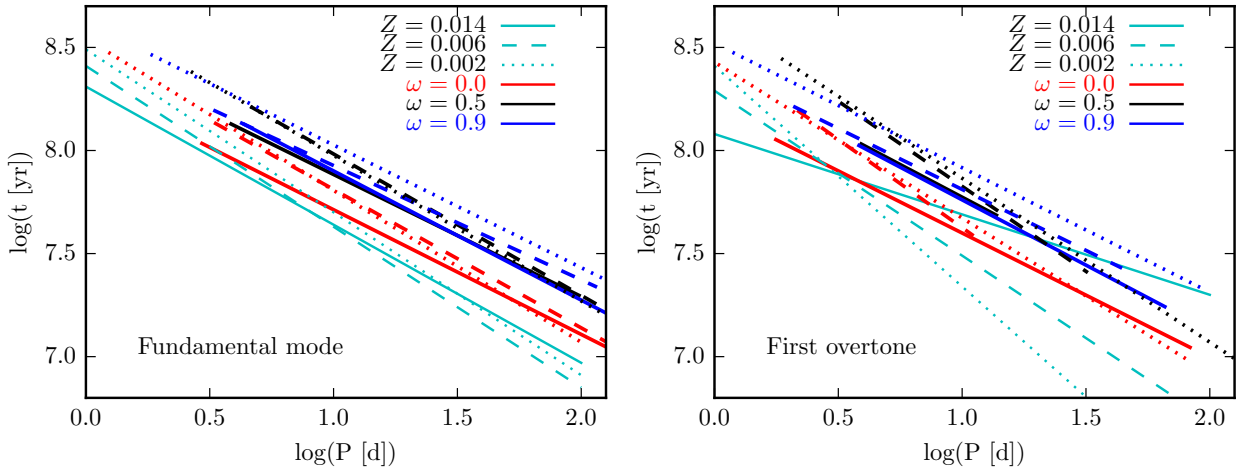


Figure 1.15: Theoretical period-age relation for fundamental-mode (*left*) and first-overtone (*right*) Cepheids, as a function initial rotation rate ω and metallicity Z . These plots show that the age of Cepheids t decreases with increasing pulsation period, and that, at a fixed period, adopting higher rotation rates in stellar evolution models results in older Cepheid ages. The cyan lines represent the period-age relations from [Bono et al. \(2005\)](#). *Image credit:* Figure 10 from [Anderson et al. \(2016\)](#). Reproduced by permission of the authors and the *Astronomy & Astrophysics (A&A)* journal.

has offered a unique opportunity to test these consistencies. This served as motivation for the work presented in Chapter 2.

On the importance of classical Cepheids for Galactic studies

Since the discovery of the PL relation (also known as the Leavitt Law) at the beginning of the 20th century ([Leavitt, 1908](#); [Leavitt & Pickering, 1912](#)), Cepheids have been extensively used as standard candles ([Jacoby, 1989](#); [Branch & Tammann, 1992](#); [Kasen & Woosley, 2009](#); [Muraveva et al., 2018](#); [Avelino et al., 2019](#); [Parada et al., 2021](#)). Owing to their intrinsic brightness (typically in the range $-6 < M_V < -2$), they are ideal distance indicators on Galactic and extragalactic scales (e.g., [Madore, 1982](#); [Madore & Freedman, 1991](#); [Caputo et al., 2000](#); [Riess et al., 2016](#)), covering distances from a few hundreds of parsecs to ~ 50 Mpc. This makes them a fundamental step of the cosmic distance ladder²⁷, as they are the most precise standard candles available for calibrating extragalactic distance indicators, allowing for precise measurements of the current expansion rate of the Universe (through the local Hubble constant H_0 ; [Riess et al., 1998, 2011](#); [Freedman et al., 2001](#)).

Extensive literature exists from decades of research aiming to calibrate the Cepheid PL and PW relation ([Feast & Catchpole, 1997](#); [An, Terndrup, & Pinsonneault, 2007](#); [Benedict et al., 2007](#); [Turner, 2010](#); [Ngeow et al., 2012a,b](#); [Ripepi et al., 2020](#); [Breuval, Riess, & Kervella, 2022](#)). In order to accurately calibrate these relations, however, it is necessary to estimate the distances to Cepheids from alternative methods. These methods include the use of geometric stellar parallaxes (e.g., [Perryman et al., 1997](#); [Benedict et al., 2007](#);

²⁷Other steps of the distance ladder include geometrical distances (e.g., via parallaxes), supernovae type Ia, and the use of the Tully-Fischer relation.

Breival et al., 2020), independent distance determination to the stellar systems that host them (see e.g. Anderson, Eyer, & Mowlavi, 2013; Chen, de Grijs, & Deng, 2017; Breival et al., 2021), and the parallax-of-pulsation technique (PoP; e.g., Fouque & Gieren, 1997; Mérand et al., 2015; Breitsfelder et al., 2016; Kervella et al., 2017; Gallenne et al., 2017, 2021; Trahin et al., 2021). The latter consists of determining the distance of pulsating stars from the correlation between their angular diameters (estimated from, e.g., interferometry), their linear diameters, and their distances. If the angular diameter is measured by applying surface brightness-colour relations, this method is referred as the Baade–Wesselink (BW) technique (Lindemann, 1918; Wesselink, 1946; Baade, 1948; Gautschy, 1987; Liu & Janes, 1990).

Because classical Cepheids are young, they have been widely used to model the disc and to trace their birthplace in the spiral arms of the Galaxy, where star formation is continuously occurring. Dékány et al. (2015), for instance, used the presence of numerous classical Cepheids in the central regions of the Galaxy to prove that it contains very young stellar populations (< 100 Myr old), and identified a young inner thin disc along the Galactic mid-plane. Their results suggested that this disc has a smooth transition from both the nuclear bulge and the Galactic thin disk that encompasses the bulge region. More recently, Chen et al. (2019) found that the stellar disc extends to ~ 20 kpc and follows the gas disc, using classical Cepheids, and Skowron et al. (2019a) built a three-dimensional map of the MW, shedding light into the warped shape of the disc and proposing a simple model of star formation in the spiral arms. Also recently, Dékány et al. (2019) conducted a census of distant classical Cepheids along the highly attenuated southern Galactic midplane using near-infrared photometry from the VVV survey (Minniti et al., 2010). Their study revealed a steep near-infrared extinction curve toward the inner bulge, and used Cepheids to trace the Galactic warp, together with Galactic disc substructures and radial age gradients of the thin disk population at the far side of the MW. In addition, Poggio et al. (2021) mapped the distribution of classical Cepheids through density variations, and found that overdensities extend the spiral arm portion on scales ~ 10 kpc from the Sun. Even further conclusions can be reached when the positions of Cepheids are combined with their chemical abundances. For instance, Cepheids have been used to show that the metallicity gradient of the Galaxy covers a broad range of Galactocentric distances (between 5 and 20 kpc; Lemasle et al., 2007, 2008, 2013; Genovali et al., 2014; Luck, 2018), and that the azimuthal variations of light element abundances are largest in the inner Galaxy (probably induced by the rotating bar) and the outer disc (e.g., Kovtyukh et al., 2022). This resembles the results from chemodynamical models of the MW (e.g., Spitoni et al., 2019; Mollá et al., 2019).

1.6.2 RR Lyrae stars

The pioneer studies of Solon I. Bailey on globular clusters (Bailey, 1902; Bailey & Pickering, 1913) led to the discovery of hundreds of variable stars that were originally labeled as *cluster variables*, and are now known as RR Lyrae stars (RRLs, or RRL for single stars). RR Lyrae variables are old (> 10 Gyr) population II pulsating variable stars in the horizontal giant branch (HB) that lie in its intersection with the instability strip, and that are found only in systems that contain old stellar populations. The period of variability of these stars spans between ~ 0.2 and 1 d (that is, between ~ 4.8 and 24 hr; see e.g. Smith, 1995;

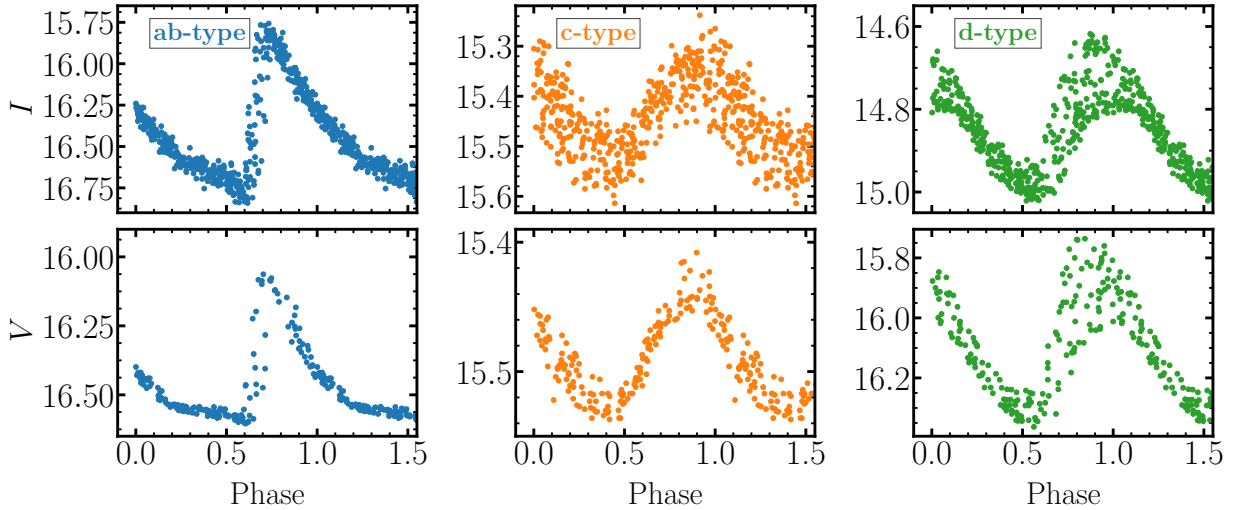


Figure 1.16: Example of light curves for the three subclasses of RRLs discussed in Section 1.6.2, in two different bandpasses (I and V). The light curves of a fundamental-mode pulsator (an RRab star; OGLE-BLG-RRLYR-09255) is displayed on the *left* panels, show their characteristic saw-tooth shapes and large amplitudes (larger for redder filters). The *middle* panels show the more sinusoidal light curves of a first-overtone RRL (an RRC star; OGLE-BLG-RRLYR-10769). The light curves of a double-mode pulsator (an RRd star; OGLE-BLG-RRLYR-10510) is displayed on the *right* panels. The data used in these plots are taken from the OGLE-IV database of Galactic bulge RRLs (Soszyński et al., 2014).

Catelan, 2009; Catelan & Smith, 2015), and their V -band amplitudes is in the range 0.2–2.0 mag (e.g., Kholopov et al., 1998; Dorfi & Feuchtinger, 1999; Abbas et al., 2014). The brightness variation of these variables declines with increasing wavelength (Stetson et al., 2014; Fiorentino et al., 2015; Bono et al., 2016). RR Lyrae variables have masses below Solar, typically between 0.6 and 0.8 M_{\odot} , diameters of 4–6 R_{\odot} (hence, they are considered giant stars; Smith, 1995), absolute V magnitudes of ~ 0.6 mag, and mean effective temperatures from $\sim 6,000$ K to 7,300 K in the red and blue edge of the IS, respectively (e.g., Catelan, Pritzl, & Smith, 2004). These stars are considered metal-poor, and their metallicity distribution (measured as their $[\text{Fe}/\text{H}]$ ratio) ranges between ~ -3 and 0 dex (see e.g. Layden, 1994; Preston, 1959; Hansen et al., 2011; Liu et al., 2020; Prudil et al., 2021; Crestani et al., 2021a; Dékány, Grebel, & Pojmański, 2021; Fabrizio et al., 2021).

Nowadays, RRLs can be split mainly into three sub-groups, according to their pulsation properties:

- ab-type RRLs, or RRab stars, combine two of the sub-classes defined by Bailey (1902), and pulsate in the fundamental mode (Schwarzschild, 1940). These stars have luminosity variations (amplitudes) in the V -band ranging from ~ 0.3 to 1.5 mag. The variation in observed radial velocities for RRab stars are of the order of 40–70 km s^{-1} (e.g., Sesar, 2012; Catelan & Smith, 2015). For this subclass, both the light curves and the radial velocity curves are “saw-tooth” shaped, that is, with steep rises and a gradual decline. An example of the light curve of an RRab star is provided in Figure 1.16. The majority (~ 90 per cent) of the RRLs known fall into this subclass (e.g., Bailey, 1902; Smith, 2004; Abbas et al., 2014).

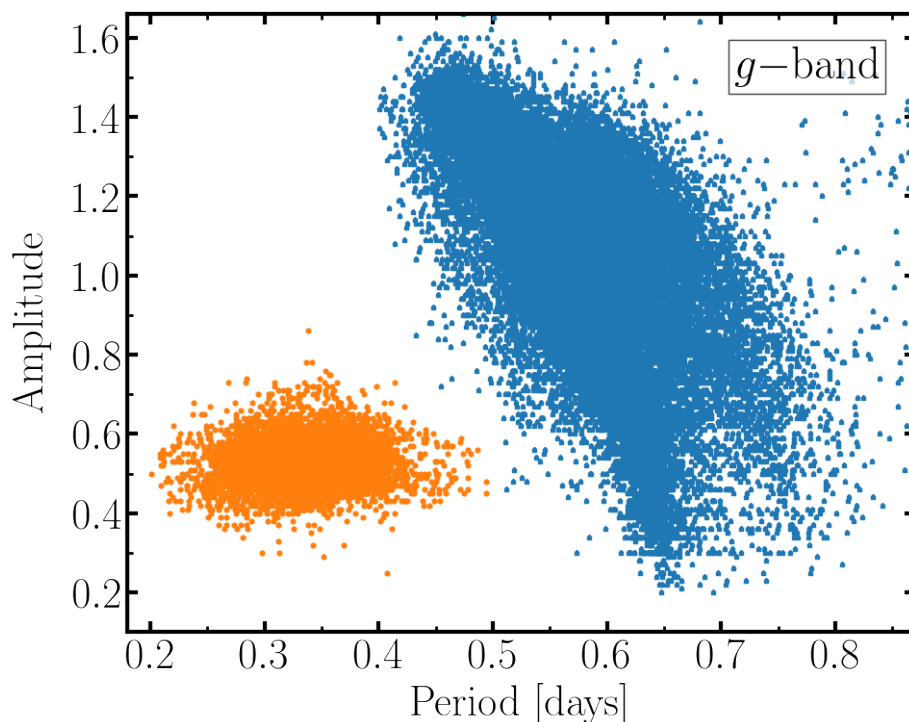


Figure 1.17: Bailey diagram of RRLs from the PS-1 survey (Sesar et al., 2017), showing the distribution and separation between RRab and RRc stars according to their periods and amplitudes of pulsation. The stars shown in these plots are those from the PS-1 catalogue that display a high probability of belonging to any of these subclasses (with classification scores > 0.90 , as defined by Sesar et al. 2017).

- c-type RRLs, or RRc stars, are first-overtone pulsators whose luminosity and radial velocity amplitudes variations are a factor of two smaller than those of RRab variables (e.g., Bono et al., 2016). Their periods are typically shorter than 0.4 d. The light curves and radial velocity variations of RRc stars are also smoother and more sinusoidal than RRab’s over the entire pulsation cycle (see Figure 1.16). RRc variables are found toward the blue side of the instability strip. In terms of numbers, only ~ 10 per cent of the RRLs observed are classified as RRc stars.
- d-type RR Lyrae stars, or RRd stars, are found in smaller numbers than the previous two classes, and pulsate simultaneously in the fundamental and first-overtone modes (Nemec, 1985a,b). In the HR diagram, RRd stars occur in between RRab and RRc stars.

These sub-classes, especially the RRLs of types ab and c, are clearly separated in the period-amplitude space, which is also often called the Bailey diagram. This is illustrated in Figure 1.17, using g -band data from the PS-1 catalogue of RRLs (Sesar et al., 2017).

Evolution

In the HR diagram, RR Lyrae variables occur in the region where the HB crosses the IS. Because they are low-mass stars, RRLs are already older than 10 Gyr when they reach the IS, and they have evolved from the MS, gone through the red giant phase, and undergone the He flash (e.g., [Catelan, 2007](#)). Thus, they are burning helium quiescently in their convective cores, and hydrogen in a shell, and their pulsations are driven by the κ and γ mechanisms. Considering that a star in the HB does not spend all of its core helium burning time within the IS, the maximum time that an HB star can remain an RRL is of the order of $\sim 10^8$ yr. After they exhaust the He in their cores, these stars leave the HB and become AGB stars.

The Blazhko effect

The light curves of some RR Lyrae variables do not repeat perfectly from one pulsation cycle to another. The observed cycle-to-cycle changes, a quasi-periodic modulation, are commonly referred as the *Blazhko effect* ([Blažko, 1907](#); [Shapley, 1914](#)). This phenomenon has been observed in all RRLs subtypes (see e.g. [Smolec, 2005](#); [Netzel et al., 2018](#)), affecting nearly 50 per cent of the fundamental-mode RRab stars ([Szeidl, 1988](#); [Moskalik & Poretti, 2002](#); [Jurcsik et al., 2009](#); [Benkő et al., 2010](#); [Kovacs, 2016](#); [Prudil & Skarka, 2017](#)), and from 5 to 40 per cent of the first-overtone RRC (Kolenberg et al., 2010; Kunder et al., 2013; [Catelan & Smith, 2015](#)). In fact, the star RR Lyrae itself (the prototype of this class of variables) is affected by the Blazhko effect ([Shapley, 1916](#)). The Blazhko modulation period is typically much longer than that of the primary pulsation period, and can be as short as ~ 5 d and may extend up to a few decades ([Catelan & Smith, 2015](#); [Netzel et al., 2018](#); [Prudil & Skarka, 2017](#); [Jurcsik & Smitola, 2016](#)). RR Lyrae variables affected by the Blazhko modulation vary the phase of their light curves and their amplitudes of pulsation (from a few mmag up to ~ 1 mag), hence the shape of their light curves. Thus, the Blazhko effect can also introduce uncertainties on the determination of physical quantities that are computed from the shape of the RRLs light curves (e.g., mean magnitudes, distances, and metallicities; [Benkő, Szabó, & Papp, 2011](#); [Benkő et al., 2014](#); [Skarka, Prudil, & Jurcsik, 2020](#)). There is still no consensus on the origin of the Blazhko effect even after decades of proposed theories (see e.g. [Kluyver, 1936](#); [Cousens, 1983](#); [Nowakowski & Dziembowski, 2003](#); [Kolenberg et al., 2009](#); [Smolec et al., 2011](#)), which include combining the effects of turbulent convection with magnetic fields ([Stothers, 2006](#)), mixing non-radial pulsation modes with the dominant radial mode (e.g., [Cox, 2013](#)), 9:2 nonlinear resonances between the fundamental-mode and the ninth-overtone radial mode ([Buchler & Kolláth, 2011](#)), and shock waves that perturb the pulsation in the fundamental mode ([Gillet, 2013](#)).

RR Lyrae stars as standard candles

Similar to classical Cepheids, RRLs can be used as standard candles given that they follow a PL relation in the near-infrared ([Longmore, Fernley, & Jameson, 1986](#); [Coppola et al., 2011](#); [Marconi et al., 2015](#)), and that they are located in the HB stage of the evolution of low-mass stars. The PL relation of these variables becomes more defined for redder bandpasses ([Catelan, Pritzl, & Smith, 2004](#); [Catelan & Smith, 2015](#)). Moreover, these stars obey a well-defined luminosity-metallicity relation (e.g., [Sandage, 1990](#); [Caputo, Santolamazza, &](#)

Marconi, 1998; Caputo et al., 2000; Di Criscienzo, Marconi, & Caputo, 2004) in optical bands, and follow tight PLZ relations (e.g., Catelan, Pritzl, & Smith, 2004; Sollima, Cacciari, & Valenti, 2006; Braga et al., 2015; Sesar et al., 2017; Marconi et al., 2022) and PWZ relations in toward the red (e.g., Braga et al., 2015; Neeley et al., 2019; Marconi et al., 2022; Ngeow et al., 2022). Thus, calibrations of the mean absolute magnitude of RRLs, $\langle M \rangle$, typically have the form

$$\langle M \rangle = A \log(P) + B [\text{Fe}/\text{H}] + C, \quad (1.9)$$

where P is the pulsation period, $[\text{Fe}/\text{H}]$ is iron abundance ratio, A and B are constants that describe the dependence of the absolute magnitude on the period and metallicity, and C is a zero-point. In order to calibrate these relations, a variety of approaches have been used throughout the years, including stellar parallaxes (e.g., Neeley et al., 2019; Muhie et al., 2021), the Baade-Wesselink method (Carney, Storm, & Jones, 1992; Kovács, 2003), and in general, methods that determine (independent) distances to systems that host RRLs (e.g., globular clusters and dwarf galaxies; see e.g. Nemeč, Nemeč, & Lutz, 1994; Vivas et al., 2017; Bhardwaj et al., 2021; Cusano et al., 2021; Ngeow et al., 2022).

The Oosterhoff dichotomy

Oosterhoff (1939), studying RRLs in five globular clusters (M 3, M 5, M 15, M 53, and Omega Cen), was the first to report that these systems could be mainly separated into two groups, now called the *Oosterhoff groups*. In his work, Oosterhoff (1939) recognized that the period distribution of the RRab stars in two of these clusters had a mean of $\langle P_{\text{ab}} \rangle \sim 0.55$ d, whereas the mean period of the RRab stars in the other three clusters were closer to 0.65 d. This difference has been confirmed using larger samples of MW globular clusters hosting RRLs (Catelan, 2009), and the literature concerning this dichotomy has grown to include theoretical (e.g., Lee, Demarque, & Zinn, 1994; Cassisi et al., 2004), photometric (Lee & Carney, 1999; Prudil et al., 2019a,b; Jurcsik, Hajdu, & Juhász, 2021), and spectroscopic studies (van den Bergh, 1993; Fabrizio et al., 2021). Nowadays, the group containing clusters with shorter mean period RRLs is called Oosterhoff I (OoI), and the clusters that host RRLs with mean periods near 0.65 d belong to the Oosterhoff II (OoII) group. Another difference is that the fraction of RRc stars with respect to the total number of RRLs is larger for OoII clusters than for OoI (~ 45 and 30 per cent for OoII and OoI, respectively; Braga et al., 2016). Furthermore, globular clusters in the OoI group have been found to be more metal-rich ($[\text{Fe}/\text{H}] \sim -1.3$ dex) than those in the OoII group ($[\text{Fe}/\text{H}] \sim -2.0$ dex; Smith 1995; Catelan & Smith 2015 and references therein).

The Oosterhoff dichotomy is depicted in Figure 1.18, which shows the mean periods of field MW RRLs as a function of their V -band amplitudes, and their iron abundance distributions. This region located between the locus of the OoI and the OoII groups is often denoted as the Oosterhoff gap (Catelan, Pritzl, & Smith, 2004; Catelan, 2009). The bimodal distribution observed for MW globular clusters in the $[\text{Fe}/\text{H}]$ vs. $\langle P_{\text{ab}} \rangle$ space does not occur among all systems. In fact, the Oosterhoff gap is only (well) populated if we consider dSphs in the Local Group. The systems located in this region are classified as Oosterhoff-intermediate (Oo-int), with $\langle P_{\text{ab}} \rangle$ typically between 0.58 and 0.62 d. Because RRLs hosted by OoI and OoII systems lie in different regions of the Bailey diagram, the position of individual halo

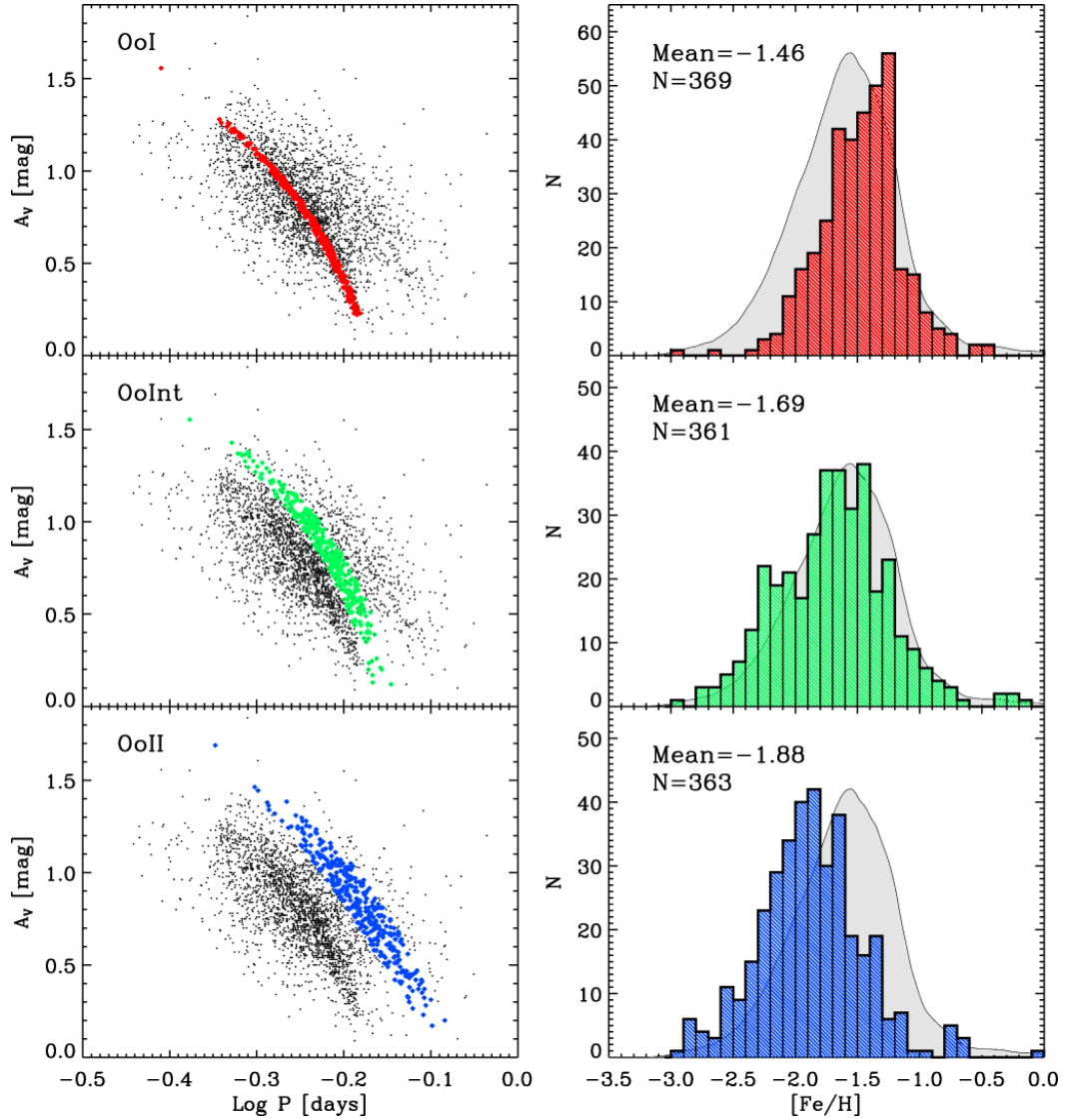


Figure 1.18: Positions in the Bailey diagram (*left panels*) and metallicity distributions (*right panels*) of a sample of field RRLs. These plots show the distinction between RRLs associated with the OoI, Oo-int, and OoII, based on their periods, amplitudes, and metallicities. Normalized distributions are represented by the grey solid areas in the *right panels*. *Image credit:* Figure 16 from [Fabrizio et al. \(2021\)](#). Reproduced by permission of the authors and the American Astronomical Society (AAS) journal.

RRLs can be used to associate them with one of the Oosterhoff groups. In this regard, and similar to the case of globular clusters, the distribution of field halo RRLs has shown to be bimodal, although with a preference for the OoI group (see e.g. [Miceli et al., 2008](#); [Simion et al., 2014](#); [Zinn et al., 2014](#)). With respect to the RRc population ratio, RRLs in the field have been found to follow trends more complex than in clusters, with higher numbers of RRc found in the more metal-poor regime ([Fabrizio et al., 2021](#)).

Several physical origins have been proposed to explain the Oosterhoff dichotomy, including higher helium abundances in the more metal-poor OoII clusters (which would explain their longer periods; [Sandage, 1981](#)), the existence of a hysteresis zone in the instability strip that would make RRLs in OoI clusters populate the IS from the red keeping a fundamental-mode pulsation (hence, with a preference for RRab; [van Albada & Baker, 1973](#); [Stellingwerf, 1975](#)), and the lack of metal-intermediate globular clusters ([Fabrizio et al., 2019](#)).

On the importance of RR Lyrae stars for Galactic studies

Similar to classical Cepheids, RRLs are one of the most useful types of variable stars, although, unlike the former, they are important for studies involving systems with old stellar populations. In particular, RR Lyrae variables have served as powerful probes of the chemical and dynamical evolution of the disc and halo of our Galaxy (e.g., [Vivas, Zinn, & Gallart, 2005](#); [Keller et al., 2008](#); [For et al., 2011a,b](#); [Hansen et al., 2011, 2016](#); [Belokurov et al., 2018a](#); [Li & Binney, 2022](#)), given that the small scatter in their mean absolute magnitudes and PL relations, with which distances can be easily determined at a 5 per cent level precision (see e.g. [Christy, 1966](#); [Catelan & Smith, 2015](#); [Neeley et al., 2017](#); [Beaton et al., 2018](#)). Given the relatively high luminosity and characteristic pulsation properties of RRLs (e.g., their light curve shapes), they are easily identifiable in time-domain surveys, and have been widely used as tracers of Galactic substructures ([Vivas & Zinn, 2006](#); [Watkins et al., 2009](#); [Sesar et al., 2013a,b](#); [Dékány et al., 2018](#); [Mateu, Read, & Kawata, 2018](#); [Martínez-Vázquez et al., 2019](#); [Prudil et al., 2019a](#); [Torrealba et al., 2019](#); [Cook et al., 2022](#)).

Because RRLs are ubiquitous in the halo and dwarf galaxies, they are used for numerous astrophysical applications, and are useful in different but complementary ways. [Sesar et al. \(2014\)](#), for instance, proposed that RRLs can be used as tracers of yet undiscovered low luminosity satellites, and [Baker & Willman \(2015\)](#) suggested that even small groups of halo RRLs can serve this purpose ([Torrealba et al., 2019](#)), thus contributing to bridge the gap between current cosmological simulations and observations ([Pillepich et al., 2014](#); [Hargis, Willman, & Peter, 2014](#); [Jethwa, Erkal, & Belokurov, 2018](#); [Engler et al., 2021](#)). By tagging RRLs according to their pulsation properties (e.g., their periods and amplitudes) it is possible to shed light onto the genesis of the stellar halo, as they are excellent tracers of old stellar populations in Local Group Galaxies and halo substructures. Thus, they have provided clues on the nature of the accretion events that formed the halo (e.g., [Catelan, Pritzl, & Smith, 2004](#); [Vivas et al., 2004](#); [Vivas & Zinn, 2006](#); [Fiorentino et al., 2015](#); [Torrealba et al., 2015](#); [Belokurov et al., 2018a](#); [Martínez-Vázquez et al., 2019](#); [Deason et al., 2017](#); [Dékány et al., 2018](#); [Hernitschek et al., 2018](#); [Mateu, Read, & Kawata, 2018](#); [Prudil et al., 2019a, 2021](#); [Monelli & Fiorentino, 2022](#)). For instance, they can be used to characterize the stellar streams resulting from these accretions ([Hendel et al., 2018](#); [Price-Whelan et al., 2019](#); [Abbas, Grebel, & Simunovic, 2021](#); [Prudil et al., 2021](#)), to find new streams and accretion events (e.g., [Duffau et al., 2006](#); [Sesar et al., 2010](#); [Iorio & Belokurov, 2019](#)), and as evidence of

the extragalactic origin of overdensities in the disc (e.g., [Mateu et al., 2009](#); [Price-Whelan et al., 2015](#)). Thus, by combining their precise distances with kinematics (proper motions and line-of-sight velocities), RRLs can be easily used to reconstruct the accretion history of the Galaxy, as notably done for the characterization of the Gaia-Enceladus merger event (e.g., [Belokurov et al., 2018b](#); [Helmi et al., 2018](#)).

Given that their distances are known with great precision, the spatial distribution of RRLs is also pivotal to study the radial density profile of the Galaxy ([Wetterer & McGraw, 1996](#); [Vivas & Zinn, 2006](#); [Cohen et al., 2016](#); [Iorio et al., 2018](#)). Their role as precise distance indicators also makes them excellent tracers of the outermost limits of our Galaxy, as well-characterized stars at such large distances (beyond 100 kpc) are scarce ([Sesar et al., 2017](#); [Medina et al., 2018](#); [Stringer et al., 2021](#)). Furthermore, distant RRLs are ideal to estimate the MW mass, as its value is most strongly constrained by tracers in the outermost regions of the Galaxy (see e.g. [Eadie & Harris, 2016](#); [Deason, Belokurov, & Sanders, 2019](#); [Deason et al., 2021](#); [Rodriguez Wimberly et al., 2021](#); [Prudil et al., 2022](#)). Finally, RRLs in the halo are also valuable to probe the chemical enrichment of the old component of the MW (e.g., [Clementini et al., 1995](#); [Kolenberg et al., 2010](#); [Hansen et al., 2011](#); [Pancino et al., 2015](#); [Gilligan et al., 2021](#); [Liu et al., 2020](#); [Fabrizio et al., 2021](#)).

1.7 This thesis

So far, I have highlighted the importance of using stellar populations in different regions of the Galaxy as tools to uncover its formation history, stressing the role that variable stars have played throughout the history to this end. However, there is a wealth of fundamental questions that remain unanswered, mainly due to the intricate nature of the processes responsible for the continuous evolution of the Galaxy (at all scales), and the amount of detail required to thoroughly disentangle them (e.g., what the fraction of field stars formed in clusters is, and to what extent haloes are formed in-situ/ex-situ).

In this thesis, I use archetypes of two distinct but complementary classes of variable stars, namely Cepheids and RR Lyrae variables, as tracers of young and old stellar populations, exploiting their properties (e.g., as distance indicators) in the context of Galactic archaeology. I use these variables to study where, how, and under which conditions these stars were formed, and how they contribute to our understanding of the formation and evolution of our Galaxy as a whole. For this, I employ the three observational techniques introduced earlier in this chapter: astrometry (extensively used in [Chapter 2](#)), photometry (as the foundations of [Chapter 3](#)), and spectroscopy (used in [Chapter 4](#)). More specifically:

- In [Chapter 2](#), I use classical Cepheids and open clusters as testbeds for studying the origin of intermediate-mass stars, the fundamental properties of Cepheids, and cluster dissolution mechanisms by addressing questions such as:
 - What is the fraction of clustered Cepheids in the MW, and how does the usage of new data change their established cluster membership scenario?
 - Is the fraction of clustered Cepheids consistent with cluster dissolution models?
 - Are young open clusters suitable laboratories for empirical tests of the Cepheid period-age relation?

Here I present the results of an all-sky search for classical Cepheids in Galactic open clusters, taking advantage of the unprecedented astrometric precision and homogeneity of recent *Gaia* data releases. In order to do this, I determine the membership of Cepheids to clusters using the newest available catalogues, following a Bayesian approach, and taking the spatial and kinematic information of the potential cluster-Cepheid pairs into account. I also explore the feasibility of using open clusters hosting Cepheids to empirically test the Cepheid period-age relation through the use of a semi-automated method to derive cluster ages. Together with the description of the methodology followed, I discuss the implications of my findings and their impact in the current understanding of the birthplace of Cepheids, their period-age relation, the clustered Cepheid fraction in the MW, and the dynamical dissolution of young clusters.

- In Chapter 3, I use RRLs to dig into the most remote regions of the MW, focusing on questions such as:
 - What is the role of dedicated time-domain photometric surveys on the census of RRLs in the outer halo of the MW?
 - How homogeneous is the distribution of these stars in the halo?
 - How does their distribution relate to our current understanding of past and ongoing mergers, and is it compatible with current Galactic assembly models?

Here I describe a systematic search for RRLs in the Galactic halo carried out in the context of the Halo Outskirts With Variable Stars (HOWVAST) survey. I use proprietary data (time series) obtained with the Dark Energy Camera to identify and characterize these variable stars, with an emphasis on regions beyond 100 kpc from the Galactic centre. I use the properties of the detected RRLs (e.g., their classification and their positions) to speculate about the fraction of distant RRLs with an in-situ and ex-situ origin. I study the radial distribution of these tracers adopting an ellipsoidal halo model, following a Markov chain Monte Carlo methodology. With this, I look for evidence of the separation between the inner and outer halo using power-laws, compare my results with MW assembly simulations from the literature, and analyse the isotropy of their distribution throughout the halo.

- Chapter 4, is dedicated to exploring the role of distant halo RRLs in our current understanding of the MW assembly history. Here, I cover questions such as:
 - Given the low brightness and short period of outer halo RRLs, what are the current limitations of using them to unveil the Galactic history at large distances?
 - On what level is it possible to derive the kinematics, atmospheric parameters, and abundances for outer halo RRLs?
 - What do the chemistry and kinematics of these stars tell us about their origin (in-situ or ex-situ)?
 - How does the infall of the LMC affect the orbits of distant stars?

To address these questions, I present the spectroscopic analysis of 20 outer halo RRLs with distances between 15 and 165 kpc (including RRLs discovered in Chapter 3)

conducted using proprietary medium-resolution spectra from the Magellan Inamori Kyocera Echelle spectrograph. In combination with *Gaia* data, I model the orbits of our stars considering the gravitational perturbation of the halo by the LMC, and study the atmospheric parameters and chemical abundance ratios (including α -elements, Fe, and neutron-capture elements) for a subsample of them. I search for associations between these distant RRLs with known satellites and accretion events by studying their chemodynamics and speculate about their parent populations and origins (formed in-situ vs. accreted). I test the hypothesis that the accretion of sub-haloes largely contributes to the outer halo stellar populations, and report on the limitations of state-of-the-art distant halo RRL spectroscopic surveys. Finally, I discuss the implications of my findings, and their impact on the preparation for the analysis of large samples of halo RRLs in the upcoming era of large scale photometric and spectroscopic surveys.

- Chapter 5 summarizes the main outcomes of this thesis. In addition, I discuss ideas on future avenues expanding on the results of this work, providing perspectives for the field of Galactic archaeology with Cepheids and RRLs in the near future.

2

A study of Cepheids in open clusters and the Cepheid period-age relation in the *Gaia* era

The content of this chapter is based on the published article “A revisited study of Cepheids in open clusters in the *Gaia* era” (Medina, Lemasle, & Grebel, 2021a), of which I am the first author. For this work, I was in charge of processing and analysing the data, as well as reaching the conclusions. This study was developed under the supervision of Prof. Dr. Eva K. Grebel and Dr. Bertrand Lemasle. The text was written by me and includes input from the co-authors of the published work. The final version of the text also takes the suggestions from an anonymous referee into account.

In this chapter, we describe our investigation of Cepheid cluster membership taking advantage of the large, rich, and homogeneous *Gaia* data, complemented (if needed) by other recent surveys. To achieve this goal, we follow a Bayesian approach and use state-of-the-art publicly available data. We also use the host clusters as laboratories to age-date Cepheids and to investigate the Cepheid period-age relation. In Section 2.1, we provide an overview of the importance of studying Cepheids in open clusters, and how this field has evolved since the first discoveries of these associations. Section 2.2 describes the catalogues used for our study. In Sections 2.3 and 3.2, we describe the Bayesian method used to search for cluster membership, and justify its applicability to the data characterized in Section 2.2. In Section 2.5, we report and discuss in detail new cluster Cepheid candidates and compare our results to previous studies. In Section 2.6, we estimate the age of our sample of cluster Cepheids by age-dating the clusters they are hosted by, and we investigate the feasibility of obtaining an empirical Cepheid period-age relation from our results. Finally, in Section 4.6 we summarize the contents of our study and describe their implications.

2.1 Motivation

Identifying Cepheid variables that are part of stellar associations and open clusters has attracted scientific attention of many astronomers, starting with Irwin (1955), and remains an important research topic. Since they are young objects, Cepheids are, in principle, expected to be found in stellar associations and young open clusters.

As explained in Chapter 1, Cepheids and young clusters can be used to trace recent star formation events, both in the external galaxies (see e.g. Payne-Gaposchkin, 1974; Efremov, 2003; Glatt, Grebel, & Koch, 2010), and in the MW, wherein they are expected to trace the spiral arms (e.g., Magnier et al., 1997a; Pietrzyński et al., 2002; Skowron et al., 2019a). Cepheids are intrinsically rare since the duration of the yellow supergiant stage

for intermediate and high mass stars is short, which makes them valuable for constraining models of post-MS evolution (e.g., [Bono et al., 2000](#)).

Cepheids in open clusters present several specific interests: first, the clusters can be used as benchmarks for abundance determinations of the Cepheids they host, which are complicated by their pulsating nature (e.g., [Fry & Carney, 1997](#); [Lemasle et al., 2017](#)). Moreover, because Cepheids are young and massive, they can provide useful constraints on the dynamical effects that drive the evolution of young clusters (e.g., tidal dissolution and mass segregation; [Dinnbier, Anderson, & Kroupa, 2022](#); [Dinnbier, Kroupa, & Anderson, 2022](#)). In addition, the presence of Cepheids in Galactic open clusters has proven to be extremely helpful for the calibration of the Cepheid PL relation (see e.g. [Turner & Burke, 2002](#); [Breuval et al., 2020](#)) first found by [Leavitt & Pickering \(1912\)](#), which makes Cepheids cornerstones of the distance scale as it provides a fundamental constraint on the Hubble constant (e.g., [Madore & Freedman, 1991](#); [Riess et al., 2018](#)). Conversely, the existence of a PL relations also allows cluster Cepheids to be used as tools to provide an independent measurement of the distance of the clusters that host them. Finally, in addition to PL relations, theoretical PA relations have been established and can be tested by studying cluster-Cepheid associations and age-dating the clusters through isochrone fitting (see e.g. [Grebil & Chu, 2000](#); [von Hippel et al., 2006](#); [Senchyna et al., 2015](#); [Yen et al., 2018](#); [Bossini et al., 2019](#)) or with alternative methods (e.g., from the morphology of their tidal tails; [Dinnbier et al., 2022](#)).

In spite of their importance, only a small number of bona fide classical Cepheids in open clusters has been reported so far. The available literature illustrates the numerous attempts to increase the list of reliable cluster-Cepheid pairs, starting with the identification of the Cepheids S Nor and U Sgr as members of NGC 6087 and M 25, respectively ([Irwin, 1955](#)), and extending throughout the last decades (e.g., [van den Bergh, 1957](#); [Kraft, 1962](#); [Efremov, 1964](#); [Turner, 1986](#); [Turner, Forbes, & Pedreros, 1992](#); [Turner et al., 1998b](#); [Baumgardt, Dettbarn, & Wielen, 2000](#); [Hoyle, Shanks, & Tanvir, 2003](#); [Turner et al., 2005](#); [An, Terndrup, & Pinsonneault, 2007](#); [Majaess, Turner, & Lane, 2008](#); [Turner et al., 2008](#); [Turner, 2010](#); [Anderson, Eyer, & Mowlavi, 2013](#); [Chen, de Grijs, & Deng, 2015](#); [Lohr et al., 2018](#); [Negueruela, Dorda, & Marco, 2020](#)). These studies have provided approximately two tens of the currently identified cluster Cepheids, and have faced a common obstacle: the scarcity and the inhomogeneity of the input data. In particular, photometry originated from different sources and instruments, and accurate astrometry was rarely available. Spectroscopic information, albeit sparse, was used by several authors when available (e.g., [Turner et al., 2008](#); [Anderson, Eyer, & Mowlavi, 2013](#); [Usenko et al., 2019](#)).

Large-scale astrometry-focused surveys are required to provide homogeneous catalogues for the study of the Galactic cluster Cepheid populations. The HIPPARCOS mission ([ESA, 1997](#)) has been an invaluable source of data, allowing astronomers to investigate the association of many Cepheids with open clusters (see e.g. [Lyngå & Lindegren, 1998](#); [Turner & Burke, 2002](#)). HIPPARCOS' successor, the ongoing ESA *Gaia* mission ([Gaia Collaboration et al., 2016](#)) revolutionized the study of stellar populations within the MW. Indeed, the second, early third, and third data releases of the *Gaia* catalogues (hereafter *Gaia* DR2, eDR3, and DR3, respectively) reach limiting magnitudes close to 21 in the *G* band with an unparalleled astrometric precision (uncertainties < 0.7 mas for stars brighter than $G = 20$), and include parallaxes and proper motions for more than a billion stars, with photometric precisions at the millimag level ([Gaia Collaboration et al., 2018, 2020, 2022](#)). In particular,

as far as this work is concerned, *Gaia* has allowed several authors to discover hundreds of new open cluster candidates and to perform membership determinations based on a full astrometric solution of the sources (e.g., [Ferreira et al., 2019](#); [Liu & Pang, 2019](#); [Torrealba, Belokurov, & Koposov, 2019](#); [Cantat-Gaudin et al., 2019](#); [Hunt & Reffert, 2021](#)). With such new data at hand, it becomes possible to take the study of Cepheids in open clusters to a next level by updating the list of bona-fide cluster-Cepheids (i.e., confirming/rejecting their associations) and expanding it with new discoveries. Lastly, the updated census of Cepheids in Galactic open clusters can subsequently be exploited to investigate the feasibility of using of these associations as testbeds for the empirical Cepheid PA relation, which have not yet been extensively studied using open clusters in the *Gaia* era.

2.2 Cepheids and open clusters samples

To carry out this study, we focused on astrometric and kinematic information for both open clusters and Cepheids.

2.2.1 Open clusters

We rely first on two large public catalogues of known Galactic open clusters: the compilation made by [Dias et al. \(2002, hereafter D02\)](#), for which the last update was published in 2015, and the catalogue from [Kharchenko et al. \(2013, hereon K13\)](#). The former compilation (D02) consists of 2,167 optically visible clusters and candidates, and is based on the Web version of the Base Données Amas (WEBDA) database ([Mermilliod, 1988](#))²⁸, whereas the latter catalogue (K13) contains 3,006 clusters. Combining the clusters from D02 and K13 resulted in a total of 3,135 unique clusters, after removing sources classified as globular clusters by K13. We complemented those with new MW open cluster or open cluster candidates from works published prior to the preparation of this study, based on *Gaia* data:

- from *Gaia* DR2, [Cantat-Gaudin et al. \(2018b, hereafter CG18b\)](#) and [Cantat-Gaudin et al. \(2020, henceforth CG20\)](#) derived the properties of > 1200 clusters. From these we include 70 and 102 clusters that do not appear in the D02/K13 catalogue, respectively;
- from *Gaia* DR2, [Castro-Ginard et al. \(2018\)](#) identified 23 nearby open clusters (within 2 kpc from the Sun);
- from *Gaia* DR2, [Castro-Ginard et al. \(2019\)](#) added 53 new open clusters in the Galactic anticentre and the Perseus arm;
- from *Gaia* DR2, [Cantat-Gaudin et al. \(2019, hereafter CG19\)](#) added 41 clusters, most of which (33 clusters) located within 2 kpc from the Sun;
- still from *Gaia* DR2, [Ferreira et al. \(2019\)](#) found three clusters in the field of the intermediate-age cluster NGC 5999, and [Ferreira et al. \(2020\)](#) discovered 25 new open cluster candidates. We added to our sample the 34 open clusters discovered by [Ferreira et al. \(2021\)](#);

²⁸<https://webda.physics.muni.cz>

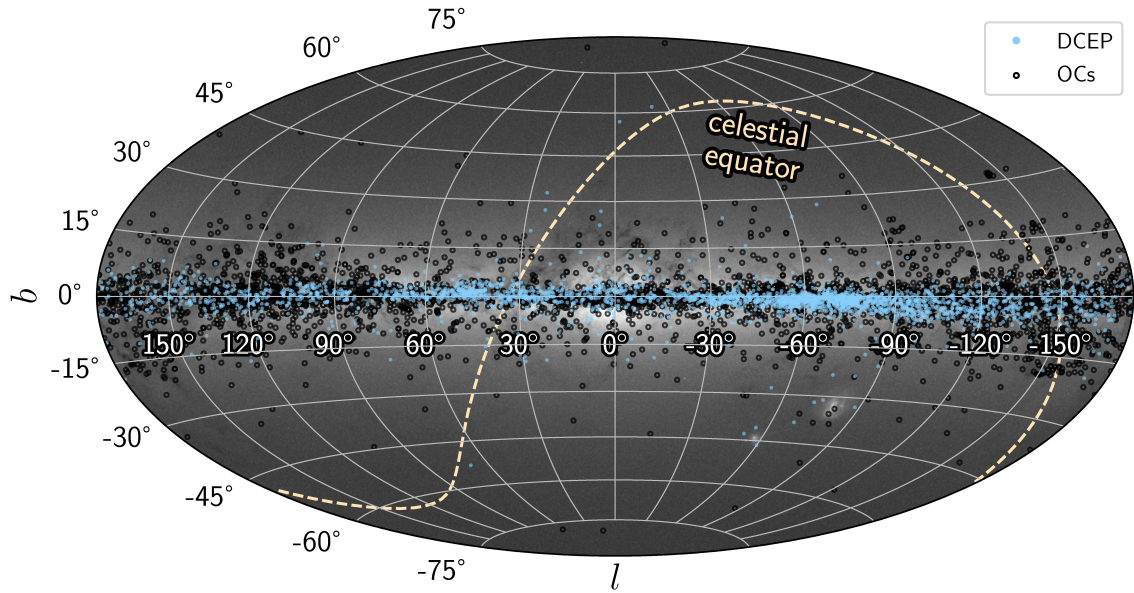


Figure 2.1: Spatial distribution in Galactic coordinates of the Cepheids (DCEP; *light blue points*) and open clusters (OCs; *open circles*) used in this work. The *Gaia* all-sky map in the background is shown as a reference. *Background Image Credit: Gaia Data Processing and Analysis Consortium (DPAC); A. Moitinho / A. F. Silva / M. Barros / C. Barata, University of Lisbon, Portugal; H. Savietto, Fork Research, Portugal.*

- from *Gaia* DR2, [Sim et al. \(2019\)](#) found 207 open cluster candidates (187 totally new), all located within 1 kpc from the Sun;
- [Liu & Pang \(2019\)](#) identified 76 (mostly old) open cluster candidates (39 totally new) within 4 kpc in the *Gaia* DR2 data
- the clusters found by [Torrealba, Belokurov, & Koposov \(2019\)](#) using *Gaia* DR2 were also added, excluding those potentially associated with the Magellanic Clouds (DES 4, DES 5, To 1, and Gaia 3);
- the 582 Galactic disc open clusters recently discovered by [Castro-Ginard et al. \(2020\)](#) using again *Gaia* DR2 data were also incorporated in our catalogue;
- finally, the 41 open cluster candidates detected by [Hunt & Reffert \(2021\)](#) were also included.

We gave priority to the data from D02 over K13. Both were superseded by *Gaia* DR2 astrometric/kinematic data from the aforementioned studies when available. We checked for duplicated clusters by performing over this compilation an internal cross-match on the cluster center, checking individually all clusters whose centres fell within 3.5 arcmin from each other. After removing evident repeated entries from this list (with astrometric parameters within one standard deviation from each other), our final catalogue contains a total of 4,140 Galactic open clusters. Their spatial distribution is shown in Figure 2.1.

2.2.2 Cepheids sample

Our catalogue of classical Cepheids relies firstly on the OGLE database (Udalski, Szymański, & Szymański, 2015). We compiled the MW classical Cepheids in the disc reported by Udalski et al. (2018) and those in the inner disc towards the bulge found by Soszyński et al. (2017). We added the additional Cepheids recently added by Soszyński et al. (2020). A number of additional sources list Cepheids, for instance *Gaia* DR2 and DR3 (Clementini et al., 2019; Ripepi et al., 2019, 2022), the General Catalogue of Variable Stars (GCVS; Kukarkin et al., 1969; Samus’ et al., 2017), the Wide-field Infrared Survey Explorer (WISE; Chen et al., 2018), and the VVV survey (Ferreira Lopes et al., 2020). We note in passing that the *Gaia* DR3 catalogue was not available when this work was carried out. Therefore, it is not included in our sample. It is notoriously difficult to classify variable stars in the near- and mid-infrared. This is because their light curves become more symmetric and their amplitudes decrease, leading to confusion with other types of pulsating variables, eclipsing binaries and spotted stars. The purity of the infrared catalogues is then significantly lower than the purity of the optical ones (Udalski et al., 2018; Dékány et al., 2019). Therefore, we supplemented our catalogue with Cepheids only when they could be detected in the optical as well; hence, we did not include the 640 distant Cepheids recently discovered by Dékány et al. (2019) in the Galactic midplane and bulge. We rely for this on the cross-survey validation performed by the OGLE team, which also includes targets from the Asteroid Terrestrial-impact Last Alert System survey (ATLAS; Heinze et al., 2018) and the All Sky Automated Survey for Supernovae (ASAS-SN; Jayasinghe et al., 2018, 2019a,b) surveys. The Cepheids discovered by Clark et al. (2015) in the cluster BH 222 and by Lohr et al. (2018) in the clusters Berkeley 51 and Berkeley 55 entered our catalogue via this list. The extended catalogue of Cepheids has been used by Skowron et al. (2019a,b) to map the Galactic disc. Once compiled, we cross-matched this catalogue against *Gaia* eDR3. After removing Cepheids possibly related to the Magallanic Clouds (sources in the region $254^\circ < l < 324^\circ$, $-54^\circ < b < -22.6^\circ$), with negative parallaxes or with parallax-based distances > 10 kpc, our final sample of MW classical Cepheids contains 2,921 Cepheids with *Gaia* eDR3 coordinates and proper motions. Their location is indicated in Figure 2.1.

2.3 Membership determination

We follow the Bayesian approach adopted by Anderson, Eyer, & Mowlavi (2013, hereafter A13) to address the membership determination (albeit with differences, which will be detailed in Section 2.3.3). The Bayesian approach enables us to quantify the likelihood of a given Cepheid being a member of an open cluster. We refer to a Cepheid-cluster pair as a “combo”, following the convention initiated by A13. To determine the membership probabilities, we use positional and kinematic constraints on both Cepheids and clusters: projected on-sky distances, parallaxes, proper motions, and radial velocities where available.

Using Bayes’ theorem (see e.g. Jaynes, 2003), the posterior $P(A|B)$, i.e., the membership probability, is computed from:

$$P(A|B) \propto P(B|A) \times P(A), \quad (2.1)$$

where $P(B|A)$ is the conditional probability of obtaining the cluster and Cepheid data assuming that their association is real (the likelihood), and $P(A)$ (the prior) represents the probability distribution that expresses our belief of membership before the evidence used for $P(B|A)$ is considered. We emphasize that this methodology relies on a hypothesis test that assumes membership. Thus, the association between a Cepheid and a cluster cannot be proven but only refuted by following this approach.

In Equation 2.1, a normalization term associated with the probability of observing the data is neglected, given that we possess no knowledge to quantify it. In the rest of this subsection, we detail the procedure and assumptions on which the determination of the probabilities $P(B|A)$ and $P(A)$ are based.

2.3.1 On-sky selection and prior $P(A)$

As other works have done in the past, we perform an initial cross-match based on the on-sky position of Cepheids and open clusters, taking into account the actual size of the clusters. The goal is to identify possible combos and to rule out Cepheids easily recognizable as non-members. This also reduces the computation time of the next steps of our analysis.

To achieve this, we first estimate the apparent size of each cluster. K13 provide a list of cluster size parameters denoted as r_0 , r_1 , and r_2 , which represent the angular radius of the core, the central part, and the entire cluster, respectively. They were fitted by eye to describe the shape of the clusters radial density profiles (Kharchenko et al., 2012). Clusters from sources other than K13 do not provide these particular parameters as estimators of the cluster sizes. However, A13 demonstrated that r_1 and r_2 given by Kharchenko et al. (2012) are correlated with the core and limiting radius of the clusters provided by Kharchenko et al. (2005a) and Kharchenko et al. (2005b), respectively. Then, A13 used the trend between the core and limiting radii and the values from D02 to finally get an estimate of these clusters' sizes. In the case of clusters that are only present in D02, they do have an estimation of their sizes, but in the form of an angular apparent diameter. Unsurprisingly, we found correlations between the apparent radius, r_{app} , and r_1 and r_2 , but they show considerable scatter. This is shown in Figure 2.2. The correlations are:

$$\begin{aligned} r_1 &= 0.3037 \cdot r_{\text{app}} + 0.0688, \\ r_2 &= 0.6060 \cdot r_{\text{app}} + 0.1252, \end{aligned} \tag{2.2}$$

which we used to estimate r_1 and r_2 for this subsample of clusters.

In CG18b, CG19, and CG20, the authors present the value r_{50} , which represents the radius containing half the members. For these clusters, we assumed $r_1 = r_{50}$, and $r_2 = 1.957 \cdot r_1$, where the scaling factor is the ratio between r_2 and r_1 in K13, and their correlation factor is 0.962. We made the same assumptions for the clusters from Hunt & Reffert (2021), for which r_{50} is provided. In a recent work, Sánchez, Alfaro, & López-Martínez (2020) determined the radii of a sub-sample of open clusters available in the literature based on *Gaia* DR2 proper motions. As a comparison, the median difference between the clusters' r_{50} in CG20 and the cluster radii from Sánchez, Alfaro, & López-Martínez (2020) is 1.19 pc for the 357 clusters in common.

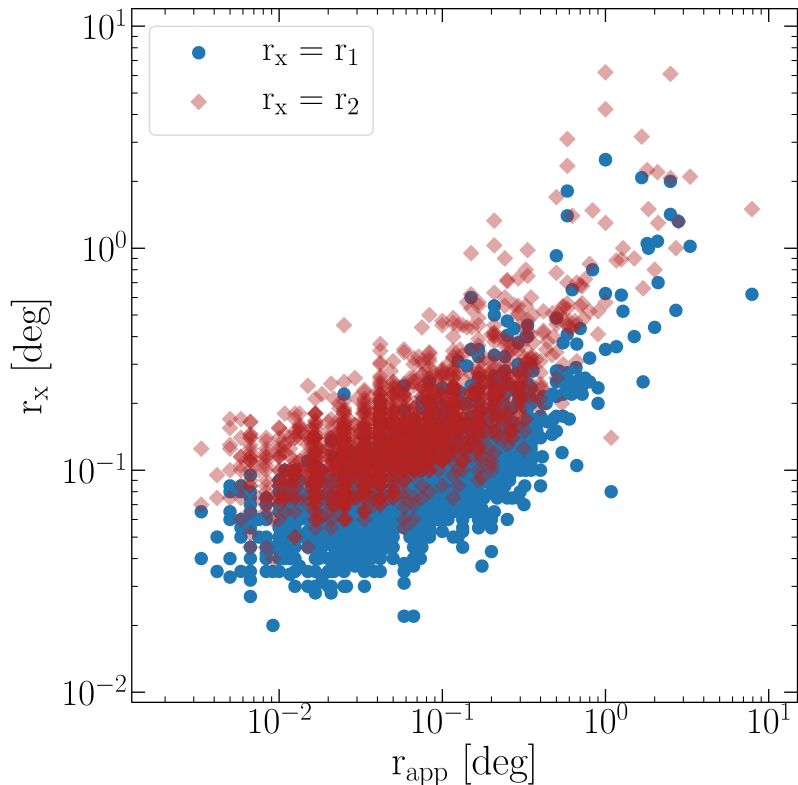


Figure 2.2: Correlation between the open cluster apparent radii listed in D02 and the radii r_1 and r_2 presented by K13, plotted with blue dots and red diamonds, respectively.

For the clusters provided by [Ferreira et al. \(2019, 2020\)](#), we use directly the values given in their work, as they provide estimations for both the core radius and the limiting radius. We assumed those values to be good representations of r_1 and r_2 , respectively. [Ferreira et al. \(2021\)](#) provide only an estimation of the clusters limiting radius r_{lim} . Thus, for those clusters we assumed $r_2 = r_{\text{lim}}$, and $r_1 = r_2/1.957$. Regarding the nine clusters from [Torrealba, Belokurov, & Koposov \(2019\)](#), the authors provide a direct estimation of the half-light radius (r_h). In order to obtain r_1 and r_2 , we assume $r_1 = r_h$, and applied the scaling factor 1.957 to estimate r_2 .

The case of the clusters discovered by [Liu & Pang \(2019\)](#) and [Sim et al. \(2019\)](#) is similar. The catalogue published by [Liu & Pang \(2019\)](#) provides the distance of the furthest member to the average member position as a proxy of the clusters' size, r_{MAX} . We considered $r_2 = r_{\text{MAX}}$ in those cases. The catalogue that characterizes the cluster candidates found by [Sim et al. \(2019\)](#) gives the core radius as an estimation of the clusters size. We adopted those values as the clusters' r_1 . For both the [Liu & Pang \(2019\)](#) and the [Sim et al. \(2019\)](#) clusters, we again assumed the values of r_2 to be about twice as large as r_1 .

For the clusters from the works by [Castro-Ginard et al. \(2018, 2019, 2020\)](#), a list of tentative cluster members was also published by the authors. With this information we computed the radii r_1 and r_2 using the previously mentioned scaling factor and setting $r_1 = r_{50}$, the median cluster member distance (as provided by [Castro-Ginard et al., 2018, 2019, 2020](#)) with respect to their tabulated central coordinates.

With an estimated cluster size, it is possible to perform the initial cross-match based on the on-sky position of the Cepheid-open cluster pairs. To minimize the list of possible combinations for which we compute probabilities, we selected all Cepheids within the largest distance between 2 deg from a given cluster centre, or five times the cluster’s r_1 . This is similar to the procedure followed by A13. With the median r_1 of the entire sample at 0.08 deg and with ~ 95 per cent of the clusters having values of $r_1 < 0.4$ deg, we consider that finding a Cepheid at more than 2 deg from the cluster centre makes its membership unlikely and justifies such an arbitrary choice. For the remaining clusters, for which the median r_1 is 0.6 deg, choosing the limit at $5 \cdot r_1$ allows for some flexibility, even when computing probabilities for nearby associations with $r_1 > 1$ deg, such as Collinder 285.

A total of $\sim 44,300$ possible combos results from this procedure. We focus on these combinations in the next steps of our membership analysis, starting with the determination of the prior.

We define the prior $P(A)$ following A13’s approach: we only take into account the on-sky separation between a Cepheid and a cluster, and the apparent size of the latter based on its core and limiting radius. By defining the quantity x as:

$$x = \frac{r - r_1}{2 \cdot r_2 - r_1}, \quad (2.3)$$

where r is the on-sky separation, r_1 is a proxy for the core radius, and r_2 a proxy for the limiting radius, we can measure the relative position of the Cepheid with respect to the centre of the cluster, weighted by its size. Then, for the value of the probability we define:

$$\begin{aligned} P(A) &\equiv 1, & x < 0 \\ P(A) &\equiv 10^{-x}, & x \geq 0. \end{aligned} \quad (2.4)$$

From this definition, a combo’s prior probability will be 1 if the Cepheid falls within the core of the cluster, and will reach 10 per cent at $x = 1$, inspired by the exponential decline of the radial profile of star clusters. We note that in the study by A13 the authors define the prior such that it reaches 0.1 per cent at $x = 1$. Considering only the prior, this means that we are more flexible than A13 when computing probabilities.

We modified the prior with respect to A13 to take into account the recent results of e.g., [Meingast, Alves, & Rottensteiner \(2021\)](#): from a sample of young open clusters with ages between 30 and 300 Myr (perfectly matching the ages of Cepheids), they found that almost all clusters are surrounded by a large halo of stars they call coronae and which extend further than 100 pc from the clusters’ centre. Most clusters show evidences of expansion along one or more spatial axes, a feature also observed by, e.g., [Pang et al. \(2020\)](#). Although reminiscent of tidal features observed in older clusters, such features are most likely primordial and related to filamentary star formation (e.g., [Beccari, Boffin, & Jerabkova, 2020](#); [Tian, 2020](#)). With a somewhat relaxed prior, we are more likely to recover bona-fide cluster Cepheids located at large distances from the cluster centre, but also more exposed to spurious detections. We note in passing that for a Cepheid located at $5 \cdot r_1$ from a cluster’s centre (one of the pre-selection criteria adopted above), Equation 2.4 would return $P(A) \approx 0.05$ when $r_2 \approx 2 \cdot r_1$.

2.3.2 The likelihood $P(B|A)$

As other authors have done in the past (Robichon et al. 1999; Baumgardt, Dettbarn, & Wielen 2000; A13; Hanke et al. 2020b; Prudil et al. 2021), we determine the likelihood of membership $P(B|A)$ as a hypothesis test based on the Mahalanobis distance (introduced by Mahalanobis, 1936), which is a measure of the distance between a point (a Cepheid) and a distribution (an open cluster). The task of calculating quantiles for multivariate normal distributions is not as simple as in the one-dimensional case, since these quantiles can be considered ellipsoids in dimensions higher than two. However, calculating the Mahalanobis distance is a rather simple method to describe all points on the surface of such a multidimensional ellipsoid.

Given a vector \vec{z} built as the difference Δ between the Cepheid and the mean cluster parameters (here we consider the parallaxes ϖ , proper motion in right ascension μ_α^* and declination μ_δ , and the radial velocities V_r):

$$\vec{z} = (\Delta\varpi, \Delta\mu_\alpha^*, \Delta\mu_\delta, \Delta V_r), \quad (2.5)$$

the square of the Mahalanobis distance between the Cepheid and the cluster, c , can be expressed as:

$$c = \vec{z}^T \Sigma^{-1} \vec{z}, \quad (2.6)$$

where \vec{z}^T is the transpose of \vec{z} , and Σ^{-1} denotes the inverse of the sum of the covariance matrices of a cluster and a Cepheid when systematic effects and correlations are taken into account. It should be noted that, for the purpose of these calculations, we compute c under the assumption that the Cepheid was not used to measure the mean cluster parameters.

An additional quantity that we used to determine Σ^{-1} is the re-normalized unit weight error (RUWE), which is given as a parameter in the *Gaia* DR2 and eDR3 catalogues and which accounts for the fitting effects when the astrometric solution is poor (Lindegren et al., 2018). For sources where the *Gaia* single-star model is well fitted, the RUWE is expected to be close to 1.0, and values significantly greater than 1.0 reflect problems in the astrometric solution or non-single objects. To account for this, for stars with $\text{RUWE} > 1.4$ we scaled the elements of the covariance matrix that are taken from the *Gaia* catalogues by the square of their RUWE values. If a given Cepheid has a non-numerical RUWE, we set its value to 22, which corresponds to the maximum value of the original list of Cepheids in the *Gaia* catalogue.

We assume the clusters' covariance matrices to be diagonal whenever the data collected come from several sources, and we possess no information about possible correlations. If correlations between the cluster parameters are known and given in the cluster sources or can be inferred from, for example, *Gaia* data, the mean values from the clusters members are included in the corresponding cluster's covariance matrix. For the Cepheids' matrices we used the correlations between parallaxes and proper motions explicitly provided by the *Gaia* eDR3 catalogue. Finally, we assume the correlation between the properties of clusters and Cepheids to be negligible.

It is possible to show that, under these conditions, and assuming Gaussian distributions, the Mahalanobis distance c is actually χ^2 -distributed. It is worth mentioning that the shape of the χ^2 distribution depends on the number of dimensions of \vec{z} , i.e., the number of constraints considered for the combo. Finally, the likelihood is the result of:

$$P(B|A) = 1 - p(c), \quad (2.7)$$

where $p(c)$ represents the probability of finding a value at least as extreme as the observed c under the null hypothesis of (true) membership, that is, is the p-value of c .

2.3.3 Differences with A13

Although our study follows the Bayesian approach of A13, there are also significant differences, both in the method and in the data, since we benefit from greatly improved data quality thanks to *Gaia* in particular. We discuss these differences here below:

A13 initially considered 2,168 clusters. In our study, many more entered the catalogue, since the D02 database has been continuously updated and thanks to the discovery of numerous open clusters after *Gaia* DR2. Our catalogue contains over 4,000 clusters. Moreover, cluster parallaxes and proper motions have been updated to *Gaia* DR2 values for roughly half of our cluster catalogue.

Our initial catalogue of Cepheids is also much larger than the one used in A13 (2,921 vs. 1,821) thanks to numerous surveys having provided a large number of new Cepheids. Parallaxes in A13 are taken directly from the Hubble Space Telescope (8 stars, [Benedict et al., 2007](#)), from the study by [Storm et al. \(2011\)](#) for 33 stars, and from HIPPARCOS ([van Leeuwen, 2007](#)) for a good fraction of their sample. For 622 Cepheids, parallaxes are derived by inverting the distance to the Cepheid, computed using a period-luminosity relation in the V -band since the largest photometric datasets are available in this band. Although computed with the greatest care, this method suffers from the intrinsic width of the instability strip, which is much larger than in the near-infrared for instance, from the metallicity dependence of V -band period-luminosity relations (e.g., [Romaniello et al., 2008](#)), from the heterogeneity of the photometric datasets used, and from very large uncertainties on the adopted values for the colour excess $E(B - V)$. We benefit instead from the great quality of *Gaia* eDR3 parallaxes. Finally, the proper motions for Cepheids in A13 are taken from HIPPARCOS ([van Leeuwen, 2007](#)) when available and from the Position and Proper Motion Extended-L catalogue (PPMXL; [Roeser, Demleitner, & Schilbach, 2010](#)) otherwise, while ours are also from *Gaia* eDR3. Radial velocities are comparable in terms of data availability, accuracy, and precision.

In Figure 2.3, we compare the astrometric and kinematic datasets, after cross-matching the $\sim 4,000$ pairs investigated by A13 against our $\sim 44,300$ candidates. Since no other comparison data are available, we compare the difference between a given Cepheid and its potential host in both datasets. On the other hand, such a comparison relates directly to possible differences in the probabilities $P(B|A)$ derived by each study. We note that even small discrepancies may be significant in the computation of $P(B|A)$. In terms of proper motions, the spreads of the distributions are of the order of tens of mas yr^{-1} , and can be as high as $\sim 180 \text{ mas yr}^{-1}$.

We mentioned earlier that we adopted a different prior for cluster membership, to take

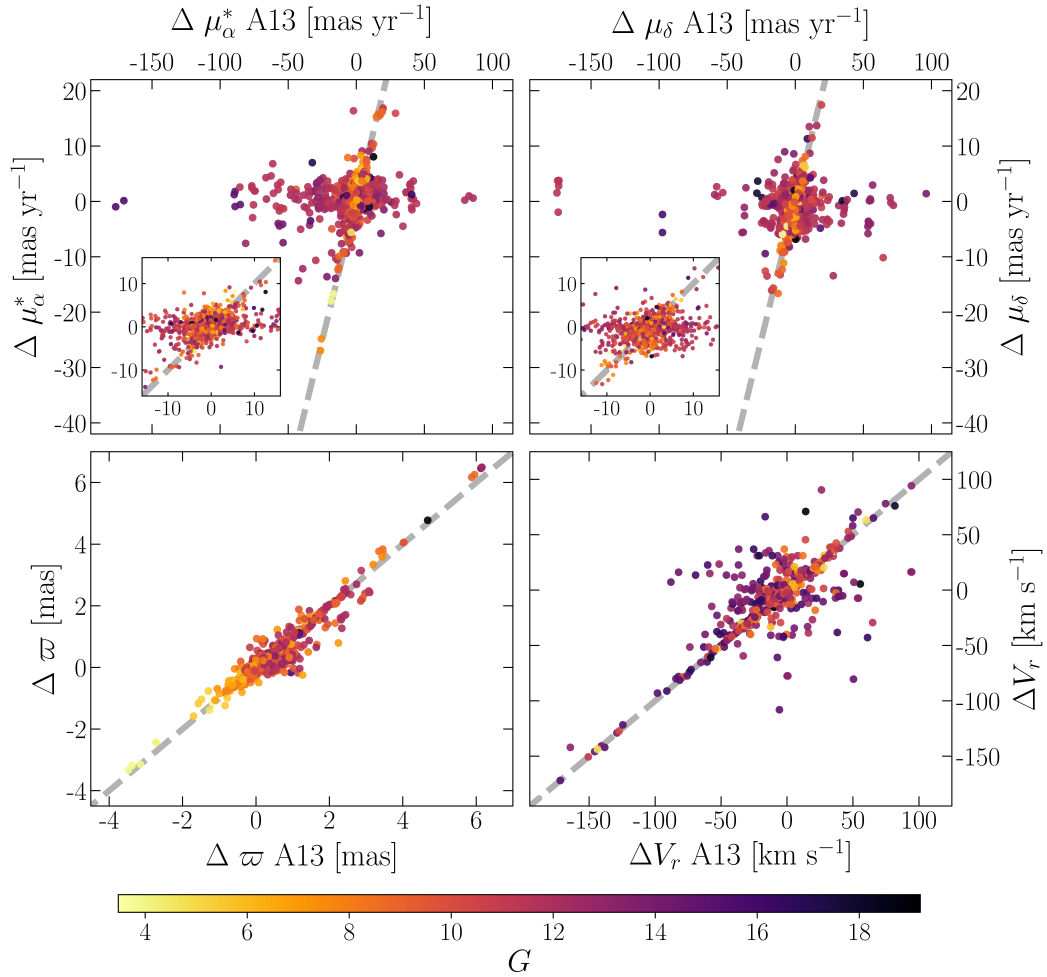


Figure 2.3: Comparison of the differences in proper motions, parallaxes, and radial velocities between clusters and Cepheids for the combos in common with A13. The filled circles shown are colour-coded by the Cepheids’ mean G magnitudes. A grey dashed line representing the identity function is plotted in each panel as a reference. In the plots displaying proper motion differences (*upper* panels) we include an enlargement of the central distribution of points.

into account the mounting evidence of large spatial extensions even for young clusters. Since this particular property had not been discovered yet, A13 adopted a stricter prior that is less sensitive to the clusters' outskirts but conversely less prone to false positives. We note in passing that an even looser prior has been used by [Hanke et al. \(2020b\)](#) in a search for extra-tidal halo stars in the neighborhood of globular clusters.

Another important difference is that, in contrast to A13, who took into account up to six dimensions when computing the square of the Mahalanobis distance, we only consider up to four (ϖ , μ_{α}^* , μ_{δ} , and V_r), and neither ages nor metallicities, in the computation of c .

If we were to include ages in our analysis, we would necessarily have computed the Cepheids' ages from period-age relations. This is, however, impossible in our case since one of our goals is to constrain such relations. Moreover, ages derived from period-age relations with an average stellar rotation ($\Omega_{\text{ZAMS}}/\Omega_{\text{crit}} = 0.5$; [Anderson et al. 2016](#)) are 50-100 per cent higher than those derived from period-age relations without rotation (e.g., [Bono et al., 2005](#)). As far as clusters are concerned, for 93 per cent of the clusters in D02 ages were provided. From the numerous clusters discovered in *Gaia* DR2 data, a good fraction has ages available (see e.g. [Bossini et al., 2019](#), or CG20, without quoted uncertainties for the vast majority). However, the difficulty to properly identify the main-sequence turn-off (MSTO) compromises the age determination via the isochrone-fitting method for young clusters, that is, those potentially hosting Cepheids, especially when using an automated algorithm as we experienced ourselves (see Section 2.6 for a more detailed discussion). The difficulty is reduced towards higher ages, when the MSTO and the RGB region become more populated, and A13 allowed for varying uncertainties in age to take this effect into account. As pointed out by A13, even large uncertainties are useful, in the sense that they allow us to filter out pairs for which ages definitely mismatch. Our concern here is that pairs could be rejected on the basis of an inaccurate age determination, even when allowing for large uncertainties.

The situation is even worse in the case of the metallicity, since $[\text{Fe}/\text{H}]$ is available only for a small fraction of the clusters, and often relies on disparate techniques (photometric estimates, low-resolution spectroscopy, high-resolution spectroscopy) and very few cluster members. Many have attempted to provide homogeneous metallicity scales in the recent past, either within a given large spectroscopic survey or by collecting data from various sources (e.g., [Netopil et al., 2016](#)), but the number of clusters with available metallicities falling in the age range considered here is very small. Studies of the MW radial abundance gradient indicate a good agreement between < 1 Gyr old open clusters and Cepheids, both for $[\text{Fe}/\text{H}]$ and other elements (e.g., [Lemasle et al., 2008](#); [Genovali et al., 2015](#); [Magrini et al., 2017](#)), but detailed comparisons are still missing. [Fry & Carney \(1997\)](#) found a good agreement (≈ 0.1 dex) between the metallicity of two main-sequence stars and the Cepheid U Sgr in M25, but the comparison is limited to $[\text{Fe}/\text{H}]$. [Lemasle et al. \(2017\)](#) found a similarly good agreement between 6 Cepheids and a large number of RGB stars analysed by [Mucciarelli et al. \(2011\)](#) in the young LMC cluster NGC 1866, which contains 24 Cepheids ([Musella et al., 2016](#)) and is therefore not representative of MW young clusters.

On the basis of the above, we decided to search for possible cluster-Cepheid combos relying on astrometry and kinematics only, awaiting for a membership confirmation from studies including a detailed age and chemical analysis.

2.4 The data

2.4.1 Parallaxes

For the open clusters in our list (see Section 2.2) we used the parallaxes and their associated uncertainties directly from their original sources, if available. If not (as for the D02 clusters), we derived the parallaxes ϖ from the published distances d in parsecs, following:

$$\begin{aligned}\varpi &= \frac{1000}{d} \text{ (mas)}, \\ \sigma_{\varpi} &= \frac{1000}{d^2} \cdot \sigma_d \text{ (mas)},\end{aligned}\tag{2.8}$$

where σ_d represents the distance uncertainty, and σ_{ϖ} the corresponding assumed parallax uncertainty. We consider this approximation justified since there is an overall good agreement between parallaxes computed this way and those provided by CG20 using *Gaia* DR2 data with a median difference of 0.08 mas for the clusters in common between that study and D02. In such a case we enforced a distance uncertainty of 20 per cent (as done by A13) to account for various effects impacting the distance determination such as stellar rotation and binarity.

In any case, older values are superseded by parallaxes and parallax errors from *Gaia* DR2 when available. Moreover, [Lindegren et al. \(2018\)](#) reported a (global) zero-point shift of -0.03 mas for *Gaia* DR2 parallaxes. Unless this was explicitly accounted for in the original papers, we shifted the *Gaia* DR2 parallaxes accordingly.

In addition, parallaxes of *Gaia* sources located close to each other on the sky are highly correlated, especially when they are separated by less than one degree. Following the recommendations of [Lindegren et al. \(2018\)](#) for sources separated by an angle θ , we computed the mean spatial covariance of the parallax errors $V_{\varpi}(\theta)$ of the members of each cluster in our sample based on *Gaia* DR2 data, if a list of members was available in the source catalogue, and if these spatial covariances were not originally considered. Otherwise, spatial covariances were neglected. The corresponding systematic uncertainties and additional correlations are then included in the covariance matrices of the clusters.

For the Cepheids, parallaxes from *Gaia* eDR3 are available for all the stars in our sample. We corrected them for the *Gaia* eDR3 zero-point parallax offset following [Lindegren et al. \(2021\)](#)²⁹, and we increased the uncertainties by 10 per cent to account for their likely underestimation, based on the work of [Fabricius et al. \(2021\)](#). As in the case of the clusters, these changes were included in the covariance matrices of the Cepheids.

2.4.2 Proper motions

The (mean) proper motions in right ascension and declination and their respective uncertainties were first taken from D02. Some clusters are registered only in K13, where a single value σ_{μ} is given for the proper motion uncertainties. We therefore adopted $\sigma_{\mu\alpha}^* = \sigma_{\mu\delta} = \sigma_{\mu}/\sqrt{2}$. These values were replaced by proper motions based on *Gaia* DR2 when available. In this case, we adopted the values tabulated in the respective source catalogues for the proper

²⁹https://gitlab.com/icc-ub/public/gaiadr3_zeropoint

motions and their uncertainties.

Similarly to the $V_{\varpi}(\theta)$ correction described above, we corrected the *Gaia* DR2 proper motion uncertainties by taking into account the spatial covariances $V_{\mu}(\theta)$ that affect sources located close to each other in the sky (Lindgren et al., 2018), in this case the members of a given cluster, and added the mean $V_{\mu}(\theta)$ of such a cluster as a systematic uncertainty when this effect was not already accounted for in the original studies. For the clusters with *Gaia* DR2 proper motions but no list of members (which have sizes as small as ~ 0.01 deg), we added a systematic uncertainty of $0.066 \text{ mas yr}^{-1}$ following the recommendations of Vasiliev (2019) (see their Figure 3). These changes were propagated in the cluster covariance matrices.

In the case of the Cepheids, we take their proper motions directly from the *Gaia* eDR3 catalogue. It is worth noting that the proper motions (and their uncertainties) listed in this catalogue are equivalent to those in the *Gaia* DR3. We revised these values using the *Gaia* eDR3 proper motion bias correction recently described by Cantat-Gaudin & Brandt (2021), and added a systematic error of $-10 \mu\text{as yr}^{-1}$ to the uncertainties of the Cepheids with $G < 13$ listed in the catalogue to account for the remaining color-dependent systematics discussed by these authors. These changes were included in the covariance matrices of the Cepheids.

2.4.3 Radial velocities

For the radial velocity of the open clusters, we use the mean values and uncertainties listed in D02. We note, however, that for a given cluster, the uncertainty on the radial velocity provides a good estimate of the intrinsic velocity dispersion (σ_{ocRV}) only when the number of stars analysed is large. For clusters only present in K13, where no uncertainty is given, we follow A13's reasoning and estimate this value by computing $\sigma_{ocRV} = 10/\sqrt{N_{RV}} \text{ km s}^{-1}$, where N_{RV} is the number of stars used to compute the radial velocity of the cluster. If N_{RV} is also missing, we assume a value of 15 km s^{-1} , which matches the maximum velocity dispersion for open clusters recently analysed by, e.g., Carrera et al. (2019) and Donor et al. (2020).

To update the radial velocities and associated uncertainties of our cluster catalogue we used the information of 131 clusters listed in Carrera et al. (2019), obtained by data mining the APOGEE (DR14; Abolfathi et al., 2018; Holtzman et al., 2018) and the GALAH survey (DR2; Buder et al., 2018). Of these open clusters, 127 are in common with the original D02 + K13 catalogues, of which 72 have previously derived radial velocities (in D02 + K13). We also considered the radial velocities of the 128 clusters listed in Donor et al. (2020), who examined APOGEE data (DR16; Jönsson et al., 2020). Of these clusters, 126 are listed in the catalogue of D02 and K13. We note that the mean absolute radial velocity difference between the values listed in the D02 and K13 catalogues, and those catalogued by Carrera et al. (2019) and Donor et al. (2020) is $12.1 \pm 26.1 \text{ km s}^{-1}$ and $7.5 \pm 13.9 \text{ km s}^{-1}$, respectively. For the clusters for which more than one radial velocity measurement is available, we give priority to the more recent studies over older ones (including those in D02 and K13, since we favour the homogeneity of the data). In any case, we impose a minimum velocity dispersion of 2 km s^{-1} , a value also in line with the compilations of Carrera et al. (2019) and Donor et al. (2020) for clusters in which the measured velocity dispersion relies on more than 10 stars.

As classical Cepheids are pulsating stars, monitoring observations are required to derive their systemic velocity (or alternatively radial velocity templates). Such data are in general

not available, and we rely on the compilation made by Mel'nik et al. (2015), in which they provide heliocentric radial velocities and their uncertainties for ~ 320 Cepheids from different sources (see references in Mel'nik et al. 2015). To take into account possible phase coverage biases or binarity (up to 80 per cent of Cepheids are in binary systems; Kervella et al., 2019), we impose an arbitrary minimum uncertainty for the Cepheids' radial velocities of 2 km s^{-1} .

2.5 Membership determination: the outcome

Of the total $\sim 44,300$ possible combos for which we computed the likelihood of membership, only a small fraction displays relatively high probabilities, and the sample is strongly dominated by cluster-Cepheid pairs with probabilities $\leq 10^{-5}$. From the cluster-Cepheid pairs with higher membership probabilities, 164 have probabilities higher than 1 per cent, 69 have probabilities over 10 per cent, and only 45 over 25 per cent. The thresholds mentioned here are only meant to give an overview of the results and bear no implication on membership, as our methodology relies on a hypothesis test that assumes membership in the first place. Cluster-Cepheid pairs with posterior probabilities higher than 0.10 are shown in Table 2.1. Those with membership probabilities from 0.01 to 0.10 can be found in the appendix (Table A2).

In Section 2.5.1, we briefly discuss a few combos from the literature that we consider recovered, relying mostly on the cluster Cepheid catalogues from David Turner³⁰, A13, and Chen, de Grijs, & Deng (2015). In Section 2.5.2, we briefly discuss six combos reported in at least three previous studies (from the aforementioned ones plus Röck 2012) for which we obtain marginal membership probabilities. In Table A1, we show the results of these comparisons with literature combos. In Section 2.5.4, we discuss a few arbitrarily selected combos.

2.5.1 A few bona fide combos from the literature

The Cepheids around NGC 7790

We recover the three Cepheids CE Cas A, and CE Cas B, CF Cas paired to the cluster NGC 7790 (widely known as the only Galactic open cluster hosting three Cepheids), with relatively high association probabilities. The three Cepheids are bright ($G \sim 10 \text{ mag}$) fundamental-mode pulsators with similar periods of $\sim 5 \text{ d}$ (Ripepi et al., 2019), indicating they have a similar age.

Our algorithm also reports a non-negligible probability of association of these three Cepheids with LP 888 (Liu & Pang, 2019, even with a slightly larger probability for CE Cas A) or with UBC 404. Although they are close to each other in the vicinity of NGC 7790, LP 888 and UBC 404 are reported as different structures by Liu & Pang (2019) and Castro-Ginard et al. (2020), respectively. From previous knowledge (e.g., Sandage, 1958; Mateo & Madore, 1988; Matthews et al., 1995; Majaess et al., 2013b) and given $P(A)=1$, the three Cepheids are clearly members of NGC 7790, but the quite high likelihoods computed suggest a dynamical association between NGC 7790 and the other structures newly discovered nearby.

³⁰<http://www.ap.smu.ca/~turner/cdlist.html>

2 A study of Cepheids in open clusters and the Cepheid period-age relation in the Gaia era

Table 2.1: Cluster - Cepheid pairs with membership probabilities $P(A|B) > 0.10$. The table lists the cluster names as well as their Milky Way Star Clusters Catalog (MWSC) identification in the K13 catalogue, the Cepheid names, the ratio between the separation of the pair and the cluster's r_1 (Sep/r_1), the list of constraints used to derive the membership probability, the prior $P(A)$, the likelihood $P(B|A)$ and the membership probability $P(A|B)$.

Open cluster	MWSC ID	Cepheid	Sep/ r_1	Constraints	$P(A)$	$P(B A)$	$P(A B)$
Trumpler 14	1846	OGLE-GD-CEP-1673	0.50	$\varpi, \mu_\alpha^*, \mu_\delta$	1.00	1.00	1.00
UBC 553	–	OGLE-GD-CEP-1194	0.54	$\varpi, \mu_\alpha^*, \mu_\delta$	1.00	0.99	0.99
Berkeley 55	3490	ASASSN-V J211659.90+514558.7	0.38	$\varpi, \mu_\alpha^*, \mu_\delta$	1.00	0.94	0.94
Gaia 5	–	V0423 CMa	0.81	ϖ	1.00	0.94	0.94
ASCC 79	2288	OGLE-GD-CEP-1752*	0.77	$\varpi, \mu_\alpha^*, \mu_\delta$	1.00	0.94	0.94
Berkeley 51	3280	ASASSN-V J201151.18+342447.2	0.66	$\varpi, \mu_\alpha^*, \mu_\delta$	1.00	0.85	0.85
Harvard 16	2616	OGLE-BLG-CEP-041	0.85	$\varpi, \mu_\alpha^*, \mu_\delta$	1.00	0.83	0.83
FSR 0951	849	RS Ori	0.20	$\varpi, V_r, \mu_\alpha^*, \mu_\delta$	1.00	0.82	0.82
Lynga 6	2348	TW Nor	0.18	$\varpi, V_r, \mu_\alpha^*, \mu_\delta$	1.00	0.82	0.82
NGC 6664	2962	EV Sct	0.40	$\varpi, V_r, \mu_\alpha^*, \mu_\delta$	1.00	0.80	0.80
NGC 7790	3781	CF Cas	0.36	$\varpi, V_r, \mu_\alpha^*, \mu_\delta$	1.00	0.80	0.80
Gulliver 9	–	AM Vel	1.33	$\varpi, \mu_\alpha^*, \mu_\delta$	0.77	1.00	0.77
IC 4725	2940	U Sgr	0.13	$\varpi, V_r, \mu_\alpha^*, \mu_\delta$	1.00	0.75	0.75
NGC 129	53	DL Cas	0.33	$\varpi, V_r, \mu_\alpha^*, \mu_\delta$	1.00	0.75	0.75
Czernik 41	3192	J297.7863+25.3136	0.45	$\varpi, \mu_\alpha^*, \mu_\delta$	1.00	0.73	0.73
vdBergh 1	934	CV Mon	0.49	$\varpi, \mu_\alpha^*, \mu_\delta$	1.00	0.67	0.67
NGC 6193	2444	OGLE-GD-CEP-1175*	0.71	$\varpi, \mu_\alpha^*, \mu_\delta$	1.00	0.67	0.67
NGC 6067	2370	V0340 Nor	0.14	$\varpi, \mu_\alpha^*, \mu_\delta$	1.00	0.66	0.66
BH 222	2564	OGLE-BLG-CEP-110	0.19	$\varpi, \mu_\alpha^*, \mu_\delta$	1.00	0.65	0.65
NGC 6649	2949	V0367 Sct	0.82	$\varpi, \mu_\alpha^*, \mu_\delta$	1.00	0.63	0.63
Kronberger 84	3532	ASASSN-V J213533.70+533049.3	0.27	$\varpi, \mu_\alpha^*, \mu_\delta$	1.00	0.62	0.62
UBC 266	–	OGLE-GD-CEP-1676	1.08	$\varpi, \mu_\alpha^*, \mu_\delta$	0.94	0.62	0.58
FSR 1755	–	OGLE-BLG-CEP-175	1.00	μ_α^*, μ_δ	1.00	0.57	0.57
UBC 130	–	SV Vul	1.41	$\varpi, \mu_\alpha^*, \mu_\delta$	0.73	0.71	0.52
UBC 229	–	V0335 Pup	0.48	$\varpi, \mu_\alpha^*, \mu_\delta$	1.00	0.51	0.51
NGC 7790	3781	CE Cas B	0.62	$\varpi, \mu_\alpha^*, \mu_\delta$	1.00	0.50	0.50
FSR 0172	3218	Dauban V16	1.25	$\varpi, \mu_\alpha^*, \mu_\delta$	0.82	0.59	0.49
ASCC 12	427	SV Per	1.81	$\varpi, \mu_\alpha^*, \mu_\delta$	0.53	0.90	0.48
LP 1937	–	DF Cas	1.58	$\varpi, \mu_\alpha^*, \mu_\delta$	0.64	0.71	0.45
UBC 608	–	ASASSN-V J040516.13+555512.9	0.63	$\varpi, \mu_\alpha^*, \mu_\delta$	1.00	0.45	0.45
LP 1370	–	DT Gem	1.77	$\varpi, \mu_\alpha^*, \mu_\delta$	0.55	0.78	0.43
NGC 6087	2382	S Nor	0.07	$\varpi, V_r, \mu_\alpha^*, \mu_\delta$	1.00	0.38	0.38
LP 2134	–	VY Per	1.53	$\varpi, \mu_\alpha^*, \mu_\delta$	0.66	0.56	0.37
NGC 6631	2916	OGLE-BLG-CEP-164	1.31	$\varpi, \mu_\alpha^*, \mu_\delta$	0.78	0.46	0.36
LP 888	–	CE Cas B	1.91	$\varpi, \mu_\alpha^*, \mu_\delta$	0.50	0.71	0.35
LP 2134	–	UY Per	1.01	$\varpi, \mu_\alpha^*, \mu_\delta$	0.99	0.35	0.35
FSR 0158	3182	GQ Vul	2.22	$\varpi, \mu_\alpha^*, \mu_\delta$	0.38	0.89	0.34
LP 888	–	CE Cas A	1.91	$\varpi, \mu_\alpha^*, \mu_\delta$	0.50	0.66	0.33
UBC 106	–	CM Sct	1.30	$\varpi, \mu_\alpha^*, \mu_\delta$	0.79	0.40	0.32
DBSB 179	2544	OGLE-BLG-CEP-173	0.66	$\varpi, \mu_\alpha^*, \mu_\delta$	1.00	0.31	0.31
BH 121	1960	OGLE-GD-CEP-1688	0.91	$\varpi, \mu_\alpha^*, \mu_\delta$	1.00	0.29	0.29
UBC 291	–	OGLE-GD-CEP-1719	2.21	$\varpi, \mu_\alpha^*, \mu_\delta$	0.40	0.72	0.28
IC 2395	1537	OGLE-GD-CEP-0270*	1.99	$\varpi, \mu_\alpha^*, \mu_\delta$	0.46	0.61	0.28
LP 888	–	CF Cas	1.98	$\varpi, \mu_\alpha^*, \mu_\delta$	0.47	0.59	0.28
NGC 7790	3781	CE Cas A	0.60	$\varpi, \mu_\alpha^*, \mu_\delta$	1.00	0.28	0.28
Ruprecht 79	1701	CS Vel	0.69	$\varpi, V_r, \mu_\alpha^*, \mu_\delta$	1.00	0.23	0.23
Loden 143	1807	OGLE-GD-CEP-0507	2.74	$\varpi, \mu_\alpha^*, \mu_\delta$	0.21	0.95	0.20
UBC 290	–	X Cru	2.04	$\varpi, \mu_\alpha^*, \mu_\delta$	0.45	0.41	0.18
Gulliver 29	–	OGLE-BLG-CEP-172	2.20	$\varpi, \mu_\alpha^*, \mu_\delta$	0.39	0.47	0.18
UBC 406	–	CG Cas	1.72	$\varpi, \mu_\alpha^*, \mu_\delta$	0.58	0.30	0.17
Schuster 1	1756	GDS J1004164-555031	2.21	$\varpi, \mu_\alpha^*, \mu_\delta$	0.39	0.44	0.17
LP 699	–	DK Vel	3.29	$\varpi, \mu_\alpha^*, \mu_\delta$	0.17	0.97	0.17
BH 99	1831	OGLE-GD-CEP-0507	3.06	$\varpi, \mu_\alpha^*, \mu_\delta$	0.20	0.85	0.17
UBC 553	–	OGLE-GD-CEP-1196	0.90	$\varpi, \mu_\alpha^*, \mu_\delta$	1.00	0.16	0.16
UBC 80	–	ASAS J060722+0834	3.24	$\varpi, \mu_\alpha^*, \mu_\delta$	0.18	0.91	0.16
LP 1332	–	VV Cas	2.63	$\varpi, \mu_\alpha^*, \mu_\delta$	0.29	0.55	0.16
Teutsch 145	2978	GDS J1842359-051557	1.94	$\varpi, \mu_\alpha^*, \mu_\delta$	0.48	0.29	0.14
UFMG 69	–	OGLE-BLG-CEP-057	2.98	$\varpi, \mu_\alpha^*, \mu_\delta$	0.21	0.62	0.13
Loden 153	1824	CS Car	1.71	$\varpi, \mu_\alpha^*, \mu_\delta$	0.46	0.28	0.13
UFMG 70	–	OGLE-BLG-CEP-057	1.91	$\varpi, \mu_\alpha^*, \mu_\delta$	0.49	0.27	0.13
NGC 4609	2062	WISE J124231.0-625132	1.01	$\varpi, \mu_\alpha^*, \mu_\delta$	1.00	0.13	0.13

Table 2.1: (Continued)

Open cluster	MWSC ID	Cepheid	Sep/ r_1	Constraints	$P(A)$	$P(B A)$	$P(A B)$
Collinder 228	1845	OGLE-GD-CEP-1673	3.66	$\varpi, \mu_{\alpha}^*, \mu_{\delta}$	0.13	0.93	0.12
UBC 345	–	V0459 Sct	3.77	$\varpi, \mu_{\alpha}^*, \mu_{\delta}$	0.12	1.00	0.12
LP 699	–	GDS J0909005-533555	2.62	$\varpi, \mu_{\alpha}^*, \mu_{\delta}$	0.29	0.41	0.12
UBC 409	–	V0824 Cas	2.71	$\varpi, \mu_{\alpha}^*, \mu_{\delta}$	0.27	0.39	0.10
Trumpler 16	1850	OGLE-GD-CEP-1673	2.97	$\varpi, \mu_{\alpha}^*, \mu_{\delta}$	0.21	0.49	0.10
Loden 143	1807	OGLE-GD-CEP-1669	3.28	$\varpi, \mu_{\alpha}^*, \mu_{\delta}$	0.13	0.82	0.10
UBC 286	–	OGLE-GD-CEP-1707	1.36	$\varpi, \mu_{\alpha}^*, \mu_{\delta}$	0.76	0.14	0.10
LP 925	–	ASASSN-V J062542.07+082944.4	2.95	$\varpi, \mu_{\alpha}^*, \mu_{\delta}$	0.22	0.45	0.10

* Uncertain Cepheid classification, as noted by the OGLE team.

Open clusters with identification names starting with UBC correspond to clusters found by [Castro-Ginard et al. \(2018, 2019, 2020\)](#). The cluster names starting with LP are discoveries of [Liu & Pang \(2019\)](#), whereas those starting with UFMG are from [Ferreira et al. \(2021\)](#). Cepheid names are taken from the International Variable Star Index (VSX; [Watson, Henden, & Price, 2006, 2014](#)), or from the OGLE catalogue ([Udalski et al., 2018](#)).

The Cepheids in NGC 6067

A second case of well-known cluster-Cepheid associations are the Cepheids V0340 Nor and QZ Nor and the cluster NGC 6067. An extensive discussion addressing the possible membership of, especially, QZ Nor is available in the literature (see e.g. [Eggen, 1980](#); [Walker, 1985b](#); [Coulson & Caldwell, 1985](#); [An, Terndrup, & Pinsonneault, 2007](#); [Turner, 2010](#); [Majaess, Turner, & Lane, 2008](#)). A dedicated study performed by [Majaess et al. \(2013a\)](#) confirmed both stars as members of NGC 6067. Recently, [Breuval et al. \(2020\)](#) interpreted the proper motion difference between the cluster and QZ Nor as a hint that the Cepheid is leaving the cluster. The striking difference in the membership probability (66 per cent for V0340 Nor vs. < 1 per cent for QZ Nor) is a strong indication that the dynamical state of the cluster can have a strong impact on the membership probability. This is the reason why we provide a list of potential combos with a low membership probability, ranging from 1 to 10 per cent (Table A2) as it may contain similar cases. Finally, [Breuval et al. \(2020\)](#) proposes GU Nor as a potential member of NGC 6067 as well. We find a posterior probability < 0.01 for this pair, as both its prior and likelihood are not significant.

GQ Vul and FSR 0158

For the combo consisting of the distant open cluster FSR 0158 ([Froeblich, Scholz, & Raftery, 2007](#)) and the Cepheid GQ Vul we also obtain a high association probability (0.34). This result is a combination of the position of the Cepheid close to the cluster’s centre and the excellent agreement between their proper motions and parallaxes. It had been reported so far only by A13 with a probability of 43 per cent. We note, however, a discrepancy between the distance of FSR 0158 according to CG20 ($\sim 6,100$ pc) and the distance of GQ Vul ($\sim 4,500$ pc) derived by [Wang et al. \(2018\)](#) using a PL relation in the mid-infrared. Similarly, GQ Vul is about ~ 35 Myr old from the theoretical PA relation of [Bono et al. \(2005\)](#), whereas the cluster age as determined by CG20 is < 10 Myr, a value incompatible with the presence of a Cepheid. However, it is noteworthy that only 27 stars are considered as cluster members with a probability higher than 50 per cent, and only 14 with probabilities higher than 70 per cent (CG18b, CG20), which may significantly affect the determination of FSR 0158’s distance and age.

Combos for which we obtain $P(A|B) > 0.01$ and that appear at least once in Turner’s database, A13 (with membership probability > 0.10 from their work), or [Chen, de Grijs, & Deng \(2015\)](#), together with the spectroscopically confirmed cluster Cepheids described by [Lohr et al. \(2018\)](#) and [Clark et al. \(2015\)](#), and the association recently found by [Negueruela, Dorda, & Marco \(2020\)](#), are listed at the top of Table A1 (19 in total).

2.5.2 Missed combos from the literature

Beyond the fact that combos previously reported in the literature might simply be discarded in the light of new, more accurate data, we could be unable to recover real combos for several reasons:

We exclude the fact that a cluster, and especially a Cepheid are missing in our catalogue. Both the lists of clusters and Cepheids have been regularly updated and are much larger than the ones used for previous studies. Of course, there is always the possibility that an object is retracted, and this is actually the case for the Cepheid ASAS J155149–5621.8 ([Pojmanski & Maciejewski, 2004](#)) located 0.1 deg away from the centre of the cluster NGC 5999, within its limiting radius ($r_{\text{lim}} \sim 0.15$ deg; [Ferreira et al. 2019](#)). A potential association has been hypothesised by [Chen, de Grijs, & Deng \(2015\)](#), based on good agreement in proper motion, although they noted a mismatch for the computed age and distance modulus. However, the star is not considered as a classical Cepheid anymore: it is listed as a type II Cepheid by [Clementini et al. \(2019\)](#) and as “other” by [Ripepi et al. \(2019\)](#). It is considered a non-periodic variable in ASAS-SN ([Jayasinghe et al., 2019b](#)).

Another possibility is that an insignificant membership probability originates from a low prior $P(A)$. The projected distance between the Cepheid and the cluster centre has obviously not substantially changed, and since we opted for a looser prior, the only possibility for this to happen is that the cluster apparent size has been modified after its core radius, limiting radius, or both, were modified. This could be the case for the potential association between the Cepheid X Cyg and the cluster Ruprecht 175. This pair has been considered a bona-fide association by other authors in the past ([Turner, 1998](#); [Chen, de Grijs, & Deng, 2015](#)), but the pair’s projected separation is 0.37 deg (28.6 pc, assuming membership), which, given a tabulated value of $r_1=0.05$ deg for Ruprecht 175 (3.8 pc, K13) gives a prior probability of virtually zero. We note in addition that the difference in parallax and proper motions between the cluster and the Cepheid are about ten times higher than their respective uncertainties, which leads to a negligible association probability.

As mentioned above, updated values of the input parameters and their uncertainties with respect to those used in previous studies may result in smaller posterior probabilities, which may even become negligible and inconsistent with membership. This could have happened for the Cepheid BB Sgr, associated with the cluster Collinder 394 by many authors ([Tsarevsky, Ureche, & Efremov, 1966](#); [Turner, 1984](#); [Usenko et al., 2019](#)). It has a relatively high prior $P(A)=0.59$, but there is a noticeable difference in the parallax and proper motions in right ascension and declination of the cluster and the Cepheid, which are 0.20 mas, 1.83 mas yr⁻¹, and 0.85 mas yr⁻¹, respectively. An analogous case occurs for the

combo WZ Sgr and Turner 2, where the difference in parallax and proper motions in right ascension and declination of the cluster and the Cepheid is 0.22 mas , 0.25 mas yr^{-1} , and 0.57 mas yr^{-1} (respectively), the latter being larger than three times the cluster’s proper motion dispersion. Similarly, the Cepheid CG Cas has been considered for a long time a likely member of the cluster Berkeley 58 ($r_{50} = 3.6 \text{ pc}$; Turner et al. 2008; Chen, de Grijs, & Deng 2015), of which it is separated by 0.09 deg (5.4 pc). In spite of having $P(A) = 0.66$, we found a negligible membership probability for this pair due to their differences in parallax and proper motion. Interestingly, we found instead higher probabilities for CG Cas to be associated with UBC 406 (0.17) or LP 888 (0.09). In the case of CG Cas and UBC 406, the angular separation corresponds to $1.7 \cdot r_1$ (0.17 deg ; 10.6 pc , assuming membership), whereas the Cepheid is located at $2.7 \cdot r_1$ from the centre of LP 888 (0.74 deg ; 37.2 pc). We note in addition that the Cepheid V0997 Cas shows signs of an association with the cluster LP 888, albeit with a low probability of 2 per cent.

The case of RU Sct is more complicated, because the Cepheid has been associated with the cluster Trumpler 35 (Turner, 1980; Chen, de Grijs, & Deng, 2015) as well as with other hosts, like Dolidze 32 (A13). In fact, A13 computed a membership probability of 0.52 with Dolidze 32 and of only 15 per cent with Trumpler 35. In our study, we obtain a prior of 0.30 and 0.02 for the association of RU Sct with Dolidze 32 and Trumpler 35, respectively, and posterior probabilities smaller than 1 per cent in both cases. These insignificant $P(A|B)$ are mostly due to the large difference in proper motions, which exceed the uncertainties by about one order of magnitude, and due to the large radial velocity difference of 19 km s^{-1} in the case of the pair Dolidze 32 – RU Sct, where the individual uncertainties used are 7.4 and 2 km s^{-1} , respectively. A third possible host for RU Sct could be the cluster Dolidze 34, for which $P(A) = 0.07$ (RU Sct lies at approximately four times the cluster’s r_1). However, in that case we also obtain an insignificant membership probability, based on a radial velocity, parallax, and proper motion comparison.

Moreover, we could end up with a very low posterior probability because uncertainties have been underestimated. This could for instance be the reason why we do not recover the Cepheid SU Cyg associated with the cluster Turner 9 (Turner et al. 1998b; Turner 2010; A13). SU Cyg is located near the centre of the cluster, which returns $P(A)=0.66$ in our analysis. However, parallax and proper motion differences between the pair are much larger than their corresponding uncertainties (about one order of magnitude), and we obtain therefore a small association probability for Turner 9 and SU Cyg.

Hanke et al. (2020b) advocate for an additional unknown systematic error on *Gaia* DR2 proper motions. Analysing stars with a possible globular cluster origin, they find that, from their position in the colour-magnitude diagram and their absolute proper motion deviation with respect to the globular cluster M 13’s mean value (see their Figure 2), the bright stars in their sample are obvious members of M13. However, those stars would not qualify as cluster members when taking into account the relative proper motion deviation. This result is a consequence of their membership likelihoods, computed from proper motions only and based on Mahalanobis distances, becoming very small for such stars. Since those stars have G magnitudes of the order of $G = 14$ to 15 mag , the effect might be similar for the open cluster members considered here, and even stronger for the somewhat brighter Cepheids in our sample. This could in turn artificially lower the value of our posterior probabilities.

Finally, we already mentioned in Section 2.3.1 that we adopted a looser prior as compared with A13 to accommodate for possible primordial or tidal features surrounding open clusters. However, it might be necessary to relax in addition the conditions related to parallaxes, proper motions, and radial velocities, in order to properly account for the dynamical state of the clusters. It could indeed be that the larger uncertainties in the pre-*Gaia* era were masking this effect, which could not be omitted anymore in the light of *Gaia*'s accuracy and precision. We note in passing that inflating the uncertainties in the astrometric data by a factor of two would also increase the total number of combos with $P(A|B) > 0.01$ by a factor of two (from 164 to 328 pairs).

2.5.3 Combos with high likelihood but low prior

In Table 2.1, where we list combos with probabilities higher than 0.10, the large majority of stars have a high prior. There are also a few stars with a lower prior, compensated by a high likelihood. In other words, their properties match extremely well with those of their potential host cluster, and they end up with a low probability only due to their large projected distance to the cluster. This is for instance the case of DK Vel in LP 699, OGLE GD-CEP-0507 in Loden 143 (MWSC 1807), SV Per in ASCC 12 (MWSC 427), and V0459 Sct in UBC 345.

When inspecting stars with lower membership probabilities ($0.01 < P(A|B) < 0.10$, Table A2), the number of these cases increases, including for instance OGLE GD-CEP-0964 and OGLE GD-CEP-0968 in UFMG 54, RW Cam in UPK 300, and OGLE GD-CEP-1167 in UBC 545. A handful of such stars are associated with 2–4 clusters, but with high likelihoods only with 1–2 hosts, such as AQ Pup and LP 1428, and OGLE GD-CEP-1669 with Loden 143 and UBC 259.

A high likelihood is obviously not a guarantee of membership, as it can in particular be driven by issues in the determination of the astrometric parameters and/or large uncertainties. Nevertheless, we highlight these cases as interesting pairs to further investigate. We note that if we do not restrict ourselves to combos with membership probabilities $P(A|B) > 0.01$, we find 258 additional combos with likelihood $P(B|A) > 0.85$. They are listed in Table A3 in the Appendix. Within this sample, 66 per cent of the stars lie within $35 \cdot r_1$, a value after which the distribution of projected radial distance drops drastically.

2.5.4 Some combos of interest

In this section we select arbitrarily a small number of combos for a more detailed discussion, focusing mostly on newly discovered clusters as potential hosts (not necessarily those with the highest membership probabilities).

Clusters potentially hosting several Cepheids

In our sample of combos with membership probabilities $P(A|B) > 0.01$, we find clusters that appear to be associated with several stars. We list them here below for further investigation and provide a few comments for each of them. With the current data at hand, in addition to

the astrometric and kinematic constraints used in this work, we conclude that only a couple of them are robust detections.

The Cepheids AQ Pup and V620 Pup present probabilities of association with LP 1429 (Liu & Pang, 2019) of 0.04 and 0.01, respectively, mostly due to their likelihoods (0.42 and 0.40). Possible associations of these Cepheids with overdensities, or putative clusters in their surroundings have been suggested in the past (Turner et al., 2012), including Ruprecht 43, Ruprecht 44, and Turner 12. We report negligible membership probabilities in these cases, even considering the relatively high prior of AQ Pup and Turner 12 (0.25).

Three Cepheids are listed with non-negligible membership probability in BH 131: OGLE GD-CEP-0785 is the closest one (at 17 pc from the cluster centre, assuming membership) and therefore also has the highest prior (~ 0.43), while OGLE GD-CEP-0790 and OGLE GD-CEP-0795 lie farther away, with priors of 0.12 and 0.01. Only the latter has a higher likelihood (0.82), thus the three Cepheids have an overall membership probability of only 0.01–0.02. Other clusters in the neighborhood of BH 131 are BH 132 and UBC 521. Both the priors and the likelihoods are negligible for the association of OGLE GD-CEP-0785, OGLE GD-CEP-0790, and OGLE GD-CEP-0795 with these clusters.

Collinder 228 might host three Cepheids, namely V720 Car, OGLE GD-CEP-1672, and OGLE GD-CEP-1673. They have priors > 0.10 but relatively low likelihoods (with the exception of OGLE GD-CEP-1673) and therefore end up with membership probabilities ranging from 1 to 12 per cent.

For the Cepheids VY Per, UY Per, and SZ Cas we report a $P(A|B)$ of 0.37, 0.35, and 0.07 with LP 2134 (Liu & Pang, 2019), respectively, as a combination of their high priors and likelihoods. These relatively high membership probabilities make LP 2134 a case of interest, for which we consider further studies might be required. Other clusters within our list with which these Cepheids could be associated with because of their on-sky proximity, are Czernik 8, FSR 0591, UBC 190, ASCC 8, and SAI 17. However, for all of them the resulting $P(A|B)$ are near zero, including the pair Czernik 8–UY Per, which has been considered a real association in previous works (e.g., Turner, 1977; Chen, de Grijs, & Deng, 2015). For this pair in particular, the reason for its low probability is their low $P(B|A)$, which is not compensated by its slightly higher, but still poor prior (0.02 per cent).

Five Cepheids are seemingly related to LP 699 (GDS J0909005-533555, DK Vel, V0530 Vel, OGLE-GD-CEP-0341, EX Vel), with combinations of priors and likelihoods leading to membership probabilities from 1 to 17 per cent, with the larger value corresponding to DK Vel. We note that four of these Cepheids, GDS J0909005-533555, DK Vel, V0530 Vel, and OGLE-GD-CEP-0341, were not included in the analysis of A13, whereas EX Vel was paired with the cluster Teutsch 48, although with a null membership probability from that work. We confirm this result. The other four Cepheids are initially crossmatched with other clusters in the field in our study. However, the membership probabilities of these pairs are not significant overall.

Finally, six Cepheids are potentially associated with LP 925, namely VW Mon, V480 Mon, V966 Mon, ASAS J062855+1107.3, OGLE GD-CEP-0040, ASASSN-V J062542.07+082944.4, but they have either a low prior or a low likelihood. Their membership probabilities range from 2 to 10 per cent, making their association with LP 925 rather unlikely.

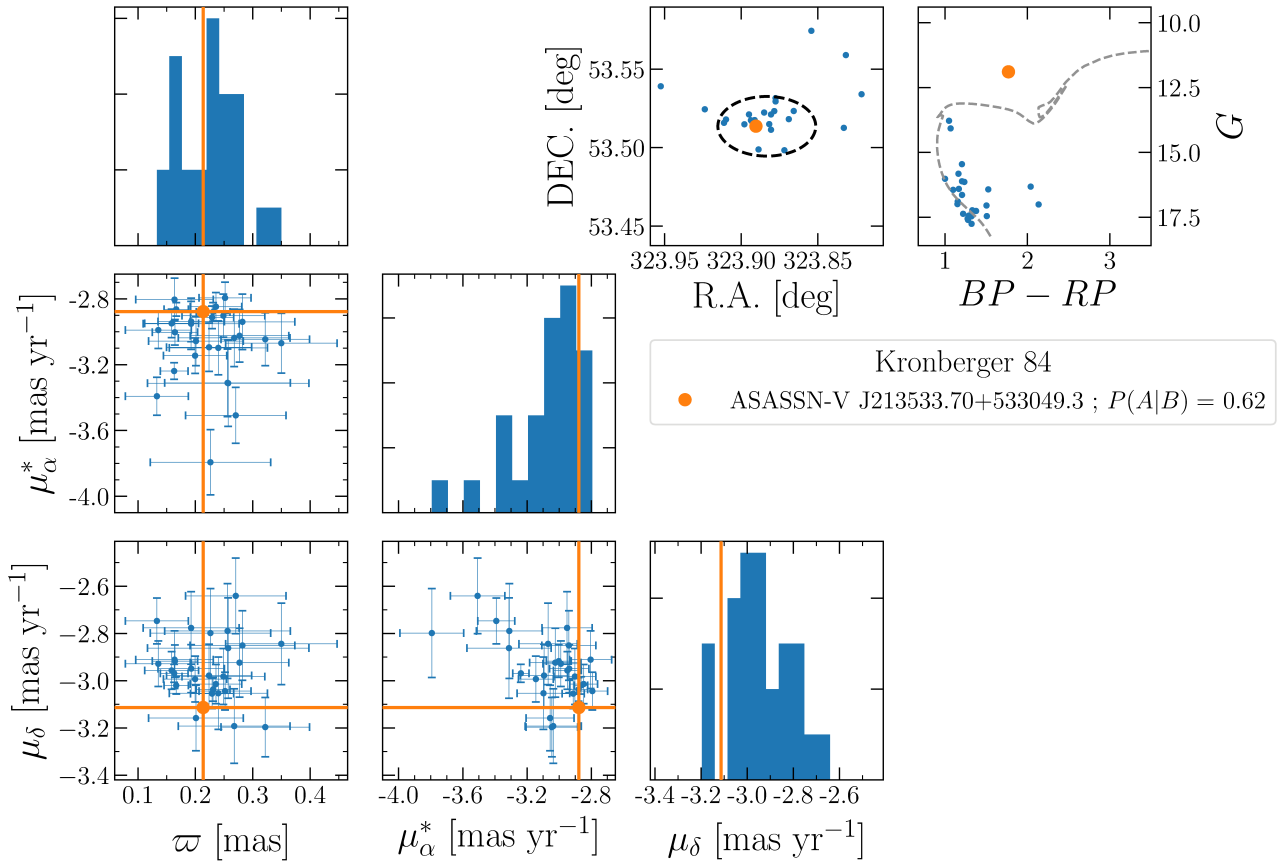


Figure 2.4: Distribution of the *Gaia*-based astrometry (parallaxes, proper motions, and positions) and colour-magnitude diagram for the cluster Kronberger 84 and the Cepheid ASASSN-V J213533.70+533049.3, described in Section 2.5.4 as a new potential combo. For Kronberger 84 a list of cluster members is provided by CG20. The information of the members (from CG20) is represented in blue, while the Cepheid properties are shown in orange. In the panels displaying the equatorial coordinates of the members, a black dashed line represent the clusters' r_1 . PARSEC isochrones of solar metallicity are plotted in the colour-magnitude diagram with a grey dashed line using the values derived by CG20 as a reference.

Gaia 5 and V0423 CMa

The Cepheid V0423 CMa lies within the half-light radius of the recently discovered cluster Gaia 5 (2 pc; Torrealba, Belokurov, & Koposov, 2019). In the cluster discovery publication, the authors discard a possible association between Gaia 5 and V0423 CMa, arguing that the distance modulus difference determined in their study (~ 1.7) make the pair likely unrelated. We analysed the pair based on parallaxes only, since this is the only information available for both the cluster and the Cepheid. Our method outputs a membership probability of 0.94. Translated into distances, parallax values give a distance difference of ~ 120 pc only between the Cepheid and the cluster, a small value when compared with the cluster distance (6.8 kpc; Torrealba, Belokurov, & Koposov, 2019).

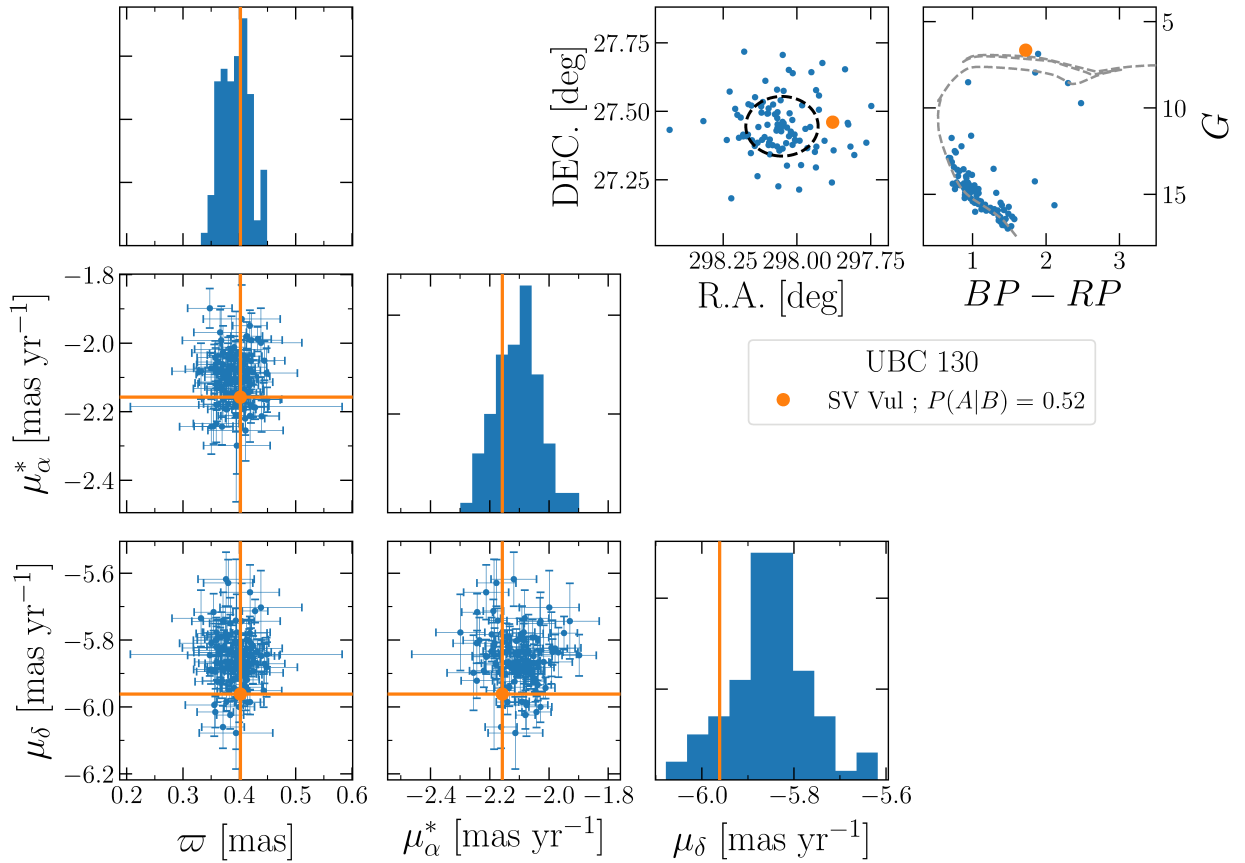


Figure 2.5: Same as Figure 2.4 but for the combo UBC 130-SV Vul.

Kronberger 84 and ASASSN-V J213533.70+533049.3

For the first-overtone Cepheid ASASSN-V J213533.70+533049.3 ($P = 3.2$ d) we find a possible association with the cluster Kronberger 84 (MWSC 3532, K13). In this case, the Cepheid lies close to the centre of the cluster (at 0.30 pc), well within its r_{50} (0.02 deg, 1.34 pc). This results in $P(A) = 1$. The posterior membership probability of this pair is 0.62, as a combination of both its high prior and likelihood. As a list of members of this cluster is provided by CG20, we display in Figure 2.4 the astrometry and colour-magnitude diagram of this pair to illustrate its compatibility.

UBC 130 and SV Vul

SV Vul falls in a region of the sky with numerous clusters and star-forming regions, including Vul OB1 with which the Cepheid has been associated for a long time (Turner, 1984). We find a high probability of association (~ 0.52) between SV Vul and the open cluster UBC 130 (Castro-Ginard et al., 2020). The distance of SV Vul to the centre of UBC 130 is 6 pc (0.15 deg) assuming membership, about 50 per cent larger than the cluster's r_{50} . It turns out that UBC 130 is another designation for the cluster Alicante 13, for which the membership of SV Vul has been recently demonstrated by Negueruela, Dorda, & Marco (2020). The astrometric parameters of SV Vul as compared with those of the members of UBC 130 (from

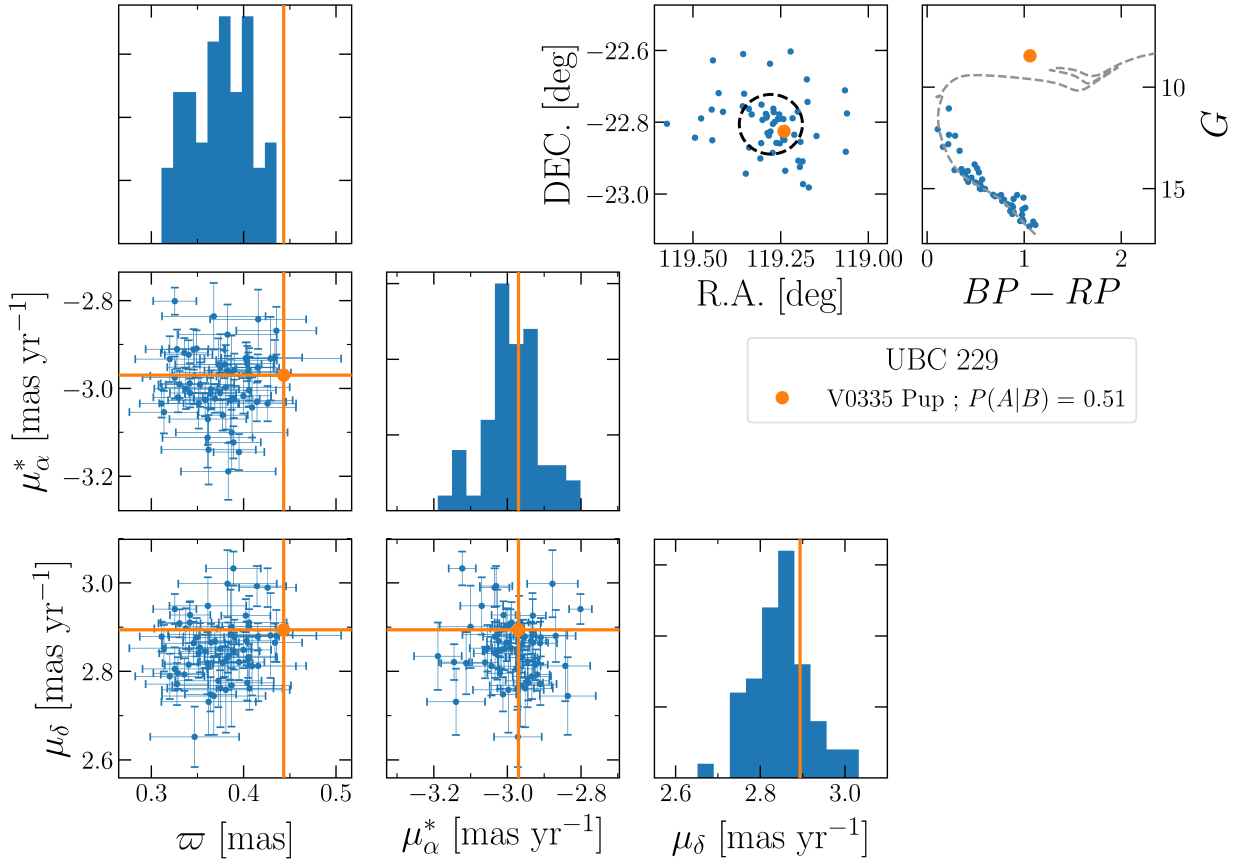


Figure 2.6: Same as Figure 2.4 but for the combo UBC 229-V0335 Pup.

CG20) are depicted in Figure 2.5.

UBC 229 and V0335 Pup

The angular separation between the Cepheid and the cluster’s centre (0.04 deg) corresponds to 1.8 pc assuming membership, which locates V0335 Pup within the r_{50} of UBC 229 (3.6 pc) and secures a prior of $P(A)=1$. The constraints analysed in this case are the pair’s parallaxes and proper motions (Figure 2.6). They lead to an association probability of 0.51. Moreover, the position of the Cepheid in the CMD of UBC 229 and its distance are both compatible with membership.

LP 1937 and DF Cas

DF Cas is located at 0.24 deg of the centre of the newly discovered cluster candidate LP 1937 (Liu & Pang, 2019), within the cluster’s r_2 (0.486 deg; 25.2 pc). The value of $P(A)$ for this pair is 0.64, and the small ϖ , μ_α^* , and μ_δ differences between the Cepheid and the cluster yield a likelihood $P(B|A)$ of 0.71, hence a posterior membership probability of 0.45. We note the presence of other clusters in the neighborhood, such as NGC 1027, for which we get a membership probability < 0.01 ($P(A)=0.80$, $P(B|A) \sim 0$), in agreement with the results of A13.

UBC 106 and CM Sct

We find a prior of 0.79 and a likelihood of 0.40 for CM Sct, hence a membership probability to UBC 106 of 0.32, based on parallax and proper motion. CM Sct is located outside of the cluster's r_{50} (~ 4.9 pc or 0.12 deg), with a physical distance of 6.6 pc assuming the cluster and the Cepheid equidistant. The position of the Cepheid in the cluster's colour-magnitude diagram is compatible with membership, as depicted in Figure A1 (in the appendix). We highlight this combo as A13 report a high likelihood for the combos CM Sct/Dolidze 32 and CM Sct/Dolidze 33, but with small membership probabilities of < 1 and 1.6 per cent, respectively. Their probability is slightly higher with Teutsch 145 (2.8 per cent) thanks to a higher prior (0.21), but with a reduced likelihood of 0.13. We checked that the aforementioned clusters are distinct from UBC 106.

Our results indicate another Cepheid potentially associated with UBC 106, Z Sct, which is located ~ 700 pc away in heliocentric distance from CM Sct (and half a degree away on the sky) and has similar likelihood but a much lower prior than CM Sct. With an angular separation between Z Sct and the centre of UBC 106 (0.48 deg, which corresponds to 19.7 pc), the membership probability drops below 0.01. We note that the period of Z Sct is significantly larger than that of CM Sct, making it significantly younger. Our determination of the age of UBC 106 shows a quite large uncertainty, but overall matches $\log(t) = 8.2$ provided by CG20. It then also supports a higher membership probability for CM Sct than for Z Sct, whatever the PA relation we consider. We note in passing that A13 mention Z Sct in eight potential combos, all of them with negligible membership probability although with a likelihood $P(B|A) = 1$ for three of them (Dolidze 32, Dolidze 33, Andrews-Lindsay 5).

UBC 290 and X Cru

The combo composed of the cluster UBC 290 (Castro-Ginard et al., 2020) and the fundamental-mode pulsator X Cru ($P = 6.22$ d) is another case of a relatively high $P(A|B)$ association, as the Cepheid lies at 8.6 pc from the center of the cluster of size $r_{50} = 0.15$ deg (4.24 pc), which, together with a high likelihood, yields a posterior probability of 0.18 (Figure A1). We note that neither the cluster nor the Cepheid are included in the study of A13.

2.6 Age determination of open clusters

In this section, we derive ages for a subsample of clusters believed to host Cepheids in the literature, or where the Cepheid has a high membership probability according to our study (see Section 2.5, and Table 2.1). We compare these estimates with age determinations from the literature, and check their consistency with theoretical Cepheid pulsation and evolution models.

2.6.1 Methodology

Age-dating resolved star clusters via isochrone fitting is a task for which several techniques have been used along the years, from pure visual inspection to recently developed algorithms

(see e.g. von Hippel et al. 2006; Monteiro, Dias, & Caetano 2010; Dias et al. 2012; Yen et al. 2018; Liu & Pang 2019; Sim et al. 2019; CG20). In most cases, the codes used for these calculations are not made publicly available. However, in spite of the application of new methodologies, determining the age of young clusters remains as a challenging goal because in addition to stellar contamination, binarity, and age spreads, the MSTO of these clusters is commonly not clearly defined.

We adopted two approaches: a χ^2 -based isochrone selection developed on our own, and the AURIGA neural network (henceforth ANN; Kounkel, Covey, & Stassun, 2020), which predicts the age, extinction, and distance of clusters from the photometry and astrometry of the cluster members. We did not use the software BASE 9 (von Hippel et al., 2006) as in Bossini et al. (2019) since these authors mention that its use together with only *Gaia* magnitudes does not allow one to lift the degeneracy between the distance modulus and the extinction.

For our own method, we used the PARSEC stellar evolution models. The models were computed for the *Gaia* DR2 passbands (Evans et al., 2018), and in the 2MASS photometric system. From the available models, we selected evolutionary tracks with initial chemical compositions ranging from $Z = 0.006$ to $Z = 0.029$ and a grid size of 0.001 dex. Approximately 90 per cent of the clusters in the catalogue of Carrera et al. (2019) younger than 800 Myr (with ages from CG20) lie in this range of Z . The ages selected vary from $\log(t) = 6.6$ (~ 5 Myr), with t in units of years, to $\log(t) = 8.9$ (~ 800 Myr) with a minimum resolution of 0.01 dex, including extreme values of $\log(t)$ for a proper uncertainty determination. Since rotationally-induced instabilities strongly affect the evolution of stars, as studied specifically in the case of Cepheids by Anderson et al. (2016), we also adopted models that take stellar rotation into account, namely the MIST set of evolutionary tracks, which are based on the publicly available stellar evolution tool MESA (Paxton et al., 2011, 2013; Dotter, 2016; Choi et al., 2016). We chose evolutionary tracks with a range of initial iron abundances $[\text{Fe}/\text{H}]$ from -0.5 to 0.5 dex with a grid size of 0.25 dex, and logarithmic ages between 6.6 and 8.9 dex, with a step size of 0.05 dex.

The selection of the best model isochrone for a given cluster is based on a χ^2 minimization criterion when comparing it with the cluster colour-magnitude diagram³¹. We repeated the process twice, first using *Gaia* photometry only and then using 2MASS photometry only. In the latter case, the near-infrared J , H , and K magnitudes of the cluster members are taken from Roeser, Demleitner, & Schilbach (2010).

In order to perform the isochrone fitting, we limited ourselves to cluster members as established in previous studies, and we discarded clusters for which the main sequence was not clearly defined. In the case of the clusters in CG18b, who provide a membership probability, we included all stars with membership probabilities larger than 30 per cent and within $2.5 \cdot r_1$ from the cluster centre. For the clusters from Castro-Ginard et al. (2020), we simply used the list of members provided by the authors. Additionally, a number of stars was further excluded during the fitting process via sigma-clipping. As initial conditions for the fitting routine, we adopted the values provided in the literature. From this original value, we explored an age window of ± 0.5 in logarithmic scale, using 0.05 as a grid size and a metallicity window of ± 0.03 dex in Z , with a grid size of 0.01 dex. For the reddening, we allowed for an

³¹The Cepheids were excluded from the computation of the χ^2 values.

excursion of ± 0.6 mag from the initial value, in steps of 0.15 mag. The extinction values were computed assuming $R_V = 3.1$ (Schultz & Wiemer, 1975; Cardelli, Clayton, & Mathis, 1989), adopting the ratios $A_G/A_V = 0.85926$, $A_{G_{BP}}/A_V = 1.06794$, $A_{G_{RP}}/A_V = 0.65199$, $A_J/A_V = 0.29434$, $A_H/A_V = 0.18128$, and $A_K/A_V = 0.11838$ ³², and without considering differential reddening. Finally, we allow distances to vary in a range of ± 500 pc from the initial value, in steps of 50 pc.

To account for the magnitude errors on the stars' G , G_{BP} , and G_{RP} magnitudes, we assumed:

$$\sigma_{\text{mag}}^2 = \left(1.09 \frac{\sigma_{\text{Flux}}}{\text{Flux}}\right)^2 + \sigma_{\text{zp}}^2, \quad (2.9)$$

where σ_{mag} is the magnitude error of a star in a given *Gaia* bandpass, Flux is the mean flux of the star in that filter, and σ_{Flux} its uncertainty. We used this formula since no errors are provided in the *Gaia* catalogues because of the asymmetric error distribution of the sources in magnitude space, as stated in the table description of the *Gaia* DR2³³. We adopted $\sigma_{\text{zp}} = 0$ as we possess no knowledge of the behaviour of this zero-point, and its effects should be negligible for the purpose of our study.

The uncertainties on the age determination were estimated by inspecting the distribution of the minimum χ^2 as a function of age in the range explored for a given cluster. We computed the significance of the global minimum by looking for the local maxima around it. For this we used the methodology described by Yen (2019), with which asymmetric errors can be computed.

In a few cases, when the fit appeared inconsistent with the cluster members in a visual inspection, we applied small adjustments, setting the age to a local rather than a global minimum or correcting for small distance/reddening imprecisions when the best value would fall in between two consecutive grid points. We did so for seven clusters analysed with *Gaia* photometry and PARSEC isochrones, five clusters with *Gaia* photometry and MIST isochrones, two clusters with 2MASS photometry and PARSEC isochrones, and four clusters with 2MASS photometry and MIST isochrones. The median shift in age is 0.20 in logarithmic scale, with a maximum of 0.60 for the cluster Ruprecht 100 in a *Gaia*+PARSEC configuration. The case of Ruprecht 100 in the 2MASS+PARSEC configuration remained nevertheless an unsatisfactory fit and was fitted using a visual inspection only, as displayed in Figure 2.7.

Alternatively, we employed the ANN³⁴ to derive the cluster properties. The ANN is a neural network trained on a mix of artificial stellar populations and real clusters. We provided as input for each cluster photometry in the *Gaia* and near-infrared bands (G , BP , RP , J , H , K), and the *Gaia* DR2 parallaxes. Kounkel, Covey, & Stassun (2020) indicate that the ANN underestimates the age for clusters older than ~ 120 Myr and overestimates it for clusters younger than ~ 120 Myr, in both case by ~ 0.1 dex. They remark that this threshold roughly corresponds to the age at which all low-mass pre-main-sequence stars would have reached the main sequence, and very few high-mass stars would have evolved off the main sequence towards the RGB. Unfortunately, this is also the expected age range

³²http://stev.oapd.inaf.it/cgi-bin/cmd_3.3

³³<https://dc.zah.uni-heidelberg.de/tableinfo/gaia.dr2light>

³⁴<https://github.com/mkounkel/Auriga>

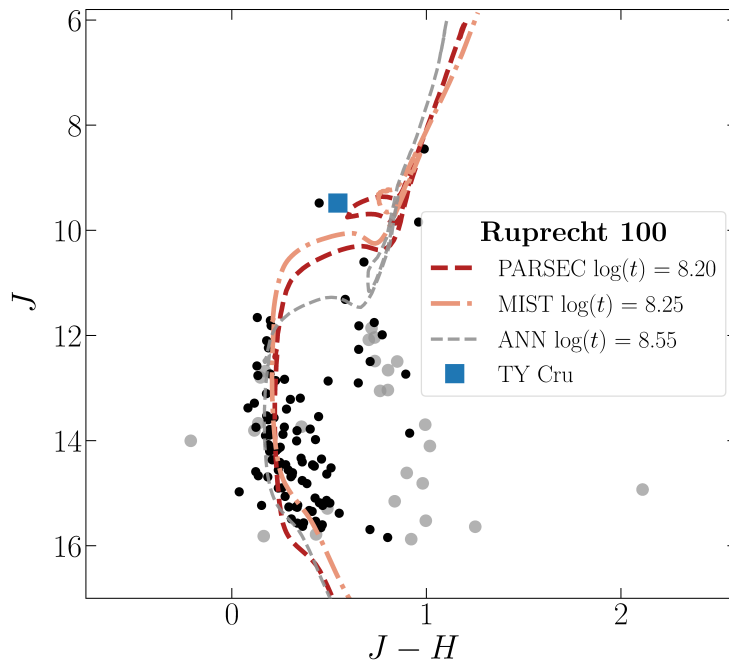


Figure 2.7: Colour-magnitude diagram of the cluster Ruprecht 100, with PARSEC (red) and MIST (orange) isochrones fitted (as an exception) by visual inspection. Cluster members are taken from CG18b and shown as grey filled circles, while the cleaned sample of stars used during the isochrone fitting procedure is shown as black dots. For this cluster, automatic fits based on a χ^2 minimization did not converge to an acceptable solution, even when allowing for a manual shift of the age. A PARSEC isochrone computed with the parameters derived by the ANN analysis and assuming solar metallicity is also plotted in grey.

for clusters hosting Cepheids. In general, neural networks do not provide uncertainties in the predicted parameters. However, it is possible to treat the scatter between the solutions from independent realizations as a measure of these errors. Thus, for each cluster we ran 100 ANN iterations to estimate the parameter uncertainties. For more details about the ANN design, we refer the reader to [Kounkel, Covey, & Stassun \(2020\)](#).

2.6.2 Results and comparison with previous studies

It is no surprise that our analysis of clusters hosting Cepheids provides only young ages, ranging from $\log(t)=7.4$ (25 Myr) to $\log(t)=8.8$ (630 Myr), depending on the cluster, the method and the data considered. For reasons that will become clear later in this Section, we discuss here and list in Table 2.2 only 11 clusters (12 Cepheids) whose ages are considered relatively reliable (considering the accuracy and precision of the estimations) and with which we could potentially constrain the Cepheid period-age relation (see Section 2.6.5). Figure 2.8 displays the results for two representative clusters. The first one, NGC 6067, is a relatively evolved system with a well-defined main sequence, two Cepheids, and already a number of stars populating the RGB. With such favorable circumstances, all analyses lead to a similar

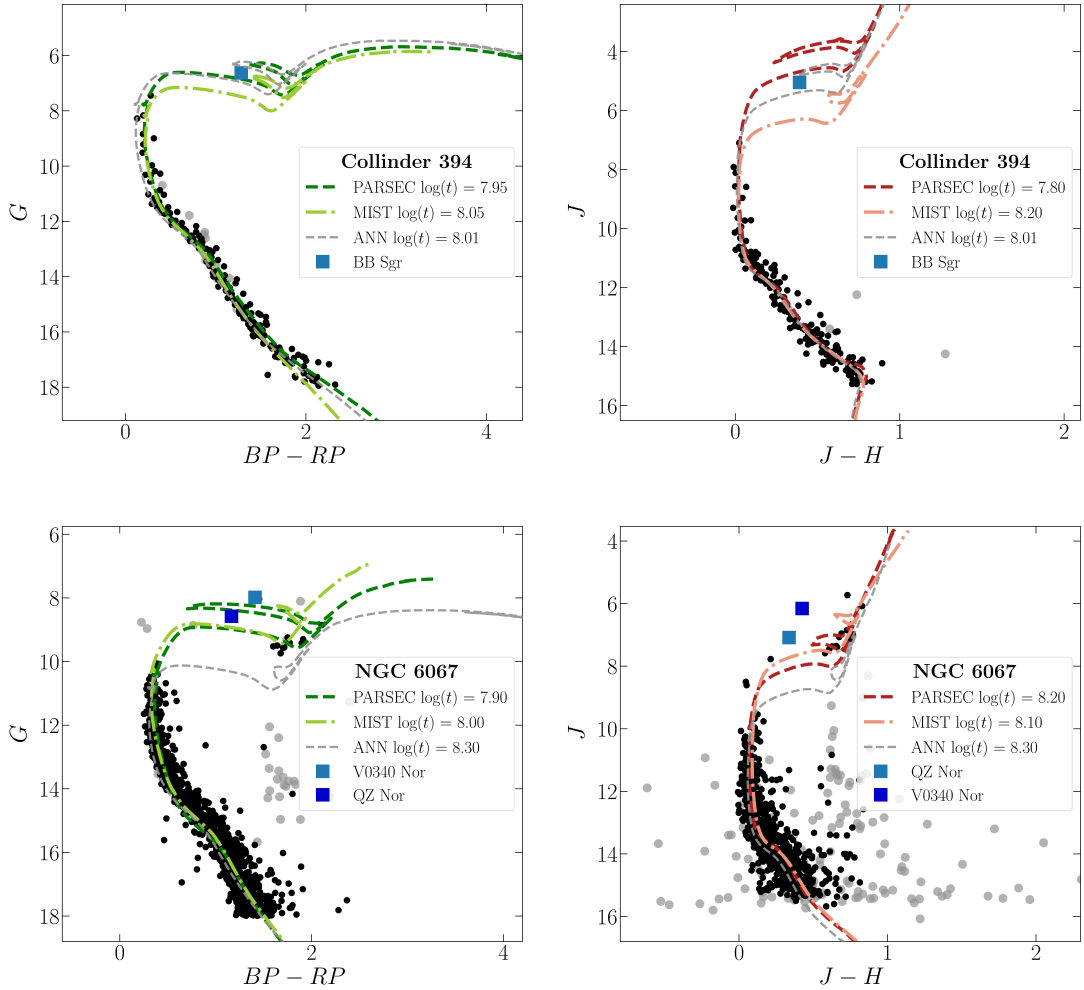


Figure 2.8: Colour-magnitude diagrams of two clusters: Collinder 394 (*top* panels) and NGC 6067 (*bottom* panels) representative of clusters hosting Cepheids. The left panels show colour-magnitude diagrams in the *Gaia* passbands while the *right* panels display them in the 2MASS passbands. Presumed cluster members from the input catalogues are shown as grey filled circles while those selected by sigma-clipping during the isochrone fitting procedure are shown as black dots. The best-fitting isochrones are shown with a colour-code related to the photometric system and the stellar evolution model used in the analysis. We also show in grey a PARSEC isochrone computed with the parameters derived by the ANN analysis and assuming solar metallicity.

age between $\log(t)=7.9$ (80 Myr) and $\log(t)=8.3$ (200 Myr). The second one, Collinder 394, is in contrast less massive, it contains only one Cepheid and no other evolved member has been reported in *Gaia* DR2 so far. Fortunately, it possesses a narrow main sequence and a quite well defined MSTO, allowing for a similar dispersion (~ 0.4 dex) around an age of $\log(t)\approx 8.05$ (110 Myr). The resulting isochrones and cluster colour-magnitude diagrams of our whole sample are shown in the Appendix (Figure A2). It is clear that our “good” sample is biased toward higher ages since we report $\log(t) < 7.8$ for only two clusters.

In the rest of this subsection we compare the age estimates from our first approach with previous studies, namely the compilations of D02 and K13, the analysis of [Bossini et al. \(2019\)](#) who derived ages for 269 low reddening (not very young) Galactic open clusters using *Gaia* DR2 data (two clusters in common with our work), and the recent work of CG20 who used an artificial neural network to determine the ages of 1,867 clusters from *Gaia* DR2 photometry. The outcome of the comparison is shown in Figure 2.9, from which we draw the following conclusions (which we emphasize are drawn from low-number statistics):

- we find an overall agreement between all the literature ages we compared our results with (within 0.8 dex);
- the agreement of our ages with D02 is better than that our agreement with K13, most likely due to the cluster membership selection. The median absolute differences are 0.16 and 0.33 in logarithmic scale, respectively, for the seven clusters in common with both works;
- we reach an overall good agreement with the [Bossini et al. \(2019\)](#) (two clusters in common) and CG20 age estimates (11 clusters in common, median absolute difference of 0.15 dex). However, for clusters younger than $\log(t)\sim 8.0$ (100 Myr), our ages tend to be lower than those of CG20, and higher for $\log(t) > 8.2$ (~ 160 Myr);
- there are no other clear trends of $\Delta\log(t)$ as a function of $\log(t)$;
- the choice of a specific isochrone set (PARSEC or MIST) seems to have marginal influence.

We believe that the age difference between earlier studies (as compiled by D02 and K13) and the more recent ones resides mainly in the capability to select the cluster membership based on *Gaia* DR2 parallaxes and proper motions. However, the assumed reddening and distance for each cluster (in both earlier and recent studies) likely play an important role as well. Finally, we consider important to keep in mind the typical values of $\Delta\log(t)$ when analysing the cluster ages from different works (and their spread), in particular for interpreting the results shown in Section 2.6.5.

2.6.3 A critical view on cluster Cepheids to test period-age relations

To illustrate the difficulty of deriving accurate ages for young open clusters via isochrone fitting, we study the theoretical behaviour of the stellar occupation of the members of a given cluster in the *Gaia* colour-magnitude diagram, using simple models based on stellar population synthesis. We used PARSEC isochrones to generate ten simulated clusters of solar

Table 2.2: Ages for a reliable subsample of clusters. We show the logarithmic cluster ages obtained with two sets of isochrones (PARSEC or MIST) using either *Gaia* DR2 or 2MASS photometry, and those obtained with ANN using *Gaia* DR2 and 2MASS simultaneously.

Open cluster	Cepheid	Period ¹ [days]	Pulsation Mode ¹	GDR2		log(<i>t</i>)		ANN	CG20 ²	Lit. log(<i>t</i>) Bossini et al. (2019)
				PARSEC	MIST	PARSEC	MIST			
Collinder 394	BB Sgr	6.64	F	7.95 ^{+0.20} _{-0.40}	8.05 ^{+0.20} _{-0.25}	7.80 ^{+0.30} _{-0.30}	8.20 ^{+0.15} _{-0.15}	8.01 ± 0.09	7.96	7.97 ^{+0.06} _{-0.02}
NGC 5662	V Cen	5.49	F	7.95 ^{+0.20} _{-0.15}	7.95 ^{+0.15} _{-0.15}	7.85 ^{+0.25} _{-0.25}	8.45 ^{+0.30} _{-0.20}	8.22 ± 0.12	8.30	—
NGC 6067	QZ Nor	3.79	1O	7.90 ^{+0.50} _{-0.30}	8.00 ^{+0.35} _{-0.40}	8.20 ^{+0.30} _{-0.35}	8.10 ^{+0.45} _{-0.20}	8.30 ± 0.14	8.10	—
NGC 6067	V0340 Nor	11.29	F	7.90 ^{+0.30} _{-0.30}	8.00 ^{+0.35} _{-0.40}	8.20 ^{+0.30} _{-0.35}	8.10 ^{+0.45} _{-0.20}	8.30 ± 0.14	8.10	—
NGC 6087	S Nor	9.75	F	7.75 ^{+0.70} _{-0.70}	7.90 ^{+0.20} _{-0.20}	7.90 ^{+0.35} _{-0.35}	8.05 ^{+0.55} _{-0.55}	7.92 ± 0.10	8.00	8.05 ^{+0.02} _{-0.03}
NGC 6649	V367 Sct	6.29 (4.38)	F1O	7.45 ^{+0.20} _{-0.20}	7.40 ^{+0.60} _{-0.60}	7.75 ^{+0.20} _{-0.20}	7.70 ^{+0.35} _{-0.35}	7.18 ± 0.39*	7.85	—
Ruprecht 79	CS Vel	5.90	F	7.80 ^{+0.25} _{-0.20}	7.80 ^{+0.35} _{-0.35}	7.90 ^{+0.60} _{-0.60}	7.60 ^{+0.55} _{-0.40}	7.77 ± 0.24	7.79	—
Ruprecht 100	TY Cru	5.00	F	8.40 ^{+0.10} _{-0.60}	8.00 ^{+0.55} _{-0.10}	†8.20 ^{+0.55} _{-0.55}	8.25 ^{+0.25} _{-0.45}	8.55 ± 0.23	8.31	—
UBC 106	CM Sct	3.92	F	8.20 ^{+0.30} _{-0.15}	8.15 ^{+0.25} _{-0.15}	8.00 ^{+0.35} _{-0.35}	7.85 ^{+0.25} _{-0.25}	7.96 ± 0.43	8.20	—
UBC 130	SV Vul	44.88	F	7.45 ^{+0.15} _{-0.40}	7.20 ^{+0.15} _{-0.15}	7.40 ^{+0.30} _{-0.30}	7.20 ^{+0.40} _{-0.30}	7.53 ± 0.32*	7.44	—
UBC 156	V1077 Cyg	4.64	F	8.80 ^{+0.65} _{-0.65}	8.45 ^{+0.50} _{-0.50}	8.60 ^{+0.15} _{-0.55}	8.80 ^{+0.35} _{-0.35}	8.19 ± 0.18	8.40	—
UBC 290	X Cru	6.22	F	8.05 ^{+0.20} _{-0.35}	7.90 ^{+0.35} _{-0.35}	8.00 ^{+0.35} _{-0.35}	7.80 ^{+0.10} _{-0.10}	7.83 ± 0.11	8.28	—

¹ From Ripepi et al. (2019), except for R Cru, V367 Sct (VSX; Watson, Henden, & Price, 2014) and for OGLE-GD-CEP-1012 (OGLE; Udalski et al., 2018).

In the pulsation mode column, F stands for fundamental mode, 1O for first overtone, and F1O for double mode. For the double mode Cepheid V367 Sct the first-overtone period is shown in parentheses.

² The uncertainties associated with the log(*t*) determinations of CG20 range from 0.1 to 0.25 dex.

† Unsatisfactory χ^2 fitting procedure. Age determined by visual inspection.

* Clusters for which high values of the extinction A_V (> 1.6 , CG20; > 1.9 , ANN) affected the ANN parameter determination.

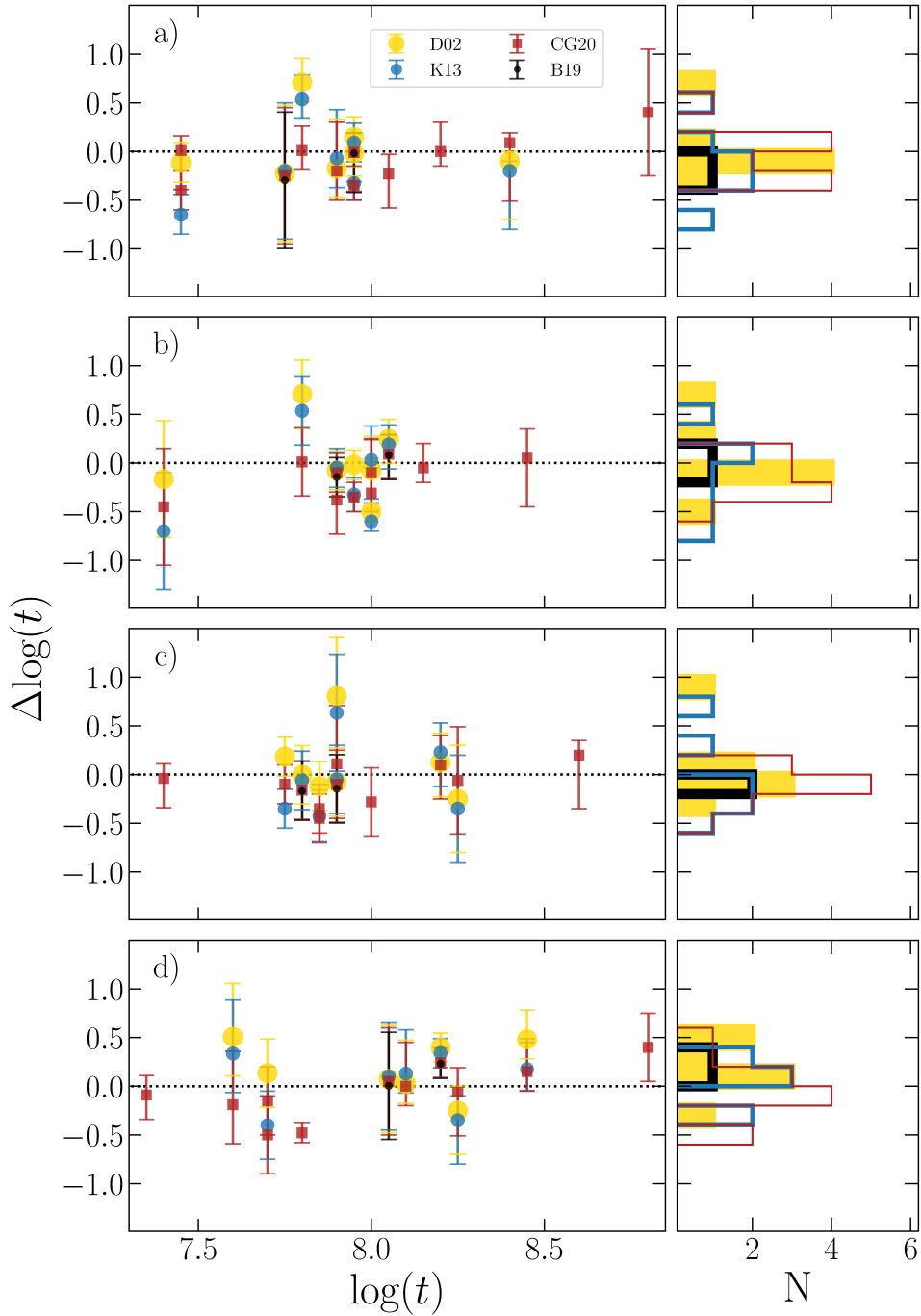


Figure 2.9: *Left panels:* Difference in logarithmic ages, $\Delta \log(t)$, between the values obtained in this work and those published in previous studies, for the sub-sample of clusters shown in Table 2.2. *Right panels:* Dispersion of the residuals in $\Delta \log(t)$ using a bin size of 0.25 in age logarithmic scale. The sources of literature ages are D02 (yellow), K13 (blue), Bossini et al. (2019) (B19, black), and CG20 (red). The panels from top to bottom display: *a*): our ages from PARSEC isochrones, using *Gaia* photometry, *b*): our ages from MIST isochrones, using *Gaia* photometry, *c*): our ages from PARSEC isochrones, using 2MASS photometry, *d*): our ages from MIST isochrones, using 2MASS photometry. The error bars take into account the age uncertainties from this work and from the literature, when available.

metallicity at two specific ages (five random realizations per age). The ages selected for these models are 7.4 to 8.2 in logarithmic scale (approximately 25 and 160 Myr, respectively), for a massive Galactic open cluster ($1,000 M_{\odot}$; based on the cluster mass functions shown by, e.g., Lada & Lada 2003, Zinnecker et al. 2009, and Röser et al. 2010). To compute the stellar occupation along the isochrones we adopted a Chabrier (2001) IMF, together with a Salpeter (1955) IMF for stars with masses larger than a solar mass. To transform the modeled absolute magnitudes to apparent magnitudes, we assumed a distance of 1 kpc, and $E(B - V) = 0.175$, which are representative values for a Galactic cluster such as NGC 6087. We included photometric uncertainties based on the typical magnitude errors for the NGC 6087 members in the *Gaia* passbands, re-drawing the magnitudes assuming Gaussian distributions. In addition, we adopted a binary fraction of 0.6 to roughly reproduce the characteristic widening produced in the evolutionary tracks by the presence of binary companions. Finally, we added field contamination (foreground/background) based on the Besançon models³⁵ (Robin et al., 2003; Czekaj et al., 2014; Robin et al., 2014) of Galactic stellar populations for the *Gaia* magnitudes, including only a random selection of stars with distances between 0.8 and 1.2 kpc as possible contaminants. The results of this exercise are depicted in Figure 2.10.

Isochrones of different ages, in the ideal scenario in which the true distance, reddening, and metallicity of the cluster are known, are fitted to the populations plotted in the different panels of Figure 2.10. The scatter in the fitted logarithmic ages with respect to the isochrone ages from which the populations are drawn shows the sensitivity to different effects (e.g., photometric errors and contamination) of the age determination of a stellar cluster via isochrone fitting, and one expects it to only increase if small variations in the isochrone distances and reddenings were allowed.

A factor that is not being considered here is related to the fraction of observed stars that are recovered from the theoretical stellar populations, due to the survey photometric completeness, or to possible biases in the cluster census made by the studies that selected cluster members. In the example populations depicted in Figure 2.10 it can be seen that, for a 25 Myr old cluster ($\log(t) = 7.4$) with $1,000 M_{\odot}$, missing only a couple of bright members near the MSTO of the cluster might easily result in an age determination offset of 75 Myr (0.6 in logarithmic scale). Therefore, for the younger clusters in our sample, large age uncertainties are expected to be found, making them inadequate as observable checks of the PA relation of Cepheids.

In this regard, since the IMFs are sampled stochastically, fewer stars are formed overall in less massive clusters, and as a consequence, the probability of forming intermediate and high-mass stars decreases, especially when the star formation rate of a cluster is rather low (see e.g. Weidner & Kroupa, 2006; Eldridge, 2012). In fact, the stochastic sampling that affects the observed mock cluster colour-magnitude diagrams coupled with the relatively young age of the clusters, in addition to the natural limitations of the *Gaia* photometry (saturation, for instance, and crowding for distant clusters; Boubert & Everall, 2020), translates into not well defined stellar main-sequence turn-offs and an evident dearth of cluster members at the turn-offs and post-main-sequence evolutionary stages. For more details regarding the effects of stochasticity in cluster populations we refer the reader to more dedicated works, such as those carried out by Fouesneau & Lançon (2010) and Popescu & Hanson (2010).

As a final remark, we would like to highlight that in order to overcome the limitation

³⁵https://model.obs-besancon.fr/modele_home.php

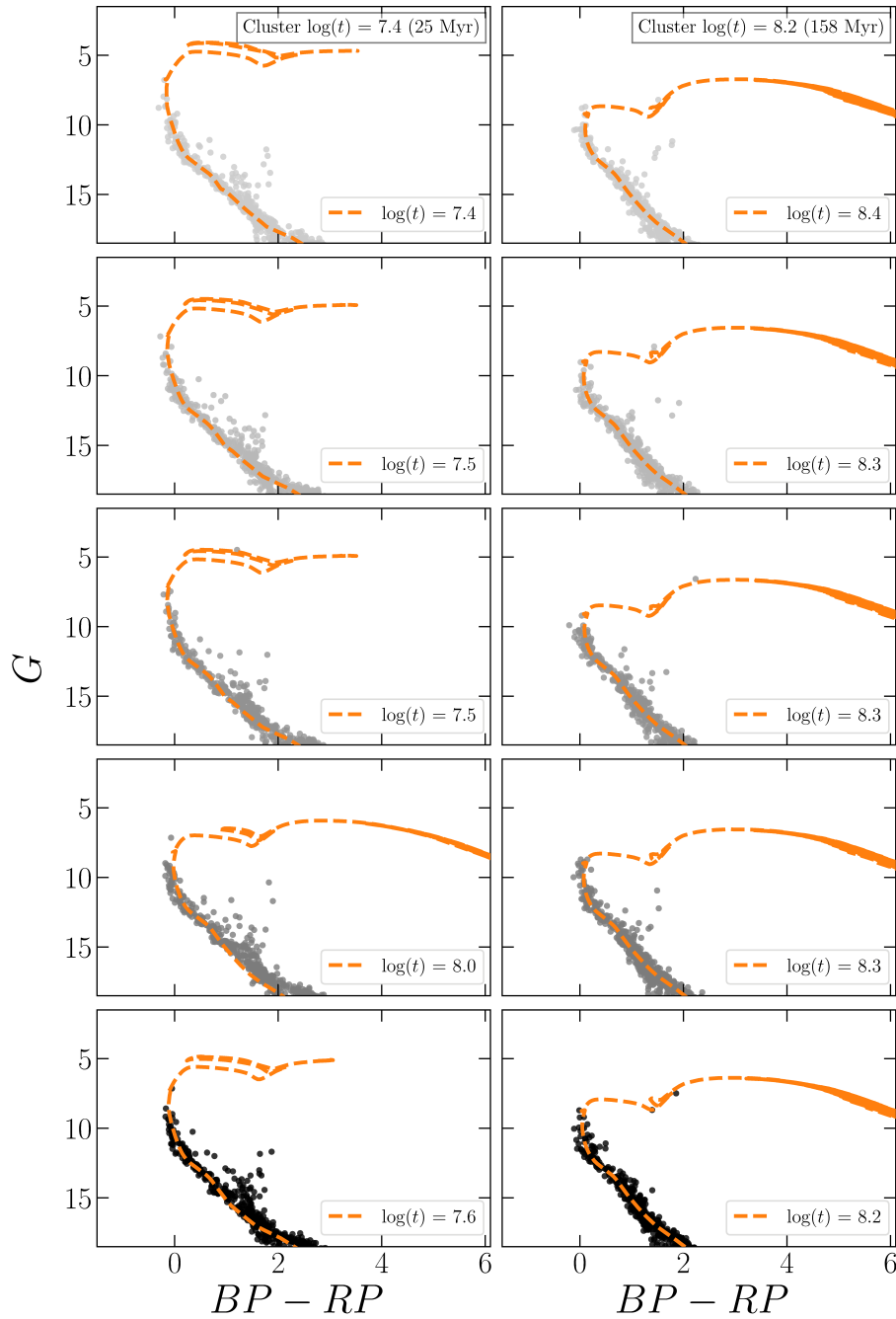


Figure 2.10: Simulated colour-magnitude diagrams for a cluster of $\log(t) = 7.4$ (*left* panels) and $\log(t) = 8.2$ (*right* panels), and a total initial mass of $1,000 M_{\odot}$. Each panel shows a different population randomly generated using a [Chabrier \(2001\)](#) + [Salpeter \(1955\)](#) IMF. Observational effects, such as photometric errors, the presence of a binary sequence, and field contamination are included in each diagram. PARSEC isochrones are fitted to the observed CMDs and displayed with orange dashed lines. The isochrones were fitted assuming the exact same distance, extinction, and metal content as those of the theoretical population, but allowing for shifts in age.

described above, extremely high levels of both purity and completeness in the open cluster member catalogues are mandatory for an age determination at the accuracy required (a few tens of Myr) to constrain Cepheid PA relations. In particular, no turn-off or further evolved members should be missing or falsely included. The use of reliable spectral types, in addition to high-precision reddening estimates should become beneficial to better constrain the cluster ages. If these requirements are not met, only such clusters with well-defined MSTO can in practice be used with confidence, which biases the cluster Cepheid sample selection towards older and more massive hosts. Similar conclusions were reached by [Senchyna et al. \(2015\)](#) in their study of the PA relation of Cepheids in M31, in which they attribute the broad constraints in their PA fits to the difficulty of assigning an age to low-mass clusters at large distances.

This is a reason why, from all the high probability combos obtained in Section 2.5, we retain only 11 cluster-Cepheid pairs in an attempt to characterize Cepheids' PA relations in the next section.

2.6.4 Alternative methods for cluster age determination

So far we have described the limitations of determining precise ages for young clusters using the isochrone fitting technique, which is also sensitive to stellar evolution processes that are not yet fully understood (e.g. convective overshooting, rotational mixing, and internal gravity waves). These limitations directly hinder our ability to use these ages to constrain the PA relation. However, other methods have been considered in order to age-date clusters which do not directly rely on the use of isochrones, such as the study of the clusters' lithium depletion boundary and the consideration of stellar kinematics (or cluster dynamics).

The lithium depletion boundary method is based on the presence (or absence) of Li in low-mass stars and brown dwarfs (see e.g. [Galindo-Guil et al., 2022](#)). The lithium depletion boundary is typically seen in young open clusters (with ages between 20 to few hundred Myr), and is the point at the bottom of the MS below which low-mass stars cannot reach the necessary internal temperature for Li destruction. This temperature limit, combined with convective mixing makes it possible to estimate the age of a cluster since stellar evolution depends on mass (the Li surface abundance decreases with age, and for low-mass stars the decay is very rapid). It is worth mentioning that this method is considered to be as or more accurate than isochrone fitting (both methods based on stellar evolution), and that the former yields, in general, cluster ages ~ 50 per cent older than those from isochrone fitting (see e.g. [Stauffer, Schultz, & Kirkpatrick, 1998](#); [Binks et al., 2021](#)). The use of this technique, however, is limited to nearby clusters due to the low luminosity of the target stars. Thus, the number of clusters with ages determined by this method remains low to this day (about a dozen).

Recently, [Dinnbier et al. \(2022\)](#) developed a method to estimate the ages of open clusters from the morphology of their extended tidal tails, based on the tilt angle of the tails with respect to the direction of the cluster orbit around the Galaxy and the width of the tidal structure. In their work, [Dinnbier et al. \(2022\)](#) show that the tilt angle of a tidal tail is only a function of the object's age (at a given Galactocentric distance), and not of other properties such as its initial mass or radius. This method is suitable for clusters on circular orbits with ages between ~ 40 and 300 Myr, where it provides an accuracy of 10-20 per cent. Because

this technique is (in principle) independent from stellar evolution models, it offers a new opportunity to not only test but to independently calibrate the Cepheid PA relation. The age-dating via tidal tails is, however, only applicable to early formed structures resulting from gas expulsion (i.e., it is not suitable for classical tidal tails formed by gradual evaporation of stars) and requires studying clusters with clear evidence of tidal disruption with well characterized tails.

We refer the reader to the review of [Soderblom \(2010\)](#) for a comprehensive description of these and other methods used for the determination of stellar ages. In this thesis, we do not attempt to use either of these methods mainly due to the aforementioned challenges. Nevertheless, we would like to highlight the potential of their applicability to Cepheid-hosting clusters when more suitable (e.g., larger and deeper) datasets become available in the future (see Chapter 5).

2.6.5 The Cepheid period-age relation

[Bono et al. \(2005\)](#) provided the first theoretical PA relations for Cepheids with Magellanic or solar-like chemical compositions. More recently, models including rotation have been developed ([Anderson et al., 2014, 2016](#)) predicting that, as rotation increases the main-sequence lifetime of the stars, higher Cepheid ages are expected in comparison with ages determined using non-rotating models (by $\Delta \log(t) \sim 0.2$ to 0.3). Taking advantage of updated evolutionary ([Hidalgo et al., 2018](#)) and pulsation ([De Somma et al., 2020a](#)) models, [De Somma et al. \(2020b\)](#) derived new PA relations and PAC relations in the *Gaia* passbands.

It is natural to overlay the age of a cluster Cepheid as provided by the determination of the age of the hosting cluster (following the traditional assumption that they are coeval) on the prediction of the Cepheids' age as given by a theoretical PA relation. As described above, we take into account only those (11) clusters for which we consider the ages relatively well constrained. Considering this small number together with their bias towards larger ages, we do not consider fitting an empirical PA relation. For the same reason, we only consider fundamental-mode Cepheids, since only a single first-overtone Cepheid falls in this restricted sample.

The comparison with the theoretical PA relations of [Bono et al. \(2005\)](#) (no stellar rotation), [Anderson et al. \(2016\)](#) ($\Omega_{\text{ZAMS}}/\Omega_{\text{crit}} = 0.5$), and [De Somma et al. \(2020b\)](#) (no rotation) is displayed in Figure 2.11. Assuming a PA relation of the shape $\log(t) = \alpha + \beta \cdot \log(P)$, where the value of the age t is represented in years, the former study reports $\alpha = 8.41 \pm 0.10$ and $\beta = -0.78 \pm 0.01$ for fundamental-mode Cepheids and for $Z = 0.01$ (Table 4 in [Bono et al., 2005](#)). In the case of [Anderson et al. \(2016\)](#) we used the average PA relation slope and intercept for a Cepheid with $Z = 0.014$ in their second and third crossing of the instability strip (Table 4 in [Anderson et al., 2016](#)), where $\alpha = 8.48 \pm 0.09$ and $\beta = -0.59 \pm 0.09$ for fundamental-mode Cepheids. The uncertainty assumed represents the standard deviation of these values with respect to the averages. Finally, for the models of [De Somma et al. \(2020b\)](#) we adopt the results obtained in the case of a canonical mass-luminosity relation, when neglecting rotation, mass-loss, and overshooting, with a mixing length parameter equal to 1.5, and $Z = 0.020$ (Table 2 in [De Somma et al., 2020b](#)). In this case $\alpha = 8.39 \pm 0.01$ and $\beta = -0.70 \pm 0.01$ for fundamental-mode Cepheids.

From the plots shown in Figure 2.11, we do not observe well-defined relations between

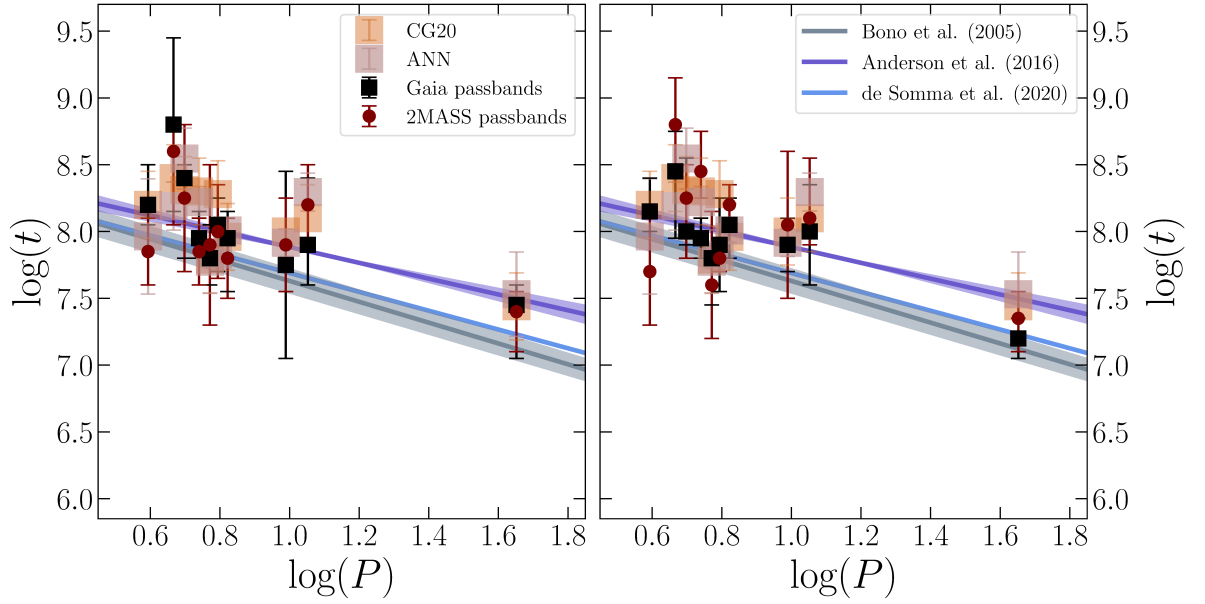


Figure 2.11: Comparison between the logarithm of the Cepheid periods in days (Udalski et al., 2018; Ripepi et al., 2019) and the cluster logarithmic ages (in years), obtained with different isochrone sets: PARSEC (*left* panel) and MIST (*right* panel) for the combos shown in Table 2.2. We do not include in the plot the unique first-overtone Cepheid recovered as high probability cluster member. Black symbols represent the cluster ages obtained using *Gaia* DR2 photometry and red stars those obtained using the 2MASS passbands. For comparison, we overplot these values to the theoretical PA relation for fundamental-mode Cepheids derived by Bono et al. (2005), in grey, Anderson et al. (2016), in blue, and De Somma et al. (2020b) in light blue, for $Z = 0.010$, $Z = 0.014$, and $Z = 0.020$, respectively. The cluster ages obtained by CG20 and by our ANN analysis are also shown as a reference, setting a constant uncertainty budget at 0.25 dex for the former. The errors on the period are negligible and therefore not included in the plots.

the Cepheid periods and the cluster ages, regardless of the choice of photometric system, isochrone models (with and without stellar rotation), or source of the cluster ages (from the use of the ANN, or from CG20). The large scatter of the cluster ages as compared to the theoretical predictions for the Cepheids' ages reveals the lack of accuracy and precision of our age determinations for this purpose, and makes it impossible to discriminate between the various theoretical Cepheid PA relations. Although not a factor here, we stress that a proper comparison between theoretical and empirical ages should be carried out with models making the same assumptions on overshooting, rotation, etc.

2.7 Discussion and concluding remarks

Considering that the number of known open clusters and classical Cepheids has increased considerably in recent years, and taking advantage of the unprecedented quality of the data provided by the *Gaia* mission (DR2 and eDR3), we revisited the membership of classical

Cepheids in Galactic open clusters. We follow the Bayesian approach proposed by [Anderson, Eyer, & Mowlavi \(2013\)](#), focusing only on the relative position and kinematics of the Cepheid and its potential host.

After investigating more than 40,000 possible combinations (combos) selected by their on-sky projected distance, we found 69 with a probability of association larger than 10 per cent, including 45 with a posterior probability larger than 25 per cent. Additionally, we found 95 possible associations with probabilities between 1 and 10 per cent, mostly in newly discovered open clusters. Within the list of combos with probabilities > 0.01 (164 in total), we report 19 that are consistent with previously known cluster Cepheids. Six literature combos are unlikely associations given their extremely small membership probabilities.

We advocate for dedicated follow-up studies including a detailed chemical investigation (chemical tagging; [Freeman & Bland-Hawthorn, 2002](#)) and an accurate age determination. For combos with a membership probability higher than 10 per cent, logarithmic ages range from 6.42 (2.6 Myr) and 8.72 (525 Myr), with a median age of 7.80 (63 Myr), according to the age determinations of [Cantat-Gaudin et al. \(2020\)](#).

In an attempt to compare the age of Cepheids as given through isochrone fitting of the cluster population with the age given by theoretical period-age relations, we derived cluster ages using our own method and a publicly available code based on artificial neural networks. Despite an overall good agreement with literature values, we conclude that current age determinations for young open clusters do not reach the required accuracy ($\log(t) < 0.2$) for the proposed goal. We argue that the reason is intrinsic to young open clusters, especially the less massive ones, due to the lack of MSTO stars. Such conclusions have already been reported by, e.g., [Senchyna et al. \(2015\)](#). We believe that upcoming *Gaia* data releases will allow us to overcome this difficulty by providing colour-magnitude diagrams with extremely high levels of completeness and purity. Other approaches to possibly avoid some of these difficulties could come from the comparison of their observed and theoretical luminosity functions (see e.g. [Piskunov et al., 2004](#)), or by complementing *Gaia* data by reddening-free indices and spectral types for upper main-sequence stars. We note in passing that [Peña Ramírez et al. \(2021\)](#) pre-selected potential cluster members via their *Gaia* DR2 proper motions using Gaussian mixture models, and assigned membership probabilities using the same unsupervised machine learning method (UPMASK) as in [Cantat-Gaudin et al. \(2018b\)](#) and [Cantat-Gaudin & Anders \(2020\)](#), but on near-infrared data instead of *Gaia* DR2 photometry. For the six clusters in their study, they report on average 45 per cent more cluster members than [Cantat-Gaudin et al. \(2018b\)](#) and [Cantat-Gaudin & Anders \(2020\)](#).

Despite a much larger number of clusters and Cepheids in the input catalogues, the number of high probability cluster-Cepheid pairs in the MW did not increase much. Even assuming that all cluster Cepheids pairs with $P(A|B) > 0.01$ represent a true association, which is far from being realistic, we infer 4.1 per cent ($121/2921$)³⁶ as an upper limit to the fraction of classical Cepheids in open clusters. [Anderson & Riess \(2018\)](#), using the bona-fide cluster Cepheids described in A13, report an upper limit of 8.5 per cent for the clustered fraction of fundamental-mode Cepheids within 2 kpc from the Sun. [Anderson & Riess \(2018\)](#) also estimated the clustered fraction of fundamental-mode Cepheids in the Small and Large Magellanic Clouds to 6 and 11 per cent, respectively, and to 2.5 per cent in M31. Although

³⁶For this, we also impose that a given Cepheid is associated with a unique cluster, therefore we consider 121 combos instead of 164.

the fraction presumably varies from galaxy to galaxy, even within a given galaxy, and also with time, these numbers all suggest a low fraction of Cepheids in clusters.

Since very young (< 20 Myr) clusters are overabundant, it is known that young clusters dissolve quickly, whether it is a consequence of gas expulsion or of their stellar dynamic and stellar evolution-driven expansion (e.g., Lada & Lada, 2003; Goodwin & Bastian, 2006; Moeckel et al., 2012), and these dissolutions can occur as fast as 100 Myr even for relatively massive clusters (of $\sim 1,000 M_{\odot}$; Shukirgaliyev et al., 2018). In contrast, Cepheids have ages ranging from a few tens to a few hundred Myr (e.g., Anderson et al., 2016). The low fraction of Cepheids in clusters could then be related to the rapid dissolution of young clusters, or alternatively indicate that they are born elsewhere.

In a recent study, Dinnbier, Anderson, & Kroupa (2022) investigated the occurrence of classical Cepheids in star clusters evolving to an age of ~ 300 Myr using N-body simulations. The results of these simulations agree with the picture that a small fraction of Cepheids reside in clusters, although this depends on the cluster mass (Cepheid progenitors are more likely to escape from low-mass clusters) and the Cepheids masses (higher-mass Cepheids are more likely to be found in clusters), on the distance to the galactic centre (smaller distances involve more rapid cluster dissolutions), and on metallicity (a lower Z imply a delayed Cepheid formation). Dinnbier, Anderson, & Kroupa (2022) predicted that the upper limit for the fraction of clustered Cepheids in the MW ranges from 30 to 36 per cent when neglecting cluster dissolving mechanisms other than gas expulsion, internal dynamics, and the Galactic tidal field, and a fraction of 1.5 to 2.6 per cent when adopting an analytical model to match empirical findings. A possible solution for this disagreement could arise from considering cluster disruption mechanisms not considered in these numerical simulations (e.g. cluster encounters with giant molecular clouds), from the discovery of a large number of clusters that could host Cepheids (not considered in previous works; e.g., Castro-Ginard et al., 2022), or from adapting the current methodologies to associate Cepheids to clusters. These future avenues for the study of cluster Cepheids are discussed in more detail in Chapter 5.

After estimating the age distribution of Galactic open clusters within a cylinder of 2 kpc radius from the Sun (taking into account age-dependent completeness limits), Anders et al. (2021) derived the star formation rate in clusters in the Solar vicinity, compared it to the total star formation rate in the solar vicinity (Mor et al., 2019), and concluded that only ~ 16 per cent of stars formed in bound clusters. This result is in line with recent findings where star formation takes place at all scales and in unbound structures rather than in clusters (see e.g. Ward, Kruijssen, & Rix 2020, or the review by Adamo et al. 2020). This view has been challenged by Dinnbier, Kroupa, & Anderson (2022), who found that the fraction of stars (not only Cepheids) observed in star clusters is consistent with the hypothesis that all stars originate from gravitationally bound systems, when cluster dynamics, early gas expulsion, and the influence of realistic galactic environments are properly taken into account. In Chapter 5 the role that Cepheids will play in future studies for bridging the gaps between these views of the formation of stars in our Galaxy is further addressed.

3

RR Lyrae stars in the Halo Outskirts With Variable STars survey (HOWVAST)

The content of this chapter is partially based on the work “A Systematic DECam Search for RR Lyrae in the Outer Halo of the Milky Way” published on the *Astronomical Society of the Pacific Conference Series* (Medina et al., 2021b), and was adapted from the article in preparation “Discovery of remote RR Lyrae stars in the Halo Outskirts With Variable Stars (HOWVAST) survey” (Medina et al., in preparation). The latter will be submitted to the *Monthly Notices of the Royal Astronomical Society (MNRAS)* journal in the upcoming months. I am the first author of both of these works, and have been in charge of collecting, processing, and analysing the data, as well as reaching the conclusions.

In this study, we introduce the Halo Outskirts With Variable Stars (HOWVAST) survey, with which we aim to extend the reach of known well-characterized outer halo RRLs surveys. Thus, our goal is to detect and derive the properties of faint RRLs. We use this knowledge to study their spatial distribution and their connection with the accretion history of the MW. Section 3.1 provides an overview of the importance of the halo outermost regions for Galactic studies, highlighting the role of RRLs in this regard. In Section 3.2, we describe the survey strategy, the observations carried out for this study, and the methodology followed for data processing. In Section 3.3, we provide a detailed description of our RRLs selection and classification pipelines, as well as the methods used for the determination of their heliocentric distances, periods, and amplitudes. Additionally, we contrast our detected RRLs with those from the literature and use these comparisons as an indicator of our detection completeness. In Section 3.4, we focus our attention on the most distant RRLs in our sample (those with $d_{\text{H}} > 100$ kpc). Finally, in Section 3.5 we study the spatial distribution of our RRLs via an Markov chain Monte Carlo analysis, and discuss the similarities and differences between our results and studies of other regions of the halo. We conclude this chapter by summarizing our results and outlining the implications of our findings in Section 3.6.

3.1 Motivation

In the currently favoured cosmological framework, the Λ -CDM model, galaxies are assembled hierarchically through the accretion of smaller systems. The MW and similar galaxies (MW-like), as large disc galaxies, had likely undergone violent mergers in their early history as part of their hierarchical formation (see, e.g., Press & Schechter, 1974; Blumenthal et al., 1984; Bullock & Johnston, 2005; Montalbán et al., 2021). The stellar haloes of galaxies provide key information to help reconstruct their formation conditions. For the MW, in particular,

compelling evidence for these (past and ongoing) accretion events have been identified in present-day inner and outer halo stellar populations, unveiling details of gravitational interactions with massive satellites such as the Sagittarius stream (e.g., [Ibata, Gilmore, & Irwin, 1994](#); [Majewski et al., 2003](#); [Vivas & Zinn, 2006](#)), Gaia-Sausage-Enceladus (GSE; e.g., [Belokurov et al., 2018b](#); [Helmi et al., 2018](#); [Haywood et al., 2018](#)), and the infall of the Magellanic Clouds (e.g., [Mathewson, Cleary, & Murray, 1974](#); [Besla et al., 2007](#); [Zaritsky et al., 2020](#); [Erkal et al., 2021](#)).

As stated in Chapter 1, the shape of the halo radial density profile is sensitive to key properties of the MW that help reconstruct its accretion history (see e.g. [Bullock & Johnston, 2005](#); [Pillepich et al., 2014](#)). Of particular importance is the slope of the distribution of outer halo stars, which can be used to constrain the relative fraction of stars with an accreted origin in the outskirts of the MW, where they are not expected to have formed in-situ (see e.g. [Jurić et al., 2008](#); [Pillepich et al., 2014](#); [Merritt et al., 2016](#); [Naidu et al., 2020](#)). The spatial distribution of halo stars can also be used to study the presence of large-scale overdensities (and underdensities) in the halo, that appear as a consequence of the dynamical response of the MW to the infall of massive satellites (e.g., the LMC; [Erkal, Belokurov, & Parkin, 2020](#); [Conroy et al., 2021](#)). Thus, the degree of radial (an-)isotropy and the wakes that characterize the dynamical effects of the infalling satellites are key to disentangle the events that formed the halo, especially at large distances where they are expected to be more noticeable ([Pandey, 2022](#)). But well-characterized (e.g., with reliable classifications and precisely determined distances) MW stars at large distances are rare, in particular close to the “edge” of the MW (292 ± 61 kpc, when defined as the point at which virialized material has completed at least two pericentric passages; [Deason et al., 2020](#)). Commonly used stellar distance tracers include RGB stars (e.g., [Helmi et al., 2003](#); [Xue et al., 2014](#)), blue horizontal branch stars (e.g., [Schlaufman et al., 2009](#); [Thomas et al., 2018](#)), M giants (e.g., [Bochanski et al., 2014](#)), and the old and metal-poor RRLs (e.g., [Drake et al., 2013b](#); [Medina et al., 2018](#); [Stringer et al., 2021](#); [Huang & Koposov, 2022](#)), which are ubiquitous in the halo and dwarf galaxies.

RR Lyrae variables have become essential tools to uncover the formation history of the MW and its neighborhood not only because of their role as precise distance indicators. For example, RRLs in the distant halo have been shown to be valuable tracers of known and yet undiscovered low luminosity satellites and associations (e.g., [Sesar et al., 2014](#); [Baker & Willman, 2015](#); [Sanderson et al., 2017](#); [Torrealba et al., 2019](#)), especially when they are found in groups at distances $d_H > 50$ kpc. Furthermore, the periods and amplitudes of RRLs can be used to support the evidence about their origins and, in particular, of the nature of the mergers responsible for the formation of the halo (e.g., [Catelan, Pritzl, & Smith, 2004](#); [Vivas & Zinn, 2006](#); [Torrealba et al., 2015](#); [Belokurov et al., 2018a](#); [Deason et al., 2017](#); [Dékány et al., 2018](#); [Prudil et al., 2019a, 2021](#); [Monelli & Fiorentino, 2022](#)). In addition, these stars are useful to study stellar streams and the imprints of past and ongoing accretion events occurring under different physical conditions (see e.g. [Duffau et al., 2006](#); [Sesar et al., 2010](#); [Iorio & Belokurov, 2019](#); [Belokurov et al., 2018b](#); [Helmi et al., 2018](#); [Abbas, Grebel, & Simunovic, 2021](#); [Prudil et al., 2021](#)). The spatial distribution of RRLs in the halo is also essential to investigate the radial density profile of the MW, given that they are intrinsically bright stars that can be identified (relatively) easily in time-domain surveys ([Wetterer & McGraw, 1996](#); [Sesar et al., 2011](#); [Medina et al., 2018](#); [Stringer et al., 2021](#)).

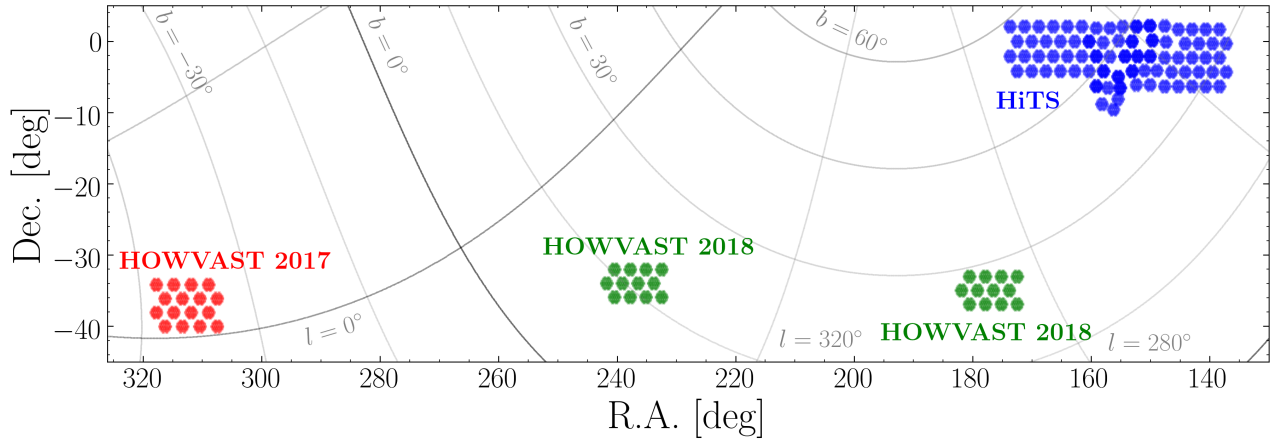


Figure 3.1: Spatial distribution of the surveys used for this work, shown in equatorial and Galactic coordinates. The DECam fields corresponding to the HOWVAST survey are plotted in red and green, while the fields observed by the HiTS survey are shown in blue.

Moreover, complementing the photometric characterization of halo RRLs with spectroscopic information (e.g., chemical abundances and line-of-sight velocities) is key to paint a complete portrait of the early chemical enrichment of the Galaxy (Clementini et al., 1995; Hansen et al., 2011; Pancino et al., 2015; Liu et al., 2020; Fabrizio et al., 2021) and to obtain precise estimates of its mass (see e.g. Deason et al., 2021; Prudil et al., 2022), even if a small number of stars is used for these purposes (e.g., Eadie & Harris, 2016).

Given their important role in Galactic astronomy, a large number of RRLs catalogues have been produced over the years from their classification in existing large-sky surveys, which cover a wide range of photometric depths (hence distances) and different regions of the sky. These systematic searches include the Quasar Equatorial Survey Team (QUEST) and the La-Silla QUEST surveys (Vivas et al., 2004; Zinn et al., 2014), the SDSS (Sesar et al., 2007, 2010), the Catalina surveys (Drake et al., 2014, 2017; Torrealba et al., 2015), the Pan-STARRS-1 survey (or PS-1; Chambers et al., 2016; Sesar et al., 2017), the High cadence Transient Survey (HiTS; Förster et al., 2016; Medina et al., 2017, 2018; Martínez-Palomera et al., 2018), the second and third data releases of the *Gaia* mission (Holl et al. 2018, and Clementini et al. 2019 and Clementini et al. 2022 using the Specific Objects Study pipeline SOS), the DES (Dark Energy Survey Collaboration et al., 2016; Stringer et al., 2021), and the ZTF survey (Masci et al., 2019; Chen et al., 2020; Huang & Koposov, 2022). Nevertheless, even though thousands of RRLs are predicted to be found in the halo between 100 and 300 kpc (Sanderson et al., 2017), only a small subset of these surveys have allowed astronomers to reliably detect RRLs beyond 100 kpc (mostly due to instrumental limitations). Thus, current censuses of the distant RRLs populations are still likely incomplete, and the outer limits of the halo have yet to be comprehensively mapped.

3.2 The data

3.2.1 Observations

The data used in this work were obtained as part of three independent campaigns carried out with the Dark Energy Camera (DECam; [Flaugher et al., 2015](#)), which is mounted on the 4m telescope at Cerro Tololo Inter-American Observatory (CTIO) in Chile. The first campaign corresponds to the HiTS survey, which was originally designed to characterize the early stages of supernovae explosions in real time ([Förster et al., 2016](#)). Specifically, we use the data from HiTS that were observed between 2015 February 17 and 22. This region of the HiTS survey consists of 50 Galactic halo fields (~ 150 sq. deg.) and includes 14 fields that were observed in previous HiTS campaigns. The HiTS 2015 fields were observed up to five times per night, and are located between 137 and 160 deg in right ascension, and -7 and 2.6 deg in declination, as shown by [Förster et al. \(2016\)](#) in their Figure 4. The data were taken mainly in the g -band, with 87 s exposures and a cadence of 1.6 hr. Observations in the r -band were performed as well, with individual exposures ranging from 81 to 102 s, which allowed the inclusion of $g-r$ colours for our analysis. This configuration summed up a total of 20 to 29 epochs in g , and from one to ten in r , per field. The data reduction was performed using the DECam community pipeline ([Valdes et al., 2014](#)). It is worth mentioning that the data obtained in this campaign have not been analysed for the purpose of this work, i.e., the data were not included in the analysis of [Medina et al. \(2018\)](#). For a more detailed description of HiTS' design, its observing strategy, and a comprehensive review of its characteristics we refer the reader to the work by [Förster et al. \(2016\)](#).

The second and third observing campaigns took place in 2017 and 2018, in the context of the HOWVAST ([Medina et al., 2021b](#)) survey. For HOWVAST we selected DECam fields to cover a considerable range of Galactic latitudes of the MW halo. The footprint of HOWVAST was chosen to avoid overlaps with deep large-sky surveys, such as the DES ([The Dark Energy Survey Collaboration, 2005](#); [Dark Energy Survey Collaboration et al., 2016](#)) and PS-1 ([Chambers et al., 2016](#)). In the first HOWVAST observing run, we observed 16 DECam fields during four consecutive half-nights, with 180 s exposures in the r -band and a cadence of approximately one hour. The second HOWVAST campaign consists of 24 fields, separated into two groups of 12 fields at different Galactic latitudes, observed in the r -band during four consecutive nights. As in the first run, the integration times for this campaign was 180 s, but with a cadence of ~ 40 min. This results in a combined area of ~ 120 sq. deg. mapped in the halo surveyed by HOWVAST, and time series containing from 15 to 30 observations per star. In addition, we obtained from two to four 240 s-exposure observations per field in the g -band HOWVAST each year, in order to facilitate the process of identification of RRLs in our analysis. The coordinates in the equatorial system of the HOWVAST fields are provided in [Table 3.1](#), making the distinction between the high- and low-Galactic latitude fields observed during our second campaign. As in the case of the HiTS data, the data of this survey was reduced using the DECam community pipeline.

Therefore, we analysed a total of ~ 270 sq. deg. when combining the footprints of footprint of HiTS and HOWVAST. The sky coverage of these surveys is shown in [Figure 3.1](#) in equatorial and Galactic coordinates.

Table 3.1: Identification numbers and equatorial coordinates of the DECam fields observed by HOWVAST in 2017 and 2018. The fields of the second campaign are labeled according to their positions with respect to the Galactic plane (2018A and 2018B represent the high- and low-Galactic latitude fields, respectively).

Campaign	Field ID	R.A. (deg)	Dec. (deg)
2017	1	307.50000	-40.00000
2017	2	308.96859	-38.05144
2017	3	307.50000	-36.10289
2017	4	308.96859	-34.15433
2017	5	310.43715	-40.00000
2017	6	311.90575	-38.05144
2017	7	310.43715	-36.10289
2017	8	311.90575	-34.15433
2017	9	313.37434	-40.00000
2017	10	314.84293	-38.05144
2017	11	313.37434	-36.10289
2017	12	314.84293	-34.15433
2017	13	316.31149	-40.00000
2017	14	317.78008	-38.05144
2017	15	316.31149	-36.10289
2017	16	317.78008	-34.15433
2018A	1	172.50000	-33.00000
2018A	2	173.84140	-34.94856
2018A	3	172.50000	-36.89711
2018A	4	175.18282	-33.00000
2018A	5	176.52423	-34.94856
2018A	6	175.18282	-36.89711
2018A	7	177.86563	-33.00000
2018A	8	179.20704	-34.94856
2018A	9	177.86563	-36.89711
2018A	10	180.54845	-33.00000
2018A	11	181.88986	-34.94856
2018A	12	180.54845	-36.89711
2018B	13	232.50000	-32.00000
2018B	14	233.82657	-33.94856
2018B	15	232.50000	-35.89711
2018B	16	235.15315	-32.00000
2018B	17	236.47973	-33.94856
2018B	18	235.15315	-35.89711
2018B	19	237.80630	-32.00000
2018B	20	239.13288	-33.94856
2018B	21	237.80630	-35.89711
2018B	22	240.45945	-32.00000
2018B	23	241.78602	-33.94856
2018B	24	240.45945	-35.89711

3.2.2 Data processing

Pre-processing

The data from the HiTS 2015 campaign were pre-processed as part of the work by [Medina \(2017\)](#). Thus, in order to create a catalogue with the sources in these fields, we followed the methodology from [Medina et al. \(2018\)](#). We first defined an x,y pixel coordinate system based on the output information generated by the SExtractor photometry software ([Bertin & Arnouts, 1996](#)). To do this, we selected a reference frame for both the g - and the r -band, for which the observing conditions were closer to optimal. For the g filter we chose the second epoch, whereas for r the reference chosen was the first epoch. Subsequently, we used the scaling constants found by the HiTS pipeline ([Förster et al., 2016](#)) to perform the alignment of the individual observations with respect to the reference. Then, we crossmatched the catalogues aligned in the common x,y coordinate system and rejected sources with fewer than five detections in the g -band for the rest of the analysis. In order to keep sources with a preliminary indications of variability for further processing, we disregarded sources for which the uncertainties in the mean flux exceeded by more than two times their flux standard deviations. Finally, we applied an x,y pixel to equatorial coordinate transformation following the procedure described by [Förster et al. \(2016\)](#), i.e., using quadratic transformations.

To pre-process the HOWVAST observations we adopted an alternative approach, based on the data processing pipeline in development for the Rubin Observatory Legacy Survey of Space and Time (LSST; [LSST Science Collaboration et al., 2009](#); [Bosch et al., 2019](#)). This pipeline was used to detect sources in the images, measure aperture fluxes, and perform a source point spread function (PSF) fitting. Because the sources of interest of this work are stars, we use PSF fluxes and magnitudes throughout the HOWVAST data treatment. For the subsequent variable star analysis, we only examined stellar sources with more than 15 data points in their time series, and with flux standard deviations at least 2.5 times larger than their mean flux uncertainties.

Photometric calibration

In order to account for atmospheric effects affecting the epochs in our time series, we determined a photometric zero-point relative to the reference frame chosen for HiTS and HOWVAST separately. For this, we computed instrumental magnitudes following

$$\text{mag}_{\text{inst}} = -2.5 \log \left(\frac{\text{Flux}}{t_{\text{exp}}} \right) - a_g - k_g A, \quad (3.1)$$

where mag_{inst} represents the instrumental magnitude either in the g or the r filter, Flux is the source flux, t_{exp} corresponds to the exposure time, a and k are the filter-dependant DECam photometric zero-point and first-order extinction coefficient per CCD³⁷ (respectively), and A is the airmass at the time of the observations.

To calibrate the photometry of the HiTS 2015 fields, we first anchored our instrumental magnitudes to the reference frames in g and r . For the photometric calibration of the HOWVAST 2017 and 2018 data we also selected reference frames, similar to what was done

³⁷ Available at <http://www.noirlab.edu/science/documents/scidoc1571>

for the HiTS 2015 data pre-processing. We selected the first and second epoch in g , and the eighth and fourth in r (respectively), as the average PSF of the sources were minimum in these cases. We compared our instrumental magnitudes with those in the reference frame, so that $\text{mag}_{\text{ref}} = \text{mag}_{\text{inst}} + \Delta_{\text{rel}}$, where Δ_{rel} is the zero-point relative to the reference epoch, and mag_{ref} is the object magnitude calibrated with respect to said epoch.

We calibrated the photometry of the references using the archival data stored in the National Optical-Infrared Astronomy Research Laboratory (NOIRLab) Source Catalog (NSC; [Nidever et al., 2021](#)), as all the surveys considered in our work overlap the catalogues published in the second data release of this database. The photometric calibration of the NSC is based on the PS-1 survey, on the Skymapper and the ATLAS all-sky stellar reference catalogues ([Wolf et al., 2018](#); [Tonry et al., 2018](#), respectively), and on model magnitudes from linear combinations of photometry from catalogues such as the 2MASS survey ([Skrutskie et al., 2006](#)) and the American Association of Variable Star Observers (AAVSO) Photometric All-Sky Survey (APASS; [Henden et al., 2015](#)). For the calibration, we limited the NSC data to star-like sources, with *starClass* flags larger than 0.85 (a *starClass* value of 0 is assigned for extended sources in the NSC, and a value of 1 is used for point-like sources). The sample was selected to include the NSC stars within two arcseconds from the sources in our catalogue. We used only NSC stars with g and r magnitudes between 16.5 and 20.5, and magnitude errors smaller than 0.05, in addition to a two sigma clipping process performed over the median magnitude difference to remove outliers. From this comparison, we obtained an additional zero-point and colour term on a chip-by-chip basis, for each DECam field. Therefore, the calibrated magnitudes are given by

$$\text{mag} = \text{mag}_{\text{ref}} - A_{\text{NSC}} - B_{\text{NSC}} (g - r), \quad (3.2)$$

where mag represents the calibrated magnitudes, A_{NSC} and B_{NSC} are the zero-point and the colour coefficient resulting from the magnitude comparison with the NSC data, and $g - r$ is the colour of a given star.

Finally, the mean magnitudes were corrected for extinction using the dust maps of [Schlafly & Finkbeiner \(2011\)](#), adopting $A_g = 3.237 E(B - V)$ and $A_r = 2.176 E(B - V)$. Magnitude errors were computed by propagation of uncertainties.

3.3 Search and characterization of RR Lyrae stars

3.3.1 Selection of the RR Lyrae candidates

Since the data used in this work were obtained from two different surveys, we adopted two slightly different methodologies to process the data for the search and characterization of RRLs.

To reduce the amount of data to be analysed when looking for RRL candidates in the HiTS 2015 survey, objects with a magnitude variation smaller than 0.2 magnitudes were filtered out from the original source catalogues. Additionally, only the sources redder than -0.2 in $g - r$, and bluer than 0.6 were considered for further processing.

The period of the sources in the HiTS 2015 catalogues were determined by running a generalized version Lomb-Scargle period detection routine (the GLS; [Zechmeister & Kürster,](#)

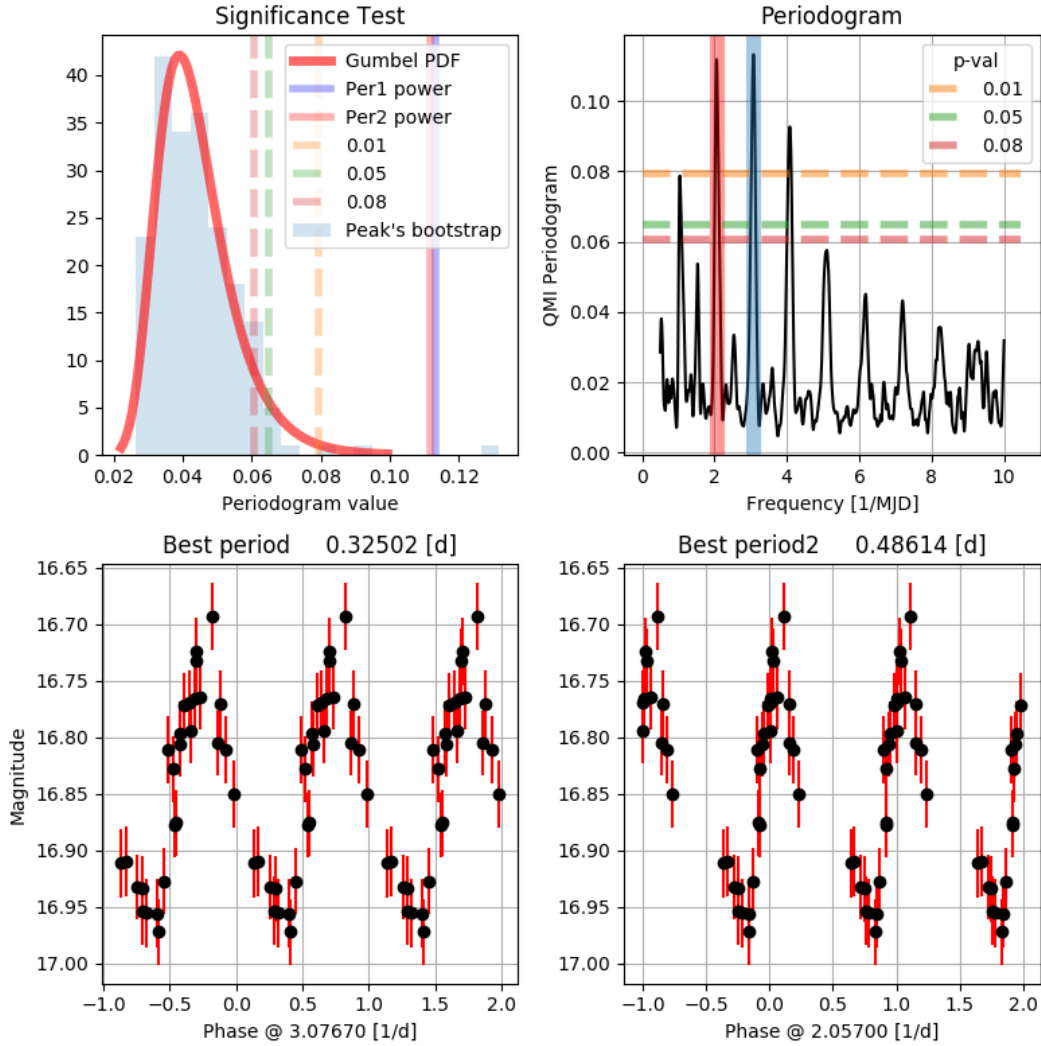


Figure 3.2: Outcome of the period detection analysis for an RRL in our sample (HV210233-341321). The *top left* panel shows the QMI periodogram power distribution after bootstrapping and highlights the limits corresponding to a p-value of 0.08 (red dashed line), 0.05 (green dashed line), and 0.01 (yellow dashed line), in addition to the power of the two most significant periods detected (Per1 and Per2). The Gumbel probability density function (PDF), as computed by the routine P4J, is represented with a red solid line. The *top right* panel depicts the dependence between the QMI periodogram power and the inverse of the periods tested (the frequency). The *bottom* panels show the light curve of this RRL phased by the two most significant periods. Based on these periods, the amplitude of variation, and the shape of the phased light curve, we classify this RRL as ab-type.

2009), which incorporates a constant to the typical Lomb-Scargle sinusoid fitting procedure. By doing this, the results are overall less susceptible to aliasing and provide a more accurate frequency selection in the power spectrum. To compute the statistics and period selection, the GLS tool within the *astroML* Python module (VanderPlas et al., 2012) was used. Only sources with periods longer than 4.8 hours (0.2 d) and shorter than 21.6 hours (0.9 d) were considered to reduce the number of RRL pre-candidates, as well as those for which with a GLS statistical level detection were smaller than 0.08. Finally, the two most significant periods were chosen and further inspected when more than one period were detected and met the aforementioned requirements. The last step for the selection of RRL candidates in the HiTS 2015 fields was to visually inspect the light curves resulting from the previous cuts, and to look for objects with light-curve shapes, periods, and amplitudes typical of RRLs. The search resulted in a total of 98 RRL candidates in the fields that do not overlap those inspected by Medina et al. (2018).

The selection criteria for RRL candidates in HOWVAST data is similar to the one followed for HiTS. For the sake of preliminary rejecting spurious sources from our list of potential candidates, we filtered out sources with minimum to maximum magnitude variability smaller than 0.2 magnitudes, and those with $g - r$ colours clearly differing from the expectations for RRLs. Thus, we adopted a more conservative cut and only considered stars with $g - r$ between -0.45 and 1.0 .

To determine periods for the remaining sources, we used the Python package P4J³⁸, which was specifically designed for period detection on irregularly sampled and heteroscedastic time series, using the Cauchy-Schwarz QMI as the criterion to be maximized by this routine (Huijse et al., 2018). We first inspected the two periods with highest likelihoods, as long as they were longer than 0.2 d and shorter than 0.95 d (typical of RRLs). Periods detected with a statistical significance lower than 0.01 were not further considered for the analysis. Finally, we visually inspected the phased light curves and selected only RRL-like sources as candidates, based on their light curve shapes, periods, and amplitudes. For candidates exhibiting more than two high probability signals in the power spectrum, we examined the four most likely periods before choosing the star’s main period. In Figure 3.2, we show the outcome of this procedure for the RRL HV210233-341321 as an example.

The final list of RRL candidates from the HOWVAST data only consists of 399 stars. Thus, we report the detection of a total of 497 RRLs, whose main properties are provided in Table B1. The distribution of the mean g and r magnitudes for our entire sample is depicted in Figure 3.3, and their spatial distribution is shown in Figure 3.4.

3.3.2 Distance determination

We determined the absolute magnitude of our RRLs in the g - and r -bands (M_g and M_r , respectively) using the period-luminosity-metallicity relations from Sesar et al. (2017) and assuming halo metallicity ($[\text{Fe}/\text{H}] = -1.5$; see e.g. Suntzeff, Kinman, & Kraft 1991; Prantzos 2008; Conroy et al. 2019):

$$\begin{aligned} M_g &= (-1.7 \pm 0.3) \log\left(\frac{P}{0.6}\right) + (0.69 \pm 0.04) + (0 \pm 0.07) \\ M_r &= (-1.6 \pm 0.1) \log\left(\frac{P}{0.6}\right) + (0.51 \pm 0.04) + (0 \pm 0.06), \end{aligned} \quad (3.3)$$

³⁸Available at <http://github.com/phuijse/P4J>

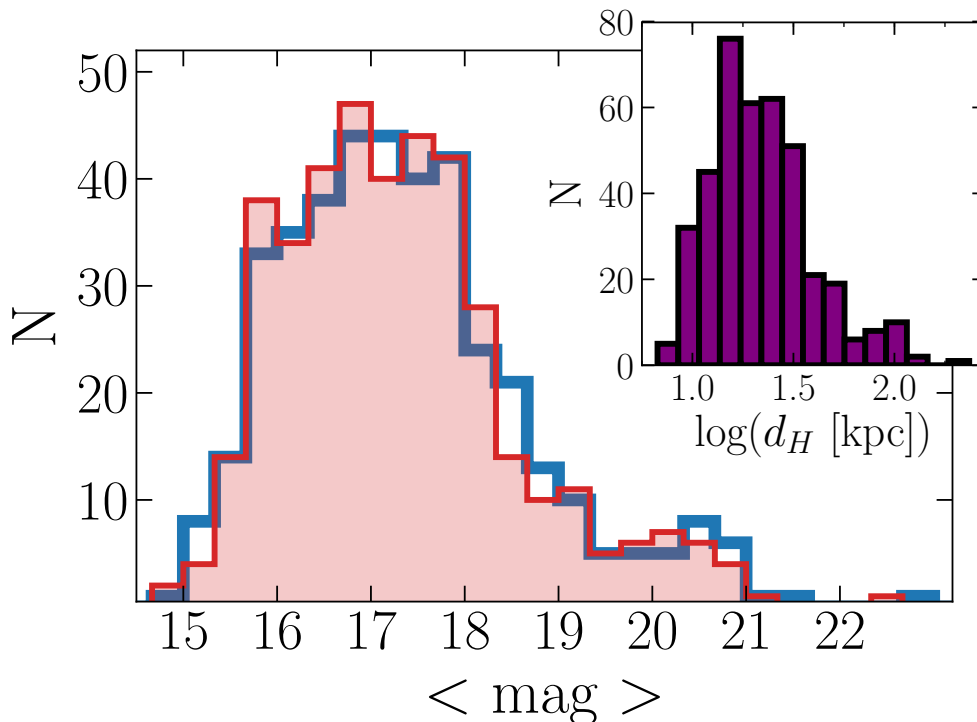


Figure 3.3: Histogram of the mean g and r magnitudes of the RRLs detected in this work (blue and red distributions, respectively). The inner plot depicts the logarithmic distribution of the heliocentric distances d_H obtained in Section 3.3.2.

where P stands for the periods of the RRLs. We note in passing that these relations are only valid for fundamental-mode periods. Thus, for RRc stars we “fundamentalize” their periods prior to using Equation 3.3 by following:

$$\log(P_F) = \log(P) + 0.128, \quad (3.4)$$

where P_F is the fundamentalized period (Catelan, 2009). Heliocentric distances d_H are then computed through distance modulus, and their uncertainties determined from error propagation. The effects of the metallicity assumption on the resulting distances in Equation 3.3 are expected to be small. In fact, an offset of 0.5 and 1.0 dex in $[\text{Fe}/\text{H}]$ would lead to differences in d_H smaller than 4 and 8 kpc for remote RRLs (> 100 kpc), respectively.

Along with the mean magnitude distribution of our RRLs, Figure 3.3 displays their heliocentric distance distribution. Our sample consists of RRLs with d_H spanning from 6 to ~ 270 kpc. Most of the stars lie within 50 kpc (434 RRLs; 87.3 per cent), whereas 52 of them have d_H between 50 and 100 kpc (10.5 per cent), and 11 (2.2 per cent) lie beyond 100 kpc. We further describe the most distant subsample in Section 3.4. An overdensity of 16 RRLs near 90 kpc ($\langle g \rangle \sim 20.5$ or $\langle r \rangle \sim 20.2$) is clear from the figure, and is associated with RRLs in the Sextans dSph that were not detected by Medina et al. (2018). All of these stars are found in the catalogue of Vivas et al. (2019) when crossmatching within a radius of seven arcseconds, with the exception of HiTS 100752-020827.

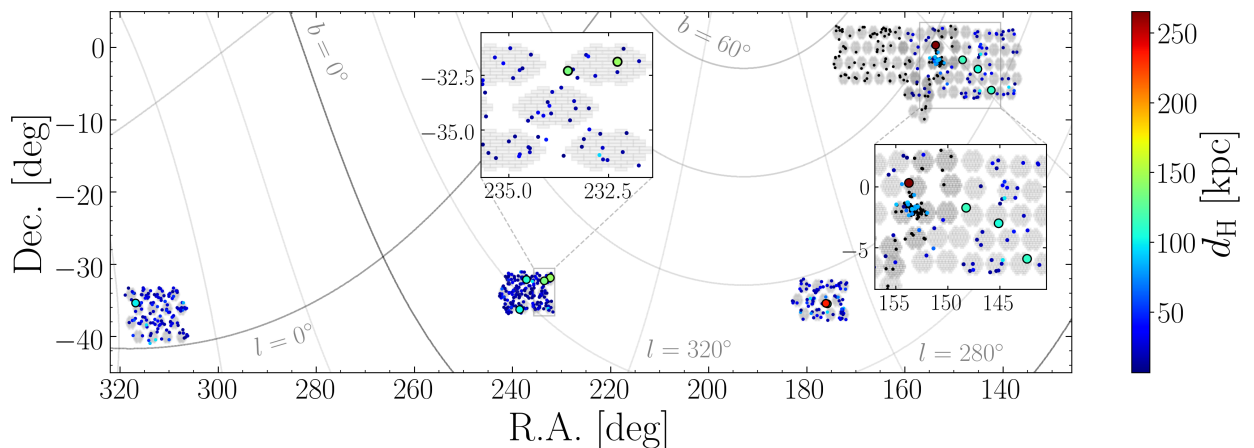


Figure 3.4: Spatial distribution of the RRL candidates detected in this work, colour-coded by their heliocentric distance d_H in kpc. The stars from the HiTS campaign analysed by [Medina et al. \(2018\)](#) are plotted with small black symbols, and the RRLs from this work with distances larger than 100 kpc (described in Section 3.4) are plotted with large colour-coded circles. An approximation of the footprint of each DECam field observed is shown in grey in the background as a reference. An enlargement of the two regions containing RRLs beyond 100 kpc with similar distances (and potentially associated with each other) is provided.

3.3.3 Classification and Bailey diagram

In order to classify the RRL candidates in our catalogue, we adjusted the light curve templates from the SDSS Stripe 82 ([Sesar et al., 2010](#)) to our phased light curves. This was performed using the templates in the g - and r -bands available in the Python package GATSPY ([Vanderplas, 2015](#); [VanderPlas & Ivezić, 2015](#)). The final classification of RRLs into ab- and c- subtypes was based on the inspection of the best-fitting templates, their amplitudes, and periods. This resulted in 335 RRab stars (67 per cent), 157 RRc stars (32 per cent), and 5 RRLs (1 per cent) that do not fall in either category, with indications of pulsations in the fundamental mode and first overtone simultaneously. We classified the latter as RRd stars. The distribution of these stars in the period-amplitude space, colour-coded by type, is shown in Figure 3.5. From the figure, we identify seven RRLs classified as ab-type with periods shorter than 0.4 d and V -band amplitudes smaller than 0.75. Because this region of the Bailey diagram is expected to be populated mostly by RRc-stars, we label these RRLs as most likely misclassified. A similar case is that of the RRL HiTS101456-022025, which is identified as an RRc star but whose period (~ 0.5 d) and V -band amplitude (~ 0.65) are typical of RRab stars. Thus, for these special cases we highlight that the reported classification is tentative.

The position of RRLs in the Bailey diagram can be used as a tool to help discern RRLs coming from the halo general population and those coming from UFDs. This is possible by taking the Oosterhoff types ([Oosterhoff, 1939](#)) into account, as cluster RRLs can be split into two distinct groups based on their periods and amplitudes, in a dichotomy that is not present in most MW UFDs (which are mostly Oo-int and OoII) and field stars. Figure 3.5

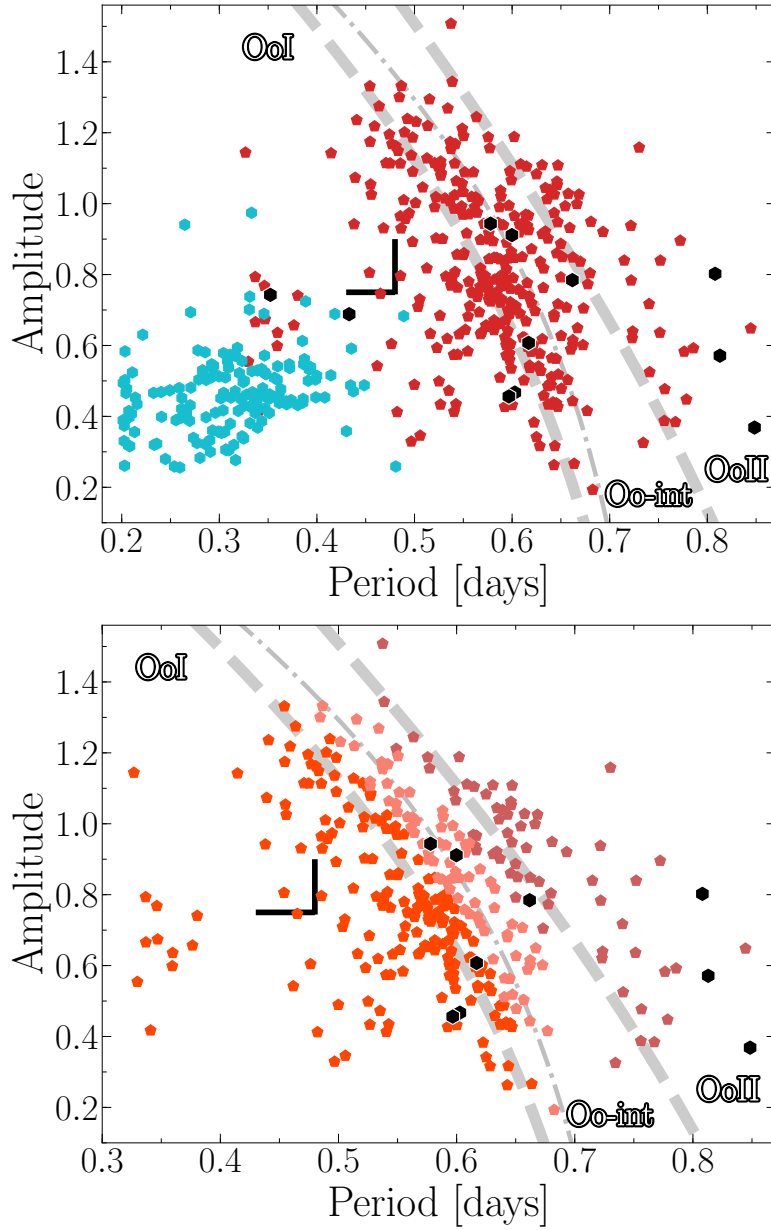


Figure 3.5: Bailey diagrams of the RRLs detected in this work. In the *top* panel, RRab stars are displayed with red pentagons, whereas light blue hexagons represent c-type RRLs. The amplitudes represent the minimum-to-maximum variation of the fitted light curves in the V -band, obtained by scaling the g and r magnitude amplitudes by a factor of 0.90 and 1.21, respectively (Sesar, 2012). Stars with estimated heliocentric distances larger than 100 kpc are plotted with black symbols. The dashed regions depict the fiducial lines for OoI, Oo-int, and OoII defined by Fabrizio et al. (2019). The *bottom* panel shows RRab stars only, colour-coded by the likelihood of the RRLs belonging to these groups based on their distance to the fiducial lines in the period-amplitude space (red, salmon, and brown representing OoI, Oo-int, and OoII, respectively). In both plots, black solid lines delimit the region containing HASP RRab variables, as defined by Fiorentino et al. (2015).

shows the OoI, OoII, and Oo-int fiducial lines in the Bailey diagram as defined by [Fabrizio et al. \(2019\)](#) for V -band RRL amplitudes. To account for the differences between RRL amplitudes in the g and r -bands from our work and those in the V -band, we scaled our amplitudes by a factor of 0.90 and 1.21, respectively ([Sesar, 2012](#)). In the bottom panel of [Figure 3.5](#) we colour-code the RRab stars according to their proximity to either of the Oosterhoff groups' fiducial lines. From this grouping, we conclude that most of the RRab stars in our sample could be considered OoI or Oo-int, as only ~ 21 per cent lies close to the OoII curve.

High Amplitude Short Period (HASP) variables, that is, those with periods shorter than 0.48 d, and V band amplitudes larger than 0.75, have been interpreted as coming from progenitors or regions in the Galaxy with populations more metal-rich than $[\text{Fe}/\text{H}] = -1.5$ ([Fiorentino et al., 2015](#)). Therefore, RRLs lying in this region of the Bailey diagram can provide insights on the building of the halo and its progenitors. In fact, most MW dSph lack HASP variables, and these stars are not rare in the halo and among the globular clusters and massive dwarf irregulars. We find 17 RRab stars populating the HASP region, which corresponds to only 5 per cent of our full RRab star sample. The heliocentric distance of these stars (see [Section 3.3.2](#)) ranges between 9 to 38 kpc. Thus, the relatively low fraction of HASP RRLs in our sample might be an indication of the dual origin of the outer halo (and its dependence on Galactocentric distance), as further discussed in [Section 3.5](#).

3.3.4 Comparison with previous surveys

A common approach to measure the completeness of variable star surveys is to compare with previous surveys with overlapping footprints. With this, it is possible to understand the limitations of each survey, and to quantify the effects of the assumptions on which the RRL detection pipelines rely, among other selection biases.

Because the strategy followed to detect RRLs in the HiTS 2015 fields is nearly identical to that of [Medina et al. \(2018\)](#), we assume that the detection efficiency and completeness of the survey in those regions are equivalent. That is, the ability to detect an RRL and to estimate its period within 10 per cent of its real value varies between 85 and 90 per cent for RRLs with mean g in the range 18.5-21, and drops to < 70 per cent for $g > 22$. The completeness, estimated from the comparison with surveys containing brighter sources (e.g., the La Silla-QUEST survey; [Zinn et al., 2014](#)), is expected to range between 75 and 80 per cent.

To investigate the ratio of RRLs that we are missing over the entire distance range covered by HOWVAST, it would be ideal to compare with a survey from data taken with a telescope with equal or similar capabilities as the DECam, such as the DES. That is not possible in our case given that HOWVAST and the DES have a minor overlap (by design), and only three likely RRLs from the latter are found in the region in common. Of these, we are able to recover two (DES Y6 ID's 993068652 and 899681846, at $d_{\text{H}} \sim 40$ and 50 kpc; [Stringer et al. 2021](#)), and attribute the non-detection of the third (DES 884429730, at 100 kpc) to its proximity to the border of the CCD (~ 100 pixels).

Here we crossmatch our sample with the RRLs in the CRTS catalogues ([Drake et al., 2013a, 2014, 2017](#); [Torrealba et al., 2015](#)) and with the *Gaia* catalogues generated with the SOS pipeline. For the latter, we use the catalogue based on *Gaia* DR2 ([Clementini et al., 2019](#)), which has been widely used and analysed in the literature and for which estimates of

Table 3.2: Total number (N) and recovered RRLs (N_x) from previous surveys as a function of heliocentric distance d_H . This table shows that, while our survey is partially limited to sources with mean magnitudes fainter than 17.5 in g and r , we are able to recover over 75 per cent of the candidate RRLs beyond 20 kpc. In this table, we abbreviate HOWVAST as HV for conciseness.

Literature	Survey	All			$d_H > 20$ kpc			$20 < d_H < 40$ kpc			$40 < d_H < 80$ kpc			$d_H > 80$ kpc		
		N	N_x	N_x/N	N	N_x	N_x/N	N	N_x	N_x/N	N	N_x	N_x/N	N	N_x	N_x/N
<i>Gaia</i> DR2	HV	430	210	0.49	89	67	0.75	78	62	0.79	8	3	0.38	3	2	0.67
<i>Gaia</i> DR3	HV	651	291	0.45	171	118	0.69	131	101	0.77	31	11	0.35	9	6	0.67
PS-1	HV	–	–	–	–	–	–	–	–	–	–	–	–	–	–	–
CRTS	HV	391	180	0.46	101	80	0.79	96	75	0.78	5	5	1.00	–	–	–
ZTF	HV	–	–	–	–	–	–	–	–	–	–	–	–	–	–	–
DES	HV	5	2	0.40	3	2	0.67	–	–	–	2	2	1.00	1	0	0.00
<i>Gaia</i> DR2	HITS 2015 + HV	476	232	0.49	95	71	0.75	82	64	0.78	10	5	0.50	3	2	0.67
<i>Gaia</i> DR3	HITS 2015 + HV	896	395	0.44	292	180	0.62	173	125	0.72	75	32	0.43	44	23	0.52
PS-1	HITS 2015 + HV	467	150	0.32	104	58	0.56	32	22	0.69	31	17	0.55	41	19	0.46
CRTS	HITS 2015 + HV	554	253	0.46	152	113	0.74	137	102	0.74	15	11	0.73	–	–	–
ZTF	HITS 2015 + HV	87	38	0.44	13	7	0.54	11	6	0.55	2	1	0.50	–	–	–
DES	HITS 2015 + HV	5	2	0.40	3	2	0.67	–	–	–	2	2	1.00	1	0	0.00

the amount of spurious detections it contains are currently available (e.g., Iorio & Belokurov, 2021). We also considered the recently published catalogue based on *Gaia* DR3 (Clementini et al., 2022). This catalogue almost doubles the size of its previous version but no cleaned RRL samples (or clear metrics that could be used to remove contaminants) are available at the moment this thesis work was prepared. Thus, in terms of the completeness of our survey, we consider the number of missed stars from *Gaia* DR2 a lower limit, and those from *Gaia* DR3 an upper limit. We note in passing that, by design, HOWVAST does not overlap the area covered by other large surveys such as the OGLE catalogue (Soszyński et al., 2016), and has minor overlap with the ZTF (Chen et al., 2020; Huang & Koposov, 2022) and the PS-1 (Sesar et al., 2017) surveys. The results of our comparisons, including the few overlapping RRLs from the ZTF and the PS-1 surveys, are summarized in Table 3.2 and depicted in Figures B4, B5, and B6.

Using all the stars from the CRTS and *Gaia* DR2 (DR3) that lie within HOWVAST’s footprint for the comparison, we are able to recover only 46 and 49 (45) per cent of the RRLs, respectively. These numbers can be explained by the fact that a large number of the RRLs in these catalogues are located closer than the d_{H} corresponding to the saturation limit of HOWVAST ($\lesssim 10$ kpc). Thus, we inspect the variation of the number of recovered RRLs with d_{H} assuming $M_V = 0.69$ for the RRLs in the Catalina catalogue (Tsujiimoto, Miyamoto, & Yoshii, 1998), and using distances from the period-Wessenheit-metallicity relation of Garofalo et al. (2022) for the *Gaia* RRLs (for halo metallicity).

When limiting the comparison to RRLs between 20 and 40 kpc, observed at least 70 pixels from the edge of the CCDs (and with detections in the *Gaia* bandpasses, *BP* and *RP*), the number of recovered RRLs increases to about 80 per cent in each case. Only five RRLs from the CRTS and eight (31) from *Gaia* DR2 (DR3) lie in the regions mapped by HOWVAST in the range from 40 to 80 kpc. We are able to recover all five CRTS RRLs, and only three (11) of *Gaia*’s. A possible explanation for this difference, albeit the low number statistics, is the contamination in the *Gaia* SOS catalogue at these distances, as it has been shown that artefacts and spurious detections can be abundant in crowded areas (e.g., close to the Galactic plane; Holl et al., 2018; Clementini et al., 2019; Rimoldini et al., 2019), and attempting to remove them can reduce the *Gaia* SOS catalogue size by 17 per cent (Iorio & Belokurov, 2021). Beyond 80 kpc, no RRLs from the CRTS that fulfill our selection cuts are found, while we recover ~ 70 per cent of the reliably detected RRLs from *Gaia*. In the case of *Gaia* DR2, the only missed RRL in this distance range (*Gaia* 3466180307433981952) displays a relatively high *G*-band absorption (0.48 mag), and a large ratio between the combined flux in *BP* and *RP* with respect to *G* ($phot_bp_rp_excess_factor = 1.21$), which might be an indication of a blended source. The case is similar for the three RRLs missed at these distances from *Gaia* DR3, all of which have $phot_bp_rp_excess_factor > 1.25$.

We detect 108, 91, and 87 RRLs that are not listed in the concatenation of the aforementioned catalogues, when crossmatching using a search radius of 1, 5, and 10 arcsec, respectively. These stars are located from ~ 7 to 265 kpc in heliocentric distance, and the majority of them (57 per cent) lie in the low Galactic latitude fields of the second HOWVAST campaign. Interestingly, 83 per cent of the 71 RRLs with $d_{\text{H}} \leq 80$ kpc are classified as c-type, which might be a consequence of contamination by blended sources (for RRLs near the Galactic plane) and/or the misclassification of variable objects (e.g., eclipsing binaries). This does not occur for the stars further than 80 kpc, where 75 per cent of the new RRL

candidates are detected as ab-type. The most distant portion of this subsample is described in detail in Section 3.4.

3.4 RR Lyrae stars beyond 100 kpc

3.4.1 Main properties of the sample

We identify 11 RRLs with mean g and r magnitudes fainter than 20.7 and 20.6, respectively, which corresponds to heliocentric distances larger than 100 kpc. None of these stars are listed in the catalogues used for comparison in Section 3.3.4. Among these RRLs, two stars are located beyond 200 kpc. The number of observations in the light curves of these RRLs spans from 22 to 27 in the g -band, and from 15 to 28 in the r -band. The folded light curves of these RRLs are shown in Figure 4.1, and their main properties are summarized in Table 3.3.

It is noteworthy that most of the stars in this subsample are classified as ab-type (75 per cent), which we attribute to the fact that this subclass is easier to identify at larger distances (based on their light curves shapes), and that ab-type RRLs seem to be more abundant in general. Additionally, the flux-based cut used to filter the number of sources to be analysed in the pre-processing stage (i.e., only considering sources whose flux standard deviations are larger than 2 or 2.5 times their flux errors) biases our results against the detection of distant RRc stars, given their smaller amplitudes of pulsation. The location of these stars in the Bailey diagram (bottom panel in Figure 3.5), does not suggest a strong association with the locus of the fiducial line of the OoII group, albeit their tendency for periods of pulsation longer than 0.60 d. In fact, the average period of these R Rab stars is 0.70 d, similar to the mean period of distant RRLs found by Medina et al. (2018) and the collection of RRLs in MW UFDs studied by Vivas et al. (2016) (0.67 d). Observing a clear trend towards the OoII group could be interpreted as an indication of the contribution of these galaxies to the stellar populations in the outer halo. This is, however, not observed in our sample. Nevertheless, Figure 3.5 shows that the distribution of distant RRLs does not follow the overall trend of R Rab stars within 100 kpc. In particular, they are not preferably located near the locus of the OoI group. Finally, none of the RRLs in this subgroup lie in the HASP region.

To examine the overall consistency of the number of distant RRLs found in our work with the results of previous studies of similar photometric depth, we can perform a direct comparison assuming high completeness out to similar distances. Stringer et al. (2021) detected 6,971 ab-type RRL candidates in the $\sim 5,000$ sq. deg of the DES' footprint, among which 4,569 do not belong to the known substructures and galaxies considered by the authors. Of this subsample, 18 per cent are located beyond 100 kpc, which implies a rough density of six distant halo RRLs every 40 sq. deg (or 0.16 per sq. deg), without accounting for their estimated completeness (expected to be > 70 per cent at ~ 150 kpc). This number is a factor of two larger than the number of distant RRLs that we find in our study (three R Rab stars beyond 100 kpc every 40 sq. deg, or 0.065 per sq. deg.). Nonetheless, our density is more consistent with the findings of Stringer et al. (2021) if we only consider their candidates with more than 25 observations in total (considering g , r , i , z , and Y) and with an R Rab score > 0.90 as assigned by their classifier. In this case, the DES R Rab star density decreases to

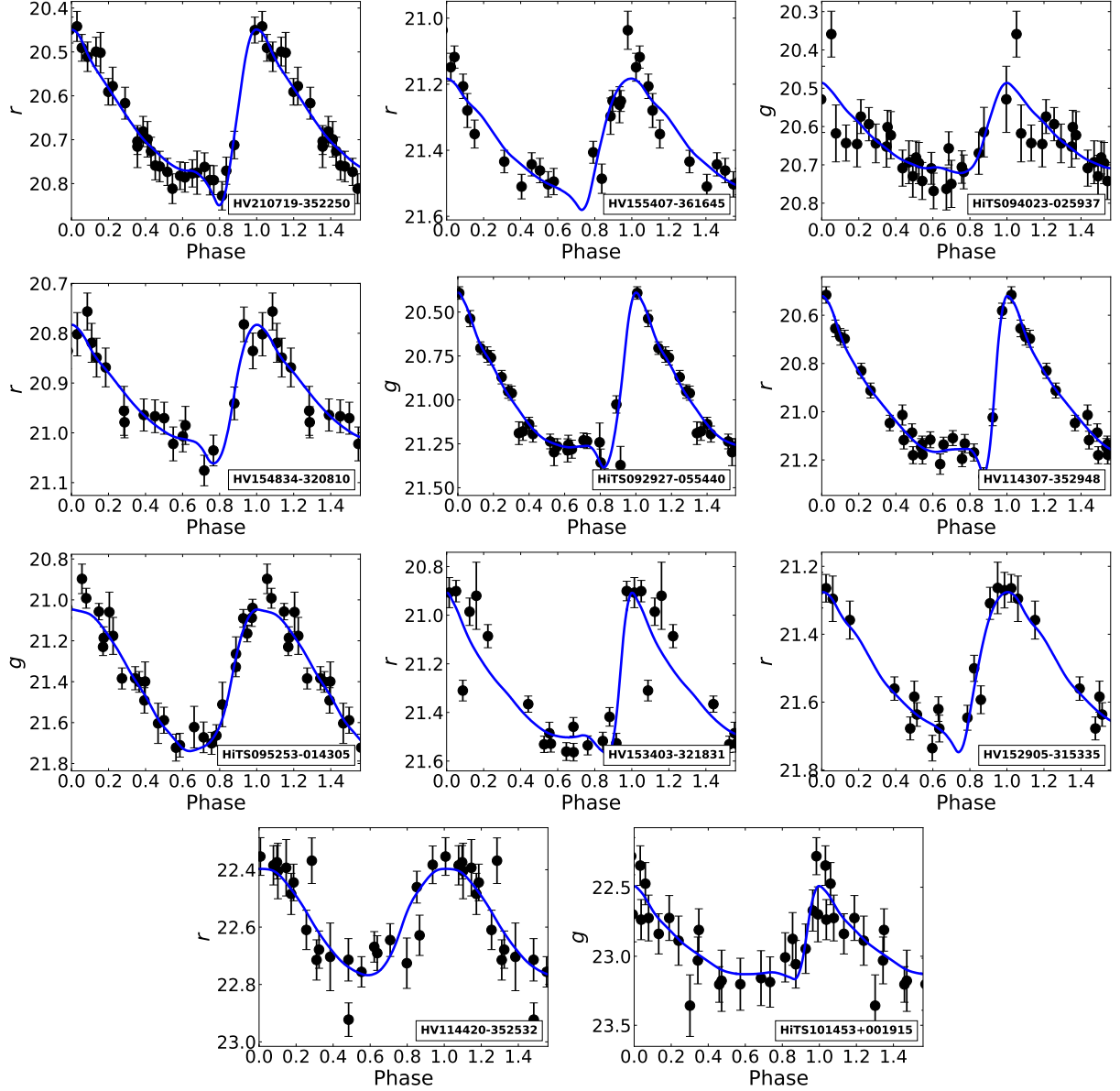


Figure 3.6: Folded light curves in g and r of our sample of RRLs with $d_H > 100$ kpc, and out to ~ 270 kpc. For each star, we overplot the best-fitting model from the Python module GATSPY (Vanderplas, 2015; VanderPlas & Ivezić, 2015) with a blue solid line, which are obtained from the SDSS Stripe 82 RRLs light curve templates (Sesar et al., 2010). The main properties of these RRLs are summarized in Table 3.3.

0.083 distant RRLs per sq. deg (or three RRLs every 40 sq. deg), in better agreement with our results.

3.4.2 Potential associations of distant RR Lyrae stars

In Figure 3.4, we highlight the spatial distribution of the RRL candidates detected beyond 100 kpc. From the figure, we identify two groups of stars with similar on-sky positions and heliocentric distances. Associations and groups at large distances (especially at $d_{\text{H}} > 100$ kpc) are unlikely to happen by chance from halo stars. Using mock stellar haloes and focusing on RRLs beyond 100 kpc, Sanderson et al. (2017) showed that the median of the minimum angular distance to the nearest star for bound (unbound) RRLs beyond 100 kpc is of ~ 0.01 deg (3.0 deg), where the bulk of the angular distance distribution is found to be between zero and 0.03 deg (~ 0.3 to 10.0 deg). Moreover, Sanderson et al. (2017) found that the closest pairs of RRLs tend to originate from the same building block (regardless of their bound/unbound status). For still-bound satellites, this occurs roughly 60 per cent of the time, whereas for unbound structures the number decreases to 50 per cent of the time. Therefore, we analysed these groups looking for indications of their potential association with known substructures.

The first group consists of the stars HV153403-321831 and HV152905-315335, two RRab stars located at 135 ± 5 and 144 ± 5 kpc, respectively (with right ascensions of ~ 233 deg). These stars are separated by 1.1 deg (or 3 kpc at $d_{\text{H}} \sim 140$ kpc) and have a mean period of 0.81 d. The second group, at right ascensions ~ 142 -148 deg, corresponds to the stars HiTS095253-014305, HiTS094023-025937, and HiTS092927-055440, with distances of 116 ± 5 , 105 ± 5 , and 112 ± 4 kpc, respectively. The first of these stars is classified as an RRC star, whereas the other two are of ab-type. These two RRab stars have a mean period of 0.71 d. The second group shows an angular extension of ~ 7.2 deg (or 14 kpc at $d_{\text{H}} \sim 110$ kpc). Thus, the stars in the second group are too separated to be considered part of an intact (or not heavily disrupted) bound satellite. We note in passing that we detect other three ab-type RRLs within ~ 2 deg from the stars in this group (HiTS093847-060049, HiTS093807-005552, and HiTS091510-052952, at d_{H} of 99 ± 4 , 98 ± 4 , and 94 ± 4 kpc, respectively). We consider the association of the second group with these stars less likely.

As these RRLs might be associated with the ongoing tidal disruption of MW satellites, we inspected the Python library *galstreams* (Mateu, 2022), which collects celestial, distance, proper motion, and radial velocity information for ~ 97 distinct stellar streams. Nevertheless, we find no streams within the *galstreams* database with distances similar to those of our groups (most streams close to the position of our groups have $d_{\text{H}} < 40$ kpc). Comparing the positions and distances of these groups to the model of the Sagittarius stream by Dierickx & Loeb (2017) shows that only the group with higher right ascension is in proximity to the stream, but at larger distances (most Sagittarius stream stars at this right ascension are located at $d_{\text{H}} \sim 50$ kpc). Moreover, all of the stars in these groups have latitude-like coordinates in the Sagittarius stream system (B_{Sgr} ; Majewski et al. 2003) larger than 16.6 deg, making their association with the stream unlikely. Because the stream-like shaped second group is located near the Sextans dSph (of $d_{\text{H}} \sim 84$ kpc; Medina et al. 2018), we also considered a potential connection between the dwarf and our group, even though the closest of these RRLs is ~ 5 deg from Sextans' centre. Taking into account Sextans' distance, radial

Table 3.3: Main properties of the detected RRLs with $d_H \geq 100$ kpc. The period and amplitude of pulsation are computed using the photometric band with more observations.

ID	R.A. (deg)	Dec (deg)	$\langle g \rangle$	$\langle r \rangle$	N_g	N_r	Period (days)	Amplitude	Type	d_H (kpc)
HV210719-352250	316.82756	-35.38046	20.79 ± 0.03	20.68 ± 0.01	3	28	0.60	0.39	ab	100 ± 3
HV155407-361645	238.52769	-36.27926	22.01 ± 0.03	21.31 ± 0.01	2	19	0.66	0.65	ab	104 ± 4
HiTS094023-025937	145.09730	-2.99360	20.66 ± 0.01	20.33 ± 0.02	26	-	0.85	0.41	ab	106 ± 5
HV154834-320810	237.14125	-32.13607	21.57 ± 0.02	20.94 ± 0.01	2	19	0.60	0.38	ab	110 ± 4
HiTS092927-055440	142.36180	-5.91120	21.09 ± 0.01	20.98 ± 0.01	25	-	0.58	1.05	ab	112 ± 4
HV114307-352948	175.78118	-35.49667	21.27 ± 0.02	21.01 ± 0.01	3	24	0.60	0.75	ab	115 ± 4
HiTS095253-014305	148.22270	-1.71800	21.35 ± 0.01	21.48 ± 0.02	27	-	0.35	0.83	c	116 ± 5
HV153403-321831	233.51328	-32.30856	21.45 ± 0.02	21.31 ± 0.01	2	18	0.81	0.66	ab	135 ± 5
HV152905-315335	232.27196	-31.89316	21.97 ± 0.03	21.50 ± 0.01	2	16	0.81	0.47	ab	144 ± 5
HV114420-352532	176.08172	-35.42548	23.24 ± 0.05	22.57 ± 0.02	3	22	0.43	0.57	d	234 ± 8
HiTS101453+001915	153.71970	0.32090	22.88 ± 0.03	22.39 ± 0.05	22	-	0.62	0.67	ab	265 ± 11

velocity, and proper motions (McConnachie & Venn, 2020) indicates however that the stars are not aligned with the orbit of the dwarf galaxy. Therefore, we find no clear indications of associations between our groups and known satellites or streams. Nevertheless, we suggest that the association of the stars in these groups is likely.

In the following section we address in more detail the radial density distribution of our entire sample.

3.5 Space density distribution

3.5.1 Radial density model

Many observational studies and simulations have suggested that the properties of the radial distribution of stars in the halo is connected with their origin (e.g., Zinn, 1993; Vivas & Zinn, 2006; Pillepich et al., 2014). From the slope(s) of the radial distribution, for instance, one can infer the existence of an inner halo thought to contain both accreted and formed in-situ stars, and an outer halo, expected to have been formed largely from the accretion of satellites (e.g., Watkins et al., 2009; Bullock & Johnston, 2005; Zolotov et al., 2009; Naidu et al., 2020).

In order to characterize the spatial distribution of our RRLs in the halo, we follow the methodology of Medina et al. (2018). We adopt two models to represent the data – one assuming a spherical halo, and one adopting an ellipsoidal halo. To account for the oblateness of the latter, we assume $q = c/a = 0.7$ (Sesar et al., 2011), where a and c are the axes in the disc plane and along the vertical direction, respectively. Thus, prior to binning our sample in distance, we transform our computed distances from heliocentric to spheroidal and ellipsoidal Galactocentric (R_{GC} and R_{el}) using:

$$\begin{aligned} R_{GC}^2 &= (R_{\odot} - d_H \cos b \cos l)^2 + d_H^2 \cos^2 b \sin^2 l + d_H^2 \sin^2 b \\ R_{el}^2 &= (R_{\odot} - d_H \cos b \cos l)^2 + d_H^2 \cos^2 b \sin^2 l + (d_H/0.7)^2 \sin^2 b, \end{aligned} \quad (3.5)$$

where R_{\odot} stands for the distance from the Sun to the Galactic centre (assumed to be 8 kpc), and b and l are the Galactic latitude and longitude, respectively.

We adopt a power-law model to describe the radial density $\rho(R_{GC})$ of our halo RRLs. Thus, $\rho(R) = \rho_{\odot} (R/R_{\odot})^n$, where ρ_{\odot} is the local RRL number density and n is the slope of the profile. Given that vast observational evidence suggest the existence of a break in the halo radial density profile between 20 and 35 kpc (e.g., Saha, 1985; Watkins et al., 2009; Deason et al., 2011; Sesar et al., 2011), we also model the explored regions with broken-power-laws with a breaks at R_{break} , so that, in logarithmic form:

$$\begin{aligned} \log(\rho(R)) &= A_1 + n_1 \log(R/R_{\odot}) \\ \log(\rho(R)) &= A_2 + n_2 \log(R/R_{\odot}) \\ A_1 + n_1 \log(R_{break}/R_{\odot}) &= A_2 + n_2 \log(R_{break}/R_{\odot}), \end{aligned} \quad (3.6)$$

where $A = \log(\rho_{\odot})$, and the subindices denote each side of the density profile (i.e., A_1 and A_2 correspond to the inner and outer density, respectively).

To explore the parameter space and their distribution, we employ *emcee* (Foreman-Mackey et al., 2013), a Python implementation of the invariant Markov chain Monte Carlo method

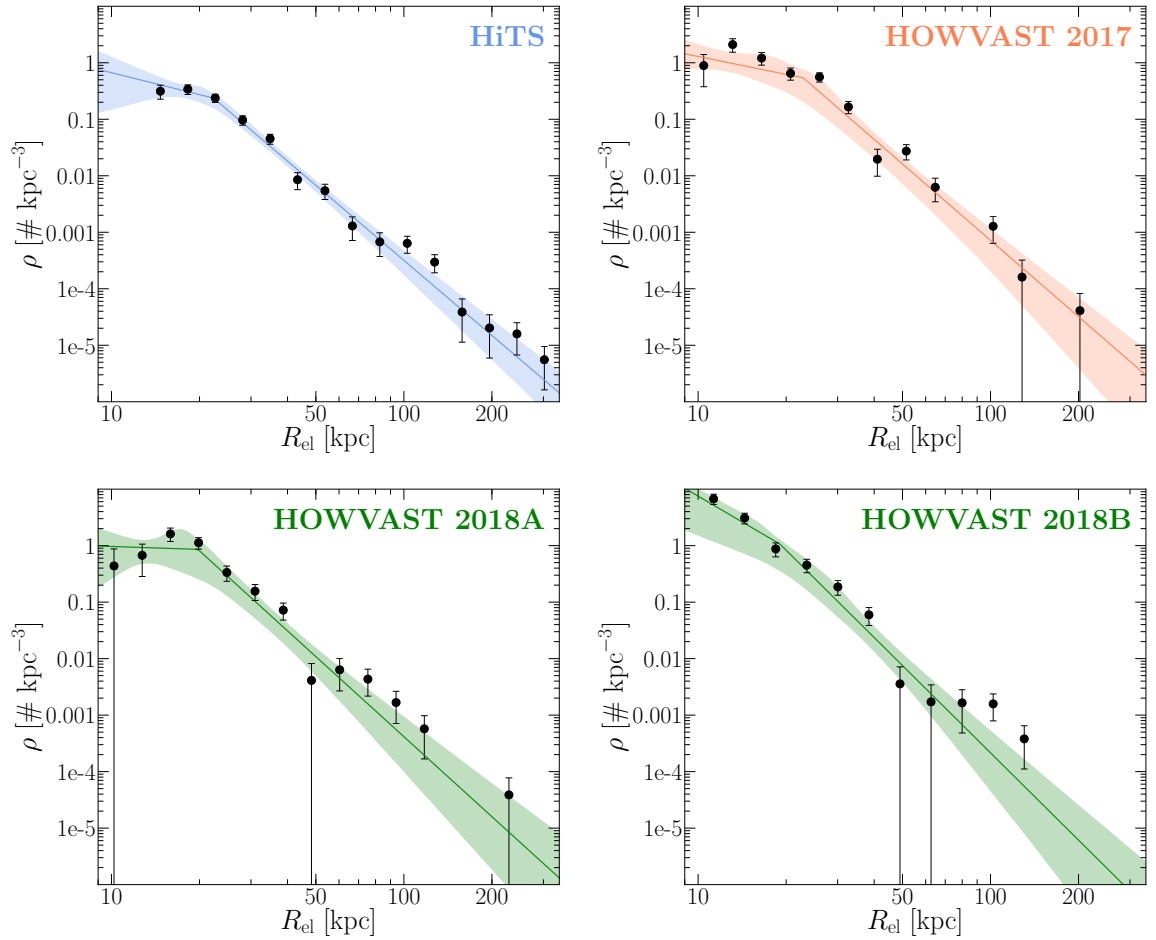


Figure 3.7: Binned RRL number density profiles of the regions studied in this work. The region corresponding to the HiTS fields is shown with blue curves, whereas that of HOWVAST 2017 is shown in orange. Green curves depict the high- and low-Galactic latitude areas surveyed by HOWVAST in 2018 (*left* and *right*, respectively). The best solution determined via MCMC is shown as a solid line in each panel, and the shaded regions depict the 3σ confidence levels. The uncertainty shown for each density bin represents Poisson noise.

(MCMC). For this, we leave A_2 , n_1 , n_2 , and R_{break} , as free parameters, and adopt the priors used by [Medina et al. \(2018\)](#). We find that running *emcee* with 200 walkers and a chain of 500 steps is sufficient to reach convergence. The selected values correspond to the median of the marginalized posterior parameter distributions, and their errors represent their 16th and 84th percentiles.

3.5.2 Number density profiles

We report the results of the aforementioned methodology for our catalogue excluding the subsample of stars belonging to the Sextans dSph. Based on the estimations of our detection efficiency and completeness, we constrain our analysis to RRLs with distances smaller than 145 kpc (this is the limit at which the RRL recovery rate decreases to ~ 85 per cent). Addi-

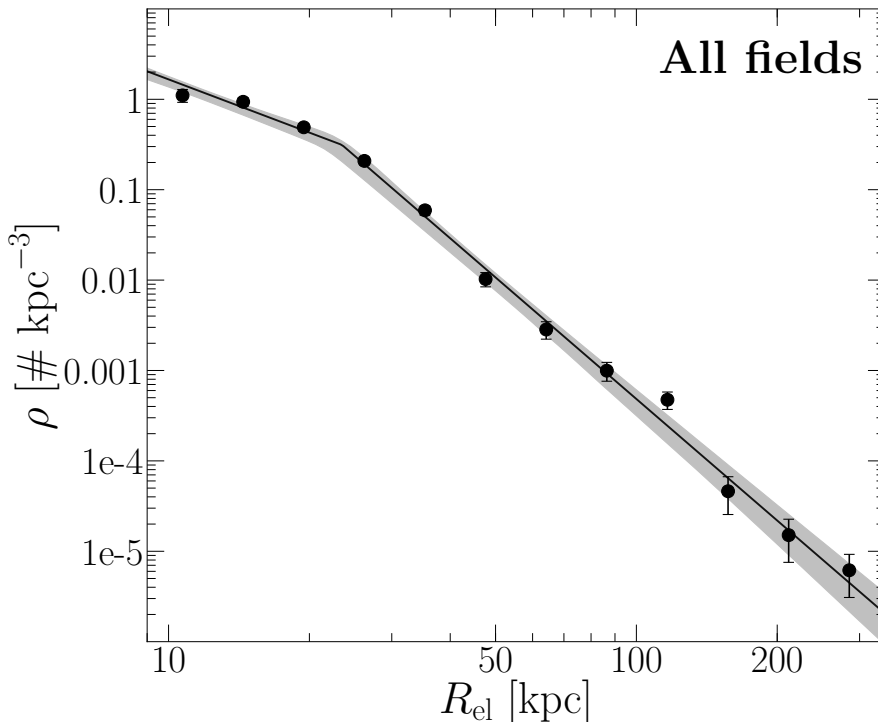


Figure 3.8: Same as Figure 3.7 but showing the number density profile obtained when considering the entire region studied in this work.

tionally, in order to inspect the (in-)homogeneity of the RRLs radial distribution, we follow two approaches: one computing the density profile of our entire sample of RRL candidates, and one measuring the profile in the four distinct regions covered by our survey. By doing this we could, in principle, directly inspect anisotropies in the halo distribution of stars at relatively small scales, albeit the additional challenge of low-number statistics.

Our results are shown in Figures 3.7 and 3.8, and summarized in Table 3.4. The posterior probability distribution for the obtained parameters of the broken-power-law model (when using R_{el}) and the parameter convergence from the MCMC chains are depicted in Figures B1, B2, and B3.

A first look into Figure 3.7 reveals that, regardless of the region considered, a break is visible between 20 and 30 kpc. This feature is, however, less clear in the fields closer to the Galactic plane, where more RRLs are detected overall at distances < 20 kpc, but might also include a higher number of contaminants. Moreover, from Table 3.4 we conclude that broken-power-law models yield better fits than simple-power-laws, in general (from their reduced χ^2 values, χ^2_{ν}). The break in the profile is also clearly observed in Figure 3.8, which depicts the radial distribution of RRLs when using all the regions combined. In that case, we find R_{break} separating the halo populations at $23.3^{+1.6}_{-1.9}$ kpc, where the profile displays an inner slope of $n_1 = -1.96^{+0.20}_{-0.12}$ and a steeper outer halo slope of $n_2 = -4.45^{+0.16}_{-0.22}$.

We find that the break radii from the different regions are consistent within their uncertainties (Table 3.4), whereas n_2 displays a larger dispersion. These values vary between

Table 3.4: Simple and broken-power-law parameters from the sampled posterior probability distributions described in Section 3.5. We report the results from using the RRLs in all our regions combined, and from the individual areas of the survey, as well as the adopted shape of the halo (spheroidal and oblate, denoted as R_{GC} and R_{el} , respectively). For each of the studied regions the best-fitting model corresponds to the broken-power-law profile.

Region	Dist. type	A	n	Simple χ^2_{ν}	A_1	A_2	n_1	n_2	R_{break} (kpc)	Broken χ^2_{ν}
All	R_{GC}	$0.05^{+0.03}_{-0.03}$	$-2.74^{+0.04}_{-0.04}$	31.35	$0.22^{+0.05}_{-0.05}$	$1.51^{+0.13}_{-0.14}$	$-1.06^{+0.23}_{-0.20}$	$-4.41^{+0.13}_{-0.17}$	$20.1^{+1.9}_{-1.3}$	2.47
All	R_{el}	$0.40^{+0.03}_{-0.03}$	$-3.09^{+0.04}_{-0.04}$	17.41	$0.39^{+0.04}_{-0.05}$	$1.57^{+0.16}_{-0.19}$	$-1.96^{+0.20}_{-0.12}$	$-4.45^{+0.16}_{-0.22}$	$23.3^{+1.6}_{-1.9}$	2.88
2017	R_{GC}	$0.48^{+0.07}_{-0.08}$	$-3.26^{+0.11}_{-0.11}$	6.15	$0.47^{+0.09}_{-0.13}$	$1.95^{+0.38}_{-0.34}$	$-1.32^{+0.51}_{-0.50}$	$-4.97^{+0.43}_{-0.59}$	$20.2^{+2.5}_{-2.3}$	1.90
2017	R_{el}	$0.54^{+0.08}_{-0.09}$	$-3.17^{+0.11}_{-0.11}$	7.09	$0.30^{+0.14}_{-0.18}$	$1.85^{+0.52}_{-0.43}$	$-1.19^{+0.74}_{-0.79}$	$-4.60^{+0.39}_{-0.72}$	$23.4^{+2.5}_{-4.4}$	2.78
2018A	R_{GC}	$0.35^{+0.13}_{-0.15}$	$-2.98^{+0.18}_{-0.18}$	4.67	$0.01^{+0.27}_{-0.46}$	$1.80^{+0.52}_{-0.47}$	$-0.65^{+2.13}_{-1.29}$	$-4.76^{+0.53}_{-0.80}$	$21.0^{+4.4}_{-3.2}$	2.97
2018A	R_{el}	$0.40^{+0.12}_{-0.15}$	$-3.01^{+0.18}_{-0.18}$	4.56	$0.03^{+0.28}_{-0.44}$	$1.81^{+0.43}_{-0.47}$	$-0.46^{+1.91}_{-1.45}$	$-4.75^{+0.54}_{-0.70}$	$20.4^{+3.1}_{-2.4}$	2.51
2018B	R_{GC}	$0.70^{+0.06}_{-0.06}$	$-3.22^{+0.07}_{-0.07}$	9.75	$0.93^{+0.06}_{-0.18}$	$2.00^{+0.20}_{-0.34}$	$-1.71^{+0.26}_{-0.27}$	$-4.69^{+0.29}_{-0.33}$	$18.3^{+1.9}_{-1.5}$	2.63
2018B	R_{el}	$1.13^{+0.04}_{-0.04}$	$-3.83^{+0.08}_{-0.08}$	3.72	$1.21^{+0.05}_{-0.15}$	$2.01^{+0.66}_{-0.36}$	$-3.10^{+0.32}_{-0.21}$	$-5.18^{+0.58}_{-0.92}$	$20.9^{+5.3}_{-5.1}$	1.93
HiTS	R_{GC}	$0.45^{+0.07}_{-0.08}$	$-3.43^{+0.10}_{-0.10}$	6.23	$-0.34^{+0.42}_{-0.73}$	$1.31^{+0.22}_{-0.15}$	$-0.61^{+2.71}_{-1.33}$	$-4.40^{+0.22}_{-0.29}$	$22.1^{+3.0}_{-4.2}$	2.17
HiTS	R_{el}	$0.68^{+0.08}_{-0.08}$	$-3.61^{+0.11}_{-0.12}$	4.06	$-0.10^{+0.30}_{-0.52}$	$1.35^{+0.21}_{-0.16}$	$-1.18^{+1.55}_{-0.84}$	$-4.42^{+0.23}_{-0.28}$	$22.3^{+2.7}_{-2.3}$	1.83

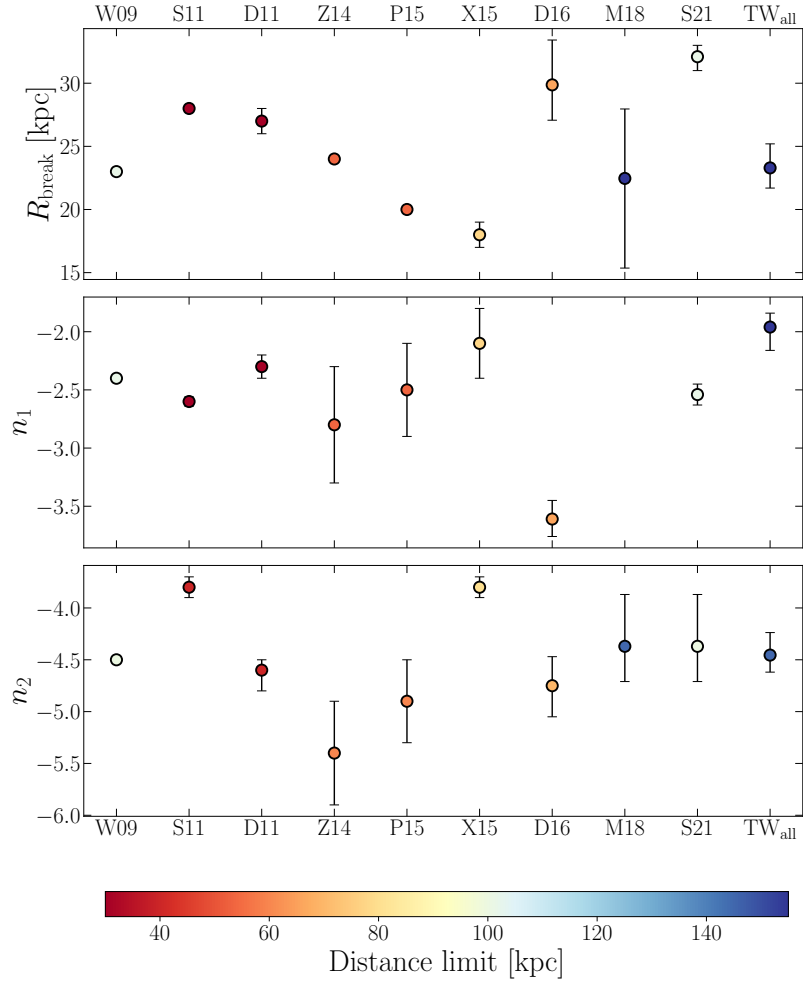


Figure 3.9: Comparison between our best-fitting radial density profile parameters (broken-power-law) and those from other RRL studies in the literature. The markers are colour-coded to illustrate the distance limits of each work, and the error bars depict the uncertainties in the parameters estimation, when available. We denote our values as TW_{all}, and the references for the literature works are as follows: W09 (Watkins et al., 2009), S11 (Sesar et al., 2011), D11 (Deason et al., 2011), Z14 (Zinn et al., 2014), P15 (Pila-Díez et al., 2015), X15 (Xue et al., 2015), D16 (Das et al., 2016), M18 (Medina et al., 2018), and S21 (Stringer et al., 2021).

$20.4_{-2.4}^{+3.1}$ and $23.4_{-4.5}^{+2.5}$ kpc for the R_{break} , and $-4.42_{-0.28}^{+0.23}$ and $-5.18_{-0.92}^{+0.58}$ for the outer halo slopes. The largest differences are seen when contrasting the inner slopes n_1 , which tend to be steeper for the fields near the Galactic plane (as mentioned above).

In Figure 3.9, we display our best-fitting parameters and contrast them with broken power law fits of the density profile from the literature. These works generally cover large areas and different regions of the halo. In this regard, we note that that our survey maps a smaller area than previous studies, but we are able to better trace the halo beyond 40 kpc. We find that our measured break radii are consistently smaller than those found by [Stringer et al. \(2021\)](#) and [Das et al. \(2016\)](#) (who find R_{break} closer to ~ 30 kpc), regardless of the adopted halo flattening, and are most similar to those from [Watkins et al. \(2009\)](#), [Zinn et al. \(2014\)](#), and [Pila-Díez et al. \(2015\)](#). Regarding to the inner slope values, we observe that our results are consistent with those from the literature, especially when neglecting the contamination from the disc. The measured outer slopes from each of our regions are broadly consistent with previous studies, and our value from using all the fields lies within 2σ of the n_2 of most other works in the literature.

3.6 Discussion and summary

We have described our search for RRLs in different directions of the remote MW halo using DECam data from the HiTS and the ongoing HOWVAST survey. We constructed light curves from time series containing from 16 to 38, and from 15 to 32 observations in the g and r -bands, respectively. Considering all of the studied fields in HiTS and HOWVAST, we detected a total of 497 RRL candidates (399 in the HOWVAST fields) in a combined area of ~ 270 sq. deg., including at least 91 RRL candidates not listed by previous surveys. The heliocentric distances of our RRLs range between 7 and 270 kpc. We identified 11 RRL candidates beyond 100 kpc, which we add to the still small list of well-characterized tracers of the old component of the MW at large distances.

We found that the bulk of the distribution of RRab stars in the Bailey diagram is consistent with OoI and Oo-int groups, as is often the case for the general halo population (see e.g. [Catelan & Smith, 2015](#), and references therein). The most distant RRLs are not preferentially located towards a unique Oo-group, and are rather distributed uniformly in the period-amplitude space for periods longer than 0.6 d. Within this sample we identified two groups containing RRLs with similar distances (at around 110 ± 5 and 140 kpc) located within a few degrees from each other, and with a mean period of 0.76 d, consistent with them being linked to the OoII group. This might be an indication of their accreted origin. Moreover, previous studies have shown that neighboring stars at these distances are unlikely to occur by chance ([Sesar et al., 2014](#); [Baker & Willman, 2015](#); [Sanderson et al., 2017](#)), which makes them potential tracers of known or undiscovered substructures. We found that the position of these groups is inconsistent with those of previously known satellites (e.g., the Sextans dSph) and streams (e.g., the Sagittarius stream), and cannot directly associate these stars with the accretion of UFDs with our data only. We conclude that the stars in these groups are likely associated, and advocate for additional data and follow-up studies to confirm their association and to determine their parent populations. None of the remote RRLs lie in the HASP region of the diagram, which is often interpreted as coming from populations with $[\text{Fe}/\text{H}] > -1.5$.

We characterized the (radial) spatial distribution of our RRLs with power-law profiles, by adopting a spherical halo model ($q = 1$) and an ellipsoidal model (oblate, with $q = 0.7$). Furthermore, we analysed the density profiles from the RRLs in our entire sample, and from different directions in the halo. For this, we followed an MCMC approach and considered RRLs located at distances < 145 kpc from the Galactic centre. We found that the profiles are better described by broken-power-laws, as it has been shown by previous works. Our best-fitting model suggests a break in the halo RRLs distribution at $23.3_{-1.9}^{+1.6}$ kpc, with an inner slope of $-1.96_{-0.12}^{+0.20}$, and a steeper outer slope of $-4.45_{-0.22}^{+0.26}$.

Stellar haloes are important testbeds sensitive to various aspects of galaxy formation models, and comparing observations (e.g., the properties of their density profiles) with simulations is an important requirement to draw meaningful conclusions. In recent years, several authors have measured the stellar distribution of MW-like galaxies using sophisticated cosmological simulation suites (e.g., the IllustrisTNG project; [Pillepich et al., 2018](#)). In these simulations, outer halo slopes are typically found in the range $-5.5 < n < -3.5$, where recently formed haloes or those with a large fraction of their total stellar mass originating from mergers have shallower slopes. Steeper slopes correspond to quiescent recent accretion histories ([Pillepich et al., 2014](#)). In particular, our measured density profiles are remarkably consistent with the results reported by [Merritt et al. \(2020\)](#), who predicted a median outer slope (beyond 20 kpc) of -4.5 for MW-like galaxies using the TNG100 simulation of the IllustrisTNG project (e.g., [Pillepich et al., 2018](#); [Nelson et al., 2019](#)).

The observed position of the break in the halo and the outer slope of the radial density distribution has been shown to be different at different directions halo regions. These differences in the stratification of the halo density profile seem to be an indication of the anisotropic distribution of RRLs throughout the halo. Recently, various authors have discussed the dynamical response of the Galactic halo to the first passage of the LMC’s orbit, which causes a substantial disequilibrium state ([Conroy et al., 2021](#); [Rozier et al., 2022](#)). Evidence of the disequilibrium phenomena is found in the density variations over thousands of square degrees, and the observed overdensities and “voids” in different regions of the (“smooth”) distant halo appear to be a consequence of the dynamical effect of the LMC in the outer MW, i.e., they are likely associated with the local wake and the collective response to the MW-LMC interaction. In a similar vein, [Han et al. \(2022a\)](#) suggested that two major stellar overdensities in the halo (the Virgo Overdensity and the Hercules-Aquila Cloud; [Vivas et al., 2001](#); [Belokurov et al., 2007](#)) are most likely associated with the GSE merger, and that the MW dark matter halo is tilted with respect to the disc. This halo-disc misalignment has been observed in recent cosmological simulations (e.g., [Prada et al., 2019](#); [Emami et al., 2021](#); [Dillamore et al., 2022](#)). Extended studies of the RRL distribution in the outer halo, covering a wide range of distances and in different directions, is therefore key to collect further empirical evidence of these features, and to shed new light onto the events that formed the MW.

4

Probing the Galactic outer halo using chemodynamics of RR Lyrae stars

The content of this chapter was adapted from the article “RR Lyrae stars as probes of the outer Galactic halo: Chemical and kinematic analysis of a pilot sample” (Medina et al. 2022, submitted to MNRAS), of which I am the lead author. For this work, I was in charge of collecting and processing the data, performing the scientific analysis, and reaching the conclusions. This study was co-authored by Dr. C. J. Hansen, Prof. Dr. R. R. Muñoz, Prof. Dr. E. K. Grebel, Dr. A. K. Vivas, Dr. J. L. Carlin, and Dr. C. E. Martínez-Vázquez. The text was written by me, taking into account the suggestions from the co-authors of the submitted article.

In this chapter, we describe our effort to spectroscopically analyse a selection of distant RRLs aiming to assess their parent populations, and to use these information to investigate the accreted/in-situ origin of the outer halo. We performed this study using proprietary spectroscopic data collected over the course of my PhD studies. In Section 4.1, we address the importance of spectroscopically characterizing distant RRLs, and the inherent challenges that need to be considered in order to carry out these studies. Section 4.2 briefly describes the sample of RRLs selected for our analysis (which is taken from publicly available catalogues including our own previous work; see Chapter 3), and the data acquired for it. In Section 4.3, we describe the derivation of our sample’s systemic velocities, stellar parameters, element abundance, and integrated orbits. We present the results of our spectroscopic and kinematic analysis in Section 4.4 and use them to identify potential parent population for our RRL sample in Section 4.5. Finally, in Section 4.6 we summarize the outcomes of this study, and put them into a broader Galactic context to draw our conclusions.

4.1 Motivation

In recent years, growing evidence of the tidal interactions that built up our Galaxy, and in particular of the accretion of massive satellites, has been found by studying the dynamics and chemical patterns of MW stars. This is the case of the Sagittarius (Sgr) merger event (Ibata, Gilmore, & Irwin, 1994), the GSE merger (Belokurov et al., 2018b; Haywood et al., 2018; Helmi et al., 2018), Kraken (Massari, Koppelman, & Helmi, 2019; Kruijssen et al., 2019), and Sequoia (Myeong et al., 2019), among many other examples (see Section 1.5). As explained in Chapter 1, investigating the observed six-dimensional phase-space of present-day stellar populations is pivotal to piece together the assembly history of our Galaxy via signatures of tidal stripping. This can be achieved by measuring the positions and velocities

(tangential and in the line-of-sight) of stars with great precision, which can (and should) be complemented by the derivation of their chemical abundance patterns. Performing these studies is particularly useful in the halo (due to its long dynamical time-scales), where it is even possible to associate single stars with potential parent populations. However, the phase-space and detailed abundance patterns of outer halo stars remain vastly unexplored, mostly due to distance determination limitations. This makes, in principle, RR Lyrae variables perfect targets for studies aiming to reconstruct the formation history of the halo at large distances (given that they are old, metal-poor, and precise distance indicators).

Radial velocity measurements and spectroscopic metallicity derivations are more challenging to conduct in RRLs, owing to their variability on short time-scales. In spite of these difficulties, different authors have measured these quantities using both low- and high-resolution spectra. In terms of metallicities, the usage of the former began with introduction of the ΔS method by [Preston \(1959\)](#) which relates the absorption line strengths of hydrogen and calcium K-lines to the metallicity, and was recently revised by [Crestani et al. \(2021a\)](#). Other methods rely on the use of a known correlation between the Ca II triplet and RRLs metallicities ([Wallerstein et al., 2012](#); [Kunder et al., 2016](#); [Martínez-Vázquez et al., 2016](#)), or the determination of photometric and luminosity-based metallicities (e.g., [Jurcsik & Kovacs, 1996](#); [Smolec, 2005](#); [Hajdu et al., 2018](#); [Dékány, Grebel, & Pojmański, 2021](#); [Mullen et al., 2021, 2022](#); [Garofalo et al., 2022](#)). The most precise methods to estimate RRLs metallicities are based on high-resolution spectra. However, the number of RRLs observed and later analysed with this method is still relatively low (see e.g. [Clementini et al., 1995](#); [Kolenberg et al., 2010](#); [For et al., 2011b](#); [Hansen et al., 2011](#); [Pancino et al., 2015](#); [Chadid, Sneden, & Preston, 2017](#); [Sneden et al., 2017](#); [Gilligan et al., 2021](#); [Crestani et al., 2021b](#)). For distant RRLs, in particular, this is mainly due to the need for large telescopes and long exposure times, which is in clear conflict with their short-term pulsations. The determination of centre-of-mass radial velocities has also proven to be a challenging task given the pulsation phase of the RRLs that needs to be considered. To take this effect into account, observations can be conveniently scheduled so they take place at pulsation phases where the pulsation contributes the least to the observed radial velocity, or the measured velocities can be corrected by assuming a pulsation model.

Because of these observational challenges, only a handful of spectroscopic studies have been performed specifically on halo RRLs (e.g., [Liu et al., 2020](#); [Fabrizio et al., 2021](#)), and even fewer have focused on RRLs at large heliocentric distances, mostly due to the low number of RRLs detected in these regions, and due to instrumental limitations. At these limits one would expect, for instance, RRLs as faint as $g \sim 21.0$ or $V \sim 20.6$ at distances of $d_{\text{H}} \sim 100$ kpc, and correspondingly fainter magnitudes with increasing distance. However, the increasing amount of data from deep photometric surveys has allowed astronomers to detect significant samples of distant RRLs, as the ones found using the Catalina surveys ([Drake et al., 2014, 2017](#); [Torrealba et al., 2015](#)), the PS-1 survey ([Chambers et al., 2016](#); [Sesar et al., 2017](#)), the HiTS survey ([Förster et al., 2016](#); [Medina et al., 2018](#)), the DES (Dark Energy Survey Collaboration et al., 2016; [Stringer et al., 2021](#)), the ZTF ([Chen et al., 2020](#); [Huang & Koposov, 2022](#)), and those reported in Chapter 3 of this thesis (from HOWVAST). [Medina et al. \(2018\)](#) found 16 RRL candidates beyond 100 kpc in a survey area of ~ 120 sq. deg using HiTS data, whereas more recently [Stringer et al. \(2021\)](#) identified 800 RRLs candidates further than 100 kpc using the footprint of the DES ($> 5,000$ sq. deg)

with a limiting magnitude of $g \sim 23.5$, in line with the predicted number of RRLs from current accretion models (Bullock & Johnston, 2005; Sanderson et al., 2017). These stars, together with other samples including RRLs between 20 and 100 kpc (from the Catalina survey, for example) have thus become intrinsically alluring targets for spectroscopic follow-up observations, which is what motivates this chapter.

4.2 Sample selection and observations

4.2.1 Sample selection

We selected a subsample of halo RRLs from previous studies, namely the Catalina surveys (Drake et al., 2014, 2017; Torrealba et al., 2015), the HiTS survey (Medina et al., 2018), and the HOWVAST survey (Medina et al., 2021b). The Catalina surveys consist of an extensive database of V -band photometry for thousands of variable sources observed over $\sim 33,000$ sq. deg., carried out with three dedicated telescopes (of 0.5, 0.7, and 1.5 m primary mirror diameter, respectively). HiTS and HOWVAST, on the other hand, observed a combined total of ~ 350 sq. deg. of the halo with deep g and r images using the DECam (Flaugher et al., 2015), which is mounted on the Blanco 4 m telescope at the CTIO in Chile (see Chapter 3). HiTS was originally planned to look for the early phases of SNe explosions in real time, whereas HOWVAST was specifically designed to detect RRLs at the outskirts of the MW. We focused on RRLs with estimated heliocentric distances ranging from 15 to 165 kpc, classified as ab-type and with pulsation periods longer than 0.48 days. Our target sample consists of nine stars from the Catalina surveys, seven stars from HiTS, and four stars from HOWVAST. Thus, we observed a total of 20 RRab. Their main properties are summarized in Table 4.1.

We designed our observations to avoid pulsation phases ϕ in which the stars were predicted to be close to their minimum radii, where major distortions are expected to affect their spectral features. Thus, we preferred phases close to the quiescent stages of their atmospheres, at around 0.4 and 0.8 (Kolenberg et al., 2010). For the faintest subsample, in particular, we selected ϕ near maximum radii, in the descending branch of the light curves (ϕ between 0.15 and 0.60). However, in a few cases, pulsation phases involving rapid changes in the targets' atmospheres were difficult to avoid. In addition, the long-period modulation that leads to variations in the period and amplitude of RRLs (the Blazhko effect, described in Section 1.6.2; Blažko, 1907) could affect part of our sample, since it is thought to be a common effect among ab-type RRLs (observed in 20-30 per cent of the RRab stars; Szeidl, 1988; Moskalik & Poretti, 2003; Buchler & Kolláth, 2011; Gillet, 2013; Hernitschek & Stassun, 2022). As a reminder, these modulations affect RRLs on timescales from weeks to months, and they modify their amplitude of pulsation by a few tenths of magnitudes. It is noteworthy that the periods obtained by Medina et al. (2018) were computed using a relatively low number of observations (from 20 to 30 data points), and the ephemerides of the stars from the Catalina survey might have slightly varied since their times of observation. Therefore, our phase predictions might in addition suffer deviations from the actual pulsation values. The RRL light curves, and the estimated pulsation phases in which we performed our observations are provided in Table 4.1 and displayed in Figure 4.1.

4 Probing the Galactic outer halo using chemodynamics of RR Lyrae stars

Table 4.1: Summary of the stars observed in our program, including the estimated time of maximum light T_0 and the phase of observation ϕ of our RRLs.

ID	RA (deg)	DEC (deg)	<mag>	Filter	Period (days)	$d\mu$ (kpc)	T_0 (MJD)	ϕ	Run	Slit size (arcsec \times arcsec)	Binning (spatial \times spectral)	Coadded spectra	S/N ¹
J051424.2-595954 (J051424)	78.59417	-59.99483	19.1	V	0.4838	47.1 \pm 2.4	53647.1685	0.46	1	1.0 \times 5.0	3 \times 8	5 (\times 900 s)	14
J050226.9-395429 (J050226)	75.61042	-39.91011	19.2	V	0.5200	47.9 \pm 2.4	53597.4055	0.53	1	1.0 \times 5.0	3 \times 8	2 (\times 900 s)	14
H1TS112524-024348 (H1TS112524)	171.35042	-2.73200	20.2	g	0.6373	85.7 \pm 3.7	56717.4255	0.04	1	1.0 \times 5.0	3 \times 8	3 (\times 900 s)	12
H1TS100956+013212 (H1TS100956)	152.48583	1.53700	20.3	g	0.6220	88.6 \pm 3.8	56717.2142	0.33	1	1.0 \times 5.0	3 \times 8	4 (\times 900 s)	8
H1TS101243+022118 (H1TS101243)	153.17958	2.35514	20.5	g	0.5346	90.6 \pm 3.5	56717.4971	0.15	1	1.0 \times 5.0	3 \times 8	3 (\times 900 s)	8
H1TS104009-063304 (H1TS104009)	160.04083	-6.55275	20.7	g	0.6376	104.7 \pm 4.5	56717.1908	0.18	1	1.0 \times 5.0	3 \times 8	2 (\times 900 s)	5
H1TS103943-021726 (H1TS103943)	159.93375	-2.29472	20.7	g	0.6956	110.8 \pm 5.1	56717.4797	0.46	1	1.0 \times 5.0	3 \times 8	5 (\times 900 s)	3
H1TS102414-095518 (H1TS102414)	156.06000	-9.92625	21.5	g	0.7641	166.8 \pm 8.3	56717.1339	0.53	1	1.0 \times 5.0	3 \times 8	6 (\times 900 s)	6
CS 22874.042 (CS 22874)	219.50710	-24.97972	14.0	V	—	—	—	0.26	1	1.0 \times 5.0	3 \times 8	2 (\times 240s)	114
J054653.1-020350 (J054653)	86.72131	-2.06410	18.6	V	0.6144	14.4 \pm 0.7	53650.0886	0.02	2	1.5 \times 5.0	2 \times 2	4 (\times 1200 s)	15
J040422.4-012011 (J040422)	61.09358	-1.33642	18.3	V	0.6354	25.2 \pm 1.3	53627.1991	0.98	2	1.5 \times 5.0	2 \times 2	3 (\times 1200 s)	17
J050902.1-123926 (J050902)	77.25909	-12.65738	18.2	V	0.6180	25.6 \pm 1.3	53620.2295	0.03	2	1.5 \times 5.0	2 \times 2	4 (\times 1200 s)	19
J034239.9-000009 (J034239)	55.66652	-0.00260	18.1	V	0.6118	26.9 \pm 1.3	53626.4146	0.84	2	1.5 \times 5.0	2 \times 2	4 (\times 1200 s)	21
HV205840-342000 (HV205840)	314.66548	-34.33322	17.6	r	0.6664	27.1 \pm 0.9	57992.3662	0.72	2	1.5 \times 5.0	2 \times 2	4 (\times 1200 s)	21
J023001.9-011146 (J023001)	37.50817	-1.19623	18.2	V	0.6491	30.5 \pm 1.5	53627.2430	0.72	2	1.5 \times 5.0	2 \times 2	4 (\times 1200 s)	22
HV210205-341427 (HV210205)	315.52120	-34.24092	17.9	r	0.6454	32.2 \pm 1.1	57992.1996	0.87	2	1.5 \times 5.0	2 \times 2	3 (\times 1200 s)	18
HV204704-382019 (HV204704)	311.76850	-38.33850	18.1	r	0.6104	35.5 \pm 1.2	57992.1393	0.38	2	1.5 \times 5.0	2 \times 2	3 (\times 1200 s)	13
J044339.2-005841 (J044339)	70.91353	-0.97819	18.7	V	0.6433	38.2 \pm 1.9	53651.2801	0.76	2	1.5 \times 5.0	2 \times 2	3 (\times 1200 s)	11
J051213.6-151041 (J051213)	78.05674	-15.17828	18.9	V	0.6660	39.4 \pm 2.0	53598.0793	0.72	2	1.5 \times 5.0	2 \times 2	4 (\times 1200 s)	10
H1TS091050-055917 (H1TS091050)	137.70940	-5.98800	19.4	g	0.6468	61.4 \pm 2.7	57070.1314	0.81	2	1.5 \times 5.0	2 \times 2	3 (\times 1200 s)	6
HV210918-335828 (HV210918)	317.32527	-33.97447	19.4	r	0.6340	62.3 \pm 2.1	57992.5420	0.82	2	1.5 \times 5.0	2 \times 2	4 (\times 1200 s)	9
HD 76483	133.83150	-27.68186	4.9	V	—	—	—	—	2	1.5 \times 5.0	2 \times 2	1 (\times 3s)	154

¹The S/N ratio is estimated from the continuum surrounding H_{α} . For J050226 it is measured around H_{β} instead.

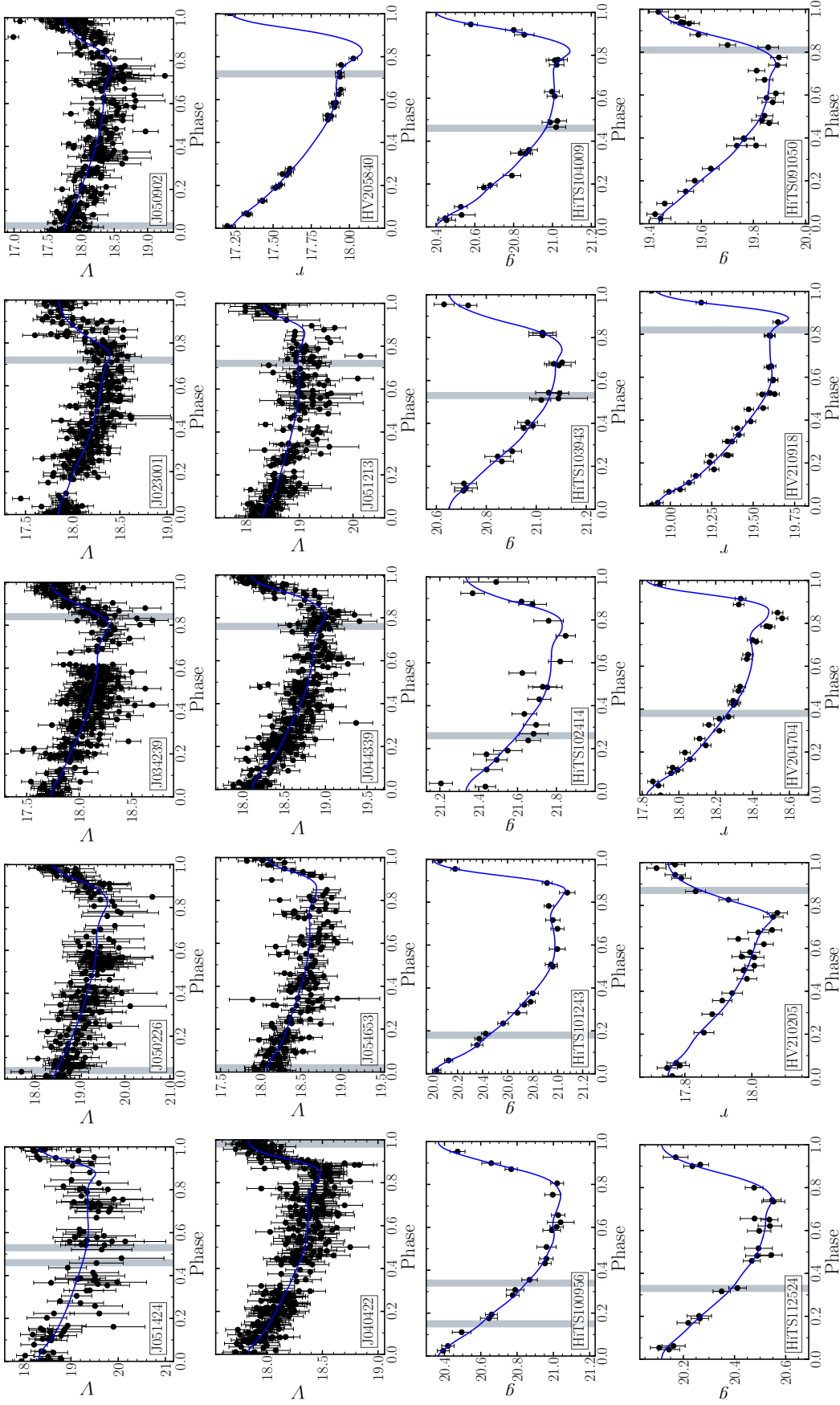


Figure 4.1: Folded light curves of our program stars, based on time series from the Catalina survey, HiTS, and HOWVAST. On each panel, a solid blue line displays a model generated with GATSPY (VanderPlas & Ivezić, 2015), which is based on the light curve templates from the SDSS Stripe 82 RRLs (Sesar et al., 2010). The grey vertical regions represent the estimated phase of the pulsation period of the RRLs in which the spectra were obtained, and their widths approximate the duration of the co-added observations.

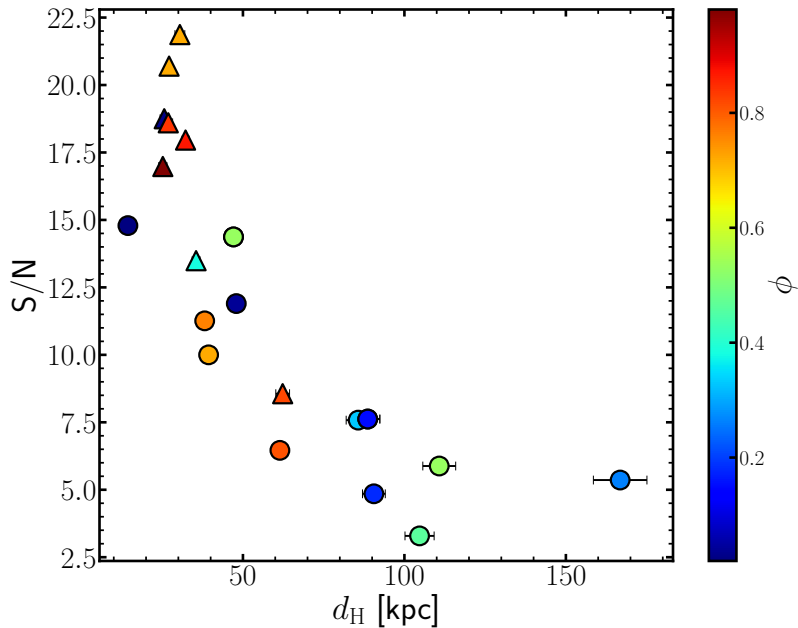


Figure 4.2: Signal-to-noise ratio of our target stars, as a function of heliocentric distance and colour-coded by their phase of observation. Stars for which we obtain spectroscopic atmospheric parameters (the primary sample, as defined in Section 4.3.4) are plotted with triangle markers.

4.2.2 Observation and data reduction

The spectroscopic observations took place on two separate runs, carried out on 2019 January 14 and 15, and on 2020 November 9 and 11 (four nights in total), with the Magellan Inamori Kyocera Echelle (MIKE) double echelle spectrograph mounted at the 6.5-m Clay Magellan telescope at the Las Campanas Observatory (LCO) in Chile. The wavelength interval covered by this instrument ranges from $\sim 3,500$ to $\sim 9,500$ Å with a few gaps at the reddest wavelengths. The wavelength range covered by MIKE allows us to study spectral regions with absorption lines of interest for the characterization of RRLs, such as the Ca II triplet (at 8,498 Å, 8,542 Å, and 8,662 Å), the Mg I triplet (5,167 Å, 5,173 Å, and 5,183 Å), and the Balmer lines (H_α at 6,563 Å, H_β at 4,861 Å, H_γ at 4,340 Å, and H_δ at 4,102 Å). For the targets observed during the first run, we used a 1 arcsec slit, with which MIKE provides a resolution of $\sim 19,000$ and 25,000 in the red and the blue side of the detector, respectively. Since the targets observed during the first run are the faintest in our sample, we selected a configuration with a slow readout time and a strong binning in the spectral direction ($\times 8$) in order to increase the signal-to-noise ratio (S/N). Thus, we decreased the resolution with respect to the values assumed for a 1 arcsec slit with MIKE resulting in $R \sim 2,000$ and 3,000.

For the second run, we adopted a different observing strategy by increasing the slit width to 1.5 arcsec with which, in principle, a resolution of $\sim 15,000$ and 18,000 is achieved in the red and the blue, respectively. However, for this run we used a 2×2 binning, leading to half of the respective resolutions.

In order to obtain a reasonable S/N per star yet avoiding spectral line smearing owing to the pulsations, we observed the RRLs with 900 and 1,200 s exposures in the first and second observing campaigns, respectively, and proceeded to stack the individual (consecu-

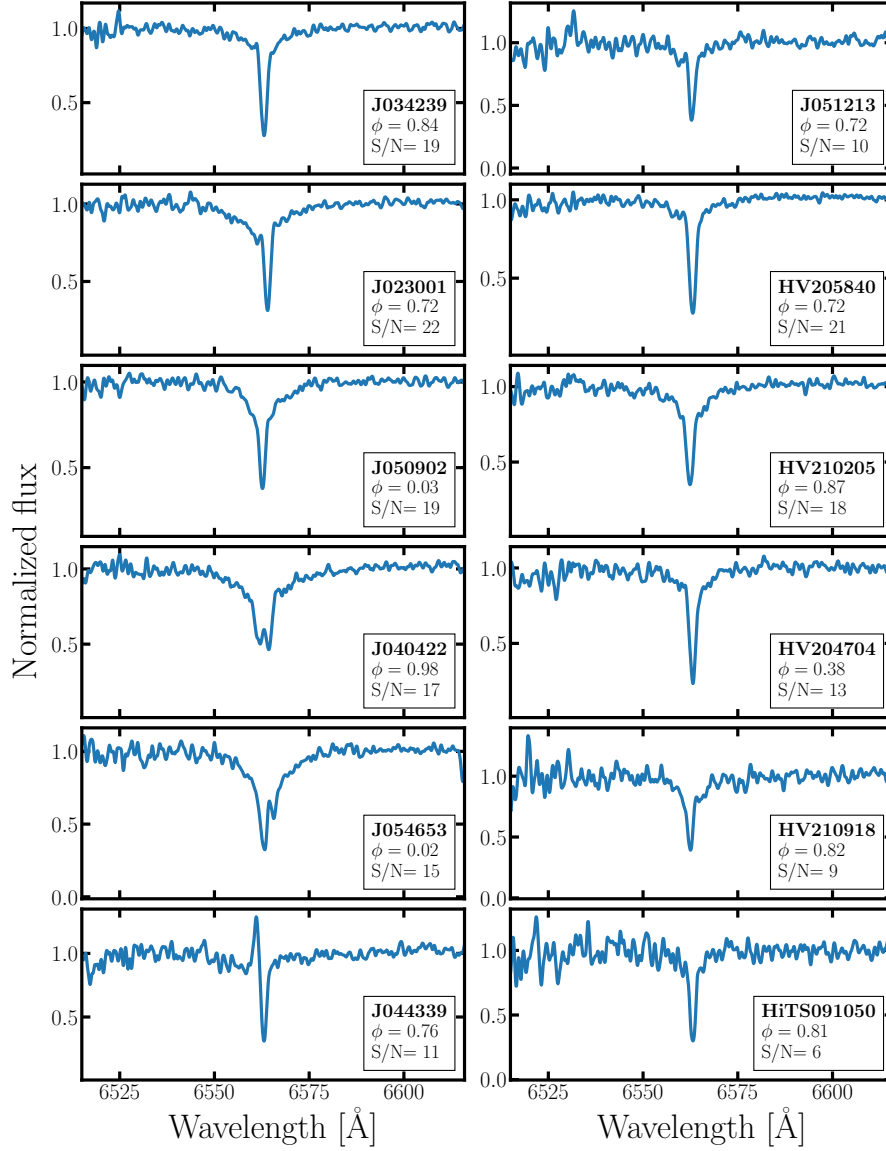


Figure 4.3: Spectral region surrounding the H_{α} line for the stars observed during our second campaign. A Gaussian convolution with $\sigma = 3$ was applied to smooth the spectra in order to help visualize the emission lines affecting the H_{α} profile in certain phases during the RRLs pulsation cycle.

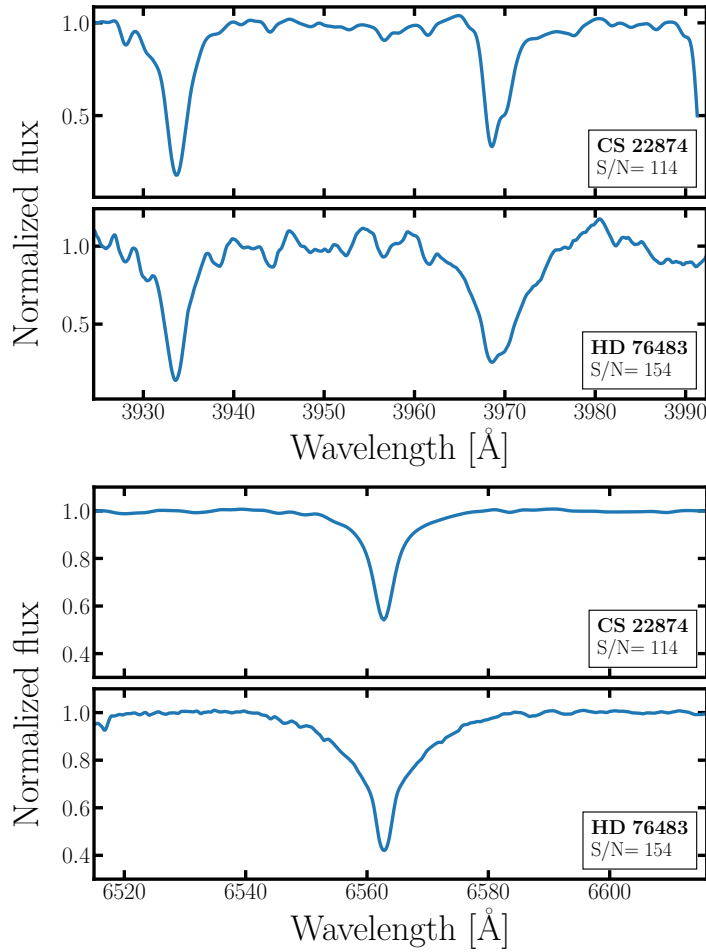


Figure 4.4: Same as Figure 4.3 but for the spectral regions surrounding the Ca K and H ϵ lines (*top* panels), and the H α line (*bottom* panel) for our radial velocity standard stars (at 3,933, 3,970, and 6,563 Å, respectively).

tive) spectra later on. The fraction of the periods of the stars observed in a single exposure during both campaigns range from 1.3 to 2.3 per cent. To avoid the smearing of the spectral lines, we stacked only 2–6 spectra for each star, with which a total of 3.9 to 10.8 per cent of the star’s periods are covered by our observations. The S/N of the continuum in the order in which the H α absorption line lies, resulting from the coadded spectra, are provided in the last column of Table 4.1 and displayed in Figure 4.2 colour-coded by the estimated ϕ , showing that higher S/N was achieved for brighter (closer) RRLs.

For wavelength calibration, thorium-argon comparison lamp exposures were obtained at each star position during each night. Two reference stars were also observed in order to be used as radial velocity standards (CS 22874-042 and HD 76483).

The data reduction, and the flux and wavelength calibrations were executed using the Carnegie Python tools pipeline (CarPy; Kelson et al., 2000; Kelson, 2003). This pipeline produces spectra separated in orders covering < 100 Å in both detectors. These orders are not merged afterwards. Finally, the spectra were normalized in an order-by-order basis, and shifted in wavelength, as explained in Section 4.3. Part of the spectra of a subsample

of our program stars and our radial velocity standards is displayed in Figures 4.3 and 4.4. Additional spectral regions of RRLs in our sample are provided in the Appendix C1.

4.3 Spectral analysis

4.3.1 Radial velocities

To determine the radial velocities to be used for posterior spectral analysis, we used the tools available in the Image Reduction and Analysis Facility (IRAF; Tody, 1993) software. We used the blue metal-poor star CS 22874 (Preston & Sneden, 2000), obtained during our first run, and the star HD 76483 (Layden, 1994), obtained in the second run, as standards for the radial velocity shifts as these two stars have been widely studied in the past, and their spectra should resemble those of RRLs. We ran the IRAF cross-correlation function routine FXCOR and RVCORRECT to determine the radial velocity shift of the spectra, using both the blue and red arms of the detector, and focusing on three different orders on average in each arm. Because our targets are remote and metal-poor, we only rely on orders with fairly strong and well-defined lines. In this regard, the most valuable regions were those containing Balmer lines (mainly H_α and H_β), the Ca II triplet, and the Mg I triplet. The final radial velocity used to shift the spectra resulted from averaging the shifts measured from those orders individually, when available.

The outcome of the radial velocity determinations is shown in Table 4.2, where the propagated uncertainties $e v_{\text{los}}$ and the scatter in the measured radial velocities from different orders σ_{RV} are displayed as a reference. It is worth mentioning that the scatter found when comparing velocities computed from different orders (lines), for the stars with several measurements available is in broad agreement with Sesar (2012) (Figure 3 in his work), who measured the scatter of the radial velocities when using different spectral lines. Sesar (2012) showed that such scatter generally ranges between 1 and 18 km s^{-1} , and is smaller for phases < 0.6 and for RRLs with larger light curve amplitudes.

We note that for the star J023001 the radial velocity shifts obtained from orders containing Balmer lines significantly differ from those obtained using orders with metallic features (with differences of $\sim 40 \text{ km s}^{-1}$) as expected for RRLs in phases of rapid atmospheric changes (< 0.2 and > 0.8 ; For et al., 2011b), although this also depends on the amplitude of the stars' light curve (Sesar, 2012). In fact, differences of the order of 40 km s^{-1} can easily be found for halo RRLs observed at phases > 0.80 . Thus, the difference in velocities measured for J023001 might indicate that our initial phase estimation ($\phi \sim 0.70$) is slightly off. In this specific case, taking advantage of the relatively high S/N of J023001, additional orders were used to better constrain its metallic-line-based radial velocity. We only used these orders for the radial velocity correction of J023001.

If one wishes to use the spectra of RRLs to perform kinematic and orbital analyses, it is necessary to subtract the velocity associated with the pulsations to obtain their so-called systemic (centre-of-mass) velocity v_{sys} . In this sense, it is important to consider that the line-of-sight velocities of RRLs obtained from their spectra depend on the lines used to determine them, and their depth in the stellar atmosphere. Thus, the amplitude and shape of the line-of-sight velocity curves vary depending on what lines are measured. Larger line-

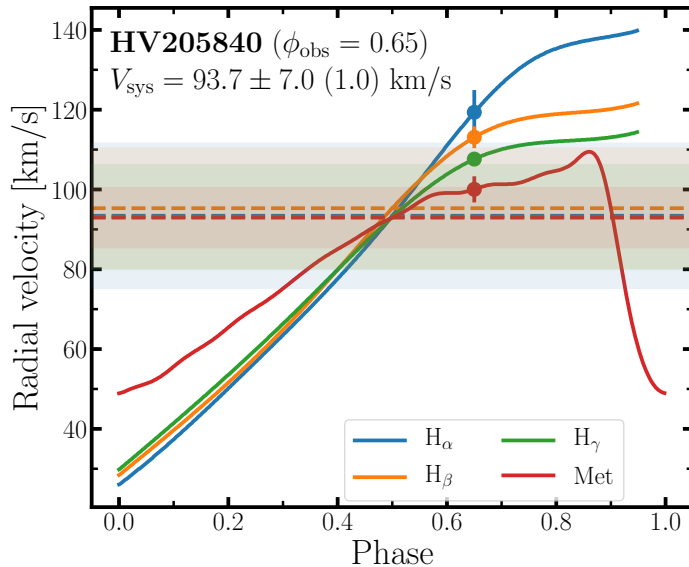


Figure 4.5: Example of the determination of the systemic velocity V_{sys} for one star, based on Balmer and metallic lines. The model radial velocity curves are those provided by Sesar (2012) derived from H_α (blue), H_β (orange), H_γ (green), and metallic lines (red). The radial velocities measured at the observed phase (v_{los}) are plotted with filled circles. The systemic velocities derived from the use of each set of absorption lines are shown with horizontal dashed lines, with shaded regions representing their uncertainties. This figure illustrates that, for a given V_{sys} , the difference between line-of-sight velocities from Balmer and metallic lines depends on the observed phase, and can be up to $\sim 40 \text{ km s}^{-1}$ even for $\phi < 0.8$.

of-sight velocity variations are expected for lines formed in the upper atmosphere (such as the Balmer lines), in comparison with metallic lines formed deeper in the atmospheres (see e.g. Liu, 1991; Sesar, 2012). To estimate v_{sys} for our sample, we used the line-of-sight velocity templates provided by Sesar (2012) in addition to our knowledge of the observed pulsation phases of our targets. Because those velocity templates scale with the V -band amplitude of the RRLs pulsation, we transformed the g and r light curve amplitudes to the V -band using the transformations provided by Sesar (2012) ($A_V = 0.9 A_g$, $A_V = 1.21 A_r$). The final v_{sys} were obtained by using the measured line-of-sight velocities and the corresponding templates of the Balmer lines, Ca triplet, and Mg triplet (when available) independently, and minimizing the scatter of the resulting v_{sys} after allowing for small shifts in ϕ (± 0.1 around the expected phase). Figure 4.5 depicts the differences between v_{los} and v_{sys} for one of the RRLs in our sample. It is clear from the figure that observing an RRL at a quiescent phase (e.g., $\phi \sim 0.4$) results in a smaller scatter in the final value of v_{sys} .

4.3.2 Atmospheric parameters

We derive stellar parameters such as temperature and metallicity. Using various techniques, the gravity turned out to be the hardest as is often the case (see, e.g., Jofré et al. 2010 or Hanke et al. 2020a). First, we use photometry and the Infra-Red Flux method (IRFM) to determine the temperature, and parallaxes to compute gravities (following Nissen, Høg, & Schuster 1997). The metallicity was computed using different spectroscopic tracers and

Table 4.2: Radial velocity measurements for our targets after heliocentric correction. In addition to line-of-sight velocities (v_{los}), we include the number of MIKE orders used to estimate such velocities in both the blue and the red side of the detector (N_{ap}), their propagated uncertainties ($e v_{\text{los}}$), and the scatter in the measurements from different orders ($\sigma_{v_{\text{los}}}$). In the case of the systemic velocities (v_{sys}), we provide the uncertainties propagated from using the Balmer and metallic line-based radial velocity templates ($e v_{\text{sys}}$), and the scatter in the best fits ($\sigma_{v_{\text{sys}}}$).

ID	N_{ap} red	N_{ap} blue	v_{los} (km s^{-1})	$e v_{\text{los}}$ (km s^{-1})	$\sigma_{v_{\text{los}}}$ (km s^{-1})	v_{sys} (km s^{-1})	$e v_{\text{sys}}$ (km s^{-1})	$\sigma_{v_{\text{sys}}}$ (km s^{-1})
J051424	3	3	221.2	1.7	9.6	216.9	7.7	4.0
	3	3	247.7	0.8	7.6	240.3	8.0	0.2
J050226	3	–	79.3	1.6	3.9	132.3	7.9	8.4
HiTS112524	3	3	188.4	0.7	7.3	205.4	4.3	2.8
HiTS100956	1	1	58.6	0.9	0.0	75.4	12.7	0.0
	3	3	51.5	1.5	4.8	66.0	4.3	9.3
HiTS101243	1	1	293.8	1.4	6.4	305.6	3.8	1.0
HiTS104009	1	1	146.5	1.9	3.3	140.5	7.6	1.9
HiTS103943	–	2	171.2	1.8	0.6	167.0	12.7	0.0
HiTS102414	–	2	50.0	0.8	1.9	72.3	12.7	0.0
J054653	2	1	–66.0	1.6	7.4	3.4	6.8	12.5
J040422	3	3	–122.3	0.5	4.5	–138.4	6.1	2.6
J050902	3	2	102.7	0.7	5.2	145.7	6.2	5.1
J034239	3	4	–101.2	0.8	3.4	–117.6	5.9	9.5
HV205840	3	4	105.5	1.1	7.8	93.7	7.0	1.0
J023001	2	9	–142.6*	0.7	3.8	–137.1	5.9	8.0
HV210205	3	3	97.3	0.3	10.5	72.0	5.5	26.0
HV204704	3	4	97.6	0.2	4.7	108.6	6.6	4.0
J044339	3	2	–27.5	0.2	2.8	–44.5	6.7	5.2
J051213	3	3	78.6	0.6	2.6	66.1	6.4	4.1
HiTS091050	2	2	60.7	0.3	0.7	46.2	5.4	9.0
HV210918	3	2	–78.1	0.7	10.7	–108.7	6.8	25.0

*The v_{los} used for J023001’s radial velocity correction was computed using orders with metallic lines only.

empirical methods (including the ΔS). However, deriving the stellar parameters in these faint, variable stars turned out to be challenging and the above mentioned methods and their results were instead used as initial guesses in a purely spectroscopic approach. For details we refer to the following subsections. Our final stellar parameters are spectroscopically derived as described in Section 4.3.3.

Metallicities

An initial estimation of the metallicity of our sample followed different approaches, taking advantage of the broad spectral coverage of our spectra.

For the stars with clearly defined Ca II triplet lines and higher S/N ($\gtrsim 10$), we used the correlation between $[\text{Fe}/\text{H}]$ and the equivalent width (EW) of the Ca line at 8,498 Å described by Wallerstein et al. (2012). In some stars, the 8,498 Å Ca line was not reliably detected, so here we estimated the EW based on an empirical scaling using the 8,498 Å and the 8,542 Å obtained from the spectra of CS 22874, HD 76483, and of the metal-poor r -process-rich star HD 20 (Hanke et al., 2020a). The latter is a well-known giant for which accurate stellar parameters and high-resolution spectra are available and we use it as a benchmark star. The scaling coefficient used was $\text{EW}(8,498 \text{ \AA})/\text{EW}(8,542 \text{ \AA}) = 0.5119$. The EW’s measured for this approach were obtained using Gaussian profiles, as they better fit the shape of the lines.

Singh et al. (2020) presented empirical relations that predict $[\text{Fe}/\text{H}]$ and are valid for carbon-enhanced metal-poor (CEMP) stars as well as carbon-normal stars. These relations were tested for seven elements with strong features at low metallicities, and showed Cr and Ni as the best $[\text{Fe}/\text{H}]$ tracers. In that work, linear scaling relations were also obtained for the Mg I absorption lines at 5,173 Å and 5,184 Å, valid for lines with $\text{EW} < 1,000 \text{ mÅ}$ (although with an accuracy within ~ 0.4 dex). The empirical Mg I- $[\text{Fe}/\text{H}]$ relation was obtained via private communication with the authors. Thus, we also used these correlations to obtain an estimate of the star’s metallicity (iron abundance), by measuring the Mg lines using Gaussians.

Additionally, we estimated the metallicity using an updated version of the ΔS method (Crestani et al., 2021a). This method relies on the correlations between the EW of the Ca K line (3,933 Å) and those from the Balmer lines. As Crestani et al. (2021a) provide correlation coefficients for different combinations of Balmer lines with the Ca K line, we determined the metallicity for each combination, using Gaussian and Lorentzian profiles, and with different levels of spectral convolution to mimic the low resolution of their work, i.e., none, medium (convolution box size of 5 pixels), and drastic convolution (box size of 50 pixels). Applying medium convolutions results in spectral resolutions close to those of Crestani et al. (2021a). Moreover, given the overall higher resolution and lower S/N of our spectra, as compared with those from Crestani et al. (2021a), we reduced the EW integration region around each line from 20 Å, as used by the authors, to 10 Å. In a few cases, the region was even further reduced (down to 5 Å around the lines) to provide a sensible fit. For each combination of lines, we selected the line profile that best fit the lines centres, and their wings, for each convolved level. This typically corresponds to Lorentzian and Gaussian profiles for the Balmer and Ca lines, respectively. An example of the outcome of these calculations is shown in Figure 4.6. The combination of lines that generally showed lower dispersion between the methods used, of the order of 0.15 dex, are single comparisons (CaK with either H_β , H_γ , or H_δ), whereas using multiple Balmer lines results in $[\text{Fe}/\text{H}]$ scatter closer to 0.2 dex. We also find that, for our RRLs, the metallicity estimates from the ΔS method are on average 0.17 dex higher than those from Wallerstein et al. (2012)’s correlation (Figure 4.7).

In Figure 4.7, we compare the metallicity estimates resulting from the aforementioned methods. We note that the metallicity estimates obtained from the relation derived by Singh et al. (2020) are consistently more metal-poor than those obtained from the Ca II triplet and from the ΔS method. In fact, they lead to $[\text{Fe}/\text{H}]$ values that are 0.30 and 0.60 dex smaller on average, respectively. Given these large differences, and that the validity of the Mg I-Fe relations for the stars in our sample is not certain, we computed the average of the resulting metallicities from the other two methods, as it should represent a sensible range of metallicities to be used as initial guesses for the rest of the analysis. We consider this justified since, in theory, it reduces possible biases from the choice of a given metallicity scale, in order to ensure the convergence of the atmospheric parameter determination described in Section 4.3.3. The resulting mean metallicities are displayed in Table 4.3.

Another method commonly used for deriving the metallicity of RRLs relies on the correlation between their periods, light curve shapes (mainly through the phase parameter ϕ_{31} , obtainable through Fourier decomposition analysis), and $[\text{Fe}/\text{H}]$ (see, e.g., Jurcsik & Kovacs, 1996; Smolec, 2005; Nemeč et al., 2011, 2013; Dékány, Grebel, & Pojmański, 2021; Mullen

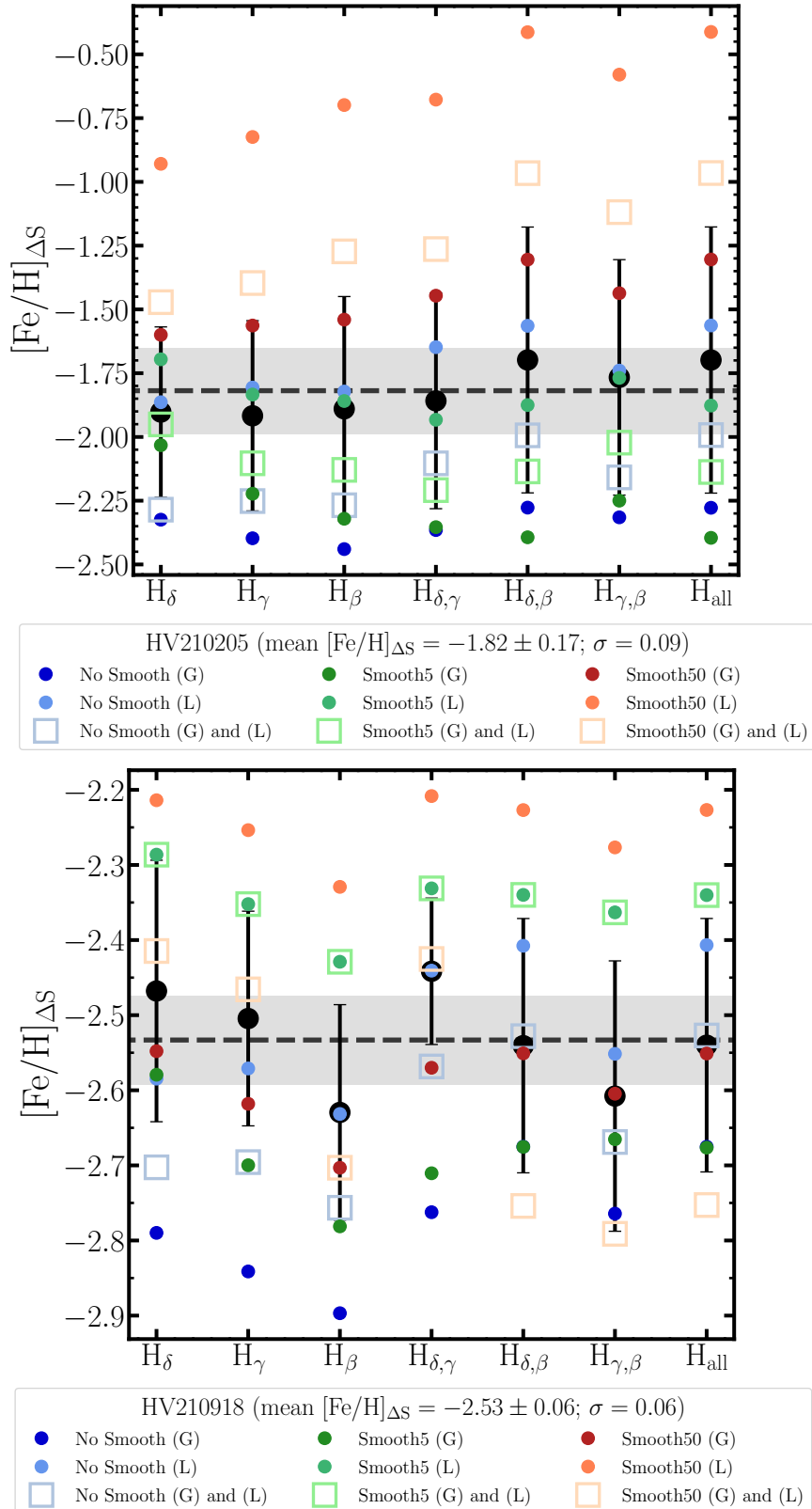


Figure 4.6: Iron abundance estimations from the ΔS method and different combinations of Balmer lines, for two stars in our sample. The average iron abundances from the best-measured lines (considering spectral smoothing and line shapes) are shown with black filled circles, and the average from using all the combinations of Balmer lines is represented by an horizontal dashed line. The standard deviation of the latter (σ) is depicted as a shaded region. These figures show the strong dependency of the resulting $[\text{Fe}/\text{H}]$ on the resolution of the input spectra (colour-coded), and the line profiles used, i.e., Gaussian (G) and/or Lorentzian (L). 133

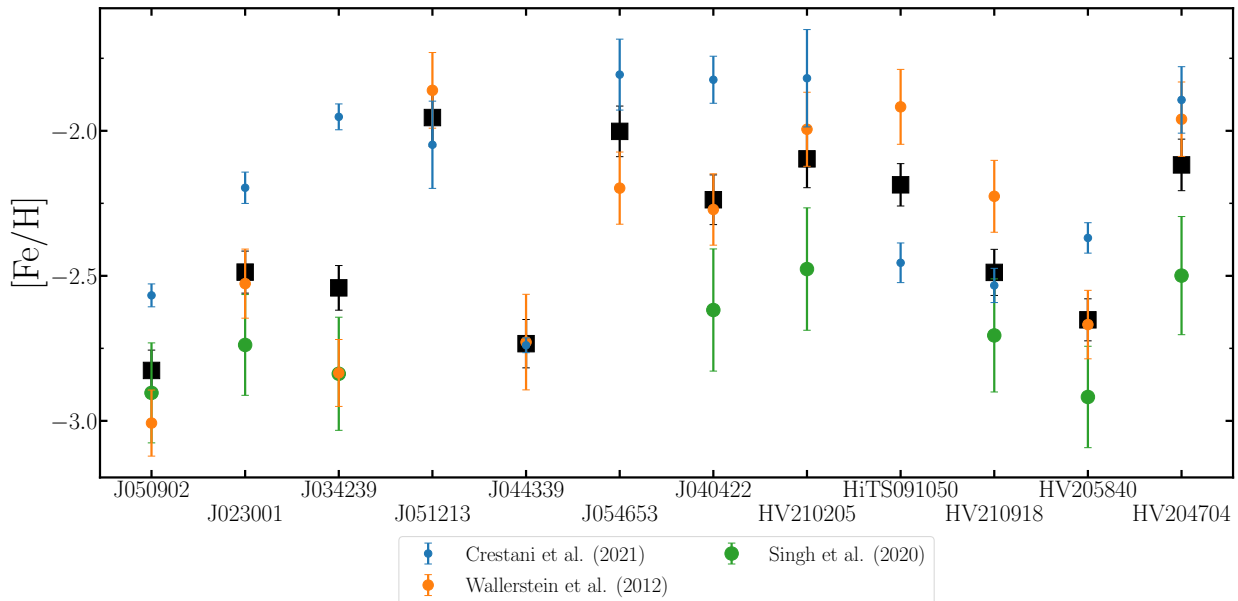


Figure 4.7: $[\text{Fe}/\text{H}]$ estimation based on the method of Wallerstein et al. (2012), Crestani et al. (2021b), and Singh et al. (2020), for the stars in our second run. The iron abundances shown are derived from empirical relations based on the Ca II triplet, the Balmer lines, and Mg lines (respectively), as described in the Section 4.3.2. Black squares represent the average of the aforementioned measurements weighted by their uncertainties.

et al., 2021, 2022). This approach, however, is inherently sensitive to the uncertainties in the light curve measurements and its phase coverage. Because almost half of our targets are taken from the Catalina survey (good phase coverage but large photometric uncertainties), and the other half from our independent surveys (modest phase coverage and small uncertainties), this method is, in principle, not the best suited for our study. In addition, the $[\text{Fe}/\text{H}]$ from photometric formulae depends on the metallicity scale used, the $[\text{Fe}/\text{H}]$ range in which is valid, and can reach a scatter of 0.5 dex when compared with high-resolution spectra (see, e.g., Figure 6 from Dékány, Grebel, & Pojmański 2021 or Figure 11 from Mullen et al. 2021). Recently, Dékány, Grebel, & Pojmański (2021) obtained new empirical relations between the iron abundance of RRLs and their light-curve parameters based on near-infrared photometry. The training set used by these authors consisted of high-resolution spectra of 80 RRab with $[\text{Fe}/\text{H}]$ from solar to ~ -2.5 , collected from the datasets of Crestani et al. (2021a), For et al. (2011b), Chadid, Sneden, & Preston (2017), and Sneden et al. (2017). Also recently, Mullen et al. (2021) reported new period- ϕ_{31} - $[\text{Fe}/\text{H}]$ relations in the optical (including V), from stars in a similar $[\text{Fe}/\text{H}]$ range and calibrated with the same metallicity scale. In Figure 4.8, we depict two examples of RRLs in our sample with metallicities derived from the Fourier decomposition of their light curves, following the relations of Mullen et al. (2021):

$$\phi_{31} = \phi_3 - 3 \phi_1 \quad (4.1)$$

$$[\text{Fe}/\text{H}] = a_M + b_M (P - 0.58) + c_M (\phi_{31} - 5.25),$$

where a_M , b_M , and c_M are constants, ϕ_1 and ϕ_3 the first and third coefficient of the Fourier

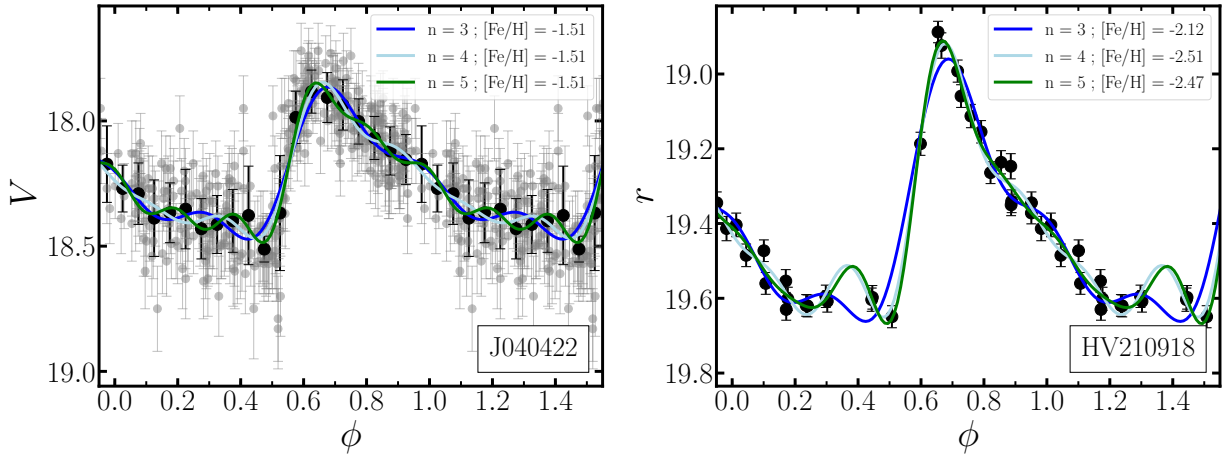


Figure 4.8: Models of the light curves of two RRLs in our sample (J040422 and HV210918) using Fourier decomposition. In the *left* panel the light curve of an RRL from the Catalina survey is shown. In that plot, the black transparent circles are all the observations from Catalina, and the normal black circles represent the points of the light curve binned in steps of 0.05 phase units. The *right* panel shows an RRL from the HOWVAST survey. In both panels, the blue, light-blue, and green solid lines represent the Fourier decomposition of the light curves with three, four, and five degrees of freedom, respectively. These two RRLs are examples of an RRL with good phase coverage but large photometric uncertainties (J040422) and of an RRL with small photometric uncertainties but a modest phase coverage (HV210918).

series (respectively), and P is the RRLs' period. In these examples we perform three, four, and five-degree Fourier decompositions for an RRL from the Catalina survey, and one from HOWVAST. In the first case, due to the large number of observations and their relatively large uncertainties, we first binned the data in boxes of width 0.05 in phase. It is clear from the figure that using light curves with imprecise photometry leads to imprecise metallicities (the results are unreliable due to the large errors, even when the three $[\text{Fe}/\text{H}]$ ratios shown are the same). In a similar vein, small photometric errors with an incomplete phase coverage leads to inconclusive estimations (e.g., due to the challenge of characterizing the feature before and during the steep rise of the light curve). Thus, we do not further consider this method to estimate the metallicity of our sample.

For a quick comparison with our work, we note that one of our stars, J051424, is included in the list of LMC RRLs with I -band based $[\text{Fe}/\text{H}]$ from [Dékány, Grebel, & Pojmański \(2021\)](#). For this star, their model predicts $[\text{Fe}/\text{H}] = -1.68$, whereas the relation of [Mullen et al. \(2021\)](#) yield -2.21 (from Catalina's V -band photometry), and the use of the ΔS method from our spectra results in -2.34 . As a second comparison, using the formula from [Mullen et al. \(2021\)](#) on J040422 (for which we possess relatively high signal-to-noise spectra with clearly defined metallic lines) yield $[\text{Fe}/\text{H}] = -1.51$, while following the ΔS method and the EW technique (see Section 4.3.5) we obtain $[\text{Fe}/\text{H}] = -1.82$ and -1.56 , respectively.

Effective temperatures

As a rough effective temperature estimation for these RRLs we used the photometric colour transformations from [Casagrande et al. \(2010\)](#), which rely on Johnson-Cousins photometry. These transformations are of the type:

$$T_{\text{eff}}^{-1} = 5,040 (A_0 + A_1 \cdot C + A_2 \cdot C^2 + A_3 \cdot C \cdot [\text{Fe}/\text{H}] + A_4 \cdot [\text{Fe}/\text{H}] + A_5 \cdot [\text{Fe}/\text{H}]^2), \quad (4.2)$$

where C is the colour used in the relation ($V - R$, $B - V$, $R - I$, or $V - I$), and the coefficients A_x depend on such colour. The stars' mean $[\text{Fe}/\text{H}]$ values derived above were used for these transformations. Prior to performing any computation, we dereddened the magnitudes of our halo RRLs targets by using the dust maps from [Schlafly & Finkbeiner \(2011\)](#), adopting $R_V = 3.1$ ([Schultz & Wiemer, 1975](#); [Cardelli, Clayton, & Mathis, 1989](#)). For the brighter RRLs in our sample, the usage of the relations from [Casagrande et al. \(2010\)](#) is straightforward given that photometry for their mean magnitudes in the Johnson-Cousins system is available with relatively small uncertainties (from the Catalina survey, for instance). In the case of the fainter RRLs, we used PS-1 photometry and converted those magnitudes to Johnson-Cousins using the photometric relations provided by [Tonry et al. \(2012\)](#). When neither Johnson-Cousins nor PS-1 magnitudes were directly available, but the star is listed in the *Gaia* third data release (DR3) catalogue, we adopted the photometric transformations given in the *Gaia* documentation to derive Johnson-Cousins magnitudes³⁹.

In [Figure 4.9](#), we plot the results from our photometric effective temperature determinations. The figure shows that the T_{eff} obtained from a given set of filters (either *Gaia* or PS-1) is in general self consistent at a ~ 300 K level, but in some cases a clear disagreement is observed. These differences more significant when considering different photometric systems (e.g., in the case of J050902 and J040422). We attribute this to the different limiting magnitudes of each survey, and to the accuracy and precision of the transformations used to transform their photometry to the Johnson-Cousins system (including the colour range in which they are valid).

It is worth mentioning that in our study, the effective temperatures and gravities obtained from photometric indices are used as initial guesses for the method described in [Section 4.3.3](#) and mostly as a test, due to their high dependence on the phase in which such photometry was obtained (as stated by, e.g., [Kolenberg et al. 2010](#)), which is in general rather uncertain.

³⁹https://gea.esac.esa.int/archive/documentation/GDR2/Data_processing/chap_cu5pho/sec_cu5pho_calibr/ssec_cu5pho_PhotTransf.html

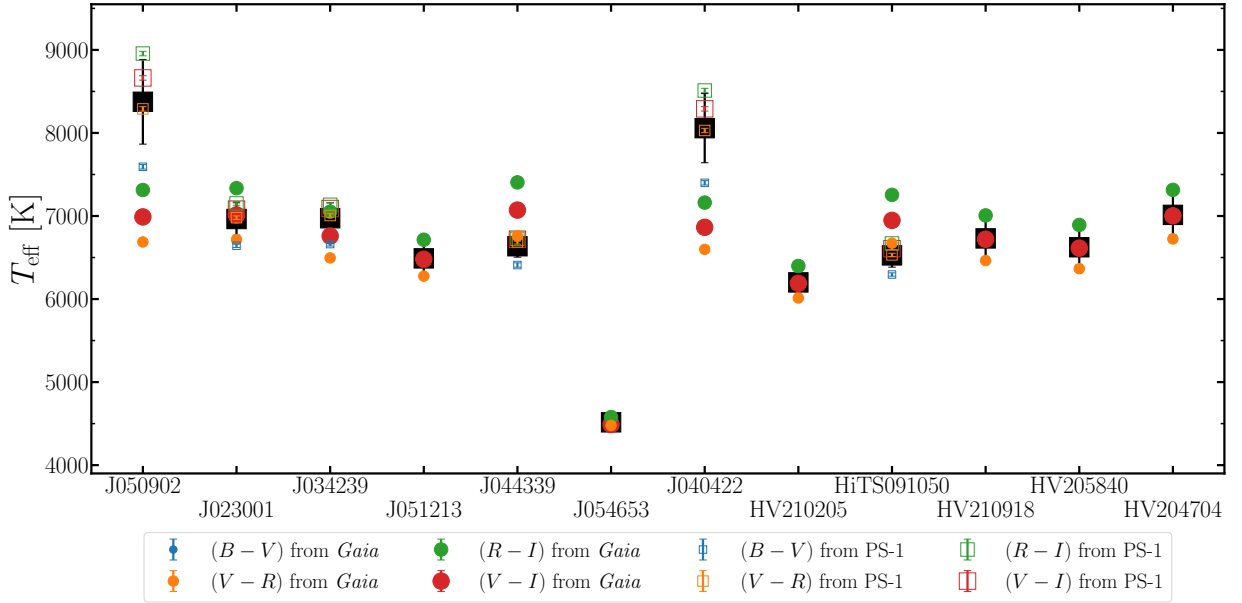


Figure 4.9: Photometric effective temperatures of those stars obtained using the relations from Casagrande et al. (2010), after transforming the stars’ *Gaia* magnitudes (and PS-1 magnitudes, when available; Tonry et al., 2012) to the Johnson-Cousins system. The colours used to get T_{eff} for a subset of the stars are based on PS-1 photometry and/or *Gaia*’s passbands (G , BP , and RP), depending on the availability of photometric measurements for these faint stars. Black squares represent the average of the T_{eff} estimations (from PS-1 photometry only when available, from *Gaia* otherwise). For J054653 using the colours (based on *Gaia* photometry) $V - R$, $R - I$, and $V - I$ yield temperatures that is not typical of RRLs, as a result of the overall red colour of this distant star, making it a limit case for the use of the photometric transformations ($V - R$ is for most RRLs in our sample between 0.2 and 0.3, whereas it is 0.6 for J054653).

Surface gravity - $\log g$

The surface gravity of stars accounts for the acceleration of their moving atmospheres and can, in principle, be modelled by differentiating the radial velocity curve (when available). Since we do not possess radial velocity curves for our stars, we first employed the empirical relation from Nissen, Høg, & Schuster (1997) in order to have a rough estimate of the observed surface gravity of RRLs. This relation relies on the knowledge of the stars’ mass, T_{eff} , V magnitude, bolometric correction (BC), and parallax ϖ , and is of the form:

$$\log(g/g_{\odot}) = \log(M/M_{\odot}) + 4 \log(T_{\text{eff}}/T_{\text{eff},\odot}) + 0.4 V + 0.4 \text{BC} + 2 \log(\varpi/1000) + 0.12. \quad (4.3)$$

For this work, we used the empirical BC described by Flower (1996) and Torres (2010):

$$\text{BC} = c_0 + c_1 \log(T_{\text{eff}}) + c_2 \log(T_{\text{eff}})^2 + c_3 \log(T_{\text{eff}})^3 + c_4 \log(T_{\text{eff}})^4, \quad (4.4)$$

where the values c_x are constants and the parallaxes are taken from *Gaia* DR3, adopting a fixed RRL mass of $0.8 M_{\odot}$ (Simon, 1989; Clement & Shelton, 1997; Catelan & Smith, 2015). However, this approach resulted in imprecise gravities overall, mostly due to the stellar parallaxes of our rather distant sources (small parallaxes and large relative uncertainties).

Thus, we assumed $\log g = 2.0$ as sensible initial estimates (For et al., 2011b) for all the RRLs.

Microturbulence - V_t

The micro/macroturbulence velocities were estimated applying the same empirical relation used by Blanco-Cuaresma et al. (2014b), based on the GES Ultraviolet and Visual Echelle Spectrograph (UVES) data release 1 and the *Gaia* FGK benchmark stars (Jofré et al., 2014). We note that, for a star of $T_{\text{eff}} = 6,500$ K, $[\text{Fe}/\text{H}] = -1.5$, and $\log g = 2.0$, using the empirical relation derived by Mashonkina et al. (2017) (based on very- and extremely-metal poor stars) results in a microturbulence velocity 0.3 km s^{-1} higher than that based on the *Gaia* FGK benchmark stars' scaling. In the case of the star HD 76483, we used the literature values $[\text{Fe}/\text{H}] = -0.5$, $T_{\text{eff}} = 8,600$ K, and $\log g = 3.77$ as initial estimates (David & Hillenbrand, 2015).

4.3.3 Spectroscopic stellar parameters

To determine the atmospheric parameters of our program stars, we used the spectral analysis tool iSpec (Blanco-Cuaresma et al., 2014a; Blanco-Cuaresma, 2019), which outputs the best fitting parameters based on a χ^2 minimization criterion. For this, we worked with synthetic spectra generated by MOOG (Snedden, 1973, version 2019) and ATLAS9 model atmospheres (Castelli & Kurucz, 2003), relying on the Vienna Atomic Line Database (VALD) atomic line lists in the range $3,000 - 11,000 \text{ \AA}$ (Piskunov et al., 1995; Ryabchikova et al., 2015).

The atmospheric parameters were determined following different approaches. In the first case, considering that the orders of our spectra are not merged, we chose five non-contiguous orders at different wavelengths in each side of the detector (ten in total), in which strong parameter-sensitive lines are present. Due to the narrow wavelength range covered in each order, however, the statistics of the lines fit remains poor, which negatively affects the resulting parameters, especially when the (few) targeted lines are affected by noise or stellar pulsations. Moreover, using a single order to determine stellar parameters can bias the metallicity due to the small number of metal tracers in the order's wavelength range. These biases might also affect the estimation of T_{eff} , as it can easily differ by 400-500 K when determined from, e.g., H_α and H_β . Thus, we ran iSpec on the concatenation of the aforementioned orders. In the second approach, we used a selection of orders numbered with odd and even identifiers, in order to cover a broader wavelength range and in turn more lines to improve the precision of the parameter determination. Separating the orders into odd and even allows for the use of the overlapping regions between orders without having to merge the orders. Because ~ 70 per cent of the entire wavelength range covered by MIKE is measured in more than one (contiguous) order, the resulting atmospheric parameters from odd and even concatenations are not independent from each other. From hereon, we use the results from the concatenation of even orders as derived parameters, given that they resemble those from the ten selected orders but with smaller uncertainties overall. The only exceptions for this are HV210205, for which using the odd orders results in significantly smaller uncertainties (due to the presence of distorted lines in the even orders, at $\phi \sim 0.87$), and J051213, for which neither even nor odd orders provide sensible solutions (due to the low number of visible lines

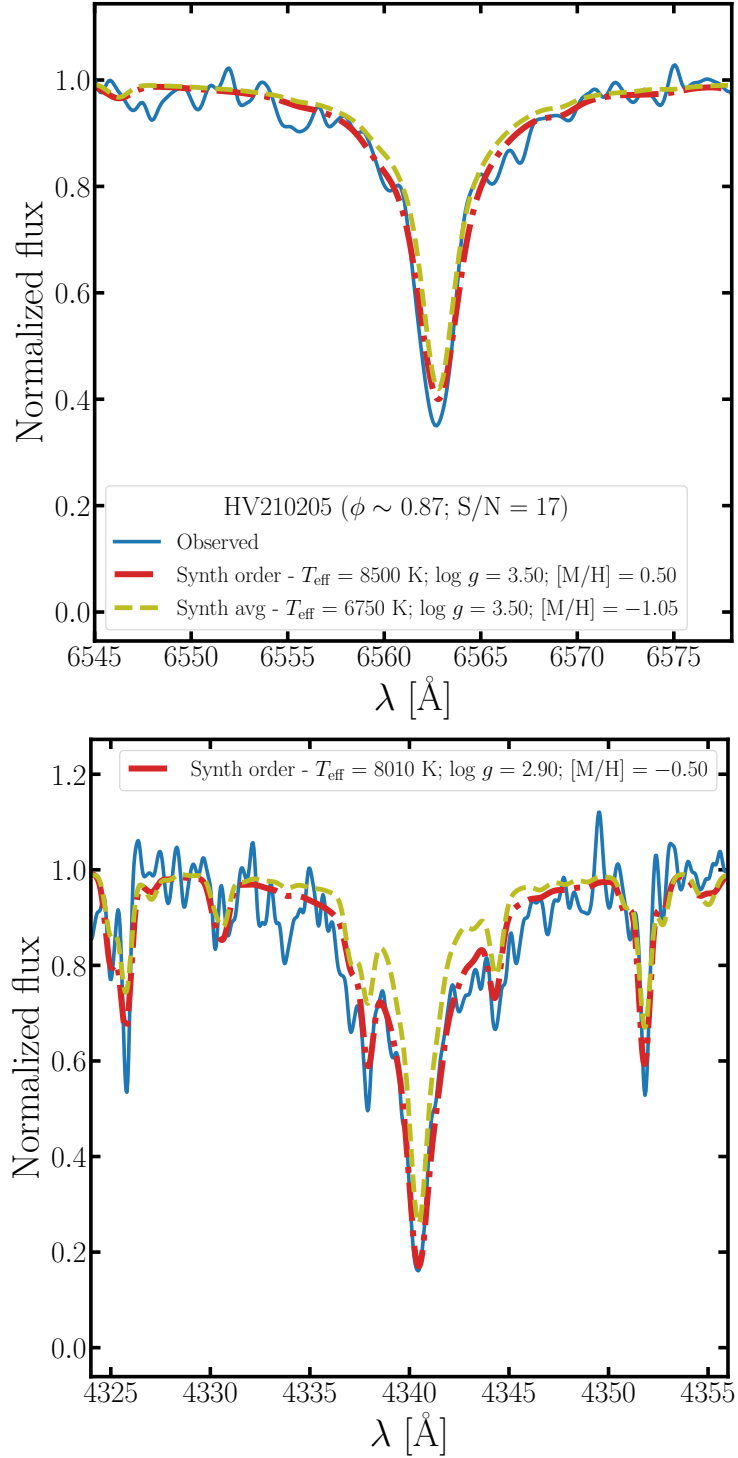


Figure 4.10: H_α and H_γ profiles of an RRL from our primary sample (HV210205). The observed spectra are represented by blue solid lines. In these panels we overplot, for comparison, the best stellar atmosphere fit for the selected orders (red lines) and the average from all the used orders (yellow dashed lines). This figure shows the discrepancies that can be observed in the stellar parameters computed from different (single) orders.

at $\phi \sim 0.72$ and low S/N). Thus, for these two stars we use the odd and ten selected orders instead, respectively.

The fitting process was carried out with a maximum of six iterations of the code leaving the effective temperatures, metallicity, and $\log g$ as free parameters, while fixing the rest of the required parameters (micro/macro turbulence velocities, rotation, resolution, and limb darkening coefficient). We used the values obtained in Section 4.3.2 and 4.3.2 as initial estimations for the [Fe/H] and effective temperatures. For all the stars we adopted a fixed value for the limb darkening coefficient (0.6) and $v \sin i = 2.0 \text{ km s}^{-1}$. Figure 4.10 shows an example of spectra with the best fitting parameters from using a single order, and the average of all the orders considered.

An exception in this treatment is made for J023001 and J040422. For these RRLs, the use of our method results in a metallicity of -1.23 ± 0.30 and -0.61 ± 0.23 , which is not compatible with the visible Fe lines in the range 3,800-5,000 Å (including Fraunhofer lines), after a visual comparison with synthetic spectra. This might be attributable to their observed phases (between 0.70 and 0.80 for J023001, and > 0.90 for J040422). Therefore, we re-estimated J023001's and J040422's [Fe/H] by following the EW approach (Section 4.3.5) on clean Fe lines in this wavelength range, from which we obtain [Fe/H] = -1.80 ± 0.10 and -1.56 ± 0.17 , respectively. We adopted these values for the rest of their analysis.

Our results are shown in Figure 4.11, and summarized in Table 4.3. We note in passing that the parameters derived in this section represent the atmosphere of the stars at the moment of the observations, which in most cases corresponds to phases of atmospheric contraction, with a decrease in luminosity, and a plateau in T_{eff} (ϕ between 0.40 and 0.85; For et al., 2011b; Kolenberg et al., 2010). A star-by-star description of the atmospheric parameters of a subsample of our program stars is provided in the appendix (Section C2).

4.3.4 Stellar parameters and uncertainties

The observed phase and S/N of an RRL define its suitability for the method described above, which might result in unreliable stellar parameters and/or large uncertainties. Thus, we subdivide our target stars into two groups depending on their spectrum quality and phase: a primary sample, containing stars with relatively high S/N, ideal observing phases, and well constrained atmospheric parameters, and a secondary sample for which the spectra were not observed in optimal conditions and/or low S/N, which resulted in loosely constrained atmospheric parameters. We include J054653 in the secondary sample since, albeit its relatively high S/N (≥ 15), it was observed close to maximum light. J044339, J051213, and HiTS091050 are included in the secondary sample due to their low S/N (≤ 10) and phase of observation ~ 0.75 , at a stage of abrupt atmospheric kinetic energy changes (Kolenberg et al., 2010).

For both the primary and secondary sample, the errors in the atmospheric parameters are computed by propagating the uncertainties resulting from the iSpec routine only if the derived values are well defined for a given method. Hence if a parameter does not make physical sense or does not return a reasonable uncertainty, we define it as a limit or flag the values. Table 4.3 shows the atmospheric parameters together with their uncertainties, and the scatter σ originating from the empirical relations employed and the spectroscopic measurements.

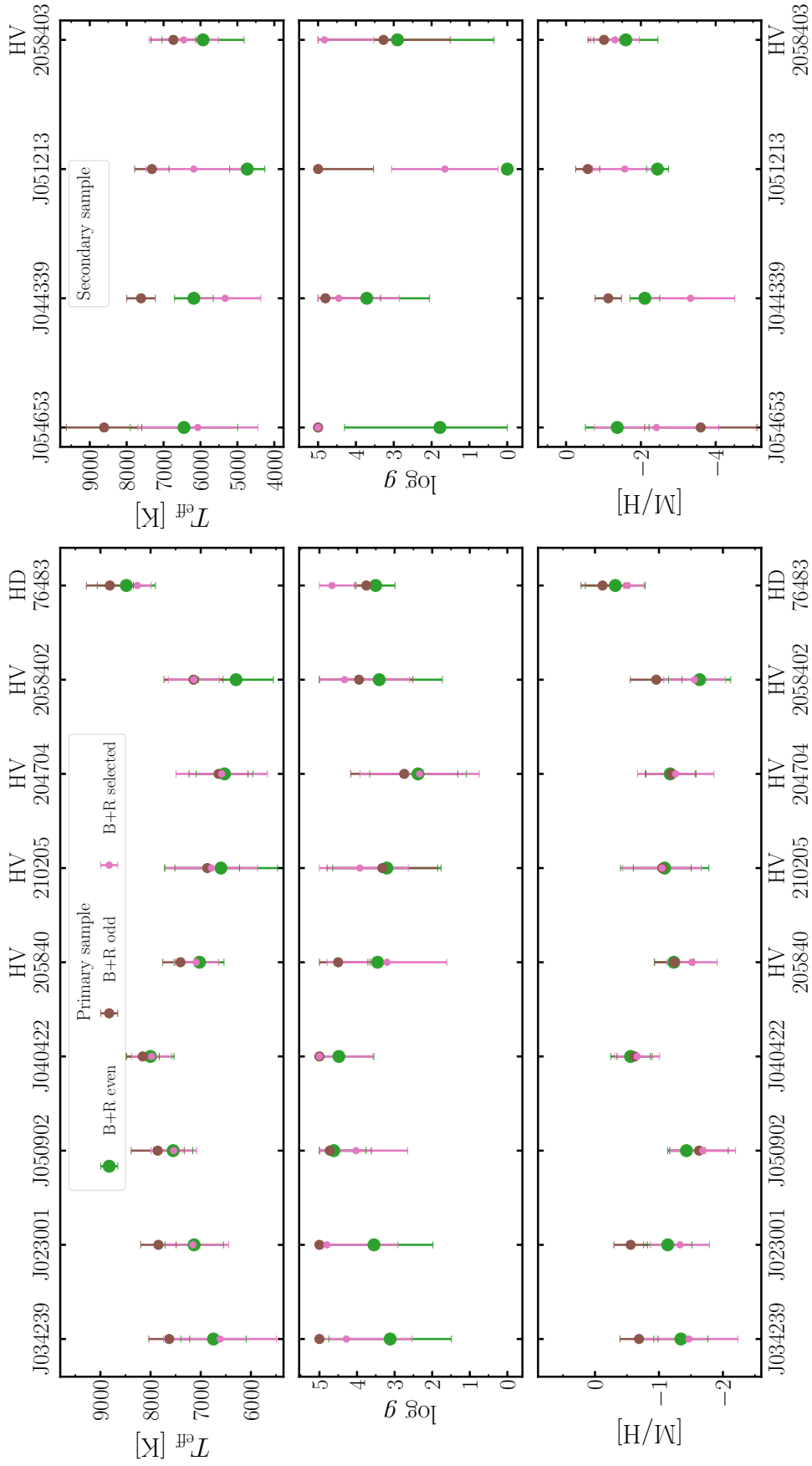


Figure 4.11: Stellar parameters (as returned by iSpec) and uncertainties of the subsample of our program stars with higher resolution (including the radial velocity standard HD 76483). The values derived from the use of even/odd/ten selected orders in both sides of the detector (B+R) are shown with green/brown/pink symbols. The *left* panels depict the RRLs that we consider part of our primary sample, whereas those in our secondary sample are plotted on the *right*, respectively. These plots illustrate (in-)consistencies in the stellar parameters obtained when using different sets of orders, as well as the the overall higher uncertainties obtained for the secondary sample.

Table 4.3: Summary of the atmospheric parameters determined for the RRLs with higher S/N in our sample using empirical estimations (emp) and spectrum synthesis (synth).

ID	[Fe/H]	$e_{\text{[Fe/H]}}$	$\sigma_{\text{[Fe/H]}}$	[Fe/H]	$e_{\text{[Fe/H]}}$	$\sigma_{\text{[Fe/H]}}$	T_{eff}	$\sigma_{T_{\text{eff}}}$	T_{eff}	$e_{T_{\text{eff}}}$	$\sigma_{T_{\text{eff}}}$	$\log g$	$e_{\log g}$	$\sigma_{\log g}$
	(dex)	(dex)	(dex)	(dex)	(dex)	(dex)	(K)	(K)	(K)	(K)	(K)	(cgs)	(cgs)	(cgs)
Primary sample														
J040422	-2.24	0.09	0.32	-1.56	0.17	-	8057	416	8003	473	12	4.5	0.9	0.3
J050902	-2.83	0.07	0.19	-1.43	0.29	0.11	8375	509	7548	389	147	4.6	0.9	0.3
J034239	-2.54	0.08	0.42	-1.34	0.42	0.06	6973	185	6746	650	66	3.1	1.6	0.6
HV205840	-2.65	0.07	0.22	-1.23	0.31	0.13	6623	215	7025	488	164	3.5	0.3	0.6
J023001	-2.49	0.07	0.22	-1.80	0.10	-	6963	195	7131	583	13	3.5	1.6	0.6
HV210205	-2.10	0.10	0.28	-1.05	0.45	0.02	6200	157	6870	645	114	3.3	1.5	0.3
HV204704	-2.12	0.09	0.27	-1.18	0.39	0.04	7013	241	6526	563	48	2.4	1.3	0.2
HV210918	-2.49	0.08	0.20	-1.64	0.49	0.30	6730	222	6296	743	397	3.4	1.7	0.4
HID 76483	-	-	-	-0.32	0.47	0.16	-	-	8482	579	224	3.5	0.5	0.5
Secondary sample														
J054653	-2.00	0.09	0.20	-1.37	0.85	0.00	4515	45	6447	1456	0	1.8	2.5	0.0
J044339	-2.73	0.08	0.01	-2.11	0.40	0.90	6635	131	6179	524	940	3.7	1.7	0.5
J051213	-1.95	0.10	0.09	-1.57	0.87	0.00	6489	178	6182	1295	0	1.6	1.4	0.0
HITS091050	-2.19	0.07	0.27	-1.60	0.86	0.24	6525	141	5931	1111	332	2.9	2.5	0.8

The uncertainties derived for the stellar $[\text{Fe}/\text{H}]$ from spectrum synthesis range from ~ 0.10 to ~ 0.49 dex with a mean error of 0.34 dex and low scatter overall (0.02-0.30 dex), for the stars in the primary sample. For the stars in the secondary sample, the uncertainties are larger in general, with a mean of ~ 0.70 dex (these large errors are one of the reasons for them to be considered in the secondary sample). In contrast, the $[\text{Fe}/\text{H}]$ values obtained from empirical models (Section 4.3.2) display a mean propagated uncertainty of ~ 0.10 dex for both the primary and the secondary sample, displaying a scatter between methods that ranges from 0.02 to 0.42 dex. We note that the $[\text{Fe}/\text{H}]$ values derived from spectrum synthesis are systematically more metal-rich than those from scaling methods, regardless of the metallicity scale used.

The resulting propagated error on the temperature is typically 400-600 K, whereas the scatter of the derived T_{eff} for this sample ranges from 10 K to 400 K, and lies below 70 K for three stars. The stars in the secondary sample display, on the other hand, a mean uncertainty of about twice that of the primary sample. We note in passing that for J054653 neither the estimations of Section 4.3.2 nor the spectrum synthesis comparison gave satisfactory results. We thus consider it a secondary sample star.

We observe a mean difference of ~ 100 K when comparing our derived spectroscopic and photometric temperatures (the latter being hotter), with a standard deviation of 460 K. This is consistent with the results of Mucciarelli & Bonifacio (2020), who found the spectroscopic T_{eff} from giant stars to be lower than the photometric ones, with discrepancies increasing with decreasing metallicity, and reaching differences of ~ 350 K at $[\text{Fe}/\text{H}] \sim -2.5$ dex (as shown in Figure 9 in their work). Mucciarelli & Bonifacio (2020) concluded that these differences cannot be interpreted as being due to systematic errors, and are likely due to the physics adopted for the spectroscopic studies. Thus, they rely on the choice between temperatures that reproduce the stellar flux and those that reproduce the depths of individual metallic lines.

Finally, we stress that the temperatures obtained here represent those at the moment of observation, and that the range of T_{eff} that an RRL can exhibit can easily reach 2,000 K (Peña et al., 2009; For et al., 2011b). For later reference, we list the observed phases in Table 4.1.

In the case of the stellar surface gravities, we were only able to derive them using spectrum synthesis. Thus, we use those values hereafter. The typical uncertainty on the derived $\log g$ for the stars in the primary sample is 0.8 dex (mean), and this group displays standard deviations (from the use of different order combinations) ranging from 0.2–0.6 dex. The uncertainties are significantly larger for the secondary sample, where the mean error exceeds 1 dex. As the overall uncertainties in the surface gravities are rather large, we highlight that the derived values of $\log g$ should be taken with caution. It is worth having in mind that, in general, the typical minimum-to-maximum variations of $\log g$ of RRLs throughout their pulsation cycle can reach values of ~ 1.5 dex (Peña et al., 2009; For et al., 2011b). Additionally, Mucciarelli & Bonifacio (2020) found that even for non-variable stars the discrepancies between spectroscopic and photometric surface gravities can be as high as ~ 1 dex. As a result, we loosely fix the $\log g$ of the secondary sample to ~ 2 dex (which is a reasonable assumption considering the work by For et al., 2011b) and only use this to complete our stellar parameters and metallicities. No abundances have been computed for the secondary sample owing to the large uncertainties in stellar parameters. In Figure 4.11, we display the

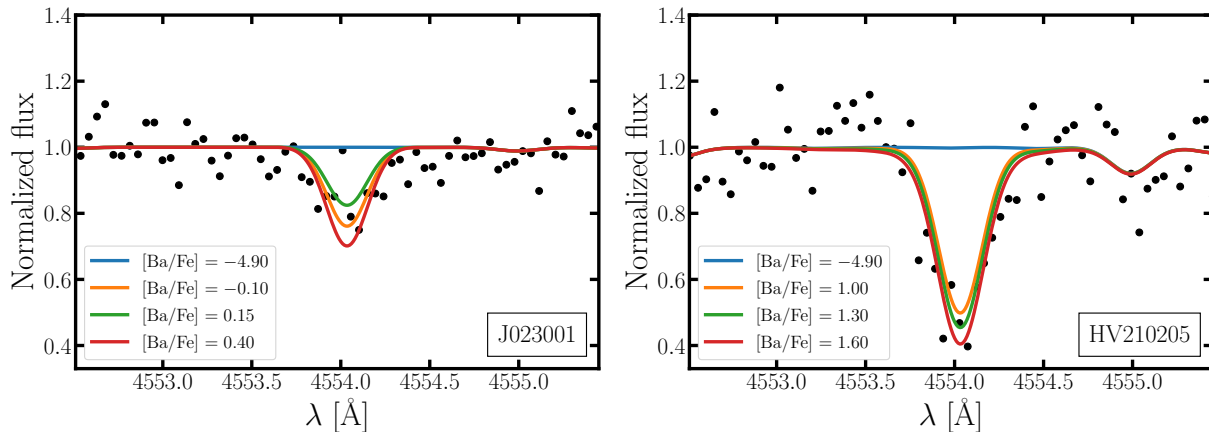


Figure 4.12: Ba absorption line at 4554.03 Å for two of the program RRLs (J023001 and HV210205 in the *top* and *bottom* panels, respectively), displaying the estimated $[\text{Ba}/\text{Fe}]$, illustrative variations around the estimated values (of 0.25 dex in the *top* panel and 0.30 dex in the *bottom* panel), and continuum levels.

derived stellar parameters and associated uncertainties for the stars in both samples.

4.3.5 Chemical abundances

In addition to determining the stellar parameters described above, we derive local thermodynamic equilibrium (LTE) abundances for O, Na, Mg, Ca, Ti II, Sr II, and Ba II employing the EW method. For this purpose, we used the direct integration of Gaussian profiles fitted to the observed lines using IRAF. We only use the lines if they appear clean, free of emission owing to the variability, and have a clearly defined continuum on at least one side of the line. The line list is taken from Hansen et al. (2011) and complemented with information from the National Institute of Standards and Technology (NIST) atomic spectra database⁴⁰. The abundances were derived using a Python implementation of MOOG with the input parameters reported in Section 4.3.3. Given that our program stars are faint, and as a consequence of overall low S/N, we are forced to mainly use strong lines (e.g., Fraunhofer lines).

We then checked the consistency of the results from the EW approach with spectrum syntheses from MOOG. For Ba II and Sr II, however, we relied on the use of synthetic spectra only, to handle the hyperfine splitting and isotopic substructure of the atomic lines considered. Figure 4.12 shows examples of the results of the abundance determination of Ba II in two of our stars, via synthetic spectra. In general, we disregarded lines with an EW larger than 300 mÅ, full-width-at-half-maximum outside the range 0.1–0.5, with shifts in central wavelength greater than 0.3 Å, or the ones that were based on unclear features, due to the noise or blends.

To estimate the uncertainties of individual line measurements, we varied the input parameters of the models ($[\text{Fe}/\text{H}]$, T_{eff} , and $\log g$) one by one based on their scatter while keeping the others fixed, and finally adding the variations in quadrature. On top of that, from the manual inspection of our spectra, we find that determining abundances at a level better than

⁴⁰<https://www.nist.gov/pml/atomic-spectra-database>

0.1–0.15 dex is, in general, unfeasible. Therefore, a systematic uncertainty, or a ground level for the errors, should be considered.

To correct for LTE departures, we used the online interface hosted by the Max-Planck-Institut für Astronomie (MPIA)⁴¹. These non-LTE (NLTE) corrections apply for O (Sitnova, Mashonkina, & Ryabchikova, 2013), Mg (Bergemann et al., 2017), Ca (Mashonkina, Korn, & Przybilla, 2007), and Ti (Bergemann, 2011).

We note in passing that the RRLs’ abundance ratios are not expected to vary significantly throughout their pulsation cycles (see, e.g., Figure 13 from For et al., 2011b), even if the changes in the RRLs’ effective temperatures amount to ~ 800 K. For spectra taken at phase $\phi \sim 0.35$, however, atomic lines are expected to suffer from minimal blending, and are therefore best suited for chemical composition analyses. On the other hand, observing RRLs at their descending/ascending branches is beneficial, for instance, for metal lines with low excitation potentials (that saturate at cooler parts of RRLs cycles), as they are weaker at hotter phases.

We compute abundance ratios $[X/Fe]$ relative to the solar abundances of Asplund et al. (2009). In Table 4.4, we provide the averaged abundance ratios for each element, weighted by our confidence in the line measurement (limits and saturated lines were given half weight and flagged in the list). Additionally, we list the dispersion of the abundances when more than one line is available and passed the aforementioned cuts. The line-by-line atomic data of the line list used is presented in Table C1, including excitation potentials, $\log gf$, EWs, individual abundances, and NLTE corrections.

4.3.6 Orbital analysis

We combine the radial velocities derived in Section 4.3.1 with proper motions in right ascension and declination (μ_α^* and μ_δ , respectively) from *Gaia* DR3 to estimate the orbital parameters and history of our sample of halo RRLs. We exclude three of the stars from this part of the analysis (HiTS101243, HiTS103943, and HiTS102414, at $d_H \sim 90, 110,$ and 165 kpc, respectively) as they are not listed in the *Gaia* catalogue. Together with the kinematic information of our targets, we take advantage of the RRLs being standard candles to obtain a precise distance estimation for each star. We estimated the heliocentric distance d_H of our RRLs by adopting the PLZ relation from Sesar et al. (2017), using the periods from Table 4.1 and the metallicities from Section 4.3.3. For the stars with no metallicity information, we adopted $[Fe/H] = -1.5$ as a reasonable representation of the Galactic halo metallicity distribution function (see e.g. Suntzeff, Kinman, & Kraft, 1991; Prantzos, 2008; Liu et al., 2018; Conroy et al., 2019).

In order to integrate the stellar orbits, we use the Python package GALPY (Bovy, 2015)⁴², adopting an *isolated* model MW potential consisting of a spherical nucleus and bulge (Hernquist potential), a Miyamoto-Nagai disc model, and a spherical Navarro-Frenk-White dark matter halo. In GALPY this corresponds to the *MWPotential2014*. We used a second potential (hereafter called *perturbed* potential) that takes into account the growing evidence of the perturbations caused by a massive LMC to the MW gravitational potential (van

⁴¹https://nlte.mpia.de/gui-siuAC_secE.php

⁴²<http://github.com/jobovy/galpy>

Table 4.4: Summary of the abundance ratios obtained in Section 4.3.5, for seven RRLs in our sample. For each element measured, the weighted mean is shown, in addition to its propagated uncertainty, standard deviation, and number of lines used. We use the symbol $<$ to flag abundances that we consider limits.

ID	$[\alpha/\text{Fe}]$	e $[\alpha/\text{Fe}]$	σ $[\alpha/\text{Fe}]$	N α	$[\text{Na}/\text{Fe}]$	e $[\text{Na}/\text{Fe}]$	σ $[\text{Na}/\text{Fe}]$	N Na
J023001	0.35	0.25	0.15	12	0.00	0.15	0.15	2
J034239	0.40	0.30	0.10	8	–	–	–	–
J050902	–0.05	0.20	0.15	8	< -0.50	0.20	–	1
HV205840	–0.20	0.25	0.20	6	–0.60	0.25	0.15	2
J040422	0.60	0.40	0.10	8	–	–	–	–
HV210205	0.40	0.15	0.10	10	0.25	0.15	–	1
HV204704	0.25	0.10	0.15	11	0.30	0.10	0.10	2

$[\text{O}/\text{Fe}]$	e $[\text{O}/\text{Fe}]$	σ $[\text{O}/\text{Fe}]$	N O	$[\text{Mg}/\text{Fe}]$	e $[\text{Mg}/\text{Fe}]$	σ $[\text{Mg}/\text{Fe}]$	N Mg	$[\text{Ca}/\text{Fe}]$	e $[\text{Ca}/\text{Fe}]$	σ $[\text{Ca}/\text{Fe}]$	N Ca
< 0.65	0.3	0.15	2	0.25	0.20	0.05	5	< 0.45	0.15	–	1
0.45	0.30	–	1	0.30	0.35	–	1	< 0.10	0.10	–	1
–0.10	0.20	–	1	–0.05	0.20	0.15	3	–0.10	0.20	0.20	2
–	–	–	–	–0.25	0.25	0.15	5	–	–	–	–
0.60	0.35	0.10	2	0.55	0.40	0.20	2	–	–	–	–
0.25	0.15	0.05	2	0.45	0.20	0.10	5	0.45	0.10	0.15	3
0.30	0.15	0.15	3	0.30	0.05	0.15	3	0.05	0.05	0.15	2

$[\text{Ti}/\text{Fe}]$	e $[\text{Ti}/\text{Fe}]$	σ $[\text{Ti}/\text{Fe}]$	N Ti	$[\text{Sr}/\text{Fe}]$	e $[\text{Sr}/\text{Fe}]$	σ $[\text{Sr}/\text{Fe}]$	N Sr	$[\text{Ba}/\text{Fe}]$	e $[\text{Ba}/\text{Fe}]$	σ $[\text{Ba}/\text{Fe}]$	N Ba
0.35	0.30	0.05	4	–	–	–	–	0.15	0.25	–	1
0.40	0.30	0.10	5	< 0.45	0.15	–	1	0.35	0.25	0.30	2
0.10	0.20	0.00	2	< 0.10	0.20	–	1	< 0.20	0.20	–	1
0.05	0.35	–	1	< 1.15	0.25	0.05	2	–	–	–	–
0.65	0.40	0.05	4	0.40	0.40	0.05	2	0.55	0.40	–	1
–	–	–	–	< 1.40	0.15	0.05	2	< 1.45	0.15	0.2	2
0.30	0.10	0.15	3	< 1.45	0.10	–	1	< 0.25	0.10	–	1

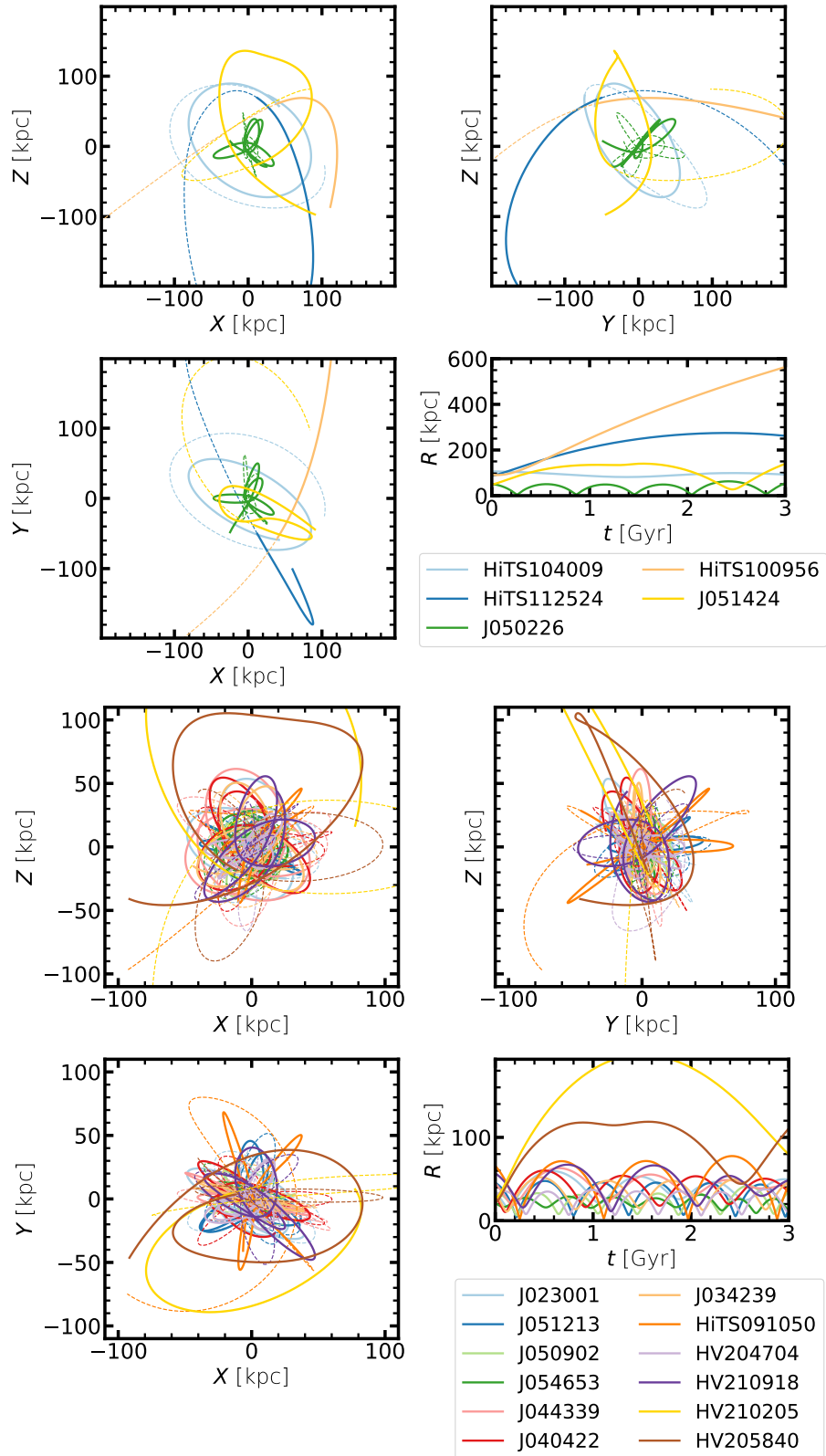


Figure 4.13: Orbits of the 17 stars for which we possess 3D kinematic information, computed with GALPY, accounting for the LMC infall, and integrated for 3 Gyr forward and backward (solid and dashed lines, respectively). The *top* panels show the five RRLs observed in our first run (with lower spectral resolution and S/N), and the *bottom* panels show the RRLs from our second run. These figures illustrate that the gravitational perturbation of the LMC can affect the orbit of the stars significantly in some cases (e.g., J051424 and HV205840).

der Marel & Kallivayalil, 2014; Laporte et al., 2018; Erkal et al., 2018; Erkal & Belokurov, 2020; Vasiliev, Belokurov, & Erkal, 2021; Cunningham et al., 2020). For the LMC, we adopted a right ascension and declination of 78.77 deg and -69.01 deg, respectively, a distance $d_{\text{LMC}} = 49.6$ kpc (Pietrzyński et al., 2019), proper motions $\mu_{\alpha^*} = 1.85$ mas yr $^{-1}$ and $\mu_{\delta} = 0.234$ mas yr $^{-1}$ (Gaia Collaboration et al., 2018), and 262.2 km s $^{-1}$ as its systemic line-of-sight velocity (van der Marel et al., 2002). Additionally, we multiply the MW halo mass by 1.5 for the isolated and the perturbed potentials to correct for the fact that the LMC is unbound in *MWPotential2014*⁴³.

For the mass of the LMC we adopted a value of $1.88 \times 10^{11} M_{\odot}$, based on the recent estimation of Shipp et al. (2021) from stellar streams. In addition, we assumed a scale length $a_{\text{LMC}} = 20.22$ kpc, with which the input parameters used match the observed circular velocity 91.7 km s $^{-1}$ at 8.7 kpc from the LMC centre (van der Marel & Kallivayalil, 2014). Given that the LMC is a massive MW satellite, we decided to take the Chandrasekhar dynamical friction into account for its orbit integration. In this work, we ignore the impact of other massive perturbers of the MW potential, such as the Sagittarius dSph.

For the isolated potential, we integrate the orbits for 10 Gyr backward and forward, with a step size of 1 Myr. In the case of the perturbed potential, the integrations are limited to 3 Gyr in both directions, assuming that the perturbations in the MW potential beyond these limits are likely not significant. In order to obtain uncertainties for the derived orbital parameters, we draw 100 input parameters assuming Gaussian distributions and using the covariance matrices of the stars, from the *Gaia* DR3 catalogue. Then, we select the median value of the resulting parameters, and the 16 and 84 percentiles as errors to represent the asymmetry of their distributions. Finally, we treat the fraction of bound solutions over the total number of integrated orbits as a proxy of the bound likelihood for each star.

Figure 4.13 displays the resulting orbits for the *MWPotential2014* perturbed by the infall of the LMC. The figure illustrates that the majority of the stars' orbits are not significantly affected by the choice of the potential, with a few exceptions (HV205840, HV210918, and J051424). Figure 4.13 also shows RRLs with loosely bound orbits, namely HiTS112524 and HiTS100956. A detailed model of the orbits computed for a subsample of our stars is provided in the appendix (from Figure C3 to C6). Tables 4.5 and 4.6 summarize the main orbital parameters of our target stars, obtained from the isolated and the perturbed potential, respectively.

⁴³Following <https://docs.galpy.org/en/v1.5.0/orbit.html>

Table 4.5: Orbital parameters of the stars in our sample, integrated for 3 Gyr using GALPY's *MWPotential2014*.

ID	d_{H} (kpc)	R (kpc)	μ_{α^*} (mas yr $^{-1}$)	μ_{δ} (mas yr $^{-1}$)	V (km s $^{-1}$)	E (10^5 km 2 s $^{-2}$)	L (10^3 kpc km s $^{-1}$)	r_{peri} (kpc)	r_{apo} (kpc)	e	Orb. Period (Myr)	Bound Likelihood
HITS104009	105 ± 5	107 $^{+2}$ ₋₆	-0.53 ± 1.09	-0.26 ± 1.25	168.6 $^{+85.4}$ _{-36.8}	0.25 $^{+0.15}$ _{-0.07}	19.04 $^{+7.46}$ _{-4.78}	90 $^{+15}$ ₋₃₆	120 $^{+180}$ ₋₁₂	0.37 $^{+0.22}$ _{-0.14}	2.77 $^{+3.76}$ _{-0.73}	0.13
HITS112524	86 ± 4	86 $^{+4}$ ₋₄	-0.84 ± 0.88	-0.81 ± 0.63	231.7 $^{+35.6}$ _{-113.5}	0.27 $^{+0.11}$ _{-0.18}	18.14 $^{+5.01}$ _{-10.40}	71 $^{+10}$ ₋₅₀	153 $^{+131}$ ₋₅₄	0.50 $^{+0.15}$ _{-0.13}	3.02 $^{+2.80}$ _{-1.58}	0.24
J050226	48 ± 2	51 $^{+2}$ ₋₂	0.39 ± 0.19	-0.42 ± 0.22	88.4 $^{+37.5}$ _{-27.6}	-0.16 $^{+0.04}$ _{-0.03}	3.66 $^{+2.22}$ _{-1.62}	9 $^{+8}$ ₋₅	53 $^{+2}$ ₋₂	0.72 $^{+0.15}$ _{-0.18}	0.67 $^{+0.08}$ _{-0.05}	1.00
HITS100956	89 ± 4	92 $^{+4}$ ₋₄	-0.24 ± 0.73	0.38 ± 0.67	228.9 $^{+45.6}$ _{-34.5}	0.30 $^{+0.11}$ _{-0.18}	19.87 $^{+4.90}$ _{-5.37}	79 $^{+8}$ ₋₄₆	172 $^{+158}$ ₋₁₇₈	0.47 $^{+0.22}$ _{-0.13}	3.49 $^{+3.40}$ _{-3.87}	0.29
J051424	47 ± 2	48 $^{+2}$ ₋₂	1.42 ± 0.27	1.20 ± 0.28	316.7 $^{+49.9}$ _{-23.2}	0.26 $^{+0.13}$ _{-0.06}	14.36 $^{+2.58}$ _{-0.99}	44 $^{+3}$ ₋₃	169 $^{+74}$ ₋₈	0.60 $^{+0.21}$ _{-0.15}	2.87 $^{+1.25}$ _{-0.72}	0.64
J023001	30 ± 2	36 $^{+2}$ ₋₂	-0.17 ± 0.18	-1.57 ± 0.14	225.1 $^{+23.4}$ _{-40.0}	-0.11 $^{+0.05}$ _{-0.04}	5.90 $^{+0.98}$ _{-2.23}	17 $^{+4}$ ₋₄	56 $^{+8}$ ₋₆	0.55 $^{+0.03}$ _{-0.13}	0.79 $^{+0.10}$ _{-0.07}	1.00
J051213	39 ± 2	46 $^{+2}$ ₋₂	0.45 ± 0.24	-0.53 ± 0.22	93.4 $^{+22.0}$ _{-21.1}	-0.20 $^{+0.04}$ _{-0.03}	3.02 $^{+1.40}$ _{-0.73}	7 $^{+8}$ ₋₄	48 $^{+2}$ ₋₂	0.75 $^{+0.24}$ _{-0.11}	0.61 $^{+0.07}$ _{-0.05}	1.00
J050902	26 ± 1	32 $^{+1}$ ₋₁	0.29 ± 0.16	-1.08 ± 0.13	99.3 $^{+21.2}$ _{-19.2}	-0.36 $^{+0.03}$ _{-0.06}	3.09 $^{+0.70}$ _{-0.56}	8 $^{+3}$ ₋₃	32 $^{+1}$ ₋₁	0.61 $^{+0.11}$ _{-0.11}	0.42 $^{+0.03}$ _{-0.03}	1.00
J054653	14 ± 1	22 $^{+1}$ ₋₁	4.35 ± 0.31	-0.81 ± 0.27	239.8 $^{+19.2}$ _{-11.8}	-0.31 $^{+0.04}$ _{-0.04}	4.82 $^{+0.56}$ _{-1.34}	17 $^{+2}$ ₋₂	30 $^{+4}$ ₋₂	0.29 $^{+0.02}$ _{-0.03}	0.47 $^{+0.07}$ _{-0.04}	1.00
J044339	38 ± 2	45 $^{+2}$ ₋₂	0.02 ± 0.18	-1.38 ± 0.17	203.3 $^{+19.7}$ _{-22.5}	-0.05 $^{+0.05}$ _{-0.06}	6.83 $^{+1.33}$ _{-1.08}	20 $^{+5}$ ₋₄	64 $^{+7}$ ₋₇	0.53 $^{+0.03}$ _{-0.04}	0.93 $^{+0.14}$ _{-0.16}	1.00
J040422	25 ± 1	31 $^{+1}$ ₋₁	-0.01 ± 0.17	-1.98 ± 0.13	253.3 $^{+12.7}$ _{-16.3}	-0.10 $^{+0.04}$ _{-0.05}	4.37 $^{+0.66}$ _{-0.62}	10 $^{+2}$ ₋₃	62 $^{+5}$ ₋₆	0.71 $^{+0.03}$ _{-0.05}	0.80 $^{+0.09}$ _{-0.10}	1.00
J034239	27 ± 1	33 $^{+1}$ ₋₁	0.24 ± 0.17	-2.08 ± 0.13	219.0 $^{+16.9}$ _{-15.7}	-0.16 $^{+0.04}$ _{-0.04}	4.32 $^{+0.62}$ _{-0.62}	11 $^{+2}$ ₋₂	52 $^{+6}$ ₋₆	0.66 $^{+0.05}$ _{-0.12}	0.69 $^{+0.07}$ _{-0.07}	1.00
HITS091050	61 ± 3	66 $^{+3}$ ₋₃	0.02 ± 0.28	-0.54 ± 0.25	154.3 $^{+17.6}$ _{-13.2}	0.02 $^{+0.08}$ _{-0.03}	5.19 $^{+2.07}$ _{-0.50}	12 $^{+18}$ ₋₆	85 $^{+14}$ ₋₅	0.75 $^{+0.20}$ _{-0.10}	1.13 $^{+0.38}$ _{-0.09}	1.00
HV204704	35 ± 1	30 $^{+1}$ ₋₁	-0.07 ± 0.14	-1.80 ± 0.11	149.3 $^{+13.2}$ _{-9.5}	-0.32 $^{+0.03}$ _{-0.03}	2.59 $^{+0.50}$ _{-0.89}	6 $^{+2}$ ₋₂	36 $^{+2}$ ₋₁	0.71 $^{+0.10}$ _{-0.06}	0.45 $^{+0.03}$ _{-0.04}	1.00
HV210918	62 ± 2	56 $^{+2}$ ₋₂	0.19 ± 0.39	-1.04 ± 0.34	179.4 $^{+54.6}$ _{-50.1}	0.02 $^{+0.11}$ _{-0.10}	9.07 $^{+3.79}$ _{-2.92}	31 $^{+14}$ ₋₈	67 $^{+27}$ ₋₁₈	0.41 $^{+0.26}$ _{-0.13}	1.14 $^{+0.52}$ _{-0.30}	0.99
HV210205	32 ± 1	27 $^{+1}$ ₋₁	-2.38 ± 0.15	-2.29 ± 0.11	394.6 $^{+26.0}$ _{-20.9}	0.28 $^{+0.11}$ _{-0.09}	10.47 $^{+0.83}$ _{-0.83}	26 $^{+1}$ ₋₁	200 $^{+143}$ ₋₆₁	0.76 $^{+0.09}$ _{-0.08}	3.21 $^{+2.87}$ _{-1.06}	0.80
HV205840	27 ± 1	22 $^{+1}$ ₋₁	-2.77 ± 0.10	-2.38 ± 0.09	393.8 $^{+16.7}$ _{-18.5}	0.19 $^{+0.08}$ _{-0.09}	8.58 $^{+0.70}$ _{-0.70}	22 $^{+1}$ ₋₁	140 $^{+36}$ ₋₃₈	0.73 $^{+0.06}$ _{-0.07}	2.09 $^{+0.67}$ _{-0.62}	1.00

Table 4.6: Orbital parameters of the stars in our sample, integrated for 3 Gyr using the perturbed potential.

ID	d_H (kpc)	R (kpc)	μ_{α^*} (mas yr $^{-1}$)	μ_δ (mas yr $^{-1}$)	V (km s $^{-1}$)	E (10 5 km 2 s $^{-2}$)	L (10 3 kpc km s $^{-1}$)	r_{peri} (kpc)	r_{apo} (kpc)	e	Orb. Period (Myr)	Bound Likelihood
HITS104009	105 \pm 5	105 $^{+5}_{-5}$	-0.53 \pm 1.09	-0.26 \pm 1.25	196.5 $^{+72.0}_{-45.6}$	0.19 $^{+0.18}_{-0.05}$	19.77 $^{+7.69}_{-3.40}$	53 $^{+33}_{-17}$	109 $^{+113}_{-5}$	0.44 $^{+0.23}_{-0.14}$	1.57 $^{+2.68}_{-1.38}$	0.13
HITS112524	86 \pm 4	86 $^{+4}_{-3}$	-0.84 \pm 0.88	-0.81 \pm 0.63	255.1 $^{+34.1}_{-83.2}$	0.26 $^{+0.11}_{-0.16}$	19.59 $^{+4.36}_{-6.30}$	48 $^{+16}_{-23}$	155 $^{+86}_{-51}$	0.57 $^{+0.09}_{-0.17}$	2.42 $^{+1.98}_{-0.93}$	0.34
J050226	48 \pm 2	51 $^{+3}_{-2}$	0.39 \pm 0.19	-0.42 \pm 0.22	94.5 $^{+31.6}_{-26.8}$	-0.33 $^{+0.05}_{-0.13}$	4.13 $^{+1.98}_{-1.70}$	9 $^{+7}_{-5}$	54 $^{+10}_{-3}$	0.72 $^{+0.17}_{-0.17}$	0.61 $^{+0.19}_{-0.12}$	1.00
HITS100956	89 \pm 4	90 $^{+5}_{-2}$	-0.24 \pm 0.73	0.38 \pm 0.67	235.1 $^{+68.9}_{-103.5}$	0.25 $^{+0.13}_{-0.19}$	21.12 $^{+5.38}_{-11.88}$	68 $^{+10}_{-40}$	170 $^{+209}_{-156}$	0.52 $^{+0.17}_{-0.12}$	2.91 $^{+4.50}_{-1.95}$	0.32
J051424	47 \pm 2	47 $^{+2}_{-2}$	1.42 \pm 0.27	1.20 \pm 0.28	332.5 $^{+49.9}_{-48.9}$	0.03 $^{+0.12}_{-0.06}$	15.23 $^{+2.37}_{-1.85}$	43 $^{+7}_{-4}$	200 $^{+126}_{-94}$	0.67 $^{+0.15}_{-0.02}$	3.38 $^{+2.11}_{-0.21}$	0.88
J023001	30 \pm 2	35 $^{+3}_{-1}$	-0.17 \pm 0.18	-1.57 \pm 0.14	225.3 $^{+19.9}_{-21.2}$	-0.22 $^{+0.06}_{-0.05}$	5.78 $^{+1.65}_{-1.01}$	16 $^{+4}_{-4}$	59 $^{+9}_{-5}$	0.58 $^{+0.03}_{-0.03}$	0.75 $^{+0.21}_{-0.21}$	1.00
J051213	39 \pm 2	46 $^{+1}_{-1}$	0.45 \pm 0.24	-0.53 \pm 0.22	101.7 $^{+21.2}_{-24.0}$	-0.33 $^{+0.04}_{-0.03}$	3.64 $^{+1.38}_{-1.69}$	6 $^{+4}_{-5}$	49 $^{+11}_{-3}$	0.77 $^{+0.18}_{-0.09}$	0.52 $^{+0.26}_{-0.08}$	1.00
J050902	26 \pm 1	32 $^{+1}_{-1}$	0.29 \pm 0.16	-1.08 \pm 0.13	101.0 $^{+19.4}_{-17.2}$	-0.49 $^{+0.03}_{-0.03}$	3.05 $^{+0.79}_{-0.55}$	3 $^{+2}_{-2}$	44 $^{+4}_{-8}$	0.87 $^{+0.06}_{-0.07}$	0.41 $^{+0.05}_{-0.22}$	1.00
J054653	14 \pm 1	22 $^{+1}_{-1}$	4.35 \pm 0.31	-0.81 \pm 0.27	241.8 $^{+16.1}_{-12.5}$	-0.43 $^{+0.05}_{-0.06}$	4.91 $^{+0.46}_{-0.41}$	12 $^{+4}_{-4}$	43 $^{+7}_{-12}$	0.57 $^{+0.07}_{-0.13}$	0.43 $^{+0.22}_{-0.14}$	1.00
J044339	38 \pm 2	45 $^{+2}_{-2}$	0.02 \pm 0.18	-1.38 \pm 0.17	196.7 $^{+25.2}_{-18.8}$	-0.18 $^{+0.04}_{-0.05}$	6.50 $^{+1.31}_{-0.96}$	18 $^{+5}_{-4}$	63 $^{+9}_{-5}$	0.55 $^{+0.06}_{-0.06}$	0.91 $^{+0.14}_{-0.16}$	1.00
J040422	25 \pm 1	32 $^{+1}_{-1}$	-0.01 \pm 0.17	-1.98 \pm 0.13	255.1 $^{+18.8}_{-19.2}$	-0.21 $^{+0.05}_{-0.04}$	4.52 $^{+0.96}_{-0.58}$	11 $^{+2}_{-2}$	61 $^{+8}_{-3}$	0.70 $^{+0.05}_{-0.02}$	0.79 $^{+0.16}_{-0.13}$	1.00
J034239	27 \pm 1	33 $^{+1}_{-1}$	0.24 \pm 0.17	-2.08 \pm 0.13	214.6 $^{+15.2}_{-15.7}$	-0.28 $^{+0.04}_{-0.04}$	4.31 $^{+0.82}_{-0.58}$	11 $^{+2}_{-2}$	53 $^{+3}_{-3}$	0.66 $^{+0.02}_{-0.02}$	0.58 $^{+0.13}_{-0.08}$	1.00
HITS091050	61 \pm 3	66 $^{+3}_{-3}$	0.02 \pm 0.28	-0.54 \pm 0.25	155.7 $^{+33.7}_{-31.7}$	-0.06 $^{+0.06}_{-0.04}$	5.50 $^{+2.82}_{-2.79}$	12 $^{+13}_{-9}$	83 $^{+16}_{-10}$	0.73 $^{+0.19}_{-0.19}$	1.13 $^{+0.48}_{-0.10}$	1.00
HV204704	35 \pm 1	30 $^{+1}_{-1}$	-0.07 \pm 0.14	-1.80 \pm 0.11	145.4 $^{+12.0}_{-11.5}$	-0.46 $^{+0.03}_{-0.03}$	2.32 $^{+0.66}_{-0.84}$	3 $^{+4}_{-2}$	38 $^{+3}_{-1}$	0.88 $^{+0.10}_{-0.18}$	0.34 $^{+0.10}_{-0.07}$	1.00
HV210918	62 \pm 2	57 $^{+2}_{-2}$	0.19 \pm 0.39	-1.04 \pm 0.34	160.9 $^{+58.2}_{-43.8}$	-0.12 $^{+0.12}_{-0.06}$	8.18 $^{+4.14}_{-3.11}$	14 $^{+6}_{-7}$	89 $^{+72}_{-110}$	0.76 $^{+0.10}_{-0.10}$	1.15 $^{+1.29}_{-0.45}$	0.99
HV210205	32 \pm 1	27 $^{+1}_{-1}$	-2.38 \pm 0.15	-2.29 \pm 0.11	400.8 $^{+35.3}_{-22.8}$	0.18 $^{+0.13}_{-0.09}$	10.70 $^{+3.11}_{-0.88}$	27 $^{+1}_{-1}$	201 $^{+110}_{-25}$	0.77 $^{+0.07}_{-0.03}$	3.85 $^{+1.45}_{-0.88}$	0.98
HV205840	27 \pm 1	22 $^{+1}_{-1}$	-2.77 \pm 0.10	-2.38 \pm 0.09	392.3 $^{+13.0}_{-21.9}$	0.06 $^{+0.07}_{-0.11}$	8.52 $^{+0.53}_{-0.81}$	22 $^{+1}_{-1}$	147 $^{+54}_{-60}$	0.74 $^{+0.06}_{-0.12}$	2.64 $^{+1.14}_{-1.68}$	1.00

4.4 Results

Given that the dynamical time-scales in the outer halo are long, the partial phase-mixing of accreted systems allows for the detection of tidal disruption signatures as overdensities (e.g., [Haywood et al., 2018](#)). Thus, halo stars with a common origin (same progenitor) tend to share similar orbital parameters and kinematics (e.g., [Belokurov et al., 2018b](#)), even if these stars do not lie close to each other when projected on-sky (e.g., [Hanke et al., 2020b](#)). In addition, chemical tagging allows one to trace back the stars’ origins to their parent populations, based on their shared elemental abundances pattern (e.g., [Freeman & Bland-Hawthorn, 2002](#); [Buder et al., 2022](#)), as stated in Chapter 1. Assessing especially the stellar $[\alpha/\text{Fe}]$ vs. $[\text{Fe}/\text{H}]$ is a useful chemical diagnostic, as the level of the α -element abundance ratio can help separate in-situ from ex-situ formed stars. Thus, with multi-dimensional stellar chemodynamics it is possible to hypothesize about the origin of a star by looking at tentative associations with known substructures.

Here we compare the resulting chemical abundances and orbital parameters of our target RRLs to those of MW halo stars. For these comparisons, we use data from the APOGEE survey (DR16; [Ahumada et al., 2020](#)) combined with distances from the Bayesian isochrone-fitting code StarHorse ([Queiroz et al., 2020](#)), to select stars from the halo program with metallicities $[M/\text{H}]$ between -5.0 and -1.0 , and Cartesian coordinates $Z > 2$ kpc. Subsequently, we computed the orbits of these stars following the procedure described in Section 4.3.6.

A brief chemodynamical description of a subsample of our program stars, including individual orbits and chemical abundance ratios, is presented in the appendix (Section C2).

4.4.1 Chemical comparison

In this section we compare our stellar abundances to other studies to expand on the chemical origin of our metal-poor RRLs. As tracers we have selected elements with strong lines that carry information on the early nucleosynthesis in the MW’s outskirts. Using α -elements (O, Mg, Ca, and Ti), we can comment on the mass of the previous SNe progenitors as well as the stellar origin (in situ vs. accreted). Combining these abundances with heavy element abundances of neutron-capture elements (Sr and Ba) from intrinsically strong lines, we can assess the early production of such heavy elements in the most remote parts of the Galaxy.

Figure 4.14 depicts the abundance of α -elements with respect to Fe as a function of $[\text{Fe}/\text{H}]$. These quantities are computed as the average of O, Mg, Ca, and Ti, weighted by their uncertainties. In Figure 4.15, we display individual element abundance ratios (α , Na, Ba, and Sr), and compare them with those from field RRLs ([For et al., 2011b](#)), halo stars (from APOGEE and [Hansen et al. 2012](#)), and stars from massive mergers (GSE and Sequoia; [Aguado et al., 2021](#)).

As explained in Chapter 1, several Galactic chemical evolution studies have shown that the Galactic halo follows a bimodal α -element abundance trend, $[\alpha/\text{Fe}]$ (see e.g. [Nissen & Schuster, 2010](#); [Ivezić, Beers, & Jurić, 2012](#)). The outer halo shows, owing to it being predominantly accreted, lower α -element abundances while the inner halo tends to exhibit higher abundances of the α -elements. This roots in a less efficient star formation history typically causing fewer (and/or less) massive SNe events owing to the poorer gas reservoir

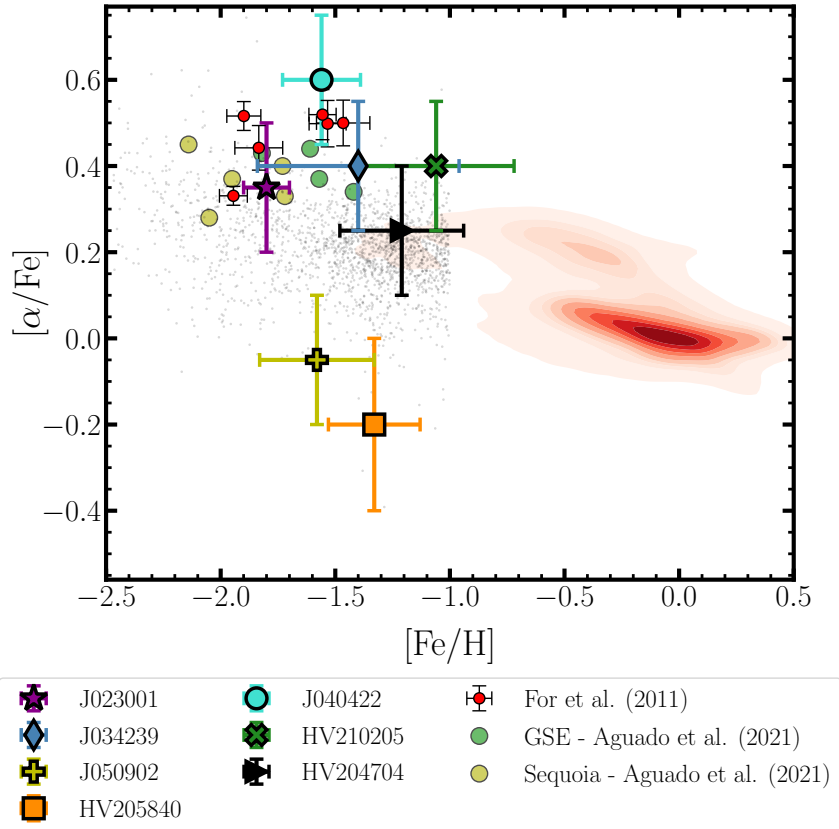


Figure 4.14: Relative abundance of α -elements as a function of $[\text{Fe}/\text{H}]$ for our target stars, computed assuming LTE. APOGEE-based abundance patterns of the MW non-halo and halo populations are displayed as red contours and grey dots, respectively. The red filled circles represent the chemical abundances of the RRLs studied by For et al. (2011b), whereas those corresponding to stars in GSE and Sequoia (from Aguado et al., 2021) are plotted in green and yellow, respectively. The error bars in the abundances represent their standard deviations σ from Table 4.4. It is clear from this figure that two of our RRLs, HV205840 and J050902, display an underabundance of α -elements for their metallicity.

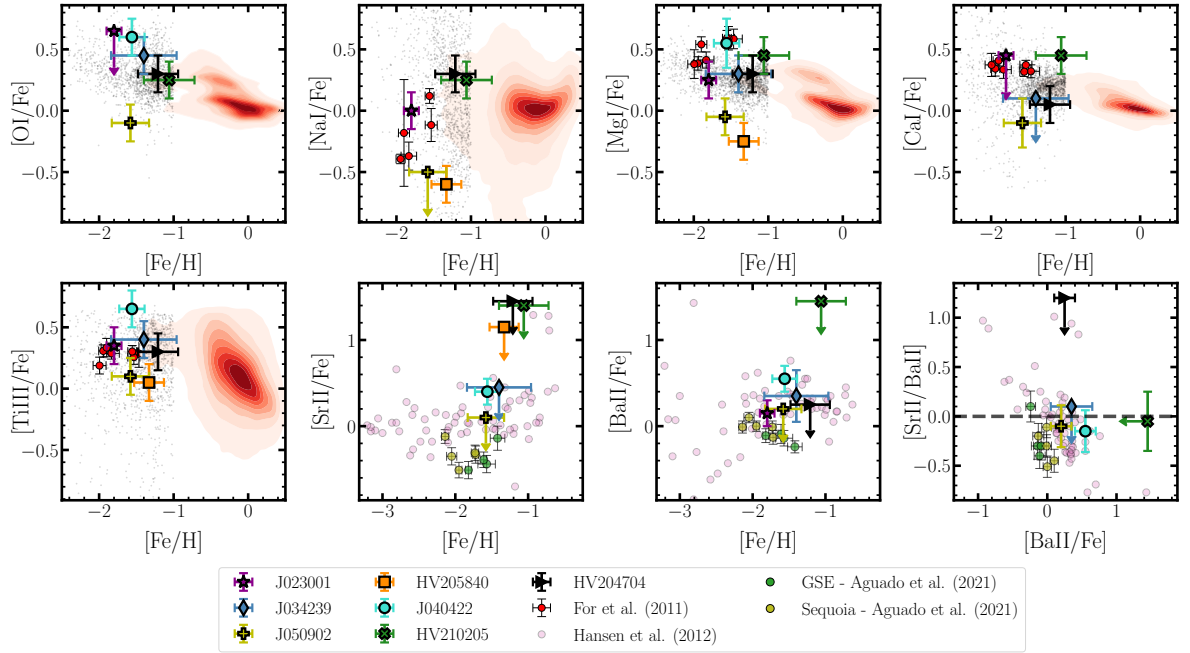


Figure 4.15: Same as Figure 4.14, but showing the abundance ratios of individual elements as a function of iron abundance. The *bottom right* panel includes a dashed horizontal line representing Solar values as a reference. An arrow of arbitrary length (0.3) is used instead of error bars for the abundances considered upper limits. These panels show the similarities in abundance patterns between different groups of RRLs (e.g., J050902 and HV205840, and HV210205 and HV204704), which we use in Section 4.5 to speculate about their origins.

and/or stronger gas loss due to winds in the accreted dwarf galaxies. Thus, the mass of the SN directly correlates with the amount of ejected α -elements (Tinsley & Larson, 1978), and tidal remnants tend to show lower $[\alpha/\text{Fe}]$ ratios at a given (low) $[\text{Fe}/\text{H}]$ than stars formed in-situ (see, e.g., Lanfranchi, Matteucci, & Cescutti, 2008; Sakari et al., 2019).

In our sample, J050902 and HV205840 show lower α abundance ratios as compared with normal halo stars at their metallicity, thus suggesting an accreted origin. We note that taking into account NLTE corrections for O, Mg, and Ti does not significantly change the apparent α -poor nature of these stars. J034239, J023001, J040422, HV210205, and HV204704, on the other hand, show enhanced Na and α -abundances (Mg, Ca, O, and Ti) that are comparable with halo stars, which suggests an in-situ formation.

Numerous studies have shown that the heavy neutron-capture elements exhibit a large star-to-star scatter in the halo (e.g., Aoki et al., 2013). We measure the abundance of two such elements, Sr and Ba, owing to the strong transitions in the blue/visual part of the spectra (as seen in Figure C1). Both Sr and Ba can be produced by either of the neutron-capture processes - namely the slow and the rapid n-capture process. However, keeping in mind that our RRL sample focuses on old, low-mass stars, it is unlikely that we are tracing s -process yields from AGB stars (Käppeler et al., 2011; Karakas & Lattanzio, 2014), but rather see the early production made by the r -process. The r -process is associated with neutron star mergers or rare magneto-hydrodynamic supernova explosions (MHD SN), as

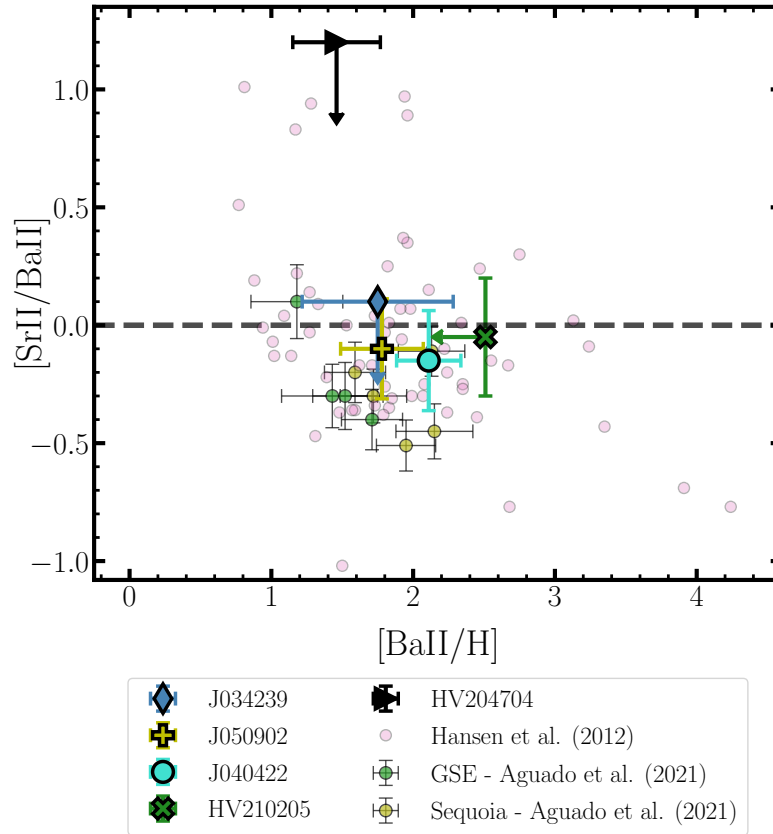


Figure 4.16: Abundance ratios of the n-capture process elements Sr and Ba of our stars and those from [Aguado et al. \(2021\)](#) and [Hansen et al. \(2012\)](#). The solar $[\text{Sr II}/\text{Ba II}]$ value is depicted as a dashed horizontal line for reference. An arrow of arbitrary length (0.3) is used instead of error bars for HV204704 and J034239, to represent that their Sr measurement are upper limits. For HV204704, the high $[\text{Sr}/\text{Ba}]$ ratio could be indicative of a fast rotating massive star origin ([Frischknecht et al., 2016](#)).

shown in the recent review by [Cowan et al. \(2021\)](#). When comparing the n-capture process element abundances of our sample, Sr and Ba (those that are not merely limits), to the halo sample of [Hansen et al. \(2012\)](#) we find that J034239 and J050902 follow the halo-like trend for both elements. This is depicted in Figure 4.16. For HV204704, even though we are only able to derive upper limits for Sr, the high $[\text{Sr}/\text{Ba}]$ ratio could be indicative of yet another origin of these heavy elements, namely fast rotating massive stars that produce (relatively) more Sr than Ba in an early *s*-process ([Frischknecht et al., 2016](#)). The $[\text{Sr}/\text{Ba}]$ ratio also carries important nucleosynthetic information on metal-poor stars, as Sr and Ba can be produced in a number of different formation sites, as detailed above. This ratio has also been used to trace carbon-enhanced metal-poor (CEMP) stars, as these are bona fide second generation stars, and as such provide pure insight into the pristine gas composition and ejecta from the first stars. With a $[\text{Sr}/\text{Ba}] < 1.2$, HV204704 might belong to the CEMP-no group (CEMP stars with low abundances of n-capture elements; [Beers & Christlieb, 2005](#); [Yong et al., 2013](#); [Hansen et al., 2019](#)), however, the spectrum quality and high temperature of HV204704 prevented a detection of carbon. Another CEMP RRL candidate is HV210205.

In this case, however, both the Sr and Ba detections are considered upper limits. Thus, a detailed study of HV204704 and HV210205 is required to test their Sr and Ba formation scenario, along the same lines as the study of Kennedy et al. (2014) (who analysed CEMP RRLs).

4.4.2 Kinematics

The Toomre diagram illustrates the orbital velocity V_Y of stars against their velocity perpendicular to the Galactic rotation $\sqrt{V_X^2 + V_Z^2}$, where V_X , V_Y , and V_Z are the Cartesian velocity components relative to the local standard of rest (LSR). This diagram is usually used to distinguish between thin disc/thick disc, and halo populations based on their kinematics (see, e.g., Bensby, Feltzing, & Lundström, 2003; Venn et al., 2004; Nissen & Schuster, 2010), with a total velocity between 180 and 220 km s⁻¹ often used as a discriminant (e.g., Bonaca et al., 2017; Amarsi, Nissen, & Skúladóttir, 2019; Buder et al., 2019). Figure 4.17 (*right* panel) depicts the Toomre diagram for the studied RRLs and halo stars from APOGEE, and shows that the studied RRLs are roughly consistent with being halo stars.

It is also worth mentioning that MW halo stars' orbits consistent with satellite accretion or with retrograde motion could be an indication of an extragalactic origin (Roederer, Hattori, & Valluri, 2018; Sakari et al., 2018a, 2019). Figure 4.17 shows that approximately half of our sample consists of stars with retrograde orbits. We note that one of the stars with α -abundances below Solar (J050902) also displays a retrograde orbit, which supports the hypothesis of its accreted origin.

Lastly, the total velocity as a function of Galactocentric distance of the stars in our sample place them within the escape velocity limit for the MW when using both of the adopted potentials (Figure 4.17). Thus, the bound likelihood of the stars determined as the fraction of computed orbits with valid solutions is most likely only associated with their large proper motion uncertainties, and does not necessarily represent their actual bound/unbound status.

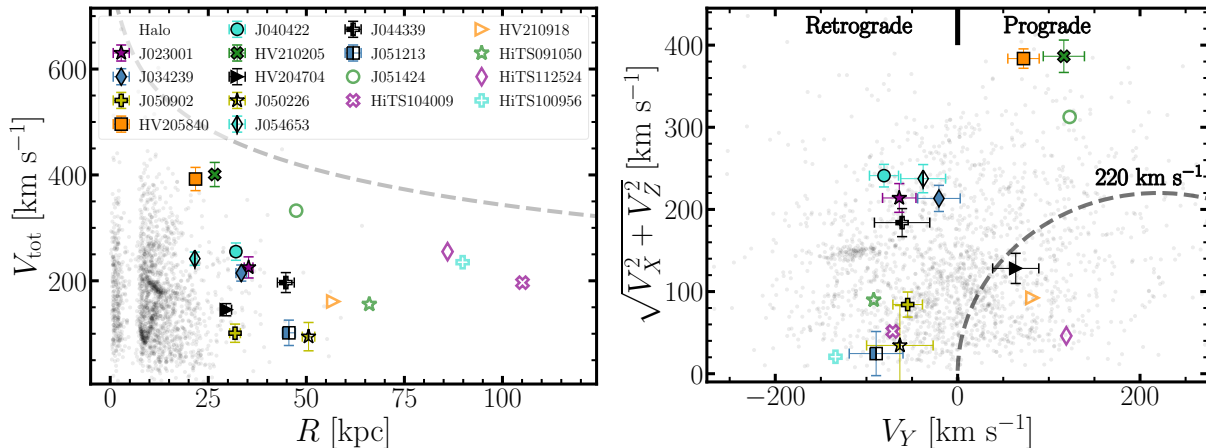


Figure 4.17: *Left:* Total velocity as a function of Galactocentric distance for the stars in our sample (large symbols) and halo stars from APOGEE (black dots), using the symbols defined in Figure 4.14. The dashed line represents the escape velocity from the MW when assuming a *MWPotential2014* as a reference. We see in this figure that all the stars in our sample have total velocities consistent with them being gravitationally bound to the MW. *Right:* Toomre diagram depicting $\sqrt{V_X^2 + V_Z^2}$ as a function of the orbital velocity V_Y . The dashed line marks the regions with $\sqrt{V_X^2 + (V_Y - 220)^2 + V_Z^2} > 220$ km s⁻¹, as a kinematic discriminant between MW halo and disc components. Stars from our primary sample are plotted with large (fully) filled symbols, whereas open symbols represent the stars with loosely constrained parameters. For clarity, the (large) uncertainties of the latter are not shown in these panels. From this figure we conclude that approximately half of our sample display retrograde orbits, suggesting accreted origins.

4.5 Discussion

One of the criteria used for the selection of our target RRLs was the length of their pulsation periods (see Section 4.2). Selecting RRLs based on their periods does not only allow for optimizing the observing strategy (e.g., allowing longer integration times), but can also be valuable to assess their connection with the accretion of MW satellites through the Oosterhoff classification (Oosterhoff, 1939). As a reminder, this dichotomy is not commonly observed in satellite galaxies (e.g., Catelan, 2009; Clementini, 2014; Martínez-Vázquez et al., 2017; Vivas et al., 2022), which are often classified as Oo-int (or OoII). Thus, although this is not a unique criterion and works best on large statistical samples, the agreement between the period of our RRLs and those of the Oo groups can provide additional hints about their origin.

Our sample consists of RRab stars with periods between 0.48 and 0.76 d, with a majority displaying pulsations longer than 0.60 d (85 per cent), and five stars (25 per cent) with periods ≥ 0.65 d. Thus, most of our stars could be classified as Oo-int or OoII. Here we inspect their derived chemical abundances and positions in phase space and compare them with those of known satellites and streams, looking for evidence of an accreted origin.

4.5.1 J051424 and the LMC

One of our stars, J051424, is located at the outskirts of the LMC, and has an heliocentric distance compatible with that of the LMC (~ 48 kpc). Here we analyse the possibility that J051424 is a member of this satellite galaxy.

J051424 lies close to the limits of the LMC’s asymmetrical (with respect to its distribution and dynamical centre) extended halo at ~ 8 kpc (9 deg) from its centre, in the region opposing the Magellanic bridge (Jacyszyn-Dobrzyniecka et al., 2017). This star has been catalogued as an LMC member by the Optical Gravitational Lensing Experiment team (OGLE; Soszyński et al., 2016)⁴⁴, under the ID LMC581.17.130 (or alternatively OGLE-LMC-RRLYR-30511). The proper motions of J051424, as listed in the *Gaia* DR3 catalogue ($\mu_\alpha^* = 1.42 \pm 0.27$ mas yr⁻¹, $\mu_\delta = 1.20 \pm 0.28$ mas yr⁻¹), are consistent with the proper motion distribution of the LMC (1.76 ± 0.45 mas yr⁻¹, 0.30 ± 0.64 mas yr⁻¹; Gaia Collaboration et al. 2021). There is also a rough agreement between J051424’s systemic line-of-sight velocity (228.2 ± 5.5 km s⁻¹) with the velocity distribution of the LMC (262.2 ± 3.4 km s⁻¹; van der Marel et al. 2002). The observed radial velocity difference might be attributable to the small number of observations (in phase) used to determine J051424’s systemic velocity.

We find a [Fe/H] from -2.34 to -2.57 dex when using the ΔS method on J051424 (based on Crestani et al., 2021b) from different line combinations, which is consistent with the spectroscopic metallicity range of LMC RRLs found by Haschke et al. (2012b) (from -1.97 to -2.67 dex). Additionally, from Haschke et al. (2012a), the metallicity distribution of the old component of the LMC from the Fourier decomposition of RRLs light curves is Gaussian, with a mean [Fe/H] of -1.22 and -1.49 dex (on the Jurcsik 1995 and Zinn & West 1984 scales, respectively), and a dispersion of 0.26 dex. Using a recent photometric metallicity calibration based on a large sample of RRLs with high-resolution metallicities (on data from Crestani et al. 2021a, For et al. 2011b, Chadid, Sneden, & Preston 2017, and Sneden et al. 2017), Dékány, Grebel, & Pojmański (2021) found these [Fe/H] values to be systematically overestimated by up to 0.4 dex. These authors find that the mode of the RRLs’ metallicity distribution function in the LMC is -1.83 dex, with a mean absolute error for individual stars of 0.16 dex from their calibration. We are not able to reliably estimate J051424’s [Fe/H] with other methods, nor other element abundances in this work to confirm/reject membership. However, we consider that J051424 is likely an LMC member, lying in the more metal-poor end of its metallicity distribution function.

4.5.2 J023001, Whiting 1, and Sagittarius

We discuss here the possibility that the RRL J023001 is a member of either the Galactic halo globular cluster Whiting 1 or the Sgr stream.

J023001 is located at $\sim 30.5 \pm 1.5$ kpc from the Sun, similar to the cluster Whiting 1 (Whiting, Hau, & Irwin, 2002), which is thought to be a former member of the disrupting Sgr dwarf spheroidal galaxy, and which is located at a heliocentric distance of $\sim 30.6 \pm 1.2$ kpc (Baumgardt & Vasiliev, 2021). Carraro (2005) estimated Whiting 1’s metallicity to be ~ -1.2 dex, whereas Carraro, Zinn, & Moni Bidin (2007) concluded that its [Fe/H] probably lies within the range of -0.4 to -1.1 . Both of these works determined the cluster’s

⁴⁴<http://www.astrouw.edu.pl/ogle/ogle4/OCVS/lmc/rrlyr>

metallicity by fitting isochrones to its colour-magnitude diagrams. This shows that the consistency of J023001’s metallicity, i.e., -1.2 ± 0.3 dex from synthesis and -1.8 ± 0.1 dex from EW measurements with that of Whiting 1 strongly depends on the literature value and the method used for the comparison. In any case, J023001 is located at 7 deg from Whiting 1’s centre, a comparatively large angular distance given the cluster’s angular radius (~ 0.5 arcmin; Dias et al., 2002; Carraro, 2005). Additionally, the cluster age estimated by Carraro, Zinn, & Moni Bidin (2007) is $6.5_{-0.5}^{+1.0}$ Gyr, which makes it one of the youngest globular clusters in the halo, and is incompatible with it hosting RRLs. The mean V magnitude of J023001 is 18.2, also incompatible with the horizontal branch position in the cluster’s colour-magnitude diagram.

The RRL J023001 also lies relatively close to the footprint of the Sgr stream, with a latitude-like coordinate (B_{Sgr}) of ~ 3 deg in the Sgr stream coordinate system (Majewski et al., 2003). Several authors have studied the chemical abundance patterns and orbital parameters of Sgr (e.g., Chou et al., 2007; Carlin et al., 2018; Hansen et al., 2018; Hayes et al., 2020; Johnson et al., 2020; del Pino et al., 2021; Hasselquist et al., 2021), including the identification of Sgr stream stars using APOGEE (Hasselquist et al., 2019). These studies have shown that the bulk of the $[\text{Fe}/\text{H}]$ distribution spans between -0.8 and 0 dex for Sgr’s core, that the Sgr stream’s $[\text{Fe}/\text{H}]$ is ~ 0.5 dex more metal-poor than its main body, and that the more metal-rich stars in Sgr display $[\text{X}/\text{Fe}]$ abundances below the MW abundance trends. Recently, Hasselquist et al. (2021) reported Sgr’s $[\alpha/\text{Fe}]$ to smoothly decline from the MW halo-like high- α plateau at the metal-poor end of its $[\text{Fe}/\text{H}]$ distribution ($[\alpha/\text{Fe}] > 0.2$ for $[\text{Fe}/\text{H}] < -1.5$) to below the MW low- α disc trend at $[\text{Fe}/\text{H}] > -1.0$ ⁴⁵. For J023001 we obtain $[\alpha/\text{Fe}] = 0.35 \pm 0.25$ (with a scatter of 0.15 dex). Additionally, Hasselquist et al. (2019) found the locus of the eccentricity e distribution of Sgr stream members to be between 0.4 and 0.7, and their apocentric distances r_{apo} to vary between 30 and 80 kpc (see their Figure 6). For J023001, we find $e \sim 0.55$ regardless of the adopted potential ($0.52_{-0.05}^{+0.05}$ for the perturbed model), and $r_{\text{apo}} \sim 70$ kpc (68_{-8}^{+15} kpc). Thus, our results indicate that J023001 is more likely to be associated with Sgr than Whiting 1.

4.5.3 Association with known substructures

Various studies have suggested that the bulk of the halo is built from accreted satellite systems and the heating of the disc (see, e.g., Robertson et al., 2005; Font et al., 2006; Naidu et al., 2020; Ibata et al., 2021), and evidence of these substructures can be observed in the energy-vertical angular momentum space (E - L_Z).

Figure 4.18 shows the position of our RRLs and halo stars in the E - L_Z diagram determined for orbits under an isolated and a perturbed MW potential. The figure highlights the regions where the majority of stellar distributions of known substructures are located (for GSE, Sgr, Wukong, the Helmi streams, Thamnos, and Arjuna+Sequoia+I’itoi), as shown by Naidu et al. (2020). We point out that the energies and L_Z computed from both models are only significant for the stars without loosely constrained orbits. It is clear from the figure that the RRLs display total energies higher than those of the considered substructures (at least at the high end of the distributions), and that their main uncertainty is in L_Z .

⁴⁵It is worth noticing that metal-poor members of Sgr with high α -abundances have also been found in the literature (see, e.g., Hansen et al., 2018).

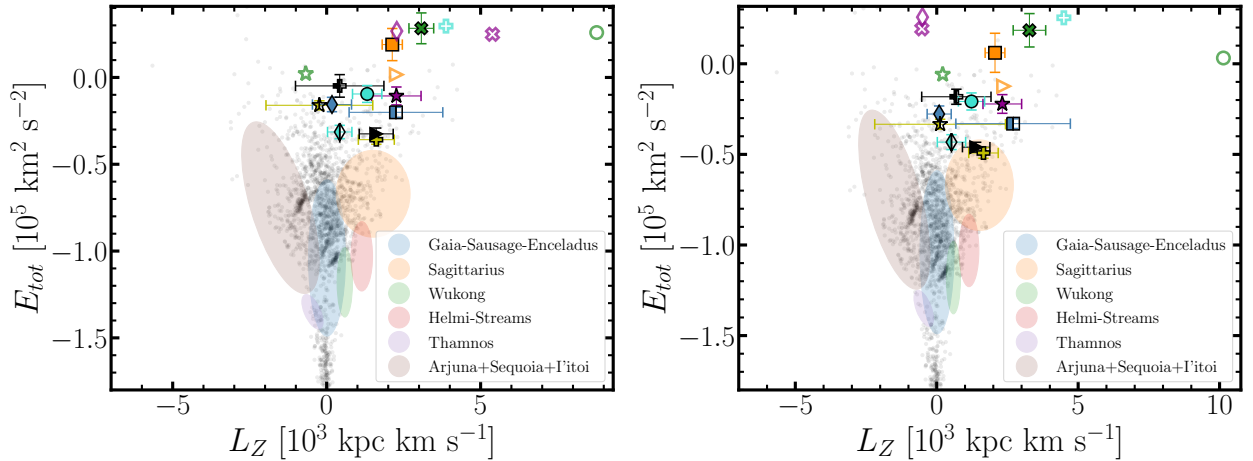


Figure 4.18: Energy vs. vertical angular momentum for the stars in our sample assuming an isolated potential (*left*) and a perturbed potential (*right*), using the symbol scheme of Figure 4.17. Shaded regions represent an approximation of the area occupied by the substructures studied by Naidu et al. (2020). These plots show that, regardless of the adopted potential, our RRLs display total energies higher than those of the considered substructures, and that their main uncertainty is in their vertical angular momenta.

In terms of α -abundances, even though J034239, HV210205, and HV204704 show an enhancement compared with normal halo stars from APOGEE (Figure 4.14 and Figure 4.15), their $[\alpha/\text{Fe}]$ ratios are also compatible with those of the GSE and Sequoia stars analysed by Aguado et al. (2021) (see their Figure 4), with $0.2 < [\alpha/\text{Fe}] < 0.4$.

Our stars show, however, $[\text{Sr}/\text{Fe}]$ and $[\text{Ba}/\text{Fe}]$ that are overall higher than those of the GSE and Sequoia stars analysed by Aguado et al. (2021), who reported an underabundance of Sr as compared to halo stars, and Ba around the solar value for both GSE and Sequoia stars. This is clearly visible in Figure 4.15. Furthermore, their distances are not compatible with those expected from these merger events.

4.5.4 Streams and other associations

Overdensities in the phase-space (positions and velocities) can, in principle, be used to trace recently accreted substructures, and even undiscovered satellites. From the phase-space location of our stars, displayed in Figure 4.19, we identify two groups that appear to be coherent with each other, i.e., with similar Cartesian coordinates and velocities.

The first group consists of HV205840, HV210205, and HV204704, which display similar Cartesian coordinates X , Y , and Z (with a dispersion in these coordinates < 2 kpc). HV205840 and HV210205 have also similar total velocities (390 ± 16 and 405 ± 24 km s^{-1} , respectively), which differ from that of HV204704 (147 ± 12 km s^{-1}). Additionally, the element ratios of HV210205 and HV204704 are similar (see Figure 4.15). Based on its low α -to-Fe abundance ratio (-0.2 at $[\text{Fe}/\text{H}] = -1.23$), HV205840 is one of the potential accreted stars. Moreover, the orbits of HV205840 and HV210205 have pericentres within 5 kpc, similarly large apocentres (both uncertain), and eccentricities that are alike (~ 0.75 , with a difference of 0.03), and more certain.

The other group includes J050902, J040422, and J034239. These three stars are not only

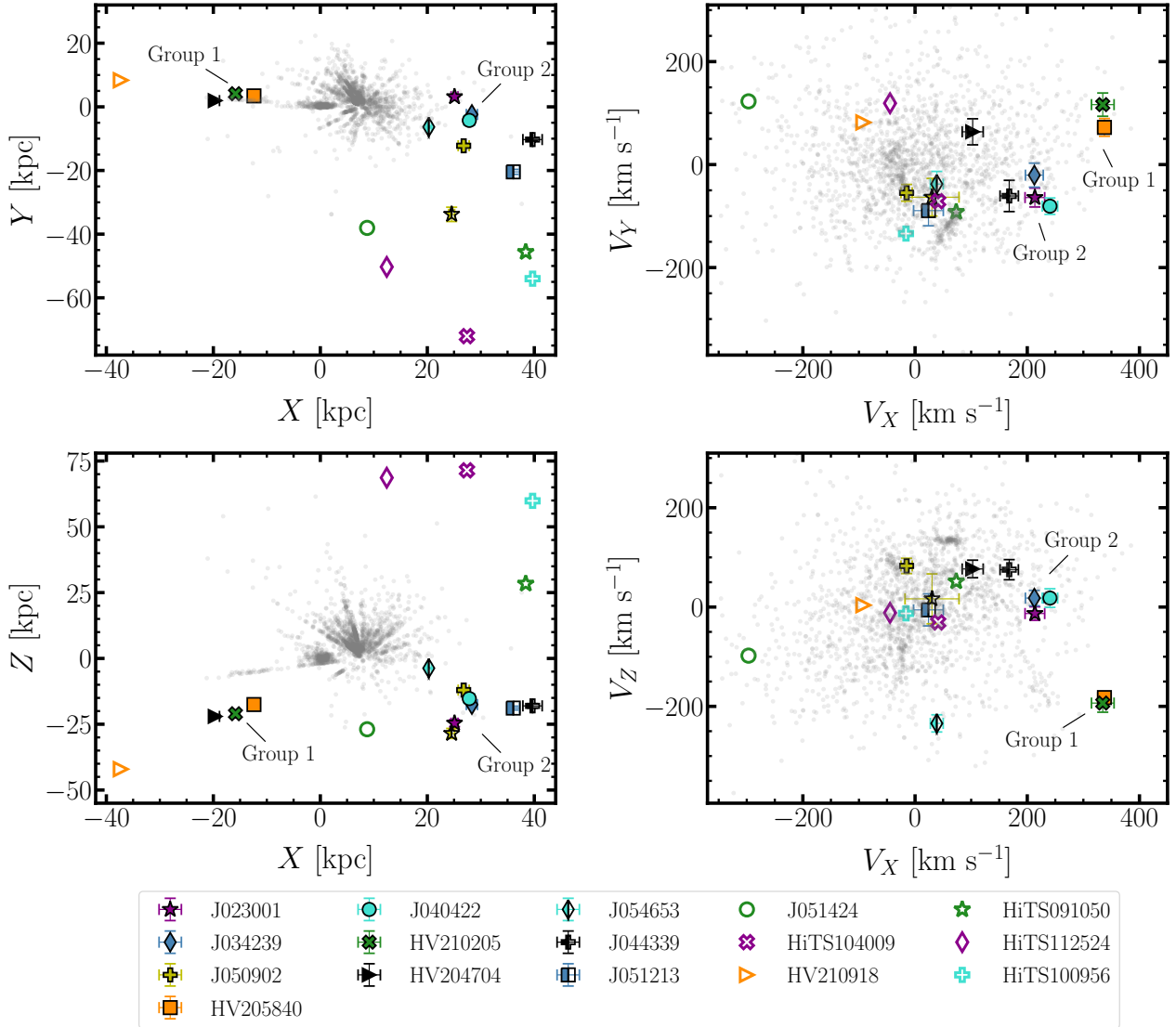


Figure 4.19: Positions and velocities of our sample in Galactic Cartesian coordinates. The location of the two groups of RRLs with similar positions and velocities (discussed in Section 4.5.4) is marked in each panel.

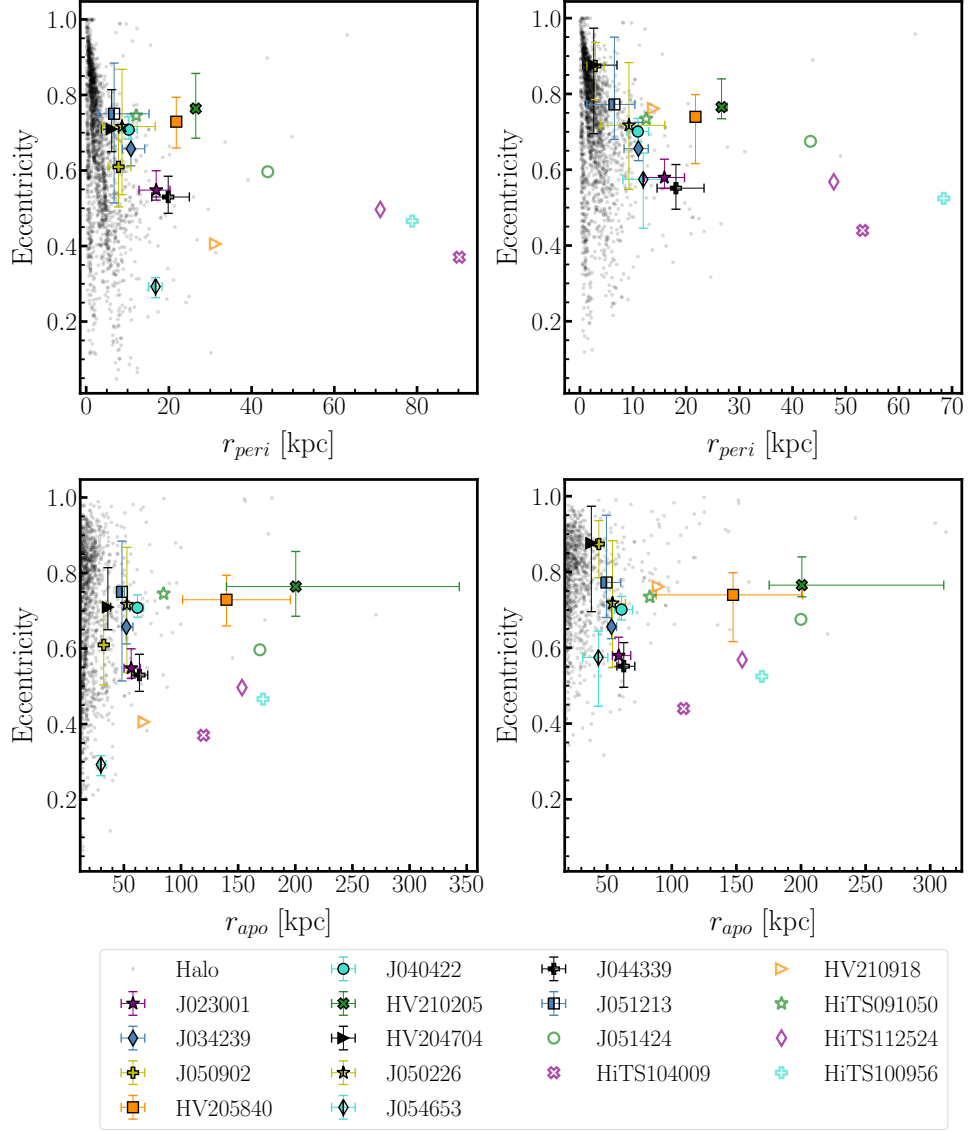


Figure 4.20: Eccentricity of the integrated orbits of our RRLs (large symbols) and halo stars (black dots), as a function of pericentric and apocentric distance (*upper* and *lower* panels, respectively). The *left* panels are computed using the isolated MW potential model, and the *right* panels consider the perturbed potential.

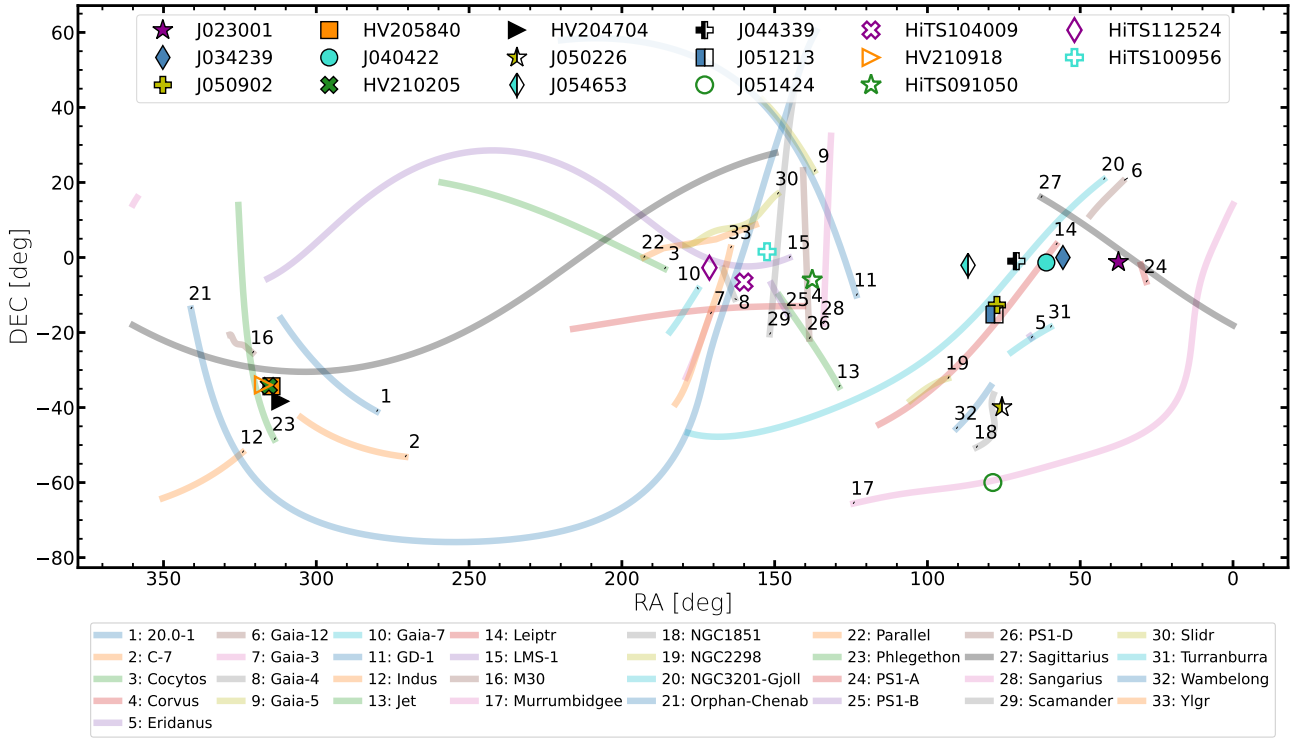


Figure 4.21: Footprint of 33 of the stream tracks in *galstreams* (Mateu, 2022) discussed in Section 4.5.4, shown in equatorial coordinates.

coincident in the phase-space, but also share similar n-capture process element abundances. However, only J034239 and J040422 are alike in their α -elements abundances, whereas J050902 displays a significantly lower $[\alpha/\text{Fe}]$ (~ 0.5 dex lower). Additionally, the apocentric and pericentric distance, and the eccentricities of J034239 and J040422 are substantially congruent (see Figure 4.20), with differences $\Delta r_{\text{peri}} \lesssim 2$ kpc, $\Delta r_{\text{apo}} \lesssim 10$ kpc, and $\Delta e \lesssim 0.05$ regardless of the model adopted to determine them. This is an indication of a common origin for these two RRLs.

To investigate the connection between our RRLs and the past and ongoing tidal dissolution of satellites, we used the recently updated Python library *galstreams* (Mateu, 2022), which contains celestial, distance, proper motion, and radial velocity information for 125 stream tracks corresponding to 97 distinct stellar streams (proper motions and velocities when available). Figures 4.21 and 4.22 show 33 tracks from *galstreams* located in the proximity of our targets in equatorial and Galactic coordinates, respectively.

For a given stream, we examine case by case all the RRLs in our sample that lie within 15 deg (on-sky projection) from the its footprint. The following streams pass this filter: Phlegethon, C-7, Ylgr, NGC 3201-Gjoll, Leiptr, NGC 1851 (Ibata, Malhan, & Martin, 2019; Ibata et al., 2021), M30 (Sollima, 2020; Harris, 1996), LMS-1 (Yuan et al., 2020), Orphan-Chenab (Grillmair, 2006; Shipp et al., 2018; Koposov et al., 2019), Gaia-4 (Malhan & Ibata, 2018), Corvus (Mateu, Read, & Kawata, 2018), Scamander, Sangarius (Grillmair, 2017a), PS1-D (Bernard et al., 2016), Murrumbidgee (Grillmair, 2017b). The main properties of these streams, as well as those of the RRLs in our sample located close to the streams in equatorial coordinates, are provided in Table 4.7. Most of these streams, however, are

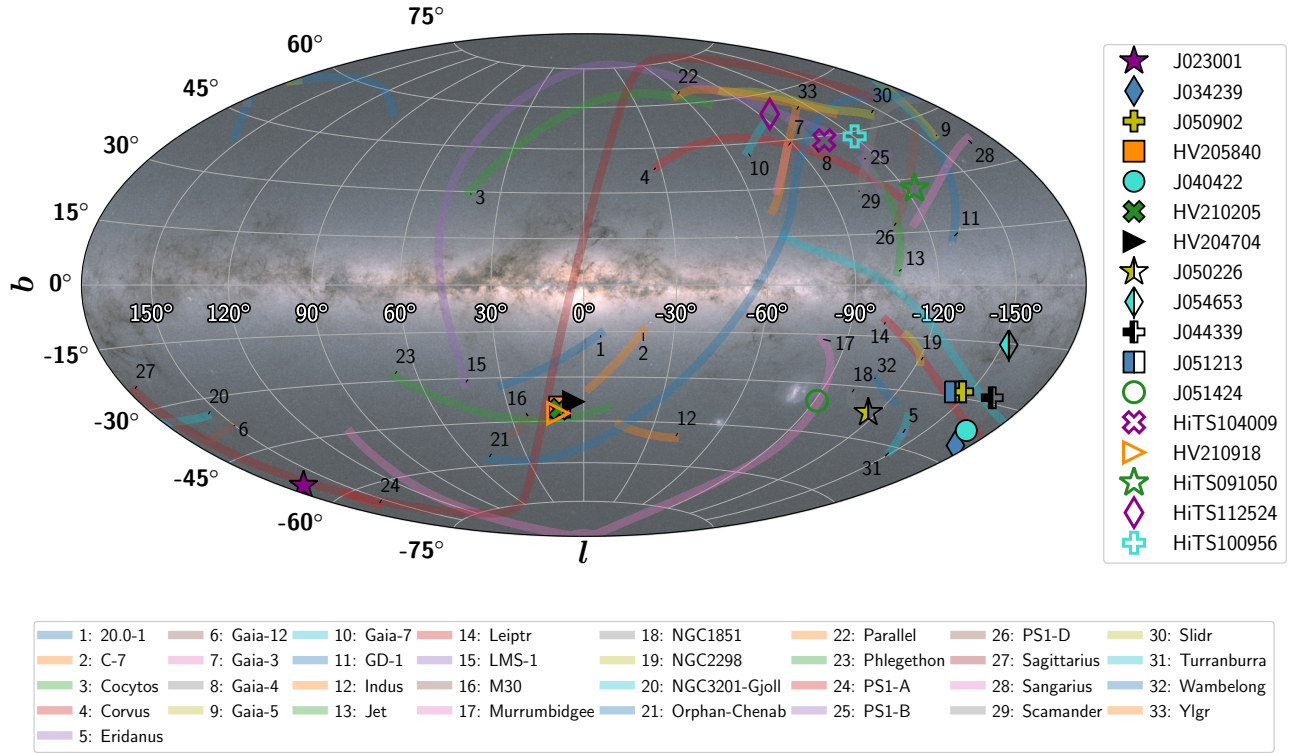


Figure 4.22: Same as Figure 4.21, but with the stars and streams represented in Galactic coordinates. The *Gaia* all-sky map is shown in the background as a reference. *Background Image Credit: Gaia Data Processing and Analysis Consortium (DPAC); A. Moitinho / A. F. Silva / M. Barros / C. Barata, University of Lisbon, Portugal; H. Savietto, Fork Research, Portugal.*

located in the inner Galaxy, i.e., with distances < 10 kpc and with proper motions clearly dissimilar to those of our RRLs.

Among the cases of interest (Table 4.7) we confirm J023001 as a likely Sgr stream member (as discussed in Section 4.5.2), and find four other RRLs possibly associated with the stream (including proper motions and radial velocities within the expected ranges; Mateu, 2022, and references therein), namely HV205840, HV210205, HV204704, and HV210918. Additionally, the position of these stars in the E - L_Z space is consistent with the region that contains the bulk of stars from the Sgr stream. Furthermore, given their longitudes in the Sgr stream coordinate system (Λ_{Sgr}) defined by Majewski et al. (2003) ($\Lambda_{\text{Sgr}} \sim 109.79, 26.17, 26.89, 23.49,$ and 28.41 deg for J023001, HV205840, HV210205, HV204704, and HV210918), their velocities are compatible with them being part of the Sgr trailing arm (see e.g. Johnson et al., 2020; Hasselquist et al., 2019; Ramos et al., 2020). In addition, the latitude of these stars with respect to the Sgr stream is $\lesssim 4.3$ deg, with the exception of HV204704 for which B_{Sgr} is ~ 8 deg. Of these stars, however, only J023001 and HV205840 are observed with α -element ratios compatible with those of the Sgr α -abundance trends at their metallicity. We do not possess abundance information for HV210918 to check its concordance with the stars in the stream and the dwarf galaxy. Nonetheless, this does not rule out their potential connection with the stream, given the wide range of Sagittarius' $[\alpha/\text{Fe}]$ (see Figure 5 from Hasselquist et al., 2021).

4 Probing the Galactic outer halo using chemodynamics of RR Lyrae stars

Table 4.7: Information of the streams considered in Section 4.5.4, as reported by *galstreams* (Mateu, 2022), in contrast to those of our RRLs. This table includes the range of proper motions of the stream members, and the angular separation (Sep.) in degrees between the RRLs and the stream tracks.

Stream	Stream d_H (kpc)	μ_α^* range (mas s^{-1})	μ_δ range (mas s^{-1})	RRL ID	RRL d_H (kpc)	RRL μ_α^* (mas s^{-1})	RRL μ_δ (mas s^{-1})	Sep. (deg)
Sgr	[19.0, 52.3]	[-2.68, 0.40]	[-2.89, -0.46]	J023001	30.5 ± 1.5	-0.17 ± 0.18	-1.57 ± 0.14	3.0
				HV210918	62.3 ± 2.1	0.19 ± 0.39	-1.04 ± 0.34	4.2
				HV205840	27.1 ± 0.9	-2.77 ± 0.10	-2.38 ± 0.09	4.3
				HV210205	32.2 ± 1.1	-2.38 ± 0.15	-2.29 ± 0.11	4.3
Orphan-Chenab	[16.0, 100.0]	[-4.46, 0.30]	[-3.57, 2.85]	HV204704	35.5 ± 1.2	-0.07 ± 0.14	-1.80 ± 0.11	8.1
				HITS104009	104.7 ± 4.5	-0.53 ± 1.09	-0.26 ± 1.25	3.2
				HITS112524	85.7 ± 3.7	-0.84 ± 0.88	-0.81 ± 0.63	8.6
				HITS10918	62.3 ± 2.1	0.19 ± 0.39	-1.04 ± 0.34	2.2
Phlegethon	[3.2, 4.1]	[-6.96, 1.32]	[-37.81, -21.07]	HV205840	27.1 ± 0.9	-2.77 ± 0.10	-2.38 ± 0.09	4.2
				HV210205	32.2 ± 1.1	-2.38 ± 0.15	-2.29 ± 0.11	3.5
				HV204704	35.5 ± 1.2	-0.07 ± 0.14	-1.80 ± 0.11	5.1
				HV210918	62.3 ± 2.1	0.19 ± 0.39	-1.04 ± 0.34	9.1
M30	7.9	-	-	HV205840	27.1 ± 0.9	-2.77 ± 0.10	-2.38 ± 0.09	10.4
				HV210205	32.2 ± 1.1	-2.38 ± 0.15	-2.29 ± 0.11	9.9
				HV204704	35.5 ± 1.2	-0.07 ± 0.14	-1.80 ± 0.11	15.0
				HV210918	62.3 ± 2.1	0.19 ± 0.39	-1.04 ± 0.34	12.9
C-7	[5.7, 6.1]	[-15.46, -9.60]	[-15.17, -7.67]	HV205840	27.1 ± 0.9	-2.77 ± 0.10	-2.38 ± 0.09	11.2
				HV210205	32.2 ± 1.1	-2.38 ± 0.15	-2.29 ± 0.11	11.7
				HV204704	35.5 ± 1.2	-0.07 ± 0.14	-1.80 ± 0.11	6.6
				HITS112524	85.7 ± 3.7	-0.84 ± 0.88	-0.81 ± 0.63	2.2
LMS-1	[15.4, 18.9]	[-0.25, 1.63]	[-4.42, -0.81]	HITS104009	104.7 ± 4.5	-0.53 ± 1.09	-0.26 ± 1.25	4.2
				HITS100956	88.6 ± 3.8	-0.24 ± 0.73	0.38 ± 0.67	3.4
				HITS104009	85.7 ± 3.7	-0.84 ± 0.88	-0.81 ± 0.63	5.0
				HITS10918	62.3 ± 2.1	0.19 ± 0.39	-1.04 ± 0.34	4.2
Ylgr Gata-4 Corvus	[7.6, 11.6] [10.7, 11.5] [4.9, 14.8]	[-0.63, -0.30]	[-11.23, -5.02]	HITS104009	104.7 ± 4.5	-0.53 ± 1.09	-0.26 ± 1.25	4.6
				HITS091050	61.4 ± 2.7	0.02 ± 0.28	0.38 ± 0.67	7.6
				HITS100956	88.6 ± 3.8	-0.24 ± 0.73	0.38 ± 0.67	3.2
				HITS091050	61.4 ± 2.7	0.02 ± 0.28	-0.54 ± 0.25	1.7
Scamander PS1-D Sangarius NGC3201-Gjoll	21.0 22.9 21.0 [3.1, 6.2]	-	[-23.51, -0.48]	HITS091050	61.4 ± 2.7	0.02 ± 0.28	-0.54 ± 0.25	4.2
				J054653	14.4 ± 0.7	4.35 ± 0.31	-0.81 ± 0.27	11.6
				J044339	38.2 ± 1.9	0.02 ± 0.18	-1.38 ± 0.17	1.4
				J050902	25.6 ± 1.3	0.29 ± 0.16	-1.08 ± 0.13	2.6
Leiptr	[6.0, 8.9]	[7.82, 10.32]	[-10.87, -4.62]	J051213	39.4 ± 2.0	0.45 ± 0.24	-0.53 ± 0.22	3.9
				J044339	38.2 ± 1.9	0.02 ± 0.18	-1.38 ± 0.17	6.5
				J050902	25.6 ± 1.3	0.29 ± 0.16	-1.08 ± 0.13	3.0
				J051213	39.4 ± 2.0	0.45 ± 0.24	-0.53 ± 0.22	1.8
NGC1851 Murrumbidgee	[13.5, 14.7] 20.0	[2.19, 2.37]	[-0.59, -0.21]	J040422	25.2 ± 1.3	-0.01 ± 0.17	-1.98 ± 0.13	4.0
				J050226	47.9 ± 2.4	0.39 ± 0.19	-0.42 ± 0.22	2.5
				J051424	47.1 ± 2.4	1.42 ± 0.27	1.20 ± 0.28	0.5
				J051424	47.1 ± 2.4	1.42 ± 0.27	1.20 ± 0.28	0.5

Lastly, we find two RRLs (HiTS112524 and HiTS104009) relatively close to the Orphan-Chenab stream projected in the sky. However, given the large physical distance of both of these stars to the stream, and their inconsistency with the proper motions and predicted systemic velocities trends for Orphan-Chenab’s members at right ascension between 160 and 170 ($\mu_\alpha^* \sim -1.6 \text{ mas yr}^{-1}$, $\mu_\delta \sim 0.8 \text{ mas yr}^{-1}$, $v_{\text{sys}} \sim 200 \text{ km s}^{-1}$; Kozlov et al. 2019; Prudil et al. 2021), we consider their association unlikely.

For the rest of the stars in our sample we do not find clear indications of association with satellites and known substructures. As discussed in Section 4.5.4, the stars J040422 and J034239 (at $d_{\text{H}} \sim 25$ and 27 kpc , respectively) are coincident in phase-space and have α -abundances comparable to those of the sample of halo stars from APOGEE. This might also be interpreted as an indication of them having been formed in-situ. Along the same lines, the pulsation periods of two of the RRLs with lower-resolution spectra in our sample (J050226 and HiTS101243, at $d_{\text{H}} \sim 48$ and 91 kpc , and periods $\sim 0.53 \text{ d}$) are similar to the periods typical of RRLs in the OoI group. Because the majority of the RRLs in the general halo population follow the locus of the OoI, this might be a hint of their origins being in agreement with the main trend of nearby field RRLs. Without chemical abundances and more precise orbital parameters, however, it becomes challenging to set solid constraints on the formation conditions of the most distant stars in our sample (including J050226 and HiTS101243).

4.6 Summary and conclusions

We have conducted a pilot study to characterize spectroscopically remote halo RR Lyrae stars, to better understand the limiting factors in determining their stellar parameters, abundances, and kinematics, and to explore their role in understanding the Milky Way’s accretion history. We have obtained MIKE@Magellan medium-resolution optical spectroscopy for a sample of 20 halo RRLs with precise heliocentric distance information, between 15 and 165 kpc. These stars were selected from the HiTS, HOWVAST, and Catalina surveys, based on their pulsating properties (ab-type RRLs with periods $\gtrsim 0.5 \text{ d}$). Given the combination of distance and variable nature of our targets, the signal-to-noise of our coadded spectra ranges from ~ 5 to 20.

We derived (systemic) radial velocities for our whole sample with typical uncertainties of $\sim 5\text{--}10 \text{ km s}^{-1}$. By combining proper motions from *Gaia* DR3 with these velocities and period-luminosity-based distances we computed orbital parameters for more than half of our sample (with great precision out to 50 kpc from the Galactic centre), and estimated their iron abundances by following various approaches.

We derived atmospheric parameters and chemical abundances (including α -element abundance ratios and n-capture elements, and considering NLTE corrections) for seven stars in our sample that have distances between 20 kpc and 40 kpc. We found the estimated atmospheric parameters consistent with their observed phases of pulsation, and the spread of their spectroscopic [Fe/H] values (from -1.80 to -1.05 dex) in general agreement with the peak of the halo metallicity distribution.

For computing the orbital parameters of our RRLs, we considered two models: one assuming an isolated evolution of the MW potential, and one taking the gravitational effects of the infall of the LMC into account, in line with recent studies (e.g., Vasiliev, Belokurov,

& Erkal, 2021). Based on the number of valid solutions resulting from determining the orbits of our RRLs we computed their likelihood to be gravitationally bound to the MW, and find two stars with loosely constrained orbits. Interestingly, the velocity of the potentially unbound stars lie within the bounds of the MW escape velocity curve at their respective distances. From the data at hand, we conclude that the biggest limitations in exploring the full six-dimensional phase-space, and the bound likelihood of the orbits, come from the large uncertainties in the proper motions of stars beyond 30 kpc.

By combining the stars' orbital parameters and their derived chemical abundances, we speculated about their origin and associate them with potential parent populations, including the LMC. We found two RRLs with an underabundance of α -elements for their metallicity (HV205840 and J050902), which is not compatible with in-situ formed MW stars and suggests an accreted origin. Applying NLTE corrections does not change the abundances significantly. Furthermore, we deduced the early production of two n-capture process elements (via the r -process) for three of our stars, two of which follow the expected halo-like trend (J034239 and J050902). For the third star (HV204704), we find a [Sr/Ba] ratio that suggests a CEMP classification, which could be explained by pollution from a fast rotating massive star. Further studies are required to confirm this classification. Additionally, about half of our sample is found in counter-rotating orbits, which might indicate an extragalactic origin. We confirm one of our stars (J051424) as an LMC outskirts member, and find a likely association of another RRL with Sagittarius (J023001). We also found other RRLs for which additional data are required to confirm an association with Sagittarius (HV205840, HV210205, HV204704, HV210918). We analysed other substructures, including major merger events (e.g., GSE and Sequoia) and streams, but did not find convincing evidence of their connections with our RRLs. Observing larger samples of RRLs with dedicated medium- and high-resolution spectroscopy at large aperture telescopes (throughout their pulsation cycles or at specific phases) might render it possible to associate single halo RRLs with known or yet undiscovered substructures, and is required to recover a more complete scenario of their origins, together with dedicated spectroscopic studies of satellites and streams in the halo (e.g., Ji et al., 2020, 2021; Li et al., 2021; Martin et al., 2022a,b). Our results indicate that a $S/N > 15$ is sufficient for determining the RRLs' systemic velocities and abundances to assess these associations.

5

Conclusions and future work

5.1 Summary and outlook

In this thesis, we have used pulsating variable stars as tools to unveil the formation and evolution our Galaxy. More specifically, we studied Cepheids and RR Lyrae variables and their connection with stellar systems (star clusters and dwarf galaxies) in order to reconstruct how these systems have contributed to building up the Galaxy at different times. We analysed the fraction of classical Cepheids in MW open clusters, the suitability of open clusters as laboratories for testing the Cepheid PA relation, the distribution of RRLs in the MW outskirts, the chemodynamics of outer halo RRLs, and how these properties can be used to assess their origin (formed in-situ vs. ex-situ). We summarize the main conclusions and the implications of our findings below:

- **Chapter 2:** We revisited the problem of identifying bona fide cluster Cepheids by performing an all-sky search using state-of-the-art catalogues for both Cepheids and open clusters. For this, we exploited the unparalleled astrometric precision of the second and early third data releases of the *Gaia* satellite. We confirmed 19 Cepheid-cluster associations considered in previous studies as bona-fide, and questioned the established cluster membership of six other associations. In addition, we identified 139 cluster Cepheid candidates of potential interest, mostly in recently discovered open clusters. We reported on at least two new clusters possibly hosting more than one Cepheid. Furthermore, we explored the feasibility of using open clusters hosting Cepheids to empirically determine the Cepheid period-age relation through the use of *Gaia* and 2MASS photometry and a semi-automated method to derive cluster ages. We concluded that the usage of cluster Cepheids as tentative probes of the period-age relation still faces difficulties when determining cluster ages via isochrone fitting. This is a consequence of the quick dissolution, the sparsely populated RGB region, and the stochastically sampled main-sequence turn-off of young open clusters, which subsequently biases the age-datable cluster selection for Cepheid period-age studies towards older and higher-mass clusters.
- **Chapter 3:** As part of our efforts to better characterize the outer halo, we hunt for faint RRLs employing data from the HiTS and the HOWVAST surveys, both of which rely on data taken with the DECam. The footprints of these surveys do not overlap with each other and is partially covered by large-scale surveys from the literature.

We detected a total of ~ 500 RRL candidates (~ 400 of them in the HOWVAST fields), including previously identified RRLs and at least 91 candidates not reported by previous surveys. We identified 11 new RRL candidates beyond 100 kpc from the Sun, most of which are classified as ab-type. The periods and amplitudes of these distant RRLs do not place them toward the locus of either Oosterhoff group and suggests that our sample might contain stars coming from UFDs and with other origins (i.e., RRLs formed in-situ and ex-situ). Within our distant sample, we detected two groups containing RRL candidates with similar heliocentric distances and coordinates, which we interpret as an indication of their association with undiscovered bound or unbound satellites. We studied the halo density profile using an ellipsoidal model and following an MCMC methodology. We found that our radial profiles are consistent with broken-power-laws with break radii from $20.4^{+3.1}_{-2.4}$ to $23.4^{+2.5}_{-4.5}$ kpc separating the inner and the outer halo, confirming that the break in the density profile is a feature visible in different directions of the halo. The mean value of the outer slope of our profiles probing the smooth halo is $-4.45^{+0.16}_{-0.22}$, with individual values that range between $-4.75^{+0.54}_{-0.70}$ and $-4.42^{+0.23}_{-0.28}$. The similarity of these radial distributions to previous values reported in the literature depends on the regions of the sky surveyed. We attributed these differences to the an-isotropic distribution of RRLs throughout the halo as a result of the dynamical response of the Galaxy to the infall of massive satellites, such as the LMC. Our findings are compatible with simulations that predict that the outer regions of MW-like galaxies are mainly composed of accreted material.

- **Chapter 4:** We reported the spectroscopic analysis of 20 halo ab-type RRLs with heliocentric distances between 15 and 165 kpc, conducted using medium-resolution spectra from the MIKE spectrograph. These stars were selected from the Catalina and the HOWVAST surveys. We obtained the systemic line-of-sight velocities of our targets with typical uncertainties of 5–10 km s⁻¹, and computed orbital parameters with great precision for a subsample of them (out to ~ 50 kpc) from the Galactic centre using proper motion data from *Gaia* DR3. The orientation of our stars' orbits, determined for an isolated MW and for a model perturbed by the LMC, appears to suggest an accreted origin for at least half of the sample. In addition, we derived atmospheric parameters and chemical abundance ratios (including O, Na, Mg, Ca, Ti, Fe, Sr, Ba) for seven stars beyond 20 kpc. The derived α -abundances of five of these stars follow a MW halo-like trend, while the other two display an underabundance of α -elements for their [Fe/H], indicating an association with accretion events. Furthermore, based on the [Sr/Ba] ratio, we speculated about the conditions for the formation of a potential chemically peculiar CEMP RRL. By analysing the stars' orbital parameters and abundance ratios, we found hints of association of two of our stars with two massive satellites, namely the LMC and the Sgr dSph. Overall, our results are in line with the suggestion that the accretion of sub-haloes largely contributes to the outer halo stellar populations.

5.2 Future research directions

In this section, I outline future avenues to be explored in order to extend the results presented in this thesis. The aims of these research directions are: (i) to increase the known number of Cepheids associated with open clusters in the MW and in neighboring galaxies, (ii) to refine the empirical Cepheid period-age(-metallicity) relation from precise cluster age determinations, (iii) to further explore the MW outskirts with RRLs and to investigate their chemodynamics on large scales and at larger distances, and (iv) to improve the census of MW satellites and streams.

5.2.1 Cepheids and open clusters in the Milky Way and beyond

The number of bona-fide classical Cepheids in Galactic open clusters remains relatively small, in spite of the vast amount of Cepheids and clusters have been discovered in recent years (e.g., [Soszyński et al., 2020](#); [Castro-Ginard et al., 2021](#)). This might be due to the fact that Cepheids are inherently rarely associated to clusters, or because of observational biases (e.g. lack of astrometric precision to assess memberships). In fact, as highlighted in [Chapter 2](#), it is expected that the occurrence of cluster Cepheids in the MW (< 5 per cent) is not significantly different than those of the SMC and the LMC, which are expected to range between 6 and 11 per cent ([Anderson & Riess, 2018](#)).

A low-hanging fruit to better investigate the birthplace of Cepheids in the MW involves performing updated censuses using larger databases relying on *Gaia* data. Recent studies have shown that the list of known clusters within 2 kpc from the Sun is still likely incomplete (less complete than the list of known Cepheids). In the last couple of months only, for instance, $\sim 1,000$ new cluster candidates have been discovered within the Galactic disc and at higher Galactic latitude regions (see e.g. [Castro-Ginard et al., 2022](#); [He et al., 2022](#)). The newly discovered cluster candidates are mostly located at beyond 1 kpc, which is a direct consequence of the improved astrometric precision of the newest *Gaia* data releases. Additionally, one could envision adapting the prior used in the Bayesian analysis presented in [Chapter 2](#) (which only relies on the on-sky separation between clusters and Cepheids) to take into account the dynamical state of the cluster. More specifically, the prior should consider the possible ongoing dissolution of the cluster, in line with the recent detection of vast stellar coronae of open clusters (that extend for > 100 pc; e.g., [Meingast, Alves, & Rottensteiner, 2021](#)) and the increased number of clusters with tidal tails reported in the literature (e.g., [Sharma et al., 2020](#); [Bhattacharya et al., 2021](#)). A practical way to quantify these effects might involve incorporating the density of stars in and around the cluster into the prior, or adopting a prior that computes a probability based on the distance to the cluster's core and its integrated orbit. This could already provide higher membership probabilities for Cepheids about to leave a cluster as it seems to be the case for QZ Nor and the cluster NGC 6067, as reported by [Breuval et al. \(2020\)](#), or those who just left it. An even more promising alternative would be to employ conservative integrals of motion, as is done in the halo to identify globular cluster escapees and link them to their original cluster (see e.g. [Hanke et al., 2020b](#)). Furthermore, the likelihood of membership defined in [Chapter 2](#) could be adapted to exploit the synergies between *Gaia* and large spectroscopic surveys (e.g., LAMOST, GALAH, and APOGEE), which would increase the number of clusters and Cepheids

with homogeneously derived velocities (radial and three dimensional), chemical abundances, and dynamical properties (such as orbit, eccentricity, angular momenta, total energy; [Fu et al., 2022](#)) to be used in the analysis. To this end, future endeavors using the next generation of instruments and surveys with multiplex capabilities, such as the William Herschel (4.2 m) Telescope Enhanced Area Velocity Explorer (WEAVE, with a spectral resolution R between 2,000 and 20,000 and a field of view of ~ 4 sq. deg.; [Dalton et al., 2012](#))⁴⁶ and the 4-metre Multi-Object Spectroscopic Telescope (4MOST, at the VISTA 4.1 m telescope, with R between 4,000 and 18,000 and a field of view of ~ 4 sq. deg.; [de Jong et al., 2014](#))⁴⁷ will be key to substantially expand the number of stars with available high-quality multidimensional information. With the addition of chemical tagging to the analysis, these synergies might render it possible to associate a given Cepheid and other nearby young stars with a unique birthplace, of any nature whatsoever.

Studies of Cepheids in MW clusters have consistently shown that the majority of Cepheids do not reside in these systems, and that the clusters that do host Cepheids typically contain only one. It has also been shown that the fraction of clustered Cepheids is typically higher for the younger long-period Cepheids ([Anderson & Riess, 2018](#); [Dinnbier, Anderson, & Kroupa, 2022](#)). In contrast, in very massive clusters in the LMC such as NGC 1866 or NGC 2031 (with masses $\sim 5 \times 10^4 M_{\odot}$) up to 24 Cepheids have been detected, most of which pulsate with somewhat short periods (see e.g. [Testa et al., 2007](#); [Musella et al., 2016](#)). Thus, extending our study to the LMC would allow us to shed light on the factors that define the occurrence of cluster Cepheids and the survivability of clusters (e.g. mass, age, metallicity, and distance to the host galaxy). Moreover, the more massive clusters that belong to the MCs are better suited laboratories to set constraints on the Cepheids period-age relation (and its metallicity dependence), since they contain more Cepheids and evolved stars, and better defined MSTOs. Thus, investigating Cepheids in LMC open clusters will contribute to answer the following questions: (i) how does the usage of state-of-the-art data (e.g., [Gatto et al., 2020](#)) change the number of bona-fide cluster Cepheids in the MCs? (ii) how will it impact the age determination of the (more massive) MC's host clusters, and the subsequent empirical calibration of the Cepheid period-age relation? (iii) how does the MC fraction of clustered Cepheids compare with the current predictions from N-body simulations and evolutionary models (e.g., [Lewis et al., 2021](#); [Dinnbier, Anderson, & Kroupa, 2022](#))? (iv) are Cepheids predominantly formed in clusters that quickly dissolve, or in other type of systems, such as unbound OB associations? If future endeavors aimed at following these research paths with *Gaia* data, however, they will need to address the challenge of distilling useful astrometric information of Cepheids and clusters at large distances. The situation would be similar if these studies focused on open clusters in M31, which would serve as an excellent laboratory to constrain survivability of Cepheids in clusters and their PA relation at high metallicity (e.g., [Senchyna et al., 2015](#)).

Finally, new approaches (or ideal conditions) are required to overcome the limitation of deriving precise cluster ages suitable for a detailed empirical study of the Cepheid PA relation, especially given the sensitivity of the cluster ages from isochrone fitting to the number of stars near the main-sequence turn-off point and the number of post-main-sequence stars. In this regard, higher precisions might be achievable from the comparison of the observed and

⁴⁶<https://www.ing.iac.es/astronomy/instruments/weave/weaveinst.html>

⁴⁷<https://www.4most.eu/cms/>

predicted cluster luminosity functions (e.g., [Piskunov et al., 2004](#)), from the use of reddening-free indices and spectral types for upper main-sequence stars, or by developing a framework to complement different methodologies to derive young cluster ages (e.g., isochrone fitting, lithium depletion, and kinematic ages from the clusters' expansion and tidal disruption; [Crundall et al., 2019](#); [Dinnbier et al., 2022](#); [Galindo-Guil et al., 2022](#)). Naturally, this would also require a proper census of the clusters members (with extremely high completeness and low contamination), a proper characterization of their spatial distributions, and an increase in the number of clusters for which the aforementioned techniques are applicable. Refining these methods will permit, however, calibrations of the Cepheid PA relation (and its metallicity dependence) from approaches that do not rely on stellar evolution models necessarily, from clusters in the MW, the Magellanic Clouds, and M31.

5.2.2 The Galactic outskirts: Pushing the boundaries with RR Lyrae stars

In recent years, the fields of Galactic archaeology and time-domain astronomy have been revolutionized by the development of large-scale surveys mapping the halo, dwarf galaxies, and streams, such as the DES ([Dark Energy Survey Collaboration et al., 2016](#)), the CRTS ([Drake et al., 2009](#)), the PS-1 survey ([Kaiser et al., 2002](#)), the ZTF ([Bellm et al., 2019](#)), the DECam Local Volume Exploration survey (DELVE; [Drlica-Wagner et al., 2021, 2022](#)), and the Southern Stellar Stream Spectroscopic Survey (S5; [Li et al., 2019](#)). This revolution will continue in the near future with the advent of the ten-year Rubin Observatory Legacy Survey of Space and Time (LSST; [LSST Science Collaboration et al., 2009](#))⁴⁸. The LSST will carry out observations with an 8.4m telescope and the ability to cover a third of the southern-hemisphere sky each night. This will allow the LSST to detect millions of transients and variable object over a wide-sky area. In fact, with its deep images, long baseline, and short cadence, the LSST is expected to recover a complete catalogue of $\sim 10^5$ well-sampled RRLs out to the edge of the MW (~ 300 kpc; [Deason et al. 2020](#)) by the completion of the survey (with single images down to $r \sim 24.5$; [Oluseyi et al. 2012](#); [Hernitschek & Stassun 2022](#)). Moreover, the start of operations of large spectroscopic campaigns such as 4MOST and the Subaru Prime Focus Spectrograph (PFS) survey (at the 8.2m Subaru telescope, with $R \sim 2,000$ -5,000 and a field of view of ~ 1.2 sq. deg.; [Takada et al., 2014](#))⁴⁹ will play an important role on enlarging the number of RRLs with precise radial velocities and chemical abundances within and beyond 20 kpc. In this subsection, I address the synergies between the surveys mentioned above in the context of this thesis.

A further exploration of the distant halo

In this thesis, I have stressed the relevance of the slope of the number density profile of outer halo stars in investigating the halo accretion history of our Galaxy. Numerous studies focusing on the detection of RRLs, including our own (Chapter 3), have been used to assess the amount of variation in stellar density at large radii (subject to the limitations of current instruments). Key to this endeavor is the development of deep and dedicated surveys specifi-

⁴⁸<https://www.lsst.org/>

⁴⁹<https://pfs.ipmu.jp/>

cally designed to map the outer halo with RRLs (such as HOWVAST), properly dealing with the pulsating properties of these stars (e.g., with their short-period variations). Moreover, in addition to probing the (an-)isotropy of the RRL distribution in large-scale surveys, any new distant (> 100 kpc) stars discovered represent a key contribution to the list of potential substructures and to the few existing tracers of the MW outermost regions' potential. Thus, larger number statistics (with large scale halo surveys of high completeness) resulting from the advent of large and deep photometric campaigns will be crucial to reconstruct a more complete local and global picture of the outer halo's history, structure, inclination, and shape. These studies will permit, e.g., to assess the amount of variation in stellar density at large radii, where asymmetries are expected to be more evident (Pandey, 2022). In this regard, the highly complete sample of outer halo RRLs recovered by the LSST and its precursors (e.g., Ivezić et al., 2008; Oluseyi et al., 2012; Hernitschek & Stassun, 2022) will serve as uniquely valuable tools to disentangle the MW formation in unprecedented detail.

Future studies should exploit the synergies between the available photometric surveys covering different regions of the halo and independent campaigns to further characterize attractive RRL candidates. To achieve this, a combination of data mining expertise with a focus on low signal-to-noise sources (for distant RRLs) will be essential, in particular to complement the tools developed for variable star classification from the LSST data (e.g., alert brokers)⁵⁰ and novel methodologies based on machine learning. Increasing the amount of photometrically characterized distant halo RRLs will also bring a larger number of targets suitable for dedicated spectroscopic follow-ups. These targets will be used as stellar tracers of the vastly unexplored outer halo RRL chemical abundance patterns and kinematics.

Tagging RRLs according to their location in the period-amplitude diagram, their phase-space information, and their chemical abundances is key to shedding light on the genesis of the halo. Therefore, complementing the upcoming samples of distant RRL catalogues by spectroscopic follow-up studies will allow us to determine their accreted origin (e.g., parent populations and stellar streams) in large numbers. If the studied stars are debris from accreted dwarf galaxies, we can additionally use the well-known mass-metallicity relation for MW dwarfs (e.g., Kirby et al., 2013) to perform an order of magnitude estimation of the masses of the progenitors building up the outer MW. The study of the systemic velocities of distant halo RRLs will contribute to placing our Galaxy in a proper cosmological context through precise estimations of its total mass, as current models (and their comparison with observations) are highly sensitive to the halo mass (e.g., Geha et al., 2017). Currently, MW mass estimates beyond the disc rely on different groups of dynamical tracers (e.g., globular clusters, dwarf galaxies, stellar streams). Because the widest dispersion in the mass estimations of the MW correspond to the most distant tracers (Eadie & Harris, 2016; Deason, Belokurov, & Sanders, 2019; Wang et al., 2020; Deason et al., 2021; Rodriguez Wimberly et al., 2021), even single remote stars (at ~ 100 kpc) with precise distance determinations and velocities could provide valuable insights into the full gravitational potential of our Galaxy (Watkins, Evans, & An, 2010).

Only the chemodynamical analysis of large numbers of halo RRLs as part of the next generation of surveys will help us unveil the real nature of the entire halo, and its connection

⁵⁰The list of dedicated software developed for this purpose include the Automatic Learning for the Rapid Classification of Events (ALeRCE) broker (Förster et al., 2021; Sánchez-Sáez et al., 2021) and the Arizona-NOIRLab Temporal Analysis and Response to Events System (ANTARES; Matheson et al., 2021).

with old populations in dwarf galaxies and streams. However, spectroscopically characterizing faint halo RRLs is an inherently challenging task, and will continue to be so in the near future, given the conflict between the long exposure times required and their short pulsation periods.

Upcoming spectroscopic surveys will allow astronomers to derive radial velocities (at a $\sim 3 \text{ km s}^{-1}$ level) and chemical abundances (at a 0.2 dex level) for millions of stars in the Galactic thick disc, halo, in tidal streams, and in several dwarf galaxies (Takada et al., 2014; Tamura, 2016; Christlieb et al., 2019; Helmi et al., 2019), sampling different stellar populations in the MW and the Magellanic Clouds, and measuring Ca II triplet-based RRLs metallicities. Studies based on current 4-m-class telescopes, such as 4MOST, WEAVE, and the Dark Energy Spectroscopic Instrument (DESI, with $R \sim 2,000\text{-}5,000$ and a field of view of $\sim 3 \text{ sq. deg.}$; DESI Collaboration et al., 2016)⁵¹, will derive these velocities and metallicities over large portions of the inner halo ($< 20 \text{ kpc}$). The 4MOST Gaia RR Lyrae Survey (4GRounds), for instance, as one of the selected 4MOST Galactic surveys⁵² will provide the community an exquisite sample of RRLs processed with a dedicated pipeline. Spectroscopic surveys conducted with larger telescopes and the next generation of instruments (e.g., the $R \sim 5,000\text{-}20,000$ MOSAIC spectrograph at the 39 m European Extremely Large Telescope, ELT; Evans et al., 2015) will render it possible to map the MW with high-precision RRL studies out $\sim 100 \text{ kpc}$. Current efforts (e.g., Chapter 4) are then key to lay the groundwork to better understand the limitations of determining radial velocity measurement for faint RRLs, and the offsets between spectroscopic and Ca II triplet-based RRLs metallicities (aiming for setting past and future observations on similar metallicity scales). The complementarity of surveys such as the aforementioned with the LSST and future *Gaia* data releases, with their corresponding improvements in astrometric precision and accuracy⁵³, will then be pivotal to recover a complete picture of the Galactic history out to large radii.

The hunt for ultra-faint dwarf galaxies and streams

The lowest-luminosity MW satellite galaxies are the oldest, most metal-poor, most dark matter-dominated, and least chemically evolved stellar systems known (Simon, 2019), and comparing the predicted number of satellites with theoretical expectations is key to test the current cosmological and galaxy evolution models (see, e.g., Engler et al., 2021). From an observational perspective, the number of detected satellite galaxies around the MW has continuously grown into the ultra-faint regime in recent years (see, e.g., Bechtol et al., 2015; Koposov et al., 2015), mostly due to the availability of large-sky deep photometric surveys. However, only a fraction of the expected number of dwarf galaxies have yet been observed, in part due to observational limitations, and it has been predicted that $\sim 100\text{-}300$ dwarfs will be discovered by the LSST (e.g., Hargis, Willman, & Peter, 2014; Jethwa, Erkal, & Belokurov, 2018). In the near future, spectroscopic surveys such as 4MOST (through its 4DWARFS community survey) and the PFS will characterize a large number of already discovered dwarf galaxies in the southern and northern sky, and it is natural to expect that surveys focusing on the new dwarfs will continue developing.

⁵¹<https://www.desi.lbl.gov/>

⁵²<https://www.eso.org/sci/observing/PublicSurveys/4most-surveys-projects.html>

⁵³<https://www.cosmos.esa.int/web/gaia/release>

Throughout this thesis I have highlighted that groups of RRLs in the distant halo can be used to trace undiscovered substructures and ultra-faint satellites (e.g., [Baker & Willman, 2015](#); [Medina et al., 2017](#); [Sanderson et al., 2017](#); [Torrealba et al., 2019](#)). Relevant to this idea are the groups of remote RRLs with coincident positions (in equatorial coordinates and heliocentric distances) detected in Chapter 3, and those with similar positions and velocities reported in Chapter 4. In order to search for the faintest dwarf galaxies in the MW neighborhood, detailed studies of halo overdensities like these in celestial coordinates, *Gaia*-based parallaxes and proper motions, orbital parameters, chemical abundances, and deep colour-magnitude diagrams (e.g., from coadded frames) are ideal and necessary. In fact, [Brauer et al. \(2022\)](#) found that the vast majority of overdensities found by clustering algorithms using kinematic data only do not correspond to real accreted remnants of UFDs, and that generally less than 10 per cent of the true remnants (mostly recently accreted) can be recovered. Thus, future studies in this field should take advantage of precise distance indicators in the halo and exploit the synergies between the wide and deep-field photometry from upcoming surveys (e.g., the LSST, which will reach $r \sim 26$ with its yearly stacks; [Oluseyi et al., 2012](#)), their precursors (e.g., the DES and DELVE), and large-scale spectroscopic surveys. Notably important will be a focus on the low signal-to-noise regime making use of state-of-the-art clustering algorithms, machine learning tools, and methodologies for membership determinations (e.g., HDBSCAN or the *simple* algorithm; [Hunt & Reffert 2021](#); [Cerny et al. 2021](#)). An alternative outcome of this research direction is the detection of new stellar streams to be used as targets for spectroscopic follow-ups. These detections will significantly contribute to improving our understanding of the accretion history of the MW ([Bovy et al., 2016](#); [Li et al., 2021](#)), particularly at the still elusive outermost regions of the halo.

5.3 Concluding remarks

We are witnesses and participants of a golden era for Galactic archaeology studies. The construction of massive telescopes and their ground-based and in-space deployment, the development of advanced instruments, large-scale surveys observing both hemispheres and producing a myriad of data that challenge our traditional data-handling methodologies, statistical tools and complex computational simulations that tackle problems offering innovative solutions, the establishment of large international and interdisciplinary collaborations, and a continuously growing community. All of the aforementioned contribute significantly to settling us into a position that previous generations of astronomers perhaps only imagined.

This thesis, in which I used a combination of the techniques most commonly used to characterize stellar populations in the Milky Way, is a good representation of the current efforts that the Galactic archaeology community is performing in order to prepare for the next generation. The work presented here was developed with the aim of contributing to the state-of-the-art of two complementary research fields, namely variable stars and Galactic astronomy. And it is with little steps that we face this scientific revolution. A revolution that has already started and will continue, and that will hopefully give us the tools needed to disentangle the complex (and captivating) history of our home in the Universe.

A1 Complementary tables and figures

Here we provide additional material to complement the information presented in Chapter 2. In Table A1, we provide the prior, likelihood and membership probability for literature combos, in addition to the separation between the Cepheid and the cluster centre, and the constraints used for the membership determination. Table A2 lists the cluster-Cepheid pairs with membership probabilities $P(A|B)$ between 0.01 and 0.10, as a complement to Table 2.1 (which displays combos with $P(A|B) > 0.10$). In Table A3, the full list of combos described in Section 2.5.3 (i.e., those with low priors $P(A)$ but $P(B|A) > 0.85$) is presented. Figure A1 displays the *Gaia*-based astrometry and colour-magnitude diagrams for two of the new combos reported in Section 2.5.4 (in addition to those shown in said section). Finally, the colour-magnitude diagrams of the clusters studied in Section 2.6, with isochrones representing the results of Section 2.6.1 (from which the cluster ages are obtained) are displayed in Figure A2.

Table A1: Prior, likelihood and membership probability for literature combos. We list the cluster and Cepheid names, their angular separation as a function of r_1 , and the constraints used in the analysis. For the combos in the top list, which appear at least once in David Turner’s database (only potential combos with open clusters), A13 (with $P(A|B) > 0.10$, from that work), or [Chen, de Grijs, & Deng \(2015\)](#), we obtain membership probabilities >1 per cent. We included in this list the cluster Cepheids recently confirmed by [Clark et al. \(2015\)](#), [Lohr et al. \(2018\)](#), and [Negueruela, Dorda, & Marco \(2020\)](#), as we considered them in the combo descriptions presented in Section 2.5. Combos in the bottom part of this table are those considered missed, and are listed as true associations in at least three of the aforementioned catalogues plus [Röck \(2012\)](#). In the last column we list references where the Cepheid membership to the cluster is discussed: a – [Lohr et al. \(2018\)](#), b – [Negueruela et al. \(2018\)](#), c – [Anderson, Eyer, & Mowlavi \(2013\)](#), d – [Walker \(1985a\)](#), e – [An, Terndrup, & Pinsonneault \(2007\)](#), f – [Turner \(2010\)](#), g – [Majaess et al. \(2011\)](#), h – [Turner \(1976\)](#), i – [Schmidt \(1982\)](#), j – [Turner & Burke \(2002\)](#), k – [Chen, de Grijs, & Deng \(2015\)](#), l – [Sandage \(1958\)](#), m – [Mateo & Madore \(1988\)](#), n – [Matthews et al. \(1995\)](#), o – [Irwin \(1955\)](#), p – [Kholopov \(1956\)](#), q – [Feast \(1957\)](#), r – [Pel \(1985\)](#), s – [Turner, Forbes, & Pedreros \(1992\)](#), t – [Turner, Pedreros, & Walker \(1998c\)](#), u – [Coulson & Caldwell \(1985\)](#), v – [Walker \(1985b\)](#), w – [Hoyle, Shanks, & Tanvir \(2003\)](#), x – [Clark et al. \(2015\)](#), y – [Flower \(1978\)](#), z – [Turner \(1981\)](#), α – [Negueruela, Dorda, & Marco \(2020\)](#), β – [Turner \(1986\)](#), γ – [Walker \(1987\)](#), δ – [Turner \(1982\)](#), ϵ : [Claria, Lapasset, & Bosio \(1991\)](#), ζ – [Turner et al. \(2008\)](#), η – [Turner & Pedreros \(1985\)](#), θ – [Turner \(1998\)](#), ι – [Yilmaz \(1966\)](#), κ – [Turner \(1980\)](#), λ – [Turner et al. \(1993\)](#), ν – [Turner et al. \(1998b\)](#).

Bona fide combos recovered

Open cluster	Cepheid	Sep/ r_1	Constraints	$P(A)$	$P(B A)$	$P(A B)$	References
Berkeley 55	ASASSN-V J211659.90+514558.7	0.38	$\varpi, \mu_\alpha^*, \mu_\delta$	1.00	0.94	0.94	a
Berkeley 51	ASASSN-V J201151.18+342447.2	0.66	$\varpi, \mu_\alpha^*, \mu_\delta$	1.00	0.85	0.85	a, b
Lynga 6	TW Nor	0.18	$\varpi, V_r, \mu_\alpha^*, \mu_\delta$	1.00	0.82	0.82	c, d, e, f, g
NGC 6664	EV Sct	0.40	$\varpi, V_r, \mu_\alpha^*, \mu_\delta$	1.00	0.80	0.80	h, i, j
NGC 7790	CF Cas	0.36	$\varpi, V_r, \mu_\alpha^*, \mu_\delta$	1.00	0.80	0.80	c, k, l, m, n
IC 4725	U Sgr	0.13	$\varpi, V_r, \mu_\alpha^*, \mu_\delta$	1.00	0.75	0.75	c, e, k, o, p, q, r
NGC 129	DL Cas	0.33	$\varpi, V_r, \mu_\alpha^*, \mu_\delta$	1.00	0.75	0.75	c, k, p, s
vdBergh 1	CV Mon	0.49	$\varpi, \mu_\alpha^*, \mu_\delta$	1.00	0.67	0.67	c, k, t
NGC 6067	V0340 Nor	0.14	$\varpi, \mu_\alpha^*, \mu_\delta$	1.00	0.66	0.66	c, e, f, u, v, w
BH 222	OGLE-BLG-CEP-110	0.19	$\varpi, \mu_\alpha^*, \mu_\delta$	1.00	0.65	0.65	a, x
NGC 6649	V0367 Sct	0.82	$\varpi, \mu_\alpha^*, \mu_\delta$	1.00	0.63	0.63	c, y, z
UBC 130	SV Vul	1.41	$\varpi, \mu_\alpha^*, \mu_\delta$	0.73	0.71	0.52	α
NGC 7790	CE Cas B	0.62	$\varpi, \mu_\alpha^*, \mu_\delta$	1.00	0.50	0.50	c, k, l, m, n
NGC 6087	S Nor	0.07	$\varpi, V_r, \mu_\alpha^*, \mu_\delta$	1.00	0.38	0.38	c, k, o, p, q, β
FSR 0158	GQ Vul	2.22	$\varpi, \mu_\alpha^*, \mu_\delta$	0.38	0.89	0.34	c
NGC 7790	CE Cas A	0.60	$\varpi, \mu_\alpha^*, \mu_\delta$	1.00	0.28	0.28	c, k, l, m, n
Ruprecht 79	CS Vel	0.69	$\varpi, V_r, \mu_\alpha^*, \mu_\delta$	1.00	0.23	0.23	f, γ
NGC 5662	V Cen	1.24	$\varpi, V_r, \mu_\alpha^*, \mu_\delta$	0.83	0.12	0.10	e, f, k, δ , ϵ
ASCC 69	S Mus	4.66	$\varpi, V_r, \mu_\alpha^*, \mu_\delta$	0.06	0.58	0.03	c, k

Combos missed

Open cluster	Cepheid	Sep/ r_1	Constraints	$P(A)$	$P(B A)$	$P(A B)$	References
Berkeley 58	CG Cas	1.53	$\varpi, V_r, \mu_\alpha^*, \mu_\delta$	0.66	0.00	0.00	k, ζ
Collinder 394	BB Sgr	1.67	$\varpi, V_r, \mu_\alpha^*, \mu_\delta$	0.59	0.00	0.00	c, f, k, η
Ruprecht 175	X Cyg	7.52	$\varpi, \mu_\alpha^*, \mu_\delta$	0.00	0.00	0.00	k, θ
Trumpler 35	RU Sct	5.87	$\varpi, V_r, \mu_\alpha^*, \mu_\delta$	0.02	0.00	0.00	c, f, w, ι , κ
Turner 2	WZ Sgr	2.56	$\varpi, \mu_\alpha^*, \mu_\delta$	0.21	0.00	0.00	c, k, λ
Turner 9	SU Cyg	1.53	$\varpi, V_r, \mu_\alpha^*, \mu_\delta$	0.66	0.00	0.00	c, f, ν

Table A2: Cluster - Cepheid pairs with membership probabilities $P(A|B)$ between 0.01 and 0.10. The table lists the cluster names as well as their MWSC identification in the K13 catalogue, the Cepheid names, the angular separation of the pair over the cluster's r_1 (Sep/r_1), the list of constraints used to derive the membership probability, the prior $P(A)$, the likelihood $P(A|B)$, and the membership probability $P(B|A)$.

Open cluster	MWSC ID	Cepheid	Sep/ r_1	Constraints	$P(A)$	$P(B A)$	$P(A B)$
UFMG 54	-	OGLE-GD-CEP-0964	11.56	$\varpi, \mu_\alpha^*, \mu_\delta$	0.10	1.00	0.10
NGC 5662	2234	V Cen	1.24	$\varpi, V_r, \mu_\alpha^*, \mu_\delta$	0.83	0.12	0.10
LP 888	-	CG Cas	2.69	$\varpi, \mu_\alpha^*, \mu_\delta$	0.27	0.35	0.09
LP 58	-	AM Vel	4.09	$\varpi, \mu_\alpha^*, \mu_\delta$	0.09	1.00	0.09
BH 99	1831	OGLE-GD-CEP-1669	1.76	$\varpi, \mu_\alpha^*, \mu_\delta$	0.55	0.16	0.09
UBC 135	-	GI Cyg	0.98	$\varpi, \mu_\alpha^*, \mu_\delta$	1.00	0.08	0.08
Collinder 228	1845	GDS J1046447-601605	2.76	$\varpi, \mu_\alpha^*, \mu_\delta$	0.26	0.32	0.08
Loden 1409	2249	OGLE-GD-CEP-0998	3.46	$\varpi, \mu_\alpha^*, \mu_\delta$	0.10	0.81	0.08
FSR 0451	3766	CE Cas A	3.84	$\varpi, \mu_\alpha^*, \mu_\delta$	0.11	0.74	0.08
Platais 8	1629	OGLE-GD-CEP-0507	3.74	$\varpi, \mu_\alpha^*, \mu_\delta$	0.12	0.66	0.08
SBB 2	3612	ASASSN-V J222004.81+560339.3	3.19	$\varpi, \mu_\alpha^*, \mu_\delta$	0.16	0.46	0.08
LP 2134	-	SZ Cas	2.23	$\varpi, \mu_\alpha^*, \mu_\delta$	0.39	0.19	0.07
LP 386	-	V0731 Pup	3.32	$\varpi, \mu_\alpha^*, \mu_\delta$	0.17	0.42	0.07
IC 2602	1841	OGLE-GD-CEP-0507	4.02	$\varpi, \mu_\alpha^*, \mu_\delta$	0.09	0.69	0.06
Trumpler 27	2639	OGLE-BLG-CEP-187	0.63	$\varpi, \mu_\alpha^*, \mu_\delta$	1.00	0.06	0.06
LP 909	-	VV Cas	3.46	$\varpi, \mu_\alpha^*, \mu_\delta$	0.15	0.38	0.06
NGC 5045	2096	OGLE-GD-CEP-1719	1.59	$\varpi, \mu_\alpha^*, \mu_\delta$	0.64	0.09	0.06
UBC 407	-	V0824 Cas	4.21	$\varpi, \mu_\alpha^*, \mu_\delta$	0.09	0.66	0.06
Hogg 17	2232	OGLE-GD-CEP-0991	1.71	$\varpi, \mu_\alpha^*, \mu_\delta$	0.57	0.10	0.06
LP 925	-	V0966 Mon	2.05	$\varpi, \mu_\alpha^*, \mu_\delta$	0.45	0.12	0.05
UBC 672	-	OGLE-GD-CEP-1194	3.22	$\varpi, \mu_\alpha^*, \mu_\delta$	0.18	0.29	0.05
ASCC 79	2288	OGLE-GD-CEP-0998	4.78	$\varpi, \mu_\alpha^*, \mu_\delta$	0.05	0.95	0.05
LP 925	-	ASAS J062855+1107.3	4.79	$\varpi, \mu_\alpha^*, \mu_\delta$	0.05	0.87	0.05
UPK 604	-	OGLE-GD-CEP-1742	4.47	$\varpi, \mu_\alpha^*, \mu_\delta$	0.07	0.67	0.05
UBC 658	-	OGLE-GD-CEP-1676	4.64	$\varpi, \mu_\alpha^*, \mu_\delta$	0.06	0.73	0.04
LP 699	-	ASASSN-V J091548.19-523008.5	4.30	$\varpi, \mu_\alpha^*, \mu_\delta$	0.08	0.56	0.04
NGC 6231	2481	OGLE-GD-CEP-1194	3.55	$\varpi, \mu_\alpha^*, \mu_\delta$	0.13	0.31	0.04
DBSB 45	1792	OGLE-GD-CEP-0479	3.85	$\varpi, \mu_\alpha^*, \mu_\delta$	0.09	0.44	0.04
FSR 0451	3766	CE Cas B	3.84	$\varpi, \mu_\alpha^*, \mu_\delta$	0.11	0.38	0.04
LP 1429	-	AQ Pup	4.11	$\varpi, \mu_\alpha^*, \mu_\delta$	0.09	0.42	0.04
UBC 404+	-	CE Cas A	4.85	$\varpi, \mu_\alpha^*, \mu_\delta$	0.05	0.73	0.04
UBC 525	-	OGLE-GD-CEP-1715	4.52	$\varpi, \mu_\alpha^*, \mu_\delta$	0.07	0.54	0.04
UPK 300	-	RW Cam	5.25	$\varpi, \mu_\alpha^*, \mu_\delta$	0.04	0.94	0.04
UBC 323	-	OGLE-GD-CEP-1194	2.95	$\varpi, \mu_\alpha^*, \mu_\delta$	0.22	0.16	0.04
LP 925	-	VW Mon	2.45	$\varpi, \mu_\alpha^*, \mu_\delta$	0.33	0.11	0.04
LP 386	-	ASAS J080822-3222.6	4.66	$\varpi, \mu_\alpha^*, \mu_\delta$	0.06	0.58	0.04
LP 925	-	OGLE-GD-CEP-0040	3.99	$\varpi, \mu_\alpha^*, \mu_\delta$	0.10	0.34	0.03
ASCC 69	1996	S Mus	4.66	$\varpi, V_r, \mu_\alpha^*, \mu_\delta$	0.06	0.58	0.03
NGC 6193	2444	OGLE-GD-CEP-1167	4.67	$\varpi, \mu_\alpha^*, \mu_\delta$	0.06	0.59	0.03
Hogg 15	2063	WISE J124231.0-625132	4.26	$\varpi, \mu_\alpha^*, \mu_\delta$	0.08	0.40	0.03
LP 1328	-	OP Cas	5.09	$\varpi, \mu_\alpha^*, \mu_\delta$	0.04	0.69	0.03
IC 2395	1537	AM Vel	5.45	$\varpi, \mu_\alpha^*, \mu_\delta$	0.03	1.00	0.03
Platais 9	1639	AM Vel	5.13	$\varpi, \mu_\alpha^*, \mu_\delta$	0.04	0.72	0.03
Trumpler 27	2639	ASAS J173848-3304.4	5.03	$\varpi, \mu_\alpha^*, \mu_\delta$	0.03	0.78	0.03
UBC 545	-	OGLE-GD-CEP-1167	5.83	$\varpi, \mu_\alpha^*, \mu_\delta$	0.02	0.99	0.02
Trumpler 22	2226	OGLE-GD-CEP-0988	5.06	$\varpi, \mu_\alpha^*, \mu_\delta$	0.04	0.60	0.02
UBC 420	-	DF Cas	3.75	$\varpi, \mu_\alpha^*, \mu_\delta$	0.12	0.20	0.02
LP 699	-	V0530 Vel	3.46	$\varpi, \mu_\alpha^*, \mu_\delta$	0.15	0.16	0.02
Alessi 52	-	OGLE-GD-CEP-0758	4.64	ϖ	0.04	0.54	0.02
FSR 1744	2474	OGLE-GD-CEP-1188*	3.21	$\varpi, \mu_\alpha^*, \mu_\delta$	0.10	0.23	0.02
LP 888	-	V0997 Cas	4.75	$\varpi, \mu_\alpha^*, \mu_\delta$	0.06	0.40	0.02
Dolidze 34	2976	OGLE-GD-CEP-1218	2.07	$\varpi, \mu_\alpha^*, \mu_\delta$	0.34	0.06	0.02
UBC 609	-	V0359 Cam	4.76	$\varpi, \mu_\alpha^*, \mu_\delta$	0.06	0.39	0.02
FSR 0451	3766	CF Cas	3.93	$\varpi, \mu_\alpha^*, \mu_\delta$	0.10	0.22	0.02
Juchert 13	1992	OGLE-GD-CEP-0743	2.64	$\varpi, \mu_\alpha^*, \mu_\delta$	0.27	0.08	0.02
NGC 129	53	V0379 Cas	4.45	$\varpi, V_r, \mu_\alpha^*, \mu_\delta$	0.07	0.32	0.02
UBC 541	-	OGLE-GD-CEP-1136	5.69	$\varpi, \mu_\alpha^*, \mu_\delta$	0.03	0.73	0.02

Table A2: (Continued).

Open cluster	MWSC ID	Cepheid	Sep/ r_1	Constraints	$P(A)$	$P(B A)$	$P(A B)$
Loden 807	2117	OGLE-GD-CEP-1722	4.11	$\varpi, \mu_\alpha^*, \mu_\delta$	0.03	0.57	0.02
ASCC 79	2288	OGLE-GD-CEP-1023	3.83	$\varpi, \mu_\alpha^*, \mu_\delta$	0.11	0.18	0.02
LP 925	–	V0480 Mon	4.05	$\varpi, \mu_\alpha^*, \mu_\delta$	0.10	0.20	0.02
UBC 421	–	UY Per	5.33	$\varpi, \mu_\alpha^*, \mu_\delta$	0.04	0.53	0.02
LP 1428	–	AQ Pup	6.07	$\varpi, \mu_\alpha^*, \mu_\delta$	0.02	0.93	0.02
UBC 156	–	V1077 Cyg	5.41	$\varpi, \mu_\alpha^*, \mu_\delta$	0.03	0.52	0.02
UFMG 54	–	OGLE-GD-CEP-0968	19.55	$\varpi, \mu_\alpha^*, \mu_\delta$	0.02	1.00	0.02
UBC 404 ⁺	–	CE Cas B	4.85	$\varpi, \mu_\alpha^*, \mu_\delta$	0.05	0.33	0.02
Ruprecht 136	2765	OGLE-BLG-CEP-131	2.75	$\varpi, \mu_\alpha^*, \mu_\delta$	0.18	0.09	0.02
Platais 1	3519	V1077 Cyg	2.71	$\varpi, \mu_\alpha^*, \mu_\delta$	0.32	0.05	0.02
UFMG 2	–	OGLE-GD-CEP-1759	5.27	$\varpi, \mu_\alpha^*, \mu_\delta$	0.03	0.48	0.02
BDSB 102	2625	GDS J1733264-322920	2.05	$\varpi, \mu_\alpha^*, \mu_\delta$	0.31	0.05	0.02
Trumpler 15	1849	OGLE-GD-CEP-1673	5.78	$\varpi, \mu_\alpha^*, \mu_\delta$	0.02	0.72	0.02
Collinder 173	–	AH Vel	1.59	ϖ, V_r	0.63	0.02	0.02
BH 131	2030	OGLE-GD-CEP-0790	3.51	$\varpi, \mu_\alpha^*, \mu_\delta$	0.12	0.13	0.02
Ruprecht 169	–	OGLE-BLG-CEP-131	1.91	$\varpi, \mu_\alpha^*, \mu_\delta$	0.46	0.03	0.02
FSR 0927	858	OGLE-GD-CEP-0031	7.06	$\varpi, \mu_\alpha^*, \mu_\delta$	0.02	0.64	0.02
PHOC 24	–	T Mon	4.86	$\varpi, \mu_\alpha^*, \mu_\delta$	0.05	0.30	0.01
NGC 5045	2096	OGLE-GD-CEP-1715	5.24	$\varpi, \mu_\alpha^*, \mu_\delta$	0.04	0.33	0.01
UBC 259	–	OGLE-GD-CEP-1669	6.58	$\varpi, \mu_\alpha^*, \mu_\delta$	0.01	0.98	0.01
NGC 6611	2886	NSV 10617	4.79	$\varpi, \mu_\alpha^*, \mu_\delta$	0.05	0.27	0.01
UFMG 45	–	OGLE-GD-CEP-1104	0.55	$\varpi, \mu_\alpha^*, \mu_\delta$	1.00	0.01	0.01
Collinder 228	1845	V0720 Car	2.42	$\varpi, \mu_\alpha^*, \mu_\delta$	0.34	0.04	0.01
Dolidze 4	–	V1046 Cyg	3.05	μ_α^*, μ_δ	0.18	0.07	0.01
UBC 272	–	WISE J111429.0-620100	3.46	$\varpi, \mu_\alpha^*, \mu_\delta$	0.15	0.09	0.01
NGC 7788	3777	CE Cas B	5.56	$\varpi, \mu_\alpha^*, \mu_\delta$	0.03	0.47	0.01
UBC 491	–	DP Vel	1.51	$\varpi, \mu_\alpha^*, \mu_\delta$	0.67	0.02	0.01
BH 131	2030	OGLE-GD-CEP-0795	5.91	$\varpi, \mu_\alpha^*, \mu_\delta$	0.01	0.82	0.01
NGC 6231	2481	OGLE-GD-CEP-1196	3.68	$\varpi, \mu_\alpha^*, \mu_\delta$	0.12	0.10	0.01
LP 699	–	EX Vel	5.37	$\varpi, \mu_\alpha^*, \mu_\delta$	0.04	0.34	0.01
LP 1429	–	V0620 Pup	5.58	$\varpi, \mu_\alpha^*, \mu_\delta$	0.03	0.40	0.01
Gulliver 59	–	OGLE-GD-CEP-1715	6.18	$\varpi, \mu_\alpha^*, \mu_\delta$	0.02	0.71	0.01
IC 2948	1961	OGLE-GD-CEP-1688	0.54	$\varpi, \mu_\alpha^*, \mu_\delta$	1.00	0.01	0.01
NGC 7788	3777	CE Cas A	5.57	$\varpi, \mu_\alpha^*, \mu_\delta$	0.03	0.43	0.01
Collinder 228	1845	OGLE-GD-CEP-1672	1.44	$\varpi, \mu_\alpha^*, \mu_\delta$	0.71	0.02	0.01
IC 1848	236	DF Cas	6.62	$\varpi, V_r, \mu_\alpha^*, \mu_\delta$	0.01	0.95	0.01
BH 131	2030	OGLE-GD-CEP-0785	1.99	$\varpi, \mu_\alpha^*, \mu_\delta$	0.43	0.02	0.01
ASCC 59	1793	WISE J102221.6-574822	1.63	$\varpi, \mu_\alpha^*, \mu_\delta$	0.53	0.02	0.01

* Uncertain Cepheid classification, as noted by the OGLE team.

⁺ Coincidence with a cluster in the catalogues of Liu & Pang (2019) or Sim et al. (2019), according to Castro-Ginard et al. (2020).

Table A3: Same as Table A2 for combos pairs with low priors $P(A)$, but high likelihood, $P(B|A) > 0.85$.

Open cluster	MWSC ID	Cepheid	Sep/ r_1	Constraints	$P(A)$	$P(B A)$	$P(A B)$
FSR 1580	1944	GI Car	48.36	$\varpi, \mu_\alpha^*, \mu_\delta$	0.00	1.00	0.00
UBC 339	–	AP Sgr	46.17	$\varpi, \mu_\alpha^*, \mu_\delta$	0.00	1.00	0.00
UBC 613	–	IN Aur	44.19	$\varpi, \mu_\alpha^*, \mu_\delta$	0.00	1.00	0.00
UBC 355 ^k	–	GDS J1843309-021501	44.04	$\varpi, \mu_\alpha^*, \mu_\delta$	0.00	1.00	0.00
FSR 1580	1944	V0419 Cen	41.81	$\varpi, \mu_\alpha^*, \mu_\delta$	0.00	1.00	0.00
UBC 93	–	V0767 Sgr	42.55	$\varpi, \mu_\alpha^*, \mu_\delta$	0.00	1.00	0.00
FSR 1580	1944	WISE J111821.4-591416	36.60	$\varpi, \mu_\alpha^*, \mu_\delta$	0.00	1.00	0.00
UBC 40	–	V1016 Cas	35.63	$\varpi, \mu_\alpha^*, \mu_\delta$	0.00	1.00	0.00
UBC 355 ^k	–	TY Sct	34.27	$\varpi, \mu_\alpha^*, \mu_\delta$	0.00	1.00	0.00
UBC 355 ^k	–	RU Sct	34.23	$\varpi, \mu_\alpha^*, \mu_\delta$	0.00	1.00	0.00
UBC 336	–	V0773 Sgr	32.61	$\varpi, \mu_\alpha^*, \mu_\delta$	0.00	1.00	0.00
PHOC 9	–	YZ Aur	30.54	$\varpi, \mu_\alpha^*, \mu_\delta$	0.00	1.00	0.00
UBC 336	–	V0767 Sgr	30.92	$\varpi, \mu_\alpha^*, \mu_\delta$	0.00	1.00	0.00
PHOC 9	–	Y Aur	29.94	$\varpi, \mu_\alpha^*, \mu_\delta$	0.00	1.00	0.00
UBC 339	–	V5738 Sgr	30.26	$\varpi, \mu_\alpha^*, \mu_\delta$	0.00	1.00	0.00
UFMG 54	–	OGLE-GD-CEP-0966	95.87	$\varpi, \mu_\alpha^*, \mu_\delta$	0.00	1.00	0.00
UBC 339	–	OGLE-BLG-CEP-135	27.84	$\varpi, \mu_\alpha^*, \mu_\delta$	0.00	1.00	0.00
UFMG 54	–	GDS J1417363-611600	90.79	$\varpi, \mu_\alpha^*, \mu_\delta$	0.00	1.00	0.00
FSR 1580	1944	V1048 Cen	24.80	$\varpi, \mu_\alpha^*, \mu_\delta$	0.00	1.00	0.00
UFMG 54	–	OGLE-GD-CEP-1733	86.73	$\varpi, \mu_\alpha^*, \mu_\delta$	0.00	1.00	0.00
UFMG 54	–	OGLE-GD-CEP-0972	83.76	$\varpi, \mu_\alpha^*, \mu_\delta$	0.00	1.00	0.00
UBC 643	–	OGLE-GD-CEP-0173	23.01	$\varpi, \mu_\alpha^*, \mu_\delta$	0.00	1.00	0.00
UFMG 54	–	GDS J1415024-624409	77.93	$\varpi, \mu_\alpha^*, \mu_\delta$	0.00	1.00	0.00
UFMG 54	–	OGLE-GD-CEP-0973	77.93	$\varpi, \mu_\alpha^*, \mu_\delta$	0.00	1.00	0.00
UBC 355 ^k	–	FT Sct	22.64	$\varpi, \mu_\alpha^*, \mu_\delta$	0.00	1.00	0.00
UFMG 54	–	GDS J1405095-602844	72.11	$\varpi, \mu_\alpha^*, \mu_\delta$	0.00	1.00	0.00
UFMG 54	–	OGLE-GD-CEP-1729	71.66	$\varpi, \mu_\alpha^*, \mu_\delta$	0.00	1.00	0.00
UFMG 54	–	ASAS J140742-6315.4	68.09	$\varpi, \mu_\alpha^*, \mu_\delta$	0.00	1.00	0.00
UBC 102	–	CM Sct	18.35	$\varpi, \mu_\alpha^*, \mu_\delta$	0.00	1.00	0.00
UFMG 43	–	OGLE-GD-CEP-1055	18.64	$\varpi, \mu_\alpha^*, \mu_\delta$	0.00	1.00	0.00
UBC 345	–	X Sct	16.20	$\varpi, \mu_\alpha^*, \mu_\delta$	0.00	1.00	0.00
UFMG 54	–	OGLE-GD-CEP-1732	52.62	$\varpi, \mu_\alpha^*, \mu_\delta$	0.00	1.00	0.00
UFMG 54	–	OGLE-GD-CEP-0971	51.21	$\varpi, \mu_\alpha^*, \mu_\delta$	0.00	1.00	0.00
PHOC 9	–	ER Aur	14.75	$\varpi, \mu_\alpha^*, \mu_\delta$	0.00	1.00	0.00
UBC 339	–	AV Sgr	14.97	$\varpi, \mu_\alpha^*, \mu_\delta$	0.00	1.00	0.00
UFMG 43	–	OGLE-GD-CEP-1091	14.86	$\varpi, \mu_\alpha^*, \mu_\delta$	0.00	1.00	0.00
UFMG 16	–	OGLE-GD-CEP-1145	14.76	$\varpi, \mu_\alpha^*, \mu_\delta$	0.00	1.00	0.00
UFMG 54	–	OGLE-GD-CEP-0960	47.33	$\varpi, \mu_\alpha^*, \mu_\delta$	0.00	1.00	0.00
UFMG 43	–	GDS J1552281-550452	14.45	$\varpi, \mu_\alpha^*, \mu_\delta$	0.00	1.00	0.00
UBC 82	–	T Mon	13.77	$\varpi, \mu_\alpha^*, \mu_\delta$	0.00	1.00	0.00
PHOC 9	–	ASASSN-V J052240.06+414302	12.99	$\varpi, \mu_\alpha^*, \mu_\delta$	0.00	1.00	0.00
UBC 40	–	Mis V1348	11.97	$\varpi, \mu_\alpha^*, \mu_\delta$	0.00	1.00	0.00
UBC 345	–	TX Sct	11.91	$\varpi, \mu_\alpha^*, \mu_\delta$	0.00	1.00	0.00
UBC 345	–	V0389 Sct	10.86	$\varpi, \mu_\alpha^*, \mu_\delta$	0.00	1.00	0.00
UFMG 54	–	OGLE-GD-CEP-0965	35.13	$\varpi, \mu_\alpha^*, \mu_\delta$	0.00	1.00	0.00
UFMG 54	–	QY Cen	32.89	$\varpi, \mu_\alpha^*, \mu_\delta$	0.00	1.00	0.00
UFMG 54	–	OGLE-GD-CEP-0969	30.01	$\varpi, \mu_\alpha^*, \mu_\delta$	0.00	1.00	0.00
UBC 336	–	V5860 Sgr	9.03	$\varpi, \mu_\alpha^*, \mu_\delta$	0.00	1.00	0.00
UFMG 87	–	V0482 Sco	8.39	$\varpi, \mu_\alpha^*, \mu_\delta$	0.00	1.00	0.00
UFMG 43	–	GDS J1537406-554914	8.57	$\varpi, \mu_\alpha^*, \mu_\delta$	0.00	1.00	0.00
UFMG 54	–	OGLE-GD-CEP-0970	25.25	$\varpi, \mu_\alpha^*, \mu_\delta$	0.01	1.00	0.01
Ruprecht 63	1504	AM Vel	11.65	$\varpi, \mu_\alpha^*, \mu_\delta$	0.00	1.00	0.00
FSR 1429	1517	AM Vel	27.23	$\varpi, \mu_\alpha^*, \mu_\delta$	0.00	1.00	0.00
FSR 1441	1524	AM Vel	23.95	$\varpi, \mu_\alpha^*, \mu_\delta$	0.00	1.00	0.00
NGC 2670	1554	AM Vel	17.75	$\varpi, \mu_\alpha^*, \mu_\delta$	0.00	1.00	0.00
NGC 2660	1539	AM Vel	37.58	$\varpi, \mu_\alpha^*, \mu_\delta$	0.00	1.00	0.00
FSR 1755	–	OGLE-BLG-CEP-174	10.00	μ_α^*, μ_δ	0.00	1.00	0.00
Ruprecht 60	1485	AM Vel	49.27	$\varpi, \mu_\alpha^*, \mu_\delta$	0.00	1.00	0.00
Saurer 4	2009	WISE J122020.6-634347	23.71	$\varpi, \mu_\alpha^*, \mu_\delta$	0.00	1.00	0.00
BH 144	2098	OGLE-GD-CEP-0869	49.82	$\varpi, \mu_\alpha^*, \mu_\delta$	0.00	1.00	0.00
Pismis 8	1533	AM Vel	53.11	$\varpi, \mu_\alpha^*, \mu_\delta$	0.00	1.00	0.00
NGC 2645	–	AM Vel	38.04	$\varpi, \mu_\alpha^*, \mu_\delta$	0.00	1.00	0.00
DBSB 50	1779	OGLE-GD-CEP-0507	34.01	$\varpi, \mu_\alpha^*, \mu_\delta$	0.00	1.00	0.00
Hogg 19	2415	OGLE-GD-CEP-1167	28.79	$\varpi, \mu_\alpha^*, \mu_\delta$	0.00	1.00	0.00
Pismis 6	1520	AM Vel	15.56	$\varpi, \mu_\alpha^*, \mu_\delta$	0.00	1.00	0.00

Table A3: (Continued).

Open cluster	MWSC ID	Cepheid	Sep/ r_1	Constraints	$P(A)$	$P(B A)$	$P(A B)$
FSR 1443	1523	AM Vel	9.49	$\varpi, \mu_\alpha^*, \mu_\delta$	0.00	0.99	0.00
FSR 1518	1738	WISE J100302.3-560258	26.89	$\varpi, \mu_\alpha^*, \mu_\delta$	0.00	0.99	0.00
Loden 153	1824	OGLE-GD-CEP-0507	22.27	$\varpi, \mu_\alpha^*, \mu_\delta$	0.00	0.99	0.00
Waterloo 6	1528	AM Vel	45.45	$\varpi, \mu_\alpha^*, \mu_\delta$	0.00	0.99	0.00
NGC 4755	2072	OGLE-GD-CEP-1714	15.68	$\varpi, \mu_\alpha^*, \mu_\delta$	0.00	0.99	0.00
Trumpler 13	1800	OGLE-GD-CEP-0507	26.94	$\varpi, \mu_\alpha^*, \mu_\delta$	0.00	0.99	0.00
SAI 113	1797	CQ Car	38.07	$\varpi, \mu_\alpha^*, \mu_\delta$	0.00	0.99	0.00
NGC 3255	1804	OGLE-GD-CEP-0507	91.05	$\varpi, \mu_\alpha^*, \mu_\delta$	0.00	0.99	0.00
Ruprecht 66	1530	GDS J0833314-382650	34.98	$\varpi, \mu_\alpha^*, \mu_\delta$	0.00	0.99	0.00
ASCC 59	1793	OGLE-GD-CEP-0507	7.38	$\varpi, \mu_\alpha^*, \mu_\delta$	0.00	0.99	0.00
Loden 153	1824	OGLE-GD-CEP-1669	19.23	$\varpi, \mu_\alpha^*, \mu_\delta$	0.00	0.99	0.00
BH 63	1653	OGLE-GD-CEP-0328	23.97	$\varpi, \mu_\alpha^*, \mu_\delta$	0.00	0.99	0.00
UBC 258	–	OGLE-GD-CEP-0507	16.81	$\varpi, \mu_\alpha^*, \mu_\delta$	0.00	0.99	0.00
IC 2581	1805	OGLE-GD-CEP-0507	22.84	$\varpi, \mu_\alpha^*, \mu_\delta$	0.00	0.99	0.00
UBC 667	–	OGLE-GD-CEP-1167	44.53	$\varpi, \mu_\alpha^*, \mu_\delta$	0.00	0.99	0.00
SAI 113	1797	OGLE-GD-CEP-0507	21.44	$\varpi, \mu_\alpha^*, \mu_\delta$	0.00	0.99	0.00
Westerlund 1	2461	OGLE-GD-CEP-1174	58.40	$\varpi, \mu_\alpha^*, \mu_\delta$	0.00	0.99	0.00
Saurer 4	2009	OGLE-GD-CEP-0774	27.71	$\varpi, \mu_\alpha^*, \mu_\delta$	0.00	0.99	0.00
Westerlund 2	1801	OGLE-GD-CEP-0507	60.38	$\varpi, \mu_\alpha^*, \mu_\delta$	0.00	0.99	0.00
UBC 259	–	OGLE-GD-CEP-0507	10.58	$\varpi, \mu_\alpha^*, \mu_\delta$	0.00	0.99	0.00
UBC 613	–	NEV44	23.56	$\varpi, \mu_\alpha^*, \mu_\delta$	0.00	0.99	0.00
Ruprecht 69	1548	AM Vel	27.64	$\varpi, \mu_\alpha^*, \mu_\delta$	0.00	0.99	0.00
ESO 260 06	1559	AM Vel	24.22	$\varpi, \mu_\alpha^*, \mu_\delta$	0.00	0.99	0.00
UBC 498	–	OGLE-GD-CEP-0507	18.11	$\varpi, \mu_\alpha^*, \mu_\delta$	0.00	0.99	0.00
Ruprecht 83	1718	GDS J0953141-550539	25.09	$\varpi, \mu_\alpha^*, \mu_\delta$	0.00	0.99	0.00
BH 84	1743	OGLE-GD-CEP-0455	59.79	$\varpi, \mu_\alpha^*, \mu_\delta$	0.00	0.98	0.00
Westerlund 2	1801	OGLE-GD-CEP-1669	88.20	$\varpi, \mu_\alpha^*, \mu_\delta$	0.00	0.98	0.00
NGC 3293	1826	OGLE-GD-CEP-0507	23.14	$\varpi, \mu_\alpha^*, \mu_\delta$	0.00	0.98	0.00
NGC 3255	1804	OGLE-GD-CEP-1669	78.75	$\varpi, \mu_\alpha^*, \mu_\delta$	0.00	0.98	0.00
UBC 499	–	OGLE-GD-CEP-0507	16.36	$\varpi, \mu_\alpha^*, \mu_\delta$	0.00	0.98	0.00
Ruprecht 78	1675	GDS J0935268-542134	31.69	$\varpi, \mu_\alpha^*, \mu_\delta$	0.00	0.98	0.00
NGC 6200	2450	OGLE-GD-CEP-1167	14.03	$\varpi, \mu_\alpha^*, \mu_\delta$	0.00	0.98	0.00
UBC 653	–	OGLE-GD-CEP-0507	16.40	$\varpi, \mu_\alpha^*, \mu_\delta$	0.00	0.98	0.00
UBC 508	–	GDS J1055122-600930	8.68	$\varpi, \mu_\alpha^*, \mu_\delta$	0.00	0.98	0.00
UBC 654	–	OGLE-GD-CEP-0507	17.01	$\varpi, \mu_\alpha^*, \mu_\delta$	0.00	0.98	0.00
DBSB 45	1792	OGLE-GD-CEP-0507	38.40	$\varpi, \mu_\alpha^*, \mu_\delta$	0.00	0.98	0.00
NGC 3324	1830	OGLE-GD-CEP-0507	32.01	$\varpi, \mu_\alpha^*, \mu_\delta$	0.00	0.98	0.00
DC 5	1838	OGLE-GD-CEP-0507	60.39	$\varpi, \mu_\alpha^*, \mu_\delta$	0.00	0.98	0.00
NGC 7067	3508	V1077 Cyg	44.84	$\varpi, \mu_\alpha^*, \mu_\delta$	0.00	0.98	0.00
UBC 318	–	OGLE-GD-CEP-1167	8.80	$\varpi, \mu_\alpha^*, \mu_\delta$	0.00	0.98	0.00
BH 90	1778	OGLE-GD-CEP-0507	45.23	$\varpi, \mu_\alpha^*, \mu_\delta$	0.00	0.98	0.00
Collinder 220	1803	OGLE-GD-CEP-0507	9.43	$\varpi, \mu_\alpha^*, \mu_\delta$	0.00	0.98	0.00
Hogg 21	2455	OGLE-GD-CEP-1167	41.58	$\varpi, \mu_\alpha^*, \mu_\delta$	0.00	0.98	0.00
SAI 113	1797	OGLE-GD-CEP-1669	34.19	$\varpi, \mu_\alpha^*, \mu_\delta$	0.00	0.98	0.00
Ruprecht 120	2426	OGLE-GD-CEP-1167	11.90	$\varpi, \mu_\alpha^*, \mu_\delta$	0.00	0.98	0.00
BH 144	2098	OGLE-GD-CEP-0873	50.61	$\varpi, \mu_\alpha^*, \mu_\delta$	0.00	0.98	0.00
UBC 502	–	OGLE-GD-CEP-0507	22.99	$\varpi, \mu_\alpha^*, \mu_\delta$	0.00	0.98	0.00
DBSB 46	1813	OGLE-GD-CEP-0507	64.40	$\varpi, \mu_\alpha^*, \mu_\delta$	0.00	0.98	0.00
DC 5	1838	GDS J1042539-610125	60.23	$\varpi, \mu_\alpha^*, \mu_\delta$	0.00	0.98	0.00
FSR 1666	2167	OGLE-GD-CEP-1727	7.25	$\varpi, \mu_\alpha^*, \mu_\delta$	0.00	0.98	0.00
BH 91	1787	OGLE-GD-CEP-0507	13.44	$\varpi, \mu_\alpha^*, \mu_\delta$	0.00	0.98	0.00
Saurer 4	2009	OGLE-GD-CEP-1699	60.72	$\varpi, \mu_\alpha^*, \mu_\delta$	0.00	0.97	0.00
UBC 261	–	OGLE-GD-CEP-1669	18.01	$\varpi, \mu_\alpha^*, \mu_\delta$	0.00	0.97	0.00
UBC 262	–	OGLE-GD-CEP-1669	26.99	$\varpi, \mu_\alpha^*, \mu_\delta$	0.00	0.97	0.00
FSR 0735	433	SV Per	39.56	$\varpi, \mu_\alpha^*, \mu_\delta$	0.00	0.97	0.00
Lynga 5	2310	OGLE-GD-CEP-1759	22.50	$\varpi, \mu_\alpha^*, \mu_\delta$	0.00	0.97	0.00
UBC 316	–	OGLE-GD-CEP-1167	15.63	$\varpi, \mu_\alpha^*, \mu_\delta$	0.00	0.97	0.00
DC 5	1838	OGLE-GD-CEP-1669	37.70	$\varpi, \mu_\alpha^*, \mu_\delta$	0.00	0.97	0.00
NGC 6167	2425	OGLE-GD-CEP-1167	10.67	$\varpi, \mu_\alpha^*, \mu_\delta$	0.00	0.97	0.00
Ruprecht 90	1819	OGLE-GD-CEP-0507	10.21	$\varpi, \mu_\alpha^*, \mu_\delta$	0.00	0.97	0.00
UBC 498	–	OGLE-GD-CEP-1669	25.88	$\varpi, \mu_\alpha^*, \mu_\delta$	0.00	0.97	0.00
Juchert 1	3095	ZTF J192214.30+143115.2	77.30	$\varpi, \mu_\alpha^*, \mu_\delta$	0.00	0.97	0.00
Trumpler 13	1800	OGLE-GD-CEP-1669	27.54	$\varpi, \mu_\alpha^*, \mu_\delta$	0.00	0.97	0.00
DBSB 48	1817	OGLE-GD-CEP-0507	17.15	$\varpi, \mu_\alpha^*, \mu_\delta$	0.00	0.97	0.00
Westerlund 2	1801	WISE J101825.7-562122	79.79	$\varpi, \mu_\alpha^*, \mu_\delta$	0.00	0.97	0.00
ESO 260 07	1570	OGLE-GD-CEP-0296	21.79	$\varpi, \mu_\alpha^*, \mu_\delta$	0.00	0.97	0.00
UBC 654	–	OGLE-GD-CEP-1669	9.72	$\varpi, \mu_\alpha^*, \mu_\delta$	0.00	0.97	0.00

Table A3: (Continued).

Open cluster	MWSC ID	Cepheid	Sep/ r_1	Constraints	$P(A)$	$P(B A)$	$P(A B)$
DBSB 51	1822	OGLE-GD-CEP-0507	33.30	$\varpi, \mu_\alpha^*, \mu_\delta$	0.00	0.97	0.00
Ruprecht 25	1280	V0612 Pup	131.78	$\varpi, \mu_\alpha^*, \mu_\delta$	0.00	0.97	0.00
DBSB 47	1784	OGLE-GD-CEP-0507	36.97	$\varpi, \mu_\alpha^*, \mu_\delta$	0.00	0.97	0.00
Ruprecht 89	1808	OGLE-GD-CEP-0507	10.05	$\varpi, \mu_\alpha^*, \mu_\delta$	0.00	0.97	0.00
Kronberger 81	3511	V0733 Cyg	26.52	$\varpi, \mu_\alpha^*, \mu_\delta$	0.00	0.97	0.00
Ruprecht 78	1675	GDS J0922126-530350	33.60	$\varpi, \mu_\alpha^*, \mu_\delta$	0.00	0.96	0.00
Saurer 4	2009	OGLE-GD-CEP-0795	58.77	$\varpi, \mu_\alpha^*, \mu_\delta$	0.00	0.96	0.00
King 21	3762	CF Cas	38.72	$\varpi, \mu_\alpha^*, \mu_\delta$	0.00	0.96	0.00
Lynga 3	2284	OGLE-GD-CEP-1028	33.71	$\varpi, \mu_\alpha^*, \mu_\delta$	0.00	0.96	0.00
UBC 291	–	WISE J132924.6-625511	29.63	$\varpi, \mu_\alpha^*, \mu_\delta$	0.00	0.96	0.00
DBSB 60	1888	OGLE-GD-CEP-0012	15.18	$\varpi, \mu_\alpha^*, \mu_\delta$	0.00	0.96	0.00
Berkeley 12	413	SV Per	29.81	$\varpi, \mu_\alpha^*, \mu_\delta$	0.00	0.96	0.00
NGC 5155	2125	OGLE-GD-CEP-1722	7.05	$\varpi, \mu_\alpha^*, \mu_\delta$	0.00	0.96	0.00
DBSB 45	1792	OGLE-GD-CEP-1669	61.23	$\varpi, \mu_\alpha^*, \mu_\delta$	0.00	0.96	0.00
Gulliver 41	–	OGLE-GD-CEP-1790	55.84	$\varpi, \mu_\alpha^*, \mu_\delta$	0.00	0.96	0.00
DBSB 60	1888	OGLE-GD-CEP-1677	58.85	$\varpi, \mu_\alpha^*, \mu_\delta$	0.00	0.96	0.00
Saurer 4	2009	WISE J120011.9-632951	51.51	$\varpi, \mu_\alpha^*, \mu_\delta$	0.00	0.96	0.00
Schuster 1	1756	GDS J1004009-551114	28.14	$\varpi, \mu_\alpha^*, \mu_\delta$	0.00	0.95	0.00
LP 1831	–	V0407 Cas	8.60	$\varpi, \mu_\alpha^*, \mu_\delta$	0.00	0.95	0.00
UBC 499	–	OGLE-GD-CEP-1669	7.69	$\varpi, \mu_\alpha^*, \mu_\delta$	0.01	0.95	0.01
UBC 505	–	OGLE-GD-CEP-1669	28.33	$\varpi, \mu_\alpha^*, \mu_\delta$	0.00	0.95	0.00
DBSB 43	1754	OGLE-GD-CEP-0433	14.16	$\varpi, \mu_\alpha^*, \mu_\delta$	0.00	0.95	0.00
Loden 172	1809	OGLE-GD-CEP-0507	14.05	$\varpi, \mu_\alpha^*, \mu_\delta$	0.00	0.95	0.00
Hogg 7	1810	OGLE-GD-CEP-0507	37.09	$\varpi, \mu_\alpha^*, \mu_\delta$	0.00	0.95	0.00
FSR 1686	2241	OGLE-GD-CEP-0998	22.30	$\varpi, \mu_\alpha^*, \mu_\delta$	0.00	0.95	0.00
UBC 502	–	OGLE-GD-CEP-1669	12.94	$\varpi, \mu_\alpha^*, \mu_\delta$	0.00	0.95	0.00
Schuster 1	1756	OGLE-GD-CEP-0434	24.44	$\varpi, \mu_\alpha^*, \mu_\delta$	0.00	0.94	0.00
LP 699	–	GDS J0914201-512930	8.29	$\varpi, \mu_\alpha^*, \mu_\delta$	0.00	0.94	0.00
BH 144	2098	GDS J1313507-642626	61.91	$\varpi, \mu_\alpha^*, \mu_\delta$	0.00	0.94	0.00
Lynga 3	2284	OGLE-GD-CEP-1032	107.45	$\varpi, \mu_\alpha^*, \mu_\delta$	0.00	0.94	0.00
Czernik 29	1234	ASAS J072925-1558.6	10.85	$\varpi, \mu_\alpha^*, \mu_\delta$	0.00	0.94	0.00
FSR 1390	1494	OGLE-GD-CEP-1629	31.35	$\varpi, \mu_\alpha^*, \mu_\delta$	0.00	0.94	0.00
Patchick 94	2418	OGLE-GD-CEP-1148	91.78	$\varpi, \mu_\alpha^*, \mu_\delta$	0.00	0.94	0.00
Hogg 20	2451	OGLE-GD-CEP-1167	21.27	$\varpi, \mu_\alpha^*, \mu_\delta$	0.00	0.94	0.00
UBC 258	–	OGLE-GD-CEP-1669	15.94	$\varpi, \mu_\alpha^*, \mu_\delta$	0.00	0.94	0.00
IC 2581	1805	OGLE-GD-CEP-1669	29.03	$\varpi, \mu_\alpha^*, \mu_\delta$	0.00	0.94	0.00
Majaess 166	–	U Nor	19.86	μ_α^*, μ_δ	0.00	0.94	0.00
UBC 299	–	OGLE-GD-CEP-0998	7.54	$\varpi, \mu_\alpha^*, \mu_\delta$	0.01	0.94	0.01
BH 92	1791	WISE J102221.6-574822	72.49	$\varpi, \mu_\alpha^*, \mu_\delta$	0.00	0.94	0.00
DBSB 60	1888	GDS J1108345-620556	17.36	$\varpi, \mu_\alpha^*, \mu_\delta$	0.00	0.94	0.00
Westerlund 2	1801	OGLE-GD-CEP-0490	26.61	$\varpi, \mu_\alpha^*, \mu_\delta$	0.00	0.94	0.00
DBSB 46	1813	Y Car	47.26	$\varpi, \mu_\alpha^*, \mu_\delta$	0.00	0.94	0.00
FSR 1653	2134	OGLE-GD-CEP-1722	13.37	$\varpi, \mu_\alpha^*, \mu_\delta$	0.00	0.94	0.00
Trumpler 15	1849	OGLE-GD-CEP-1669	45.31	$\varpi, \mu_\alpha^*, \mu_\delta$	0.00	0.94	0.00
Ruprecht 90	1819	OGLE-GD-CEP-1669	9.77	$\varpi, \mu_\alpha^*, \mu_\delta$	0.00	0.94	0.00
BH 222	2564	OGLE-BLG-CEP-173	85.39	$\varpi, \mu_\alpha^*, \mu_\delta$	0.00	0.93	0.00
Ruprecht 176	2373	OGLE-GD-CEP-1136	23.31	$\varpi, \mu_\alpha^*, \mu_\delta$	0.00	0.93	0.00
DBSB 166	2390	OGLE-GD-CEP-1136	31.99	$\varpi, \mu_\alpha^*, \mu_\delta$	0.00	0.93	0.00
Trumpler 16	1850	OGLE-GD-CEP-1669	30.22	$\varpi, \mu_\alpha^*, \mu_\delta$	0.00	0.93	0.00
NGC 3324	1830	OGLE-GD-CEP-1669	21.82	$\varpi, \mu_\alpha^*, \mu_\delta$	0.00	0.93	0.00
DBSB 48	1817	OGLE-GD-CEP-1669	17.84	$\varpi, \mu_\alpha^*, \mu_\delta$	0.00	0.93	0.00
Stock 16	2105	GDS J1307179-634643	31.99	$\varpi, \mu_\alpha^*, \mu_\delta$	0.00	0.93	0.00
ESO 260 07	1570	GDS J0849274-452756	19.45	$\varpi, \mu_\alpha^*, \mu_\delta$	0.00	0.93	0.00
BH 91	1787	OGLE-GD-CEP-1669	22.61	$\varpi, \mu_\alpha^*, \mu_\delta$	0.00	0.93	0.00
Saurer 4	2009	WISE J115906.2-640201	56.88	$\varpi, \mu_\alpha^*, \mu_\delta$	0.00	0.93	0.00
Trumpler 14	1846	OGLE-GD-CEP-1669	38.30	$\varpi, \mu_\alpha^*, \mu_\delta$	0.00	0.93	0.00
Collinder 271	2126	WISE J132924.6-625511	26.12	$\varpi, \mu_\alpha^*, \mu_\delta$	0.00	0.93	0.00
Collinder 228	1845	OGLE-GD-CEP-1669	13.16	$\varpi, \mu_\alpha^*, \mu_\delta$	0.00	0.92	0.00
FSR 1530	1774	WISE J102221.6-574822	45.93	$\varpi, \mu_\alpha^*, \mu_\delta$	0.00	0.92	0.00
UBC 653	–	OGLE-GD-CEP-1669	10.75	$\varpi, \mu_\alpha^*, \mu_\delta$	0.00	0.92	0.00
Collinder 220	1803	OGLE-GD-CEP-1669	13.90	$\varpi, \mu_\alpha^*, \mu_\delta$	0.00	0.92	0.00
Saurer 4	2009	WISE J120156.6-630957	47.39	$\varpi, \mu_\alpha^*, \mu_\delta$	0.00	0.91	0.00
Teutsch 143a	1898	OGLE-GD-CEP-0618	25.57	$\varpi, \mu_\alpha^*, \mu_\delta$	0.00	0.91	0.00
FSR 0985	786	ASAS J060722+0834	61.24	$\varpi, \mu_\alpha^*, \mu_\delta$	0.00	0.91	0.00
NGC 3293	1826	OGLE-GD-CEP-1669	18.70	$\varpi, \mu_\alpha^*, \mu_\delta$	0.00	0.91	0.00
FSR 1390	1494	CO Vel	7.87	$\varpi, \mu_\alpha^*, \mu_\delta$	0.01	0.91	0.00
ESO 260 07	1570	CP Vel	20.00	$\varpi, \mu_\alpha^*, \mu_\delta$	0.00	0.91	0.00

Table A3: (Continued).

Open cluster	MWSC ID	Cepheid	Sep/ r_1	Constraints	$P(A)$	$P(B A)$	$P(A B)$
Danks 1	2092	OGLE-GD-CEP-0871	45.32	$\varpi, \mu_\alpha^*, \mu_\delta$	0.00	0.91	0.00
Berkeley 68	412	SV Per	10.46	$\varpi, \mu_\alpha^*, \mu_\delta$	0.00	0.91	0.00
NGC 4815	2075	OGLE-GD-CEP-1718	34.45	$\varpi, \mu_\alpha^*, \mu_\delta$	0.00	0.91	0.00
Ruprecht 115	2368	OGLE-GD-CEP-1146	32.96	$\varpi, \mu_\alpha^*, \mu_\delta$	0.00	0.91	0.00
Berkeley 51	3280	ZTF J202056.73+350213.7	98.33	$\varpi, \mu_\alpha^*, \mu_\delta$	0.00	0.91	0.00
NGC 3603	1926	OGLE-GD-CEP-1677	28.35	$\varpi, \mu_\alpha^*, \mu_\delta$	0.00	0.90	0.00
Stock 16	2105	OO Cen	17.31	$\varpi, V_r, \mu_\alpha^*, \mu_\delta$	0.00	0.90	0.00
Teutsch 1	–	V0621 Aur	178.47	$\varpi, \mu_\alpha^*, \mu_\delta$	0.00	0.90	0.00
NGC 6005	2336	OGLE-GD-CEP-1759	30.60	$\varpi, \mu_\alpha^*, \mu_\delta$	0.00	0.90	0.00
SBB 2	3612	ASASSN-V J221936.83+574243.6	32.56	$\varpi, \mu_\alpha^*, \mu_\delta$	0.00	0.90	0.00
Westerlund 2	1801	OGLE-GD-CEP-1661	66.20	$\varpi, \mu_\alpha^*, \mu_\delta$	0.00	0.90	0.00
Alessi 18	1284	BE Pup	51.11	$\varpi, \mu_\alpha^*, \mu_\delta$	0.00	0.90	0.00
BH 67	1669	GDS J0937286-521546	77.31	$\varpi, \mu_\alpha^*, \mu_\delta$	0.00	0.89	0.00
DBSB 45	1792	OGLE-GD-CEP-0509	33.39	$\varpi, \mu_\alpha^*, \mu_\delta$	0.00	0.89	0.00
Ruprecht 89	1808	OGLE-GD-CEP-1669	13.43	$\varpi, \mu_\alpha^*, \mu_\delta$	0.00	0.89	0.00
Saurer 4	2009	OGLE-GD-CEP-0768	43.86	$\varpi, \mu_\alpha^*, \mu_\delta$	0.00	0.89	0.00
LP 861	–	OGLE-GD-CEP-1763	42.96	$\varpi, \mu_\alpha^*, \mu_\delta$	0.00	0.89	0.00
NGC 7790	3781	CG Cas	6.71	$\varpi, V_r, \mu_\alpha^*, \mu_\delta$	0.01	0.89	0.01
Collinder 223	1815	OGLE-GD-CEP-0507	19.56	$\varpi, \mu_\alpha^*, \mu_\delta$	0.00	0.89	0.00
King 2	79	NSVS 1712247	16.04	$\varpi, \mu_\alpha^*, \mu_\delta$	0.00	0.89	0.00
Roslund 4	3246	GH Cyg	20.50	$\varpi, V_r, \mu_\alpha^*, \mu_\delta$	0.00	0.88	0.00
DBSB 45	1792	V0708 Car	49.20	$\varpi, \mu_\alpha^*, \mu_\delta$	0.00	0.88	0.00
Carraro 1	1829	OGLE-GD-CEP-0507	27.24	$\varpi, \mu_\alpha^*, \mu_\delta$	0.00	0.88	0.00
UBC 525	–	OGLE-GD-CEP-1719	15.30	$\varpi, \mu_\alpha^*, \mu_\delta$	0.00	0.88	0.00
Moffat 1	2346	OGLE-GD-CEP-1763	26.77	$\varpi, \mu_\alpha^*, \mu_\delta$	0.00	0.88	0.00
Juchert 18	893	NSVS 12485452	63.21	$\varpi, \mu_\alpha^*, \mu_\delta$	0.00	0.88	0.00
Stock 16	2105	OGLE-GD-CEP-0904	7.98	$\varpi, \mu_\alpha^*, \mu_\delta$	0.00	0.88	0.00
Bochum 9	1825	OGLE-GD-CEP-0507	17.44	$\varpi, \mu_\alpha^*, \mu_\delta$	0.00	0.88	0.00
ESO 260 07	1570	GDS J0846163-452756	19.55	$\varpi, \mu_\alpha^*, \mu_\delta$	0.00	0.88	0.00
Stock 16	2105	V1384 Cen	11.40	$\varpi, \mu_\alpha^*, \mu_\delta$	0.00	0.88	0.00
Teutsch 145	2978	GDS J1840132-055722	47.44	$\varpi, \mu_\alpha^*, \mu_\delta$	0.00	0.88	0.00
Westerlund 2	1801	OGLE-GD-CEP-0506	10.25	$\varpi, \mu_\alpha^*, \mu_\delta$	0.00	0.88	0.00
Skiff J0458+43	442	SV Per	25.57	$\varpi, \mu_\alpha^*, \mu_\delta$	0.00	0.88	0.00
Westerlund 2	1801	GDS J1027192-582311	38.18	$\varpi, \mu_\alpha^*, \mu_\delta$	0.00	0.88	0.00
SAI 116	1978	OGLE-GD-CEP-0722	18.03	$\varpi, \mu_\alpha^*, \mu_\delta$	0.00	0.87	0.00
UBC 538	–	OGLE-GD-CEP-1763	23.35	$\varpi, \mu_\alpha^*, \mu_\delta$	0.00	0.87	0.00
BH 118	1939	OGLE-GD-CEP-0633	76.30	$\varpi, \mu_\alpha^*, \mu_\delta$	0.00	0.87	0.00
Westerlund 2	1801	GDS J1025508-594416	99.68	$\varpi, \mu_\alpha^*, \mu_\delta$	0.00	0.87	0.00
NGC 6360	2591	OGLE-BLG-CEP-116	19.82	$\varpi, \mu_\alpha^*, \mu_\delta$	0.00	0.87	0.00
Danks 1	2092	OGLE-GD-CEP-1722	72.79	$\varpi, \mu_\alpha^*, \mu_\delta$	0.00	0.87	0.00
DBSB 48	1817	OGLE-GD-CEP-0567	25.80	$\varpi, \mu_\alpha^*, \mu_\delta$	0.00	0.87	0.00
Kharchenko 2	2900	ASAS J182714-1507.1	11.35	$\varpi, \mu_\alpha^*, \mu_\delta$	0.00	0.87	0.00
Loden 165	1827	OGLE-GD-CEP-0507	22.69	$\varpi, \mu_\alpha^*, \mu_\delta$	0.00	0.86	0.00
DBSB 154	2355	OGLE-GD-CEP-1763	37.24	$\varpi, \mu_\alpha^*, \mu_\delta$	0.00	0.86	0.00
Berkeley 76	1099	ASAS J070900-1228.3	17.83	$\varpi, \mu_\alpha^*, \mu_\delta$	0.00	0.86	0.00
UBC 508	–	OGLE CAR-SC01 66142	34.89	$\varpi, \mu_\alpha^*, \mu_\delta$	0.00	0.86	0.00
Collinder 232	–	OGLE-GD-CEP-1669	22.49	$\varpi, \mu_\alpha^*, \mu_\delta$	0.00	0.86	0.00
Westerlund 2	1801	WISE J102110.8-580754	26.63	$\varpi, \mu_\alpha^*, \mu_\delta$	0.00	0.86	0.00
King 21	3762	CE Cas B	38.65	$\varpi, \mu_\alpha^*, \mu_\delta$	0.00	0.86	0.00
Loden 153	1824	WISE J102221.6-574822	25.66	$\varpi, \mu_\alpha^*, \mu_\delta$	0.00	0.86	0.00
DBSB 45	1792	ASAS J100814-5856.6	52.75	$\varpi, \mu_\alpha^*, \mu_\delta$	0.00	0.86	0.00
NGC 6031	2352	OGLE-GD-CEP-1763	7.25	$\varpi, \mu_\alpha^*, \mu_\delta$	0.01	0.86	0.01
UFMG 37	–	OGLE-GD-CEP-1023	54.83	$\varpi, \mu_\alpha^*, \mu_\delta$	0.00	0.86	0.00
Ruprecht 112	2261	OGLE-GD-CEP-0998	17.49	$\varpi, \mu_\alpha^*, \mu_\delta$	0.00	0.86	0.00
ASCC 60	1823	OGLE-GD-CEP-0507	12.12	$\varpi, \mu_\alpha^*, \mu_\delta$	0.00	0.86	0.00
UBC 537	–	OGLE-GD-CEP-1763	22.24	$\varpi, \mu_\alpha^*, \mu_\delta$	0.00	0.86	0.00
LP 1831	–	EX Cas	11.04	$\varpi, \mu_\alpha^*, \mu_\delta$	0.00	0.85	0.00
BH 151	2147	WISE J132924.6-625511	215.89	$\varpi, \mu_\alpha^*, \mu_\delta$	0.00	0.85	0.00
UBC 505	–	WZ Car	25.98	$\varpi, \mu_\alpha^*, \mu_\delta$	0.00	0.85	0.00

^k Cluster with position and proper motion compatible with a cluster in K13, based on [Castro-Ginard et al. \(2020\)](#).

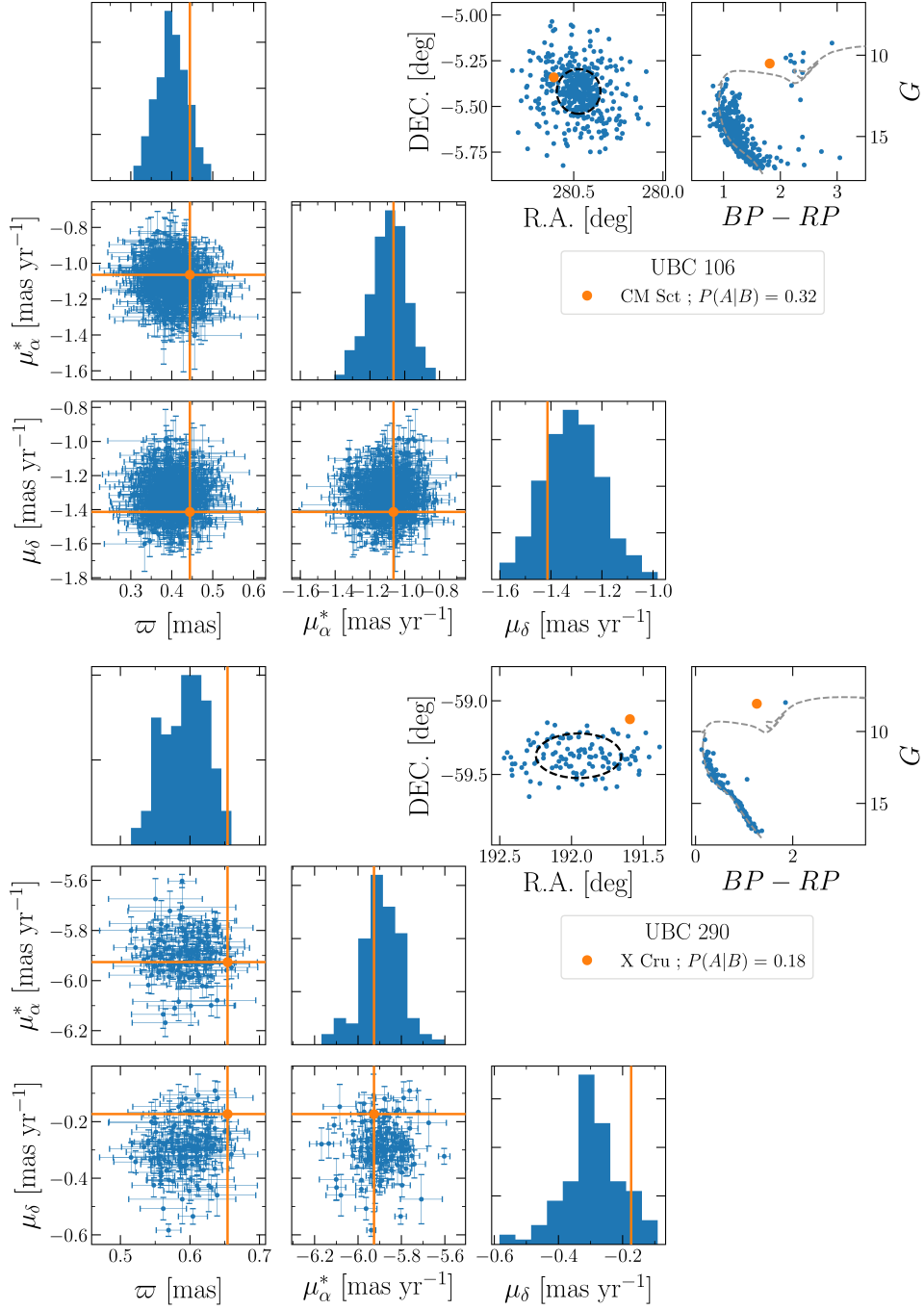


Figure A1: Distribution of the *Gaia*-based astrometry (parallaxes, proper motions, and positions) and colour-magnitude diagrams for two of the combos described in Section 2.5.4, for which a list of cluster members is provided by CG20. The information of the members (from CG20) is represented in blue, while the Cepheids properties are shown in orange. In the panels displaying the equatorial coordinates of the members, a black dashed line represent the clusters' r_1 . PARSEC isochrones of solar metallicity are plotted in the colour-magnitude diagrams with grey dashed lines using the values derived by CG20 as a reference.

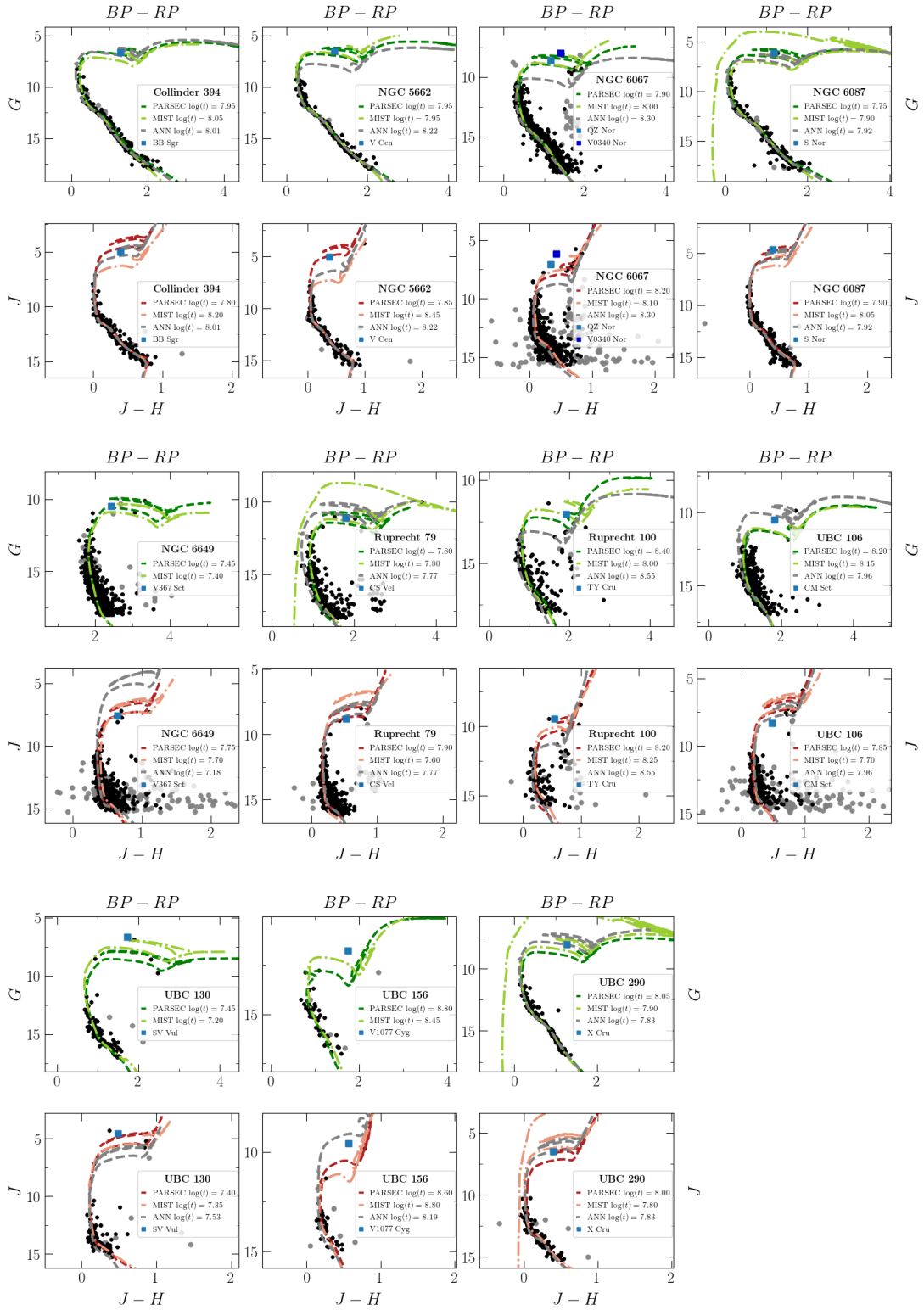
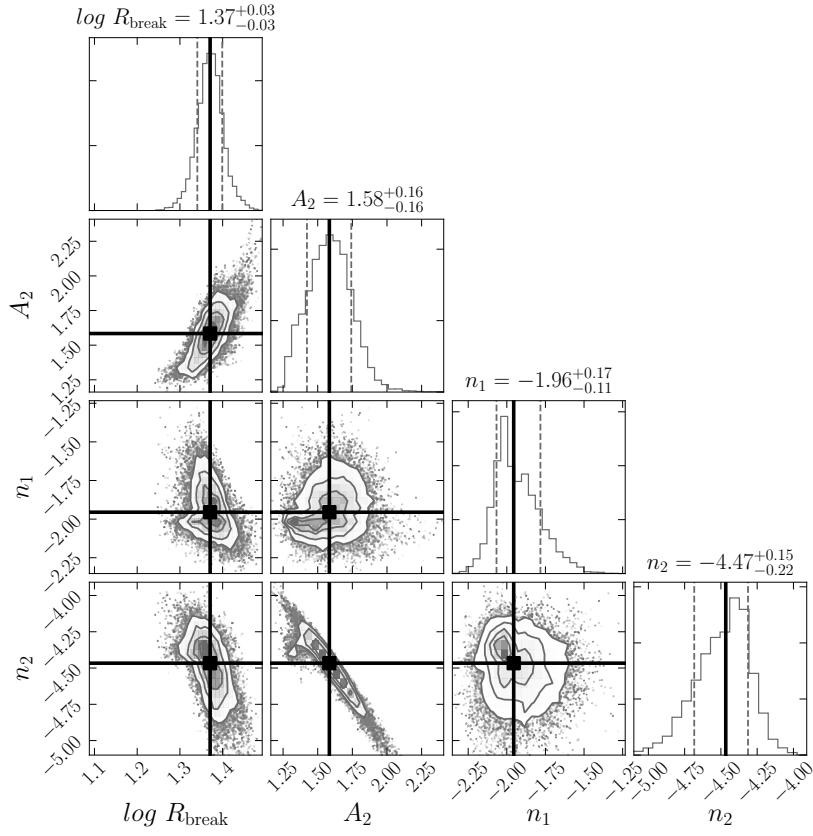


Figure A2: Colour-magnitude diagrams of the clusters studied in Section 2.6, with isochrones representing the results of Section 2.6.1. Cluster members from CG18b are shown with grey circles, whereas those used for the best-model determination are displayed in black. The outcomes of the ANN are plotted with PARSEC isochrones assuming solar metallicity (in grey), with the exception of the clusters marked as highly reddened in Table 2.2 (for the *Gaia* passband panels).

B1 Complementary material

In this appendix we provide additional material to complement the content of Chapter 3. Figures B1 to B3 show the posterior probability distribution (corner plots) and MCMC chains for the broken-power-law profiles determination described in Section 3.5, for the regions observed by HOWVAST 2017, 2018, and for our entire RRL sample. Figures B4 to B6 depict the spatial distribution of the HOWVAST RRLs, and compares it with the literature catalogues considered in Section 3.3.4. Finally, in Table B1 I present the full list of RRLs detected in Section 3.3, together with their main properties.



All fields

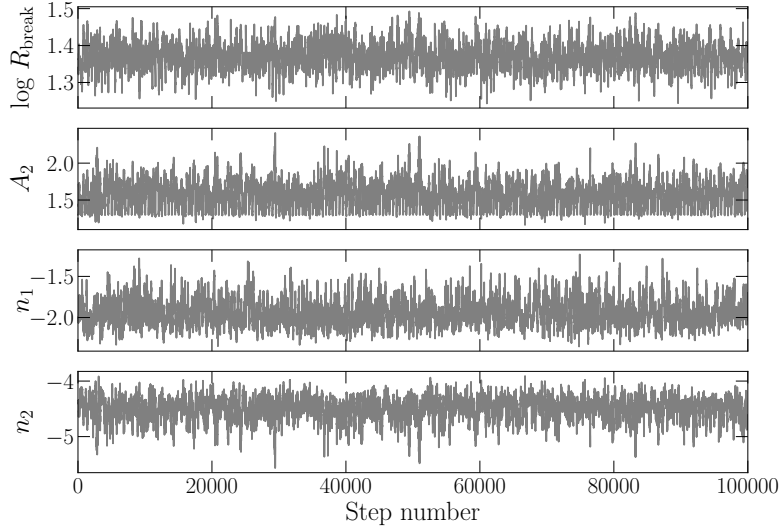
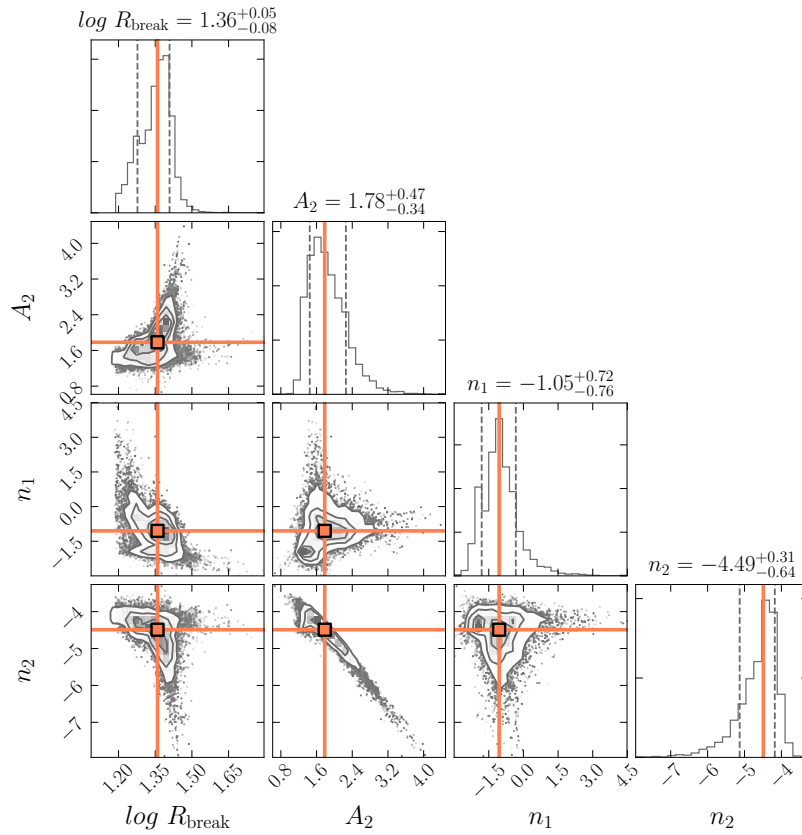


Figure B1: *Top:* Corner plot of the posterior probability distributions for the broken-power-law profiles described in Section 3.5. The adopted value of each parameter is the median of the corresponding marginalized distribution, and their uncertainties represent the 16th and 84th percentiles. *Bottom:* Convergence of the parameter chains from the MCMC model. These parameters are computed for the RRLs in all the fields studied in this work.



HOWVAST 2017

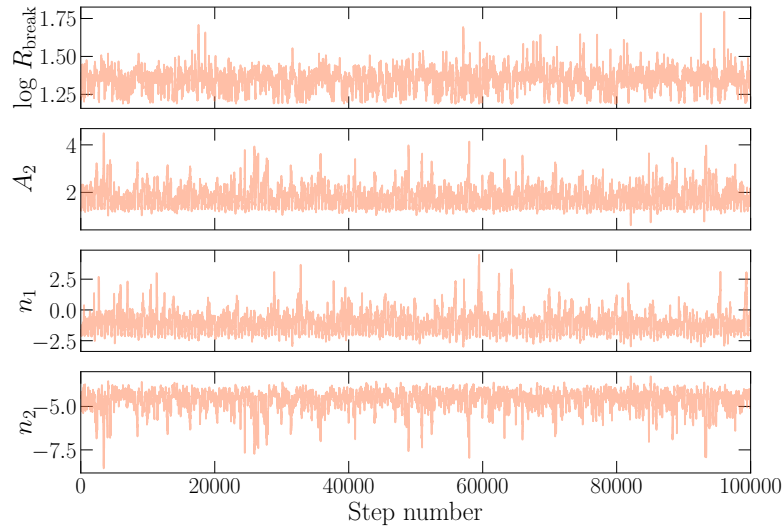
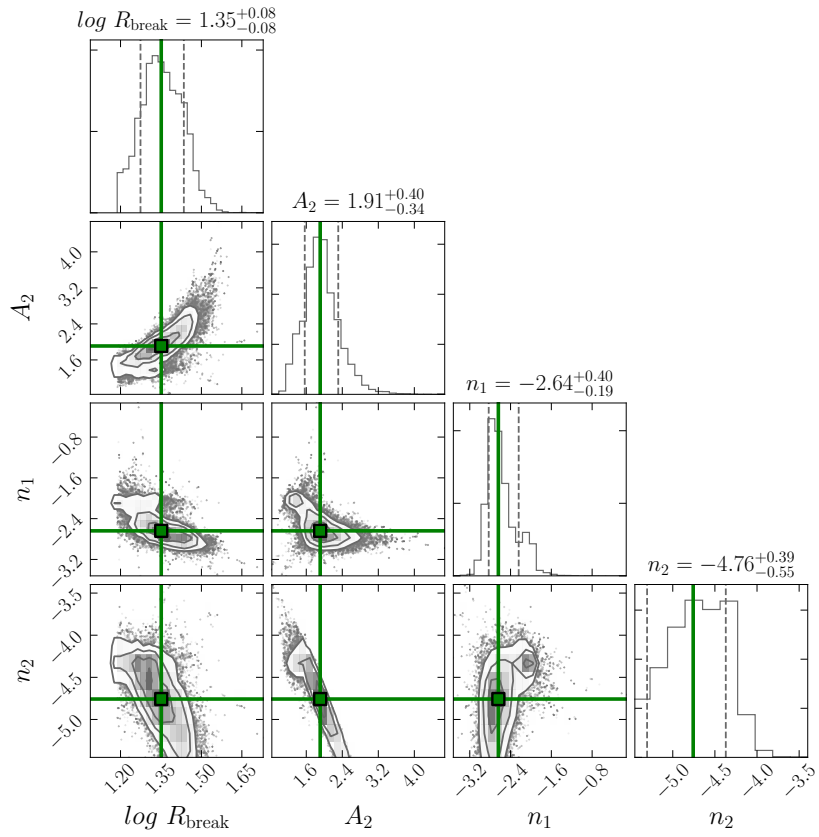


Figure B2: Same as Figure B1, but for the fields from the HOWVAST campaign in 2017.



HOWVAST 2018

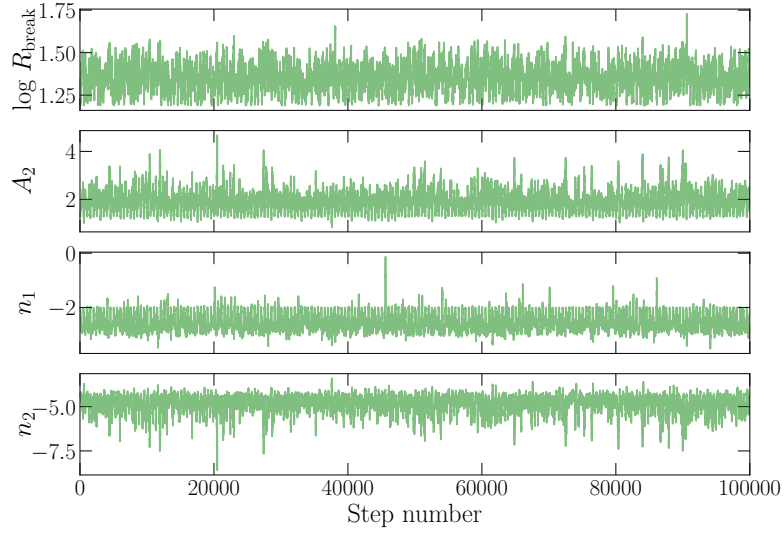


Figure B3: Same as Figure B1, but for the fields from the HOWVAST campaign in 2018.

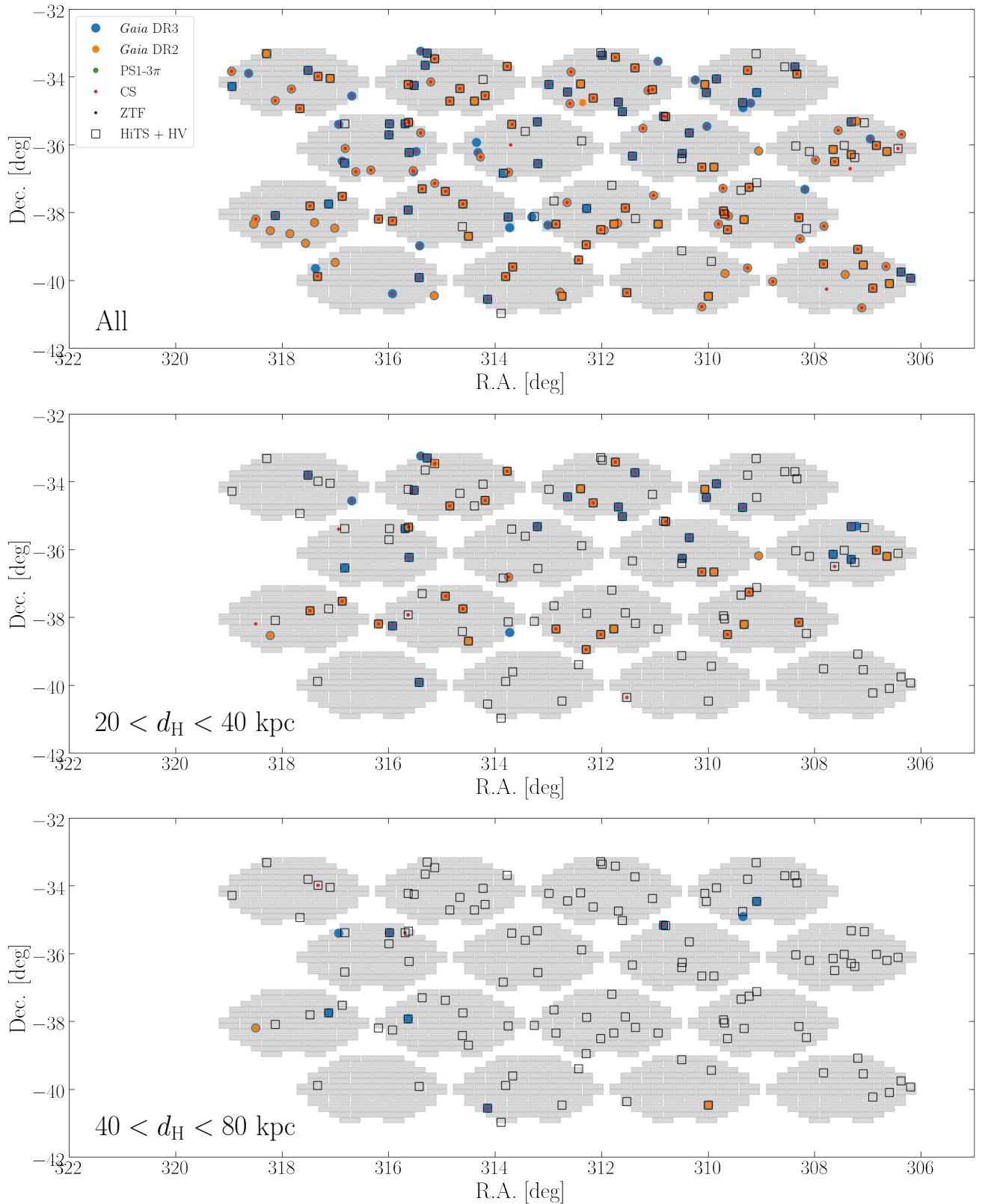


Figure B4: Spatial distribution of RRL candidates detected in the HOWVVAST 2017 fields and the (partially) overlapping surveys used in Section 3.3.4 for comparison. The footprint of the DECAM CCDs and the observed fields are shown in grey. These plots show the number of new and recovered RRL candidates as a function of heliocentric distance d_H .

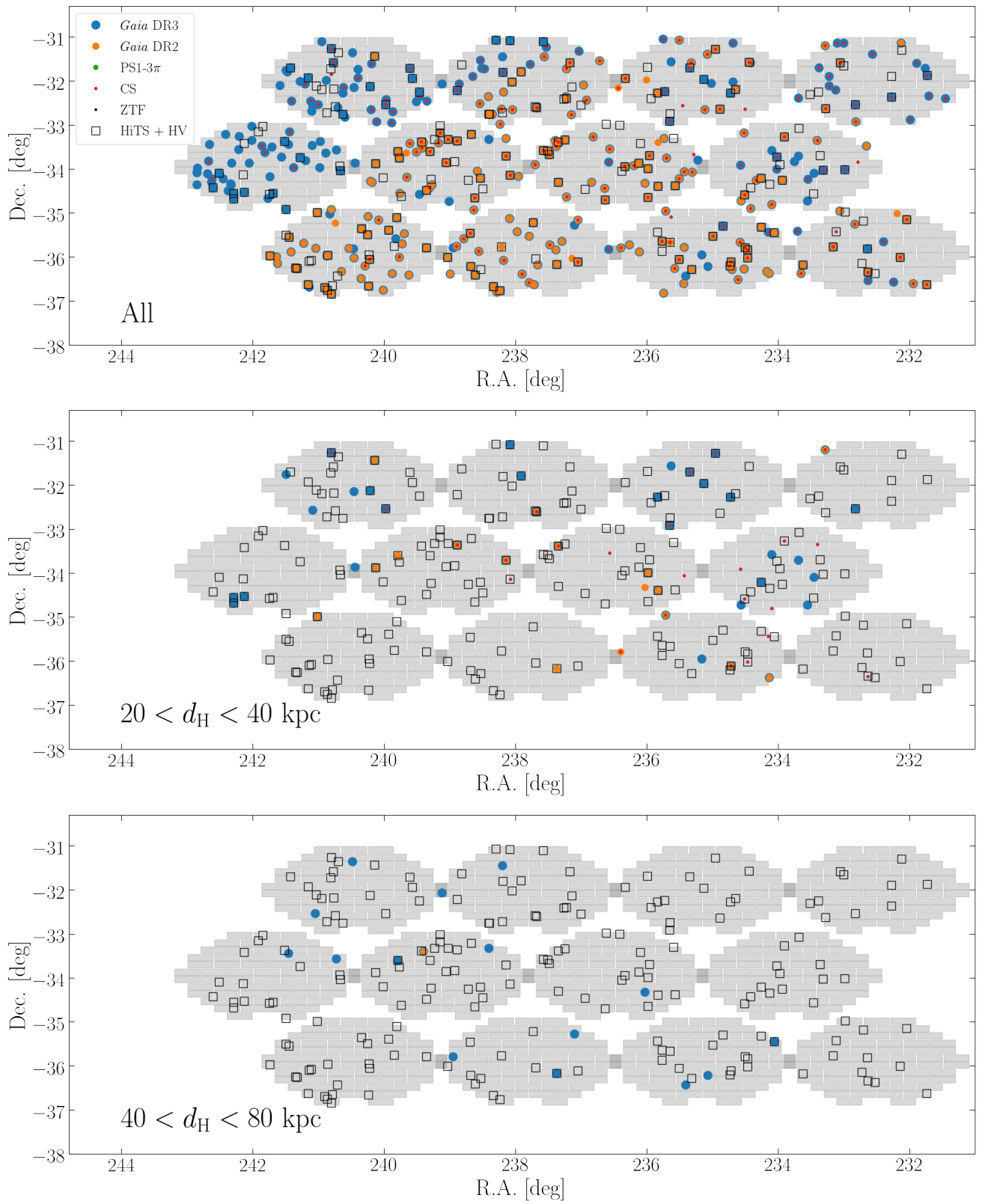


Figure B5: Same as Figure B4 but for the HOWVAST 2018A fields.

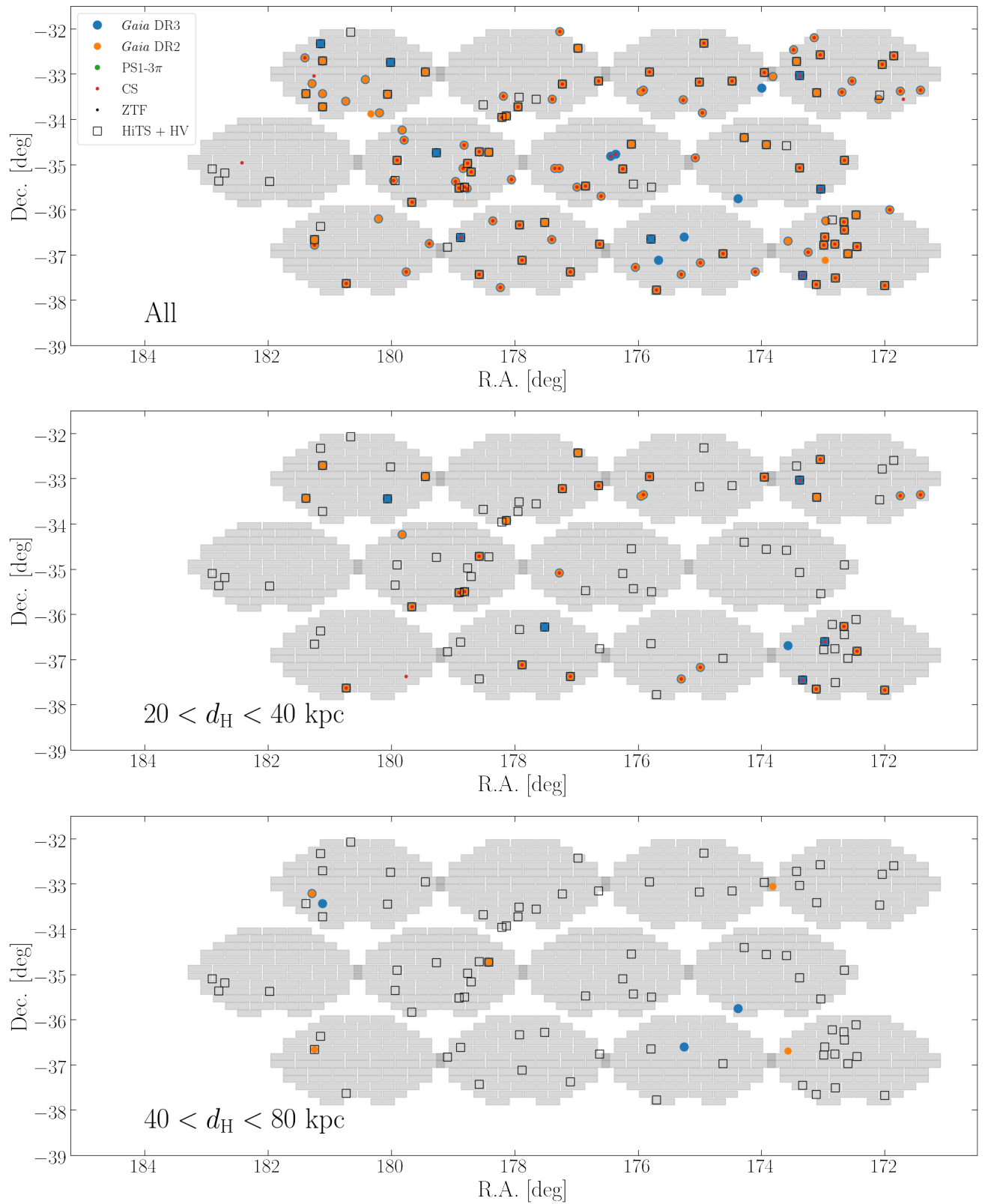


Figure B6: Same as Figure B4 but for the HOWVAST 2018B fields.

Table B1: Main properties of the entire sample of RRLs detected and used in this work. The period and amplitude of pulsation are computed from the photometric band with more observations. In this table, the mean r magnitudes for the stars from the HiTS survey are determined using photometry from the NSC.

ID	R.A. (deg)	Dec. (deg)	$\langle g \rangle$	$\langle r \rangle$	N_g	N_r	Period (days)	Amplitude	Type	d_H (kpc)
HiTS101538+022342	153.90730	2.39490	15.59	15.64	26	–	0.31	0.64	c	8.0 ± 0.3
HiTS103402-062058	158.50850	–6.34950	15.63	15.59	25	–	0.55	0.96	ab	9.0 ± 0.3
HiTS091013-050321	137.55230	–5.05570	15.66	15.78	26	–	0.54	1.24	ab	9.2 ± 0.3
HiTS103258-063715	158.24030	–6.62090	15.71	15.65	27	–	0.62	1.07	ab	9.7 ± 0.4
HiTS093950-012236	144.95780	–1.37680	15.82	15.98	25	–	0.54	0.64	ab	9.9 ± 0.4
HiTS094118-065433	145.32510	–6.90930	15.90	15.95	27	–	0.48	1.44	ab	9.9 ± 0.4
HiTS101653-013750	154.21880	–1.63050	15.84	15.69	27	–	0.58	1.02	ab	9.9 ± 0.4
HiTS102351-054146	155.96230	–5.69600	15.76	15.80	27	–	0.65	0.96	ab	10.0 ± 0.4
HiTS094714+000300	146.80960	0.05000	16.27	15.93	27	–	0.54	0.48	ab	10.4 ± 0.4
HiTS095123-065416	147.84650	–6.90450	16.21	16.12	28	–	0.49	1.24	ab	10.7 ± 0.4
HiTS101700+023314	154.24810	2.55400	16.01	16.03	26	–	0.57	0.70	ab	10.8 ± 0.4
HiTS093902-010035	144.75730	–1.00960	16.00	16.15	25	–	0.60	1.11	ab	11.1 ± 0.4
HiTS103721+015616	159.33920	1.93780	16.00	16.11	25	–	0.65	1.10	ab	11.4 ± 0.4
HiTS103003-044803	157.51080	–4.80080	16.17	15.81	27	–	0.56	1.13	ab	11.5 ± 0.4
HiTS102241+005948	155.67090	0.99670	16.34	16.58	26	–	0.35	0.58	c	11.6 ± 0.5
HiTS091945-000157	139.93730	–0.03240	16.12	15.82	27	–	0.61	1.05	ab	11.8 ± 0.4
HiTS095351-062142	148.46210	–6.36160	16.42	16.40	28	–	0.56	1.08	ab	12.7 ± 0.5
HiTS091139-003904	137.91340	–0.65120	16.48	16.60	25	–	0.47	1.33	ab	12.8 ± 0.5
HiTS091528-041929	138.86600	–4.32460	16.46	16.63	24	–	0.39	0.62	c	13.0 ± 0.5
HiTS091948+021041	139.94820	2.17810	16.66	16.86	26	–	0.29	0.60	c	13.1 ± 0.6
HiTS094109+013118	145.28620	1.52160	16.81	16.93	24	–	0.31	0.34	c	13.4 ± 0.6
HiTS091156+022530	137.98310	2.42490	16.45	16.29	27	–	0.60	1.32	ab	13.7 ± 0.5
HiTS091558-062404	138.99110	–6.40120	16.62	16.88	28	–	0.49	1.48	ab	13.7 ± 0.5
HiTS091947+011016	139.94600	1.17100	16.47	16.40	26	–	0.66	1.14	ab	14.3 ± 0.5
HiTS094842-042035	147.17670	–4.34310	16.56	16.29	26	–	0.67	1.14	ab	14.5 ± 0.6
HiTS094339-070105	145.91240	–7.01800	16.65	16.56	28	–	0.55	1.17	ab	14.5 ± 0.5
HiTS092035-042137	140.14490	–4.36040	17.09	17.11	24	–	0.26	0.43	c	15.2 ± 0.8
HiTS095209-014404	148.03850	–1.73440	16.83	16.89	27	–	0.53	1.20	ab	15.2 ± 0.6
HiTS102820-063614	157.08410	–6.60390	16.90	16.68	26	–	0.56	1.21	ab	16.0 ± 0.6
HiTS101449+000709	153.70330	0.11920	16.93	17.28	27	–	0.52	1.44	ab	16.1 ± 0.6
HiTS092103+014538	140.26190	1.76060	16.84	16.96	26	–	0.62	0.82	ab	16.5 ± 0.6
HiTS094027-065219	145.11360	–6.87200	16.87	16.75	28	–	0.63	0.69	ab	16.9 ± 0.6
HiTS090839-003849	137.16200	–0.64690	17.05	17.21	25	–	0.37	0.48	c	16.9 ± 0.7
HiTS102041+012207	155.17290	1.36850	17.17	17.34	26	–	0.46	1.42	ab	17.1 ± 0.7
HiTS103140-005140	157.91720	–0.86100	17.36	17.64	26	–	0.29	0.60	c	17.2 ± 0.8
HiTS094304-060042	145.76770	–6.01180	17.13	17.05	28	–	0.54	1.28	ab	18.0 ± 0.7
HiTS102052-035820	155.21850	–3.97230	17.39	17.65	26	–	0.30	0.39	c	18.0 ± 0.8
HiTS094710-044627	146.79040	–4.77420	17.11	16.98	26	–	0.66	0.68	ab	18.2 ± 0.7
HiTS094637-034213	146.65420	–3.70360	17.25	17.39	26	–	0.39	0.59	c	18.6 ± 0.7
HiTS093913-061915	144.80350	–6.32080	17.21	17.10	28	–	0.53	1.23	ab	18.6 ± 0.7
HiTS094032+021012	145.13440	2.16990	17.32	17.37	24	–	0.60	0.71	ab	19.9 ± 0.7
HiTS092442-062442	141.17650	–6.41180	17.55	17.83	24	–	0.30	0.52	c	19.9 ± 0.9
HiTS095017-061952	147.57210	–6.33120	17.78	17.81	28	–	0.26	0.44	c	20.1 ± 1.0
HiTS100507-032355	151.28050	–3.39870	17.41	17.42	26	–	0.51	0.91	ab	20.1 ± 0.8
HiTS093310-000612	143.29340	–0.10340	17.29	17.11	25	–	0.62	1.20	ab	20.2 ± 0.8
HiTS091512+021915	138.80090	2.32080	17.70	17.97	28	–	0.29	0.65	c	20.9 ± 1.0
HiTS093042-022248	142.67420	–2.38000	17.51	17.46	26	–	0.59	1.13	ab	21.8 ± 0.8
HiTS093704-042224	144.26610	–4.37320	17.51	17.32	27	–	0.59	0.89	ab	21.9 ± 0.8
HiTS103455+005814	158.72800	0.97050	17.79	17.70	25	–	0.45	1.48	ab	22.2 ± 0.9
HiTS102910+000310	157.29180	0.05280	17.57	17.68	27	–	0.64	0.63	ab	22.5 ± 0.8
HiTS102941-025613	157.41880	–2.93690	17.51	17.33	27	–	0.64	0.35	ab	22.5 ± 0.8
HiTS092505+015005	141.27250	1.83470	18.05	18.08	26	–	0.34	0.53	c	25.4 ± 1.0
HiTS100809-053823	152.03630	–5.63960	17.89	17.98	29	–	0.55	1.10	ab	25.6 ± 1.0
HiTS091924-063037	139.84990	–6.51020	18.29	18.29	24	–	0.36	0.67	ab	26.5 ± 1.3
HiTS103325+014710	158.35610	1.78610	17.88	17.73	25	–	0.68	0.86	ab	27.2 ± 1.0
HiTS092521+015542	141.33650	1.92830	18.37	18.46	26	–	0.27	0.77	c	27.2 ± 1.3
HiTS093056+015751	142.73530	1.96420	18.18	18.00	26	–	0.59	0.86	ab	28.1 ± 1.1
HiTS093357-005409	143.48930	–0.90260	17.95	17.81	25	–	0.68	0.21	ab	28.1 ± 1.1
HiTS102007-061151	155.02880	–6.19750	18.09	17.96	25	–	0.62	0.80	ab	28.9 ± 1.1
HiTS092916-033445	142.31770	–3.57910	18.54	18.75	26	–	0.29	0.44	c	30.6 ± 1.4
HiTS100145-024303	150.43660	–2.71760	18.14	18.35	28	–	0.78	0.50	ab	31.8 ± 1.3
HiTS100918+023801	152.32470	2.63350	18.66	18.73	28	–	0.38	0.73	ab	32.1 ± 1.5
HiTS091047+015033	137.69500	1.84240	18.30	18.05	27	–	0.60	0.94	ab	32.2 ± 1.2
HiTS091110-062237	137.78990	–6.37700	18.39	18.29	28	–	0.57	0.85	ab	32.5 ± 1.2
HiTS094242+015605	145.67660	1.93470	18.58	18.69	24	–	0.52	1.00	ab	33.1 ± 1.3

Table B1: (Continued).

ID	R.A. (deg)	Dec. (deg)	$\langle g \rangle$	$\langle r \rangle$	N_g	N_r	Period (days)	Amplitude	Type	d_H (kpc)
HiTS093851+000703	144.71130	0.11760	18.88	18.72	25	—	0.38	0.82	ab	33.4 ± 1.6
HiTS093707-000425	144.27850	-0.07370	18.48	18.41	25	—	0.60	0.77	ab	34.1 ± 1.3
HiTS095009-064914	147.53950	-6.82060	19.12	18.96	28	—	0.37	0.60	c	41.2 ± 1.6
HiTS093431-034020	143.62910	-3.67220	19.03	19.08	27	—	0.56	1.10	ab	43.1 ± 1.6
HiTS093807+002518	144.52820	0.42170	19.55	19.60	25	—	0.35	0.77	c	49.7 ± 2.0
HiTS091050-055917	137.70940	-5.98800	19.45	19.39	28	—	0.65	0.47	ab	55.6 ± 2.1
HiTS101057-033318	152.73610	-3.55500	19.77	19.82	26	—	0.64	0.76	ab	64.4 ± 2.4
HiTS100527-050335	151.36100	-5.05970	19.85	19.91	26	—	0.61	0.69	ab	65.3 ± 2.4
HiTS101551-015619	153.96060	-1.93850	20.14	20.33	27	—	0.32	0.62	c	65.9 ± 2.8
HiTS101338-015258	153.40790	-1.88280	20.08	20.19	28	—	0.44	0.66	c	71.1 ± 2.7
HiTS101128-013921	152.86680	-1.65570	20.25	19.88	28	—	0.39	0.80	c	73.4 ± 2.8
HiTS101342-021246	153.42330	-2.21280	20.26	20.30	27	—	0.40	0.57	c	75.3 ± 2.9
HiTS101734+001322	154.39120	0.22280	20.37	20.48	26	—	0.37	0.61	c	77.1 ± 3.0
HiTS101531-011841	153.87960	-1.31150	20.26	20.23	28	—	0.44	0.52	c	77.1 ± 2.9
HiTS101456-022025	153.73420	-2.34030	20.25	20.23	28	—	0.49	0.76	c	80.2 ± 3.0
HiTS101253-004020	153.21950	-0.67210	20.27	20.28	28	—	0.65	1.05	ab	80.3 ± 3.0
HiTS101227-013643	153.11060	-1.61200	20.38	20.21	27	—	0.59	1.10	ab	80.3 ± 3.0
HiTS100752-020827	151.96500	-2.14070	20.28	20.05	20	—	0.48	0.29	c	80.5 ± 3.0
HiTS101511-012700	153.79540	-1.45000	20.34	20.23	28	—	0.61	1.02	ab	81.0 ± 3.0
HiTS101527-011655	153.86430	-1.28190	20.41	20.36	27	—	0.57	0.88	ab	82.1 ± 3.1
HiTS101344-014848	153.43250	-1.81340	20.39	20.09	28	—	0.59	1.05	ab	82.1 ± 3.1
HiTS101228-014711	153.11470	-1.78650	20.38	20.27	28	—	0.63	0.85	ab	83.3 ± 3.1
HiTS101128-013643	152.86740	-1.61200	20.46	20.39	27	—	0.59	0.99	ab	84.2 ± 3.2
HiTS101337-014952	153.40450	-1.83110	20.47	20.48	28	—	0.63	0.93	ab	87.2 ± 3.3
HiTS101945-012651	154.93730	-1.44740	20.45	20.32	26	—	0.72	0.87	ab	88.2 ± 3.5
HiTS101516-011649	153.81510	-1.28040	20.45	20.22	26	—	0.73	1.29	ab	90.6 ± 3.6
HiTS091510-052952	138.79140	-5.49790	20.63	20.49	28	—	0.62	0.97	ab	93.6 ± 3.5
HiTS093807-005552	144.52890	-0.93110	20.70	20.78	25	—	0.61	0.83	ab	97.8 ± 3.7
HiTS093847-060049	144.69650	-6.01350	20.75	20.70	28	—	0.59	0.85	ab	98.6 ± 3.7
HiTS094023-025937	145.09730	-2.99360	20.66	20.33	26	—	0.85	0.41	ab	106.2 ± 4.5
HiTS092927-055440	142.36180	-5.91120	21.09	20.98	25	—	0.58	1.05	ab	112.5 ± 4.2
HiTS095253-014305	148.22270	-1.71800	21.35	21.48	27	—	0.35	0.83	c	115.7 ± 4.7
HiTS101453+001915	153.71970	0.32090	22.88	22.39	22	—	0.62	0.67	ab	265.3 ± 10.5
HV202738-401341	306.90704	-40.22804	15.28	15.48	3	32	0.52	0.92	ab	9.0 ± 0.3
HV211309-331855	318.28550	-33.31536	15.98	15.94	3	21	0.31	0.29	c	9.8 ± 0.3
HV203703-334814	309.26070	-33.80386	15.63	15.53	3	31	0.64	0.75	ab	10.0 ± 0.3
HV205158-341253	312.99054	-34.21483	16.01	15.86	3	21	0.64	0.40	ab	11.3 ± 0.4
HV203120-393116	307.83400	-39.52114	16.44	16.20	3	30	0.33	0.61	c	11.9 ± 0.4
HV210824-340157	317.09944	-34.03246	16.34	16.21	3	21	0.68	0.34	ab	13.5 ± 0.5
HV202845-390434	307.18746	-39.07624	16.47	16.30	3	31	0.60	0.36	ab	13.7 ± 0.5
HV204346-382008	310.94053	-38.33560	16.57	16.47	2	29	0.35	0.38	c	13.9 ± 0.5
HV205500-380810	313.75091	-38.13616	16.33	16.30	3	19	0.62	0.32	ab	13.9 ± 0.5
HV203238-382845	308.15717	-38.47907	16.23	16.52	3	30	0.47	0.92	ab	14.2 ± 0.5
HV205525-364955	313.85214	-36.83188	16.50	16.63	3	28	0.32	0.23	c	14.2 ± 0.5
HV205440-393635	313.66822	-39.60985	16.49	16.13	3	22	0.84	0.54	ab	14.3 ± 0.5
HV204613-375147	311.55499	-37.86298	16.54	16.38	3	29	0.64	0.36	ab	14.7 ± 0.5
HV210128-371749	315.36689	-37.29686	16.69	16.53	3	28	0.57	0.66	ab	14.9 ± 0.5
HV203850-375732	309.71040	-37.95895	16.06	16.48	3	30	0.60	0.71	ab	15.0 ± 0.5
HV211231-380515	318.12793	-38.08746	16.43	16.68	3	28	0.44	1.02	ab	15.1 ± 0.5
HV205513-395251	313.80378	-39.88095	16.43	16.67	3	28	0.35	0.47	c	15.1 ± 0.5
HV205655-340345	314.22986	-34.06253	16.37	16.56	3	25	0.59	0.78	ab	15.1 ± 0.5
HV211545-341701	318.93861	-34.28354	16.66	16.87	3	28	0.31	0.46	c	15.2 ± 0.5
HV210233-341321	315.63625	-34.22259	17.11	16.88	3	27	0.33	0.28	c	15.9 ± 0.5
HV203320-335422	308.33355	-33.90611	16.73	16.42	3	31	0.75	0.69	ab	15.9 ± 0.5
HV202946-360128	307.44191	-36.02447	17.12	17.19	3	30	0.20	0.32	c	16.2 ± 0.6
HV211039-345538	317.66448	-34.92712	16.80	16.68	3	15	0.71	0.69	ab	16.4 ± 0.6
HV204542-361942	311.42375	-36.32846	16.68	16.66	2	30	0.65	0.87	ab	16.6 ± 0.6
HV203330-334203	308.37449	-33.70077	16.71	16.66	3	31	0.63	0.44	ab	16.7 ± 0.6
HV204758-332108	311.98993	-33.35229	17.02	16.89	3	30	0.50	0.59	ab	16.9 ± 0.6
HV202623-400605	306.59755	-40.10150	16.75	16.92	3	32	0.47	0.92	ab	17.0 ± 0.6
HV204411-342215	311.04656	-34.37073	17.19	16.93	3	30	0.49	0.99	ab	17.2 ± 0.6
HV203946-392630	309.94187	-39.44173	16.99	16.93	3	31	0.39	0.41	c	17.8 ± 0.6
HV203325-360151	308.35235	-36.03096	17.06	17.19	3	31	0.28	0.23	c	18.0 ± 0.6
HV210358-354228	315.98991	-35.70781	17.19	16.97	3	28	0.60	0.58	ab	18.4 ± 0.6
HV205444-352327	313.68444	-35.39071	17.09	17.05	2	29	0.54	0.83	ab	18.4 ± 0.6
HV204945-392322	312.43676	-39.38957	17.11	16.94	3	28	0.64	0.84	ab	18.8 ± 0.6
HV203933-363920	309.88875	-36.65543	17.46	17.42	3	30	0.34	0.55	ab	19.2 ± 0.7
HV202449-395612	306.20414	-39.93669	17.16	16.95	3	32	0.69	0.76	ab	19.5 ± 0.7

Table B1: (Continued).

ID	R.A. (deg)	Dec. (deg)	$\langle g \rangle$	$\langle r \rangle$	N_g	N_r	Period (days)	Amplitude	Type	d_H (kpc)
HV205734-344244	314.39219	-34.71234	17.52	17.23	3	27	0.55	0.90	ab	20.0 ± 0.7
HV202530-394535	306.37641	-39.75973	17.54	17.13	3	31	0.68	0.66	ab	21.1 ± 0.7
HV204606-402130	311.52439	-40.35833	17.47	17.54	3	30	0.29	0.45	c	21.4 ± 0.7
HV204528-381024	311.36546	-38.17326	17.24	17.31	3	30	0.42	0.57	c	21.7 ± 0.7
HV205249-363316	313.20214	-36.55431	17.50	17.28	3	29	0.64	0.40	ab	21.9 ± 0.7
HV204627-350051	311.61221	-35.01423	17.43	17.35	3	30	0.59	0.60	ab	22.0 ± 0.7
HV210342-381435	315.92522	-38.24300	17.72	17.46	3	29	0.48	0.97	ab	22.0 ± 0.9
HV203030-362912	307.62309	-36.48678	17.83	17.58	3	30	0.30	0.48	c	22.0 ± 0.8
HV204312-350947	310.79872	-35.16313	17.36	17.31	3	30	0.62	0.58	ab	22.3 ± 0.7
HV204644-344400	311.68526	-34.73324	17.47	17.56	3	30	0.48	0.96	ab	22.6 ± 0.8
HV204935-341205	312.39637	-34.20129	17.32	17.44	3	30	0.58	0.98	ab	22.6 ± 0.8
HV204200-390727	310.49961	-39.12427	17.41	17.42	3	31	0.55	0.71	ab	22.7 ± 0.8
HV204007-342726	310.02978	-34.45732	17.51	17.55	3	31	0.35	0.50	d	22.9 ± 0.8
HV202820-393254	307.08375	-39.54820	17.71	17.81	3	30	0.33	0.46	ab	22.9 ± 0.8
HV210116-333844	315.31661	-33.64560	17.97	17.56	3	26	0.56	0.62	ab	23.0 ± 0.8
HV203312-380842	308.30036	-38.14490	17.61	17.56	3	31	0.49	0.80	ab	23.0 ± 0.8
HV205250-351857	313.20722	-35.31588	17.41	17.55	3	29	0.39	0.51	c	23.1 ± 0.8
HV203655-371513	309.22912	-37.25374	17.27	17.42	3	31	0.62	0.64	ab	23.4 ± 0.8
HV210729-373103	316.87054	-37.51752	17.45	17.54	3	28	0.54	0.88	ab	23.5 ± 0.8
HV205825-374436	314.60621	-37.74334	17.64	17.46	3	29	0.60	0.60	ab	23.5 ± 0.8
HV202722-360046	306.83964	-36.01267	17.78	17.79	3	31	0.28	0.42	c	23.7 ± 0.8
HV205304-380707	313.26767	-38.11868	17.55	17.50	3	30	0.43	0.40	c	23.8 ± 0.8
HV204803-331643	312.01338	-33.27865	17.89	17.66	3	30	0.50	0.27	ab	24.1 ± 0.8
HV204911-385709	312.29460	-38.95261	17.85	17.63	3	28	0.53	0.66	ab	24.5 ± 0.8
HV203621-370735	309.08893	-37.12626	17.72	17.58	3	31	0.57	0.83	ab	24.6 ± 0.8
HV204156-361501	310.48482	-36.25025	17.57	17.69	3	30	0.50	0.94	ab	24.6 ± 0.8
HV205840-342000	314.66548	-34.33322	17.87	17.58	3	27	0.67	0.83	ab	24.7 ± 0.8
HV210107-331724	315.28013	-33.29008	18.05	17.73	3	27	0.54	0.97	ab	24.9 ± 0.8
HV210446-381113	316.19118	-38.18686	17.66	17.55	3	29	0.64	0.36	ab	25.3 ± 0.8
HV205943-372154	314.93121	-37.36502	18.05	17.66	2	29	0.57	0.68	ab	25.3 ± 0.8
HV204126-353829	310.35907	-35.64152	18.25	18.01	3	29	0.34	0.34	ab	25.4 ± 0.9
HV203036-360800	307.64927	-36.13327	17.78	17.81	3	31	0.35	0.34	c	25.7 ± 0.9
HV210719-363223	316.82812	-36.53975	17.73	17.88	3	28	0.35	0.51	d	25.8 ± 0.9
HV210141-395458	315.42205	-39.91608	17.89	18.00	3	28	0.28	0.48	c	26.2 ± 0.9
HV205801-384145	314.50266	-38.69577	17.95	17.70	3	29	0.63	0.68	ab	27.0 ± 0.9
HV202634-361154	306.64071	-36.19827	17.94	17.81	2	31	0.56	0.59	ab	27.2 ± 0.9
HV211003-334821	317.51342	-33.80575	18.08	18.02	3	29	0.35	0.43	c	27.3 ± 0.9
HV202914-361723	307.30926	-36.28962	17.66	17.89	3	31	0.52	0.91	ab	27.5 ± 0.9
HV205507-334057	313.77754	-33.68262	18.19	18.04	3	27	0.48	0.50	ab	27.6 ± 0.9
HV205644-343233	314.18504	-34.54244	18.13	17.94	3	27	0.40	0.37	c	27.6 ± 0.9
HV204839-343705	312.16068	-34.61792	17.79	17.82	3	30	0.62	0.77	ab	27.9 ± 0.9
HV205034-342646	312.64270	-34.44608	18.18	17.97	3	30	0.54	0.47	ab	28.3 ± 0.9
HV203224-361207	308.10172	-36.20193	18.09	17.86	3	31	0.59	0.55	ab	28.3 ± 0.9
HV203846-380226	309.69318	-38.04060	17.98	17.80	3	27	0.66	0.50	ab	28.4 ± 1.0
HV204529-334345	311.37145	-33.72910	18.10	18.06	3	26	0.48	0.34	ab	28.7 ± 1.0
HV205125-382028	312.85424	-38.34105	17.93	17.99	3	30	0.52	0.84	ab	28.8 ± 1.0
HV203625-331830	309.10335	-33.30828	18.16	17.88	3	31	0.60	0.90	ab	28.8 ± 1.0
HV210231-352012	315.62713	-35.33657	18.32	18.03	3	29	0.53	0.92	ab	28.8 ± 1.0
HV210227-361337	315.61312	-36.22695	18.06	17.97	3	28	0.60	0.70	ab	29.0 ± 1.0
HV203717-381200	309.32259	-38.19993	18.11	18.21	3	31	0.29	0.42	c	29.2 ± 1.0
HV203414-334148	308.55884	-33.69664	18.08	17.97	3	31	0.55	0.80	ab	29.2 ± 1.0
HV202915-351924	307.31230	-35.32320	18.33	17.97	3	31	0.57	0.74	ab	29.2 ± 1.0
HV210205-341427	315.52120	-34.24092	18.11	17.95	3	27	0.65	0.36	ab	29.3 ± 1.0
HV204015-341323	310.06052	-34.22316	18.12	17.94	3	31	0.59	0.65	ab	29.4 ± 1.0
HV203922-340248	309.84080	-34.04655	18.01	17.93	3	28	0.62	0.76	ab	29.5 ± 1.1
HV210032-332754	315.13416	-33.46498	18.43	18.31	3	26	0.32	0.49	c	29.8 ± 1.0
HV204659-332433	311.74480	-33.40914	18.13	17.99	3	30	0.63	0.48	ab	30.3 ± 1.0
HV202544-360646	306.43492	-36.11282	18.12	17.99	3	31	0.66	0.58	ab	31.2 ± 1.0
HV204805-383020	312.02011	-38.50555	18.31	18.27	3	30	0.36	0.39	c	31.9 ± 1.1
HV203833-383027	309.63933	-38.50737	18.31	18.18	3	31	0.55	0.52	ab	31.9 ± 1.1
HV204028-363953	310.11870	-36.66477	18.10	18.11	3	30	0.61	0.51	ab	32.0 ± 1.1
HV204704-382019	311.76850	-38.33850	18.22	18.14	3	30	0.61	0.70	ab	32.3 ± 1.1
HV203725-344453	309.35279	-34.74813	18.36	18.23	3	31	0.60	0.65	ab	34.0 ± 1.1
HV205925-344235	314.85315	-34.70964	18.75	18.48	3	25	0.54	0.64	ab	35.6 ± 1.2
HV204909-375232	312.28591	-37.87553	18.35	18.37	3	29	0.67	0.54	ab	37.2 ± 1.2
HV210954-374800	317.47433	-37.80006	18.74	18.46	3	29	0.61	0.63	ab	37.7 ± 1.3
HV203731-372021	309.37766	-37.33929	18.82	18.66	3	30	0.62	0.49	ab	41.5 ± 1.4
HV210231-375511	315.63010	-37.91975	19.00	18.78	3	27	0.58	0.61	ab	42.7 ± 1.4
HV205344-353555	313.43507	-35.59859	19.36	19.32	3	27	0.24	0.27	c	44.7 ± 1.6
HV205135-373853	312.89491	-37.64809	19.00	18.70	3	30	0.77	0.32	ab	44.9 ± 1.5

Table B1: (Continued).

ID	R.A. (deg)	Dec. (deg)	$\langle g \rangle$	$\langle r \rangle$	N_g	N_r	Period (days)	Amplitude	Type	d_H (kpc)
HV210246-352242	315.69264	-35.37823	19.86	19.29	3	29	0.35	0.56	ab	45.1 ± 1.6
HV205634-403338	314.14295	-40.56045	19.22	18.94	3	28	0.58	0.53	ab	46.7 ± 1.6
HV204200-362426	310.49867	-36.40726	19.23	19.07	3	29	0.43	0.30	c	49.0 ± 1.6
HV203622-342737	309.09264	-34.46018	19.07	19.13	3	30	0.39	0.45	c	49.5 ± 1.7
HV204714-371124	311.80952	-37.18987	19.22	19.41	3	29	0.27	0.32	c	49.5 ± 1.7
HV210921-395248	317.33768	-39.87987	19.05	19.14	3	26	0.54	1.11	ab	49.6 ± 1.7
HV204930-355249	312.37476	-35.88034	19.66	19.68	3	28	0.21	0.26	c	50.8 ± 1.9
HV204320-350906	310.83300	-35.15165	19.42	19.17	3	29	0.64	0.85	ab	53.0 ± 1.8
HV210355-352305	315.98062	-35.38469	19.52	19.35	3	28	0.55	0.85	ab	53.6 ± 1.8
HV204000-402739	309.99918	-40.46079	19.22	19.22	3	30	0.63	0.76	ab	54.3 ± 1.8
HV210830-374416	317.12313	-37.73787	19.74	19.59	3	28	0.32	0.47	c	56.5 ± 1.9
HV210918-335828	317.32527	-33.97447	19.54	19.38	3	29	0.63	0.76	ab	56.7 ± 1.9
HV202900-362210	307.25049	-36.36935	19.99	20.07	3	30	0.21	0.26	c	61.4 ± 2.3
HV202817-352054	307.07153	-35.34836	21.04	20.74	3	30	0.21	0.43	c	83.9 ± 3.1
HV205533-405803	313.88689	-40.96754	20.71	20.75	3	26	0.25	0.39	c	89.3 ± 3.2
HV205828-382448	314.61624	-38.41320	20.84	20.53	3	17	0.58	0.55	ab	96.3 ± 3.2
HV205059-402816	312.74633	-40.47117	20.74	20.50	3	27	0.64	0.36	ab	97.9 ± 3.3
HV210719-352250	316.82756	-35.38046	20.79	20.68	3	28	0.60	0.39	ab	100.4 ± 3.4
HV120436-362213	181.15089	-36.37024	15.12	14.89	3	16	0.51	0.86	ab	6.7 ± 0.2
HV154531-340239	236.37927	-34.04409	17.00	16.43	2	19	0.20	0.42	c	7.6 ± 0.3
HV154357-314053	235.98828	-31.68151	15.47	15.01	2	17	0.77	0.74	ab	7.9 ± 0.3
HV154924-341748	237.35103	-34.29672	16.31	16.17	2	15	0.31	0.31	c	8.2 ± 0.3
HV153429-361038	233.62122	-36.17719	17.37	16.67	2	20	0.32	0.39	c	8.5 ± 0.4
HV160657-355828	241.73778	-35.97454	16.40	16.00	2	15	0.64	0.57	ab	8.7 ± 0.3
HV155517-313749	238.81894	-31.63018	16.47	16.13	2	20	0.21	0.33	c	8.7 ± 0.3
HV160434-360602	241.14022	-36.10062	16.75	16.20	2	16	0.38	0.36	c	8.7 ± 0.3
HV152829-311804	232.11906	-31.30125	16.79	16.25	2	19	0.21	0.34	c	9.0 ± 0.3
HV154956-334005	237.48419	-33.66800	16.07	15.57	2	20	0.78	0.48	ab	9.0 ± 0.3
HV154633-344216	236.63722	-34.70443	17.43	17.04	2	19	0.44	0.89	ab	9.3 ± 0.5
HV154520-335617	236.33410	-33.93811	16.49	16.44	2	15	0.31	0.37	c	9.3 ± 0.4
HV154235-353953	235.64485	-35.66466	16.79	16.33	2	19	0.56	1.03	ab	9.3 ± 0.3
HV155020-333455	237.58148	-33.58188	16.23	16.13	2	16	0.29	0.42	c	9.3 ± 0.3
HV155453-341500	238.72018	-34.25000	17.19	16.45	2	19	0.51	0.29	ab	9.3 ± 0.4
HV160328-364524	240.86633	-36.75662	16.56	16.29	2	15	0.59	0.65	ab	9.4 ± 0.3
HV160348-321132	240.94984	-32.19223	16.43	16.13	2	15	0.26	0.21	c	9.5 ± 0.3
HV152811-350828	232.04388	-35.14118	16.54	16.13	2	15	0.63	0.45	ab	9.5 ± 0.4
HV154305-353832	235.76887	-35.64218	17.18	16.46	2	20	0.57	0.62	ab	9.6 ± 0.4
HV160439-315534	241.16188	-31.92621	16.48	16.20	2	17	0.32	0.34	c	9.7 ± 0.4
HV154424-332511	236.09955	-33.41962	17.24	16.80	2	20	0.22	0.36	c	9.7 ± 0.5
HV155428-362428	238.61617	-36.40782	16.91	16.51	2	20	0.30	0.29	c	9.9 ± 0.3
HV160259-323450	240.74676	-32.58069	16.23	16.20	2	15	0.29	0.30	c	9.9 ± 0.4
HV160543-314159	241.42816	-31.69983	15.73	16.05	2	19	0.55	0.98	ab	10.0 ± 0.4
HV160559-345518	241.49684	-34.92157	16.81	16.41	2	18	0.32	0.41	c	10.0 ± 0.4
HV153605-334352	234.02080	-33.73120	17.00	16.78	2	20	0.33	0.36	c	10.1 ± 0.4
HV154351-334127	235.96282	-33.69092	16.64	16.64	2	20	0.26	0.37	c	10.1 ± 0.4
HV160053-360255	240.22286	-36.04861	16.84	16.37	2	19	0.49	0.80	ab	10.1 ± 0.3
HV153351-343339	233.46117	-34.56084	16.70	16.43	2	19	0.31	0.26	c	10.2 ± 0.4
HV155744-332304	239.43344	-33.38446	16.75	16.52	2	20	0.28	0.44	c	10.2 ± 0.5
HV155446-352725	238.69122	-35.45708	16.92	16.62	2	20	0.32	0.37	c	10.3 ± 0.5
HV155002-333459	237.50774	-33.58307	16.70	16.18	2	19	0.50	0.90	ab	10.4 ± 0.4
HV153240-354601	233.16552	-35.76690	17.12	16.73	2	20	0.29	0.42	c	10.5 ± 0.5
HV153702-351900	234.26027	-35.31666	17.47	16.90	2	20	0.32	0.43	c	10.7 ± 0.5
HV153921-351755	234.83939	-35.29848	17.26	16.81	2	20	0.65	0.92	ab	10.8 ± 0.4
HV154221-331754	235.58935	-33.29847	16.61	16.42	2	20	0.32	0.28	c	10.9 ± 0.4
HV153049-351041	232.70376	-35.17796	17.32	16.81	2	20	0.28	0.27	c	10.9 ± 0.4
HV154356-343852	235.98234	-34.64789	18.00	17.21	2	20	0.56	0.64	ab	11.0 ± 0.5
HV153752-354959	234.46612	-35.83309	17.16	16.73	2	19	0.45	0.67	ab	11.1 ± 0.4
HV160548-353238	241.44812	-35.54387	17.00	16.42	2	19	0.66	0.37	ab	11.1 ± 0.4
HV153958-353118	234.99360	-35.52160	17.47	16.80	2	20	0.60	0.88	ab	11.2 ± 0.4
HV155534-321228	238.89189	-32.20791	16.18	16.17	2	16	0.53	0.74	ab	11.4 ± 0.4
HV155614-335103	239.05812	-33.85073	17.42	16.68	2	19	0.48	0.95	ab	11.4 ± 0.5
HV155444-361248	238.68411	-36.21326	17.15	16.63	2	20	0.62	0.50	ab	11.4 ± 0.4
HV153157-340050	232.98893	-34.01392	16.95	16.68	2	20	0.34	0.43	d	11.5 ± 0.4
HV160315-314308	240.81095	-31.71899	17.00	16.67	2	17	0.23	0.26	c	11.6 ± 0.4
HV154116-361650	235.31727	-36.28062	17.36	16.88	2	20	0.30	0.37	c	11.6 ± 0.5
HV160058-363926	240.24047	-36.65722	17.10	16.71	2	18	0.57	0.54	ab	11.6 ± 0.4
HV154201-360254	235.50609	-36.04844	17.61	16.93	2	20	0.55	1.00	ab	11.7 ± 0.5
HV161027-342530	242.61065	-34.42511	17.06	16.64	2	19	0.39	0.37	c	11.7 ± 0.4
HV153228-352500	233.11459	-35.41676	16.96	16.60	2	20	0.58	0.63	ab	11.7 ± 0.4
HV160240-340150	240.66840	-34.03050	16.97	16.36	2	19	0.65	0.88	ab	11.7 ± 0.4

Table B1: (Continued).

ID	R.A. (deg)	Dec. (deg)	$\langle g \rangle$	$\langle r \rangle$	N_g	N_r	Period (days)	Amplitude	Type	d_H (kpc)
HV154812-360637	237.05098	-36.11028	16.71	16.63	2	20	0.59	0.51	ab	11.7±0.4
HV155428-343917	238.61849	-34.65461	17.49	17.01	2	19	0.44	0.78	ab	11.7±0.4
HV160101-352931	240.25443	-35.49207	16.73	16.52	2	19	0.37	0.37	c	11.8±0.4
HV160314-365033	240.80759	-36.84240	17.18	16.98	2	19	0.47	0.77	ab	11.8±0.4
HV160724-330134	241.85035	-33.02625	16.81	16.31	2	19	0.66	0.49	ab	11.9±0.4
HV155409-341246	238.53759	-34.21289	17.31	16.97	2	20	0.64	0.86	ab	12.0±0.4
HV114724-352819	176.85101	-35.47182	16.41	16.50	3	23	0.27	0.40	c	12.1±0.4
HV160508-334418	241.28424	-33.73825	17.05	16.52	2	19	0.62	0.28	ab	12.2±0.4
HV155858-343718	239.73968	-34.62173	16.83	16.76	2	20	0.31	0.25	c	12.2±0.5
HV153836-321134	234.65193	-32.19284	16.30	16.37	2	20	0.36	0.36	c	12.3±0.4
HV121137-350534	182.90547	-35.09273	16.42	16.32	3	24	0.34	0.37	c	12.4±0.4
HV155827-314224	239.61183	-31.70666	16.33	16.46	2	16	0.49	0.66	ab	12.5±0.4
HV115148-334333	177.94818	-33.72582	16.23	16.28	3	19	0.50	0.40	ab	12.5±0.4
HV160306-313501	240.77642	-31.58356	16.97	16.39	2	19	0.58	0.65	ab	12.6±0.4
HV113343-324307	173.42922	-32.71865	16.52	16.17	4	24	0.55	0.76	ab	12.6±0.4
HV160427-360435	241.11429	-36.07651	17.96	17.49	2	19	0.21	0.29	c	13.1±0.5
HV113024-365812	172.60025	-36.97004	16.97	16.67	3	23	0.35	0.63	ab	13.1±0.5
HV113038-362634	172.65972	-36.44279	16.40	16.38	3	23	0.54	0.66	ab	13.2±0.4
HV153746-313410	234.44097	-31.56940	16.36	16.14	2	19	0.74	0.43	ab	13.3±0.4
HV154855-322351	237.22729	-32.39748	16.65	16.51	2	20	0.36	0.38	c	13.3±0.5
HV154216-342306	235.56572	-34.38487	18.09	17.37	2	19	0.65	0.40	ab	13.4±0.6
HV155047-360238	237.69391	-36.04388	17.87	17.27	2	20	0.33	0.58	c	13.5±0.5
HV115141-362014	177.92228	-36.33716	16.18	16.33	3	23	0.60	0.80	ab	13.5±0.4
HV160409-320624	241.03929	-32.10680	17.00	17.07	2	19	0.21	0.37	c	13.5±0.5
HV154903-322431	237.26375	-32.40864	17.35	16.92	2	20	0.22	0.52	c	13.7±0.5
HV152834-360028	232.14010	-36.00766	16.98	16.76	2	20	0.72	0.77	ab	13.8±0.5
HV155441-331239	238.67165	-33.21070	17.24	16.65	2	20	0.60	0.46	ab	13.9±0.5
HV113831-365826	174.62757	-36.97377	16.80	16.48	3	18	0.58	0.78	ab	13.9±0.5
HV153316-340110	233.31770	-34.01934	17.45	17.09	2	20	0.55	0.81	ab	13.9±0.6
HV155637-330038	239.15249	-33.01068	17.34	17.06	2	20	0.25	0.21	c	14.0±0.5
HV155712-333619	239.30034	-33.60527	17.36	16.77	2	20	0.61	0.41	ab	14.0±0.5
HV155213-320059	238.05282	-32.01652	16.72	16.71	2	20	0.34	0.44	c	14.1±0.5
HV113331-350433	173.38105	-35.07571	16.55	16.41	4	24	0.58	0.60	ab	14.1±0.5
HV155636-331043	239.14920	-33.17855	17.03	16.68	2	20	0.63	0.92	ab	14.2±0.5
HV115531-363657	178.87748	-36.61578	16.31	16.51	3	23	0.53	0.51	ab	14.3±0.5
HV113114-364537	172.80813	-36.76016	16.78	16.76	3	23	0.30	0.29	c	14.3±0.5
HV113542-343321	173.92318	-34.55595	16.67	16.46	4	24	0.60	0.63	ab	14.4±0.5
HV155817-315632	239.57246	-31.94228	17.35	16.75	2	19	0.59	0.50	ab	14.5±0.6
HV113113-373008	172.80346	-37.50233	17.16	16.94	3	23	0.33	0.95	ab	14.5±0.5
HV120004-324438	180.01683	-32.74381	16.40	16.50	3	23	0.45	0.40	c	14.5±0.5
HV160122-352052	240.34279	-35.34778	17.69	17.03	2	19	0.46	0.85	ab	14.6±0.5
HV155924-354525	239.85009	-35.75690	17.49	17.20	2	19	0.39	0.45	c	14.6±0.5
HV160740-330901	241.91795	-33.15019	17.56	17.19	2	18	0.24	0.39	c	14.6±0.5
HV160330-324319	240.87674	-32.72199	17.62	17.25	2	19	0.22	0.54	c	14.7±0.5
HV113755-330908	174.48083	-33.15224	16.66	16.57	3	19	0.53	0.90	ab	14.8±0.6
HV153933-323814	234.88778	-32.63734	16.98	16.90	2	20	0.34	0.34	c	14.8±0.5
HV153803-343451	234.51281	-34.58081	18.66	18.13	2	18	0.46	0.45	ab	14.9±1.1
HV154429-335205	236.12108	-33.86807	17.68	17.25	2	20	0.57	0.78	ab	14.9±0.6
HV153740-342536	234.41751	-34.42679	18.28	17.81	2	20	0.26	0.33	c	15.1±1.0
HV154519-315604	236.32718	-31.93447	17.10	16.82	2	20	0.33	0.39	c	15.2±0.5
HV152657-363711	231.73824	-36.61962	17.35	16.82	2	20	0.59	0.69	ab	15.3±0.5
HV155943-352308	239.93101	-35.38569	17.03	17.01	2	19	0.65	0.59	ab	15.3±0.5
HV153306-323733	233.27533	-32.62578	16.95	16.89	2	20	0.40	0.42	c	15.3±0.5
HV155725-354714	239.35485	-35.78711	18.13	17.60	2	19	0.29	0.27	c	15.4±0.6
HV160605-332223	241.51956	-33.37317	17.55	17.02	2	19	0.62	0.49	ab	15.5±0.5
HV155252-354547	238.21750	-35.76309	18.08	17.57	2	20	0.35	0.35	c	15.5±0.6
HV120435-321931	181.14723	-32.32540	16.84	16.98	3	24	0.27	0.36	c	15.5±0.5
HV155359-342708	238.49633	-34.45220	18.10	17.65	2	20	0.50	1.02	ab	15.7±0.6
HV154255-321415	235.73008	-32.23757	16.60	16.68	2	19	0.59	0.67	ab	15.7±0.5
HV153544-341457	233.93473	-34.24919	17.96	17.68	2	20	0.27	0.34	c	15.7±0.6
HV155258-364555	238.24032	-36.76530	17.34	17.20	2	19	0.53	0.84	ab	15.9±0.6
HV160524-361458	241.34943	-36.24958	17.95	17.48	2	19	0.54	0.81	ab	15.9±0.5
HV152906-322156	232.27478	-32.36562	17.32	17.05	2	18	0.61	0.78	ab	16.0±0.6
HV153332-321440	233.38477	-32.24458	17.48	17.30	2	20	0.23	0.39	c	16.1±0.6
HV120427-334309	181.11305	-33.71904	16.94	16.65	3	24	0.67	0.69	ab	16.1±0.5
HV155019-310624	237.57819	-31.10674	17.16	17.02	2	20	0.33	0.35	c	16.4±0.6
HV115249-335737	178.20620	-33.96028	17.11	16.94	3	24	0.35	0.38	c	16.5±0.6
HV154842-313502	237.17384	-31.58392	16.65	16.94	2	20	0.49	0.83	ab	16.5±0.6
HV161004-340532	242.51740	-34.09234	17.77	17.46	2	19	0.34	0.32	c	16.5±0.6
HV155219-340831	238.08038	-34.14188	18.06	17.62	2	18	0.54	1.25	ab	16.7±0.7

Table B1: (Continued).

ID	R.A. (deg)	Dec. (deg)	$\langle g \rangle$	$\langle r \rangle$	N_g	N_r	Period (days)	Amplitude	Type	d_H (kpc)
HV114249-374622	175.70480	-37.77278	17.20	16.83	3	23	0.61	0.57	ab	16.8±0.6
HV160337-364119	240.90231	-36.68870	18.14	17.78	2	19	0.33	0.31	c	16.9±0.6
HV160231-324459	240.63077	-32.74965	17.22	17.21	2	18	0.52	0.82	ab	17.0±0.6
HV160518-361538	241.32381	-36.26051	18.30	17.70	2	19	0.50	0.74	ab	17.0±0.6
HV120015-332646	180.06201	-33.44602	17.19	17.25	3	24	0.34	0.66	ab	17.2±0.6
HV114630-364507	176.62677	-36.75201	17.11	17.13	2	23	0.31	0.25	c	17.3±0.6
HV115402-334022	178.50997	-33.67285	16.95	17.02	3	24	0.34	0.38	c	17.3±0.6
HV153801-354705	234.50288	-35.78464	17.91	17.47	2	20	0.63	0.38	ab	17.3±0.6
HV154859-332020	237.24680	-33.33875	17.39	16.98	2	20	0.65	0.70	ab	17.4±0.6
HV155608-360041	239.03231	-36.01134	18.12	17.82	2	20	0.30	0.42	c	17.4±0.7
HV115451-350958	178.71111	-35.16606	16.79	16.98	2	24	0.51	0.93	ab	17.4±0.6
HV152656-315158	231.73137	-31.86619	17.56	17.24	2	20	0.68	0.78	ab	17.5±0.6
HV153214-313458	233.05810	-31.58267	17.03	16.96	2	20	0.64	0.42	ab	17.6±0.6
HV121049-351040	182.70469	-35.17776	17.59	16.85	3	24	0.63	0.26	ab	17.6±0.6
HV154318-342330	235.82696	-34.39165	18.48	18.00	2	20	0.61	0.91	ab	17.8±1.0
HV120238-320417	180.65785	-32.07137	17.11	17.11	3	24	0.34	0.44	c	18.0±0.6
HV155656-331914	239.23134	-33.32054	18.11	17.80	2	20	0.20	0.31	c	18.1±0.7
HV113944-321847	174.93135	-32.31299	17.16	16.92	3	24	0.60	0.50	ab	18.1±0.6
HV155710-341336	239.29034	-34.22674	18.56	18.09	2	20	0.21	0.40	c	18.2±0.7
HV153443-330421	233.68115	-33.07250	17.63	17.34	2	20	0.63	0.86	ab	18.3±0.6
HV113157-364659	172.98727	-36.78305	17.31	17.20	3	23	0.34	0.30	c	18.3±0.6
HV160559-352959	241.49762	-35.49969	18.39	17.88	2	19	0.27	0.28	c	18.3±0.7
HV155320-364011	238.33528	-36.66972	18.26	17.55	2	20	0.58	0.54	ab	18.4±0.7
HV112811-324647	172.04662	-32.77979	17.38	17.08	4	24	0.49	0.79	ab	18.4±0.6
HV115037-333300	177.65284	-33.54987	17.25	17.14	3	24	0.49	0.77	ab	18.6±0.6
HV154746-342719	236.94055	-34.45523	18.31	17.76	2	18	0.55	0.48	ab	18.7±0.7
HV155914-350609	239.80887	-35.10242	18.10	17.90	2	19	0.29	0.27	c	18.8±0.7
HV155245-314809	238.18928	-31.80239	17.82	17.32	2	19	0.53	0.36	ab	18.9±0.7
HV160310-363905	240.79025	-36.65153	18.60	18.20	2	19	0.27	0.33	c	19.0±0.7
HV155607-331942	239.02925	-33.32825	17.80	17.34	2	20	0.59	0.56	ab	19.1±0.7
HV113038-345431	172.65944	-34.90868	17.36	17.27	4	24	0.35	0.37	c	19.4±0.7
HV113707-342412	174.27903	-34.40335	17.41	17.48	4	24	0.26	0.35	c	19.5±0.7
HV115503-345812	178.76117	-34.97010	17.50	17.18	3	24	0.58	0.74	ab	19.6±0.7
HV154628-325905	236.61840	-32.98473	17.69	17.27	2	19	0.57	0.57	ab	19.7±0.7
HV160438-363710	241.15865	-36.61948	18.63	17.85	2	19	0.66	0.22	ab	19.7±0.7
HV115938-345409	179.90957	-34.90259	17.30	17.15	3	24	0.59	0.70	ab	19.8±0.7
HV155336-324509	238.39817	-32.75237	18.41	18.03	2	20	0.20	0.27	c	19.9±0.7
HV155725-342905	239.35429	-34.48462	18.55	17.98	2	20	0.31	0.42	c	20.0±0.9
HV113210-353234	173.04204	-35.54283	17.09	17.14	4	24	0.61	0.55	ab	20.0±0.7
HV153326-334110	233.35897	-33.68610	18.93	18.43	2	20	0.20	0.38	c	20.1±0.8
HV155750-321442	239.46038	-32.24498	17.57	17.42	2	19	0.76	0.39	ab	20.1±0.7
HV155055-351301	237.73018	-35.21708	18.27	18.02	2	20	0.36	0.42	c	20.1±0.9
HV114500-350549	176.25152	-35.09701	17.36	17.25	3	24	0.58	0.96	ab	20.1±0.7
HV155542-334935	238.92386	-33.82640	18.03	17.70	2	20	0.61	0.92	ab	20.4±1.1
HV112724-323542	171.85197	-32.59487	17.22	17.16	4	24	0.62	0.48	ab	20.5±0.7
HV153032-362039	232.63357	-36.34410	18.63	17.89	2	20	0.54	0.63	ab	20.7±1.0
HV115419-372523	178.58085	-37.42296	17.14	17.17	3	23	0.67	0.50	ab	20.7±0.7
HV153005-362224	232.52253	-36.37325	18.97	18.29	2	20	0.20	0.22	c	20.8±0.8
HV155140-314738	237.91818	-31.79400	17.66	17.60	2	20	0.46	0.87	ab	20.9±0.7
HV155338-324507	238.40903	-32.75189	18.19	17.64	2	20	0.55	0.53	ab	20.9±0.7
HV153538-331608	233.90649	-33.26883	18.58	18.01	2	19	0.52	0.49	ab	21.0±0.8
HV115004-361653	177.51657	-36.28145	17.59	17.32	3	23	0.59	0.86	ab	21.1±0.7
HV153752-360053	234.46837	-36.01475	18.37	18.11	2	20	0.34	0.44	c	21.3±0.7
HV153950-311636	234.95854	-31.27679	17.81	17.56	2	20	0.47	0.62	ab	21.6±0.7
HV160031-335249	240.12751	-33.88024	18.34	17.88	2	20	0.60	0.50	ab	21.7±0.8
HV114003-331040	175.01186	-33.17768	17.49	17.28	3	24	0.65	0.73	ab	21.8±0.7
HV113212-323359	173.05096	-32.56647	17.31	17.39	4	24	0.53	1.05	ab	21.9±0.7
HV155042-323608	237.67462	-32.60214	18.01	17.44	2	20	0.64	0.80	ab	22.1±0.7
HV160646-343250	241.69320	-34.54727	18.48	17.84	2	19	0.56	0.62	ab	22.1±0.8
HV115143-333051	177.92769	-33.51430	18.07	17.91	3	24	0.21	0.34	c	22.3±0.8
HV113154-363548	172.97527	-36.59658	17.59	17.39	3	23	0.66	0.42	ab	22.5±0.7
HV153853-321632	234.72287	-32.27561	18.04	17.64	2	20	0.54	0.64	ab	22.6±0.8
HV154321-321602	235.83837	-32.26734	18.21	17.63	2	20	0.49	1.02	ab	22.7±0.8
HV160327-355740	240.86071	-35.96108	18.75	18.21	2	19	0.59	0.60	ab	22.8±0.8
HV153119-323210	232.82846	-32.53608	18.15	17.72	2	20	0.54	0.85	ab	22.8±0.8
HV120256-373719	180.73335	-37.62206	17.80	17.50	3	22	0.58	0.61	ab	23.2±0.8
HV153035-354854	232.64403	-35.81493	18.31	18.12	2	19	0.64	0.47	ab	23.2±1.0
HV160052-320725	240.21839	-32.12357	18.22	17.70	2	19	0.59	0.47	ab	23.4±0.8
HV115516-352946	178.81771	-35.49608	17.58	17.58	3	24	0.57	0.64	ab	23.8±0.8
HV160831-343153	242.12883	-34.53134	18.33	17.88	2	19	0.72	0.51	ab	23.9±0.9
HV114634-330851	176.64038	-33.14761	17.64	17.64	3	15	0.58	0.60	ab	24.6±1.0

Table B1: (Continued).

ID	R.A. (deg)	Dec. (deg)	$\langle g \rangle$	$\langle r \rangle$	N_g	N_r	Period (days)	Amplitude	Type	d_H (kpc)
HV155533-332135	238.88729	-33.35985	17.95	18.04	2	20	0.50	0.83	ab	24.8±0.9
HV160911-343318	242.29653	-34.55513	18.42	18.21	2	19	0.57	0.63	ab	25.1±0.9
HV114754-322528	176.97382	-32.42452	18.20	17.83	3	24	0.45	0.97	ab	25.3±0.9
HV155221-310438	238.08707	-31.07720	18.05	17.99	2	20	0.36	0.43	d	25.8±0.9
HV121112-352136	182.80084	-35.35990	18.02	17.90	3	24	0.36	0.42	c	26.0±0.9
HV154237-325456	235.65545	-32.91557	18.23	17.87	2	20	0.65	0.65	ab	26.2±0.9
HV153853-360629	234.71886	-36.10812	19.09	18.40	2	20	0.56	0.80	ab	26.3±0.9
HV155249-324319	238.20250	-32.72188	18.27	17.99	2	20	0.56	0.84	ab	26.3±1.1
HV113226-373850	173.11005	-37.64709	18.19	17.86	3	23	0.56	0.61	ab	26.5±0.9
HV154122-314150	235.34355	-31.69713	17.73	17.83	2	20	0.58	0.64	ab	26.6±0.9
HV154538-330004	236.40995	-33.00107	17.91	17.91	2	20	0.57	0.54	ab	26.7±0.9
HV155049-323449	237.70393	-32.58032	18.73	18.14	2	20	0.34	0.36	c	27.5±0.9
HV115537-353108	178.90369	-35.51895	18.10	18.09	2	24	0.33	0.38	c	27.6±0.9
HV155905-334458	239.76939	-33.74945	19.10	18.68	2	20	0.58	0.61	ab	27.9±1.0
HV114317-325645	175.81937	-32.94588	18.15	18.01	3	24	0.37	0.37	c	28.0±0.9
HV160247-312124	240.69526	-31.35680	19.14	18.66	2	19	0.24	0.33	c	28.3±1.0
HV115840-354947	179.66719	-35.82978	18.52	18.13	3	24	0.46	1.01	ab	28.4±1.0
HV115418-344243	178.57462	-34.71204	18.13	17.98	3	24	0.58	0.70	ab	28.5±1.0
HV113332-330136	173.38486	-33.02673	18.02	17.77	4	24	0.76	0.32	ab	28.9±1.0
HV160034-312554	240.14271	-31.43164	18.58	18.09	2	19	0.73	0.27	ab	29.6±1.0
HV160313-311537	240.80560	-31.26038	18.17	18.35	2	19	0.58	0.62	ab	29.9±1.0
HV160003-341143	240.01344	-34.19537	19.16	18.86	2	19	0.24	0.23	c	30.0±1.1
HV120427-324233	181.11264	-32.70912	18.01	17.94	3	23	0.72	0.53	ab	30.1±1.1
HV154356-335942	235.98433	-33.99506	19.68	19.33	2	19	0.33	0.41	c	30.3±2.0
HV155235-334204	238.14404	-33.70102	18.90	18.49	2	19	0.54	0.39	ab	30.4±1.0
HV115233-335519	178.13657	-33.92208	18.17	18.29	3	24	0.50	0.98	ab	31.2±1.0
HV153631-342058	234.12843	-34.34940	20.17	19.45	2	19	0.20	0.41	c	31.3±1.2
HV160911-344031	242.29392	-34.67535	19.19	18.95	2	19	0.30	0.34	c	31.4±1.1
HV153154-345835	232.97697	-34.97648	19.24	19.02	2	20	0.30	0.34	c	31.9±1.5
HV154235-324407	235.64724	-32.73536	18.41	18.37	2	20	0.52	0.52	ab	32.2±1.1
HV112801-374015	172.00379	-37.67084	18.13	18.11	3	23	0.74	0.59	ab	32.3±1.1
HV120754-352217	181.97514	-35.37136	19.17	18.78	3	24	0.20	0.48	c	32.3±1.2
HV155955-323212	239.97831	-32.53658	19.31	18.70	2	19	0.67	0.58	ab	33.1±1.5
HV115132-370642	177.88327	-37.11160	18.67	18.42	3	23	0.51	0.60	ab	33.4±1.1
HV153703-341230	234.26164	-34.20840	19.68	19.09	2	20	0.57	0.53	ab	33.6±1.2
HV153857-361159	234.73746	-36.19964	19.42	18.84	2	19	0.66	0.70	ab	34.2±1.2
HV112948-364854	172.45151	-36.81495	18.69	18.40	3	23	0.59	0.42	ab	34.5±1.2
HV154305-355149	235.76900	-35.86355	19.92	19.25	2	18	0.54	0.34	ab	34.5±1.5
HV154032-315752	235.13244	-31.96442	18.67	18.42	2	20	0.58	0.74	ab	34.7±1.2
HV120533-332545	181.38750	-33.42910	18.70	18.59	3	24	0.34	0.34	c	34.8±1.2
HV113319-372704	173.33110	-37.45111	18.73	18.45	3	23	0.59	0.35	ab	35.2±1.2
HV114823-372203	177.09669	-37.36763	18.84	18.48	3	23	0.54	0.71	ab	35.3±1.2
HV113549-325729	173.95482	-32.95808	18.37	18.44	3	24	0.55	0.56	ab	35.7±1.2
HV154923-332241	237.34747	-33.37804	19.11	18.64	2	19	0.60	0.59	ab	36.2±1.2
HV113226-332424	173.10661	-33.40674	18.77	18.44	4	24	0.62	0.44	ab	36.8±1.2
HV154321-352549	235.83565	-35.43020	20.20	19.79	2	19	0.31	0.44	c	37.2±1.4
HV160241-335543	240.67253	-33.92859	19.50	19.31	2	18	0.36	0.53	ab	37.5±1.3
HV114854-331304	177.22595	-33.21768	18.77	18.71	3	24	0.36	0.45	c	38.1±1.3
HV115749-325717	179.45383	-32.95484	18.77	18.58	3	24	0.62	0.45	ab	38.2±1.3
HV160404-345903	241.01853	-34.98406	19.33	19.29	2	18	0.41	0.94	ab	38.4±1.4
HV153555-335400	233.97782	-33.89990	20.11	19.43	2	19	0.75	0.53	ab	39.7±1.4
HV160836-340750	242.15038	-34.13062	19.46	19.04	2	17	0.60	0.44	ab	39.8±1.4
HV154929-361016	237.37228	-36.17119	19.76	19.36	2	20	0.58	0.70	ab	40.3±1.5
HV153201-313900	233.00458	-31.65003	19.53	18.95	2	19	0.41	0.37	c	41.7±1.4
HV113040-361601	172.66760	-36.26701	19.03	18.76	3	23	0.65	0.52	ab	42.0±1.4
HV155911-333559	239.79731	-33.59963	20.12	19.63	2	19	0.53	0.57	ab	43.5±1.7
HV153614-352629	234.05838	-35.44143	20.04	19.77	2	19	0.51	1.01	ab	44.5±1.5
HV160304-321037	240.76684	-32.17694	20.24	19.78	2	18	0.17	0.65	c	44.7±1.7
HV160251-362546	240.71173	-36.42934	20.05	19.69	2	19	0.41	0.43	c	44.8±1.7
HV160055-355651	240.22803	-35.94757	20.08	19.91	2	19	0.29	0.25	c	47.3±1.7
HV115945-352110	179.93851	-35.35288	19.49	19.32	3	24	0.39	0.36	c	50.9±1.7
HV160700-343410	241.74927	-34.56933	20.21	19.47	2	19	0.80	1.36	ab	51.8±1.9
HV112821-332739	172.08656	-33.46089	19.68	19.35	4	24	0.54	0.67	ab	53.7±1.8
HV113124-361257	172.84848	-36.21594	19.89	19.90	3	24	0.26	0.40	c	58.1±2.0
HV160832-332518	242.13482	-33.42160	20.65	20.10	2	18	0.33	0.81	c	61.8±2.1
HV114426-343253	176.10846	-34.54810	19.99	19.78	3	24	0.64	0.22	ab	67.8±2.3
HV113422-343446	173.59191	-34.57945	20.03	20.11	4	24	0.33	0.44	c	71.2±2.4
HV154800-323238	237.00131	-32.54377	20.43	20.48	2	19	0.26	0.78	c	74.6±2.6
HV115622-364910	179.09193	-36.81946	20.77	20.14	3	18	0.53	0.41	ab	75.1±2.5

Table B1: (Continued).

ID	R.A. (deg)	Dec. (deg)	$\langle g \rangle$	$\langle r \rangle$	N_g	N_r	Period (days)	Amplitude	Type	d_H (kpc)
HV115340-344347	178.41778	-34.72964	20.36	20.14	3	24	0.61	0.80	ab	78.3 ± 2.6
HV120459-363938	181.24417	-36.66050	20.23	20.20	3	23	0.54	0.97	ab	78.3 ± 2.6
HV155311-310412	238.29722	-31.06996	20.82	20.34	2	19	0.60	0.48	ab	80.0 ± 2.7
HV112952-360629	172.46658	-36.10819	20.60	20.41	3	23	0.58	0.70	ab	86.9 ± 2.9
HV153054-360838	232.72446	-36.14386	22.03	21.29	2	20	0.66	0.77	ab	92.8 ± 3.3
HV114310-363830	175.78972	-36.64159	20.74	20.50	3	24	0.64	0.41	ab	93.1 ± 3.1
HV115705-344426	179.26909	-34.74058	20.67	20.57	3	23	0.65	0.43	ab	97.8 ± 3.3
HV154344-322337	235.93500	-32.39366	21.10	20.49	2	16	0.79	0.49	ab	98.3 ± 3.3
HV155407-361645	238.52769	-36.27926	22.01	21.31	2	19	0.66	0.65	ab	103.5 ± 3.6
HV154834-320810	237.14125	-32.13607	21.57	20.94	2	19	0.60	0.38	ab	110.5 ± 3.7
HV114307-352948	175.78118	-35.49667	21.27	21.01	3	24	0.60	0.75	ab	115.2 ± 3.8
HV153403-321831	233.51328	-32.30856	21.45	21.31	2	18	0.81	0.66	ab	135.4 ± 4.9
HV152905-315335	232.27196	-31.89316	21.97	21.50	2	16	0.81	0.47	ab	144.4 ± 5.1
HV114420-352532	176.08172	-35.42548	23.24	22.57	3	22	0.43	0.57	d	234.4 ± 8.0

C1 Additional spectral regions and line list

Here we provide additional material to complement the content of Chapter 4. Figures C1 and C2 display the spectral regions surrounding Balmer and metallic lines used in this work (not H_α), for the RRLs observed in our second run. These figures include markers indicating the presence of metallic lines when clearly visible. Finally, Table C1 lists the absorption lines used in this work, together with their excitation potentials, $\log gf$, equivalent widths, and element abundance ratios.

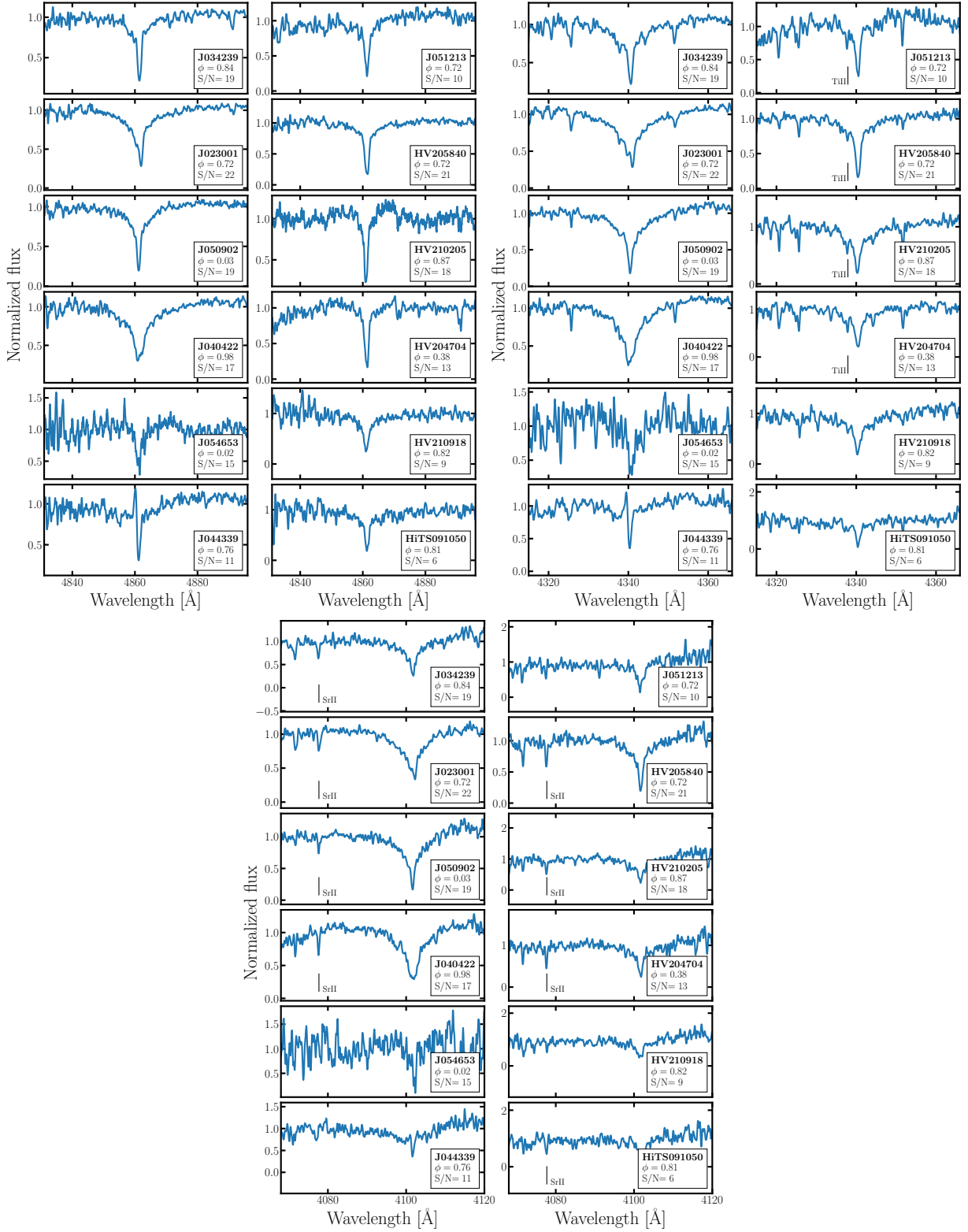


Figure C1: Spectral regions surrounding the Balmer lines for the RRLs observed in our second run (with higher resolution and S/N). A Gaussian convolution with $\sigma = 3$ was applied to smooth the spectra. Ti II and Sr II lines are marked when clearly visible in the smoothed spectra.

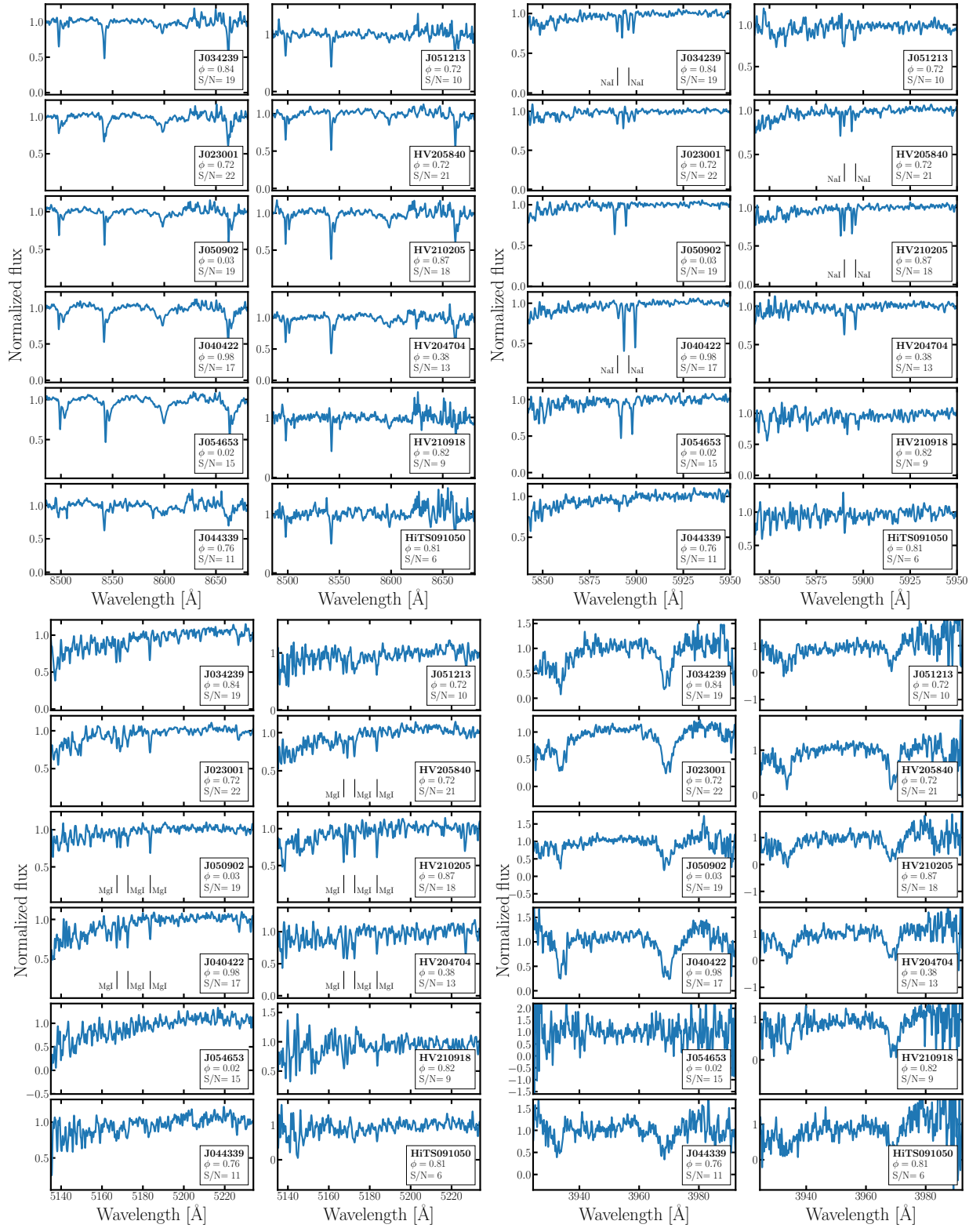


Figure C2: Same as Figure C1, but for the regions containing some of the metallic lines considered in this work. Metallic lines are marked when clearly visible in the smoothed spectra.

Table C1: (Continued)

EW	ab	rel_ab	rel_ab_e	nfte_corr	EW	ab	rel_ab	rel_ab_e	nfte_corr
HV210205	HV210205	HV210205	HV210205	HV210205	HV204704	HV204704	HV204704	HV204704	HV204704
-	-	-	-	-	-	-	-	-	-
-	-	0.30±0.15	0.15	-	-	-	0.05±0.10	0.10	-
-	-	0.25±0.15	0.15	-	-	-	0.40±0.15	0.15	-
-	-	-	-	-	-	-	0.30±0.15	0.15	-
-	-	0.25±0.15	0.15	-	-	-	0.40±0.10	0.10	-
-	-	-	-	-	-	-	0.25±0.10	0.10	-
-	-	0.45±0.15	0.15	-	-	-	-	-	-
-	-	0.50±0.20	0.20	-	-	-	0.40±0.05	0.05	-
-	-	0.50±0.25	0.25	-	-	-	-	-	-
-	-	0.40±0.25	0.25	-	-	-	0.25±0.10	0.10	-
-	-	0.35±0.10	0.10	-	-	-	-	-	-
-	-	0.65±0.10	0.10	-	-	-	0.10±0.05	0.05	-
-	-	0.45±0.10	0.10	-	-	-	-	-	-
-	-	0.30±0.10	0.10	-	-	-	0.20±0.05	0.05	-
-	-	-	-	-	-	-	-0.00±0.05	0.05	-
-	-	-	-	-	-	-	0.40±0.10	0.10	-
-	-	-	-	-	-	-	0.30±0.10	0.10	-
-	-	-	-	-	-	-	0.05±0.10	0.10	-
-	-	-	-	-	-	-	-	-	-
-	-	-	-	-	-	-	-	-	-
-	-	-	-	-	-	-	-	-	-
-	-	-	-	-	-	-	-	-	-
-	-	-	-	-	-	-	-	-	-
-	-	-	-	-	-	-	-	-	-
-	-	1.40±0.15	0.15	-	-	-	-	-	-
-	-	1.45±0.15	0.15	-	-	-	1.45±0.10	0.10	-
-	-	1.30±0.15	0.15	-	-	-	0.25±0.10	0.10	-
-	-	1.60±0.15	0.15	-	-	-	-	-	-

C2 Stellar parameters and chemodynamics of a subsample of our targets

In this section, we provide a brief description of the stellar parameters and chemodynamic properties of a subsample of our program stars. First, we compare the derived atmospheric parameters of our radial velocity standard HD 76483 with values from the literature. With this, we show that our results are compatible with previous studies. The selected subsample is used to depict RRLs at different distances, with different signal-to-noise ratios, and interesting cases. The orbital parameters described in this section assume a perturbed potential. The effects of the LMC in each of these stars is observed in the asymmetry of the computed orbits.

HD 76483

By following the methodology described in Section 4.3.3, for the radial velocity standard star HD 76483 we obtain $T_{\text{eff}} = 8,480 \pm 580$ (225) K, $[\text{Fe}/\text{H}] = -0.30 \pm 0.45$ dex (with a standard deviation of 0.15 dex), $\log g = 3.5 \pm 0.5$ (0.5), macroturbulence velocity = 43.77 ± 8.86 km s⁻¹, and $v_{\text{mic}} = 3.28$ km s⁻¹.

HD 76483 has been classified as a chemically peculiar A3IV star of effective temperature $8,204 \pm 57$ K (Zorec & Royer, 2012) and $v \sin i \sim 70$ km s⁻¹ (Díaz et al., 2011). Using the ΔS relations from Crestani et al. (2021a) on the EW measured for HD 76483 by Layden (1994), we obtain $[\text{Fe}/\text{H}] = -0.48$ dex with a dispersion of 0.40 dex (and -0.05 ± 0.12 dex when using all three Balmer lines). Thus, our results are roughly consistent with the literature (starting from the fact that for this star we adopted $v \sin i = 2$ km s⁻¹ as for the rest of our stars).

J034239

J034239 is a 0.61 d period RRL from the Catalina survey for which we derived an effective temperature of $\sim 6,745 \pm 650$ K (with a scatter of 66 K from using odd/even/ten selected orders), an iron abundance of -1.35 ± 0.42 (with a scatter of 0.06 dex), $v_{\text{mic}} \sim 2.7$ km s⁻¹, and $\log g \sim 3.1 \pm 1.6$ (0.6). We are able to measure O, Mg, Ca, Ti, Sr, and Ba, where most of these abundances rely on the measurement of one line (with the exception of Ti and Ba, which are based on five and two lines, respectively). Our analysis led to a weighted average $[\alpha/\text{Fe}]$ of 0.37 ± 0.31 (0.12), indicating that J034239 is enhanced in α elements. Additionally, we find $[\text{Sr}/\text{Fe}] = 0.45 \pm 0.15$ (based on one line only, at 4,077.71 Å, which is also an upper limit), and $[\text{Ba}/\text{Fe}] = 0.35 \pm 0.25$ (0.30) using two lines. Given that $[\text{Sr}/\text{Ba}] = 0.10$, we conclude that J034239 is a non- r -process-enhanced RRL (from the subclasses defined by Beers & Christlieb, 2005; Frebel, 2018; Hansen et al., 2019).

J034239 is located at 33 ± 1 kpc from the Galactic center. This star orbits the MW with a period of $0.87^{+0.15}_{-0.10}$ Gyr and a well-constrained eccentricity $e = 0.60^{+0.04}_{-0.02}$. Our estimation leads to a pericentric and apocentric distances (r_{peri} and r_{apo} , respectively) of $14.6^{+3.2}_{-2.7}$ and $59.1^{+8.0}_{-5.5}$ kpc for this star.

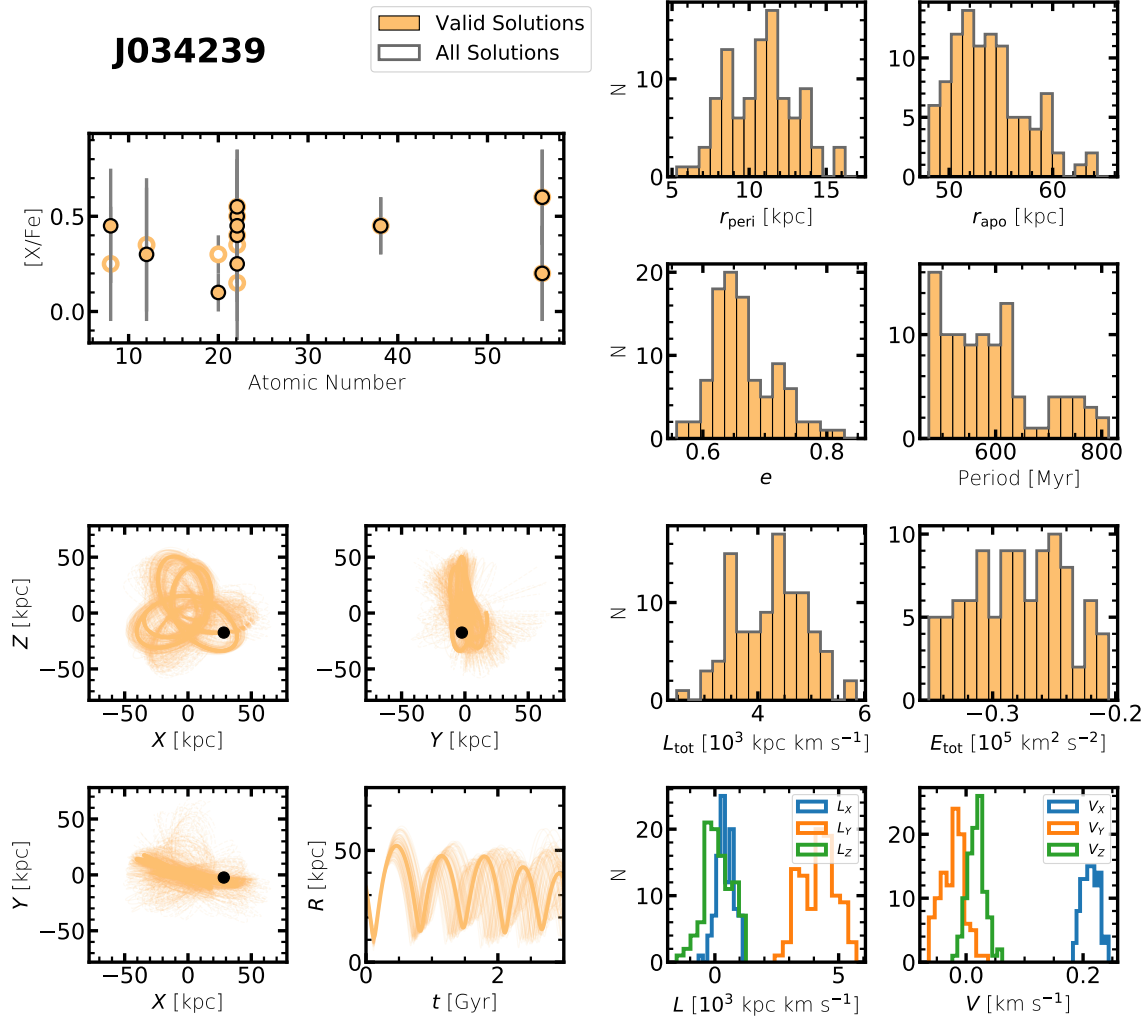


Figure C3: Relative abundances and orbits of the star J034239. In the *top left* panel, open circles represent the abundances after applying NLTE corrections. The orbits shown are integrated for 3 Gyr forward and backward using GALPY adopting a perturbed MW potential. The histograms display the distribution of the computed values from 100 orbit realisations.

J023001

J023001 is an ab-type RRL from the Catalina survey with a period of 0.65 d, observed at the phase ~ 0.70 . For J023001, we find $T_{\text{eff}} = 7,130 \pm 585$ (13) K, $[\text{Fe}/\text{H}] = -1.23 \pm 0.30$ (0.10), $v_{\text{mic}} = 2.7 \text{ km s}^{-1}$, and $\log g = 3.5 \pm 1.6$ (0.6). We observed a discrepancy between this $[\text{Fe}/\text{H}]$ and that observed in nine Fe lines in the blue side of the detector. Thus, we re-computed J023001's metallicity using the EW method, and obtained $[\text{Fe}/\text{H}] = -1.80 \pm 0.10$. We measured five Mg lines, which results in a weighted $[\text{Mg}/\text{Fe}] = 0.25 \pm 0.20$ (0.05). Using a total of 12 lines, we find evidence of J023001 having α above Solar ($[\alpha/\text{Fe}] = 0.35 \pm 0.25$ (0.15)). Additionally, we are able to estimate a $[\text{Ba}/\text{Fe}]$ of 0.15 ± 0.25 , using the $4,554.03 \text{ \AA}$ Ba line (Figure 4.12). No Sr lines are reliably detected for J023001.

The orbital period of HV210205 is $1.09^{+0.27}_{-0.16}$ Gyr, and its eccentricity is $0.52^{+0.02}_{-0.02}$. Our analysis leads to a current Galactocentric distance $R = 36 \pm 1 \text{ kpc}$, $r_{\text{peri}} = 22.2^{+3.1}_{-3.2} \text{ kpc}$, and $r_{\text{apo}} = 68.0^{+15.3}_{-8.5} \text{ kpc}$.

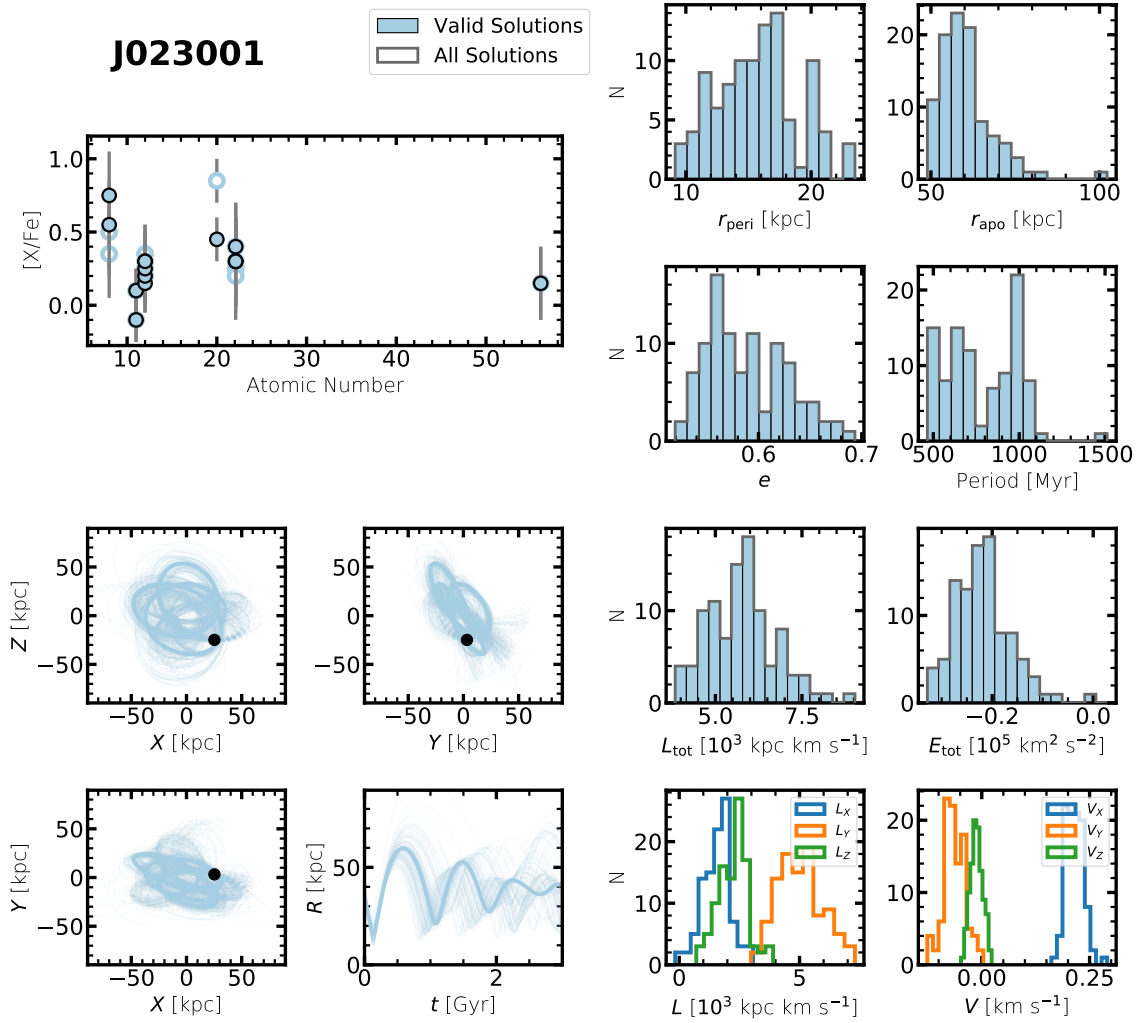


Figure C4: Same as Figure C3, but for the star J023001.

HV205840

HV205840 was observed close to minimum light (at phase 0.72), near the bump of the light curve that correlates with the shock waves produced by the collision of infalling material, before minimum radius (Christy, 1966; Fokin, 1992). For HV205840, we estimate $T_{\text{eff}} = 7,025 \pm 249$ (490) K, $[\text{Fe}/\text{H}] = -1.25 \pm 0.30$ (0.13), $v_{\text{mic}} = 2.29 \text{ km s}^{-1}$, and a surface gravity of 3.5 ± 0.3 (0.6). The high temperature of HV205840 is inconsistent with a phase of ~ 0.7 (see, e.g., Preston et al., 2019), and suggests an offset of $\sim +0.15$ on the predicted phase. Eight lines are used to compute an average $[\alpha/\text{Fe}]$ of -0.19 ± 0.26 (0.18) (Na, Mg, and Ti II), from which we conclude that HV205840 is α -poor. Two lines are used to compute the Sr content of this star, leading to $[\text{Sr}/\text{Fe}] = 1.15 \pm 0.25$ (0.05) as an upper limit.

The orbit of HV205840 ($R = 22 \pm 1 \text{ kpc}$) is highly affected by the choice of the underlying potential. The pericentric (apocentric) distance of its orbit is $21.68^{+0.8}_{-0.8} \text{ kpc}$ ($151.28^{+50.46}_{-60.50} \text{ kpc}$) for the perturbed potential, and $21.63^{+0.99}_{-0.96} \text{ kpc}$ ($135.39^{+62.11}_{-38.69} \text{ kpc}$) for the isolated model. The period of the perturbed and isolated potential are $2.67^{+1.19}_{-1.61} \text{ Gyr}$ and $2.01^{+1.08}_{-0.61} \text{ Gyr}$, respectively, in both cases with an eccentricity > 0.70 .

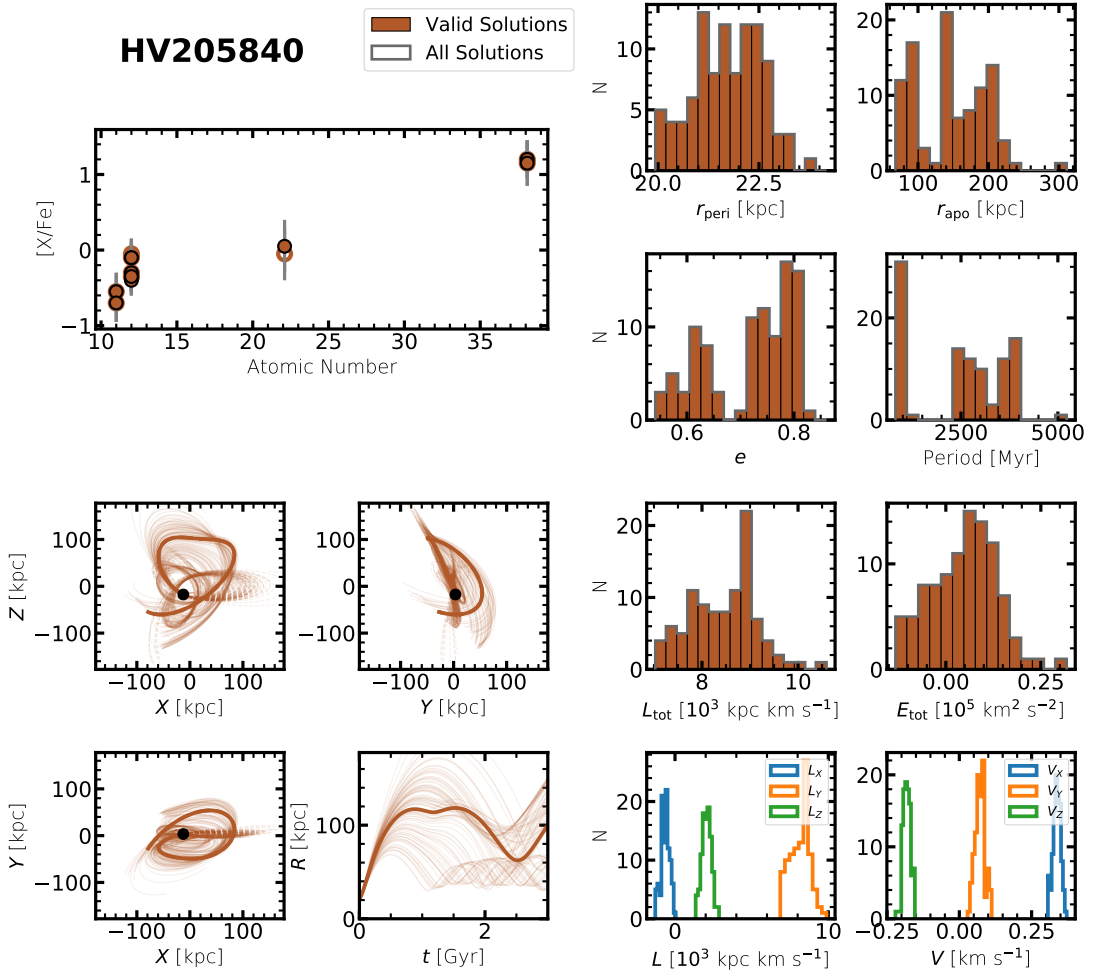


Figure C5: Same as Figure C3, but for the star HV205840.

J054653

J054653 is an RRL with a period of ~ 12 hr (0.61 d) and mean magnitude 18.6 in V . We include this RRL in our secondary sample given that it was observed near maximum light.

J054653 is located at 21.63 ± 0.82 kpc from the centre of the Galaxy, with an orbital period of $0.43^{+0.12}_{-0.07}$ Gyr. Its orbit is greatly affected by the consideration of the LMC infall, with an eccentricity of $0.58^{+0.22}$ and $0.29^{+0.03}_{-0.03}$ for the perturbed and isolated potentials, respectively. Moreover, the pericentric and apocentric distance of J054653 are $8.34^{+7.45}_{-3.19}$ and $38.43^{+10.21}_{-8.27}$ kpc for the perturbed model, and $16.91^{+1.38}_{-2.33}$ and $30.10^{+3.76}_{-2.84}$ kpc for the isolated potential.

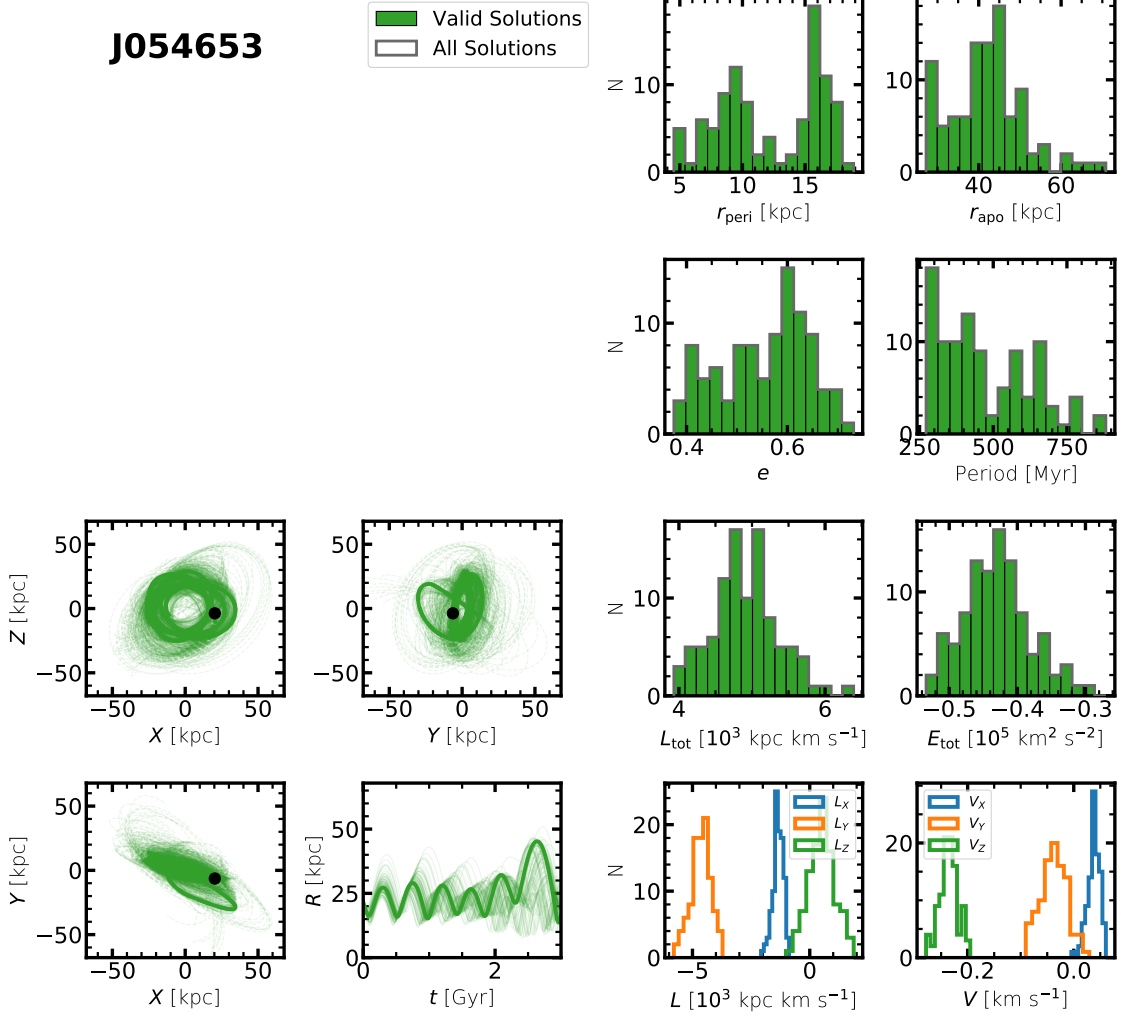


Figure C6: Same as Figure C3, but for the star J054653 and without including chemical abundances.

Frequently used acronyms

Λ-CDM	- Λ Cold Dark Matter
2MASS	- Two Micron All-Sky Survey
4MOST	- 4-metre Multi-Object Spectroscopic Telescope
AAVSO	- American Association of Variable Star Observers
AGB	- Asymptotic Giant Branch
AGN	- Active Galactic Nucleus
ANN	- AURIGA Neural Network
APASS	- AAVSO Photometric All-Sky Survey
APOGEE	- Apache Point Observatory Galactic Evolution Experiment
ASAS-SN	- All Sky Automated Survey for Supernovae
ATLAS	- Asteroid Terrestrial-impact Last Alert System survey
CCD	- Charge-Coupled Device
CEMP	- Carbon-Enhanced Metal-Poor (stars)
CMD	- Colour-Magnitude Diagram
CRTS	- Catalina Real-Time Transient Survey
CTIO	- Cerro Tololo Inter-American Observatory
dSph	- dwarf Spheroidal galaxy
DECam	- Dark Energy Camera
DELVE	- DECam Local Volume Exploration survey
DES	- Dark Energy Survey
ESO	- European Southern Observatory
EW	- Equivalent Width
GALAH	- GALactic Archaeology with HERMES
GES	- <i>Gaia</i> -ESO survey
GLS	- Generalized Lomb-Scargle
GSE	- Gaia-Sausage-Enceladus
HASP	- High Amplitude Short Period (star)
HB	- Horizontal Branch
HIPPARCOS	- High Precision Parallax Collecting Satellite
HiTS	- High cadence Transient Survey
HOWVAST	- Halo Outskirts With VArIable STars
HR	- Hertzsprung-Russel (diagram)

IMF	- Initial Mass Function
IS	- Instability Strip
ISM	- Interstellar Medium
LAMOST	- Large Sky Area Multi-Object Fibre Spectroscopic Telescope
LMC	- Large Magellanic Cloud
LS	- Lomb-Scargle
LSR	- Local Standard of Rest
LSST	- Rubin Observatory Legacy Survey of Space and Time
LTE	- Local Thermodynamic Equilibrium
MCMC	- Markov chain Monte Carlo
MESA	- Modules for Experiments in Stellar Astrophysics
MIKE	- Magellan Inamori Kyocera Echelle (spectrograph)
MIST	- MESA Isochrones and Stellar Tracks
MJD	- Modified Julian Date
MS	- Main Sequence
MSTO	- Main-Sequence Turn-Off
MW	- Milky Way
MWSC	- Milky Way Star Clusters Catalog
NLTE	- Non-Local Thermodynamic Equilibrium
NOIRLab	- National Optical-Infrared Astronomy Research Laboratory
NSC	- NOIRLab Source Catalog
OGLE	- Optical Gravitational Lensing Experiment
OoI	- Oosterhoff type I
OoII	- Oosterhoff type II
Oo-int	- Oosterhoff-intermediate
PA	- Period-Age (relation)
PAC	- Period-Age-Colour (relation)
PARSEC	- PAdova and TRieste Stellar Evolution Code
PFS	- Subaru Prime Focus Spectrograph
PL	- Period-Luminosity (relation)
PLZ	- Period-Luminosity-metallicity (relation)
PS-1	- Panoramic Survey Telescope And Rapid Response System (Pan-STARRS-1)
PSF	- Point Spread Function
PW	- Period-Wesenheit (relation)
PWZ	- Period-Wesenheit-metallicity (relation)
QMI	- Quadratic Mutual Information
QUEST	- Quasar Equatorial Survey Team (survey)
<i>r</i>-process	- rapid neutron-capture process
RAVE	- Radial Velocity Experiment
RGB	- Red Giant Branch
RRab	- ab-type RR Lyrae (star)
RRc	- c-type RR Lyrae (star)
RRd	- d-type RR Lyrae (star)
RRL	- RR Lyrae (star)
RUWE	- Re-normalized Unit Weight Error
<i>s</i>-process	- slow neutron-capture process

S/N	- Signal-to-Noise ratio
S5	- Southern Stellar Stream Spectroscopic Survey
SDSS	- Sloan Digital Sky Survey
Sgr	- Sagittarius (galaxy)
SMC	- Small Magellanic Cloud
SN	- Supernova
UFD	- Ultra-Faint Dwarf galaxy
VALD	- Vienna Atomic Line Database
VVV	- Vista Variables in the Vía Láctea Survey
WEAVE	- William Herschel Telescope Enhanced Area Velocity Explorer
WISE	- Wide-field Infrared Survey Explorer
ZAMS	- Zero-Age Main Sequence
ZTF	- Zwicky Transient Facility

List of publications

The following articles have been submitted and published in refereed journals over the course of my graduate studies, or are in preparation for publication within this year.

First author publications included in this thesis

Medina, G. E., Muñoz, R. R., Vivas, A. K., et. al., 2022,
“Discovery of remote RR Lyrae stars in the Halo Outskirts With Variable Stars (HOW-VAST) survey”,
in preparation.

[Chapter 3 of this PhD Thesis]

Medina, G. E., Hansen, C. J., Muñoz, R. R., et. al., 2022,
“RR Lyrae stars as probes of the outer Galactic halo: Chemical and kinematic analysis of a pilot sample”,
Submitted to the Monthly Notices of the Royal Astronomical Society journal.

[Chapter 4 of this PhD Thesis]

Medina, G. E., Lemasle, B., Grebel, E. K., 2021,
“A revisited study of Cepheids in open clusters in the *Gaia* era”,
[Monthly Notices of the Royal Astronomical Society](#), 505, 1342.

[Chapter 2 of this PhD Thesis]

First author publications not included in this thesis

Medina, G. E., Muñoz, R. R., Vivas, A. K., et. al., 2018,
“Discovery of Distant RR Lyrae Stars in the Milky Way Using DECam”,
[The Astrophysical Journal](#), 855, 43.

Medina, G. E., Muñoz, R. R., Vivas, A. K., et. al., 2017,
“Serendipitous Discovery of RR Lyrae Stars in the Leo V Ultra-faint Galaxy”,
[The Astrophysical Journal Letters](#), 845, L10.

Contributions to publications not included in this thesis

Martínez-Palomera, J., Förster, F., Protopapas, P., ..., **Medina, G. E.**, et al., 2018, “The High Cadence Transit Survey (HiTS): Compilation and Characterization of Light-curve Catalogs”, [The Astronomical Journal](#), 156, 5.

Förster, F., Moriya, T. J., Maureira, J. C., ..., **Medina, G. E.**, et al., 2018, “The delay of shock breakout due to circumstellar material evident in most type II supernovae”, [Nature Astronomy](#), 2, 808.

Abbott B. P., Abbott R., Abbott T. D., ..., **Medina, G. E.**, et al., 2017, “A gravitational-wave standard siren measurement of the Hubble constant”, [Nature](#), 551, 85.

Nidever D. L., Olsen K., Walker A. R., ..., **Medina, G. E.**, et al., 2017, “SMASH: Survey of the MAgellanic Stellar History”, [The Astrophysical Journal](#), 154, 199.

Cowperthwaite P. S., Berger E., Villar V. A., ..., **Medina, G. E.**, et al., 2017, “The Electromagnetic Counterpart of the Binary Neutron Star Merger LIGO/Virgo GW170817. II. UV, Optical, and Near-infrared Light Curves and Comparison to Kilonova Models”, [The Astrophysical Journal Letters](#), 848, L17.

Soares-Santos M., Holz D. E., Annis J., ..., **Medina, G. E.**, et al., 2017, “The Electromagnetic Counterpart of the Binary Neutron Star Merger LIGO/Virgo GW170817. I. Discovery of the Optical Counterpart Using the Dark Energy Camera”, [The Astrophysical Journal Letters](#), 848, L16.

Abbott B. P., Abbott R., Abbott T. D., ..., **Medina, G. E.**, et al., 2017, “Multi-messenger Observations of a Binary Neutron Star Merger”, [The Astrophysical Journal Letters](#), 848, L12.

Förster F., Maureira J. C., San Martín J., ..., **Medina, G. E.**, et al., 2016, “The High Cadence Transient Survey (HiTS). I. Survey Design and Supernova Shock Breakout Constraints”, [The Astrophysical Journal](#), 832, 155.

Bibliography

- Aarseth S. J., 1971, *Ap&SS*, 14, 118 - [24](#)
- Abadi M. G., Navarro J. F., Steinmetz M., Eke V. R., 2003a, *ApJ*, 591, 499 - [16](#)
- Abadi M. G., Navarro J. F., Steinmetz M., Eke V. R., 2003b, *ApJ*, 597, 21 - [16](#)
- Abbas, M. A., Grebel, E. K., Martin, N. F., et al. 2014, *MNRAS*, 441, 1230 - [43](#)
- Abbas M., Grebel E. K., Simunovic M., 2021, *ApJ*, 915, 49 - [48](#), [94](#)
- Abdurro'uf, Accetta K., Aerts C., Silva Aguirre V., Ahumada R., Ajgaonkar N., Filiz Ak N., et al., 2022, *ApJS*, 259, 35 - [23](#)
- Abolfathi B., Aguado D. S., Aguilar G., Allende Prieto C., Almeida A., Ananna T. T., Anders F., et al., 2018, *ApJS*, 235, 42 - [66](#)
- Adamo A., Zeidler P., Kruijssen J. M. D., Chevance M., Gieles M., Calzetti D., Charbonnel C., et al., 2020, *SSRv*, 216, 69 - [91](#)
- Adelberger E. G., García A., Robertson R. G. H., Snover K. A., Balantekin A. B., Heeger K., Ramsey-Musolf M. J., et al., 2011, *RvMP*, 83, 195 - [11](#)
- Adibekyan V. Z., Figueira P., Santos N. C., Hakobyan A. A., Sousa S. G., Pace G., Delgado Mena E., et al., 2013, *A&A*, 554, A44 - [13](#)
- Agertz O., Renaud F., Feltzing S., Read J. I., Ryde N., Andersson E. P., Rey M. P., et al., 2021, *MNRAS*, 503, 5826 - [16](#)
- Aguado D. S., Belokurov V., Myeong G. C., Evans N. W., Kobayashi C., Sbordone L., Chanamé J., et al., 2021, *ApJL*, 908, L8 - [151](#), [152](#), [154](#), [159](#)
- Ahumada R., Prieto C. A., Almeida A., Anders F., Anderson S. F., Andrews B. H., Anguiano B., et al., 2020, *ApJS*, 249, 3 - [12](#), [151](#)
- Akritas M. G., 1997, *Statistical Challenges in Modern Astronomy II*, Proceedings of the conference held 2-5 June, 1996 at Pennsylvania State University. Edited by G.J. Babu and E.D. Feigelson. Berlin: Springer-Verlag, 1997., p.105 - [33](#)
- Albert A., Anderson B., Bechtol K., Drlica-Wagner A., Meyer M., Sánchez-Conde M., Strigari L., et al., 2017, *ApJ*, 834, 110 - [27](#)
- Alves J., Zucker C., Goodman A. A., Speagle J. S., Meingast S., Robitaille T., Finkbeiner D. P., et al., 2020, *Natur*, 578, 237 - [2](#)
- Amard L., Palacios A., Charbonnel C., Gallet F., Georgy C., Lagarde N., Siess L., 2019, *A&A*, 631, A77 - [23](#)
- Amarsi A. M., Nissen P. E., Skúladóttir Á., 2019, *A&A*, 630, A104 - [155](#)
- An D., Terndrup D. M., Pinsonneault M. H., 2007, *ApJ*, 671, 1640 - [41](#), [54](#), [69](#), [180](#)
- Anders F., Chiappini C., Minchev I., Miglio A., Montalbán J., Mosser B., Rodrigues T. S., et al., 2017, *A&A*, 600, A70 - [24](#)
- Anders F., Cantat-Gaudin T., Quadrino-Lodoso I., Gieles M., Jordi C., Castro-Ginard A., Balaguer-Núñez L., 2021, *A&A*, 645, L2 - [21](#), [91](#)
- Anderson R. I., Riess A. G., 2018, *ApJ*, 861, 36 - [90](#), [171](#), [172](#)
- Anderson R. I., Ekström S., Georgy C., Meynet G., Mowlavi N., Eyer L., 2014, *A&A*, 564, A100 - [88](#)

Anderson R. I., Saio H., Ekström S., Georgy C., Meynet G., 2016, *A&A*, 591, A8 - [36](#), [37](#), [40](#), [41](#), [64](#), [78](#), [88](#), [89](#), [91](#)

Anderson R. I., Eyer L., Mowlavi N., 2013, *MNRAS*, 434, 2238 - [42](#), [54](#), [57](#), [90](#), [180](#)

Anguiano B., Majewski S. R., Hayes C. R., Allende Prieto C., Cheng X., Bidin C. M., Beaton R. L., et al., 2020, *AJ*, 160, 43 - [12](#), [15](#)

Anthony-Twarog B. J., Deliyannis C. P., Twarog B. A., Croxall K. V., Cummings J. D., 2009, *AJ*, 138, 1171 - [23](#)

Aoki W., Suda T., Boyd R. N., Kajino T., Famiano M. A., 2013, *ApJL*, 766, L13 - [153](#)

Arcones A., Janka H.-T., Scheck L., 2007, *A&A*, 467, 1227 - [14](#)

Arlandini C., Käppeler F., Wisshak K., Gallino R., Lugaro M., Busso M., Straniero O., 1999, *ApJ*, 525, 886 - [14](#)

Asplund M., Grevesse N., Sauval A. J., Scott P., 2009, *ARA&A*, 47, 481 - [8](#), [145](#)

Atkinson R. d'Escourt ., 1931, *ApJ*, 73, 250 - [10](#)

Avelino A., Friedman A. S., Mandel K. S., Jones D. O., Challis P. J., Kirshner R. P., 2019, *ApJ*, 887, 106 - [41](#)

Baade W., 1944, *ApJ*, 100, 137 - [4](#), [10](#)

Baade W., 1946, *PASP*, 58, 249 - [2](#)

Baade W., 1948, *PASP*, 60, 230 - [42](#)

Bailey, S. I. 1902, *Annals of Harvard College Observatory*, 38 - [42](#), [43](#)

Bailey S. I., Pickering E. C., 1913, *Annals of Harvard College Observatory*, 78, 1 - [42](#)

Baker N., Kippenhahn R., 1962, *ZA*, 54, 114 - [32](#)

Baker M., Willman B., 2015, *AJ*, 150, 160 - [48](#), [94](#), [117](#), [176](#)

Balachandran S., 1995, *ApJ*, 446, 203 - [23](#)

Balick B., Brown R. L., 1974, *ApJ*, 194, 265 - [2](#)

Banerjee S., Kroupa P., 2012, *A&A*, 547, A23 - [11](#)

Barbuy B., Chiappini C., Gerhard O., 2018, *ARA&A*, 56, 223 - [3](#)

Barbá R. H., Minniti D., Geisler D., Alonso-García J., Hempel M., Monachesi A., Arias J. I., et al., 2019, *ApJL*, 870, L24 - [26](#)

Bastian N., Lardo C., 2018a, *ARA&A*, 56, 83 - [26](#)

Bastian N., Kamann S., Cabrera-Ziri I., Georgy C., Ekström S., Charbonnel C., de Juan Ovelar M., et al., 2018b, *MNRAS*, 480, 3739 - [23](#)

Battaglia G., Nipoti C., 2022, *NatAs*, 6, 659 - [21](#)

Baumgardt H., Kroupa P., 2007, *MNRAS*, 380, 1589 - [24](#)

Baumgardt H., Makino J., 2003, *MNRAS*, 340, 227 - [24](#)

Baumgardt H., Vasiliev E., 2021, *MNRAS*, 505, 5957 - [26](#), [157](#)

Baumgardt H., Hilker M., Sollima A., Bellini A., 2019, *MNRAS*, 482, 5138 - [26](#)

Baumgardt H., Dettbarn C., Wielen R., 2000, *A&AS*, 146, 251 - [54](#), [61](#)

Baumgardt H., Hut P., Heggie D. C., 2002, *MNRAS*, 336, 1069 - [24](#)

Baumgardt H., 2001, *MNRAS*, 325, 1323 - [20](#)

Beaton R. L., Bono G., Braga V. F., Dall'Ora M., Fiorentino G., Jang I. S., Martínez-Vázquez C. E., et al., 2018, *SSRv*, 214, 113 - [48](#)

Beccari G., Boffin H. M. J., Jerabkova T., 2020, *MNRAS*, 491, 2205 - [60](#)

Bechtol K., Drlica-Wagner A., Balbinot E., Pieres A., Simon J. D., Yanny B., Santiago B., et al., 2015, *ApJ*, 807, 50 - [27](#), [175](#)

Becker W., Fenkart R. B., 1970, IAUS, 38, 205 - [23](#)

Becklin E. E., Neugebauer G., 1968, ApJ, 151, 145 - [2](#)

Beers T. C., Christlieb N., 2005, ARA&A, 43, 531 - [154](#), [212](#)

Beers T. C., Carollo D., Ivezić Ž., An D., Chiba M., Norris J. E., Freeman K. C., et al., 2012, ApJ, 746, 34 - [17](#)

Beers T. C., 2010, IAUS, 265, 453 - [17](#)

Bellm E. C., Kulkarni S. R., Graham M. J., Dekany R., Smith R. M., Riddle R., Masci F. J., et al., 2019, PASP, 131, 018002 - [6](#), [173](#)

Belokurov V., Zucker D. B., Evans N. W., Wilkinson M. I., Irwin M. J., Hodgkin S., Bramich D. M., et al., 2006, ApJL, 647, L111 - [16](#), [17](#), [28](#)

Belokurov V., Evans N. W., Bell E. F., Irwin M. J., Hewett P. C., Koposov S., Rockosi C. M., et al., 2007, ApJL, 657, L89 - [118](#)

Belokurov V., Walker M. G., Evans N. W., Gilmore G., Irwin M. J., Mateo M., Mayer L., et al., 2009, MNRAS, 397, 1748 - [27](#)

Belokurov V., Walker M. G., Evans N. W., Gilmore G., Irwin M. J., Just D., Koposov S., et al., 2010, ApJL, 712, L103 - [27](#)

Belokurov V., Deason A. J., Koposov S. E., Catelan M., Erkal D., Drake A. J., Evans N. W., 2018a, MNRAS, 477, 1472 - [48](#), [94](#)

Belokurov V., Erkal D., Evans N. W., Koposov S. E., Deason A. J., 2018b, MNRAS, 478, 611 - [16](#), [28](#), [49](#), [94](#), [121](#), [151](#)

Belokurov V., Deason A. J., Erkal D., Koposov S. E., Carballo-Bello J. A., Smith M. C., Jethwa P., et al., 2019, MNRAS, 488, L47 - [17](#), [18](#)

Belokurov V., 2013, NewAR, 57, 100 - [4](#)

Benedict G. F., McArthur B. E., Feast M. W., Barnes T. G., Harrison T. E., Patterson R. J., Menzies J. W., et al., 2007, AJ, 133, 1810 - [41](#), [62](#)

Benkő J. M., Kolenberg K., Szabó R., Kurtz D. W., Bryson S., Bregman J., Still M., et al., 2010, MNRAS, 409, 1585 - [45](#)

Benkő J. M., Plachy E., Szabó R., Molnár L., Kolláth Z., 2014, ApJS, 213, 31 - [45](#)

Benkő J. M., Szabó R., Papp M., 2011, MNRAS, 417, 974 - [45](#)

Bensby T., Feltzing S., Lundström I., 2003, A&A, 410, 527 - [16](#), [155](#)

Bergemann M., Collet R., Amarsi A. M., Kovalev M., Ruchti G., Magic Z., 2017, ApJ, 847, 15 - [145](#)

Bergemann M., 2011, MNRAS, 413, 2184 - [145](#)

Bernard E. J., Ferguson A. M. N., Schlafly E. F., Martin N. F., Rix H.-W., Bell E. F., Finkbeiner D. P., et al., 2016, MNRAS, 463, 1759 - [162](#)

Bertelli G., Nasi E., Girardi L., Marigo P., 2009, A&A, 508, 355 - [37](#)

Bertelli G., Bressan A. G., Chiosi C., 1985, A&A, 150, 33 - [37](#)

Bertin, E., & Arnouts, S. 1996, A&AS, 117, 393 - [98](#)

Bertulani C. A., Fuqua J., Hussein M. S., 2013, ApJ, 767, 67 - [9](#)

Besla G., Kallivayalil N., Hernquist L., Robertson B., Cox T. J., van der Marel R. P., Alcock C., 2007, ApJ, 668, 949 - [94](#)

Bethe H. A., 1939, PhRv, 55, 434 - [8](#), [10](#)

Bhardwaj A., Rejkuba M., de Grijs R., Yang S.-C., Herczeg G. J., Marconi M., Singh H. P., et al., 2021, ApJ, 909, 200 - [46](#)

Bhattacharya S., Agarwal M., Rao K. K., Vaidya K., 2021, MNRAS, 505, 1607 - [24](#), [171](#)

Bica E., Bonatto C., 2011, A&A, 530, A32 - [24](#)

Bidaran B., Pasquali A., Lisker T., Coccato L., Falcón-Barroso J., van de Ven G., Peletier R., et al., 2020, *MNRAS*, 497, 1904 - [27](#)

Binks A. S., Jeffries R. D., Jackson R. J., Franciosini E., Sacco G. G., Bayo A., Magrini L., et al., 2021, *MNRAS*, 505, 1280 - [87](#)

Binney J., Gerhard O. E., Stark A. A., Bally J., Uchida K. I., 1991, *MNRAS*, 252, 210 - [3](#)

Binney J., Gerhard O., Spergel D., 1997, *MNRAS*, 288, 365 - [3](#)

Blanco-Cuaresma S., Soubiran C., Heiter U., Jofré P., 2014a, *A&A*, 569, A111 - [6](#), [138](#)

Blanco-Cuaresma S., Soubiran C., Jofré P., Heiter U., 2014b, *A&A*, 566, A98 - [138](#)

Blanco-Cuaresma S., 2019, *MNRAS*, 486, 2075 - [138](#)

Bland-Hawthorn J., Gerhard O., 2016, *ARA&A*, 54, 529 - [1](#), [2](#), [4](#), [13](#), [14](#), [17](#), [28](#)

Bland-Hawthorn J., Peebles P. J. E., 2006, *Sci*, 313, 311 - [2](#)

Bland-Hawthorn J., Sharma S., Tepper-Garcia T., Binney J., Freeman K. C., Hayden M. R., Kos J., et al., 2019, *MNRAS*, 486, 1167 - [16](#)

Blažko S., 1907, *AN*, 175, 325 - [45](#), [123](#)

Blitz L., Spergel D. N., 1991, *ApJ*, 379, 631 - [3](#)

Blumenthal G. R., Faber S. M., Primack J. R., Rees M. J., 1984, *Nature*, 311, 517 - [2](#), [28](#), [93](#)

Bochanski J. J., Willman B., Caldwell N., Sanderson R., West A. A., Strader J., Brown W., 2014, *ApJL*, 790, L5 - [94](#)

Boesgaard A. M., Steigman G., 1985, *ARA&A*, 23, 319 - [9](#)

Boltzmann, L., 1884, Ableitung des Stefan'schen Gesetzes, betreffend die Abhängigkeit der Wärmestrahlung von der Temperatur aus der electromagnetischen Lichttheorie. In: *Annalen der Physik und Chemie*. Bd. 22, 1884, S. 291-294 - [38](#)

Bonaca A., Conroy C., Wetzel A., Hopkins P. F., Kereš D., 2017, *ApJ*, 845, 101 - [155](#)

Bonaca A., Hogg D. W., Price-Whelan A. M., Conroy C., 2019, *ApJ*, 880, 38 - [4](#)

Bonaca A., Naidu R. P., Conroy C., Caldwell N., Cargile P. A., Han J. J., Johnson B. D., et al., 2021, *ApJL*, 909, L26 - [28](#), [29](#), [30](#)

Bono G., Caputo F., Cassisi S., Marconi M., Piersanti L., Tornambè A., 2000, *ApJ*, 543, 955 - [54](#)

Bono G., Marconi M., Cassisi S., Caputo F., Gieren W., Pietrzynski G., 2005, *ApJ*, 621, 966 - [40](#), [41](#), [64](#), [69](#), [88](#), [89](#)

Bono G., Caputo F., Marconi M., Musella I., 2010, *ApJ*, 715, 277 - [39](#)

Bono G., Braga V. F., Pietrinferni A., Magurno D., Dall'Ora M., Fiorentino G., Fukue K., et al., 2016, *MmSAI*, 87, 358 - [39](#), [43](#), [44](#)

Bono G., Castellani V., Marconi M., 2000, *ApJ*, 529, 293 - [37](#), [40](#)

Borsato N. W., Martell S. L., Simpson J. D., 2020, *MNRAS*, 492, 1370 - [16](#), [28](#)

Bosch J., AlSayyad Y., Armstrong R., Bellm E., Chiang H.-F., Eggl S., Findeisen K., et al., 2019, *Astronomical Data Analysis Software and Systems XXVII*, 523, 521 - [98](#)

Bossini D., Miglio A., Salaris M., Vrad M., Cassisi S., Mosser B., Montalbán J., et al., 2017, *MNRAS*, 469, 4718 - [23](#)

Bossini D., Vallenari A., Bragaglia A., Cantat-Gaudin T., Sordo R., Balaguer-Núñez L., Jordi C., et al., 2019, *A&A*, 623, A108 - [25](#), [54](#), [64](#), [78](#), [82](#), [83](#), [84](#)

Boubert D., Everall A., 2020, *MNRAS*, 497, 4246 - [85](#)

Bouvier A., Wadhwa M., 2010, *NatGe*, 3, 637 - [8](#)

Bovy J., Rix H.-W., Liu C., Hogg D. W., Beers T. C., Lee Y. S., 2012, *ApJ*, 753, 148 - [2](#), [14](#), [17](#)

Bovy J., Bahmanyar A., Fritz T. K., Kallivayalil N., 2016, *ApJ*, 833, 31 - [176](#)

Bovy J., Erkal D., Sanders J. L., 2017, *MNRAS*, 466, 628 - [4](#), [30](#)

Bovy J., 2015, *ApJS*, 216, 29 - [145](#)

Boylan-Kolchin M., Bullock J. S., Kaplinghat M., 2011, *MNRAS*, 415, L40 - [28](#)

Boylan-Kolchin M., Bullock J. S., Kaplinghat M., 2012, *MNRAS*, 422, 1203 - [28](#)

Braga V. F., Dall’Ora M., Bono G., Stetson P. B., Ferraro I., Iannicola G., Marengo M., et al., 2015, *ApJ*, 799, 165 - [46](#)

Braga V. F., Stetson P. B., Bono G., Dall’Ora M., Ferraro I., Fiorentino G., Freyhammer L. M., et al., 2016, *AJ*, 152, 170 - [46](#)

Branch D., Tammann G. A., 1992, *ARA&A*, 30, 359 - [41](#)

Brauer K., Andales H. D., Ji A. P., Frebel A., Mardini M. K., Gomez F. A., O’Shea B. W., 2022, *arXiv*, [arXiv:2206.07057](#) - [30](#), [176](#)

Breitfelder J., Mérand A., Kervella P., Gallenne A., Szabados L., Anderson R. I., Le Bouquin J.-B., 2016, *A&A*, 587, A117 - [42](#)

Bressan A., Marigo P., Girardi L., Salasnich B., Dal Cero C., Rubele S., Nanni A., 2012, *MNRAS*, 427, 127 - [25](#)

Breuval L., Kervella P., Anderson R. I., Riess A. G., Arenou F., Trahin B., Mérand A., et al., 2020, *A&A*, 643, A115 - [42](#), [54](#), [69](#), [171](#)

Breuval L., Kervella P., Wielgórski P., Gieren W., Graczyk D., Trahin B., Pietrzyński G., et al., 2021, *ApJ*, 913, 38 - [38](#), [40](#), [42](#)

Breuval L., Riess A. G., Kervella P., 2022, *arXiv*, [arXiv:2205.06280](#) - [40](#), [41](#)

Bromm V., Larson R. B., 2004, *ARA&A*, 42, 79 - [10](#)

Buchler J. R., Kolláth Z., 2011, *ApJ*, 731, 24 - [45](#), [123](#)

Buck T., Rybizki J., Buder S., Obreja A., Macciò A. V., Pfrommer C., Steinmetz M., et al., 2021, *MNRAS*, 508, 3365 - [4](#)

Buckner A. S. M., Froebrich D., 2014, *MNRAS*, 444, 290 - [25](#)

Buck T., 2020, *MNRAS*, 491, 5435 - [16](#)

Buder S., Asplund M., Duong L., Kos J., Lind K., Ness M. K., Sharma S., et al., 2018, *MNRAS*, 478, 4513 - [66](#)

Buder S., Lind K., Ness M. K., Asplund M., Duong L., Lin J., Kos J., et al., 2019, *A&A*, 624, A19 - [155](#)

Buder S., Sharma S., Kos J., Amarsi A. M., Nordlander T., Lind K., Martell S. L., et al., 2021, *MNRAS*, 506, 150 - [23](#)

Buder S., Lind K., Ness M. K., Feuillet D. K., Horta D., Monty S., Buck T., et al., 2022, *MNRAS*, 510, 2407 - [151](#)

Bullock J. S., Boylan-Kolchin M., 2017, *ARA&A*, 55, 343 - [28](#)

Bullock, J. S., & Johnston, K. V. 2005, *ApJ*, 635, 931 - [2](#), [18](#), [19](#), [27](#), [93](#), [94](#), [112](#), [123](#)

Burbidge E. M., Burbidge G. R., Fowler W. A., Hoyle F., 1957, *RvMP*, 29, 547 - [8](#), [13](#), [14](#)

Böker T., 2010, *IAUS*, 266, 58 - [20](#)

Cameron A. G. W., 1957, *PASP*, 69, 201 - [13](#)

Cameron A. G. W., 2003, *ApJ*, 587, 327 - [14](#)

Cantat-Gaudin T., Anders F., 2020, *A&A*, 633, A99 - [90](#)

Cantat-Gaudin T., Brandt T. D., 2021, *arXiv*, [arXiv:2103.07432](#) - [66](#)

Cantat-Gaudin T., Donati P., Vallenari A., Sordo R., Bragaglia A., Magrini L., 2016, *A&A*, 588, A120 - [24](#)

Cantat-Gaudin T., Vallenari A., Sordo R., Pensabene F., Krone-Martins A., Moitinho A., Jordi C., et al., 2018a, *A&A*, 615, A49 - [24](#)

Cantat-Gaudin T., Jordi C., Vallenari A., Bragaglia A., Balaguer-Núñez L., Soubiran C., Bossini D., et al., 2018b, *A&A*, 618, A93 - [25](#), [55](#), [90](#)

- Cantat-Gaudin T., Krone-Martins A., Sedaghat N., Farahi A., de Souza R. S., Skolidis R., Malz A. I., et al., 2019, *A&A*, 624, A126 - [24](#), [55](#)
- Cantat-Gaudin T., Anders F., Castro-Ginard A., Jordi C., Romero-Gómez M., Soubiran C., Casamiquela L., et al., 2020, *A&A*, 640, A1 - [25](#), [55](#), [90](#)
- Caputo F., Marconi M., Musella I., Santolamazza P., 2000, *A&A*, 359, 1059 - [39](#), [41](#), [46](#)
- Caputo F., Bono G., Fiorentino G., Marconi M., Musella I., 2005, *ApJ*, 629, 1021 - [37](#)
- Caputo F., Santolamazza P., Marconi M., 1998, *MNRAS*, 293, 364 - [45](#)
- Capuzzo-Dolcetta R., 1993, *ApJ*, 415, 616 - [20](#)
- Cardelli J. A., Clayton G. C., Mathis J. S., 1989, *ApJ*, 345, 245 [79](#), [136](#)
- Carini R., Brocato E., Raimondo G., Marconi M., 2017, *MNRAS*, 469, 1532 - [39](#)
- Carlberg R. G., 2012, *ApJ*, 748, 20 - [30](#)
- Carlberg R. G., 2020, *ApJ*, 893, 116 - [26](#)
- Carlin J. L., Sheffield A. A., Cunha K., Smith V. V., 2018, *ApJL*, 859, L10 - [158](#)
- Carney B. W., Storm J., Jones R. V., 1992, *ApJ*, 386, 663 - [46](#)
- Carollo D., Beers T. C., Chiba M., Norris J. E., Freeman K. C., Lee Y. S., Ivezić Ž., et al., 2010, *ApJ*, 712, 692 - [17](#)
- Carollo D., Beers T. C., Bovy J., Sivarani T., Norris J. E., Freeman K. C., Aoki W., et al., 2012, *ApJ*, 744, 195 - [17](#)
- Carraro G., Baume G., Seleznev A. F., Costa E., 2017, *Ap&SS*, 362, 128 - [25](#)
- Carraro G., Subramaniam A., Janes K. A., 2006, *MNRAS*, 371, 1301 - [25](#), [26](#)
- Carraro G., Zinn R., Moni Bidin C., 2007, *A&A*, 466, 181 - [157](#), [158](#)
- Carraro G., 2005, *ApJL*, 621, L61 - [157](#), [158](#)
- Carrera R., Bragaglia A., Cantat-Gaudin T., Vallenari A., Balaguer-Núñez L., Bossini D., Casamiquela L., et al., 2019, *A&A*, 623, A80 - [66](#), [78](#)
- Carrera R., Casamiquela L., Carbajo-Hijarrubia J., Balaguer-Núñez L., Jordi C., Romero-Gómez M., Blanco-Cuaresma S., et al., 2022, *A&A*, 658, A14 - [23](#)
- Carroll B., Ostlie D., 2007, *An Introduction to Modern Astrophysics* (Pearson Addison-Wesley) - [1](#), [14](#)
- Casagrande L., Ramírez I., Meléndez J., Bessell M., Asplund M., 2010, *A&A*, 512, A54 - [136](#), [137](#)
- Casagrande L., Schönrich R., Asplund M., Cassisi S., Ramírez I., Meléndez J., Bensby T., et al., 2011, *A&A*, 530, A138 - [14](#)
- Casali G., Magrini L., Tognelli E., Jackson R., Jeffries R. D., Lagarde N., Tautvaišienė G., et al., 2019, *A&A*, 629, A62 - [23](#)
- Cassisi S., Castellani M., Caputo F., Castellani V., 2004, *A&A*, 426, 641 - [46](#)
- Castelli F., Kurucz R. L., 2003, *IAUS*, 210, A20 - [138](#)
- Castro-Ginard A., Jordi C., Luri X., Julbe F., Morvan M., Balaguer-Núñez L., Cantat-Gaudin T., 2018, *A&A*, 618, A59 - [55](#), [59](#), [69](#)
- Castro-Ginard A., Jordi C., Luri X., Cantat-Gaudin T., Balaguer-Núñez L., 2019, *A&A*, 627, A35 - [24](#), [55](#), [59](#), [69](#)
- Castro-Ginard A., Jordi C., Luri X., Álvarez Cid-Fuentes J., Casamiquela L., Anders F., Cantat-Gaudin T., et al., 2020, *A&A*, 635, A45 - [24](#), [56](#), [59](#), [67](#), [69](#), [75](#), [77](#), [78](#), [182](#), [186](#)
- Castro-Ginard A., McMillan P. J., Luri X., Jordi C., Romero-Gómez M., Cantat-Gaudin T., Casamiquela L., et al., 2021, *A&A*, 652, A162 - [23](#), [171](#)
- Castro-Ginard A., Jordi C., Luri X., Cantat-Gaudin T., Carrasco J. M., Casamiquela L., Anders F., et al., 2022, *A&A*, 661, A118 - [24](#), [91](#), [171](#)

Catelan, M., & Smith, H. A. 2015, Pulsating Stars (New York: Wiley, VCH) - [1](#), [32](#), [35](#), [37](#), [39](#), [43](#), [45](#), [46](#), [48](#), [117](#), [137](#)

Catelan M., Pritzl B. J., Smith H. A., 2004, ApJS, 154, 633 - [43](#), [45](#), [46](#), [48](#), [94](#)

Catelan M., 2007, AIPC, 930, 39 - [45](#)

Catelan M., 2009, Ap&SS, 320, 261 - [43](#), [46](#), [102](#), [156](#)

Cerny W., Pace A. B., Drlica-Wagner A., Kuposov S. E., Vivas A. K., Mau S., Riley A. H., et al., 2021, ApJL, 920, L44 - [176](#)

Chaboyer B., Demarque P., Kernan P. J., Krauss L. M., Sarajedini A., 1996, MNRAS, 283, 683 - [25](#)

Chabrier G., 2001, ApJ, 554, 1274 - [85](#), [86](#)

Chabrier G., 2003, PASP, 115, 763 - [11](#)

Chadid M., Sneden C., Preston G. W., 2017, ApJ, 835, 187 - [122](#), [134](#), [157](#)

Chambers K. C., Magnier E. A., Metcalfe N., Flewelling H. A., Huber M. E., Waters C. Z., Denneau L., et al., 2016, arXiv, arXiv:1612.05560 - [95](#), [96](#), [122](#)

Chandra V., Schlafman K. C., 2021, AJ, 161, 197 - [10](#)

Chandra V., Conroy C., Caldwell N., Bonaca A., Naidu R. P., Zaritsky D., Cargile P. A., et al., 2022, arXiv, arXiv:2207.13717 - [28](#)

Chandrasekhar S., 1931, ApJ, 74, 81 - [13](#)

Charbonnel C., Chantreau W., 2016, A&A, 586, A21 - [26](#)

Charbonnel C., Lagarde N., 2010, A&A, 522, A10 - [23](#)

Charbonnel C., Lagarde N., Jasiewicz G., North P. L., Shetrone M., Krugler Hollek J., Smith V. V., et al., 2020, A&A, 633, A34 - [23](#)

Chen B., Stoughton C., Smith J. A., Uomoto A., Pier J. R., Yanny B., Ivezić Ž., et al., 2001, ApJ, 553, 184 - [14](#)

Chen X., Wang S., Deng L., de Grijs R., Yang M., 2018, ApJS, 237, 28 - [57](#)

Chen X., Wang S., Deng L., de Grijs R., Liu C., Tian H., 2019, NatAs, 3, 320 - [42](#)

Chen X., Wang S., Deng L., de Grijs R., Yang M., Tian H., 2020, ApJS, 249, 18 - [95](#), [107](#), [122](#)

Chen X., de Grijs R., Deng L., 2015, MNRAS, 446, 1268 - [54](#), [67](#), [70](#), [71](#), [73](#), [180](#)

Chen X., de Grijs R., Deng L., 2017, MNRAS, 464, 1119 - [42](#)

Chiang H.-W., Enea Romano A., Nugier F., Chen P., 2019, JCAP, 2019, 016 -

Chiappini C., Matteucci F., Gratton R., 1997, ApJ, 477, 765 - [16](#)

Chiba M., Beers T. C., 2000, AJ, 119, 2843 - [14](#), [17](#)

Choi J., Dotter A., Conroy C., Cantiello M., Paxton B., Johnson B. D., 2016, ApJ, 823, 102 - [25](#), [78](#)

Chornock R., Berger E., Kasen D., Cowperthwaite P. S., Nicholl M., Villar V. A., Alexander K. D., et al., 2017, ApJL, 848, L19 - [14](#)

Chou M.-Y., Majewski S. R., Cunha K., Smith V. V., Patterson R. J., Martínez-Delgado D., Law D. R., et al., 2007, ApJ, 670, 346 - [158](#)

Christlieb N., Battistini C., Bonifacio P., Caffau E., Ludwig H.-G., Asplund M., Barklem P., et al., 2019, Msngr, 175, 26 - [175](#)

Christy R. F., 1966, ApJ, 144, 108 - [48](#), [215](#)

Claria J. J., Lapasset E., Bosio M. A., 1991, MNRAS, 249, 193 - [180](#)

Clark J. S., Negueruela I., Lohr M. E., Dorda R., González-Fernández C., Lewis F., Roche P., 2015, A&A, 584, L12 - [57](#), [70](#), [180](#)

Clarke D., 2002, A&A, 386, 763 - [35](#)

Clement C. M., Shelton I., 1997, *AJ*, 113, 1711 - [137](#)

Clementini G., Carretta E., Gratton R., Merighi R., Mould J. R., McCarthy J. K., 1995, *AJ*, 110, 2319 - [49](#), [95](#), [122](#)

Clementini G., Ripepi V., Molinaro R., Garofalo A., Muraveva T., Rimoldini L., Guy L. P., et al., 2019, *A&A*, 622, A60 - [57](#), [70](#), [95](#), [105](#), [107](#)

Clementini G., Ripepi V., Garofalo A., Molinaro R., Muraveva T., Leccia S., Rimoldini L., et al., 2022, *arXiv*, [arXiv:2206.06278](#) - [8](#), [95](#), [107](#)

Clementini G., 2014, *IAUS*, 301, 129 - [156](#)

Cohen, J. G., Sesar, B., Banholzer, S., 2016, in *IAU Symp. 317, The General Assembly of Galaxy Halos: Structure, Origin and Evolution*, ed. A. Bragaglia et al. (Cambridge: Cambridge Univ. Press), 91 - [49](#)

Cole S., Aragon-Salamanca A., Frenk C. S., Navarro J. F., Zepf S. E., 1994, *MNRAS*, 271, 781 - [2](#)

Colombo D., Duarte-Cabral A., Pettitt A. R., Urquhart J. S., Wyrowski F., Csengeri T., Neralwar K. R., et al., 2022, *A&A*, 658, A54 - [23](#)

Conroy C., Naidu R. P., Zaritsky D., Bonaca A., Cargile P., Johnson B. D., Caldwell N., 2019, *ApJ*, 887, 237 - [101](#), [145](#)

Conroy C., Naidu R. P., Garavito-Camargo N., Besla G., Zaritsky D., Bonaca A., Johnson B. D., 2021, *Natur*, 592, 534 - [18](#), [94](#), [118](#)

Conroy C., Weinberg D. H., Naidu R. P., Buck T., Johnson J. W., Cargile P., Bonaca A., et al., 2022, *arXiv*, [arXiv:2204.02989](#) - [4](#), [14](#), [16](#)

Cook B. T., Woods D. F., Ruprecht J. D., Varey J., Mastandrea R., de Soto K., Harburg J. F., et al., 2022, *MNRAS*, 513, 2509 - [18](#), [48](#)

Cooper A. P., D'Souza R., Kauffmann G., Wang J., Boylan-Kolchin M., Guo Q., Frenk C. S., et al., 2013, *MNRAS*, 434, 3348 - [18](#)

Coppola G., Dall'Orta M., Ripepi V., Marconi M., Musella I., Bono G., Piersimoni A. M., et al., 2011, *MNRAS*, 416, 1056 - [45](#)

Coulson I. M., Caldwell J. A. R., 1985, *MNRAS*, 216, 671 - [69](#), [180](#)

Cousens A., 1983, *MNRAS*, 203, 1171 - [45](#)

Cowan J. J., Sneden C., Lawler J. E., Aprahamian A., Wiescher M., Langanke K., Martínez-Pinedo G., et al., 2021, *RvMP*, 93, 015002 - [1](#), [14](#), [154](#)

Cox J. P., Whitney C., 1958, *ApJ*, 127, 561 - [32](#)

Cox J. P., Cox A. N., Olsen K. H., King D. S., Eilers D. D., 1966, *ApJ*, 144, 1038 - [32](#)

Cox A. N., 2013, *ASSP*, 31, 77 - [45](#)

Crestani J., Fabrizio M., Braga V. F., Sneden C., Preston G., Ferraro I., Iannicola G., et al., 2021a, *ApJ*, 908, 20 - [43](#), [122](#), [132](#), [134](#), [157](#), [212](#)

Crestani J., Braga V. F., Fabrizio M., Bono G., Sneden C., Preston G. W., Ferraro I., et al., 2021b, *arXiv*, [arXiv:2104.08113](#) - [122](#), [134](#), [157](#)

Crundall T. D., Ireland M. J., Krumholz M. R., Federrath C., Žerjal M., Hansen J. T., 2019, *MNRAS*, 489, 3625 - [173](#)

Cummings J. D., Deliyannis C. P., Maderak R. M., Steinhauer A., 2017, *AJ*, 153, 128 - [23](#)

Cunningham E. C., Garavito-Camargo N., Deason A. J., Johnston K. V., Erkal D., Laporte C. F. P., Besla G., et al., 2020, *ApJ*, 898, 4 - [148](#)

Cusano F., Moretti M. I., Clementini G., Ripepi V., Marconi M., Cioni M.-R. L., Rubele S., et al., 2021, *MNRAS*, 504, 1 - [46](#)

Cyburt R. H., 2004, *PhRvD*, 70, 023505 - [8](#)

Czekaj M. A., Robin A. C., Figueras F., Luri X., Haywood M., 2014, *A&A*, 564, A102 - [85](#)

Côté P., Marzke R. O., West M. J., 1998, *ApJ*, 501, 554 - [19](#)

Da Costa G. S., 2003, *ASPC*, 296, 545 - [21](#)

Da Rio N., Tan J. C., Covey K. R., Cottaar M., Foster J. B., Cullen N. C., Tobin J., et al., 2017, *ApJ*, 845, 105 - [23](#)

Dalton G., Trager S. C., Abrams D. C., Carter D., Bonifacio P., Aguerri J. A. L., MacIntosh M., et al., 2012, *Society of Photo-Optical Instrumentation Engineers (SPIE) Conference Series*, Vol. 8446, WEAVE: the next generation wide-field spectroscopy facility for the William Herschel Telescope, 84460P - [172](#)

DES Collaboration, Abbott T., Abdalla F. B., Aleksić J., Allam S., Amara A., Bacon D., et al., 2016, *MNRAS*, 460, 1270 - [95](#), [96](#), [122](#), [173](#)

DESI Collaboration, Aghamousa A., Aguilar J., Ahlen S., Alam S., Allen L. E., Allende Prieto C., et al., 2016, *arXiv*, arXiv:1611.00036 [175](#)

Das, P., Williams, A., & Binney, J. 2016, *MNRAS*, 463, 3169 - [116](#), [117](#)

David T. J., Hillenbrand L. A., 2015, *ApJ*, 804, 146 - [138](#)

de Boer T. J. L., Belokurov V., Beers T. C., Lee Y. S., 2014, *MNRAS*, 443, 658 - [13](#)

De Grijs R., 2010, *RSPTA*, 368, 693 - [21](#)

De Grijs, R., 2011, *An Introduction To Distance Measurement In Astronomy* (Wiley-Blackwell Academic Publishers) - [38](#)

de Jong R. S., Barden S., Bellido-Tirado O., Brynnel J., Chiappini C., Depagne É., Haynes R., et al., 2014, *SPIE*, 9147, 91470M - [172](#)

De Silva G. M., Freeman K. C., Bland-Hawthorn J., Martell S., de Boer E. W., Asplund M., Keller S., et al., 2015, *MNRAS*, 449, 2604 - [7](#)

De Somma G., Marconi M., Molinaro R., Cignoni M., Musella I., Ripepi V., 2020, *ApJS*, 247, 30 - [88](#)

De Somma G., Marconi M., Cassisi S., Ripepi V., Leccia S., Molinaro R., Musella I., 2020, *MNRAS*, 496, 5039 - [40](#), [88](#), [89](#)

Deason, A. J., Belokurov, V., & Evans, N. W. 2011, *MNRAS*, 416, 2903 - [112](#), [116](#)

Deason A. J., Belokurov V., Evans N. W., Koposov S. E., Cooke R. J., Peñarrubia J., Laporte C. F. P., et al., 2012, *MNRAS*, 425, 2840 - [17](#)

Deason A. J., Belokurov V., Koposov S. E., Gómez F. A., Grand R. J., Marinacci F., Pakmor R., 2017, *MNRAS*, 470, 1259 - [48](#), [94](#)

Deason A. J., Fattahi A., Frenk C. S., Grand R. J. J., Oman K. A., Garrison-Kimmel S., Simpson C. M., et al., 2020, *MNRAS*, 496, 3929 - [94](#), [173](#)

Deason A. J., Erkal D., Belokurov V., Fattahi A., Gómez F. A., Grand R. J. J., Pakmor R., et al., 2021, *MNRAS*, 501, 5964 - [49](#), [95](#), [174](#)

Deason A. J., Belokurov V., Sanders J. L., 2019, *MNRAS*, 490, 3426 - [16](#), [49](#), [174](#)

del Pino A., Fardal M. A., van der Marel R. P., Łokas E. L., Mateu C., Sohn S. T., 2021, *ApJ*, 908, 244 - [158](#)

DES Collaboration 2005, *arXiv:astro-ph/0510346* - [6](#), [96](#)

Di Criscienzo M., Marconi M., Musella I., Cignoni M., Ripepi V., 2013, *MNRAS*, 428, 212 - [39](#)

Di Criscienzo M., Marconi M., Caputo F., 2004, *ApJ*, 612, 1092 - [46](#)

Di Matteo P., Haywood M., Lehnert M. D., Katz D., Khoperskov S., Snaith O. N., Gómez A., et al., 2019, *A&A*, 632, A4 - [13](#)

Dias W. S., Lépine J. R. D., 2005, *ApJ*, 629, 825 - [23](#)

Dias W. S., Alessi B. S., Moitinho A., Lépine J. R. D., 2002, *A&A*, 389, 871 - [24](#), [55](#), [158](#)

Dias W. S., Monteiro H., Caetano T. C., Oliveira A. F., 2012, *A&A*, 539, A125 - [78](#)

Dias W. S., Monteiro H., Moitinho A., Lépine J. R. D., Carraro G., Paunzen E., Alessi B., et al., 2021, *MNRAS*, 504, 356 - [25](#)

Dierickx M. I. P., Loeb A., 2017, *ApJ*, 847, 42 - [110](#)

Dillamore A. M., Belokurov V., Font A. S., McCarthy I. G., 2022, *MNRAS*, 513, 1867 - [118](#)

Dinescu D. I., Girard T. M., van Altena W. F., 1999, *AJ*, 117, 1792 - [26](#)

Dinnbier F., Kroupa P., 2020, *A&A*, 640, A85 - [22](#), [24](#)

Dinnbier F., Kroupa P., Šubr L., Jeřábková T., 2022, *ApJ*, 925, 214 - [54](#), [87](#), [173](#)

Dinnbier F., Anderson R. I., Kroupa P., 2022, *A&A*, 659, A169 - [54](#), [91](#), [172](#)

Dinnbier F., Kroupa P., Anderson R. I., 2022, *A&A*, 660, A61 - [54](#), [91](#)

Donor J., Frinchaboy P. M., Cunha K., O'Connell J. E., Allende Prieto C., Almeida A., Anders F., et al., 2020, *AJ*, 159, 199 - [66](#)

Dorfi E. A., Feuchtinger M. U., 1999, *A&A*, 348, 815 - [43](#)

Dotter A., 2016, *ApJS*, 222, 8 - [25](#), [78](#)

Drake A. J., Djorgovski S. G., Mahabal A., Beshore E., Larson S., Graham M. J., Williams R., et al., 2009, *ApJ*, 696, 870 - [6](#), [173](#)

Drake A. J., Catelan M., Djorgovski S. G., Torrealba G., Graham M. J., Belokurov V., Koposov S. E., et al., 2013a, *ApJ*, 763, 32 - [105](#)

Drake A. J., Catelan M., Djorgovski S. G., Torrealba G., Graham M. J., Mahabal A., Prieto J. L., et al., 2013b, *ApJ*, 765, 154 - [94](#)

Drake A. J., Graham M. J., Djorgovski S. G., Catelan M., Mahabal A. A., Torrealba G., García-Álvarez D., et al., 2014, *ApJS*, 213, 9 - [95](#), [105](#), [122](#), [123](#)

Drake A. J., Djorgovski S. G., Catelan M., Graham M. J., Mahabal A. A., Larson S., Christensen E., et al., 2017, *MNRAS*, 469, 3688 - [95](#), [105](#), [122](#), [123](#)

Drlica-Wagner A., Mao Y.-Y., Adhikari S., Armstrong R., Banerjee A., Banik N., Bechtol K., et al., 2019, *arXiv*, arXiv:1902.01055 - [27](#)

Drlica-Wagner A., Carlin J. L., Nidever D. L., Ferguson P. S., Kuropatkin N., Adamów M., Cerny W., et al., 2021, *ApJS*, 256, 2 - [173](#)

Drlica-Wagner A., Ferguson P. S., Adamów M., Aguena M., Allam S., Andrade-Oliveira F., Bacon D., et al., 2022, *ApJS*, 261, 38 - [173](#)

Drout M. R., Piro A. L., Shappee B. J., Kilpatrick C. D., Simon J. D., Contreras C., Coulter D. A., et al., 2017, *Sci*, 358, 1570 - [14](#)

Duffau S., Zinn R., Vivas A. K., Carraro G., Méndez R. A., Winnick R., Gallart C., 2006, *ApJL*, 636, L97 - [48](#), [94](#)

Díaz C. G., González J. F., Levato H., Grosso M., 2011, *A&A*, 531, A143 - [212](#)

Dékány I., Minniti D., Majaess D., Zoccali M., Hajdu G., Alonso-García J., Catelan M., et al., 2015, *ApJL*, 812, L29 - [40](#), [42](#)

Dékány I., Hajdu G., Grebel E. K., Catelan M., Elorrieta F., Eyheramendy S., Majaess D., et al., 2018, *ApJ*, 857, 54 - [48](#), [94](#)

Dékány I., Hajdu G., Grebel E. K., Catelan M., Elorrieta F., Eyheramendy S., Majaess D., et al., 2018, *ApJ*, 857, 54 - [48](#), [94](#)

Dékány I., Hajdu G., Grebel E. K., Catelan M., 2019, *ApJ*, 883, 58 - [42](#), [57](#)

Dékány I., Grebel E. K., Pojmański G., 2021, *ApJ*, 920, 33 - [43](#), [122](#), [132](#), [134](#), [135](#), [157](#)

Eadie G. M., Harris W. E., 2016, *ApJ*, 829, 108 - [49](#), [95](#), [174](#)

Efremov, Y. N. 1964, *Peremennye Zvezdy*, 15, 242 - [54](#)

Efremov I. N., 1978, *SvA*, 22, 161 - [40](#)

Efremov Y. N., 2003, *ARep*, 47, 1000 - [40](#), [53](#)

Eggen O. J., Sandage A. R., 1964, *ApJ*, 140, 130 - [37](#)

Eggen O. J., 1980, *IBVS*, 1853, 1 - [69](#)

EHT Collaboration, Akiyama K., Alberdi A., Alef W., Algaba J. C., Anantua R., Asada K., et al., 2022, *ApJL*, 930, L12 - [2](#)

Eldridge J. J., 2012, *MNRAS*, 422, 794 - [85](#)

Emami R., Hernquist L., Alcock C., Genel S., Bose S., Weinberger R., Vogelsberger M., et al., 2021, ApJ, 918, 7 - 118

Engler C., Pillepich A., Pasquali A., Nelson D., Rodriguez-Gomez V., Chua K. T. E., Grebel E. K., et al., 2021, MNRAS, 507, 4211 - 28, 48, 175

Erkal D., Belokurov V., 2015, MNRAS, 454, 3542 - 30

Erkal D., Belokurov V. A., 2020, MNRAS, 495, 2554 - 148

Erkal D., Li T. S., Koposov S. E., Belokurov V., Balbinot E., Bechtol K., Buncher B., et al., 2018, MNRAS, 481, 3148 - 148

Erkal D., Deason A. J., Belokurov V., Xue X.-X., Koposov S. E., Bird S. A., Liu C., et al., 2021, MNRAS, 506, 2677 - 94

Erkal D., Belokurov V. A., Parkin D. L., 2020, MNRAS, 498, 5574 - 94

Erkal D., Koposov S. E., Belokurov V., 2017, MNRAS, 470, 60 - 30

ESA, 1997, ESA Special Publication, 1200 - 7, 54

Escala I., Kirby E. N., Gilbert K. M., Wojno J., Cunningham E. C., Guhathakurta P., 2020, ApJ, 902, 51 - 13

Evans C., Puech M., Afonso J., Almaini O., Amram P., Aussel H., Barbuy B., et al., 2015, arXiv, arXiv:1501.04726 175

Evans D. W., Riello M., De Angeli F., Carrasco J. M., Montegriffo P., Fabricius C., Jordi C., et al., 2018, A&A, 616, A4 - 78

Eyer L., Audard M., Holl B., Rimoldini L., Carnerero M. I., Clementini G., De Ridder J., et al., 2022, arXiv, arXiv:2206.06416 - 8

Ezzeddine R., Rasmussen K., Frebel A., Chiti A., Hinojisa K., Placco V. M., Ji A. P., et al., 2020, ApJ, 898, 150 - 14

Fabricius C., Luri X., Arenou F., Babusiaux C., Helmi A., Muraveva T., Reylé C., et al., 2021, A&A, 649, A5 - 65

Fabrizio M., Bono G., Braga V. F., Magurno D., Marinoni S., Marrese P. M., Ferraro I., et al., 2019, ApJ, 882, 169 - 48, 104, 105

Fabrizio M., Braga V. F., Crestani J., Bono G., Ferraro I., Fiorentino G., Iannicola G., et al., 2021, ApJ, 919, 118 - 43, 46, 47, 48, 49, 95, 122

Fall S. M., Zhang Q., 2001, ApJ, 561, 751 - 20

Fattahi A., Deason A. J., Frenk C. S., Simpson C. M., Gómez F. A., Grand R. J. J., Monachesi A., et al., 2020, MNRAS, 497, 4459 - 2

Feast M. W., Catchpole R. M., 1997, MNRAS, 286, L1 - 41

Feast M. W., Menzies J. W., Matsunaga N., Whitelock P. A., 2014, Natur, 509, 342 - 40

Feast M. W., 1957, MNRAS, 117, 193 - 180

Fernández-Alvar E., Tissera P. B., Carigi L., Schuster W. J., Beers T. C., Belokurov V. A., 2019, MNRAS, 485, 1745 - 13

Ferreira F. A., Santos J. F. C., Corradi W. J. B., Maia F. F. S., Angelo M. S., 2019, MNRAS, 483, 5508 - 55, 59, 70

Ferreira F. A., Corradi W. J. B., Maia F. F. S., Angelo M. S., Santos J. F. C., 2020, MNRAS, 496, 2021 - 24, 55, 59

Ferreira F. A., Corradi W. J. B., Maia F. F. S., Angelo M. S., Santos J. F. C., 2021, MNRAS, 502, L90 - 55, 59, 69

Ferreira Lopes C. E., Cross N. J. G., Catelan M., Minniti D., Hempel M., Lucas P. W., Angeloni R., et al., 2020, MNRAS, 496, 1730 - 57

Fields B. D., Olive K. A., Yeh T.-H., Young C., 2020, JCAP, 2020, 010 - 8

Fiorentino G., Caputo F., Marconi M., Musella I., 2002, ApJ, 576, 402 - 39

Fiorentino G., Marconi M., Musella I., Caputo F., 2007, A&A, 476, 863 - 39

Fiorentino G., Bono G., Monelli M., Stetson P. B., Tolstoy E., Gallart C., Salaris M., et al., 2015, *ApJL*, 798, L12 - [43](#), [48](#), [104](#), [105](#)

Fiorentino G., Musella I., Marconi M., 2013, *MNRAS*, 434, 2866 - [39](#)

Fitzpatrick E. L., Ribas I., Guinan E. F., Maloney F. P., Claret A., 2003, *ApJ*, 587, 685 - [38](#)

Flaugher B., Diehl H. T., Honscheid K., Abbott T. M. C., Alvarez O., Angstadt R., Annis J. T., et al., 2015, *AJ*, 150, 150 - [96](#), [123](#)

Flower P. J., 1978, *ApJ*, 224, 948 - [180](#)

Flower P. J., 1996, *ApJ*, 469, 355 - [137](#)

Fokin A. B., 1992, *MNRAS*, 256, 26 - [215](#)

Font A. S., Johnston K. V., Bullock J. S., Robertson B. E., 2006, *ApJ*, 646, 886 - [158](#)

For, B.-Q., Preston, G. W., & Sneden, C. 2011a, *ApJS*, 194, 38 - [48](#)

For, B.-Q., Sneden, C., & Preston, G. W. 2011b, *ApJS*, 197, 29 - [48](#), [122](#), [129](#), [134](#), [138](#), [140](#), [143](#), [145](#), [151](#), [152](#), [157](#)

Forbes D. A., Bridges T., 2010, *MNRAS*, 404, 1203 - [26](#)

Foreman-Mackey D., Hogg D. W., Lang D., Goodman J., 2013, *PASP*, 125, 306 - [112](#)

Fouesneau M., Lançon A., 2010, *A&A*, 521, A22 - [85](#)

Fouque P., Gieren W. P., 1997, *A&A*, 320, 799 - [42](#)

Franciosini E., Tognelli E., Degl'Innocenti S., Prada Moroni P. G., Randich S., Sacco G. G., Magrini L., et al., 2022, *A&A*, 659, A85 - [23](#)

Frebel A., Norris J. E., 2015, *ARA&A*, 53, 631 - [16](#)

Frebel A., Simon J. D., Geha M., Willman B., 2010, *ApJ*, 708, 560 - [27](#)

Frebel A., 2018, *ARNPS*, 68, 237 - [1](#), [9](#), [14](#), [212](#)

Freedman W. L., Madore B. F., 2011, *ApJ*, 734, 46 - [39](#)

Freedman W. L., Madore B. F., Gibson B. K., Ferrarese L., Kelson D. D., Sakai S., Mould J. R., et al., 2001, *ApJ*, 553, 47 - [41](#)

Freeman K., Bland-Hawthorn J., 2002, *ARA&A*, 40, 487 - [4](#), [5](#), [16](#), [90](#), [151](#)

Friel E. D., Janes K. A., Hong L., Lotz J., Tavaréz M., 1995, *fmw.conf*, 189 - [16](#), [23](#)

Frischknecht U., Hirschi R., Pignatari M., Maeder A., Meynet G., Chiappini C., Thielemann F.-K., et al., 2016, *MNRAS*, 456, 1803 - [154](#)

Fritz T. K., Di Cintio A., Battaglia G., Brook C., Taibi S., 2020, *MNRAS*, 494, 5178 -

Froebich D., Scholz A., Raftery C. L., 2007, *MNRAS*, 374, 399 - [69](#)

Fry A. M., Carney B. W., 1997, *AJ*, 113, 1073 - [54](#), [64](#)

Fu X., Bragaglia A., Liu C., Zhang H., Xu Y., Wang K., Zhang Z.-Y., et al., 2022, *arXiv*, arXiv:2207.09121 - [172](#)

Fux R., 1999, *A&A*, 345, 787 - [3](#)

Förster F., Maureira J. C., San Martín J., Hamuy M., Martínez J., Huijse P., Cabrera G., et al., 2016, *ApJ*, 832, 155 - [95](#), [96](#), [98](#), [122](#)

Förster F., Cabrera-Vives G., Castillo-Navarrete E., Estévez P. A., Sánchez-Sáez P., Arredondo J., Bauer F. E., et al., 2021, *AJ*, 161, 242 - [174](#)

Gaia Collaboration, Prusti T., de Bruijne J. H. J., Brown A. G. A., Vallenari A., Babusiaux C., Bailer-Jones C. A. L., et al., 2016, *A&A*, 595, A1 - [7](#), [54](#)

Gaia Collaboration, Brown A. G. A., Vallenari A., Prusti T., de Bruijne J. H. J., Babusiaux C., Bailer-Jones C. A. L., et al., 2018, *A&A*, 616, A1 - [8](#), [54](#)

Gaia Collaboration, Helmi A., van Leeuwen F., McMillan P. J., Massari D., Antoja T., Robin A. C., et al., 2018, *A&A*, 616, A12 - [148](#)

Gaia Collaboration, Brown A. G. A., Vallenari A., Prusti T., de Bruijne J. H. J., Babusiaux C., Biermann M., 2020, arXiv, arXiv:2012.01533 - 8, 54

Gaia Collaboration, Luri X., Chemin L., Clementini G., Delgado H. E., McMillan P. J., Romero-Gómez M., et al., 2021, A&A, 649, A7 - 157

Gaia Collaboration, Vallenari A., Brown A. G. A., Prusti T., de Bruijne J. H. J., Arenou F., Babusiaux C., et al., 2022, arXiv, arXiv:2208.00211 - 8, 54

Galindo-Guil F. J., Barrado D., Bouy H., Olivares J., Bayo A., Morales-Calderón M., Huéramo N., et al., 2022, A&A, 664, A70 - 87, 173

Gallenne A., Kervella P., Mérand A., Pietrzyński G., Gieren W., Nardetto N., Trahin B., 2017, A&A, 608, A18 - 42

Gallenne A., Mérand A., Kervella P., Pietrzyński G., Gieren W., Hocdé V., Breuval L., et al., 2021, A&A, 651, A113 - 42

Gallet F., Bouvier J., 2015, A&A, 577, A98 - 23

Gallino R., Arlandini C., Busso M., Lugaro M., Travaglio C., Straniero O., Chieffi A., et al., 1998, ApJ, 497, 388 - 14

Gamow G., 1939, PhRv, 55, 718 - 10

Gao X., 2020, Ap&SS, 365, 24 - 24

Garcia-Dias R., Allende Prieto C., Sánchez Almeida J., Alonso Palicio P., 2019, A&A, 629, A34 - 5

Gargiulo I. D., Monachesi A., Gómez F. A., Grand R. J. J., Marinacci F., Pakmor R., White S. D. M., et al., 2019, MNRAS, 489, 5742 - 3

Garofalo A., Delgado H. E., Sarro L. M., Clementini G., Muraveva T., Marconi M., Ripepi V., 2022, MNRAS, 513, 788 - 107, 122

Garrison-Kimmel S., Boylan-Kolchin M., Bullock J. S., Kirby E. N., 2014, MNRAS, 444, 222 - 28

Gatto M., Ripepi V., Bellazzini M., Cignoni M., Cioni M.-R. L., Dall’Ora M., Longo G., et al., 2020, MNRAS, 499, 4114 - 172

Gautschy A., 1987, VA, 30, 197 - 42

Geha M., Wechsler R. H., Mao Y.-Y., Tollerud E. J., Weiner B., Bernstein R., Hoyle B., et al., 2017, ApJ, 847, 4 - 174

Gehan C., Mosser B., Michel E., Samadi R., Kallinger T., 2018, A&A, 616, A24 - 23

Genovali K., Lemasle B., Bono G., Romaniello M., Fabrizio M., Ferraro I., Iannicola G., et al., 2014, A&A, 566, A37 - 42

Genovali K., Lemasle B., da Silva R., Bono G., Fabrizio M., Bergemann M., Buonanno R., et al., 2015, A&A, 580, A17 - 64

Georgy C., Meynet G., Maeder A., 2011, A&A, 527, A52 - 36

Gieles M., Baumgardt H., Heggie D. C., Lamers H. J. G. L. M., 2010, MNRAS, 408, L16 - 24

Gieren W., Storm J., Konorski P., Górski M., Pilecki B., Thompson I., Pietrzyński G., et al., 2018, A&A, 620, A99 - 39

Gillet D., 2013, A&A, 554, A46 - 45, 123

Gilligan C. K., Chaboyer B., Marengo M., Mullen J. P., Bono G., Braga V. F., Crestani J., et al., 2021, MNRAS, 503, 4719 - 49, 122

Gilmore G., Reid N., 1983, MNRAS, 202, 1025 - 3, 14

Gilmore G., Randich S., Asplund M., Binney J., Bonifacio P., Drew J., Feltzing S., et al., 2012, The Messenger, 147, 25 - 7

Glatt K., Grebel E. K., Koch A., 2010, A&A, 517, A50 - 53

Goodwin S. P., Bastian N., 2006, MNRAS, 373, 752 - 91

Goodwin S. P., 1997, MNRAS, 284, 785 - 24

Graham M. J., Drake A. J., Djorgovski S. G., Mahabal A. A., Donalek C., 2013a, MNRAS, 434, 2629 - 35

- Graham M. J., Drake A. J., Djorgovski S. G., Mahabal A. A., Donalek C., Duan V., Maker A., 2013b, *MNRAS*, 434, 3423 - 35
- Gran F., Zoccali M., Saviane I., Valenti E., Rojas-Arriagada A., Contreras Ramos R., Hartke J., et al., 2022, *MNRAS*, 509, 4962 - 26
- Grand R. J. J., Gómez F. A., Marinacci F., Pakmor R., Springel V., Campbell D. J. R., Frenk C. S., et al., 2017, *MNRAS*, 467, 179 - 4
- Gratton R., Bragaglia A., Carretta E., D’Orazi V., Lucatello S., Sollima A., 2019, *A&ARv*, 27, 8 - 26
- Gravity Collaboration, Abuter R., Amorim A., Bauböck M., Berger J. P., Bonnet H., Brandner W., et al., 2021, *A&A*, 647, A59 - 2
- Gray D. F., Johanson H. L., 1991, *PASP*, 103, 439 - 6
- Grebel E. K., Brandner W., 1998, in Richtler T., Braun J. M., eds, *Magellanic Clouds and Other Dwarf Galaxies*. Shaker Verlag, Aachen, p. 151 - 40
- Grebel E. K., Chu Y.-H., 2000, *AJ*, 119, 787 - 25, 54
- Grebel E. K., Gallagher J. S., Harbeck D., 2003, *AJ*, 125, 1926 - 27
- Grebel E. K., 2001a, *Dwarf galaxies and their environment*, 40th meeting of the Graduiertenkolleg The Magellanic Clouds and other dwarf galaxies, held Tue 23rd to Sat 27th January 2001 in the Physikzentrum in Bad Honnef, Germany Aachen: Shaker Verlag, 2001 317 p. *Berichte aus der Astronomie*. Edited by Klaas S. De Boer, Ralf-Juergen Dettmar, and Uli Klein. ISBN 3826592646, p.45 - 27
- Grebel E. K., 2001b, *ApSSS*, 277, 231 - 27
- Grillmair C. J., 2006, *ApJL*, 645, L37 - 28, 162
- Grillmair C. J., 2017a, *ApJ*, 847, 119 - 162
- Grillmair C. J., 2017b, *ApJ*, 834, 98 - 162
- Groenewegen M. A. T., 2008, *A&A*, 488, 25 - 39
- Groenewegen M. A. T., 2013, *A&A*, 550, A70 - 39
- Gudin D., Shank D., Beers T. C., Yuan Z., Limberg G., Roederer I. U., Placco V., et al., 2021, *ApJ*, 908, 79 - 5, 14
- Guedes J., Callegari S., Madau P., Mayer L., 2011, *ApJ*, 742, 76 - 4
- Guiglion G., Matijević G., Queiroz A. B. A., Valentini M., Steinmetz M., Chiappini C., Grebel E. K., et al., 2020, *A&A*, 644, A168 - 6
- Guillaumon P. V., Goldman I. D., 2020, arXiv, arXiv:2009.01814 - 14
- Guinan E. F., Fitzpatrick E. L., DeWarf L. E., Maloney F. P., Maurone P. A., Ribas I., Pritchard J. D., et al., 1998, *ApJL*, 509, L21 - 38
- Gustafsson B., Church R. P., Davies M. B., Rickman H., 2016, *A&A*, 593, A85 - 24
- Hajdu G., Dékány I., Catelan M., Grebel E. K., Jurcsik J., 2018, *ApJ*, 857, 55 - 122
- Halabi G. M., El Eid M. F., Champagne A., 2012, *ApJ*, 761, 10 - 37
- Han J. J., Naidu R. P., Conroy C., Bonaca A., Zaritsky D., Caldwell N., Cargile P., et al., 2022a, *ApJ*, 934, 14 - 118
- Han J. J., Conroy C., Johnson B. D., Speagle J. S., Bonaca A., Chandra V., Naidu R. P., et al., 2022b, arXiv, arXiv:2208.04327 - 18
- Hanke M., Hansen C. J., Koch A., Grebel E. K., 2018, *A&A*, 619, A134 - 6
- Hanke M., Hansen C. J., Ludwig H.-G., Cristallo S., McWilliam A., Grebel E. K., Piersanti L., 2020a, *A&A*, 635, A104 - 130, 131
- Hanke M., Koch A., Prudil Z., Grebel E. K., Bastian U., 2020b, *A&A*, 637, A98 - 26, 61, 64, 71, 151, 171
- Hanke M., 2020, “Probing the early Milky Way with stellar spectroscopy”, Doctoral thesis, Univ. Heidelberg - 7
- Hansen C. J., Nordström B., Bonifacio P., Spite M., Andersen J., Beers T. C., Cayrel R., et al., 2011, *A&A*, 527, A65 - 43, 48, 49, 95, 122, 144

Hansen C. J., Primas F., Hartman H., Kratz K.-L., Wanajo S., Leibundgut B., Farouqi K., et al., 2012, *A&A*, 545, A31 - [6](#), [14](#), [151](#), [154](#)

Hansen C. J., Rich R. M., Koch A., Xu S., Kunder A., Ludwig H.-G., 2016, *A&A*, 590, A39 - [48](#)

Hansen C. J., El-Souri M., Monaco L., Villanova S., Bonifacio P., Caffau E., Sbordone L., 2018, *ApJ*, 855, 83 - [158](#)

Hansen C. J., Hansen T. T., Koch A., Beers T. C., Nordström B., Placco V. M., Andersen J., 2019, *A&A*, 623, A128 - [154](#), [212](#)

Hansen T. T., Marshall J. L., Simon J. D., Li T. S., Bernstein R. A., Pace A. B., Ferguson P., et al., 2020, *ApJ*, 897, 183 - [28](#)

Hansen C. J., Montes F., Arcones A., 2014, *ApJ*, 797, 123 - [14](#)

Hansen C. J., 2022, arXiv, arXiv:2203.07396 - [13](#)

Hargis J. R., Willman B., Peter A. H. G., 2014, *ApJL*, 795, L13 - [48](#), [175](#)

Harris W. E., Bell R. A., Vandenberg D. A., Bolte M., Stetson P. B., Hesser J. E., van den Bergh S., et al., 1997, *AJ*, 114, 1030 - [26](#)

Harris W. E., 1996, *AJ*, 112, 1487 - [162](#)

Hartwig T., Bromm V., Klessen R. S., Glover S. C. O., 2015, *MNRAS*, 447, 3892 - [10](#)

Haschke R., Grebel E. K., Duffau S., Jin S., 2012a, *AJ*, 143, 48 - [157](#)

Haschke R., Grebel E. K., Frebel A., Duffau S., Hansen C. J., Koch A., 2012b, *AJ*, 144, 88 - [157](#)

Hasselquist S., Carlin J. L., Holtzman J. A., Shetrone M., Hayes C. R., Cunha K., Smith V., et al., 2019, *ApJ*, 872, 58 - [158](#), [163](#)

Hasselquist S., Hayes C. R., Lian J., Weinberg D. H., Zasowski G., Horta D., Beaton R., et al., 2021, *ApJ*, 923, 172 - [158](#), [163](#)

Hattori K., Erkal D., Sanders J. L., 2016, *MNRAS*, 460, 497 - [30](#)

Hawkins K., Jofré P., Gilmore G., Masseron T., 2014, *MNRAS*, 445, 2575 - [17](#)

Hawkins K., Jofré P., Masseron T., Gilmore G., 2015, *MNRAS*, 453, 758 - [5](#), [13](#)

Hawkins K., Lucey M., Ting Y.-S., Ji A., Katzberg D., Thompson M., El-Badry K., et al., 2020, *MNRAS*, 492, 1164 - [4](#)

Hawkins K., Price-Whelan A. M., Sheffield A. A., Subrahimovic A. Z., Beaton R. L., Belokurov V., Erkal D., et al., 2022, arXiv, arXiv:2205.14218 - [13](#)

Hawkins K., 2022, arXiv, arXiv:2207.04542 - [13](#)

Hayden M. R., Bovy J., Holtzman J. A., Nidever D. L., Bird J. C., Weinberg D. H., Andrews B. H., et al., 2015, *ApJ*, 808, 132 - [13](#), [16](#)

Hayes C. R., Majewski S. R., Hasselquist S., Anguiano B., Shetrone M., Law D. R., Schiavon R. P., et al., 2020, *ApJ*, 889, 63 - [158](#)

Haywood M., Di Matteo P., Lehnert M. D., Katz D., Gómez A., 2013, *A&A*, 560, A109 - [14](#), [16](#)

Haywood M., Di Matteo P., Lehnert M. D., Snaith O., Khoperskov S., Gómez A., 2018, *ApJ*, 863, 113 - [13](#), [94](#), [121](#), [151](#)

Haywood M., 2008, *MNRAS*, 388, 1175 - [16](#)

He Z., Wang K., Luo Y., Li J., Liu X., Jiang Q., 2022, arXiv, arXiv:2206.12170 - [171](#)

Heinze A. N., Tonry J. L., Denneau L., Flewelling H., Stalder B., Rest A., Smith K. W., et al., 2018, *AJ*, 156, 241 - [57](#)

Helmi A., Ivezić Ž., Prada F., Pentericci L., Rockosi C. M., Schneider D. P., Grebel E. K., et al., 2003, *ApJ*, 586, 195 - [94](#)

Helmi A., Babusiaux C., Koppelman H. H., Massari D., Veljanoski J., Brown A. G. A., 2018, *Natur*, 563, 85 - [16](#), [28](#), [49](#), [94](#), [121](#)

Helmi A., Irwin M., Deason A., Balbinot E., Belokurov V., Bland-Hawthorn J., Christlieb N., et al., 2019, *Msngr*, 175, 23 - [17](#), [175](#)

Helmi A., 2008, *A&ARv*, 15, 145 - 16

Hendel D., Scowcroft V., Johnston K. V., Fardal M. A., van der Marel R. P., Sohn S. T., Price-Whelan A. M., et al., 2018, *MNRAS*, 479, 570 - 48

Henden A. A., Levine S., Terrell D., Welch D. L., 2015, *AAS* - 99

Hernitschek N., Stassun K. G., 2022, *ApJS*, 258, 4 - 123, 173, 174

Hernitschek N., Cohen J. G., Rix H.-W., Sesar B., Martin N. F., Magnier E., Wainscoat R., et al., 2018, *ApJ*, 859, 31 - 48

Hertzprung, E., 1911, Über die Verwendung Photographischer Effektiver Wellenlaengen zur Bestimmung von Farbenaequivalenten, Publikationen des Astrophysikalischen Observatoriums zu Potsdam, 22. Bd., 1 - 11

Hidalgo S. L., Pietrinferni A., Cassisi S., Salaris M., Mucciarelli A., Savino A., Aparicio A., et al., 2018, *ApJ*, 856, 125 - 88

Hinshaw G., Larson D., Komatsu E., Spergel D. N., Bennett C. L., Dunkley J., Nolte M. R., et al., 2013, *ApJS*, 208, 19 - 8

Hirai Y., Beers T. C., Chiba M., Aoki W., Shank D., Saitoh T. R., Okamoto T., et al., 2022, *arXiv*, arXiv:2206.04060 - 14

Hoffmeister C., Kholopov P. N., 1985, *SvA*, 29, 719 - 33

Hogg D. W., Casey A. R., Ness M., Rix H.-W., Foreman-Mackey D., Hasselquist S., Ho A. Y. Q., et al., 2016, *ApJ*, 833, 262 - 5

Holl B., Audard M., Nienartowicz K., Jevardat de Fombelle G., Marchal O., Mowlavi N., Clementini G., et al., 2018, *A&A*, 618, A30 - 95, 107

Holtzman J. A., Hasselquist S., Shetrone M., Cunha K., Allende Prieto C., Anguiano B., Bizyaev D., et al., 2018, *AJ*, 156, 125 - 66

Horta D., Schiavon R. P., Mackereth J. T., Pfeffer J., Mason A. C., Kisku S., Fragkoudi F., et al., 2021, *MNRAS*, 500, 1385 - 26

Hoyle F., Shanks T., Tanvir N. R., 2003, *MNRAS*, 345, 269 - 54, 180

Hoyle F., 1960, *MNRAS*, 120, 22 - 13, 37

Huang K.-W., Kopolov S. E., 2022, *MNRAS*, 510, 3575 - 94, 95, 107, 122

Hubble E. P., 1926, *ApJ*, 64, 321 - 1

Huijse P., Estevez P. A., Protopapas P., Zegers P., Principe J. C., 2012, *IEEE Transactions on Signal Processing*, 60, 10, 5135-5145 - 35

Huijse P., Estévez P. A., Förster F., Daniel S. F., Connolly A. J., Protopapas P., Carrasco R., et al., 2018, *ApJS*, 236, 12 - 33, 34, 35, 101

Hunt E. L., Reffert S., 2021, *A&A*, 646, A104 - 24, 55, 56, 58, 176

Hénon M., 1961, *AnAp*, 24, 369 - 24

Ibata R. A., Lewis G. F., Irwin M. J., Quinn T., 2002, *MNRAS*, 332, 915 - 30

Ibata R. A., Malhan K., Martin N. F., Starkenburg E., 2018, *ApJ*, 865, 85 - 26, 30

Ibata R., Malhan K., Martin N., Aubert D., Famaey B., Bianchini P., Monari G., et al., 2021, *ApJ*, 914, 123 - 158, 162

Ibata R. A., Gilmore G., Irwin M. J., 1994, *Nature*, 370, 194 - 16, 28, 94, 121

Ibata R. A., Malhan K., Martin N. F., 2019, *ApJ*, 872, 152 - 162

Inno L., Bono G., Romaniello M., Matsunaga N., Pietrinferni A., Genovali K., Lemasle B., et al., 2015, in Points S., Kunder A., eds, *The Recent Star Formation History of the Magellanic Clouds Traced by Classical Cepheids*, Vol. 491, *Astronomical Society of the Pacific Conference Series*. p. 265 - 40

Iorio G., Belokurov V., 2019, *MNRAS*, 482, 3868 - 48, 94

Iorio G., Belokurov V., 2021, *MNRAS*, 502, 5686 - 107

Iorio G., Belokurov V., Erkal D., Koposov S. E., Nipoti C., Fraternali F., 2018, *MNRAS*, 474, 2142 - 49

Irwin M. J., Belokurov V., Evans N. W., Ryan-Weber E. V., de Jong J. T. A., Koposov S., Zucker D. B., et al., 2007, *ApJL*, 656, L13 - [27](#)

Irwin J. B., 1955, *MNSSA*, 14, 38 - [53](#), [54](#), [180](#)

Ivezić, Ž., Kahn, S. M., Tyson, J. A., Abel, B., Acosta, E., Allsman, R., Alonso, D., et al. 2008, arXiv:0805.2366 - [174](#)

Ivezić Ž., Beers T. C., Jurić M., 2012, *ARA&A*, 50, 251 - [18](#), [151](#)

Jacobson H. R., Friel E. D., Jílková L., Magrini L., Bragaglia A., Vallenari A., Tosi M., et al., 2016, *A&A*, 591, A37 - [23](#)

Jacoby G. H., 1989, *ApJ*, 339, 39 - [41](#)

Jacyszyn-Dobrzeńicka A. M., Skowron D. M., Mróz P., Soszyński I., Udalski A., Pietrukowicz P., Skowron J., et al., 2017, *AcA*, 67, 1 - [157](#)

Jaehnig K., Bird J., Holley-Bockelmann K., 2021, *ApJ*, 923, 129 - [25](#)

Janes K., Adler D., 1982, *ApJS*, 49, 425 - [23](#), [25](#)

Jayasinghe T., Kochanek C. S., Stanek K. Z., Shappee B. J., Holoiien T. W.-S., Thompson T. A., Prieto J. L., et al., 2018, *MNRAS*, 477, 3145 - [57](#)

Jayasinghe T., Stanek K. Z., Kochanek C. S., Shappee B. J., Holoiien T. W.-S., Thompson T. A., Prieto J. L., et al., 2019a, *MNRAS*, 486, 1907 - [57](#)

Jayasinghe T., Stanek K. Z., Kochanek C. S., Shappee B. J., Holoiien T. W.-S., Thompson T. A., Prieto J. L., et al., 2019b, *MNRAS*, 485, 961 - [57](#), [70](#)

Jaynes E. T. 2003, *Probability Theory - The Logic of Science*. Cambridge Univ. Press, Cambridge - [57](#)

Jeans J. H., 1902, *RSPTA*, 199, 1 - [10](#)

Jeffries R. D., Jackson R. J., Cottaar M., Koposov S. E., Lanzafame A. C., Meyer M. R., Prisinzano L., et al., 2014, *A&A*, 563, A94 - [23](#)

Jeffries R. D., Jackson R. J., Franciosini E., Randich S., Barrado D., Frasca A., Klutsch A., et al., 2017, *MNRAS*, 464, 1456 - [23](#)

Jethwa P., Erkal D., Belokurov V., 2018, *MNRAS*, 473, 2060 - [48](#), [175](#)

Ji A. P., Li T. S., Hansen T. T., Casey A. R., Koposov S. E., Pace A. B., Mackey D., et al., 2020, *AJ*, 160, 181 - [166](#)

Ji A. P., Koposov S. E., Li T. S., Erkal D., Pace A. B., Simon J. D., Belokurov V., et al., 2021, *ApJ*, 921, 32 - [30](#), [166](#)

Jofré P., Panter B., Hansen C. J., Weiss A., 2010, *A&A*, 517, A57 - [130](#)

Jofré P., Heiter U., Soubiran C., Blanco-Cuaresma S., Worley C. C., Pancino E., Cantat-Gaudin T., et al., 2014, *A&A*, 564, A133 - [138](#)

Johnson B. D., Conroy C., Naidu R. P., Bonaca A., Zaritsky D., Ting Y.-S., Cargile P. A., et al., 2020, *ApJ*, 900, 103 - [158](#), [163](#)

Johnston K. V., Carlberg R. G., 2016, *ASSL*, 420, 169 - [30](#)

Johnston K. V., Spergel D. N., Haydn C., 2002, *ApJ*, 570, 656 - [4](#)

Jordi K., Grebel E. K., 2010, *A&A*, 522, A71 - [16](#), [28](#)

Jurcsik J., Kovacs G., 1996, *A&A*, 312, 111 - [122](#), [132](#)

Jurcsik J., Smitola P., 2016, *Communications from the Konkoly Observatory*, 105, 167 - [45](#)

Jurcsik J., Sódor Á., Szeidl B., Hurta Z., Váradi M., Posztobányi K., Vida K., et al., 2009, *MNRAS*, 400, 1006 - [45](#)

Jurcsik J., Hajdu G., Juhász Á., 2021, *MNRAS*, 505, 2468 - [46](#)

Jurcsik J., 1995, *AcA*, 45, 653 - [157](#)

Jurić M., Ivezić Ž., Brooks A., Lupton R. H., Schlegel D., Finkbeiner D., Padmanabhan N., et al., 2008, *ApJ*, 673, 864 - [14](#), [18](#), [94](#)

Jönsson H., Holtzman J. A., Allende Prieto C., Cunha K., García-Hernández D. A., Hasselquist S., Masseron T., et al., 2020, *AJ*, 160, 120 - [66](#)

Kaiser N., Aussel H., Burke B. E., Boesgaard H., Chambers K., Chun M. R., Heasley J. N., et al., 2002, *SPIE*, 4836, 154 - [6](#), [173](#)

Karakas A. I., Lattanzio J. C., 2014, *PASA*, 31, e030 - [14](#), [153](#)

Kasen D., Woosley S. E., 2009, *ApJ*, 703, 2205 - [41](#)

Katz D., Sartoretti P., Guerrier A., Panuzzo P., Seabroke G. M., Thévenin F., Cropper M., et al., 2022, *arXiv*, arXiv:2206.05902 - [8](#)

Kauffmann G., White S. D. M., Guiderdoni B., 1993, *MNRAS*, 264, 201 - [2](#)

Keller S. C., Murphy S., Prior S., DaCosta G., Schmidt B., 2008, *ApJ*, 678, 851 - [48](#)

Kelly B. C., Becker A. C., Sobolewska M., Siemiginowska A., Uttley P., 2014, *ApJ*, 788, 33 - [35](#)

Kelson D. D., Illingworth G. D., van Dokkum P. G., Franx M., 2000, *ApJ*, 531, 159 - [128](#)

Kelson, D. D. 2003, *PASP*, 115, 688 - [128](#)

Kennedy C. R., Stancliffe R. J., Kuehn C., Beers T. C., Kinman T. D., Placco V. M., Reggiani H., et al., 2014, *ApJ*, 787, 6 - [155](#)

Kervella P., Trahin B., Bond H. E., Gallenne A., Szabados L., Mérand A., Breifelder J., et al., 2017, *A&A*, 600, A127 - [42](#)

Kervella P., Gallenne A., Rameau Evans N., Szabados L., Arenou F., Mérand A., Proto Y., et al., 2019, *A&A*, 623, A116 - [67](#)

Kesden M., Kamionkowski M., 2006, *PhRvD*, 74, 083007 - [30](#)

Kharchenko N. V., Piskunov A. E., Röser S., Schilbach E., Scholz R.-D., 2005, *A&A*, 438, 1163 - [58](#)

Kharchenko N. V., Piskunov A. E., Röser S., Schilbach E., Scholz R.-D., 2005, *A&A*, 440, 403 - [58](#)

Kharchenko N. V., Piskunov A. E., Schilbach E., Röser S., Scholz R.-D., 2012, *A&A*, 543, A156 - [58](#)

Kharchenko N. V., Piskunov A. E., Schilbach E., Röser S., Scholz R.-D., 2013, *A&A*, 558, A53 - [24](#), [26](#), [55](#)

Kholopov P. N., 1956, *Peremennye Zvezdy*, 11, 325 - [180](#)

Kholopov, P. N., Samus, N. N., Frolov, M. S., et al. 1998, *Combined General Catalogue of Variable Stars*, 4.1 Ed (II/214A) - [43](#)

Kippenhahn R., Smith L., 1969, *A&A*, 1, 142 - [40](#)

Kirby E. N., Cohen J. G., Guhathakurta P., Cheng L., Bullock J. S., Gallazzi A., 2013, *ApJ*, 779, 102 - [27](#), [174](#)

Kisku S., Schiavon R. P., Horta D., Mason A., Mackereth J. T., Hasselquist S., García-Hernández D. A., et al., 2021, *MNRAS*, 504, 1657 - [26](#)

Kluyver H. A., 1936, *BAN*, 7, 313 - [45](#)

Kobayashi C., Leung S.-C., Nomoto K., 2020, *ApJ*, 895, 138 - [13](#)

Koch A., Rich R. M., Reitzel D. B., Martin N. F., Ibata R. A., Chapman S. C., Majewski S. R., et al., 2008, *ApJ*, 689, 958 - [13](#), [17](#)

Koch A., Kunder A., Wojno J., 2017, *A&A*, 605, A128 - [26](#)

Kolenberg K., Guggenberger E., Medupe T., Lenz P., Schmitzberger L., Shobbrook R. R., Beck P., et al., 2009, *MNRAS*, 396, 263 - [45](#)

Kolenberg K., Fossati L., Shulyak D., Pikall H., Barnes T. G., Kochukhov O., Tsymbal V., 2010, *A&A*, 519, A64 - [45](#), [49](#), [122](#), [123](#), [136](#), [140](#)

Koposov S. E., Belokurov V., Torrealba G., Evans N. W., 2015, *ApJ*, 805, 130 - [27](#), [175](#)

Koposov S. E., Belokurov V., Li T. S., Mateu C., Erkal D., Grillmair C. J., Hendel D., et al., 2019, *MNRAS*, 485, 4726 - [162](#), [165](#)

Koppelman H. H., Helmi A., Massari D., Price-Whelan A. M., Starkenburg T. K., 2019, *A&A*, 631, L9 - [5](#)

Kounkel M., Covey K., Stassun K. G., 2020, *AJ*, 160, 279 - [78](#), [79](#), [80](#)

Kovacs G., 2016, *Communications from the Konkoly Observatory*, 105, 61 - 45

Kovtyukh V., Lemasle B., Bono G., Usenko I. A., da Silva R., Kniazev A., Grebel E. K., et al., 2022, *MNRAS*, 510, 1894 - 42

Kovács G., Kupi G., 2007, *A&A*, 462, 1007 - 35

Kovács G., 2003, *MNRAS*, 342, L58 - 46

Kraft R. P., 1962, *IAUTB*, 11B, 298 - 54

Krone-Martins A., Moitinho A., 2014, *A&A*, 561, A57 - 25

Kroupa P., Aarseth S., Hurley J., 2001, *MNRAS*, 321, 699 - 11, 24

Kruijssen J. M. D., Pfeffer J. L., Reina-Campos M., Crain R. A., Bastian N., 2019, *MNRAS*, 486, 3180 - 26, 121

Kukarkin B. V., Kholopov P. N., Efremov Y. N., Kukarkina N. P., Kurochkin N. E., Medvedeva G. I., Perova N. B., et al., 1969, *General Catalogue of Variable Stars. Volume 1. Constellations Andromeda - Grus. - Astronomical Council of the Academy of Sciences in the USSR, Sternberg State Astronomical Institute of the Moscow State University*, A121 + 474 - 57

Kunder A., Stetson P. B., Cassisi S., Layden A., Bono G., Catelan M., Walker A. R., et al., 2013, *AJ*, 146, 119 - 45

Kunder A., Rich R. M., Koch A., Storm J., Nataf D. M., De Propriis R., Walker A. R., et al., 2016, *ApJL*, 821, L25 - 122

Käppeler F., Gallino R., Bisterzo S., Aoki W., 2011, *RvMP*, 83, 157 - 14, 153

Küpper A. H. W., Kroupa P., Baumgardt H., Heggie D. C., 2010, *MNRAS*, 401, 105 - 24

Lacy C. H., 1977, *ApJ*, 213, 458 - 38

Lada C. J., Lada E. A., 2003, *ARA&A*, 41, 57 - 24, 85, 91

Lada C. J., Lombardi M., Alves J. F., 2010, *ApJ*, 724, 687 - 21, 24

Lada C. J., Margulis M., Dearborn D., 1984, *ApJ*, 285, 141 - 24

Lagarde N., Robin A. C., Reylé C., Nasello G., 2017, *A&A*, 601, A27 - 23

Lagarde N., Reylé C., Robin A. C., Tautvaišienė G., Drazdauskas A., Mikolaitis Š., Minkevičiūtė R., et al., 2019, *A&A*, 621, A24 - 4, 23

Lamers H. J. G. L. M., Gieles M., Bastian N., Baumgardt H., Kharchenko N. V., Portegies Zwart S., 2005, *A&A*, 441, 117 - 21

Lane J. M. M., Bovy J., Mackereth J. T., 2022, *MNRAS*, 510, 5119 - 16

Lanfranchi G. A., Matteucci F., Cescutti G., 2008, *A&A*, 481, 635 - 153

Laporte C. F. P., Gómez F. A., Besla G., Johnston K. V., Garavito-Camargo N., 2018, *MNRAS*, 473, 1218 - 148

Larsen S. S., 2010, *RSPTA*, 368, 867 - 21

Lattimer J. M., Schramm D. N., 1974, *ApJL*, 192, L145 - 14

Law D. R., Majewski S. R., 2010, *ApJ*, 718, 1128 - 24

Layden A. C., 1994, *AJ*, 108, 1016 - 43, 129, 212

Leavitt H. S., Pickering E. C., 1912, *Harvard College Observatory Circular*, 173 - 41, 54

Leavitt, H. S. 1908, *Annals of Harvard College Observatory*, 60, 87 - 41

Lee J.-W., Carney B. W., 1999, *AJ*, 118, 1373 - 46

Lee D. M., Johnston K. V., Sen B., Jessop W., 2015, *ApJ*, 802, 48 - 18

Lee Y.-W., Demarque P., Zinn R., 1994, *ApJ*, 423, 248 - 46

Lemasle B., François P., Bono G., Mottini M., Primas F., Romaniello M., 2007, *A&A*, 467, 283 - 42

- Lemasle B., François P., Piersimoni A., Pedicelli S., Bono G., Laney C. D., Primas F., et al., 2008, *A&A*, 490, 613 - [16](#), [42](#), [64](#)
- Lemasle B., François P., Genovali K., Kovtyukh V. V., Bono G., Inno L., Laney C. D., et al., 2013, *A&A*, 558, A31 - [35](#), [42](#)
- Lemasle B., Groenewegen M. A. T., Grebel E. K., Bono G., Fiorentino G., François P., Inno L., et al., 2017, *A&A*, 608, A85 - [54](#), [64](#)
- Lewis S., Cournoyer-Cloutier C., Tran A., Farner W., McMillan S., Mac Low M., Portegies Zwart S., et al., 2021, *American Astronomical Society meeting 238*, 53, 6 - [172](#)
- Li C., Binney J., 2022, *MNRAS*, 510, 4706 - [48](#)
- Li T. S., Kuposov S. E., Zucker D. B., Lewis G. F., Kuehn K., Simpson J. D., Ji A. P., et al., 2019, *MNRAS*, 490, 3508 - [30](#), [173](#)
- Li T. S., Kuposov S. E., Erkal D., Ji A. P., Shipp N., Pace A. B., Hilmi T., et al., 2021, *ApJ*, 911, 149 - [18](#), [30](#), [166](#), [176](#)
- Lindegren L., Hernández J., Bombrun A., Klioner S., Bastian U., Ramos-Lerate M., de Torres A., et al., 2018, *A&A*, 616, A2 - [8](#), [61](#), [65](#), [66](#)
- Lindegren L., Bastian U., Biermann M., Bombrun A., de Torres A., Gerlach E., Geyer R., et al., 2021, *A&A*, 649, A4 - [65](#)
- Lindemann F. A., 1918, *MNRAS*, 78, 639 - [42](#)
- Liu T., Janes K. A., 1990, *ApJ*, 354, 273 - [42](#)
- Liu L., Pang X., 2019, *ApJS*, 245, 32 - [55](#), [56](#), [59](#), [67](#), [69](#), [73](#), [76](#), [78](#), [182](#)
- Liu S., Du C., Newberg H. J., Chen Y., Wu Z., Ma J., Zhou X., et al., 2018, *ApJ*, 862, 163 - [145](#)
- Liu G.-C., Huang Y., Zhang H.-W., Xiang M.-S., Ren J.-J., Chen B.-Q., Yuan H.-B., et al., 2020, *ApJS*, 247, 68 - [43](#), [49](#), [95](#), [122](#)
- Liu T., 1991, *PASP*, 103, 205 - [130](#)
- Loebman S. R., Roškar R., Debattista V. P., Ivezić Ž., Quinn T. R., Wadsley J., 2011, *ApJ*, 737, 8 - [16](#)
- Lohr M. E., Negueruela I., Tabernerero H. M., Clark J. S., Lewis F., Roche P., 2018, *MNRAS*, 478, 3825 - [54](#), [57](#), [70](#), [180](#)
- Longmore A. J., Fernley J. A., Jameson R. F., 1986, *MNRAS*, 220, 279 - [45](#)
- LSST Science Collaboration, Abell P. A., Allison J., Anderson S. F., Andrew J. R., Angel J. R. P., Armus L., et al., 2009, *arXiv*, arXiv:0912.0201 - [98](#), [173](#)
- Lu Y. (Lucy) ., Ness M. K., Buck T., Zinn J. C., Johnston K. V., 2022, *MNRAS*, 512, 2890 -
- Luck R. E., 2018, *AJ*, 156, 171 - [42](#)
- Luo A.-L., Zhao Y.-H., Zhao G., Deng L.-C., Liu X.-W., Jing Y.-P., Wang G., et al., 2015, *RAA*, 15, 1095 - [7](#)
- Luque E., Queiroz A., Santiago B., Pieres A., Balbinot E., Bechtol K., Drlica-Wagner A., et al., 2016, *MNRAS*, 458, 603 - [27](#)
- Lyngå G., Lindegren L., 1998, *NewA*, 3, 121 - [54](#)
- López-Corredoira M., Cabrera-Lavers A., Gerhard O. E., 2005, *A&A*, 439, 107 -
- Mackereth J. T., Bovy J., 2020, *MNRAS*, 492, 3631 - [16](#)
- Madigan A.-M., Pfuhl O., Levin Y., Gillessen S., Genzel R., Perets H. B., 2014, *ApJ*, 784, 23 - [20](#)
- Madore B. F., Freedman W. L., 1991, *PASP*, 103, 933 - [41](#), [54](#)
- Madore B. F., 1982, *ApJ*, 253, 575 - [39](#), [41](#)
- Magnier E. A., Augusteijn T., Prins S., van Paradijs J., Lewin W. H. G., 1997a, *A&AS*, 126, 401 - [53](#)
- Magnier E. A., Prins S., Augusteijn T., van Paradijs J., Lewin W. H. G., 1997b, *A&A*, 326, 442 - [40](#)
- Magrini L., Randich S., Kordopatis G., Prantzos N., Romano D., Chieffi A., Limongi M., et al., 2017, *A&A*, 603, A2 - [64](#)

Magrini L., Lagarde N., Charbonnel C., Franciosini E., Randich S., Smiljanic R., Casali G., et al., 2021, *A&A*, 651, A84 - [23](#)

Mahalanobis P.C. 1936, On the generalised distance in statistics, *Proceedings of the National Institute of Sciences of India*, 2, 49–55 - [61](#)

Majaess D., Turner D., Moni Bidin C., Mauro F., Geisler D., Gieren W., Minniti D., et al., 2011, *ApJL*, 741, L27 - [180](#)

Majaess D., Sturch L., Moni Bidin C., Soto M., Gieren W., Cohen R., Mauro F., et al., 2013a, *Ap&SS*, 347, 61 - [69](#)

Majaess D., Carraro G., Moni Bidin C., Bonatto C., Berdnikov L., Balam D., Moyano M., et al., 2013b, *A&A*, 560, A22 - [67](#)

Majaess D. J., Turner D. G., Lane D. J., 2008, *MNRAS*, 390, 1539 - [54](#), [69](#)

Majewski S. R., Skrutskie M. F., Weinberg M. D., Ostheimer J. C., 2003, *ApJ*, 599, 1082 - [94](#), [110](#), [158](#), [163](#)

Majewski S. R., Schiavon R. P., Frinchaboy P. M., Allende Prieto C., Barkhouser R., Bizyaev D., Blank B., et al., 2017, *AJ*, 154, 94 - [7](#)

Malhan K., Ibata R. A., 2018, *MNRAS*, 477, 4063 - [162](#)

Malhan K., Ibata R. A., Sharma S., Famaey B., Bellazzini M., Carlberg R. G., D'Souza R., et al., 2022, *ApJ*, 926, 107 - [2](#), [27](#), [30](#)

Malhan K., Ibata R. A., Martin N. F., 2018, *MNRAS*, 481, 3442 - [16](#), [18](#)

Malhan K., Ibata R. A., Martin N. F., 2020, *arXiv*, arXiv:2012.05271 - [30](#)

Malhan K., Valluri M., Freese K., 2021, *MNRAS*, 501, 179 - [30](#)

Malo L., Doyon R., Lafrenière D., Artigau É., Gagné J., Baron F., Riedel A., 2013, *ApJ*, 762, 88 - [25](#)

Marconi M., Coppola G., Bono G., Braga V., Pietrinferni A., Buonanno R., Castellani M., et al., 2015, *ApJ*, 808, 50 - [45](#)

Marconi M., Molinaro R., Dall'Ora M., Ripepi V., Musella I., Bono G., Braga V., et al., 2022, *arXiv*, arXiv:2206.06470 - [46](#)

Marconi M., Musella I., Fiorentino G., 2005, *ApJ*, 632, 590 - [39](#)

Martin N. F., Ibata R. A., Bellazzini M., Irwin M. J., Lewis G. F., Dehnen W., 2004, *MNRAS*, 348, 12 - [27](#)

Martin N. F., Venn K. A., Aguado D. S., Starkenburg E., González Hernández J. I., Ibata R. A., Bonifacio P., et al., 2022a, *Natur*, 601, 45 - [26](#), [28](#), [30](#), [166](#)

Martin N. F., Ibata R. A., Starkenburg E., Yuan Z., Malhan K., Bellazzini M., Viswanathan A., et al., 2022b, *arXiv*, arXiv:2201.01310 - [166](#)

Martínez-Palomera J., Förster F., Protopapas P., Maureira J. C., Lira P., Cabrera-Vives G., Huijse P., et al., 2018, *AJ*, 156, 186 - [95](#)

Martínez-Vázquez C. E., Monelli M., Gallart C., Bono G., Bernard E. J., Stetson P. B., Ferraro I., et al., 2016, *MNRAS*, 461, L41 - [122](#)

Martínez-Vázquez C. E., Monelli M., Bernard E. J., Gallart C., Stetson P. B., Skillman E. D., Bono G., et al., 2017, *ApJ*, 850, 137 - [156](#)

Martínez-Vázquez C. E., Vivas A. K., Gurevich M., Walker A. R., McCarthy M., Pace A. B., Stringer K. M., et al., 2019, *MNRAS*, 490, 2183 - [48](#)

Masci F. J., Laher R. R., Rusholme B., Shupe D. L., Groom S., Surace J., Jackson E., et al., 2019, *PASP*, 131, 018003 - [95](#)

Mashonkina L., Jablonka P., Pakhomov Y., Sitnova T., North P., 2017, *A&A*, 604, A129 - [138](#)

Mashonkina L., Korn A. J., Przybilla N., 2007, *A&A*, 461, 261 - [145](#)

Massari D., Koppelman H. H., Helmi A., 2019, *A&A*, 630, L4 - [5](#), [121](#)

Mateo M., Madore B., 1988, *ASPC*, 4, 174 [67](#), [180](#)

Mateu C., Vivas A. K., Zinn R., Miller L. R., Abad C., 2009, *AJ*, 137, 4412 - [49](#)

Mateu C., Read J. I., Kawata D., 2018, MNRAS, 474, 4112 - [48](#), [162](#)

Mateu C., 2022, arXiv, arXiv:2204.10326 - [vii](#), [30](#), [110](#), [162](#), [163](#), [164](#)

Matheson T., Stubens C., Wolf N., Lee C.-H., Narayan G., Saha A., Scott A., et al., 2021, AJ, 161, 107 - [174](#)

Mathewson D. S., Cleary M. N., Murray J. D., 1974, ApJ, 190, 291 - [94](#)

Matteucci F., 2012, Chemical Evolution of Galaxies, Astronomy and Astrophysics Library. ISBN 978-3-642-22490-4 - [4](#)

Matthews J. M., Gieren W. P., Mermilliod J.-C., Welch D. L., 1995, AJ, 110, 2280 - [67](#), [180](#)

Mau S., Drlica-Wagner A., Bechtol K., Pace A. B., Li T., Soares-Santos M., Kuropatkin N., et al., 2019, ApJ, 875, 154 - [20](#), [26](#)

Mau S., Cerny W., Pace A. B., Choi Y., Drlica-Wagner A., Santana-Silva L., Riley A. H., et al., 2020, ApJ, 890, 136 - [27](#)

McConnachie A. W., Venn K. A., 2020, AJ, 160, 124 - [27](#), [112](#)

McConnachie A. W., 2012, AJ, 144, 4 - [27](#)

McKinney W., 2010, in van der Walt S. & Millman J., eds, Proceedings of the 9th Python in Science Conference, 56 - [61](#) -

McMillan S. L. W., Vesperini E., Portegies Zwart S. F., 2007, ApJL, 655, L45 - [24](#)

McWilliam A., Zoccali M., 2010, ApJ, 724, 1491 - [3](#)

Medina G. E., Muñoz R. R., Vivas A. K., Förster F., Carlin J. L., Martínez J., Galbany L., et al., 2017, ApJL, 845, L10 - [95](#), [176](#)

Medina G. E., Muñoz R. R., Vivas A. K., Carlin J. L., Förster F., Martínez J., Galbany L., et al., 2018, ApJ, 855, 43 - [17](#), [49](#), [94](#), [95](#), [96](#), [98](#), [101](#), [102](#), [103](#), [105](#), [108](#), [110](#), [112](#), [113](#), [116](#), [122](#), [123](#)

Medina G. E., Lemasle B., Grebel E. K., 2021a, MNRAS, 505, 1342 - [53](#)

Medina G. E., Muñoz R. R., Carlin J. L., et al., 2021b, in Kinemuchi, K., Lovekin, C., Neilson, H., and Vivas A. K., eds, ASP Conf. Ser. Vol. 529, RRLyrae/Cepheid2019: Frontiers of Classical Pulsators: Theory and Observations, p. 222 - [93](#), [96](#), [123](#)

Medina G. E., 2017, “Searching for distant RR Lyrae in the Galactic halo using the High cadence Transient Survey”, Master thesis, Universidad de Chile - [98](#)

Megeath S. T., Gutermuth R., Muzerolle J., Kryukova E., Hora J. L., Allen L. E., Flaherty K., et al., 2016, AJ, 151, 5 - [24](#)

Meingast S., Alves J., Rottensteiner A., 2021, A&A, 645, A84 - [60](#), [171](#)

Mel’nik A. M., Rautiainen P., Berdnikov L. N., Dambis A. K., Rastorguev A. S., 2015, AN, 336, 70 - [67](#)

Mermilliod J. C., 1988, Bulletin d’Information du Centre de Données Stellaires, 35, 77 [55](#)

Merritt A., van Dokkum P., Abraham R., Zhang J., 2016, ApJ, 830, 62 - [94](#)

Merritt A., Pillepich A., van Dokkum P., Nelson D., Hernquist L., Marinacci F., Vogelsberger M., 2020, MNRAS, 495, 4570 - [118](#)

Messier C., 1781, Connaissance des Temps ou des Mouvements Célestes, 227-267 - [2](#), [24](#)

Meyer-Hofmeister E., 1969, A&A, 2, 143 - [40](#)

Miceli A., Rest A., Stubbs C. W., Hawley S. L., Cook K. H., Magnier E. A., Krisciunas K., et al., 2008, ApJ, 678, 865 - [48](#)

Michalik D., Lindegren L., Hobbs D., Butkevich A. G., 2015, A&A, 583, A68 - [24](#)

Mikolaitis Š., Hill V., Recio-Blanco A., de Laverny P., Allende Prieto C., Kordopatis G., Tautvaišienė G., et al., 2014, A&A, 572, A33 - [13](#)

Milone A. P., Marino A. F., 2022, Univ, 8, 359 - [26](#)

Minchev I., Chiappini C., Martig M., 2016, AN, 337, 944 - [24](#)

Minniti D., Lucas P. W., Emerson J. P., Saito R. K., Hempel M., Pietrukowicz P., Ahumada A. V., et al., 2010, *NewA*, 15, 433 - [6](#), [42](#)

Minniti J. H., Zoccali M., Rojas-Arriagada A., Minniti D., Sbordone L., Contreras Ramos R., Braga V. F., et al., 2021, *A&A*, 654, A138 - [23](#), [26](#)

Mitschang A. W., De Silva G., Zucker D. B., Anguiano B., Bensby T., Feltzing S., 2014, *MNRAS*, 438, 2753 - [5](#)

Moeckel N., Holland C., Clarke C. J., Bonnell I. A., 2012, *MNRAS*, 425, 450 - [91](#)

Moitinho A., 2010, *IAUS*, 266, 106 - [25](#)

Mollá M., Wekesa S., Cavichia O., Díaz Á. I., Gibson B. K., Rosales-Ortega F. F., Ascasibar Y., et al., 2019, *MNRAS*, 490, 665 - [42](#)

Monelli M., Fiorentino G., 2022, *Univ*, 8, 191 - [48](#), [94](#)

Montalbán J., Mackereth J. T., Miglio A., Vincenzo F., Chiappini C., Buldgen G., Mosser B., et al., 2021, *NatAs*, 5, 640 - [2](#), [93](#)

Monteiro H., Dias W. S., Caetano T. C., 2010, *A&A*, 516, A2 - [78](#)

Moore, B., Ghigna, S., Governato, F., et al. 1999, *ApJ*, 524, L19 - [28](#)

Mor R., Robin A. C., Figueras F., Roca-Fàbrega S., Luri X., 2019, *A&A*, 624, L1 - [91](#)

Moraux E., 2016, *EAS*, 80-81, 73 - [25](#)

Moskalik P., Poretti E., 2002, *ASPC*, 259, 392 - [45](#)

Moskalik P., Poretti E., 2003, *A&A*, 398, 213 - [123](#)

Mosser B., Benomar O., Belkacem K., Goupil M. J., Lagarde N., Michel E., Lebreton Y., et al., 2014, *A&A*, 572, L5 - [23](#)

Mucciarelli A., Bonifacio P., 2020, *A&A*, 640, A87 - [143](#)

Mucciarelli A., Cristallo S., Brocato E., Pasquini L., Straniero O., Caffau E., Raimondo G., et al., 2011, *MNRAS*, 413, 837 - [64](#)

Muhie T. D., Dambis A. K., Berdnikov L. N., Kniazev A. Y., Grebel E. K., 2021, *MNRAS*, 502, 4074 - [46](#)

Mullen J. P., Marengo M., Martínez-Vázquez C. E., Neeley J. R., Bono G., Dall’Ora M., Chaboyer B., et al., 2021, *ApJ*, 912, 144 - [122](#), [132](#), [134](#), [135](#)

Mullen J. P., Marengo M., Martínez-Vázquez C. E., Bono G., Braga V. F., Chaboyer B., Crestani J., et al., 2022, *ApJ*, 931, 131 - [122](#), [134](#)

Murakami Y. S., Jennings C., Hoffman A. M., Savel A. B., Sunseri J., Baer-Way R., Stahl B. E., et al., 2022, *MNRAS*, 514, 4489 - [35](#)

Muraveva T., Palmer M., Clementini G., Luri X., Cioni M.-R. L., Moretti M. I., Marconi M., et al., 2015, *ApJ*, 807, 127 - [38](#)

Muraveva T., Delgado H. E., Clementini G., Sarro L. M., Garofalo A., 2018, *MNRAS*, 481, 1195 - [41](#)

Musella I., Marconi M., Stetson P. B., Raimondo G., Brocato E., Molinaro R., Ripepi V., et al., 2016, *MNRAS*, 457, 3084 - [64](#), [172](#)

Muñoz R. R., Côté P., Santana F. A., Geha M., Simon J. D., Oyarzún G. A., Stetson P. B., et al., 2018, *ApJ*, 860, 66 - [27](#)

Myeong G. C., Evans N. W., Belokurov V., Sanders J. L., Koposov S. E., 2018, *ApJL*, 863, L28 - [16](#)

Myeong G. C., Vasiliev E., Iorio G., Evans N. W., Belokurov V., 2019, *MNRAS*, 488, 1235 - [28](#), [121](#)

Mérand A., Kervella P., Breifelder J., Gallenne A., Coudé du Foresto V., ten Brummelaar T. A., McAlister H. A., et al., 2015, *A&A*, 584, A80 - [42](#)

Naidu R. P., Conroy C., Bonaca A., Johnson B. D., Ting Y.-S., Caldwell N., Zaritsky D., et al., 2020, *ApJ*, 901, 48 - [17](#), [18](#), [19](#), [94](#), [112](#), [158](#), [159](#)

Nataf D. M., Udalski A., Gould A., Fouqué P., Stanek K. Z., 2010, *ApJL*, 721, L28 - [3](#)

Navarro J. F., Abadi M. G., Venn K. A., Freeman K. C., Anguiano B., 2011, *MNRAS*, 412, 1203 - [12](#)

- Neeley J. R., Marengo M., Bono G., Braga V. F., Dall’Ora M., Magurno D., Marconi M., et al., 2017, *ApJ*, 841, 84 - [48](#)
- Neeley J. R., Marengo M., Freedman W. L., Madore B. F., Beaton R. L., Hatt D., Hoyt T., et al., 2019, *MNRAS*, 490, 4254 - [46](#)
- Negueruela I., Monguió M., Marco A., Tabernero H. M., González-Fernández C., Dorda R., 2018, *MNRAS*, 477, 2976 - [180](#)
- Negueruela I., Dorda R., Marco A., 2020, *MNRAS*, 494, 3028 - [54](#), [70](#), [75](#), [180](#)
- Nelson D., Springel V., Pillepich A., Rodriguez-Gomez V., Torrey P., Genel S., Vogelsberger M., et al., 2019, *ComAC*, 6, 2 - [118](#)
- Nelson T., Ting Y.-S., Hawkins K., Ji A., Kamdar H., El-Badry K., 2021, *ApJ*, 921, 118 - [5](#)
- Nemec J. M., Smolec R., Benkó J. M., Moskalik P., Kolenberg K., Szabó R., Kurtz D. W., et al., 2011, *MNRAS*, 417, 1022 - [132](#)
- Nemec J. M., Cohen J. G., Ripepi V., Derekas A., Moskalik P., Sesar B., Chadid M., et al., 2013, *ApJ*, 773, 181 - [132](#)
- Nemec J. M., Nemec A. F. L., Lutz T. E., 1994, *AJ*, 108, 222 - [46](#)
- Nemec J. M., 1985a, *AJ*, 90, 204 - [44](#)
- Nemec J. M., 1985b, *AJ*, 90, 240 - [44](#)
- Ness M., Freeman K., 2016, *PASA*, 33, e022 - [3](#)
- Ness M., Freeman K., Athanassoula E., Wylie-de-Boer E., Bland-Hawthorn J., Asplund M., Lewis G. F., et al., 2013, *MNRAS*, 432, 2092 -
- Netopil M., Paunzen E., Heiter U., Soubiran C., 2016, *A&A*, 585, A150 - [64](#)
- Netzel H., Smolec R., Soszyński I., Udalski A., 2018, *MNRAS*, 480, 1229 - [45](#)
- Newberg H. J., Carlin J. L., 2016, *ASSL*, 420 - [28](#)
- Ngeow C.-C., Marconi M., Musella I., Cignoni M., Kanbur S. M., 2012a, *ApJ*, 745, 104 - [41](#)
- Ngeow C.-C., Kanbur S. M., Bellinger E. P., Marconi M., Musella I., Cignoni M., Lin Y.-H., 2012b, *Ap&SS*, 341, 105 - [41](#)
- Ngeow C.-C., Bhardwaj A., Dekany R., Duev D. A., Graham M. J., Groom S. L., Mahabal A. A., et al., 2022, *AJ*, 163, 239 - [46](#)
- Ngeow C.-C., 2012, *ApJ*, 747, 50 - [39](#)
- Nidever D. L., Dey A., Fasbender K., Juneau S., Meisner A. M., Wishart J., Scott A., et al., 2021, *AJ*, 161, 192 - [99](#)
- Nikiforova, V. V., Kulesh, M. V., Seleznev, A. F., Carraro, G. 2020. The Relation of the Alpha Persei Star Cluster with the Nearby Stellar Stream. *The Astronomical Journal* 160 - [24](#)
- Nissen P. E., Schuster W. J., 2010, *A&A*, 511, L10 - [13](#), [14](#), [17](#), [151](#), [155](#)
- Nissen P. E., Schuster W. J., 2011, *A&A*, 530, A15 - [17](#)
- Nissen P. E., Chen Y. Q., Carigi L., Schuster W. J., Zhao G., 2014, *A&A*, 568, A25 - [17](#)
- Nissen P. E., Høg E., Schuster W. J., 1997, *ESASP*, 402, 225 - [130](#), [137](#)
- Nomoto K., Tominaga N., Umeda H., Kobayashi C., Maeda K., 2006, *NuPhA*, 777, 424 - [12](#)
- Nowakowski R. M., Dziembowski W. A., 2003, *Ap&SS*, 284, 273 - [45](#)
- Oh S., Kroupa P., Pflamm-Altenburg J., 2015, *ApJ*, 805, 92 - [24](#)
- Oluseyi H. M., Becker A. C., Culliton C., Furqan M., Hoadley K. L., Regencia P., Wells A. J., et al., 2012, *AJ*, 144, 9 - [173](#), [174](#), [176](#)
- Oort J. H., Kerr F. J., Westerhout G., 1958, *MNRAS*, 118, 379 - [21](#)
- Oort J. H., 1926, “Stars of High Velocity”, *Publications of the Kapteyn Astronomical Laboratory Groningen*, vol. 40, pp.1-75 - [4](#)

Oosterhoff P. T., 1939, *The Observatory*, 62, 104 - [46](#), [103](#), [156](#)

Oser L., Ostriker J. P., Naab T., Johansson P. H., Burkert A., 2010, *ApJ*, 725, 2312 - [19](#)

Ostriker J. P., Choi E., Chow A., Guha K., 2019, *ApJ*, 885, 97 - [28](#)

Palacios A., Talon S., Charbonnel C., Forestini M., 2003, *A&A*, 399, 603 - [23](#)

Palmer D. M., 2009, *ApJ*, 695, 496 - [35](#)

Pancino E., Britavskiy N., Romano D., Cacciari C., Mucciarelli A., Clementini G., 2015, *MNRAS*, 447, 2404 - [49](#), [95](#), [122](#)

Pandey B., 2022, arXiv, arXiv:2204.08425 - [18](#), [94](#), [174](#)

Pang X., Li Y., Tang S.-Y., Pasquato M., Kouwenhoven M. B. N., 2020, *ApJL*, 900, L4 - [60](#)

Parada J., Heyl J., Richer H., Riposte P., Rousseau-Nepton L., 2021, *MNRAS*, 501, 933 - [41](#)

Parmentier G., Baumgardt H., 2012, *MNRAS*, 427, 1940 - [21](#)

Pasquini L., Randich S., Zoccali M., Hill V., Charbonnel C., Nordström B., 2004, *A&A*, 424, 951 - [23](#)

Paxton B., Bildsten L., Dotter A., Herwig F., Lesaffre P., Timmes F., 2011, *ApJS*, 192, 3 - [25](#), [78](#)

Paxton B., Cantiello M., Arras P., Bildsten L., Brown E. F., Dotter A., Mankovich C., et al., 2013, *ApJS*, 208, 4 - [25](#), [78](#)

Payne-Gaposchkin C. H., 1974, *SCoA*, 16 - [53](#)

Pearson S., Price-Whelan A. M., Johnston K. V., 2017, *NatAs*, 1, 633 - [30](#)

Peebles P. J. E., 1965, *ApJ*, 142, 1317 - [28](#)

Pel J. W., 1985, *IAU Colloq. 82: Cepheids: Theory and Observation*, 1 - [180](#)

Penzias A. A., Wilson R. W., 1965, *ApJ*, 142, 419 - [10](#)

Perryman M. A. C., Lindegren L., Kovalevsky J., Hoeg E., Bastian U., Bernacca P. L., Crézé M., et al., 1997, *A&A*, 323, L49 - [41](#)

Peña J. H., Arellano Ferro A., Peña Miller R., Sareyan J. P., Álvarez M., 2009, *RMxAA*, 45, 191 - [143](#)

Peña Ramírez K., González-Fernández C., Chené A.-N., Ramírez Alegría S., 2021, *MNRAS*, 503, 1864 - [90](#)

Peñarrubia J., 2021, *MNRAS*, 501, 3670 - [30](#)

Pietrzyński G., Gieren W., Fouqué P., Pont F., 2002, *AJ*, 123, 789 - [53](#)

Pietrzyński G., Graczyk D., Gallenne A., Gieren W., Thompson I. B., Pilecki B., Karczmarek P., et al., 2019, *Natur*, 567, 200 - [148](#)

Pila-Díez B., de Jong J. T. A., Kuijken K., van der Burg R. F. J., Hoekstra H., 2015, *A&A*, 579, A38 - [116](#), [117](#)

Pillepich A., Vogelsberger M., Deason A., Rodriguez-Gomez V., Genel S., Nelson D., Torrey P., et al., 2014, *MNRAS*, 444, 237 - [17](#), [18](#), [48](#), [94](#), [112](#), [118](#)

Pillepich A., Nelson D., Hernquist L., Springel V., Pakmor R., Torrey P., Weinberger R., et al., 2018, *MNRAS*, 475, 648 - [118](#)

Piskunov N. E., Kupka F., Ryabchikova T. A., Weiss W. W., Jeffery C. S., 1995, *A&AS*, 112, 525 - [138](#)

Piskunov A. E., Belikov A. N., Kharchenko N. V., Sagar R., Subramaniam A., 2004, *MNRAS*, 349, 1449 - [90](#), [173](#)

Planck Collaboration, Aghanim N., Akrami Y., Ashdown M., Aumont J., Baccigalupi C., Ballardini M., et al., 2020, *A&A*, 641, A5 - [10](#)

Poggio E., Drimmel R., Cantat-Gaudin T., Ramos P., Ripepi V., Zari E., Andrae R., et al., 2021, *A&A*, 651, A104 - [42](#)

Pojmanski G., Maciejewski G., 2004, *AcA*, 54, 153 - [70](#)

Pont F., Zucker S., Queloz D., 2006, *MNRAS*, 373, 231 - [33](#)

Popescu B., Hanson M. M., 2010, ApJ, 724, 296 - [85](#)

Porras A., Christopher M., Allen L., Di Francesco J., Megeath S. T., Myers P. C., 2003, AJ, 126, 1916 - [24](#)

Portail M., Wegg C., Gerhard O., Ness M., 2017, MNRAS, 470, 1233 - [3](#)

Prada J., Forero-Romero J. E., Grand R. J. J., Pakmor R., Springel V., 2019, MNRAS, 490, 4877 - [118](#)

Prantzos N., 2008, A&A, 489, 525 - [101](#), [145](#)

Prantzos N., 2008, A&A, 489, 525 - [101](#), [145](#)

Press W. H., Schechter P., 1974, ApJ, 187, 425 - [2](#), [93](#)

Preston, G. W. & Sneden, C. 2000, AJ, 120, 1014 - [129](#)

Preston G. W., Sneden C., Chadid M., Thompson I. B., Shectman S. A., 2019, AJ, 157, 153 - [215](#)

Preston, G. W. 1959, ApJ, 130, 507 - [43](#), [122](#)

Price-Jones N., Bovy J., Webb J. J., Allende Prieto C., Beaton R., Brownstein J. R., Cohen R. E., et al., 2020, MNRAS, 496, 5101 - [5](#), [26](#)

Price-Whelan A. M., Johnston K. V., Sheffield A. A., Laporte C. F. P., Sesar B., 2015, MNRAS, 452, 676 - [49](#)

Price-Whelan A. M., Mateu C., Iorio G., Pearson S., Bonaca A., Belokurov V., 2019, AJ, 158, 223 - [48](#)

Principe J. C., 2010, Information Theoretic Learning, Springer, ISBN: 978-1-4419-1569-6 - [35](#)

Prisinzano, L., Damiani, F., Sciortino, S., Flaccomio, E., Guarcello, M.G., Micela, G., and, ...: 2022, arXiv, arXiv:2206.00249. [23](#)

Protopapas P., Huijse P., Estévez P. A., Zegers P., Príncipe J. C., Marquette J.-B., 2015, ApJS, 216, 25 - [35](#)

Prudil Z., Skarka M., 2017, MNRAS, 466, 2602 - [45](#)

Prudil Z., Dékány I., Catelan M., Smolec R., Grebel E. K., Skarka M., 2019a, MNRAS, 484, 4833 - [46](#), [48](#), [94](#)

Prudil Z., Dékány I., Grebel E. K., Catelan M., Skarka M., Smolec R., 2019b, MNRAS, 487, 3270 - [46](#)

Prudil Z., Hanke M., Lemasle B., Crestani J., Braga V. F., Fabrizio M., Koch-Hansen A. J., et al., 2021, A&A, 648, A78 - [43](#), [48](#), [61](#), [94](#), [165](#)

Prudil Z., Hanke M., Lemasle B., Crestani J., Braga V. F., Fabrizio M., Koch-Hansen A. J., et al., 2021, A&A, 648, A78 - [43](#), [48](#), [61](#), [94](#), [165](#)

Prudil Z., Koch-Hansen A. J., Lemasle B., Grebel E. K., Marchetti T., Hansen C. J., Crestani J., et al., 2022, arXiv, arXiv:2206.00417 - [49](#), [95](#)

Psaltis A., Arcones A., Montes F., Mohr P., Hansen C. J., Jacobi M., Schatz H., 2022, arXiv, arXiv:2204.07136 - [13](#)

Queiroz A. B. A., Anders F., Chiappini C., Khalatyan A., Santiago B. X., Steinmetz M., Valentini M., et al., 2020, A&A, 638, A76 - [151](#)

Quillen A. C., Nolting E., Minchev I., De Silva G., Chiappini C., 2018, MNRAS, 475, 4450 - [24](#)

Racine R., 1971, AJ, 76, 321 - [37](#)

Ramos P., Mateu C., Antoja T., Helmi A., Castro-Ginard A., Balbinot E., Carrasco J. M., 2020, A&A, 638, A104 - [163](#)

Randich S., Gilmore G., Magrini L., Sacco G. G., Jackson R. J., Jeffries R. D., Worley C. C., et al., 2022, arXiv, arXiv:2206.02901 - [23](#)

Recio-Blanco A., Piotto G., de Angeli F., Cassisi S., Riello M., Salaris M., Pietrinferni A., et al., 2005, A&A, 432, 851 - [26](#)

Recio-Blanco A., de Laverny P., Palicio P. A., Kordopatis G., Álvarez M. A., Schultheis M., Contursi G., et al., 2022, arXiv, arXiv:2206.05541 - [23](#)

Reddy B. E., Lambert D. L., Allende Prieto C., 2006, MNRAS, 367, 1329 - [16](#)

Ricker G. R., Winn J. N., Vanderspek R., Latham D. W., Bakos G. Á., Bean J. L., Berta-Thompson Z. K., et al., 2015, JATIS, 1, 014003 - [6](#)

- Riess A. G., Filippenko A. V., Challis P., Clocchiatti A., Diercks A., Garnavich P. M., Gilliland R. L., et al., 1998, *AJ*, 116, 1009 - [41](#)
- Riess A. G., Macri L., Casertano S., Lampeitl H., Ferguson H. C., Filippenko A. V., Jha S. W., et al., 2011, *ApJ*, 730, 119 - [41](#)
- Riess A. G., Macri L. M., Hoffmann S. L., Scolnic D., Casertano S., Filippenko A. V., Tucker B. E., et al., 2016, *ApJ*, 826, 56 - [39](#), [41](#)
- Riess A. G., Casertano S., Yuan W., Macri L., Anderson J., MacKenty J. W., Bowers J. B., et al., 2018, *ApJ*, 855, 136 - [54](#)
- Rimoldini L., Holl B., Audard M., Mowlavi N., Nienartowicz K., Evans D. W., Guy L. P., et al., 2019, *A&A*, 625, A97 - [107](#)
- Ripepi V., Molinaro R., Musella I., Marconi M., Leccia S., Eyer L., 2019, *A&A*, 625, A14 - [39](#), [57](#), [67](#), [70](#), [83](#), [89](#)
- Ripepi V., Catanzaro G., Molinaro R., Marconi M., Clementini G., Cusano F., De Somma G., et al., 2020, *A&A*, 642, A230 - [41](#)
- Ripepi V., Catanzaro G., Clementini G., De Somma G., Drimmel R., Leccia S., Marconi M., et al., 2022a, *A&A*, 659, A167 - [39](#), [40](#), [57](#)
- Ripepi V., Clementini G., Molinaro R., Leccia S., Plachy E., Molnár L., Rimoldini L., et al., 2022b, *arXiv*, arXiv:2206.06212 - [8](#)
- Ripepi V., Clementini G., Molinaro R., Leccia S., Plachy E., Molnár L., Rimoldini L., et al., 2022, *arXiv*, arXiv:2206.06212 - [39](#), [40](#), [57](#)
- Ritter A., 1879, *AnP*, 244, 157 - [39](#)
- Robertson B., Bullock J. S., Font A. S., Johnston K. V., Hernquist L., 2005, *ApJ*, 632, 872 - [158](#)
- Robichon N., Arenou F., Mermilliod J.-C., Turon C., 1999, *A&A*, 345, 471 - [61](#)
- Robin A. C., Reylé C., Derrière S., Picaud S., 2003, *A&A*, 409, 523 - [85](#)
- Robin A. C., Marshall D. J., Schultheis M., Reylé C., 2012, *A&A*, 538, A106 - [3](#)
- Robin A. C., Reylé C., Fliri J., Czekaj M., Robert C. P., Martins A. M. M., 2014, *A&A*, 569, A13 - [85](#)
- Robinson E., von Hippel T., Stein N., Stenning D., Wagner-Kaiser R., Si S., van Dyk D., 2016, *ascl.soft*. ascl:1608.007 -
- Rodriguez Wimberly M. K., Cooper M. C., Baxter D. C., Boylan-Kolchin M., Bullock J. S., Fillingham S. P., Ji A. P., et al., 2021, *arXiv*, arXiv:2109.00633 - [49](#), [174](#)
- Rodriguez-Gomez V., Pillepich A., Sales L. V., Genel S., Vogelsberger M., Zhu Q., Wellons S., et al., 2016, *MNRAS*, 458, 2371 - [18](#)
- Roederer I. U., Mateo M., Bailey J. I., Spencer M., Crane J. D., Sheckman S. A., 2016, *MNRAS*, 455, 2417 - [28](#)
- Roederer I. U., Hattori K., Valluri M., 2018, *AJ*, 156, 179 - [155](#)
- Roeser S., Demleitner M., Schilbach E., 2010, *AJ*, 139, 2440 - [62](#), [78](#)
- Romaniello M., Primas F., Mottini M., Pedicelli S., Lemasle B., Bono G., François P., et al., 2008, *A&A*, 488, 731 - [62](#)
- Rozier S., Famaey B., Siebert A., Monari G., Pichon C., Ibata R., 2022, *arXiv*, arXiv:2201.05589 - [118](#)
- Russell, H. N., 1914, *Popular Astronomy*, 22, 275-294 - [11](#)
- Ryabchikova T., Piskunov N., Kurucz R. L., Stempels H. C., Heiter U., Pakhomov Y., Barklem P. S., 2015, *PhyS*, 90, 054005 - [138](#)
- Röck, B., 2012, “Calibration of new period-age relations by studying Cepheids in open clusters of the Milky Way and the Magellanic Clouds”, Master thesis, Univ. Heidelberg - [67](#), [180](#)
- Röser S., Schilbach E., 2019, *A&A*, 627, A4 - [24](#)
- Röser S., Kharchenko N. V., Piskunov A. E., Schilbach E., Scholz R.-D., Zinnecker H., 2010, *AN*, 331, 519 - [85](#)
- Saha, A. 1985, *ApJ*, 289, 310 - [112](#)

Sakari C. M., Placco V. M., Hansen T., Holmbeck E. M., Beers T. C., Frebel A., Roederer I. U., et al., 2018a, *ApJL*, 854, L20 - [14](#), [155](#)

Sakari C. M., Placco V. M., Farrell E. M., Roederer I. U., Wallerstein G., Beers T. C., Ezzeddine R., et al., 2018b, *ApJ*, 868, 110 - [14](#)

Sakari C. M., Roederer I. U., Placco V. M., Beers T. C., Ezzeddine R., Frebel A., Hansen T., et al., 2019, *ApJ*, 874, 148 - [153](#), [155](#)

Salpeter E. E., 1955, *ApJ*, 121, 161 - [11](#), [85](#), [86](#)

Samus' N. N., Kazarovets E. V., Durlevich O. V., Kireeva N. N., Pastukhova E. N., 2017, *ARep*, 61, 80 - [57](#)

Sandage A., Tammann G. A., 2006, *ARA&A*, 44, 93 - [39](#)

Sandage A., 1958, *ApJ*, 128, 150 - [67](#), [180](#)

Sandage A., 1981, *ApJ*, 248, 161 - [48](#)

Sandage A., 1990, *ApJ*, 350, 631 - [45](#)

Sanderson, R. E., Secunda, A., Johnston, K. V., et al. 2017, *MNRAS*, 470, 5014 - [94](#), [95](#), [110](#), [117](#), [123](#), [176](#)

Sanders W. L., 1971, *A&A*, 14, 226 - [25](#)

Sandquist E. L., 2004, *MNRAS*, 347, 101 - [37](#)

Sarro L. M., Bouy H., Berihuete A., Bertin E., Moraux E., Bouvier J., Cuillandre J.-C., et al., 2014, *A&A*, 563, A45 - [25](#)

Sawala T., Frenk C. S., Fattahi A., Navarro J. F., Bower R. G., Crain R. A., Dalla Vecchia C., et al., 2016, *MNRAS*, 457, 1931 - [28](#)

Scargle J. D., 1982, *ApJ*, 263, 835 - [35](#)

Schlafly E. F., Finkbeiner D. P., 2011, *ApJ*, 737, 103 - [99](#), [136](#)

Schlaufman K. C., Rockosi C. M., Allende Prieto C., Beers T. C., Bizyaev D., Brewington H., Lee Y. S., et al., 2009, *ApJ*, 703, 2177 - [94](#)

Schlaufman K. C., Thompson I. B., Casey A. R., 2018, *ApJ*, 867, 98 - [10](#)

Schmeja S., 2011, *AN*, 332, 172 - [25](#)

Schmidt E. G., 1982, *AJ*, 87, 1197 - [180](#)

Schultz G. V., Wiemer W., 1975, *A&A*, 43, 133 - [79](#), [136](#)

Schwarzschild, M. 1940, *Harvard College Observatory Circular*, 437, 1 - [43](#)

Schwarzenberg-Czerny A., 1996, *ApJL*, 460, L107 - [35](#)

Schweizer F., Seitzer P., 1998, *AJ*, 116, 2206 - [26](#)

Schönrich R., Asplund M., Casagrande L., 2011, *MNRAS*, 415, 3807 - [17](#)

Searle L., Zinn R., 1978, *ApJ*, 225, 357 - [2](#), [19](#)

Seleznev A. F., 2016, *MNRAS*, 456, 3757 - [21](#), [25](#)

Senchyna P., Johnson L. C., Dalcanton J. J., Beerman L. C., Fouesneau M., Dolphin A., Williams B. F., et al., 2015, *ApJ*, 813, 31 - [40](#), [54](#), [87](#), [90](#), [172](#)

Sesar B., Ivezić Ž., Lupton R. H., Jurić M., Gunn J. E., Knapp G. R., DeLee N., et al., 2007, *AJ*, 134, 2236 - [95](#)

Sesar B., Ivezić Ž., Grammer S. H., Morgan D. P., Becker A. C., Jurić M., De Lee N., et al., 2010, *ApJ*, 708, 717 - [48](#), [94](#), [95](#), [103](#), [109](#), [125](#)

Sesar, B., Jurić, M., & Ivezić, Ž. 2011, *ApJ*, 731, 4 - [17](#), [94](#), [112](#), [116](#)

Sesar B., Ivezić Ž., Stuart J. S., Morgan D. M., Becker A. C., Sharma S., Palaversa L., et al., 2013a, *AJ*, 146, 21 - [48](#)

Sesar B., Grillmair C. J., Cohen J. G., Bellm E. C., Bhalerao V. B., Levitan D., Laher R. R., et al., 2013b, *ApJ*, 776, 26 - [48](#)

Sesar B., Banholzer S. R., Cohen J. G., Martin N. F., Grillmair C. J., Levitan D., Laher R. R., et al., 2014, *ApJ*, 793, 135 - [48](#), [94](#), [117](#)

Sesar B., Hernitschek N., Mitrović S., Ivezić Ž., Rix H.-W., Cohen J. G., Bernard E. J., et al., 2017, *AJ*, 153, 204 - [44](#), [46](#), [49](#), [95](#), [101](#), [107](#), [122](#), [145](#)

Sesar B., 2012, *AJ*, 144, 114 - [43](#), [104](#), [105](#), [129](#), [130](#)

Shapley H., 1914, *ApJ*, 40, 448 - [45](#)

Shapley H., 1916, *ApJ*, 43, 217 - [45](#)

Sharma S., Ghosh A., Ojha D. K., Pandey R., Sinha T., Pandey A. K., Ghosh S. K., et al., 2020, *MNRAS*, 498, 2309 - [24](#), [171](#)

Sharma S., Hayden M. R., Bland-Hawthorn J., 2021, *MNRAS*, 507, 5882 - [16](#)

Shen J., Rich R. M., Kormendy J., Howard C. D., De Propriis R., Kunder A., 2010, *ApJL*, 720, L72 - [3](#)

Shipp N., Drlica-Wagner A., Balbinot E., Ferguson P., Erkal D., Li T. S., Bechtol K., et al., 2018, *ApJ*, 862, 114 - [30](#), [162](#)

Shipp N., Price-Whelan A. M., Tavangar K., Mateu C., Drlica-Wagner A., 2020, *AJ*, 160, 244 - [28](#)

Shipp N., Erkal D., Drlica-Wagner A., Li T. S., Pace A. B., Koposov S. E., Cullinane L. R., et al., 2021, arXiv, arXiv:2107.13004 - [148](#)

Shipp N., 2022, AAS Division on Dynamical Astronomy meeting 53, id. 203.04, 54, 4 - [30](#)

Shukirgaliyev B., Parmentier G., Just A., Berczik P., 2018, *ApJ*, 863, 171 - [22](#), [24](#), [91](#)

Siess L., Livio M., Lattanzio J., 2002, *ApJ*, 570, 329 - [10](#)

Sim G., Lee S. H., Ann H. B., Kim S., 2019, *JKAS*, 52, 145 - [24](#), [56](#), [59](#), [78](#), [182](#)

Simion I. T., Belokurov V., Irwin M., Koposov S. E., 2014, *MNRAS*, 440, 161 - [48](#)

Simon J. D., Geha M., 2007, *AAS* - [28](#)

Simon N. R., 1989, *ApJL*, 343, L17 - [137](#)

Simon J. D., 2019, *ARA&A*, 57, 375 - [1](#), [27](#), [175](#)

Singh D., Hansen C. J., Byrgesen J. S., Reichert M., Reggiani H. M., 2020, *A&A*, 634, A72 - [131](#), [132](#), [134](#)

Sitnova T. M., Mashonkina L. I., Ryabchikova T. A., 2013, *AstL*, 39, 126 - [145](#)

Skarka M., Prudil Z., Jurcsik J., 2020, *MNRAS*, 494, 1237 - [45](#)

Skowron D. M., Skowron J., Mróz P., Udalski A., Pietrukowicz P., Soszyński I., Szymański M. K., et al., 2019a, *Sci*, 365, 478 - [42](#), [53](#), [57](#)

Skowron D. M., Skowron J., Mróz P., Udalski A., Pietrukowicz P., Soszyński I., Szymański M. K., et al., 2019b, *AcA*, 69, 305 - [57](#)

Skrutskie M. F., Cutri R. M., Stiening R., Weinberg M. D., Schneider S., Carpenter J. M., Beichman C., et al., 2006, *AJ*, 131, 1163 - [6](#), [99](#)

Slater C. T., Nidever D. L., Munn J. A., Bell E. F., Majewski S. R., 2016, *ApJ*, 832, 206 - [18](#)

Smiljanic R., Gauderon R., North P., Barbuy B., Charbonnel C., Mowlavi N., 2009, *A&A*, 502, 267 - [23](#)

Smith H. A., 1995, *Cambridge Astrophysics Series*, Vol. 27, RR Lyrae Stars. Cambridge Univ. Press, Cambridge, UK - [42](#), [43](#), [46](#)

Smith H. A., 2004, *RR Lyrae Stars*, Cambridge, UK: Cambridge University Press, ISBN 0521548179, 166 - [43](#)

Smolec R., Moskalik P., Kolenberg K., Bryson S., Cote M. T., Morris R. L., 2011, *MNRAS*, 414, 2950 - [45](#)

Smolec R., 2005, *AcA*, 55, 59 - [45](#), [122](#), [132](#)

Snedden C., Bean J., Ivans I., Lucatello S., Sobeck J., 2012, *Astrophysics Source Code Library*, record ascl:1202.009 - [6](#)

Snedden C., Preston G. W., Chadid M., Adamów M., 2017, *ApJ*, 848, 68 - [122](#), [134](#), [157](#)

- Snedden C., Cowan J. J., Gallino R., 2008, *ARA&A*, 46, 241 - 14
- Snedden, C. 1973, *ApJ*, 184, 839 - 138
- Soderblom D. R., 2010, *ARA&A*, 48, 581 - 88
- Soker N., 2019, *NewAR*, 87, 101535 - 13
- Sollima A., Cacciari C., Valenti E., 2006, *MNRAS*, 372, 1675 - 46
- Sollima A., 2020, *MNRAS*, 495, 2222 - 24, 162
- Soszyński I., Udalski A., Szymański M. K., Pietrukowicz P., Mróz P., Skowron J., Kozłowski S., et al., 2014, *AcA*, 64, 177 - 43
- Soszyński I., Udalski A., Szymański M. K., Wyrzykowski Ł., Ulaczyk K., Poleski R., Pietrukowicz P., et al., 2016, *AcA*, 66, 131 - 33, 107, 157
- Soszyński I., Udalski A., Szymański M. K., Wyrzykowski Ł., Ulaczyk K., Poleski R., Pietrukowicz P., et al., 2017, *AcA*, 67, 297 - 57
- Soszyński I., Udalski A., Szymański M. K., Pietrukowicz P., Skowron J., Skowron D. M., Poleski R., et al., 2020, *AcA*, 70, 101 - 57, 171
- Soubiran C., Cantat-Gaudin T., Romero-Gómez M., Casamiquela L., Jordi C., Vallenari A., Antoja T., et al., 2018, *A&A*, 619, A155 - 23
- Sparke L. S., Gallagher J. S., 2007, *Galaxies in the Universe: An Introduction*. Second Edition. ISBN-13 978-0-521-85593-8 (HB); ISBN-13 978-0-521-67186-6 (PB), Cambridge University Press, Cambridge, UK, 2007 - 1, 16, 26
- Spera M., Mapelli M., Jeffries R. D., 2016, *MNRAS*, 460, 317 - 24
- Spitoni E., Cescutti G., Minchev I., Matteucci F., Silva Aguirre V., Martig M., Bono G., et al., 2019, *A&A*, 628, A38 - 16, 42
- Spitzer L., 1969, *ApJL*, 158, L139 - 24
- Spoo T., Tayar J., Frinchaboy P. M., Cunha K., Myers N., Donor J., Majewski S. R., et al., 2022, *AJ*, 163, 229 - 23
- Springel V., Wang J., Vogelsberger M., Ludlow A., Jenkins A., Helmi A., Navarro J. F., et al., 2008, *MNRAS*, 391, 1685 - 28
- Stauffer J. R., Schultz G., Kirkpatrick J. D., 1998, *ApJL*, 499, L199 - 87
- Stefan, J., 1879, Über die Beziehung zwischen der Wärmestrahlung und der Temperatur. In: *Sitzungsberichte der mathematisch-naturwissenschaftlichen Classe der kaiserlichen Akademie der Wissenschaften*. Bd. 79 (Wien 1879), S. 391â€428 - 38
- Steinmetz M., Zwitter T., Siebert A., Watson F. G., Freeman K. C., Munari U., Campbell R., et al., 2006, *AJ*, 132, 1645 - 7
- Stellingwerf R. F., 1975, *ApJ*, 195, 441 - 48
- Stellingwerf R. F., 1978, *ApJ*, 224, 953 - 35
- Stetson P. B., Braga V. F., Dall'Ora M., Bono G., Buonanno R., Ferraro I., Iannicola G., et al., 2014, *PASP*, 126, 521 - 43
- Storm J., Gieren W., Fouqué P., Barnes T. G., Pietrzyński G., Nardetto N., Weber M., et al., 2011, *A&A*, 534, A94 - 62
- Stothers R. B., 2006, *ApJ*, 652, 643 - 45
- Stott J. J., 2018, *A&A*, 609, A36 - 25
- Stringer K. M., Drlica-Wagner A., Macri L., Martínez-Vázquez C. E., Vivas A. K., Ferguson P., Pace A. B., et al., 2021, *ApJ*, 911, 109 - 17, 18, 49, 94, 95, 105, 108, 116, 117, 122
- Suntzeff N. B., Kinman T. D., Kraft R. P., 1991, *ApJ*, 367, 528 - 101, 145
- Suntzeff N. B., Kinman T. D., Kraft R. P., 1991, *ApJ*, 367, 528 - 101, 145
- Szeidl B., 1988, *Multimode Stellar Pulsations*, Proceedings of the Workshop, held in Budapest, September 1-3, 1987. Edited by G. Kovacs, L. Szabados and B. Szeidl. Budapest: Konkoly Observatory, Kultura, 1988., p. 45 - 45, 123

Sánchez N., Alfaro E. J., López-Martínez F., 2020, MNRAS, 495, 2882 - [58](#)

Sánchez-Sáez P., Reyes I., Valenzuela C., Förster F., Eyheramendy S., Elorrieta F., Bauer F. E., et al., 2021, AJ, 161, 141 - [174](#)

Takada M., Ellis R. S., Chiba M., Greene J. E., Aihara H., Arimoto N., Bundy K., et al., 2014, PASJ, 66, R1 - [173](#), [175](#)

Talon S., Charbonnel C., 2003, A&A, 405, 1025 - [23](#)

Tammann G. A., 1970, IAUS, 38, 236 - [40](#)

Tamura N., 2016, IAUS, 319, 55 - [175](#)

Tanikawa A., Yoshikawa K., Okamoto T., Nitadori K., 2012, NewA, 17, 82 - [24](#)

Tarricq Y., Soubiran C., Casamiquela L., Cantat-Gaudin T., Chemin L., Anders F., Antoja T., et al., 2021, A&A, 647, A19 - [23](#)

Testa V., Marconi M., Musella I., Ripepi V., Dall’Ora M., Ferraro F. R., Mucciarelli A., et al., 2007, A&A, 462, 599 - [172](#)

The Dark Energy Survey Collaboration, 2005, arXiv, astro-ph/0510346 - [6](#), [96](#)

Thomas G. F., Famaey B., Ibata R., Lüghausen F., Kroupa P., 2017, A&A, 603, A65 - [30](#)

Thomas G. F., McConnachie A. W., Ibata R. A., Côté P., Martin N., Starkenburg E., Carlberg R., et al., 2018, MNRAS, 481, 5223 - [94](#)

Tian H.-J., 2020, ApJ, 904, 196 - [60](#)

Tinsley B. M., Larson R. B., 1978, ApJ, 221, 554 - [153](#)

Tinsley B. M., 1979, ApJ, 229, 1046 - [13](#)

Tody, D. 1993, Astronomical Data Analysis Software and Systems II, 173 - [129](#)

Tognelli E., Prada Moroni P. G., Degl’Innocenti S., Salaris M., Cassisi S., 2020, A&A, 638, A81 - [23](#)

Tolstoy E., Hill V., Tosi M., 2009, ARA&A, 47, 371 - [13](#)

Tomozeiu M., Mayer L., Quinn T., 2016, ApJL, 827, L15 - [28](#)

Tonry J. L., Stubbs C. W., Lykke K. R., Doherty P., Shivvers I. S., Burgett W. S., Chambers K. C., et al., 2012, ApJ, 750, 99 - [136](#), [137](#)

Tonry J. L., Denneau L., Flewelling H., Heinze A. N., Onken C. A., Smartt S. J., Stalder B., et al., 2018, ApJ, 867, 105 - [99](#)

Torrealba G., Catelan M., Drake A. J., Djorgovski S. G., McNaught R. H., Belokurov V., Koposov S., et al., 2015, MNRAS, 446, 2251 - [48](#), [94](#), [95](#), [105](#), [122](#), [123](#)

Torrealba G., Koposov S. E., Belokurov V., Irwin M., 2016, MNRAS, 459, 2370 - [27](#)

Torrealba G., Belokurov V., Koposov S. E., Li T. S., Walker M. G., Sanders J. L., Geringer-Sameth A., et al., 2019, MNRAS, 488, 2743 - [21](#), [27](#), [28](#), [48](#), [94](#), [176](#)

Torrealba G., Belokurov V., Koposov S. E., 2019, MNRAS, 484, 2181 - [55](#), [56](#), [59](#), [74](#)

Torres G., 2010, AJ, 140, 1158 - [137](#)

Trahin B., Breuval L., Kervella P., Mérand A., Nardetto N., Gallenne A., Hocdé V., et al., 2021, A&A, 656, A102 - [42](#)

Trippella O., Busso M., Palmerini S., Maiorca E., Nucci M. C., 2016, ApJ, 818, 125 - [14](#)

Trumpler R. J., 1930, LicOB, 420, 154 - [25](#)

Tsarevsky G. S., Ureche V., Efremov Y. N., 1966, ATsir, 367 - [70](#)

Tsujimoto T., Miyamoto M., Yoshii Y., 1998, ApJL, 492, L79 - [107](#)

Turner D. G., Burke J. F., 2002, AJ, 124, 2931 - [54](#), [180](#)

Turner D. G., Pedreros M., 1985, AJ, 90, 1231 - [180](#)

Turner D. G., van den Bergh S., Younger P. F., Danks T. A., Forbes D., 1993, ApJS, 85, 119 - [180](#)

- Turner D. G., Ibrahimov M. A., Mandushev G. I., Berdnikov L. N., Horsford A. J., 1998b, *JRASC*, 92, 145 - 54, 71, 180
- Turner D. G., Forbes D., van den Bergh S., Younger P. F., Berdnikov L. N., 2005, *AJ*, 130, 1194 - 54
- Turner D. G., Forbes D., English D., Leonard P. J. T., Scrimger J. N., Wehlau A. W., Phelps R. L., et al., 2008, *MNRAS*, 388, 444 - 54, 71, 180
- Turner D. G., van den Bergh S., Younger P. F., Majaess D. J., Pedreros M. H., Berdnikov L. N., 2012, *AJ*, 144, 187 - 73
- Turner D. G., Forbes D., Pedreros M., 1992, *AJ*, 104, 1132 - 54, 180
- Turner D. G., Pedreros M. H., Walker A. R., 1998c, *AJ*, 115, 1958 - 180
- Turner D. G., 1976, *AJ*, 81, 1125 - 180
- Turner D. G., 1977, *PASP*, 89, 277 - 73
- Turner D. G., 1980, *ApJ*, 240, 137 - 71, 180
- Turner D. G., 1981, *AJ*, 86, 231 - 180
- Turner D. G., 1982, *PASP*, 94, 1003 - 180
- Turner D. G., 1984, *JRASC*, 78, 229 - 70, 75
- Turner D. G., 1986, *AJ*, 92, 111 - 54, 180
- Turner D. G., 1996, *JRASC*, 90, 82 - 35
- Turner D. G., 1998, *AJ*, 116, 274 - 70, 180
- Turner D. G., 2010, *Ap&SS*, 326, 219 - 41, 54, 69, 71, 180
- Tyson J. A., 2019, *JPhCS*, 1290, 012001 - 5
- Udalski A., Soszyński I., Pietrukowicz P., Szymański M. K., Skowron D. M., Skowron J., Mróz P., et al., 2018, *AcA*, 68, 315 - 57, 69, 83, 89
- Udalski A., Szymański M. K., Szymański G., 2015, *AcA*, 65, 1 - 6, 57
- Ulaczyk K., Szymański M. K., Udalski A., Kubiak M., Pietrzyński G., Soszyński I., Wyrzykowski Ł., et al., 2013, *AcA*, 63, 159 - 36
- Umeda H., Nomoto K., 2003, *Natur*, 422, 871 - 10
- Usenko I. A., Kniazev A. Y., Katkov I. Y., Kovtyukh V. V., Mishenina T. V., Miroshnichenko A. S., Turner D. G., 2019, *OAP*, 32, 91 - 54, 70
- Valdes, F., Gruendl, R., & DES Project 2014, *Astronomical Data Analysis Software and Systems XXIII*, 485, 379 - 96
- van Albada T. S., Baker N., 1973, *ApJ*, 185, 477 - 48
- van den Bergh S., 1957, *ApJ*, 126, 323 - 21, 54
- van den Bergh S., 1958, *ZA*, 46, 176 - 23
- van den Bergh S., 1993, *AJ*, 105, 971 - 46
- van den Bergh S., 2008, *MNRAS*, 390, L51 - 21
- van der Marel R. P., Kallivayalil N., 2014, *ApJ*, 781, 121 - 145, 148
- van der Marel R. P., Alves D. R., Hardy E., Suntzeff N. B., 2002, *AJ*, 124, 2639 - 148, 157
- van der Walt S., Colbert S. C., Varoquaux G., 2011, *Computing in Science and Engineering*, 13, 22 -
- van Leeuwen F., 2007, *Hipparcos, the New Reduction of the Raw Data: Astrophysics and Space Science Library*, Vol. 350, Springer Science+Business Media B.V., Berlin - 62
- VanderPlas, J. T., & Ivezić, Ž. 2015, *ApJ*, 812, 18 - 103, 109, 125
- VanderPlas J., Connolly A. J., Ivezić Z., Gray A., 2012, in *Proc. Conf. Intelligent Data Understanding (CIDU)*, ed. K. Das, N.V. Chawla, & A. N. Srivastava (Boulder, CO: NCAR), 47 - 101

VanderPlas, J., Connolly, A. J., Ivezić, Z., et al. 2012, in Proc. Conf. Intelligent Data Understanding (CIDU), ed. K. Das, N.V. Chawla, & A. N. Srivastava (Boulder, CO: NCAR), 47 - 101

Vanderplas J., 2015, zndo - [103](#), [109](#)

Vasiliev E., Baumgardt H., 2021, MNRAS, 505, 5978 - [26](#)

Vasiliev E., Belokurov V., Erkal D., 2021, MNRAS, 501, 2279 - [148](#), [165](#)

Vasiliev E., 2019, MNRAS, 489, 623 - [66](#)

Venn K. A., Irwin M., Shetrone M. D., Tout C. A., Hill V., Tolstoy E., 2004, AJ, 128, 1177 - [18](#), [155](#)

Vescovi D., Reifarh R., 2021, Univ, 7, 239 - [14](#)

Villalobos Á., Helmi A., 2008, MNRAS, 391, 1806 - [16](#)

Viscasillas Vázquez C., Magrini L., Casali G., Tautvaišienė G., Spina L., Van der Swaelmen M., Randich S., et al., 2022, A&A, 660, A135 - [23](#)

Vivas A. K., Zinn R., 2006, AJ, 132, 714 - [28](#), [48](#), [49](#), [94](#), [112](#)

Vivas A. K., Zinn R., Andrews P., Baily C., Baltay C., Coppi P., Ellman N., et al., 2001, ApJL, 554, L33 - [118](#)

Vivas A. K., Zinn R., Abad C., Andrews P., Baily C., Baltay C., Bongiovanni A., et al., 2004, AJ, 127, 1158 - [48](#), [95](#)

Vivas A. K., Olsen K., Blum R., Nidever D. L., Walker A. R., Martin N. F., Besla G., et al., 2016, AJ, 151, 118 - [108](#)

Vivas A. K., Saha A., Olsen K., Blum R., Olszewski E. W., Claver J., Valdes F., et al., 2017, AJ, 154, 85 - [46](#)

Vivas A. K., Alonso-García J., Mateo M., Walker A., Howard B., 2019, AJ, 157, 35 - [102](#)

Vivas A. K., Martínez-Vázquez C. E., Walker A. R., Belokurov V., Li T. S., Erkal D., 2022, ApJ, 926, 78 - [156](#)

Vivas A. K., Zinn R., Gallart C., 2005, AJ, 129, 189 - [48](#)

von Hippel T., Jefferys W. H., Scott J., Stein N., Winget D. E., De Gennaro S., Dam A., et al., 2006, ApJ, 645, 1436 - [25](#), [54](#), [78](#)

von Weizsäcker C. F., 1951, ApJ, 114, 165 - [8](#)

Vrard M., Mosser B., Samadi R., 2016, A&A, 588, A87 - [23](#)

Walker A. R., 1985a, MNRAS, 213, 889 - [180](#)

Walker A. R., 1985b, MNRAS, 214, 45 - [69](#), [180](#)

Walker A. R., 1987, MNRAS, 229, 31 - [180](#)

Wallerstein, G., Gomez, T., & Huang, W. 2012, Ap&SS, 341, 89 - [122](#), [131](#), [132](#), [134](#)

Wallerstein G., 1962, ApJS, 6, 407 - [13](#)

Wanajo S., 2013, ApJL, 770, L22 - [14](#)

Wang S., Chen X., de Grijs R., Deng L., 2018, ApJ, 852, 78 - [69](#)

Wang W., Han J., Cautun M., Li Z., Ishigaki M. N., 2020, SCPMA, 63, 109801 - [174](#)

Ward J. L., Kruijssen J. M. D., Rix H.-W., 2020, MNRAS, 495, 663 - [91](#)

Watkins L. L., Evans N. W., Belokurov V., Smith M. C., Hewett P. C., Bramich D. M., Gilmore G. F., et al., 2009, MNRAS, 398, 1757 - [17](#), [48](#), [112](#), [116](#), [117](#)

Watkins L. L., Evans N. W., An J. H., 2010, MNRAS, 406, 264 - [174](#)

Watson D., Hansen C. J., Selsing J., Koch A., Malesani D. B., Andersen A. C., Fynbo J. P. U., et al., 2019, Natur, 574, 497 - [14](#)

Watson C. L., Henden A. A., Price A., 2006, SASS, 25, 47 - [69](#)

Watson C., Henden A. A., Price A., 2014, yCat, B/vsx - [69](#), [83](#)

Webb J. J., Carlberg R. G., 2021, MNRAS, 502, 4547 - 26

Webbink R. F., 1985, IAUS, 113, 541 - 26

Weidner C., Kroupa P., 2006, MNRAS, 365, 1333 - 85

Weiland J. L., Arendt R. G., Berriman G. B., Dwek E., Freudenreich H. T., Hauser M. G., Kelsall T., et al., 1994, ApJL, 425, L81 - 3

Werner K., Drake J. J., 2005, A&A, 434, 707 - 12

Wesselink A. J., 1946, BAN, 10, 91 - 42

Wetterer, C. J., & McGraw, J. T. 1996, AJ, 112, 1046 - 49, 94

White S. D. M., Frenk C. S., 1991, ApJ, 379, 52 - 2

White S. D. M., Rees M. J., 1978, MNRAS, 183, 341 - 19

Whiting A. B., Hau G. K. T., Irwin M., 2002, ApJS, 141, 123 - 157

Widmark A., Malhan K., de Salas P. F., Sivertsson S., 2020, MNRAS, 496, 3112 - 30

Wiescher M., Käppeler F., Langanke K., 2012, ARA&A, 50, 165 - 11

Willman B., Blanton M. R., West A. A., Dalcanton J. J., Hogg D. W., Schneider D. P., Wherry N., et al., 2005a, AJ, 129, 2692 - 21, 27

Willman B., Dalcanton J. J., Martinez-Delgado D., West A. A., Blanton M. R., Hogg D. W., Barentine J. C., et al., 2005b, ApJL, 626, L85 - 21, 27

Wolf C., Onken C. A., Luvaul L. C., Schmidt B. P., Bessell M. S., Chang S.-W., Da Costa G. S., et al., 2018, PASA, 35, e010 - 99

Wollenberg K. M. J., Glover S. C. O., Clark P. C., Klessen R. S., 2020, MNRAS, 494, 1871 - 10

Wright N. J., Jeffries R. D., Jackson R. J., Bayo A., Bonito R., Damiani F., Kalari V., et al., 2019, MNRAS, 486, 2477 - 23

Xue X.-X., Ma Z., Rix H.-W., Morrison H. L., Harding P., Beers T. C., Ivans I. I., et al., 2014, ApJ, 784, 170 - 94

Xue X.-X., Rix H.-W., Ma Z., Morrison H., Bovy J., Sesar B., Janesh W., 2015, ApJ, 809, 144 - 17, 116

Yang, Y., Zhao, J.-K., Xue, X.-X., Ye, X.-H., Zhao, G., 2022, arXiv, arXiv:2208.05176 - 30

Yeh F. C., Carraro G., Montalto M., Seleznev A. F., 2019, AJ, 157, 115 - 24

Yen S. X., Reffert S., Schilbach E., Röser S., Kharchenko N. V., Piskunov A. E., 2018, A&A, 615, A12 - 25, 54, 78

Yen S. X.-T., 2019, "Peering into the milky way disk: Gaia's perspective of our galaxy's open clusters", Doctoral thesis, Univ. Heidelberg. 79

Yilmaz F., 1966, ZA, 64, 54 - 180

Yong D., Norris J. E., Bessell M. S., Christlieb N., Asplund M., Beers T. C., Barklem P. S., et al., 2013, ApJ, 762, 26 - 154

Yoon J. H., Johnston K. V., Hogg D. W., 2011, ApJ, 731, 58 - 30

York D. G., Adelman J., Anderson J. E., Anderson S. F., Annis J., Bahcall N. A., Bakken J. A., et al., 2000, AJ, 120, 1579 - 6

Youakim K., Starkenburg E., Martin N. F., Matijević G., Aguado D. S., Allende Prieto C., Arentsen A., et al., 2020, MNRAS, 492, 4986 - 16

Yu S.-Y., Xu D., Ho L. C., Wang J., Kao W.-B., 2022, A&A, 661, A98 - 3

Yuan Z., Chang J., Beers T. C., Huang Y., 2020, ApJL, 898, L37 - 162

Zaritsky D., Conroy C., Naidu R. P., Cargile P. A., Putman M., Besla G., Bonaca A., et al., 2020, ApJL, 905, L3 - 94

Zechmeister M., Kürster M., 2009, A&A, 496, 577 - 35, 99

Zhevakin S. A., 1963, ARA&A, 1, 367 - 32

Zinn R., West M. J., 1984, ApJS, 55, 45 - [157](#)

Zinn R., Horowitz B., Vivas A. K., Baltay C., Ellman N., Hadjiyska E., Rabinowitz D., et al., 2014, ApJ, 781, 22 - [48](#), [95](#), [105](#), [116](#), [117](#)

Zinnecker H., Piskunov A. E., Kharchenko N. V., Röser S., Schilbach E., Scholz R.-D., 2009, IAUS, 254, 221 - [85](#)

Zinn, R. 1993, The Globular Cluster-Galaxy Connection, ASP Conference Series, Vol 48, 38 - [112](#)

Zoccali M., Hill V., Lecureur A., Barbuy B., Renzini A., Minniti D., Gómez A., et al., 2008, A&A, 486, 177 - [3](#)

Zolotov A., Willman B., Brooks A. M., Governato F., Brook C. B., Hogg D. W., Quinn T., et al., 2009, ApJ, 702, 1058 - [112](#)

Zorec J., Royer F., 2012, A&A, 537, A120 - [212](#)

Zucker, D. B., Belokurov, V., Evans, N. W., et al. 2006, ApJ, 643, L103 - [27](#)

Zucker S., 2016, MNRAS, 457, L118 - [35](#)

Acknowledgements

It is hard for me to assimilate that this journey, that started who knows when, is coming to an end. Pursuing my PhD in Heidelberg is a privilege that my younger self had never (really) thought about, and will become for sure a truly memorable episode of my life. There are many people that have backed me up over the course of these four somewhat hectic years, and without whom concluding this would have never been possible.

Primero, y por sobre todo, quisiera agradecer a mi familia, y en especial **a mi mamá, al Seba, y al Benja**. Gracias por estar conmigo en las buenas y en todas las malas, y por ser mi cable a tierra en todo momento. Ustedes son en el fondo la mayor razón por la cual decidí seguir este loco camino, y las palabras no alcanzan para expresar cuánto les agradezco por su apoyo incondicional (en cada etapa de mi vida). And of course I would like to thank you, **Nina**, for your constant love and support. You have been a pillar of my life and I thank you so much for that. Thanks for being an awesome partner, for believing in me, for being so understanding, for being there to listen, for dealing with me even though I'm a constant mess, and for walking this path with me from start to finish. I love you.

I would like to express my gratitude to my supervisor Eva Grebel. **Eva**, thanks for giving me the opportunity to become part of the Galaxy Evolution group at the Astronomisches Rechen-Institut (ARI), and for making it possible for me to join the Hector Fellow Academy. I am grateful for your mentoring, your valuable advice on scientific and career development matters, for your availability for improvised meetings at random times, and for giving me the freedom to follow my own research path. Oh, and I profoundly apologize for not dedicating an entire chapter of this thesis to black holes. Next time.

I am truly grateful to those who, in spite of not being my direct supervisors, put so much time and effort into guiding me both personally and professionally. **Camilla**, I deeply appreciate your role as an advisor throughout these years. Thanks for always being so friendly and kind, and for genuinely caring about me and my projects. Thanks teaching me so much, and of course, thanks for proofreading a substantial part of this thesis. Without your seemingly infinite patience and support I would have never finished this work. **Bertrand**, I would like to thank you for our many long conversations and for working with me. I am thankful for your honest advice, critical opinions, and for every time you offered your help to me. I want to also thank you for giving me confidence about my research and what I might be capable of doing. **Ricardo**, I really appreciate that we have kept in touch, and I hope that we continue to do so in the future. I will always be grateful for every time you were there for me, being open and willing to give me advice on life- and work-related matters, despite the distance. Also, thank you so much for encouraging me to follow this path. I would also like

to acknowledge all the teachers and professors that, over the course of my studies, inspired me in one way or another to choose a scientific career.

I further would like to thank **Joachim Wambsganz**, and **Luca Amendola** for being willing to take part of my examination committee. Special thanks to **Sabine Reffert** for not only being part of the examination committee, but also for agreeing to referee this dissertation (and sorry if I made it too long!).

Tambien quisiera agradecer a mis amigos en Chile por mantenerse presentes y dispuestos a ayudar durante estos cuatro años pese a la distancia. Quiero agradecer en especial a: **Cris Siegel, Nacho, Tata, Chino, Evelyn, Nicolásandoval, y Franco**.

A warm thank you goes out to the Cosmic Cells: **Maui, Volker, Thomas, and Marc**. Guys, thanks a lot for making my stay in Heidelberg a truly enjoyable experience. Thanks for fueling my mind with energy, creativity, and inspiration, and for every restless noise music-making session. Thanks for the passion, for showing me a path to follow, and for making me a member of your family. I would also like to thank the members of the Heidelberg Lions hobby team. Thanks for being so welcoming and for becoming an always needed escape from the routine.

I would like to extend my gratitude to the members of the ARI Galaxy Evolution group and to other students from the International Max Planck Research School in Heidelberg (IMPRS-HD) whose warmth and positive attitude made every interaction we had enjoyable. In particular, thanks to **Ismael Pessa, Paz Bluhm, Samantha Brown, Hitesh Lala, Andreas Koch-Hansen, Anna Pasquali, and Dongwook Lim**. Special thanks to my office mates, for helping me survive the PhD through random conversations, a very much needed regular dose of common sense, and for the overall great times we spent together. **Zdenek** and **Michael**, thanks for being so friendly and for sharing your knowledge, codes, and plotting advice with me. And for all the weird jokes. **Bahar**, thanks for tolerating and reinforcing my frequent frustrations and complains. **Fabian**, thanks for your constant willingness to help, in particular with the abstract of this thesis.

I feel fortunate to have been part of the International Max Planck Research School in Heidelberg (IMPRS-HD). I sincerely thank **Christian Fendt** and **Huong Witte-Nguy** for being the heart and soul of this institution. You have been responsible for making the doctoral studies of so many generations an incredible experience. Also thanks to the ARI's administrative staff who were always kind and friendly with me, and helped me go through so many bureaucrazy processes: **Frau Mayer, Frau Ballmann, Frau Buchhaupt, and Frau Pisch-Papendick**.

Last but not least, I would like to acknowledge the Hector Fellow Academy for the financial support of my studies, for giving me the chance of networking with other PhD students and developing useful skills for my career, and for allowing me to learn about the really exciting science that is being developed within the academy.

Declaration of Originality

Declaration of Originality

I hereby declare that this thesis is my own work and that I have used no other than the stated sources and aids.

Declaration

Ich versichere, dass ich diese Arbeit selbstständig verfasst habe und keine anderen als die angegebenen Quellen und Hilfsmittel benutzt habe.

Heidelberg, der 22. August 2022

Gustavo Enrique Medina Toledo

